



HAL
open science

Modelling the impact of fuel in aeronautical gas turbines

Jonathan Wirtz

► **To cite this version:**

Jonathan Wirtz. Modelling the impact of fuel in aeronautical gas turbines. Electric power. Institut National Polytechnique de Toulouse - INPT, 2022. English. NNT : 2022INPT0112 . tel-04248655

HAL Id: tel-04248655

<https://theses.hal.science/tel-04248655v1>

Submitted on 18 Oct 2023

HAL is a multi-disciplinary open access archive for the deposit and dissemination of scientific research documents, whether they are published or not. The documents may come from teaching and research institutions in France or abroad, or from public or private research centers.

L'archive ouverte pluridisciplinaire **HAL**, est destinée au dépôt et à la diffusion de documents scientifiques de niveau recherche, publiés ou non, émanant des établissements d'enseignement et de recherche français ou étrangers, des laboratoires publics ou privés.



Université
de Toulouse

THÈSE

En vue de l'obtention du

DOCTORAT DE L'UNIVERSITÉ DE TOULOUSE

Délivré par :

Institut National Polytechnique de Toulouse (Toulouse INP)

Discipline ou spécialité :

Energétique et Transferts

Présentée et soutenue par :

M. JONATHAN WIRTZ

le lundi 26 septembre 2022

Titre :

Modelling the impact of fuel in aeronautical gas turbines

Ecole doctorale :

Mécanique, Energétique, Génie civil, Procédés (MEGeP)

Unité de recherche :

Centre Européen de Recherche et Formation Avancées en Calcul Scientifique (CERFACS)

Directeur(s) de Thèse :

MME BÉNÉDICTE CUENOT

MME ELEONORE RIBER

Rapporteurs :

M. AYMERIC VIE, CENTRALESUPELEC GIF SUR YVETTE

Membre(s) du jury :

M. DIRK ROEKAERTS, UNIVERSITE DE DELFT, Président

M. ANTONIO ANDREINI, UNIVERSITA DEGLI STUDI DI FIRENZE, Membre

M. AXEL VINCENT-RANDONNIER, ONERA, Membre

M. GORKA EXILARD, GROUPE SAFRAN, Invité(e)

MME BÉNÉDICTE CUENOT, CERFACS, Membre

M. NEDUNCHEZHIAN SWAMINATHAN, UNIVERSITE DE CAMBRIDGE, Membre

M. PATRICK LECLERCQ, UNIVERSITAT STUTTGART, Invité(e)

Keywords : LES, ARC, multi-component, flame structure, two-phase flow

Abstract — The rise of climatic hazards, due to the human contribution, has led some governments and industries of the aeronautical sector to think about solutions to reduce combustion emissions. To create a less environmentally demanding aviation, electrical storage does not fill the power criteria and other promising fuels such as hydrogen require a change of the whole plane engine. Another short-run solution is the use of drop-in alternative fuel, which, despite some drawbacks, would reduce the emissions of the sector in the nearer future. The European H2020-JETSCREEN project, that funded this PhD, falls within this context. Indeed, the development of Large-Eddy Simulations (LES) and Analytically Reduced Chemistries (ARC) coupled with the rise of computer resources has enabled precise kinetics to be used in turbulent combustion chambers. The main topic of this PhD is the development of a methodology to analyse a stabilised turbulent two-phase flow flame with complex chemistry and heat losses for three multi-component fuels : one conventional and two alternative fuels. Before the computation, questions on the chemistry and the evaporation properties of the fuels remain. At first, ARC were developed and validated against the detailed mechanism, testifying the capability of the kinetic reduction code ARCANE to retrieve the chemical fuel sensitivities. Fuels were then analysed on every canonical case concluding that the fuel composition had an influence on the global combustion but little on the pollutants. Furthermore, the simulation of 1D ARC premixed flame explained why such complex kinetics need very few points in the flame front in order to give accurate results and underlined the prominent role of the flame foot and especially the fuel consumption that is monitoring the flame convergence. Second, evaporation properties comparisons led to results close to the experimental work of the DLR and retrieving the two-phase fuel sensitivities. Based on those results, a two-phase premixed flame was computed and the flame characteristic variables were found to depend on the degree of pre-evaporation. Furthermore, the spray counter-flow diffusion flame structure was investigated. The polydisperse two-phase flow initiating a change of the flame regime explained the exotic structure observed. Once those canonical analyses studied, the real combustion chamber simulation was tackled. Differences in terms of averaged solutions have then been drawn, showing the capability of the LES code, AVBP, to globally reproduce the experimental behaviour of those fuels whether for the dynamic quantities, the thermal fields or the two-phase flow properties. The comparison between a simple and a complex surrogate for Jet-A1 resulted in a similar stabilisation point, but a different flame structure, assessing the capability of the Takeno sensor to visualise the right flame regime. A Lean Blow-Out(LBO) methodology was suggested on the simple chemistry, starting by the evaluation of the characteristic timescales, key quantities for the transient flame evolution and followed by the right variable choice for the LBO detection. The LBO was detected slightly below the experimental value, following a flame stabilisation by hot gases process. Finally, the flame structure was compared for the three fuels and depicted differences in terms of flame structure mainly due to the evaporation properties that are impacting the thermal field and the local flame regime.

Mots clefs : LES, ARC, multi-composant, structure de flamme, écoulement diphasique

Résumé — L'augmentation des catastrophes climatiques, causée par l'activité humaine, a conduit certains acteurs du secteur aéronautique à réfléchir à des solutions pour réduire les émissions liées à la combustion et créer une aviation moins consommatrice. Cependant, le stockage sous forme de batterie ne remplit pas le critère de puissance et d'autres carburants prometteurs comme l'hydrogène nécessitent de modifier le moteur de l'avion de manière conséquente. Une solution à court terme est l'utilisation de carburants alternatifs qui sont directement utilisables et, qui, malgré certains inconvénients, réduiraient les émissions du secteur dans un futur proche. Le projet européen H2020 - JETSCREEN, qui a financé cette thèse, s'inscrit dans ce contexte. En effet, le développement des Simulations aux Grandes Echelles (SGE) et des Chimies Analytiquement Réduites (ARC) couplés à l'augmentation des ressources informatiques a permis à de la cinétique précise d'être appliquée à la combustion turbulente dans les foyers aéronautiques. Le principal sujet de cette thèse est le développement d'une méthodologie pour analyser une flamme diphasique turbulente avec des pertes thermiques et de la chimie complexe pour trois carburants multi-composants : un conventionnel et deux alternatifs. Avant de calculer ces flammes, des questions restent en suspens sur les propriétés chimiques et d'évaporation de ces carburants. Premièrement, les ARC ont été développés et comparés à des mécanismes détaillés, validant la capacité du code de réduction cinétique ARCANE à retrouver les sensibilités chimiques des carburants. Les carburants ont ensuite été analysés sur des cas canoniques concluant que la composition des carburants a une influence sur la combustion globale mais peu sur les polluants. De plus, la simulation de flammes 1D prémélangées ARC a expliqué pourquoi des cinétiques si complexes ont besoin de très peu de points dans le front de flamme pour donner des résultats précis et a mis en évidence le rôle prépondérant du pied de flamme et en particulier de la consommation du carburant qui pilote la convergence de la flamme. Deuxièmement, la comparaison des propriétés d'évaporation a conduit à des résultats proches du travail expérimental du DLR et retrouve la sensibilité des carburants au diphasique. En se basant sur ces résultats, le calcul de flammes prémélangées diphasiques a montré que les variables caractéristiques de la flamme sont dépendantes du degré d'évaporation préférentiel. De plus, la structure d'une flamme diphasique de diffusion à contre-courant a montré que l'écoulement diphasique polydisperse initie un changement de régime de flamme ce qui explique la structure exotique observée. Une fois ces deux analyses réalisées, la chambre de combustion réelle a pu être simulée. Les différences en terme de solutions moyennées ont été établies, montrant la bonne capacité du code SGE AVBP à reproduire le comportement expérimental de ces carburants pour les quantités dynamiques, les champs thermiques et les propriétés diphasiques. La comparaison entre un substitut simple et complexe pour le kérosène a conduit à un point de stabilisation similaire, mais une structure de flamme différente, montrant la capacité du senseur Takeno à visualiser globalement le bon régime de flamme. Une méthodologie pour la détection de l'extinction en limite pauvre a été suggérée sur la chimie simple, d'abord en évaluant le temps caractéristique de la chambre, quantité clé pour l'évolution de la flamme transitoire puis en choisissant les variables permettant la détection de l'extinction. L'extinction a été détectée un peu au-dessous de la valeur expérimentale, en stabilisant des flammes par un allumage de gaz chauds. Finalement, la structure de flamme a été comparée pour les trois carburants et a montré que les différences observées sont principalement dues aux propriétés d'évaporation qui impactent directement le champ thermique et le régime de flamme.

Acknowledgments

En premier lieu, je tiens à remercier les rapporteurs de ce manuscrit, Aymeric Vié et Dirk Roekaerts, pour l'avoir lu et évalué mon travail avec beaucoup d'attention. Je remercie également Nedunchezian Swaminathan, Axel Vincent-Randonnier et Antonio Andreini d'avoir évalué ce travail et contribué à l'améliorer ainsi que Gorka Exilard et Patrick Le Clercq pour leurs remarques instructives.

Je voudrais ensuite remercier Bénédicte Cuenot et Eleonore Riber. Merci pour votre encadrement qui m'a permis de progresser et de consolider mes différents raisonnements, tout en restant dans la bonne humeur !

Merci à l'équipe administration du CERFACS : Marie, Chantal, Brigitte, Nathalie, Michèle, d'avoir été très réactive à la moindre demande et qui nous permet de nous concentrer plus pleinement sur nos travaux de recherche et d'organiser les événements comme les formations plus sereinement. De même, je remercie l'équipe CSG : Isabelle, Gérard, Fabrice, Fred entre autres. De l'aide sur la compilation de Cantera à la gestion de la sécurité des macs en passant par l'installation de la salle de soutenance, cet accompagnement est précieux et fortement apprécié. Merci également aux séniors CERFACS avec qui j'ai eu l'occasion de travailler pour leur disponibilité et leur passion pour notre domaine d'étude.

Une thèse n'aboutirait pas sans les discussions échangées entre collègues, postdoctorants, doctorants ou stagiaires, qui nous permettent d'une part de progresser de l'expérience d'autrui et d'autre part de relâcher la pression lorsque cela est nécessaire. Il y a les anciens qui m'ont mis le pied à l'étrier quand je suis arrivé (Lucien, Felix, Simon, Bastien, Quentin (le 1er) et beaucoup d'autres) avec une mention toute particulière pour mon cobureau, Quentin (le 2e), qui m'a rapidement inculqué les arcanes d'ARCANE. Aux doctorants de ma génération, merci Antoine, Thomas (x3, il y en a trop), Etienne, Nicolas, Anthony, Victor, Théo, et j'en oublie très certainement, d'avoir échangé et apporté votre pierre à cet édifice. Et aux doctorants actuels et stagiaires avec qui j'ai pu échanger et à qui je souhaite la réussite.

N'oublions pas les loisirs, essentiels à l'écriture de ce manuscrit : je remercie l'équipe de volley-ball de Météo-France les Rastapem puis les Bubamines de m'avoir accueilli pour jouer un volley bienveillant, mais qui n'en reste pas moins compétitif ! Merci à Clovis et Alyssa pour les soirées passées à débattre de sujet divers et variés, mais qui nous ont tous fait évoluer.

Enfin, je remercie les amis qui ont pu faire le déplacement pour assister à la soutenance et mes amis proches qui sont loin de Toulouse, mais qui, je sais, m'ont soutenu dans cette expérience et me soutiendront encore dans le futur (aux messins, aux parisiens, aux lyonnais notamment, mais toujours messins de cœur !). Merci à ma belle-famille de m'avoir supporté pendant mes phases de travail ardues ainsi qu'à ma famille de m'avoir amené là où j'en suis actuellement. Enfin, je remercie Quentin (le 3e) de m'avoir accompagné et encouragé pendant ces années, l'avenir n'en sera que meilleur !

Contents

I	General context	1
1	Context	2
1.1	Human impact on the environment	2
1.2	Solutions for the aeronautical sector	4
1.3	Alternative drop-in fuels	6
1.4	Design of combustion chambers	9
1.5	The role of numerical simulation	11
2	Modelling of turbulent spray flames	13
2.1	Turbulent spray flames	13
2.1.1	Turbulent spray	14
2.1.2	Turbulent combustion	15
2.1.3	Spray laminar combustion	15
2.1.4	Spray turbulent combustion	18
2.2	Use of alternative fuels	18
2.2.1	Alternative fuels in combustors: state-of-the-art	20
2.2.2	Modelling alternative fuels	22
2.3	Prediction of the Lean Blow-Out: state-of-the-art	23
2.3.1	Semi-empirical methods	23
2.3.2	Numerical models	25
2.3.3	Hybrid models	26
2.4	Organisation of the manuscript	26
II	Fundamental equations for the resolution of two-phase turbulent reactive flows	28
3	Reactive flows and combustion canonical cases	29
3.1	Definitions	30
3.1.1	The combustion reaction	30
3.1.2	Chemical kinetics	31
3.2	3D reactive flow modelling	35
3.2.1	Compressible multi-species flow equations	35
3.2.2	Transport and thermodynamic properties	37
3.2.3	The AVBP code	39
3.3	Combustion canonical cases	41
3.3.1	Final state: Equilibrium	41
3.3.2	0D unsteady cases: Reactors	43
3.3.3	1D steady cases: Flames	44

4	Analysis and reduction of chemical schemes	53
4.1	From fuel definition to the reduced mechanism	53
4.1.1	Detailed mechanisms	54
4.1.2	Surrogate fuel model	55
4.1.3	Reduction methods	57
4.2	ARCANE	59
4.2.1	Reduction methods	59
4.2.2	Reduction loop	62
4.2.3	Implementation of ARC schemes in CFD codes	64
4.3	Methods for chemistry analysis	65
4.3.1	Quantitative and qualitative analyses	65
4.3.2	Spatial and time scales	68
5	Liquid phase modeling for reactive flows	70
5.1	Euler-Lagrange formulation and modelling	71
5.1.1	Spherical droplet model	72
5.1.2	Liquid injection	79
5.1.3	Spray-wall interactions	83
5.1.4	Combustion variables in spray flames	86
5.2	Two-phase combustion regimes	87
5.2.1	Group number	87
5.2.2	Single droplet burning: the MustARD model	89
6	Modelling turbulence in reactive flows	93
6.1	Turbulence	93
6.2	LES concept and equations	95
6.3	Combustion/turbulence interaction	97
6.3.1	Turbulent flame regimes	97
6.3.2	Turbulent combustion models	99
III	Chemical and two-phase canonical cases	104
7	Analysis of gaseous chemical processes	105
7.1	Reduced chemical scheme for multi-component surrogates	106
7.1.1	Blend composition	106
7.1.2	Mechanism reduction	108
7.2	ARC validation and discussion	110
7.2.1	Net heat of combustion	111
7.2.2	Auto-ignition delay time	115
7.2.3	Laminar flame speed accuracy	118
7.2.4	Pollutants emissions	120
7.2.5	Characteristic species chemical timescales	123
7.2.6	Conclusion	124
7.3	Spatial discretisation for complex kinetics	126
7.3.1	Impact of the discretisation on laminar flame speed	126
7.3.2	Effect of the mesh discretisation on the flame structure	130
7.3.3	Conclusion	137

8	Analysis of laminar spray flames	138
8.1	Evaporation properties of the surrogates	138
8.1.1	Two-phase flow properties	139
8.1.2	Evaporation properties	140
8.2	Multi-component spray flame structure	142
8.2.1	Setup for a 1D spray flame	142
8.2.2	Flame dynamics	144
8.2.3	Influence of the liquid phase on pollutants prediction	148
8.2.4	Conclusion	150
8.3	Spray counterflow diffusion flame	150
8.3.1	Presentation of the configuration and numerical set-up	151
8.3.2	Polydisperse spray flame	154
8.3.3	Flame structural analysis	155
8.3.4	Single droplet modelling	165
8.3.5	Conclusion	167
IV	Alternative fuels combustion in a turbulent combustor	169
9	Simulation of LBO in a swirl spray burner	170
9.1	From the geometry to the reactive flow numerical setup	171
9.1.1	Presentation of the burner and experimental data	171
9.1.2	Set-up and cold flow	174
9.1.3	Reactive two-phase flow	177
9.2	Stable spray flame: impact of the chemical modelling for a standard fuel	182
9.2.1	Fuel properties	182
9.2.2	Results: mean solution	185
9.2.3	Flame structure analysis	194
9.2.4	Flame structure: effect of the fuel model	199
9.2.5	Conclusion	202
9.3	Lean Blow-Out calculations	204
9.3.1	Timescales and methodology	204
9.3.2	Towards LBO	207
9.3.3	LBO detection	214
9.3.4	Discussion	216
9.3.5	Conclusions	218
10	Effect of fuel on flame structure	219
10.1	Time-averaged spray flames	219
10.1.1	Two-phase flow fields	220
10.1.2	Adiabatic temperature equilibrium	221
10.1.3	Reacting fields	222
10.2	Spray flame structures	225
10.2.1	Fuel evaporation	225
10.2.2	Combustion regime	229
10.2.3	Towards optimised SAF	234
10.3	Conclusion	237

11 Conclusion and perspectives	238
11.1 Conclusion	238
11.2 Perspectives	239

Nomenclature

Roman Symbols

$[S_i]$	Concentration of species i	mol/m^3
\mathcal{A}	Wall area	m^2
ξ	progress variable toward equilibrium	—
A	Troe function constant	—
a	Strain-rate	s^{-1}
A_j	Pre-exponential factor of reaction R_j	$mol^{(1-order^j)} / m^{3(1-order^j)} / s$
a_i	NASA coefficient	—
$a_{k,i}$	Number of atom k in species i	—
b_j	Temperature exponent of reaction R_j	—
B_M	Spalding mass number	—
B_T	Spalding thermal number	—
C_A	Consumption coefficient associated to species A	—
C_D	Drag coefficient	—
C_p	Heat coefficient	$J/kg/K$
$C_{p,k}$	Heat coefficient of species k	$J/kg/K$
$C_{v,trans}, C_{v,rot}, C_{v,vib}$	Trans, rot and vib motion of a given species	—
d	Partial derivative	—
d_f	Droplet flame diameter	m
d_p	Particle diameter	m
d_{ab}	Characteristics diameters of a droplet	m
d_{ext}	Extinction diameter	m
D_{th}	Thermal diffusion coefficient	m^2/s
Da	Damkhöler number	—

Da^{fl}	Flow Damkhöler number	—
Da_e	Evaporation Damkholer	—
E	Efficiency factor	—
E	Energy	J
E_a	Activation energy of a global reaction	J/mol
$E_{a,j}$	Activation energy of reaction R_j	J/mol
F	Gilbert function	—
F	Thickening factor	—
F_k	Species k in the fuel	—
f_w	Wall function for reactor	—
F_Δ	Filter kernel	—
$F_{p,i}$	Dynamic force associated to the particle	N
$f_{trans}, f_{rot}, f_{vib}$	Trans, rot and vib motion of a given species	$W/m/K$
G	Gibbs energy	J
$G_{annamalai}$	Group number according to Annamalai et al.	—
G_{candel}	Group number according to Candel et al.	—
G_{chiu}	Group number according to Chiu et al.	—
h	Film thickness	m
H/C	Hydrogen to Carbon ratio	—
h_i	Specific enthalpy of species S_i	J/kg
$h_{f,k}$	Specific formation enthalpy of species k	J/kg
HRR	Heat Release Rate	$J/m^3/s$
J_{ii}	Diagonal term of the Jacobian matrix associated to the chemical system	s^{-1}
$J_{k,i}$	Species diffusion flux	$kg/m^2/s$
k_B	Boltzmann constant	J/K
K_e	Equilibrium constant	—
k_j	Rate coefficient of reaction R_j	$mol^{(1-order^j)}/m^{3(1-order^j)}/s$
Ka	Karlovitz number	—
l_T	Integral length scale	m

L_v	Latent heat	J/kg
Le_i	Species i Lewis number	—
LHV	Lower Heating Value	J/kg
m	Mass	kg
m_{jk}	Reduced mass of species S_j and S_k	—
N	Number of droplet	—
n	Molar quantity	mol
N_c	Number of points in the flame front	—
N_i	Mole number of species i	—
n_k	Atom number of type k	—
N_s	Species number	—
Nu	Nusselt number	—
P	Pressure	Pa
P_A	Production coefficient associated to species A	—
P_r	Reduced pressure	—
P_{th}	Thermal power	W
Pr	Prandtl number	—
Q	PDF of volume fraction	—
q_i	Heat flux	$J/m^2/s$
Q_{loss}	Energy loss	W/m^2
R	Perfect gas constant	$J/mol/K$
R	Reactions	—
r	Modified perfect gas constant	$m^2/s^2/K$
r	Radial coordinate	m
R_a	Wall roughness	m
R_j	Reaction j	—
r_{AB}	DRG coefficient between a species A and a species B	—
R_{wall}	Wall resistance	$m^2.K/W$
Re	Reynolds number	—

Re_p	Particle Reynolds number	—
S	Entropy	J/K
S	Inter-droplet distance	m
S	Two-phase flow source term	$(\text{kg or m/s or J})/m^3/s$
S_i	Species i	—
s_L	Laminar flame speed	m/s
S_w	Swirl number	—
s_X	Molar stoichiometric ratio	—
s_Y	Mass stoichiometric ratio	—
s_k	Specific entropy of species k	$J/kg/K$
$s_{L,j}$	Part of the reaction rate contributing to the laminar flame speed	m/s
$S_{P,i}$	Sensitivity coefficient of species i	—
$s_{Y,k}$	Mass stoichiometric ratio linked to species k	—
Sc_k	Schmidt number of species k	—
Sh	Modified Sherwood number	—
Sh^0	Sherwood number	—
St	Stokes number	—
T	Takeno index	—
T	Temperature	K
t	time	s
$T^{\dot{\omega}_F}$	Takeno index conditioned by the fuel source term	—
T^{HRR}	Takeno index conditioned by HRR	—
T_1	Troe function constant	—
T_2	Troe function constant	—
T_3	Troe function constant	—
T_{pyro}	Takeno index including pyrolysis products	—
U	Internal energy	J
u_i	Speed associated to i direction	m/s
u_{bulk}	Bulk velocity	m/s

$u_{p,i}$	Velocity associated to the particle	m/s
V	Volume	m^3
V_i^c	Correction velocity	m/s
$V_{k,i}$	Hirschfelder and Curtiss approximation of the diffusion velocity	m/s
W	Molar mass	kg/mol
We	Weber number	—
X	Contraction factor for FIM-UR	—
X	Molar fraction	—
x	Number of carbon atom	—
x_i	Space direction	m
y	Number of hydrogen atom	—
Y_k	Mass fraction of species S_k	—
$Y_{F_k}^{fuel}$	Mass fraction of species F_k compared to mass fraction of fuel F	—
z	Mixture fraction	—
z_{Bilger}	Bilger mixture fraction	—
Ze	Zeldovich number	—

Greek Symbols

α_l	Liquid volume loading	—
α_l	Volume liquid loading	—
β_{Ch}	Charlette model constant	—
χ	Scalar dissipation rate	s^{-1}
Δh_j^{mol}	Molar enthalpy of reaction R_j	J/mol
Δx	Spatial discretisation	m
Δ	Difference	—
Δ	Filter length	m
δ^ω	Forward and backward reaction rate thicknesses	m
δ^{HRR}	Heat Release Rate thickness	m
δ_l^b	Blint thickness	m
δ_l^{th}	Thermal thickness	m

Δ_r	Change for a reaction	—
δ_r	Reaction thickness	m
$\delta_{i,j}$	Kronecker symbol	—
$\dot{\omega}_j$	Mass species source term	$kg/m^3/s$
$\dot{\omega}_j^{mol}$	Molar species source term	$mol/m^3/s$
ϵ	Relative error	—
ϵ_i	Collision efficiency	—
ϵ_i	Fraction of species i in the vapour of a multi-component droplet	—
η_K	Kolmogorov length scale	m
η_{comb}	Combustion efficiency	—
Γ	Gamma function	—
λ	Heat conduction coefficient	$W/m/K$
λ_k	Heat conductivity of species k	$W/m/K$
μ	Dynamic viscosity	$Pa.s$
μ_k	Viscosity of species k	$Pa.s$
ν	Kinematic viscosity	m^2/s
ν	Stoichiometric coefficient	—
ω	Molar reaction rate	$mol/m^3/s$
$\Omega^{1,1}, \Omega^{2,2}$	Collision integrals for modes (1,1) and (2,2)	—
ϕ	Equivalence ratio	—
ϕ	Fluxes to conductive fluxes	J/kg
ϕ_k^{eff}	Effective equivalence ratio	—
ϕ_g	Global equivalence ratio	—
ϕ_{loc}	Local equivalence ratio	—
Ψ	Vaporisation number	—
Ψ_n	First-order interpolation function	—
ρ	Density	kg/m^3
σ_{jk}	Collision cross section of species S_j and S_k	—
τ_i	Characteristic lifetime of species i	s

τ_p	Characteristic particle time	<i>s</i>
$\tau_{chamber}$	Characteristic chamber timescale	<i>s</i>
τ_{ev}	Evaporation timescale	<i>s</i>
τ_{fg}	Film gas shear stress	N/m^2
τ_{flow}	Flow timescale	<i>s</i>
$\tau_{i,j}$	Viscous stress tensor	N/m^2
θ_S	Half-angle of the spray	$^\circ$
Ξ	Efficiency function	—

Other symbols

—	Mean
\longleftrightarrow	Equilibrium
\longrightarrow	Forward reaction
\sim	Time-fluctuating variable

Superscripts

'	Relative to the reactants of the reaction
"	Relative to the products of the reaction
*	Quantities divided by their maximum absolute values.
<i>mol</i>	Molar quantity
<i>multi</i>	Associated to multi-component fuels
<i>order_i</i>	Order for species <i>i</i>

Subscripts

1	State before the flame front
2	State after the flame front
2	State before the combustion chamber
3	State after the combustion chamber
∞	Associated to the gaseous field far away from the droplet
ζ	Associated to the droplet surface
<i>atm</i>	Atmospheric
<i>backward</i>	Backward

<i>C</i>	Of carbon atom
<i>cc</i>	On the saturation curve
<i>cond</i>	Associated to conductive fluxes
<i>creation</i>	Associated to the creation of a given species
<i>destruction</i>	Associated to the destruction of a given species
<i>E</i>	Related to the energy equation
<i>eq</i>	At equilibrium
<i>ev</i>	Associated to evaporation fluxes
<i>F</i>	Of fuel
<i>fg</i>	Relative to the interface film/gas
<i>forward</i>	Forward
<i>H</i>	Of hydrogen atom
<i>HP</i>	High Pressure
<i>i</i>	index for species i
<i>imp</i>	Relative to the droplet impact
<i>in</i>	Entering the domain
<i>j</i>	Index for reaction j
<i>k</i>	Index for atom k
<i>loc</i>	Related to a local variable
<i>LP</i>	Low Pressure
<i>mass</i>	Related to the mass equation
<i>mom</i>	Related to the momentum equation
<i>net</i>	Net
<i>O</i>	Of oxygen atom
<i>O_x</i>	Of oxidiser
<i>out</i>	Going out of the domain
<i>p</i>	Quantity associated to a particle
<i>st</i>	At stoichiometric
<i>tot</i>	Relative to the total, i.e liquid and gaseous, contributions

tot total

w Occurring at the wall

T Turbulent

Acronyms / Abbreviations

HRR Heat Release Rate

LHV Lower Heating Value

NSCBC Navier-Stokes Characteristic Boundary Conditions

ARC Analytically Reduced Chemistry

ARCANE Analytical Reduction of Chemistry: Automatic, Nice and Efficient

ATJ Alcohol-To-Jet

CARS Coherent Anti-stokes Raman Spectroscopy

CERFACS Centre Européen de Recherche et de Formation Avancée en Calcul Scientifique

CFD Computational Fluid Dynamics

CH Catalytic Hydrothermolysis

CPU Central Processing Unit

CSP Computation Singular Perturbation

CSTR Plug Flow Reactor

DNS Direct Numerical Simulation

DoE Design of Experiment

DRG Direct Relation Graph

DRGEP Direct Relation Graph with Error Propagation

EBU Eddy Break-Up

EE Euler-Euler

EL Euler-Lagrange

FIM-UR Fuel Injection Method by Upstream Reconstruction

FT Fischer-Tropsch

FV Flame Volume

GCxGC GC by GC or Comprehensive Two-Dimensional Gas Chromatography

GHG Green House Gases

GWP	Global Warming Potential
HDCJ	Hydrotreated Depolymerized Cellulosic to Jet
HEFA	Hydroprocessed Ester and Fatty Acids
HFS	Hydroprocessed Fermented Sugars
ICE-PIC	Invariant Constrained Equilibrium edge Pre-Image Curve
ILDm	Intrinsic Low-Dimensional Manifolds
ISAT	In Situ Adaptative Tabulation
JETSCREEN	JET fuel SCREENing and optimisation
LBO	Lean Blow-Out
LCA	Life Cycle Assessment
LES	Large-Eddy Simulation
LFA	Laminar Flame Assumption
LHF	Locally Homogeneous Flow
LOI	Level Of Importance
LW	Lax-Wendroff
MMD	Mass Median Diameter
PDA	Phase Doppler Anemometry
PDF	Probability Density Function
PFA	Path Flux Analysis
PFR	Continuously Stirred Tank Reactor
PIV	Particle Image Velocimetry
PSR	Perfectly Stirred Reactors
QSS	Quasi-Steady State
RANS	Reynolds-Averaged Numerical Simulation
RMS	Root Mean Squared
SA	Sensitivity Analysis
SAF	Sustainable Aviation Fuels
SGS	SubGrid Scale
SIP	Synthetic IsoParaffins

SMD Sauter Mean Diameter

SPK Synthetic Paraffinic Kerosene

SSB Spray-Stabilised Burner

TKE Turbulent Kinetic Energy

TTGC Two-step Taylor Galerkin scheme

URANS Unsteady RANS

VoF Volume of Fluid

Part I

General context

Chapter 1

Context

Contents

1.1	Human impact on the environment	2
1.2	Solutions for the aeronautical sector	4
1.3	Alternative drop-in fuels	6
1.4	Design of combustion chambers	9
1.5	The role of numerical simulation	11

1.1 Human impact on the environment

Anthropogenic pollution can be defined by the environmental damage caused by any substances (natural, chemical or radioactive), wastes (household or industrial) or disturbances (noise, light, etc. . .) from the human activity. The aeronautical industry has to deal with several topics, for instance the noise caused by aeroplanes [212], the wastes generated by the material of old aircraft or the detrimental emissions generated by combustion [199].

Those emissions are the reason of the **global warming**, phenomenon active since the pre-industrial era and characterised by an increase of the temperature due to the human activity, as stated in several studies [101], [121], [277]. The temperature increase was evaluated at $1^{\circ}C$ since 1817 and tends to strengthen. This temperature rise is partly caused by fuel combustion, that is adding an anthropogenic component to the Earth thermal balance. Naturally, Earth receives heat from the sun, which is partly absorbed and heats the ground and the atmosphere and partly rejected through infra-red lights. **Greenhouse gases** that are existing in the atmosphere filter those infra-red lights and trap them so that the temperature is higher and life is enabled on Earth. The high amount of CO_2 in the atmosphere correlated with the quick temperature rise suggests that human world carbon consumption from oil slicks is increasing the concentration of those gases in the atmosphere. As a consequence, more heat is retained and the world temperature is rising. The harmfulness of those gases is measured with the **Global Warming Potential (GWP)** [119], a metric introduced to compare the ability of a greenhouse gas to trap heat with CO_2 . Generally, carbon dioxide (CO_2 , GWP=1, the reference), methane (CH_4 , GWP=25), nitrous oxide (N_2O , GWP=298) and fluorocarbons (CFC, various GWP) are considered to be the main **Green House Gases (GHGs)** [291]. Water (H_2O) has to

be taken apart, as the huge quantity already present in the atmosphere suggests that the human contribution is negligible, but answering this question remains unclear.

The main consequence of these gases soaring in the atmosphere is a global temperature rise, disturbing the ecosystems and inducing a **climate change**. This phenomenon has several aftermaths, most of them being detrimental to the human being:

- the coupling effects of **ice cap melting** and thermal expansion due to the temperature increase, especially in the poles, will induce the oceans and seas to rise to 6 to 9 meters [62] in a few decades according to the predictions. Because they are close to the sea level, several areas are threatened in the world, for instance the Netherlands, Florida or Sri Lanka. A land surface reduction will induce the movement of populations in several areas of the world, compelled to leave their countries. Moreover, the albedo will change, since the ice reflects the sunlight more than water because of its colour, leading to even hotter temperatures [264], [322].
- **Catastrophic events, such as hurricanes and storms, will be more intense and frequent** [314] in terms of rainfall and wind-speed because the sea surface temperature is rising. Bigger cataclysms on Earth surface will induce more deaths as well as shrink agricultural resources.
- As the **concentration of CO_2 is increasing in the oceans** [89], seas will become more acid, completely changing the flora and the fauna. For instance, jellyfish will be invading the seas whereas coral barriers, which hide an enormous diversity, are more prone to disappear.

To estimate the impact of the aeronautical sector on the climate change, two different quantities have to be considered. First, some **radiative forcing** is created by the aircraft, that is to say the net radiative flux generated to the Earth system, and is calculated the impact of combustion on the climate, therefore considering only the level of CO_2 , and is estimated at 1.6% of the total world emissions in 2018 [242]. Yet, the aeronautical sector also contributes with non- CO_2 effects, such as the interaction of NO_x , hot water and aerosols (sulphurs and soot particles) [168]. This second effect is measured through the **effective radiative forcing**, which is estimated at 3.5% of the total world emissions. The aeronautical sector contribution to these global emissions seems small in proportion, but it is expected to rise in the coming years. Although the Covid-19 crisis has dampened the human transportation, and consequently CO_2 emissions¹, fluxes are expected to get back to their normal level with a 2-year shift, as shown in Fig. 1.1.

Several pollutants are released when burning fuel [76], [77], [224]. **Carbon monoxide** CO and **nitrogen oxides** NO_x are intermediate products of combustion created with hot temperatures and recombination of the carbon coming from the fuel and nitrogen coming from the air. They do not burn totally, still remain at the end of combustion, and are harmful for the human beings. The interaction of SO_x and NO_x can cause acid rains, which is harmful to plants and wildlife and modifies the pH of soils. Photochemical smog is generated by the radiation of NO_x as well as CO interacting with ozone, leading to respiratory diseases.

As well, the released **soot particles** are dangerous for the health. They also participate in contrail formation. Soot particles are solid carbon particles, coming from the changing of soot precursors such as acetylene (C_2H_2) into carbon rings which are agglomerated into

¹<https://www.iea.org/reports/global-energy-review-2021/co2-emissions>

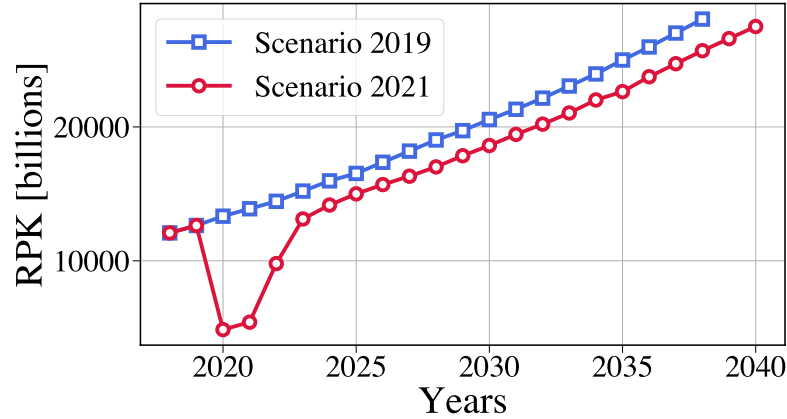


Figure 1.1: Traffic expectation from 2015-2041 (from Airbus technical report 2021).

solid particles and then oxidised. Finally, **sulphurs** SO_x are released by aeronautical engines because sulphur still remains in the Jet fuels after the refining process.

1.2 Solutions for the aeronautical sector

The reduction of polluting molecules has led instances to create numerous regulations in the aeronautic sector to prevent the emissions from increasing [78] since 2005. The aim of aeronautical industries nowadays, because of the regulations on pollutants, is to reduce the amount of pollution they produce while staying competitive in the transportation market, which is the concept of **sustainability**. Of course, challenges are not the same in the different industrial fields and the issues raised here are presented for the aeronautical field only. Industry has already started to tackle these problems by optimising the aircraft structure, but these efforts might be unfavourably compensated by the increase of the air traffic that, if nothing greater is achieved, will lead to a stagnation or a rise of the total emissions. Covid-19 crisis which conducted to a strong reduction of the air traffic has accelerated incentives from the governments and the industries to support research on future fuels. This underlines the importance of the government role in the conversion toward zero-carbon energy, which has the capacity to support research and the development of new technologies to make them as efficient as already existing technologies [101].

Therefore, several solutions are studied for aircraft propulsion to contradict the detrimental effects of pollutants release:

- historically, the **electrical energy** has emerged along with the beginning of the aeroplane history and is considered nowadays a credible solution thanks to the battery capacity increase. Indeed, as batteries are charged with ground-based facilities, the associated emissions might be handled by providing energy through wind turbines, solar panels, nuclear power-plants or **Carbon and Capture Storage (CCS)** systems. Nevertheless, while providing a great advantage in terms of emission reduction, the battery remains economically and environmentally costly [14]. Overall, the specific power released by electric batteries is not sufficient to give enough energy to a standard plane for a given weight as seen in Fig. 1.2, but could be a great opportunity for light aviation [257]. Combustion then remains very interesting, because a significant amount of energy can be carried out in a small volume, which is crucial for

a flying engine as the weight/power trade-off is optimised. Today, hybrid solutions are on the table and might provide part of the response.

- second, **drop-in alternative fuels** have been used. Either made up of synthesised matter or biomass like corn for example, these have the advantage to have been produced from organic matter and not extracted from the soil like fossil fuels, which reduces the CO_2 emissions if the fuel life cycle is considered (i.e., the climate impact from its production to its use). Furthermore, those alternative fuels can be dropped in since they are developed to fit the working point of already existing engines (and then avoid to re-design the complete engine, which would be unsustainable). A main drawback however is the following: if agricultural resources used for fuel production are also used for feeding purposes, the competition between both usages create an ethical problem. Devoting part of the fields used for growing the matter to the alternative fuel production, either may lead to less food available (while the Earth population is constantly increasing) or to forest destruction to enable more agriculture, which has to be taken into account in the total balance for CO_2 emissions. More details on that specific topic are given in the next section.
- More recently, lighter fuels such as **methane (CH_4) and even hydrogen (H_2)** have come into consideration. Indeed, those lighter fuels, already used in the spatial industry, have the advantage of releasing fewer pollutants than standard kerosene. This is especially the case for hydrogen which contains no carbon, then erasing carbon monoxide, carbon dioxide and soot production. Methane which contains only one carbon produces very little soot, as soot precursors are mainly pyrolysis products with two carbons or more that contain unsaturated HC bonds (such as C_2H_4). The main problem with hydrogen and methane is their small specific energy per unit of volume, as seen on Fig. 1.2. Indeed, those light molecules produce a lot of energy but, due to their small size, they both fill a bigger volume than the current kerosene to produce the same amount of energy. An increase of the size of the reservoir is then necessary, which induces heavier plane structure and is counter-productive. To overcome this issue, high pressure and cryogenic storage are both considered. Other problems remain concerning safety due to the high reactivity of hydrogen, its volatility and the wide flammability range in equivalence ratio. For this purpose, blends of hydrogen with other fuels are under investigation. Those mixtures take advantage of the interesting properties of hydrogen, essentially the capacity to burn fast and strong, and avoid to increase too much the fuel tank size. For instance, a CH_4/H_2 blend leads to a stabilised flame where a pure methane flame would be unstable [158]. A NH_3/H_2 blend, even if a pungent odour and a lot of NO_x are released, is also considered for improving the low velocity of ammonia [330]. This solution has the advantage of remaining carbon free while having almost the same specific energy as kerosene. A major drawback however is that those technologies can not be directly used in current aircraft engines and demand to re-design them.

All those ideas are promising, but still require time to be fully developed and operational. A common agreement in the industrial sector, at the time of this PhD, is to focus on alternative drop-in fuels to reduce carbon emissions in the short run. Indeed, hydrogen, methane and blends, which require the engine technology to be sufficiently ready, safe and certified, are predicted to be used in the horizon 2035.

In this PhD work, alternative drop-in fuels are studied. The next paragraph explains

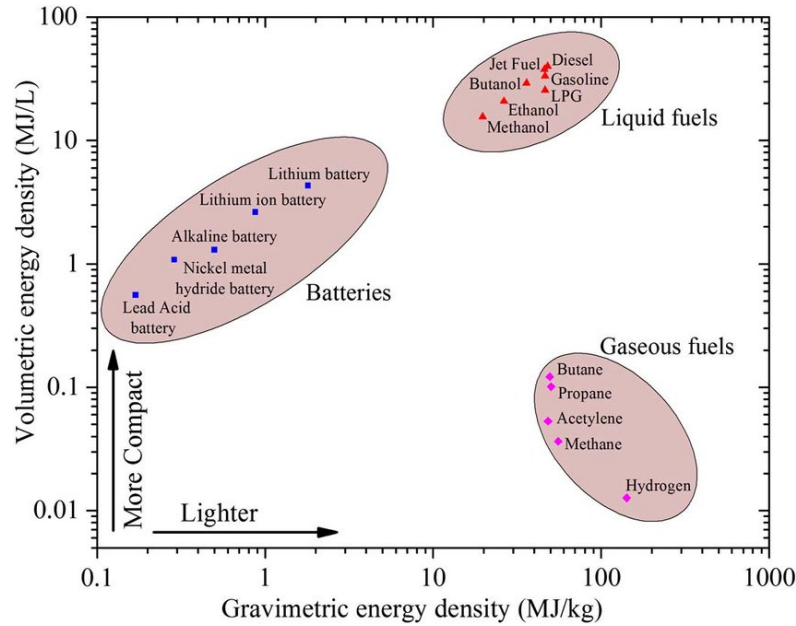


Figure 1.2: Volumetric energy vs mass energy storage for electric batteries, liquid fuels and gaseous fuels taken from [248].

which fuels are used, how they are produced and their differences compared to standard kerosene.

1.3 Alternative drop-in fuels

Alternative fuel is a term that was first used in the energy literature in the late 1970s [81], even if Germany and other countries already used it during the second world war to designate the fuel issued from the Fischer-Tropsch process and used for aeronautical propulsion. [149]. By definition, alternative fuels refer to any fuel outside the conventional petroleum fuels, namely gasoline, diesel and kerosene. As written in the previous section, alternative fuels are drop-in fuels if they can be used with the current engine technology. A further step toward environmental-friendly fuels is made with the concept of Sustainable Aviation Fuels (SAF), which have a lower carbon footprint of their production and use compared to conventional fuels. SAF may be issued from biomass, a renewable source which consumes CO_2 , and may also have a low carbon content. The aim of this section is to describe the methods as well as today's state-of-the-art of aeronautical drop-in fuels and SAF.

The petroleum-based industry started research on alternative fuels in the late 1970s, for security and self-sufficiency reasons, mainly triggered by the 1973 oil world crisis. However, when oil prices fell down again in the early 1980s, interest was lost for these more expensive synthetic fuels. In the late 1980s, the question of urban air quality brought back the subject onto the table. Still, the first flight powered with an alternative fuel took off very much later, in 2008, and was operated by Virgin Atlantic with a Boeing 747-400 flying from London to Amsterdam [5]. For this flight, a blend of 20% bio-jet fuel and 80% petroleum-based fuel was used. Since 2008, global biofuel production has more than doubled [255] but still represents only about 2% of the world aviation fuel consumption. Only 10 airports in the world provide continuous biofuel supply.

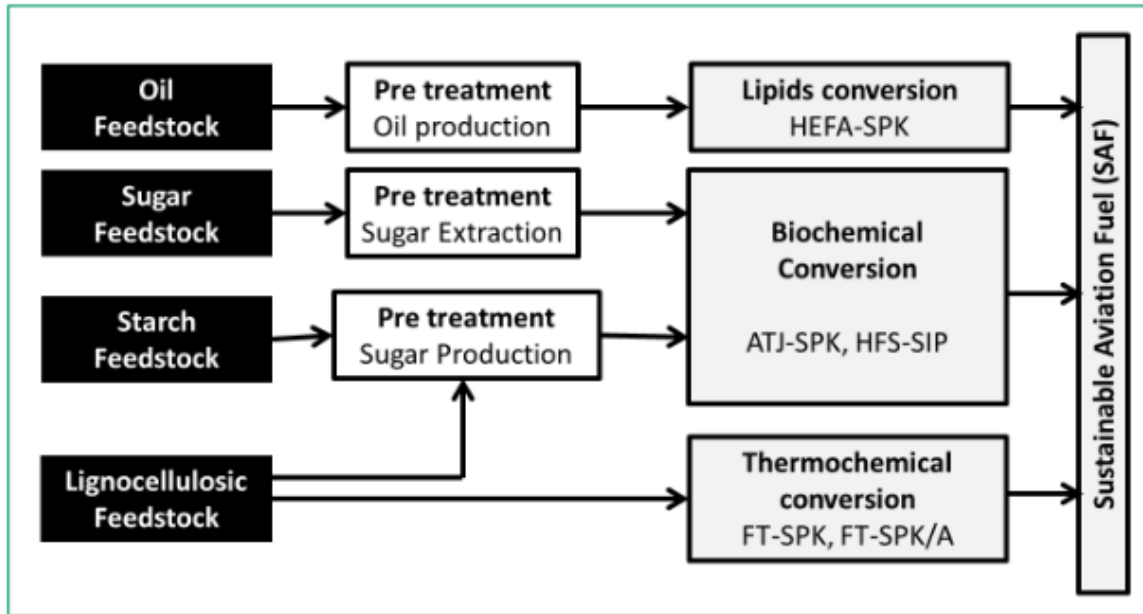


Figure 1.3: Current certified SAF pathways, adapted from [132].

One of the difficulty in introducing new aviation fuels is the certification process, which contains many criteria and is therefore quite long. Figure 1.3 displays the processes of SAF that have been certified. The detailed scheme is given in the Appendix A.

Three types of alternative fuel production pathways have been set up:

- the **thermochemical conversion**, based on lignocellulosic feedstock and algae, leads to the first certified alternative fuels. The Fischer-Tropsch - Synthetic Paraffinic Kerosene **FT-SPK** was certified in 2009 [3] and **FT-SPK/A** with added aromatics derived by alkylation of light aromatics from non-petroleum sources was certified in 2015. The Hydrotreated Depolymerized Cellulosic to Jet (HDCJ) [140] is a pathway that has not been approved yet.
- the **biochemical conversion**, based on sugar feedstock (sugar-bearing plants) and on starch feedstock is used for Alcohol-To-Jet Synthetic Paraffinic Kerosene **ATJ-SPK**, certified in 2016 with the Gevo pathway [140]. An engine can include up to 30 % in volume of ATJ-SPK. Hydroprocessed Fermented Sugars - Synthetic IsoParaffins **HFS - SIP** are created by a catalytic conversion and hydrotreatment of hydrocarbons. The process was certified in June 2014 and an engine can be fed with up to 10 % in volume of HFS-SIP.
- the **lipid conversion**, from oil feedstocks, such as oil-bearing plants or used cooking oil, can lead through hydro-cracking to Hydroprocessed Esters and Fatty Acids - Synthetic Paraffinic Kerosene **HEFA-SPK**, certified in 2011 and allowed for a use of up to 50 % in volume in aeronautical engines. SAF from Catalytic Hydrothermolysis (CH) [132] is also a pathway that has not been approved yet.

Those fuels are different from conventional kerosenes, as they all contain more isoparaffins [312] and fewer aromatics. The alternative fuels are not expected to differ greatly in terms of pollutant emissions [244] but they are interesting for their better sustainability.

The sustainability of a given energy or material is given by evaluating its **Life Cycle Assessment** (LCA) [151]. LCA evaluates the environmental impact of a product through its whole life cycle, from raw production to exploitation and final disposal. Looking at this overall cycle, alternative fuels are performing well in reducing the pollutant emissions [138], [139], mainly because the CO_2 emitted through the combustion process was captured by the raw material prior to its exploitation.

One of the main difficulty for the industry to certify and use alternative fuels is that they have to ensure the security on board, i.e. that the engine still works as for Jet-A1. Properties for Jet-A1 are give in the Table 1.1 from [171].

Properties	Value
Averaged formula	$C_{11}H_{21}$
H/C ratio	1.91
Boiling range	330 K-510 K (165 °C-265 °C)
Freeze point	-65 K (-50 °C)
Flash point	127 K (53 °C)
Net heating value	43.140 kJ/kg
Specific gravity, 16 °C (60°K)	0.81
Critical temperature	770 °F (410 °C)
Critical pressure	23 atm
Average composition	18% of aromatics, 35% of naphthalene, 45 % of paraffins, 2% of olefins

Table 1.1: Main properties of Jet-A1.

This implies several statements to be respected, to ensure the security of the airframe, of the engine fuel system and of the combustion chamber, based on properties that are similar to what is in Table 1.1 [33]:

- the density should be comprised between 775 and 840 kg/m³.
- the flashpoint should be at 38 °C minimum.
- the heating value should be at 42.8 kJ/kg minimum.
- the kinematics viscosity between 0.8 cSt and 0.88 cSt at -20 °C.
- the mass of H and C atom should be more than 99% of the blend.

The list here is not exhaustive, but should be kept in mind when dealing with alternative fuels. Other requirements for SAF include the approval that the developed alternative fuel is fully compatible with the long lifetime cycle of aero-engines.

This PhD project was funded by the **JETSCREEN** (JET fuel SCREENing and optimization)² H2020 project. The aim of this project was to screen possible alternative fuels and to evaluate their mechanical and thermochemical properties as well as their behaviour in real engines. This led to many developments such as the creation of fuel oxidation chemical schemes and their reduction, the fuel thermal and storage stability, the fuel dissolution in water and ice accretion, the fire/explosion risks, the seal performances, the fuel preparation, the flame properties (ignition, lean blow-out, stability, combustion instabilities) and

²<https://cordis.europa.eu/project/id/723525>

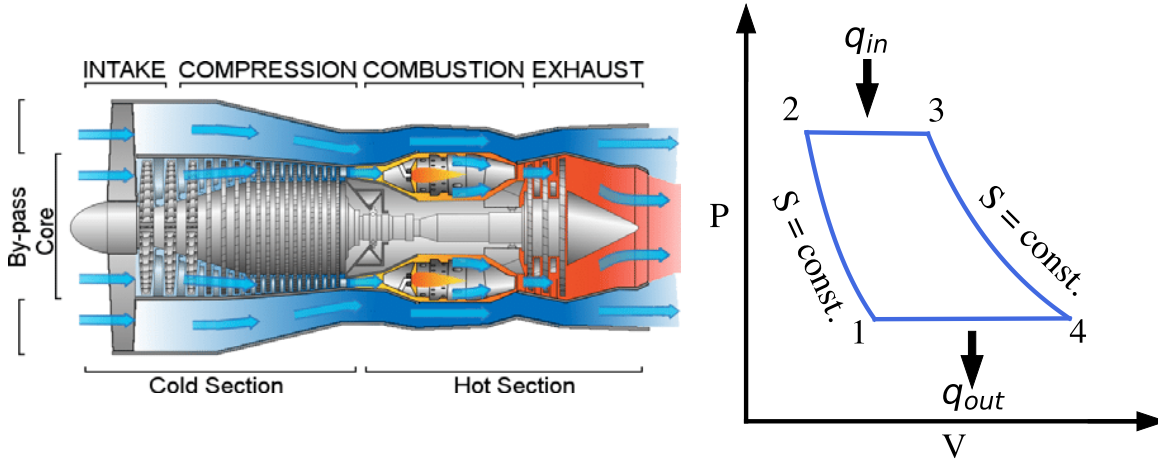


Figure 1.4: Scheme of an aeronautical gas turbine engine (left) from [2] and the Brayton ideal thermodynamic P-V diagram (right) at constant pressure.

the pollutants (NO_x , SO_x). A final result of this project was to create a screening process for the identification of fuels that can be certified, only using its detailed composition and thermochemical properties.

This PhD project contributed to JETSCREEN in the characterisation of fuel behaviour in aeronautical engines, and more specifically the Lean Blow-Out (LBO) limit. To do so, numerical simulations of a lab-scale burner, the SSB burner from the DLR, were conducted. Indeed, measurements performed in this combustion chamber [107], [109], [110] gave interesting results about parameters influencing the flame stabilisation and the LBO limit.

The next section gives details about the design of aeronautical combustion chambers, as well as the key characteristic phenomena occurring inside.

1.4 Design of combustion chambers

Gas turbines are all based on the same general architecture, with the combustion occurring with air coming from the intake (pressurised and then heated) and fuel injected in the combustor. The hot gases accelerate through various turbine stages, and their momentum is either directly used as a propulsive force or transferred to a rotating shaft. To optimise the thermodynamic cycle, the unburnt mixture is injected at a higher pressure in the **combustor**. The ideal thermodynamic Brayton cycle is shown in Fig. 1.4.

The ideal cycle is composed of three parts: an isentropic compression of the fresh gases ($1 \rightarrow 2$), a heat addition at constant pressure, i.e., the combustion step ($2 \rightarrow 3$), and an isentropic expansion of the burnt gases ($3 \rightarrow 4$). The efficiency of the cycle depends on the ratio of the net power (difference between the work gained during the isentropic compression and the work lost during the isentropic expansion) and the heat received from combustion. In other words, the area delimited by the cycle lines represents the work gained by the system. Therefore, the greater the pressure increase between steps 1 and 2, the more efficient the cycle. This increase is however limited by the maximum allowed temperature T_3 at the entry of the turbine at step 3, linked to material thermal resistance.

This PhD mainly focuses on the combustion step ($2 \rightarrow 3$). The role of a combustor is

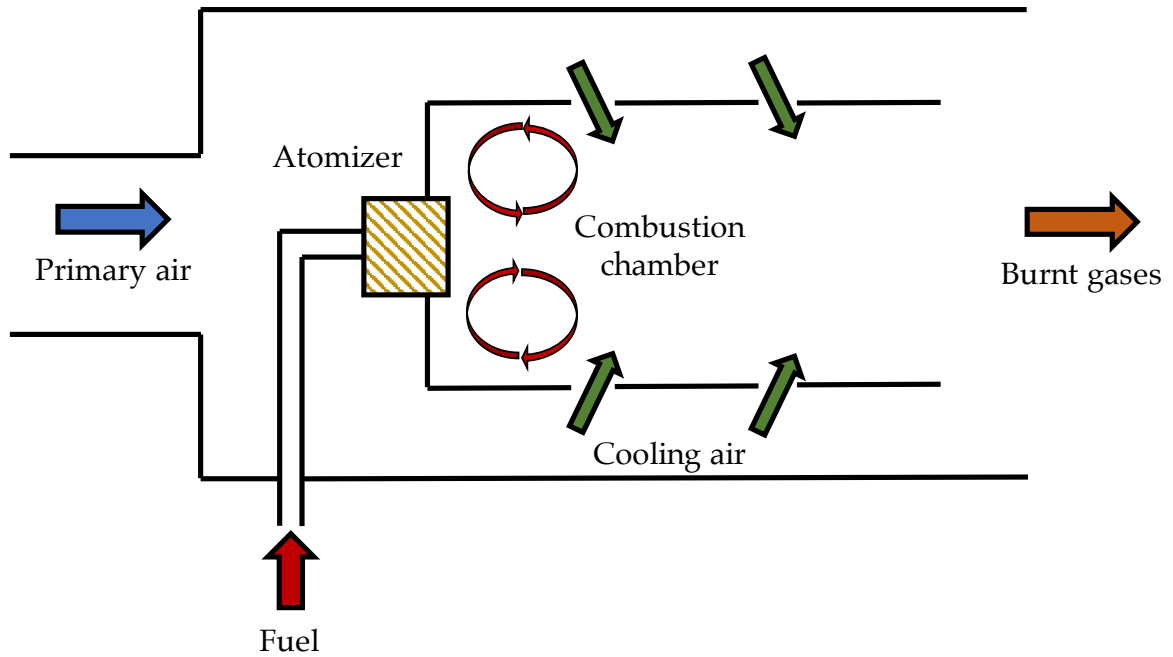


Figure 1.5: Sketch of a combustion chamber.

to generate continuous heat to produce thrust. The combustion efficiency η_{comb} is defined as the ratio between the final temperature T_3 and the theoretical adiabatic temperature T_3^{theo} in comparison to the initial temperature T_2 :

$$\eta_{comb} = \frac{T_3 - T_2}{T_3^{theo} - T_2} \quad (1.1)$$

Combustor efficiency can be changed by the wall cooling and more generally heat losses, as well as incomplete combustion and post-flame chemistry, including pollutant formation. In addition, the combustor compactness has a direct impact on its weight and therefore its manufacturing and operational costs. To better represent how the combustion chamber is integrated in the whole engine, the sketch of a combustion chamber is represented in Fig. 1.5.

The **fuel** is stored in a liquid state and separately from the air for safety reasons, i.e., to avoid auto-ignition of the mixture. Aeronautical engines indeed use liquid fuels, as liquid occupies less volume than gas. Several technologies exist for atomising and vaporising the liquid fuel into the combustion chamber, which are described later in the PhD (Chapter 5).

The subsonic turbulent flow of the combustor influences the flame shape and stability. Upstream from the combustion chamber, the injection system has a reduced section with vanes to increase the velocity and promote a better mixing with the liquid fuel. The section is then enlarged in the combustion chamber to reduce the velocity and allow the flame to stabilise. Most combustors inject swirling flows, which creates recirculation zones, leading to a very stable combustion. Downstream the flame burning area, additional air coming from the compressor is often injected to protect the walls from the hot burnt gas, and to lower the temperature. Eventually, at the far end of the combustion chamber, the section is reduced again to increase the velocity and generate thrust via burnt gases isentropic

expansion.

To fly in safe and reliable conditions, several key points need to be checked:

- **Combustion instabilities** may occur in a reacting flow when the heat release couples with acoustics in a closed loop with sufficient amplification factor. Instabilities may be systemic from the chamber or intrinsic from the flow [15]. Variables of interest that drive the instability are the fluctuations of heat release rate, velocity and pressure. Strong instabilities with high levels of fluctuations may lead to flame quenching or flash-back; they may damage the engine or even lead to explosion [233]. These instabilities are therefore hazardous for the engine and difficult to predict as strongly non-linear phenomena. In an attempt to control their occurrence, stability maps are drawn to determine safe operating points. Besides, optimising the geometry of the combustion chamber and the primary combustion zone might tackle the problem.
- **Ignition** is a crucial phase for a gas turbine [28]. Although the engine is always lightened on the ground, its relight during the flight at high altitude, i.e. in unfavourable low pressure and temperature conditions, must be guaranteed. Even on the ground, some bad weather conditions such as heavy rainfalls or extremely low temperatures may complicate the ignition. The ignition overall process goes through three phases: first, a hot kernel is created by a spark and produces hot gases by transferring locally a significant amount of energy to the mixture. Second, a first flame front forms and grows in the turbulent flow. Finally, the flame front propagates from the spark location to the injector.
- **Extinction** or flame-out can happen for several reasons: fuel starvation, cold temperatures, instabilities, etc... During the engine design process, the lean blow-off limit (LBO) is a critical parameter allowing to determine the operational range of the engine. Only the lean limit is considered, as aeronautical engines are never operated in globally rich conditions. To ensure that unwanted blow-off will never occur in any of the possible environmental conditions, margins are then taken to stay away from the LBO.

The overall design of the combustion chamber goes through a clearly defined process which involves several steps of design [288]. It includes both testing and numerical simulation, first to evaluate the feasibility of the initial concept, then to optimise the engine in terms of performance, noise, pollutant emissions and other technical parameters. Numerical modelling and simulation are then essential to improve and accelerate the design process. The next section details how the development of numerical methods and computational power help for a better understanding and prediction of combustion phenomena in engines.

1.5 The role of numerical simulation

Numerical simulations aim to represent the behaviour of any real and complex physical phenomenon as accurate as possible. These computations are based on physical laws integrating various levels of modelling to enable a description of all phenomena. Even though these models may not be always accurate, the use of simulations brings clear answers to problems that can not be solved analytically, such as turbulence or most non-linear processes. The quality of numerical solutions has constantly increased, thanks to

improved modelling but mostly to the computational power increase and the accompanying programming techniques such as massively parallel computing.

The first numerical resolution of a physical problem was the Fermi-Pasta-Ulam-Tsingou experiment run in 1953 [88], where the simulation of non-linear oscillating springs connected to two weights highlighted the chaotic behaviour of the system. Since then, numerical simulation has been applied to many, if not all, fields ranging from chemistry, biochemistry to economy and physics. Among all fields, **CFD (Computational Fluid Dynamics)** emerged in the late 50s, in the pioneer work of Francis H. Harlow [117]. First simulations were only two-dimensional, and the resolution of three-dimensional multi-species flow equations only arrived in 1967 [122]. When the developed methodologies reached a sufficient level of robustness, they were implemented in commercial codes, which are now numerous.

Combustion is a sub-field of CFD, adding chemical reaction source terms to the conservation equations to describe the conversion of chemical energy into heat by fuel oxidation. Combustion simulations are particularly useful to better understand the physical phenomena, as the experiments and measurements in flames are limited due to the hot environment and presence of combustion chamber walls. Besides, combustion depends on the combustion chambers design and only simulation allows addressing the vast variety of configurations (furnaces, power station combustors, engines, etc. . .)

The proper modelling of chemical kinetics and turbulent mixing is one of the main challenges of combustion simulation. Indeed, timescales associated to the kinetics are relatively fast and the strong interaction between turbulence, chemistry and fuel spray adds complexity to the problem. Combustion simulations have benefited of the increasing computational power in two ways. First, it simply allowed to use more refined meshes, and therefore a better description of small scale phenomena. But most importantly, it allowed to improve the description of the physics: **turbulence**, which was initially modelled with RANS in a statistically-averaged approach, is now more and more computed in DNS or LES method, able to represent transient events; **chemistry** could be simplified to a global mass-balance reaction, which was sufficient to correctly locate the flame front and give a first evaluation of the combustion efficiency, but not for more complex phenomena such as pollutant formation of complex fuel effects, is today described with more complex sets of reactions that form a reduced mechanism and keeps an acceptable computational cost; finally, **two-phase flow** phenomena such as atomisation and evaporation have been introduced.

Chapter 2

Modelling of turbulent spray flames

Contents

2.1	Turbulent spray flames	13
2.1.1	Turbulent spray	14
2.1.2	Turbulent combustion	15
2.1.3	Spray laminar combustion	15
2.1.4	Spray turbulent combustion	18
2.2	Use of alternative fuels	18
2.2.1	Alternative fuels in combustors: state-of-the-art	20
2.2.2	Modelling alternative fuels	22
2.3	Prediction of the Lean Blow-Out: state-of-the-art	23
2.3.1	Semi-empirical methods	23
2.3.2	Numerical models	25
2.3.3	Hybrid models	26
2.4	Organisation of the manuscript	26

It was recalled in the previous chapter how important is the numerical simulation of combustion chambers. Both the chamber design and the fuel composition and state drive the flame shape, which results from the competition of several phenomena. Turbulence is another driving process, introducing intermittency and stochasticity, both challenging features for deterministic calculations.

Therefore, the aim of this second chapter is to introduce the major phenomena associated with LBO of aeronautical combustors, discussed in this PhD. Section 2.1 recalls the parameters influencing the combustion of turbulent spray flames. Section 2.2 then focuses on the modelling of real fuels. Section 2.3 gives the major methods used for the prediction of LBO. Finally, Section 2.4 introduces the goals of this PhD work and the manuscript organisation.

2.1 Turbulent spray flames

As depicted in the previous chapter, fuel is stored in aeroplanes in a liquid state in order to get a high volumetric energy. The resulting flame is then influenced by the turbulent

flow, by the chemical reactions occurring in the mixture and by the two-phase flow. Figure 2.1, adapted from [222], [266], displays how these different features influence each other.

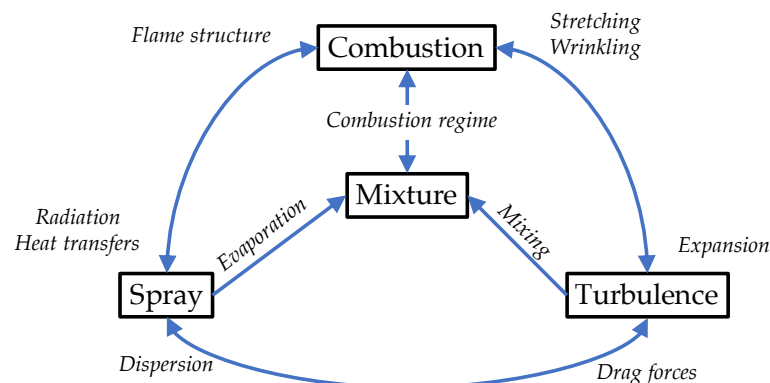


Figure 2.1: Interaction between spray, turbulence and combustion for a given mixture, adapted from [222], [266].

The interactions between those individual processes are detailed in the next sections before introducing the complexity of the resulting flame analysis.

2.1.1 Turbulent spray

Depending on the size and the velocity of the different eddies and of the droplet inertia, the spray may be spread uniformly or gathered in some areas, as illustrated in Fig. 2.2. This phenomenon is called **preferential segregation** or **inertial clustering** [73] and is characterised by the Stokes number:

$$St = \frac{\tau_p}{\tau_g} \quad (2.1)$$

where τ_p is the characteristic droplet time and τ_g the characteristic flow time. If $St \ll 1$, the particle time is smaller than the flow time and the particle follows the flow as a tracer. If $St \gg 1$, the particle has a high inertia and it is influenced only by the biggest eddies. The characteristic time τ_p depends on the droplet diameter and the expression will be detailed in Section 5.1.1.1. In industrial burners, the droplet diameters at injection and inside the combustion chamber are not uniform, meaning that small and big droplets coexist with a different response to turbulence.

The spray segregation is important for combustion as it directly influences the mixture composition via evaporation, leading to possibly strongly stratified fields of gaseous fuel concentration.

Conversely, droplets may influence the local turbulence with several contradictory phenomena [10]. On the one hand, the friction forces at the droplet surface locally dissipate the Turbulent Kinetic Energy (TKE), leading to a decrease of TKE. On the other hand, the surface shear stress and the eddies formed in the droplet wake increase locally the TKE. The classical turbulent Kolmogorov cascade is then perturbed by the liquid flow, which may be significant for high liquid loading α_l . Typically, for $10^{-6} < \alpha_l < 10^{-3}$, the turbulence/particle interaction is a two-way coupling and for $10^{-3} < \alpha_l$, a four-way coupling is needed as particle-particle interactions become important [272]).



Figure 2.2: Experimental image of a laser sheet going through a spray at $St = 0.6$ for isotropic homogeneous turbulence, showing the preferential droplet segregation phenomenon, taken from [320].

2.1.2 Turbulent combustion

When considering a gaseous turbulent reactive flow, the main effect of turbulence on combustion is the increase of the combustion rate. Indeed, the larger vortices tend to wrinkle and stretch the flame front, increasing its surface area and therefore leading to a higher turbulent flame speed. This effect is clearly visible in jet flames, which exhibit a shorter length when subjected to turbulence [235].

On the other hand, the flame also modifies the turbulent flow field. This effect is mainly due to the temperature increase on one side, which is tantamount to a viscosity rise and therefore Reynolds number decrease: the flow may even go back to laminar in the hot gas side. Conversely, pressure and density gradients in the flame front generate small vortices, which add to the turbulence. This was investigated by [205].

2.1.3 Spray laminar combustion

The interaction between the spray and the combustion depends on the time taken by the droplets to fully evaporate, to be compared to the travel time between the injection and the flame front. Indeed, the droplet may fully evaporate before the flame front, within the flame front or only after the flame front, thus influencing the flame shape and structure.

Three spray/combustion regimes, presented in Fig. 2.3, may be classified:

- in the **pre-evaporated case**, droplets are fully evaporated before the flame front, the spray and the combustion zones are separated and the flame is purely gaseous, only depending on the spray via the gaseous fuel distribution.
- in the **homogeneous two-phase combustion case**, droplets reach the flame front, where they complete their evaporation. This leads to a thickened reaction zone, where combustion occurs similarly as in a purely gaseous mixture.

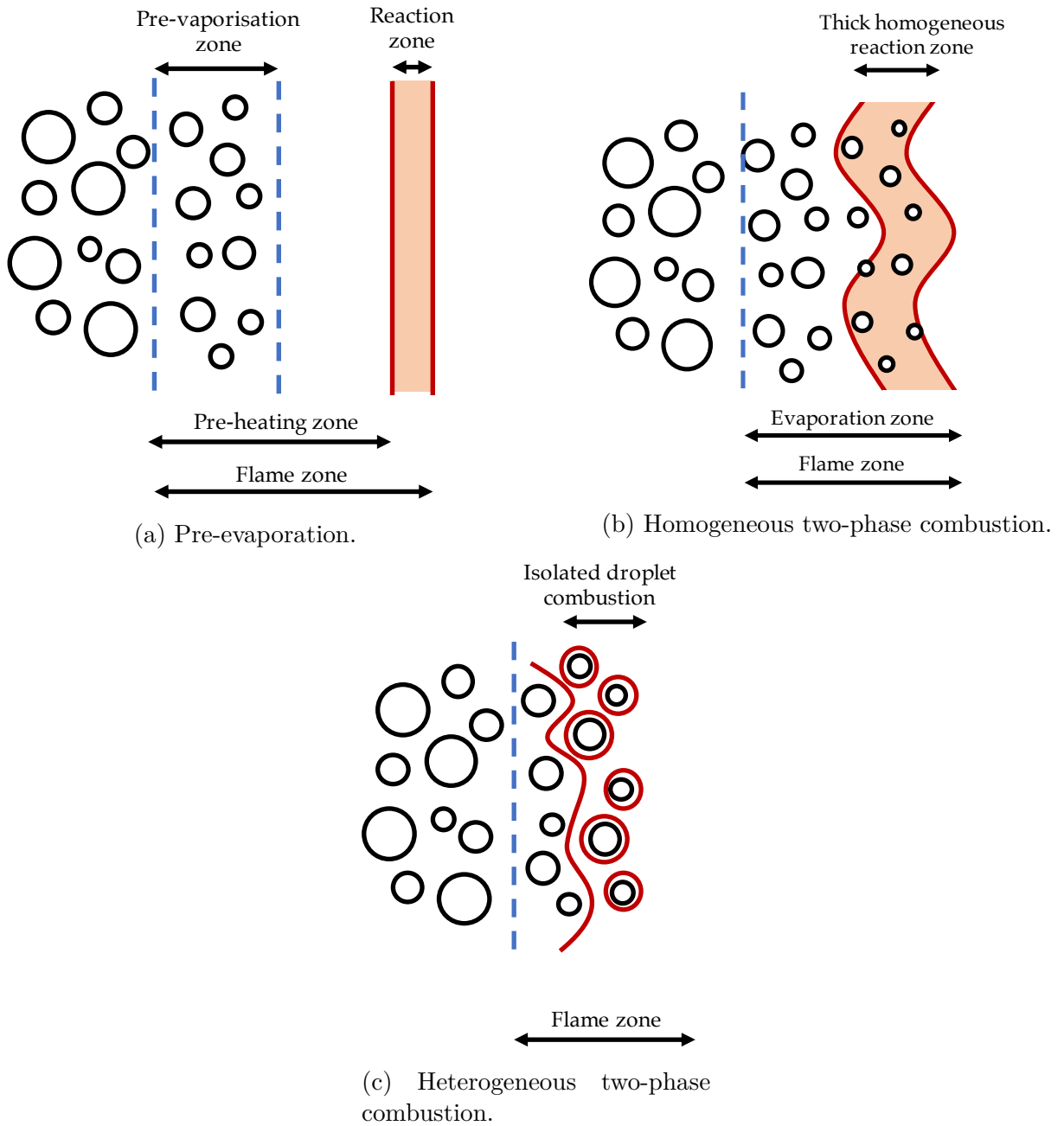


Figure 2.3: Scheme of the different interaction levels between spray and combustion adapted from [31].

- in the **heterogeneous two-phase combustion case**, droplets reach the flame front, but they survive and cross the flame front, completing evaporation and burning in the hot gas. The combustion regime is said to be heterogeneous, as droplets burn in the individual droplet combustion mode in the hot gas.

When droplets directly interact with the flame zone, i.e., do not fully pre-evaporate, the combustion and the spray are strongly coupled and the inner flame structure may significantly differ from a gaseous flame.

In a given flow, the different combustion modes are classified with the group number [46], which compares the droplet evaporation rate and the diffusion rate of hot gases in the droplet cloud. Details on this number are presented in Section 5.2.1. A major parameter of

which the group number depends on is the droplet spacing. The three combustion regimes defined above may be placed in a droplet-spacing/temperature diagram as shown in Figure 2.4.

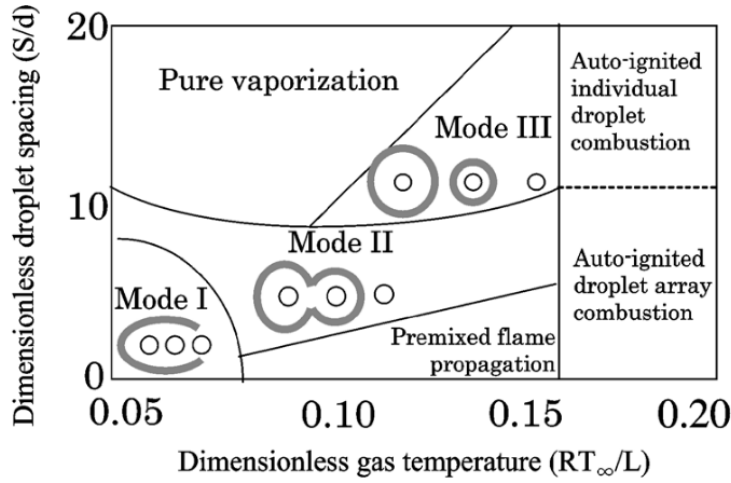


Figure 2.4: Inter-droplet flame propagation mode map from [309].

The plot shows the spray combustion regime as a function of the inter-droplet spacing S divided by the flame diameter d , and the gaseous temperature T multiplied by the perfect gas constant R_∞ and divided by the heat vaporisation of the fuel L . For high temperatures, the droplets ignite spontaneously, either individually for higher droplet spacing or collectively for low droplet spacing. On the contrary, for high droplet spacing and low gas temperature, no flame appears and the droplet is only vaporising. In between, several regimes are possible:

- **Premixed flame propagation:** As the droplet spacing is small, individual flames around droplets can not form and the high temperature leads to a fast droplet evaporation. The resulting vapour-air mixture burns as a gaseous mixture in a premixed flame. This corresponds to the above pre-evaporated case.
- **Mode I:** For low inter-droplet spacing, if the gas temperature is not high enough droplets hardly evaporate and subsist in the reaction zone which behaves like a premixed flame. Generally, the flame is thicker and the laminar flame speed may be different from the one of a purely gaseous mixture. This is the homogeneous two-phase combustion.
- **Mode II:** As the inter-droplet spacing becomes more important, the droplets may auto-ignite if the temperature is high enough. In that case, combustion occurs in the non-premixed regime between the fuel vapour layer around the droplet and the surrounding air. These diffusion individual droplet flames are close enough to merge, creating an envelope around the droplets. This is one of the possible combustion regimes of the heterogeneous two-phase combustion.
- **Mode III:** Finally, when the inter-droplet spacing is large, the droplets burn individually in surrounding diffusion flames which do not merge anymore. This is another possible combustion regime of the heterogeneous two-phase combustion.

The spray/flame interaction greatly impacts the laminar flame speed, which is essential for flame stabilisation in a real burner. Studies investigating the relation between the two-phase flow burning mode and the combustion [13], [175] have shown that the presence of droplets lead to strong variations of the local equivalence ratio, mainly depending on the droplets' diameter and the relative velocity between the liquid and the gaseous phase [213]. For rich mixtures, it was found that a maximum flame speed exists when the effective equivalence ratio seen by the flame is close to the stoichiometric value.

2.1.4 Spray turbulent combustion

When the different phenomena are taken into account, the prevalence of one parameter compared to the others may be evaluated with different timescales [63]:

- **the evaporation timescale** τ_{ev} evaluates the time of the droplet to fully evaporate.
- **the eddies timescales** τ_T for the biggest and τ_K for the smallest evaluate the turbulent motion.
- **the chemical timescale** τ_c evaluates the time taken to convert the reactants into products.

Complex 3D turbulent flows, with possible recirculation zones, may lead to the simultaneous presence of different spray combustion regimes, i.e., premixed or diffusion modes, homogeneous or heterogeneous (with individual droplet burning) modes. Complex flame structures may then be generated [188] and can be analysed with the Takeno index [323], taking the following expression:

$$T = \frac{\nabla Y_F \cdot \nabla Y_O}{|\nabla Y_F \cdot \nabla Y_O|} \quad (2.2)$$

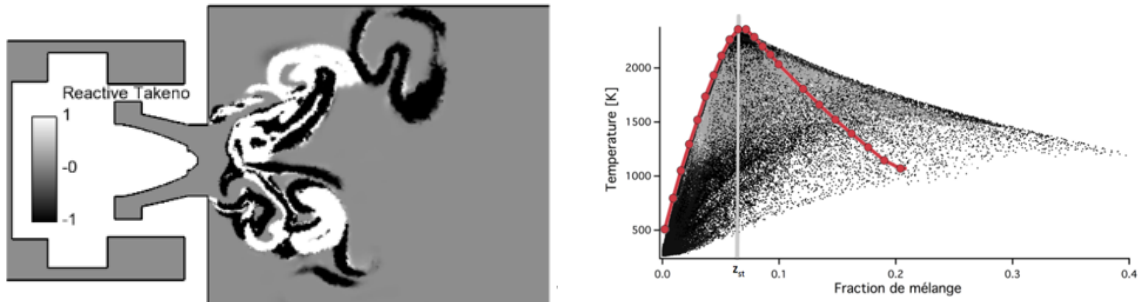
with Y_F the fuel mass fraction, Y_O the oxidiser mass fraction and ∇ the gradient operator. Discussion on its interpretation is presented in Section 3.3.3.3.

The Takeno index field presented in Fig. 2.5 for the Mercato configuration [219] depicts complex structures with reactive fronts detaching from the flame due to the droplet burning in the burnt gases [116]. Indeed, the droplets released in the hot gases generate a high amount of fuel with little oxygen, leading to a late diffusion flame. The scatter plot representing the temperature as a function of the mixture fraction is as well very different from the equilibrium line calculated for a gaseous mixture.

Most of the standard tools used to analyse flame regimes and structures (see Section 3.3.3.3) have been developed for purely gaseous flames. The question of their adequacy for two-phase flames will be addressed in this PhD, (see Chapter 9), as well as the need for additional tools to analyse the specificities of these flames.

2.2 Use of alternative fuels

When used alone, a fuel molecule is said to be a **mono-component** fuel, which is the case for hydrogen or methane, often used alone for example in rocket engines or gas turbines. Other examples are heptane, propane or ethylene, usually taken as good models of more complex fuels in lab-scale experiments. On the contrary, Diesel, gasoline or jet-fuel do not have an exactly known composition. As refinement products of petroleum distillation, they are guaranteed to meet certification requirements, but their exact composition is not



(a) Takeno index field conditioned by the heat release rate, showing premixed (white) and diffusion (black) modes. (b) Scatter plot of temperature, with premixed (black) and diffusion (grey) modes. The red curve is the gaseous equilibrium.

Figure 2.5: Takeno index field (a) and scatter plot of temperature vs mixture fraction (b), in the Mercato swirled burner [276], taken from [116].

known and may differ depending on the feedstock and the local industrial process. They contain a number of species that can be classified in four main categories:

- **alkanes** or paraffins, of which the formula is C_nH_{2n+2} , are **saturated hydrocarbons**, that is to say that they only contain $C-C$ and $C-H$ bonds. A few examples of their structure is given in Fig. 2.6.

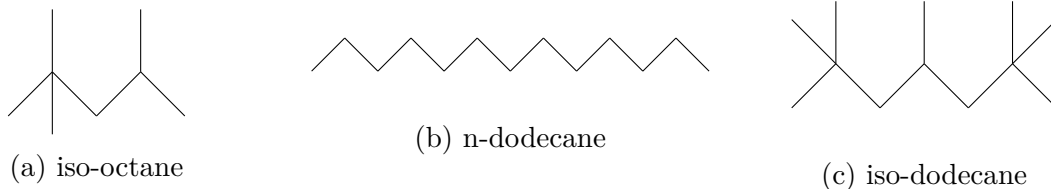


Figure 2.6: Example of several alkanes.

Alkanes may be divided in two subfamilies: n-alkane (i.e., linear alkanes) and iso-alkane (i.e., branched alkanes). Iso-alkanes are said to be more reactive than the linear alkanes. Other properties remain similar for both sub-categories. Current aviation fuels contain an average of 60% of paraffin.

- **Cycloalkanes** or naphthenes are species with the formula C_nH_{2n} and are constituted of one or several rings. Examples are given in Fig. 2.7.

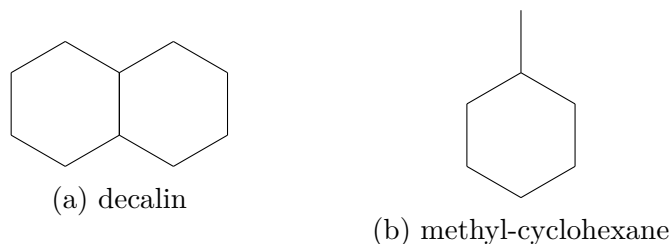


Figure 2.7: Example of several cyclo-alkanes.

Their chemical properties, such as stability, LHV (Lower Heating Value i.e. the heat released of a given fuel mass) or pollutants formation, are close to those of alkanes. Current aviation fuels contain around 25 – 35% of cycloalkanes.

- **Aromatics** are compounds with one or several rings, such as cycloalkanes but with double bonds. Examples are given in Fig. 2.8.

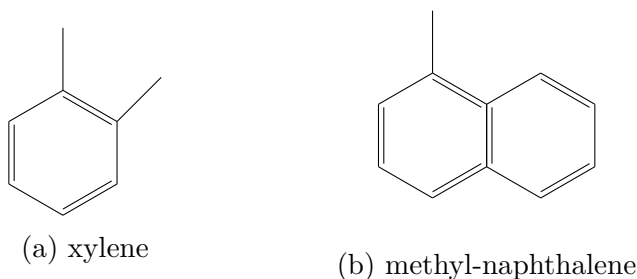


Figure 2.8: Example of several aromatics.

Their reactivity is lower than the two previous categories because they are more stable molecules as they are unsaturated. Their specific energy is also lower because of the lower hydrogen content. Furthermore, they tend to produce more soot. Current aviation fuels contain a maximum of 20% aromatics in volume. Although they are not desirable in an engine, the proportion is too high to remove them at an acceptable cost. Moreover, they play an important role in lubrication, and are today added to fuels that do not have naturally aromatics such as Alcohol-to-Jet.

Additionally, engine fuels may contain olefins, which are alkanes with a double link. Although in trace quantities they are highly undesirable and removed.

Eventually, a real fuel is a blend of all the different families with different carbon numbers. The composition may be evaluated experimentally with a GCxGC analysis, able to identify the family and give the mass percentage for each class of carbon atom number in the mixture. Such a result is given in the form of a mass distribution diagram, illustrated for Jet-A1 in Figure 2.9.

The graph shows that Jet-A1 components spread from species containing 8 carbons to species containing 18 carbons, with a peak around 10-11 carbons. Jet-A1 contains n-alkanes and iso-alkanes in high quantity, fewer cycloalkanes and mono-aromatics and close to zero di-aromatics.

Section 2.2.1 gives the major conclusions on the use of alternative jet fuels in the literature. Section 2.2.2 explains the hypotheses made to integrate such fuels in computations.

2.2.1 Alternative fuels in combustors: state-of-the-art

The combustion of alternative fuels is a wide research topic that has been broadly investigated in the past decade. Lefebvre [169] summarised the main properties required for an alternative fuel to be eligible, as well as the different types of alternative fuels that were available. Following this work and extending the database of potential alternative fuel candidates [23], several authors have started to investigate different fuels. The objective of this review is to recall the main conclusions concerning the key quantities impacting the flame in a real combustor.

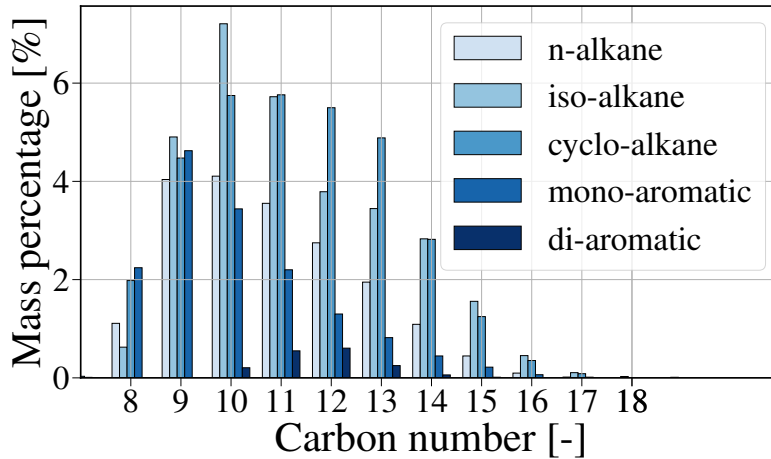


Figure 2.9: Jet-A1 experimental GCxGC mass percentage as a function of the number of carbon atoms [91]

As far as their kinetics are concerned, Dagaut [59] investigated the oxidation of kerosene and bio-kerosene experimentally in a jet-stirred reactor at high pressure and temperature, leading to the conclusion that, even if the bio-kerosene has a slightly higher reactivity, no major change in the products' distribution was observed, also stated in [218] for a wide range of alternative jet fuels. The main changes come from the oxidation phase, where every fuel species pyrolyses via its own pathway [142].

Auto-ignition time was experimentally investigated in several papers and can vary as a function of the fuel used. Kang et al. [141] compared several conventional and synthetic alternative jet fuels and found that conventional fuels showed a stronger low-temperature ignition than alternative fuels with a high content of branched alkanes. Cho et al. [47] compared a jet fuel and a blend fuel with bio-jet fuel in half and also found that the difference was significant at low temperature, which is a conclusion that was reported by other authors [327].

The laminar flame speed of several single components was investigated by Ranzi et al. [251]. This study revealed that the laminar flame speeds of normal alkanes and cycloalkanes were nearly identical for molecules containing more than four carbons and branches species a slightly lower one. Unsaturated species have higher flame speeds with increasing bond order. Wu et al. [321] compared the laminar flame speed for a conventional fuel with and without adding oxygenated molecules and concluded that there were significant differences when adding more than 10% of oxygenated fuel, increasing the flame speed. Fuel blends may then differ according to their composition and the amount of a fuel class compared to another one, especially aromatics, which tends to lower the laminar flame speed [136]. Laminar flame speed of several alternative fuels were compared in [327] for $T = 473$ K and $P = 1$ bar, showing very few differences except for standard kerosene around stoichiometry.

For pollutants emissions, Braun-Unkhoff et al. [34] reviewed the main effects for alternative fuels. CO_2 emissions are mostly identical between conventional and synthetic fuels. The CO/CO_2 equilibrium difference for fuels with a higher calorific value might shift the result to 1 to 2 % lower CO_2 emissions for synthetic fuels. A slight decrease of CO emissions have been observed for the majority of the alternative fuels studied, but results greatly depends on the amount of aromatic fuel and on the flame structure. For instance,

Kurzawska et al. [157] have compared conventional kerosene with blends of kerosene with Alcohol-to-Jet (AtJ) fuel, stating that CO emissions were higher for the blend with AtJ, depending on the loading. NO_x emissions are very dependent on the combustion parameters in the chamber, such as the temperature, the residence time and the oxygen available. Reduction of NO_x with the use of alternative fuels was observed [23]. Soot particles are as well reduced and mainly depend on the amount of aromatic species as depicted in [23] where Jet-A1 has the highest smoke number.

Evaporation properties of alternative fuels were investigated, stating that both atomisation and vaporisation key quantities may be affected by the fuel taken, impacting the flame shape and pollutants released [110]. Stöhr et al. [297] compared experimentally and numerically the diameter of a single droplet evaporating through the time, concluding to the difference of the fuels depending on the vaporisation enthalpy and the distillation curve.

Finally, the numerical simulation of real gas turbines was studied to investigate the flame structure. Chong et al. [48] compared Jet-A1 and rapeseed biodiesel at constant power output, showing very similar flow field but very different reacting behaviour. The comparison between Jet-A1 and AtJ fuels has been studied multiple times for different configurations [196], [221], [249], [285] and reveal fuel effects through experiments and LES. Indeed, they both stabilise at the same place but show a different spread of spray properties, heat release rate and intermediate species due to their different chemical and spray behaviour.

To investigate these different behaviours, modelling is then required.

2.2.2 Modelling alternative fuels

The computation of such a high number of species as presented in Fig. 2.9 in a real 3D burner is not feasible at the moment and a surrogate model, based on a reduced set of components, is designed to correctly reproduce the mechanical and thermochemical properties of the real fuel. For fuel blends, the challenge is even higher and the number of surrogate components representing the real fuel should be chosen with extreme care to avoid numerical over-costs while keeping sufficient accuracy.

The development of multi-component surrogates enables the description of different combustion behaviours [74]. The kinetics of the species chosen to build the surrogate must respect physical and chemical properties of the fuel, as well as be representative of the main families present in the blend. The surrogate algorithm that has emulated the fuel used in this PhD is described in Section 4.1.2. The impact of the chosen surrogate on the flame stabilisation, shape and regime will be investigated in Section 9.

Second, when the multi-component fuel is liquid, the question of evaporation modelling arises. In particular, each component has its own boiling temperature, leading to **preferential evaporation**. As the droplet temperature increases, the highest volatile components, i.e., with the lowest boiling temperature, evaporate first. The droplet composition then evolves, changing its properties such as molar mass, viscosity and conductivity, enthalpy, etc. . . The evaporation model must therefore take into account this composition evolution.

The model used for the multi-component modelling is described in Section 5.1.1. Overall, the importance of considering multi-component fuels will be addressed in this PhD. One complexity is the coupling between evaporation and chemical modelling, which occur nearly at the same time. Surrogates must ensure both the correct droplet evolution and

the right flame structure. Being able to identify separately the impact of evaporation and chemical characteristics is another difficulty, tackled in Chapter 10 where new tools are proposed to analyse the flame.

2.3 Prediction of the Lean Blow-Out: state-of-the-art

The Lean Blow Out phenomenon (LBO), as explained in the introduction, is a crucial safety parameter to be taken into account in the design phase of a combustion chamber. Because of the costs and limits of experiments, the capability to predict numerically LBO is essential.

No theoretical formula exists to determine the LBO limit, due to the complexity and non-linearity of chemistry, turbulence, spray and their interactions with the flame in three-dimensional configurations. Besides, the geometry of the combustion chamber also plays a key role in the flame behaviour, which adds complexity to the problem.

Therefore, for the past years scientists have been developing models that try to predict accurately the LBO limit. Methods can be categorised in three types as described in the next sections, based on [172].

2.3.1 Semi-empirical methods

The **semi-empirical** models are either based on **characteristic time ratios** or on **Perfectly Stirred Reactors** behaviours. The most well-known and validated model is the one of Lefebvre [11], [12].

Characteristic time models

These models are based on the Damköhler number Da , comparing the largest timescale of the flow τ_{flow} to the chemical timescale τ_c . A critical Damköhler number Da is used to estimate whether a flame blows off or not.

Zukoski and Marble [332] who studied the flame stabilisation over bluff bodies, estimate that the LBO limit is reached when:

$$\tau_{flow} = \tau_c \quad (2.3)$$

with

$$\tau_{flow} = \frac{L}{u_a} ; u_a = \frac{T}{T_{in}} \frac{u_{ref}}{1 - B} \quad (2.4)$$

and

$$\tau_c = \frac{\exp(E/RT)}{\phi} \quad (2.5)$$

with u_a the bulk velocity in the annular around the burner, T the shear layer temperature, T_{in} the inlet temperature, $u_{ref} = u_{in}$ the reference inlet velocity, B the blockage ratio, L the length of the bluff body, and E the activation energy of the global chemical process. Plee and Mellor [232] decided to improve this model by taking into account the presence of droplets. The condition then becomes, based on the configurations in [64], [173]:

$$\tau_{flow} > 1.36(\tau_c + 0.011\tau_{ev}) + 0.36 \quad (2.6)$$

with τ_{ev} the timescale of the evaporation of the droplets.

Perfectly Stirred Reactors (PSR)

Longwell et al. [179] were the first to derive a model based on PSRs, assuming that the unburned mixture is mixed with the burned mixture that goes through the recirculation zones. LBO is expected to occur if the amount of heat created by combustion is lower than the amount of heat needed to ignite the fresh mixture. Starting from the fuel mass balance equation, the following relation is found:

$$\frac{\dot{m}_a}{VP^n} = f(\phi, \beta) \quad (2.7)$$

with V the volume of the reactor, \dot{m}_a the mass flow rate of air, P the pressure in the recirculation zones and ϕ the global equivalence ratio and β the fraction of fuel burned. n is equal to 2 in the initial paper of Longwell and extended in the work of Kretschmer and Odgers [155] at 1.25. The function $f(\phi)$ is a result of the rewriting, taking into account the fuel reaction rate, the fuel concentration. From this equation, curves representing $\frac{\dot{m}}{VP^n}$ as a function of β can be drawn, as shown in Fig. 2.10a for a propane/air mixture.

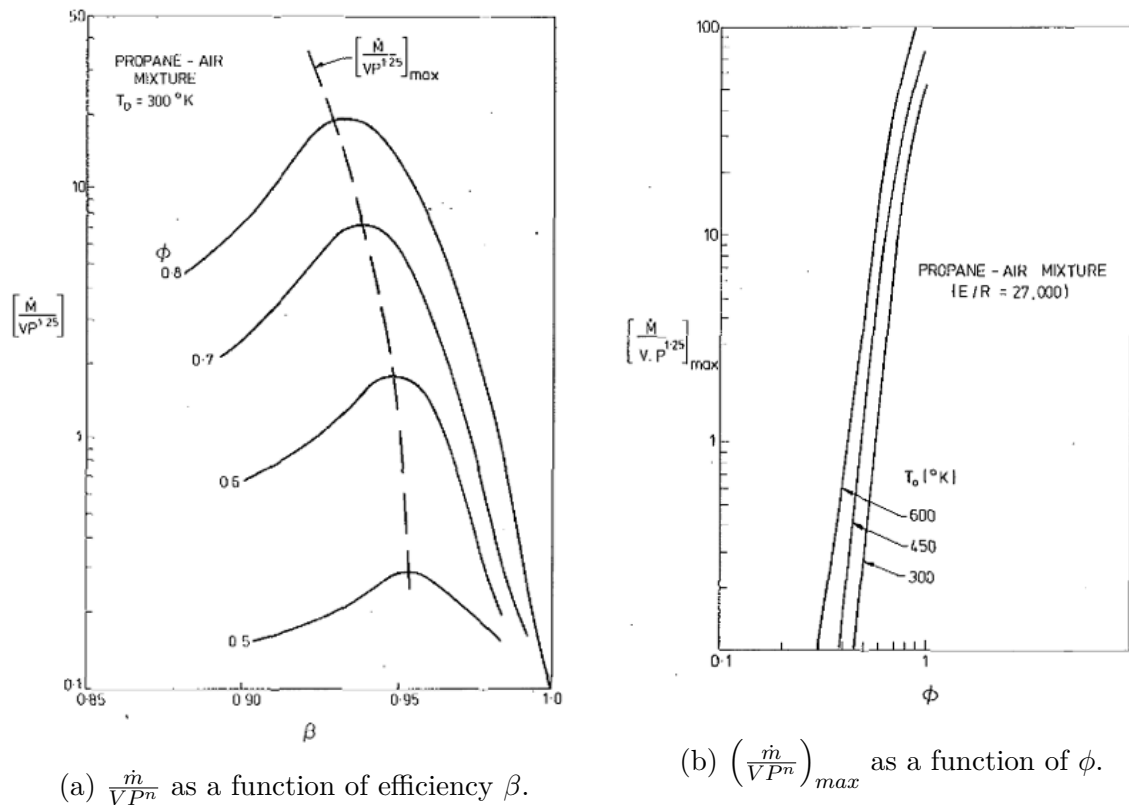


Figure 2.10: Longwell PSR model illustrations, taken from [12]

For each equivalence ratio, a maximum is reached and represents the highest possible heat release rate for the operating conditions given. By plotting this maximum as a function of the logarithm of the equivalence ratio as shown in Fig. 2.10b, a straight line relationship is shown, which represents the maximum air flow rate tolerated by the combustion area before extinction.

Lefebvre improved Longwell's model by considering that the turbulent flame zone was

also a PSR, yielding the following formula [170]:

$$\dot{m}_{LBO} = \left(\frac{A f_{PZ}}{V_{PZ}^{1+x}} \right) \left(\frac{\dot{m}_a^{1+x}}{P_3^{(1+nx)} \exp(xT_3/b)} \right) \left(\frac{d_0^2}{\lambda_{eff} LHV} \right) \quad (2.8)$$

with \dot{m}_{LBO} the mass flow rate at LBO, f_{PZ} the fraction of air employed in the primary-zone of the combustor, V_{PZ} the primary zone volume, P_3 and T_3 the injection pressure and temperature, \dot{m}_a the air mass flow rate, d_0 the droplet diameter at injection, and λ_{eff} the effective evaporation constant, defined as:

$$\lambda_{eff} = \frac{8(k/cp)_g \ln(1 + B_M)(1 + 0.22Re_{d_0}^{0.5})}{\rho_F} \quad (2.9)$$

with k and cp the gaseous heat conductivity and capacity, B_M the Spalding mass number, Re_{d_0} the injection droplet Reynolds number, and ρ_F the liquid fuel density. A is a constant whose value depends on the geometry and mixing characteristics of the combustion zone measured experimentally, n is the reaction order, b and x are model constants. The most simple values that fit the experimental values are $x = 1$, $b = 1$ and $n = 0.3$.

Some works further improves this expression for several conditions, by optimising the constants n , x and b in the q_{LBO} expression [203] or by modifying the A constant to take into account temperature-dependency [7].

2.3.2 Numerical models

The **numerical** models attempt to predict and reproduce the LBO event, but also to understand the physico-chemical mechanisms responsible for the extinction of the flame. Such numerical simulations are costly and are realised with extreme care because of the transient nature of the phenomenon, making it not straightforward to set up.

Thanks to the advent of high computing power, LBO limits are now predicted through LES and URANS. Nevertheless, it is still not possible to reproduce the exact experimental procedure which lasts over a very long, not numerically affordable time. Therefore, assumptions have to be made to set up a numerical methodology giving access to LBO. Usually, the flame is first stabilised near the lean blow-out limit and the fuel mass flow rate is then slowly decreased to reach extinction.

Attempts to simulate LBO on bluff bodies and swirled flames are numerous in the literature. The first real 3D LES simulation of LBO was realised by Smith et al. [289] for a premixed flame stabilised on a V-gutter in 2007. The impact of the Von Karman vortex was analysed as expected to be significant, but, at the end, the study concluded the contrary. LES were also performed close to blow-out, particularly in [79], [80], [200] for a bluff body, where the use of a linear-eddy mixing was attempted to predict the correct amount of pollutants. It concludes that eddies larger than the LES grid resolution $\bar{\Delta}$ and lower than $4 - 5\bar{\Delta}$ are important for the local flame quenching.

In the case of swirl-stabilised flames, the correct description of the spray characteristics is very important for the good prediction of the LBO. Several studies such as Black et al. [22] and Kim et al. [148] used LES to predict the LBO with more or less accuracy. Those studies investigated the phenomena that influence the LBO, such as the eddy resolution and the injected droplet diameter distribution. Esclapez [83], [84] studied the impact of a conventional fuel and two alternative fuels in a realistic gas turbine combustor and found a good agreement with the experiment with 14% maximum of error. These results were confirmed by Piehl et al. [229] and Hasti et al. [120] who analysed the key markers of

the LBO, such as the oxidation of formaldehyde, and improved the tools for LBO analysis (temperature vs equivalence ratio scatter plot, LBO marker). Massey et al. [194] showed that heat loss effects was important for the flame approaching blow-off. However, none of these works proposed a generic methodology that could be applied to any combustion chamber. This was done recently by Nassini et al. [211], based on numerical and experimental results on gas turbine LBO. They suggest stabilising a flame near LBO and to gradually decrease the fuel flow rate in successive steps towards the LBO. This process however depends greatly on the flame timescale: a too long timescale makes the LBO computation not affordable.

2.3.3 Hybrid models

Hybrid models are models that combine the numerical and the semi-empirical approaches. They can be divided into two different classes:

- **the numerically-based model**, where semi-empirical criteria are applied to small volumes to see if LBO can occur locally or not. In the first type of hybrid modelling, the semi-empirical approach was PSR-based. Mongia et al. [202], [260], [261] was the first to propose such model, but the dependence on experimental works or other data limits its interest. Sturgess et al. [299], [300] proposed a model that first simulated a stable operating point, second post-processed the near blowout solution to build the reactor network and finally estimated the LBO limit with computational combustion dynamics (CCD) method. The characteristic time model was also used with the Damköhler number as a criterion for flame stability [67].
- **the semi-empirically-based model**, where semi-empirical models are used on the overall combustion chamber thanks to data from 3D numerical simulations. Flame Volume LBO model of Lefebvre [170] is often employed. In some studies, some parameters are extracted from non-reacting simulations to give an indication of the flame volume and then guessing the LBO. [128], [129]

To summarise, hybrid models based on numerical methods are much more costly and depend on other data, but give a better insight on what happens in the flow. On the contrary, hybrid models based on semi-empirical correlations are much more accurate without too much computational effort, but they give a single value for the whole combustion chamber and can not be used locally.

The method as well as the key indicators for the correct detection of the LBO of complex flames will be investigated in this PhD.

2.4 Organisation of the manuscript

Given the overall context, the numerical simulation of flames in aeronautical engines is important to better understand the key processes monitoring the flame shapes along with fuel or geometry changes. The flame structures are controlled by the interactions between the combustion, the turbulent flow as well as the liquid fuel evaporation, which are difficult to study individually in the experimental works but can be decoupled in the numerical works. With this in mind, this PhD project focuses on the modelling of alternative fuels in terms of surrogate fuel and chemical kinetics in order to study their behaviour compared to conventional kerosene in terms of flame stabilisation and lean blow-out phenomenon.

The Spray-Stabilised Burner (SSB) from the DLR [110], is used to investigate the impact of the fuel and the fuel modelling on the flame shape as well as the LBO. This manuscript is therefore divided into three main parts.

The first part recalls the theoretical basis of numerical combustion, as well as the various numerical tools that have been developed recently and that will be used. To start with, **Chapter 3** explains the principles of combustion. Introducing ARCANE [40] chemical reduction code, **Chapter 4** then details how chemistry is calculated, reduced and analysed at CERFACS, before being integrated in 3D combustion chambers. **Chapter 5** describes the liquid phase system of equations and explains the assumption made in the modelling of some source terms. Theoretical explanations end with the numerical simulation of turbulent flows, detailed in **Chapter 6**.

The second part presents analysis tools for the detailed study of simulation results. At first, in **Chapter 7**, the kinetic mechanisms needed to represent accurately the simulated conventional and alternative fuels are derived and investigated to explain the flames behaviour and the pollutants released by the combustion of complex multi-species fuels. Next, the spatial and temporal integration of chemistry is investigated. Second, **Chapter 8** underlines the impacting two-phase flow phenomena as well as the accuracy of the evaporation model compared to the experiment. A two-phase 1D premixed flame is computed for each considered fuel to investigate the effect of the preferential evaporation on the flame shape and pollutant emissions. Eventually, the impact of the spray on a counter-flow diffusion flame is investigated, to better understand some flame structures appearing in real burners. This chapter was published in [319],

The third part is dedicated to the computation of the 3D two-phase turbulent Spray-Stabilised Burner (SSB). **Chapter 9** first presents the configuration, the setup of the computation, from the geometrical information to the fully reactive flow. Results are compared to the experimental work of Grohmann [108] and validated on non-reacting, two-phase flow and thermal data. Two surrogate fuels, one with simple chemistry and the other with complex one, are compared in terms of time-averaged results and flame structure. As LBO data were available in the DLR experimental work, a strategy for the LBO is investigated, looking at the behaviour of the flame near extinction and the important flow variables to consider when looking at extinction. Finally, **Chapter 10** displays the kerosene and the two alternative fuels results and flame structure, enabling a greater understanding of the phenomena involved in the flame stabilisation process.

Part II

Fundamental equations for the resolution of two-phase turbulent reactive flows

Chapter 3

Reactive flows and combustion canonical cases

Contents

3.1	Definitions	30
3.1.1	The combustion reaction	30
3.1.2	Chemical kinetics	31
3.2	3D reactive flow modelling	35
3.2.1	Compressible multi-species flow equations	35
3.2.2	Transport and thermodynamic properties	37
3.2.3	The AVBP code	39
3.3	Combustion canonical cases	41
3.3.1	Final state: Equilibrium	41
3.3.2	0D unsteady cases: Reactors	43
3.3.3	1D steady cases: Flames	44

Combustion modelling has started in the 18th century, when Lavoisier discovered in 1772 that burning phosphorus in a cup over water under a bell made water more acid (creation of phosphorus acid). The reaction consumed 1/5 of the gaseous field [143] and he called this consumed gas 'oxygen', meaning 'who creates acid' in ancient Greek. The remaining part of the gas, i.e. nitrogen N_2 , was not able to allow small animals to breath, and therefore not useful for the combustion process. During the second half of the 18th century, discoveries on the atom weight as well as the different gases supported the Lavoisier theory, leading to the beginning of combustion science. Building blocks, namely flame dynamics, particle movement theory or thermodynamics, enabled the concept of laminar flame speed in the last half of the 19th century. Flame propagation and explosions were studied because of dangers occurring in coal mines, followed by the discovery of detonation. Chemical kinetics as well as turbulence studies appeared in the 20th century, leading to the numerical and experimental methods that exist today.

The aim of this section is to recall important concepts and modellings which are used for reactive flows. First, basic definitions of combustion and chemical kinetics are given in Section 3.1. Then, the 3D compressible Navier-Stokes equations which are the simulation bases of any reactive flow are recalled in Section 3.2. Finally, several helpful simple

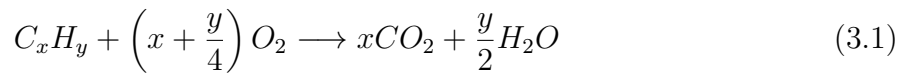
canonical cases directly derived from the system of conservation equations are detailed in Section 3.3.

3.1 Definitions

This section explains at first what is mathematically defined as a combustion reaction, in Section 3.1.1. In Section 3.1.2, basics of kinetic modelling are recalled, namely how species are converted into heat.

3.1.1 The combustion reaction

Combustion is the chemical reaction between a fuel and an oxidant, the two **reactants**, that produces heat (or exothermic). For pure hydrocarbons, the following balanced equation is given:



In other words, 1 mole of hydrocarbon (C_xH_y) reacts with $x + \frac{y}{4}$ moles of oxygen (O_2). Whatever the hydrocarbon used, the two main **products** are water (H_2O) and carbon dioxide (CO_2).

The hydrocarbon and oxidiser are said to be in **stoichiometric** conditions when their proportion match exactly the mass balance of Eq. 3.1. In such condition, there is theoretically no reactant left at the end of the combustion process. To measure the difference between the given mixture and the stoichiometric mixture, the **equivalence ratio**, involving the oxidant (O_x) and the fuel (F), is introduced as:

$$\phi = \frac{(X_F/X_{O_x})}{(X_F/X_{O_x})_{st}} = s_X \frac{X_F}{X_{O_x}} \quad (3.2)$$

with $s_X = (X_{O_x}/X_F)_{st} = \frac{\nu_{O_x}}{\nu_F} = x + \frac{y}{4}$, where ν_i is the stoichiometric coefficient of species i and X_i its molar fraction defined by:

$$X_i = n_i/n_{tot} \quad (3.3)$$

with n_i the molar quantity of species i and n_{tot} the total molar quantity. As well, the equivalence ratio can be defined with mass quantities:

$$\phi = \frac{(Y_F/Y_{O_x})}{(Y_F/Y_{O_x})_{st}} = s_Y \frac{Y_F}{Y_{O_x}} \quad (3.4)$$

with $s_Y = (Y_{O_x}/Y_F)_{st} = \frac{\nu_{O_x}W_{O_x}}{\nu_F W_F} = \frac{(x+\frac{y}{4})W_{O_x}}{xW_C+yW_H}$, where W_i is the molar mass and Y_i the mass fraction defined by:

$$Y_i = m_i/m_{tot} \quad (3.5)$$

with m_i the mass of species i and m_{tot} the total mass. The link between the mass fraction Y_i and the molar fraction X_i is then the following:

$$Y_i = \frac{X_i W_i}{W} \quad (3.6)$$

with the total molar mass W equal to:

$$\frac{1}{W} = \sum_i \frac{Y_i}{W_i} W = \sum_k X_k W_k \quad (3.7)$$

If the fuel and the oxidiser streams are injected separately, the **global equivalence ratio** ϕ_g [235] is written:

$$\phi_g = s_Y \frac{\dot{m}_F}{\dot{m}_{O_x}} \quad (3.8)$$

with \dot{m}_{O_x} the mass flow rate of the oxidiser stream and \dot{m}_F the fuel mass flow rate. This global equivalence ratio differs from the **local equivalence ratio** resulting from the mixing of both reactants. This local equivalence ratio may be computed from expressions 3.2 or 3.4 with local mole or mass fractions, but these expressions do not hold in the burnt gas. Instead, the local amounts of carbon, hydrogen and oxygen are used:

$$\phi_{loc} = \frac{2n_C + \frac{1}{2}n_H}{n_O} \quad (3.9)$$

with the molar quantity of atom k defined as:

$$n_k = a_{k,i} n_i \quad (3.10)$$

with n_i the molar quantity of species i and $a_{k,i}$ the number of atom k in species i .

The equivalence ratio is a key parameter in combustion. Indeed, burning **lean** (the fuel is in default) or **rich** (the fuel is in excess) changes the kinetics, which has an impact on macroscopic quantities. The next section provides the basics to understand chemical kinetics and their modelling.

3.1.2 Chemical kinetics

Chemical kinetics is the branch of chemistry or biochemistry that describes the chemical conversion pathways and the associated rates of reactions. **Reactions** are defined mathematically as:

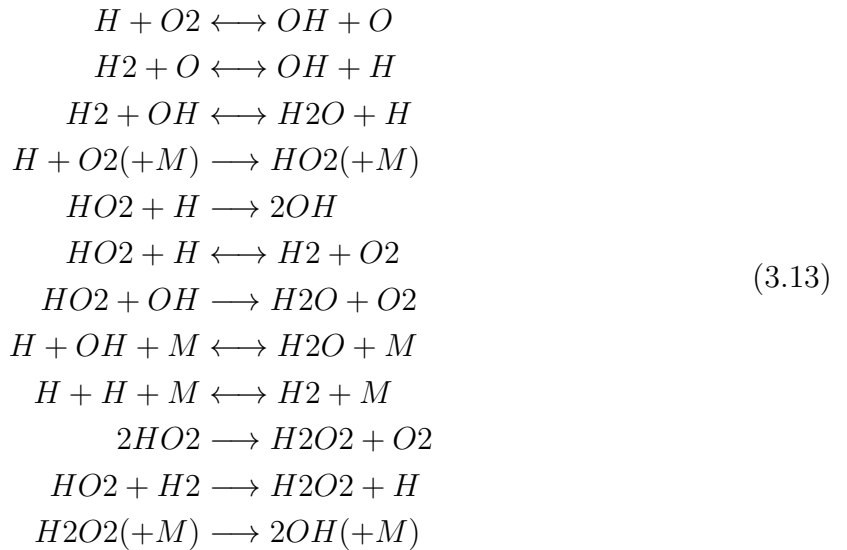


with S_i a species of the reaction, N'_s the number of **reactants**, N''_s the number of **products**, ν'_i the **stoichiometric coefficients** of the reactants and ν''_i the stoichiometric coefficients of the products.

The easiest way to describe a chemical process is to use a single reaction, called the **overall reaction** or **global reaction**, and summarising the main species conversion with a mass balance. For instance, the overall reaction between methane CH_4 and oxygen O_2 is the following:



However, most of the chemical processes involve up to tens to thousands of reactions, called **elementary reactions**, producing **intermediate species**. All those elementary reactions together are building a **chemical mechanism**. An example of such mechanism is given below for hydrogen [29]. It is a reduced mechanism describing the main steps of the overall conversion $H_2 + \frac{1}{2}O_2 \longrightarrow H_2O$:



The 4th reaction $H + O_2(+M) \longrightarrow HO_2(+M)$, as well as the overall reaction, are described with an \longrightarrow arrow sign, meaning that the reaction is **unidirectional**: only the **forward** reaction occurs, that is to say the conversion of H and O_2 in HO_2 . On the contrary, an **equilibrium**, as in reaction $H + O_2 \longleftrightarrow OH + O$, is described with an \longleftrightarrow arrow sign and the **reverse**, or **backward**, reaction can occur. The conversion of the reactants to products can therefore be incomplete, even if the reactants are inserted in stoichiometric proportions.

For a **forward reaction**, the forward **reaction rate** ω_j [$mol/m^3/s$] is defined as:

$$\omega_{forward,j}^{mol} = k_{forward,j} \prod_{i=1}^{N'_s} [S_i]^{order_i} \tag{3.14}$$

with $k_{forward,j}$ [S.I] the **forward rate constant** of reaction j , $[S_i]$ the **concentration** of species i and $order_i$ the **order of the species i in the reaction**. The unit of $k_{forward,j}$ depends on $order_i$, so that the unit of the reaction rate remains consistent. For elementary reactions, this order is equal to the stoichiometric coefficient of the given species in the reaction. This is especially the case for elementary reactions. For an equilibrium, the net reaction rate becomes:

$$\omega_{net,j}^{mol} = \omega_{forward,j}^{mol} - \omega_{backward,j}^{mol} = k_{forward,j} \prod_{i=1}^{N'_s} [S_i]^{order_i} - k_{backward,j} \prod_{i=1}^{N''_s} [S_i]^{order_i} \tag{3.15}$$

with $k_{backward,j}$ representing the **backward rate constant**, which characterises the reverse reaction rate. Since the net production rate is expected to be equal to zero at chemical equilibrium, forward and backward rate constants are linked by the **equilibrium constant** $K_{e,j}$, defined as:

$$K_{e,j} = \frac{k_{forward,j}}{k_{backward,j}} = \frac{\prod_{i=1}^{N''_s} [S_i]_{eq}^{\nu''_i}}{\prod_{i=1}^{N'_s} [S_i]_{eq}^{\nu'_i}} = \left(\frac{P_{atm}}{RT} \right)^{\sum_i (\nu''_i - \nu'_i)} \exp \left(\frac{T \Delta s_j^0 - \Delta h_j^0}{RT} \right) \tag{3.16}$$

with P_{atm} the atmospheric pressure, R the perfect gas constant, T the temperature, Δs_j^0 and Δh_j^0 the molar entropy and enthalpy changes through reaction j .

For simplicity, in the next sections the net reaction rate will be noted $\omega_j = \omega_{net,j}^{mol}$.

Different expressions can be taken for the rate constant k_j depending on the sensitivity of the given reaction to composition, temperature and pressure. These are described next.

Arrhenius and modified Arrhenius reaction rates

Consider an elementary reaction j written as:



The Arrhenius rate constant is defined as:

$$k_{forward,j} = A_j \exp\left(-\frac{E_{a,j}}{RT}\right) \quad (3.18)$$

with A_j the **pre-exponential factor** and $E_{a,j}$ the **activation energy**. The pre-exponential factor can be temperature-dependent, leading to a modified Arrhenius rate [159]:

$$k_{forward,j} = A_j T^{b_j} \exp\left(-\frac{E_{a,j}}{RT}\right) \quad (3.19)$$

with b_j the **temperature exponent**. This is the simplest way to express the rate constant with only three parameters: A , b and E_a . This rate is only temperature-dependent. Nevertheless, reaction rates may depend on other parameters, as described in the following paragraphs.

Three-body reactions

For some reactions, collisions of the reactant molecules with another molecule which is not modified by the reaction may give enough energy to enhance the conversion. This inert molecule called a **third-body** species is included in the reaction rate as:



with M being the inert third-body species. A general expression of the concentration of M writes $[M] = \sum_i \epsilon_i [S_i]$ with ϵ_i the collision efficiency of each species i , which is equal to one by default.

Fall-off reactions

A **fall-off reaction** is a pressure-dependent reaction, where three-body collisions only occur at low pressure. Two main expressions of the reaction constant are given in the literature:

- the **Lindemann** form [177] writes:

$$k_{forward,j}(T, P_r) = k_{HP,j} \left(\frac{P_r}{1 + P_r} \right) \quad (3.21)$$

with $P_r = k_{LP,j}[M]/k_{HP,j}$ and $k_{LP,j}$ and $k_{HP,j}$ defining respectively the low-pressure limit and high-pressure limit rate constants.

- the **Troe** form suggested by Gilbert et al. [102] writes:

$$k_{forward,j}(T, P_r) = k_\infty \left(\frac{P_r}{1 + P_r} F(T, P_r) \right) \quad (3.22)$$

with

$$\log_{10} F(T, P_r) = \frac{\log_{10} F_{cent}(T, P_r)}{1 + f_1^2}$$

$$F_{cent}(T) = (1 - A) \exp\left(-\frac{T}{T_3}\right) + A \exp\left(-\frac{T}{T_1}\right) + \exp\left(-\frac{T_2}{T}\right)$$

$$f_1 = \frac{(\log_{10} P_r + C)}{(N - 0.14 \log_{10} P_r + C)}$$

$$C = -0.4 - 0.67 \log_{10} F_{cent}$$

$$N = 0.75 - 1.27 \log_{10} F_{cent}$$

with T_1 , T_2 and T_3 and A which are fitted for a given molecule and bath gas.

Other expressions for the reaction rate exist, for surface reactions or other types of pressure-dependent reactions, but those are not considered in this work.

With the above definitions, the **net molar production rate** of species i $\dot{\omega}_{net,i}^{mol}$ [mol/m³/s] is defined as:

$$\dot{\omega}_{net,i}^{mol} = \frac{d[S_i]}{dt} = \sum_{j=1}^{N_R} \nu_{j,i} \omega_j \quad (3.23)$$

with N_R the number of reactions and $\nu_{j,i} = \nu'_{j,i} - \nu''_{j,i}$ the net stoichiometric coefficient of species i in reaction j . One can then detail the **species creation rate** and a **species destruction rate** defined as:

$$\dot{\omega}_{net,i}^{mol} = \dot{\omega}_{creation,i}^{mol} - \dot{\omega}_{destruction,i}^{mol} = \sum_{j=1}^{N_R} \nu'_{j,i} \omega_j - \sum_{j=1}^{N_R} \nu''_{j,i} \omega_j \quad (3.24)$$

In species mass conservation equations, the net mass production rate [kg/m³/s] is used:

$$\dot{\omega}_i = W_i \dot{\omega}_{net,i}^{mol} \quad (3.25)$$

From these quantities, the **volumetric heat release rate** HRR [J/m³/s] which defines the quantity of energy produced by the chemical conversion of a given mixture, is expressed as:

$$HRR = - \sum_{i=1}^{N_S} \dot{\omega}_i \Delta h_{f,i}^0 = - \sum_{j=1}^{N_R} \omega_j^{mol} \Delta h_j^{0,mol} \quad (3.26)$$

with $\Delta h_{f,i}^0$ [J/kg] the mass enthalpy of formation of species i . The heat of reaction $\Delta h_j^{0,mol}$ is linked to the species enthalpy of formation as:

$$\Delta h_j^{0,mol} = \sum_{i=1}^{N_S} \nu_{j,i} \Delta h_{f,i}^0 \quad (3.27)$$

In this work, a modified version of the open-source kinetic solver Cantera [103]¹ is used for computing thermochemistry in simple canonical cases used as reference solutions and for the analysis of complex chemical mechanisms.

¹Explanation on the differences with the initial version are available at <https://chemistry.cerfacs.fr>

3.2 3D reactive flow modelling

Fluid mechanics is the branch of physics that analyses the motion of fluids (gases or liquids). Two sub-fields come from this domain of study:

- **fluid statics** encompasses studies where the fluid is at equilibrium. This field of study appeared with Archimede and the concept of buoyancy [82], and is a milestone for hydrostatics and engineering for understanding fluids.
- **fluid dynamics** came later as a research field of study, because of its complexity. Starting from the experiments and observations of Da Vinci [133], several physicians have analysed the different effects of fluid mechanics, through the theorisation of inviscid (D'Alembert, Lagrange, Laplace, Poisson) and viscous flows (Poiseuille, Hagen), finally leading to the well-known Navier-Stokes equations in the first half of the 19th century, a fundamental milestone in the current fluid dynamic theory.

The unsteady flow equations are used in this work and discretized for numerical simulations with the CERFACS code AVBP [8]. Section 3.2.1 details the compressible reactive Navier-Stokes equations, incorporating the kinetics modelling of Section 3.1.2. Section 3.2.2 details the models for transport and thermodynamic properties. Finally, Section 3.2.3 presents the main features of the code AVBP.

3.2.1 Compressible multi-species flow equations

To compute the flow representing the motion of multiple species, macroscopic conservation equations were historically derived from the continuum mechanics theory, but they can also be found from Boltzmann equations without knowing the exact distribution functions [123]. Newton indexation is used to express 3D compressible Navier-Stokes equations for reactive flows:

$$\left\{ \begin{array}{l} \frac{\partial \rho}{\partial t} + \frac{\partial \rho u_i}{\partial x_i} = 0 \\ \frac{\partial \rho u_j}{\partial t} + \frac{\partial \rho u_i u_j}{\partial x_i} = -\frac{\partial P}{\partial x_j} + \frac{\partial \tau_{ij}}{\partial x_i} \\ \frac{\partial \rho Y_k}{\partial t} + \frac{\partial \rho u_i Y_k}{\partial x_i} = -\frac{\partial J_{k,i}}{\partial x_i} + \dot{\omega}_k \\ \frac{\partial \rho E}{\partial t} + \frac{\partial \rho u_i E}{\partial x_i} = -\frac{\partial q_i}{\partial x_i} - \frac{\partial u_i P \delta_{ij}}{\partial x_i} + \frac{\partial u_j \tau_{ij}}{\partial x_i} + HRR \end{array} \right. \quad (3.28)$$

with

$$\tau_{ij} = \mu \left(\frac{\partial u_i}{\partial x_j} + \frac{\partial u_j}{\partial x_i} \right) - \frac{2}{3} \mu \left(\frac{\partial u_k}{\partial x_k} \delta_{ij} \right) \quad (3.29)$$

$$J_{k,i} = \rho Y_k (V_{k,i} + V_i^c) \quad (3.30)$$

$$q_i = -\lambda \frac{\partial T}{\partial x_i} + \sum_k J_{k,i} h_k \quad (3.31)$$

defining the following variables:

- t the time and x_i the spatial coordinate in the i^{th} direction.
- ρ the density, P the pressure, u_j is the j^{th} component of the velocity, Y_k the mass fraction of the species k , E the total energy.
- HRR the heat release rate, $\dot{\omega}_k$ the net mass production rate of the species k , h_k the enthalpy of the species k .
- τ_{ij} the viscous stress tensor, $J_{k,i}$ the species diffusion flux, $V_{k,i}$ the Hirschfelder and Curtiss approximation of the diffusion velocity, V_i^c the correction velocity to keep the total mass constant and q_i the heat flux.
- $\delta_{i,j}$ the Kronecker symbol (1 if $i = j$ and 0 otherwise).
- λ the heat conduction coefficient, μ the dynamic viscosity.

In the above equations, several terms have been neglected:

- the Dufour effect, representing the diffusive energy flux associated to species gradients.
- the Soret effect, representing the diffusive species flux associated to temperature gradient.
- the volume viscosity.

The left-hand side of the equations corresponds to the derivative in time and the convective terms, while diffusive fluxes as well as sinks or sources are written on the right side. For a 3D flow with N_S species, the above system counts $1 + 3 + N_S$ independent equations for $2 + 3 + N_S$ unknowns (P , E , u_j , ρY_k). To close the system, the perfect gas equation of state is then added:

$$P = \rho r T \quad (3.32)$$

with $r = \frac{R}{W}$ the universal gas constant $R = 8.3143$ J/mol/K divided by the mean molecular weight W .

The **diffusion velocity** $V_{k,i}$ is computed using the **Hirschfelder and Curtiss approximation** [123]:

$$\rho Y_k V_{k,i} = -\rho D_k \frac{W_k}{W} \frac{\partial X_k}{\partial x_i} \quad (3.33)$$

with D_k the molecular diffusion coefficient of species k in the mixture. To ensure mass conservation, a correction velocity V_i^c is added:

$$V_i^c = \sum_{k=1}^{N_S} D_k \frac{W_k}{W} \frac{\partial X_k}{\partial x_i} \quad (3.34)$$

The transport properties D_k , μ and λ are detailed in Section 3.2.2.

3.2.2 Transport and thermodynamic properties

3.2.2.1 Transport coefficients

Three transport coefficients appear in the flow equations written in the previous section:

- the **species diffusion coefficient** D_k [m^2/s]
- the **thermal conductivity** λ [$W/m/K$].
- the **dynamic viscosity** μ [$Pa.s$].

The derivation of these parameters is directly taken from kinetic theory of gases, leading to collision integrals. This theory is described in detail in [123].

Species diffusion coefficient D_k

From the most complex to the simplest cases, diffusion coefficients are defined as follows:

- the **multi-species** or complex transport approach is the most accurate method, obeying the Stefan-Maxwell equations, but it is also the most time-consuming. The binary diffusion coefficients D_{kj} between species k and species j are computed from collision integrals, and require a matrix inversion. [123] that directly computes the diffusion fluxes without using the Hirschfelder and Curtiss approximation presented previously. This method is not used in this study.
- the **mix** transport, used for Cantera calculations, provides the best cost/accuracy trade-off as it enables the calculation of the diffusion coefficient of species k in the mixture $D_{k,mix}$ with the following approximation:

$$D_{k,mix} = \sum_k \frac{1 - Y_k}{\sum_{j \neq k} \frac{X_j}{D_{jk}}} \quad (3.35)$$

with

$$D_{kj} = \frac{3}{16} \frac{\sqrt{2\pi k_B^3 T^3 / m_{jk}}}{P \pi \sigma_{jk}^2 \Omega^{(1,1)*}} \quad (3.36)$$

with k_B the Boltzmann constant, $m_{jk} = m_j m_k / (m_j + m_k)$ the reduced mass based on the molecule mass m_k and m_j , σ_{jk} the cross-section of the collision, $\Omega^{(1,1)*}$ the collision integral associated to the mode (1,1) and P the pressure.

- the **simple** transport is based on a constant Schmidt number Sc_k for each species k , linked to the diffusion coefficient with the following relation:

$$D_k = \frac{\mu}{\rho Sc_k} \quad (3.37)$$

In reality, all Schmidt numbers vary through a flame and the question arises of the best representative values. In practice, they are usually taken in the unburnt gases of a 1D lean premixed flame. The associated error is monitored by comparison with complex transport calculations with Cantera.

Thermal conductivity λ

Similarly to molecular diffusion, thermal conductivity may be calculated in two ways:

- in the **mix** transport used by Cantera, the conductivity is approximated from a mixing formula [123]:

$$\lambda = \frac{1}{2} \left(\sum_k X_k \lambda_k + \frac{1}{\sum_k \frac{X_k}{\lambda_k}} \right) \quad (3.38)$$

with

$$\lambda_k = \frac{\mu_k}{W_k} (f_{trans} C_{v,trans} + f_{rot} C_{v,rot} + f_{vib} C_{v,vib}) \quad (3.39)$$

where the individual species heat conductivities λ_k are assumed to depend on a rotational, translational and vibrational pars. The molar heat capacities C_v depend on the shape of the considered molecule (one or several atoms, linear or non-linear arrangement, etc. . .) and f are dimensionless functions quantifying the influence of the rotational, translational and vibrational degrees of freedom, detailed in [228].

- for the **simple** transport, the conductivity is based on a constant Prandtl number, which takes the following expression:

$$\lambda = \frac{\mu C_p}{Pr} \quad (3.40)$$

with μ the dynamic mixture viscosity, C_p the mixture heat conductivity and Pr the Prandtl number.

As for the diffusion coefficients, the error of this approximation is small and, in most cases considered in this work, it is not worth to calculate all λ_k at all points in the mesh.

Dynamic viscosity μ

Various formulations also exist for the dynamic viscosity:

- for **complex** transport used in Cantera, the viscosity is approximated via the **Wilke formula** [318]:

$$\mu = \sum_k \frac{X_k \mu_k}{\sum_j X_j \phi_{kj}} \quad (3.41)$$

with

$$\mu_k = \frac{5}{16} \frac{\sqrt{(\pi m_k k_B T)}}{\pi \sigma_k^2 \Omega^{(2,2)*}} \quad (3.42)$$

and

$$\phi_{kj} = \frac{1}{\sqrt{8}} \left(1 + \frac{W_k}{W_j} \right)^{-\frac{1}{2}} \left(1 + \left(\frac{\mu_k}{\mu_j} \right)^{-\frac{1}{2}} \left(\frac{W_j}{W_k} \right)^{\frac{1}{4}} \right)^2 \quad (3.43)$$

with σ_k the species collision diameter and $\Omega^{(2,2)*}$ the collision integral associated to the mode (2,2).

- for **simple** transport, the viscosity coefficient is a function of the temperature, either via the Sutherland law:

$$\mu = \mu_0 \left(\frac{T}{T_0} \right)^{\frac{3}{2}} \frac{T_0 + S}{T + S} \quad (3.44)$$

or via a power law:

$$\mu = \mu_0 \left(\frac{T}{T_0} \right)^{\beta} \quad (3.45)$$

with μ_0 the reference viscosity at the reference temperature T_0 , and β a constant fitted for each mixture.

In this work, the power law is used, as it is well validated for the considered range of temperature and requires fewer inputs.

3.2.2.2 Thermodynamics

Thermodynamic parameters are written in the form of NASA-7 polynomials, defined as follows:

$$\begin{aligned} \frac{C_{p,k}}{R} &= a_1 + a_2 T + a_3 T^2 + a_4 T^3 + a_5 T^4 \\ \frac{h_k}{RT} &= a_1 + a_2 \frac{T}{2} + a_3 \frac{T^2}{3} + a_4 \frac{T^3}{4} + a_5 \frac{T^4}{5} + a_6 \frac{1}{T} \\ \frac{s_k}{R} &= a_1 \ln(T) + a_2 T + a_3 \frac{T^2}{2} + a_4 \frac{T^3}{3} + a_5 \frac{T^4}{4} + a_7 \end{aligned}$$

with a_i the 7 NASA coefficients, given for low (below 1000 K) and high (above 1000 K) temperature ranges. The data come from NIST-JANAF database [191].

In Cantera, as in most chemistry codes, the temperature at standard conditions is 25°C, i.e., 298K. This is different in AVBP, where the reference temperature is at 0K. Indeed, this makes it easier to compute cold flows below 25 °C, which occur in many applications. This has a direct consequence on the definition of the formation enthalpy. In Cantera, this quantity corresponds to the enthalpy at 298K, $\Delta h_{f,k}^0 = h_k(298)$, whereas in AVBP, it is simply $\Delta h_{f,k}^0 = Ra_6$.

3.2.3 The AVBP code

The in-house CERFACS code AVBP solves the 3D, fully compressible, multi-species conservation equations in the DNS (Direct Numerical Simulation) or LES (Large-Eddy Simulation, see Chapter 6) modes. The code is massively parallel, using CPU and GPU architectures, and runs on unstructured meshes. It has been widely used for simulating combustion chambers and other configurations such as turbo-machinery, but also pollutant dispersion, explosions, virus exposition in transport, or even atmospheric flows for solar or wind farms.

3.2.3.1 Numerical schemes

To predict accurately the flow behaviour, accurate temporal and convective modelling need to be implemented into the solver. More details on the schemes in AVBP are provided in [160] and are briefly recalled here:

- **The Lax-Wendroff scheme (LW)** [163] is a finite volume centred scheme of order 2 in space and time. The time integration is realised with an explicit single step. It is the cheapest scheme available in AVBP and thus usually employed when starting a simulation or when the simulation size is high.
- **The Two-step Taylor Galerkin C scheme (TTGC)** [51] is a finite element centred scheme of order 3 in space and time. The time integration is realised in two steps. It is on average 2.5 times more costly than the LW scheme, but shows better dispersion and dissipation properties.

The diffusion scheme is a finite element method of order 2. The time-step of each iteration is determined as the minimum of three different time-steps:

$$\Delta t = \min(\Delta t^i, \Delta t^v, \Delta t^{\dot{\omega}_k}) \quad (3.46)$$

with Δt^i the time-step based on the user-defined CFL number, Δt^v the time-step based on the user-defined Fourier number and $\Delta t^{\dot{\omega}_k}$ the time-step based on the local evaluation of the chemical time-step.

AVBP uses simple transport and thermodynamic properties as defined in the previous section. It is able to directly compute chemistry with explicit or semi-implicit [24], [134] time integration.

3.2.3.2 Artificial viscosity

As both numerical schemes LW and TTGC are spatially centred, they are low-diffusive but wiggles (point-to-point oscillations) may be created when gradients are too stiff. Therefore, an artificial viscosity model is added to limit spurious fluctuations. Two terms are added:

- A 2nd order viscosity term, preserving linearity in strong gradient zones.
- A 4th order viscosity term, destroying the node-to-node and chequerboard oscillations.

The terms are applied directly to the residuals of the conservation equations. To avoid over-dissipation in non-stiff zones, a sensor is applied to detect where artificial viscosity should be used. In this work, the ‘‘Colin’’ sensor [52] is always used. It is an evolution of the Jameson sensor to take into account sharp gradients of density and species.

3.2.3.3 Boundary conditions

The NSCBC (Navier-Stokes Characteristic Boundary Conditions) conditions [234] are applied to control the waves crossing the boundaries.

Several wall conditions exist in AVBP to correctly model on the one hand the heat losses, which are applied to the energy equation through a source term Q_{loss} and on the other hand the dynamic fluxes:

- the **adiabatic condition**: no heat loss at the wall, $Q_{loss} = 0$.
- the **flux condition**: a user-defined heat loss Q_{ref} is given as an input: $Q_{loss} = Q_{ref}$.

- the **relaxation condition**: a reference temperature T_{ref} is set at the boundary condition and the flux takes the following expression:

$$Q_{loss} = -\frac{K\rho C_p(T_{wall} - T_{ref})}{\Delta t} \quad (3.47)$$

where the relaxation coefficient K is set between 0 and 1 (0 for an adiabatic wall and 1 for an isothermal wall).

- the **resistance condition**: a thermal resistance R_w is applied to the wall at a given temperature and the flux takes the following expression:

$$Q_{loss} = -\frac{T_{wall} - T_{ref}}{R_{wall}} \quad (3.48)$$

- the **wall-law condition**: when the discretisation does not enable to resolve the boundary layer near the wall, a wall-law is used to correctly predict the velocity profile near the wall. The standard log-law is used, which writes:

$$u^+ = \frac{1}{k} \ln(Ey^+) \quad (3.49)$$

with $k = 0.41$ and $E = 9.2$. In the above equation, quantities are expressed in wall units: the velocity is non-dimensionalised with $u_{tau} = \sqrt{\tau_w/\rho_w}$ and the wall distance with u_{tau}/ν_w . Other wall laws exist in AVBP, but only the above log-law will be applied to the flow in this work.

3.3 Combustion canonical cases

Canonical cases are useful to understand combustion basics and validate some parts of the code. They are 0D or 1D simple laminar cases, steady or unsteady, and allow calculating important flame characteristics that are useful for the 3D turbulent complex case. The selected cases presented here are those used later in this manuscript, namely:

- **chemical equilibrium**, detailed in Section 3.3.1.
- **time-evolving 0D reactors**, characterised in Section 3.3.2.
- **1D flames**, defined in Section 3.3.3: the premixed flame, the non-premixed flame and methods to distinguish them in a 3D combustor.

The kinetic solver Cantera is able to compute these simple cases with a fast iterative numerical method. For this reason, Cantera is also used as a pre- and post-processing tool for AVBP.

3.3.1 Final state: Equilibrium

Like any thermodynamic process, chemical **equilibrium** corresponds to a **minimum of energy**. In thermochemistry, this is expressed with the **Gibbs free energy**, defined as:

$$G = H - TS = U + PV - TS \quad (3.50)$$

with H the total enthalpy of the system and S the total entropy. Taking the total derivative of G as function of the independent variables P, T, N_i with N_i the mole number of species i , chemical equilibrium corresponds to:

$$dG = VdP - SdT + \sum_i \hat{\mu}_i dN_i = 0 \quad (3.51)$$

with $\hat{\mu}_i$ the **chemical potential** of the species i , and defined for perfect gases as:

$$\hat{\mu}_i = \hat{\mu}_i^0 + RT \ln(X_i) \quad (3.52)$$

with $\hat{\mu}_i^0$ the chemical potential at reference pressure P^0 and temperature T^0 . Writing $dN_i = \nu_i d\xi$, with ξ the progress variable of the chemical evolution, the quantity $\Delta_r G$ is introduced as:

$$\Delta_r G d\xi = \sum_i \hat{\mu}_i dN_i \quad \text{so that} \quad \Delta_r G = \sum_i \nu_i \hat{\mu}_i \quad (3.53)$$

Chemical equilibrium may then be calculated in various conditions:

- at constant T and P , chemical equilibrium which corresponds to $dG = 0$ whatever the chemical path, i.e, whatever $d\xi$, is expressed as:

$$\Delta_r G = \sum_i \nu_i \hat{\mu}_i^0 + RT \sum_i \nu_i \ln(X_i) = \Delta_r G^0 + RT \ln\left(\prod_i (X_i)^{\nu_i}\right) = 0 \quad (3.54)$$

As a consequence, with an optimisation algorithm (Lagrangian multiplier for Cantera solver), the molar fractions at equilibrium can be deduced. An example is shown in Table 3.1, giving the equilibrium composition of a stoichiometric methane-air mixture at 300K and 1 bar. The chemical system contains the 53 species of the GRI-Mech 3.0 mechanism [106].

State	T [K]	P [bar]	Y_{CH_4}	Y_{O_2}	Y_{CO_2}	Y_{H_2O}	Y_{N_2}	Others
Initial state	300	1.0	0.055	0.22	0	0	0.725	0
Final state	300	1.0	0	0	0.124	0.151	0.725	0

Table 3.1: Equilibrium at fixed pressure and temperature of a methane -air mixture at $\phi = 1.0$.

The imposed temperature and pressure remain unchanged, and the composition changes from a pure methane-air mixture to products. Note that due to the fixed low temperature, no other species than the main products appear. This final composition corresponds to the lowest Gibbs energy at this temperature and pressure and the considered set of species.

Chemical equilibrium at fixed temperature and pressure may be used for two purposes:

1. to know if the local composition in a given configuration has reached equilibrium.
2. to calculate the **Lower Heating Value** (LHV), namely the amount of energy released by the consumption of one kilogram of fuel, by subtracting the enthalpy

of the $T - P$ equilibrium mixture to the enthalpy of the initial mixture. The final temperature of the mixture at equilibrium may be estimated as:

$$T_{eq} = T_0 + \frac{LHV Y_{F,0}}{C_p} = \frac{LHV \phi Y_{O,0}}{s_Y C_p} \quad (3.55)$$

with T_0 the initial temperature, T_{eq} the equilibrium temperature, $Y_{F,0}$ the initial fuel mass fraction, $Y_{O,0}$ the initial oxygen mass fraction. The heat capacity C_p was considered constant in the above expression, which therefore gives only an approximate value of T_{eq} .

- at constant enthalpy H and pressure P , the chemical equilibrium reaches the final burnt gas state of an adiabatic flame. This calculation is very useful to know precisely the equilibrium temperature and composition of a given mixture after the combustion process occurs. An example of such calculation is given in Table 3.2.

State	T [K]	P [bar]	Y_{CH_4}	Y_{O_2}	Y_{CO_2}	Y_{H_2O}	Y_{N_2}	Others
Initial state	300	1.0	0.055	0.22	0	0	0.725	0
Final state	2225	1.0	0	0.005	0.137	0.120	0.724	0.05

Table 3.2: Equilibrium at fixed pressure and enthalpy for a methane-air mixture at $\phi = 1.0$.

The temperature, called the **adiabatic flame temperature** T_{ad} , has increased to 2225 K. The composition is very much different from the previous equilibrium at fixed T and includes other species (denoted "Others" in the table) such as OH or NO which remain in the final mixture.

The adiabatic flame temperature is the maximum final temperature that can be reached from the combustion of a given initial mixture, pressure and temperature.

The chemical equilibrium corresponds to a final state. It does not depend on the chemical mechanism, but only on the thermodynamics of the considered set of species. To go further in combustion analysis, a first step is to introduce time evolution via chemical kinetics.

3.3.2 0D unsteady cases: Reactors

Reactors are defined as homogeneous mixtures in a control volume V . Variables non-dimensionalised with their maximum absolute values have the superscript $*$.

The mass flow rate $\dot{m}_{in} = \dot{m}_{out}$ determines the residence time inside the reactor. All species, i.e., reactants, products and intermediate species are supposed to be well mixed all times, that is to say that the mixture is the same everywhere.

The total mass m , species mass fraction Y_k , volume V and energy (either T the temperature, U the total internal energy or H the total enthalpy, depending on the case studied) conservation equations represent the evolution of the reactor. The equations for the ideal batch reactor without heat transfer through the wall are the following [145]:

$$\begin{cases} \frac{\partial(Y_k)}{\partial t} = \frac{\dot{\omega}_k}{\rho} \\ \rho c_v \frac{\partial T}{\partial t} = - \sum_{i=1}^{N_S} u_i \dot{\omega}_i \end{cases} \quad (3.56)$$

$$\begin{cases} \frac{\partial(Y_k)}{\partial t} = \frac{\dot{\omega}_k}{\rho} \\ \rho c_p \frac{\partial T}{\partial t} = - \sum_{i=1}^{N_S} h_i \dot{\omega}_i \end{cases} \quad (3.57)$$

for constant volume.
with:

for constant pressure.

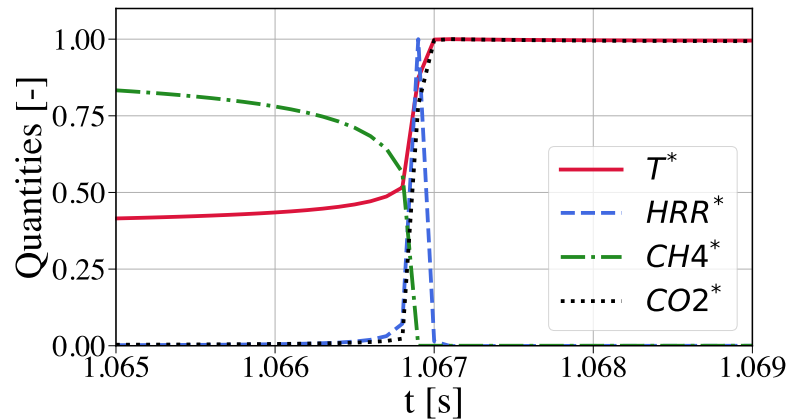


Figure 3.1: Dimensionless time-evolution profiles of an ideal gas reactor.

- $\dot{\omega}_k$ the source term of species k
- e_k and h_k the specific internal energy and enthalpy of the species k .

The energy equation can be further simplified by considering the use of the perfect gas law or a constant pressure, for instance. These equations are solved using Cantera with a time-stepping method.

After sufficient time, the mixture in the reactor ignites, allowing to determine the **auto-ignition delay** or **auto-ignition time**, which is one characteristic parameter of the chemical behaviour of a mixture. This quantity is arbitrarily defined as the time when the heat release rate is maximum in the reactor. An example is given on Fig. 3.1(right) with an auto-ignition time of 1.067 s, corresponding to the peak of HRR. The temperature increases while the fuel is consumed through the combustion reactions. The HRR profile might take more complicated shapes at higher initial temperature, but in this work the initial temperature, chosen in accordance with the target applications, always stays in the range giving a single HRR peak. The auto-ignition delay should be compared with the flow timescales in a real combustor, to assess its capability to sustain a stable flame. A too low injection temperature is tantamount to a long ignition time, which can prevent a flame from stabilising.

In this manuscript, constant volume reactors are used to analyse and reduce kinetic mechanisms, allowing to directly compare the results to measurements in shock tubes and rapid compression machines [226]. Other types of reactors exist such as the Continuously Stirred Tank Reactor (CSTR) also called Perfectly Stirred Reactors (PSR). Plug Flow Reactors PFR which may be arranged in a network to represent a complex reactive flow.

Overall, reactors allow characterising the reactivity of a fuel, which is crucial for explaining the observed flame shapes in complex configurations. However, as 0D time-dependent models, reactors do not describe flames.

3.3.3 1D steady cases: Flames

One-dimensional configurations allow understanding the structure of the flame and help the analysis of 3D complex calculations. The most simple configurations are the steady premixed flame and the steady counterflow diffusion flame, detailed in this section. More complex cases which can still be formulated in a 1D or pseudo-1D problem are for instance the impinging jet flame or the counterflow premixed flame, but are not studied in this

work. **Premixed flame** and the **counter-flow diffusion flame** designs, are described because they are used in the following chapters.

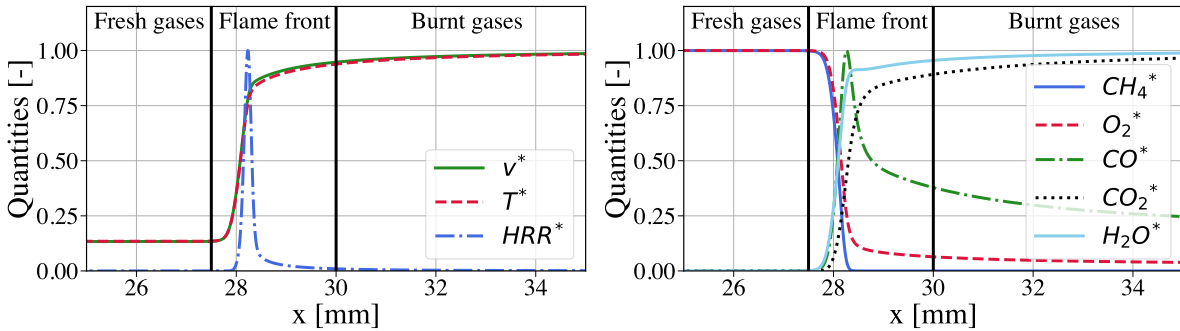
3.3.3.1 Premixed flames

In a **premixed flame**, the oxidiser and the fuel are mixed together before burning. As a consequence, such a flame is largely driven by chemistry and rates of reactions. Premixed flames are important for the analysis of the combustion process. First, direct comparisons are available with the experiments to assess the thermochemical flame structure. Second, most burners operate majorly in premixed mode because it is optimum for many technical reasons.

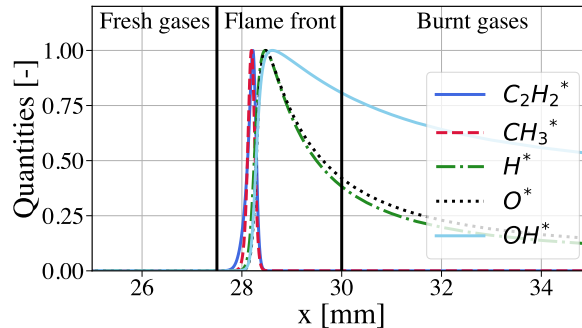
The system of conservation equations for a 1D premixed flame reduce to:

$$\left\{ \begin{array}{l} \frac{\partial \rho u}{\partial x} = 0 \\ \rho u \frac{\partial u}{\partial x} = -\frac{\partial P}{\partial x} \\ \frac{\partial \rho u Y_k}{\partial x} = -\frac{\partial J_k}{\partial x} + \dot{\omega}_k \\ \rho u C_p \frac{\partial T}{\partial x} = \frac{\partial}{\partial x} \left(\lambda \frac{\partial T}{\partial x} \right) - \frac{\partial T}{\partial x} \left(\sum_k C_{p,k} J_k \right) + HRR \end{array} \right. \quad (3.58)$$

An example is given in Fig. 3.2 showing some of the quantities representing the flame structure.



(a) Temperature, heat release rate and velocity. (b) CO , CO_2 , H_2O , O_2 and CH_4 mass fractions.



(c) C_2H_2 , OH , H , O and CH_3 mass fractions.

Figure 3.2: Dimensionless profiles for a 1D stoichiometric methane-air premixed flame.

A premixed flame can be separated in three zones:

- the **pre-heat zone** is characterised by a cold temperature and the absence of chemical reactions.
- the **flame front** is where the combustion occurs. The heat release rate is highest, the temperature rises sharply and reactants are transformed into products. Most of the intermediate species are found here. This zone is defined by the **flame thickness**, which can be calculated in three different ways:
 - the **thermal thickness** is the thickness of the temperature profile:

$$\delta_l^{th} = \frac{T_2 - T_1}{\max(|\frac{\partial T}{\partial x}|)} \quad (3.59)$$

with T_1 the temperature of the unburnt gases and T_2 the temperature of the burnt gases.

- the **Blint thickness** is an analytical expression for the thermal thickness, proposed by Blint [26]:

$$\delta_l^b = 2 \frac{D_{th}^1}{s_L} \left(\frac{T_2}{T_1} \right)^{0.7} \quad (3.60)$$

The Blint thickness is approximate but found very close to the thermal thickness.

- the **reaction thickness** is the thickness of the reaction zone. It is not easy to predict exactly, and the following correlation is used:

$$\delta_r = \frac{\delta_L^{th}}{0.5Ze} \quad (3.61)$$

with Ze the Zeldovich number, calculated as $Ze = \frac{E_a}{R} \frac{T_2 - T_1}{T_2^2}$. The above expression derives from a one-step chemistry solution.

- the **post-flame zone** is located after the flame front and is constituted of nearly non-reactive burnt gases, even though slow reactions are still occurring in this zone. At the far end, the temperature eventually reaches the equilibrium temperature.

Other definitions of the flame thickness may be useful to analyse accurately some key variables:

- the **HRR thickness**, as defined in [266], can be estimated as:

$$\delta^{HRR} = 2 \sqrt{\frac{-2HRR}{\partial^2 HRR / \partial x_i^2}} \quad (3.62)$$

- the **forward and backward reaction thicknesses** are estimated with a similar formula:

$$\begin{aligned} \delta^{\omega_j^{forward}} &= 2 \sqrt{\frac{-2|\omega_j^{forward}|}{|\partial^2 \omega_j^{forward} / \partial x_i^2|}}, j \in [1, N_{forward}] \\ \delta^{|\omega_j^{backward}|} &= 2 \sqrt{\frac{-2\omega_j^{backward}}{|\partial^2 \omega_j^{backward} / \partial x_i^2|}}, j \in [1, N_{backward}] \end{aligned} \quad (3.63)$$

The three main zones of the premixed flame explain the mechanisms that maintain the flame front: the unburnt gas arriving at the front are heated up by the burnt hot gases through a diffusion process, allowing them to reach the ignition temperature and burn, producing the heat to maintain the burnt gas temperature.

A key property of the premixed flame is the **laminar flame speed** s_L , defined as the speed at which the flame is propagating in a fresh gas mixture. If the reactants are injected at the laminar flame speed at the inlet of the domain, the flame therefore stays stationary and the problem becomes steady. The laminar flame speed can be calculated as follows:

- from the 1D species equations, the integrated fuel species source term gives the laminar flame speed:

$$s_L = -\frac{1}{\rho_1(Y_F^1 - Y_F^2)} \int_{-\infty}^{\infty} \dot{\omega}_F dx \quad (3.64)$$

with ρ_1 the fresh gas density, $\dot{\omega}_F$ the fuel source term and Y_F^1 and Y_F^2 the fuel mass fraction in the fresh and burnt gas, respectively.

- as well, from the 1D energy equation, the integrated heat release rate is also linked to the laminar flame speed:

$$s_L = -\frac{1}{\rho_1(C_{p2}T_2 - C_{p1}T_1)} \int_{-\infty}^{\infty} HRR dx \quad (3.65)$$

with C_{p1} and C_{p2} the heat capacity, T_1 and T_2 the temperature in the fresh and burnt gas, respectively.

The laminar flame speed calculated through the fuel source term is exact for a complex chemistry and gives very precise results. On the contrary, the laminar flame speed calculated with the heat release rate is less accurate because the heat coefficient is varying in the flame, and therefore some errors might occur.

In Cantera, as the flame is in a steady-state by construction, the value at the entry of the domain u_1 may be used directly to estimate the laminar flame speed:

$$s_L = u_1 \quad (3.66)$$

Those quantities (s_L and δ) are important for analysing a real combustor as:

- the mesh is often built with respect to the number of points in the flame front, then the knowledge of δ is useful.
- the speed at which the reactants are burnt drives the flame shape and the interaction of the flame with the turbulence.

Note that the laminar flame speed also changes with stretch induced by the flow, either strain or curvature applied to the flame front.

In a more pragmatic outlook, 1D premixed flames are used to ensure the proper integration of the chemistry in AVBP, by comparison with reference results from Cantera. Moreover, some premixed flame properties are input parameters for the thickened flame model (see Section 6).

3.3.3.2 Non-premixed flames

Contrary to a premixed flame, in a **non-premixed** or **diffusion** flame, the oxidiser and the fuel are not mixed together before burning. Another difference with premixed flame is that a diffusion flame does not have a steady structure without a flow, and the canonical case uses a counterflow configuration to stabilise the diffusion flame. For such flames, both reactant mixing and chemical reactions occur simultaneously.

In real systems, pure diffusion flames are not common and require very fast combustion to prevent premixing. This is the case for example in rocket engines, where the oxidiser is pure oxygen. However, diffusion flames may be locally encountered in 3D burners with secondary air injection. Spray flames also often lead to local diffusion flame fronts.

Although the counterflow configuration is not 1D, a pseudo-1D solution along the symmetry axis x can be derived, where the velocity in the transverse direction is calculated from the axial velocity through the divergence-free condition. Noting $v(x, r) = rV(x)$, and assuming temperature and mass fractions r -derivatives to be 0 on the axis, as well as a constant radial pressure gradient, the pseudo-1D equations, resolved in Cantera for example, are [145]:

$$\left\{ \begin{array}{l} \frac{\partial \rho u}{\partial x} + 2\rho V = 0 \\ \rho u \frac{\partial V}{\partial x} + \rho V^2 = -P + \frac{\partial}{\partial x} \left(\mu \frac{\partial V}{\partial x} \right) \\ \rho u \frac{\partial Y_k}{\partial x} = -\frac{\partial J_k}{\partial x} + \dot{\omega}_k \\ \rho u C_p \frac{\partial T}{\partial x} = \frac{\partial}{\partial x} \left(\lambda \frac{\partial T}{\partial x} \right) - \frac{\partial T}{\partial x} \left(\sum_k C_{p,k} J_k \right) + HRR \end{array} \right. \quad (3.67)$$

If $V = 0$, the same 1D system than for the premixed flame is recovered. The structure of such a flame is shown in Fig. 3.3 and comprises three different zones:

- the **fuel injection zone**.
- the **oxidiser injection zone**.
- the **flame front**, located at stoichiometry.

The flame maximum temperature is not obviously the equilibrium temperature, as the mixing is not perfect.

The **stagnation plane**, where the velocity is 0, is in general at a different location than the stoichiometric line, i.e., the flame. According to the global equivalence ratio and the dilution of both streams, this plane may be shifted toward the oxidiser side or the fuel side. In the case of Fig. 3.3, the global equivalence ratio is 1, but the diluted oxidiser in the air stream attracts the flame on the air side. As mixing occurs inside this flame, the flame thickness is an outcome of the flame solution, depending on the flow, and not a flame property as in premixed flames. As well, because the diffusion flame front does not propagate, there is no laminar flame speed. To characterise a diffusion flame, other quantities may be used:

1. the **strain rate** is a key element as it drives the diffusion flame thickness. It is defined as the velocity gradient along the flame front, i.e., along the stoichiometric

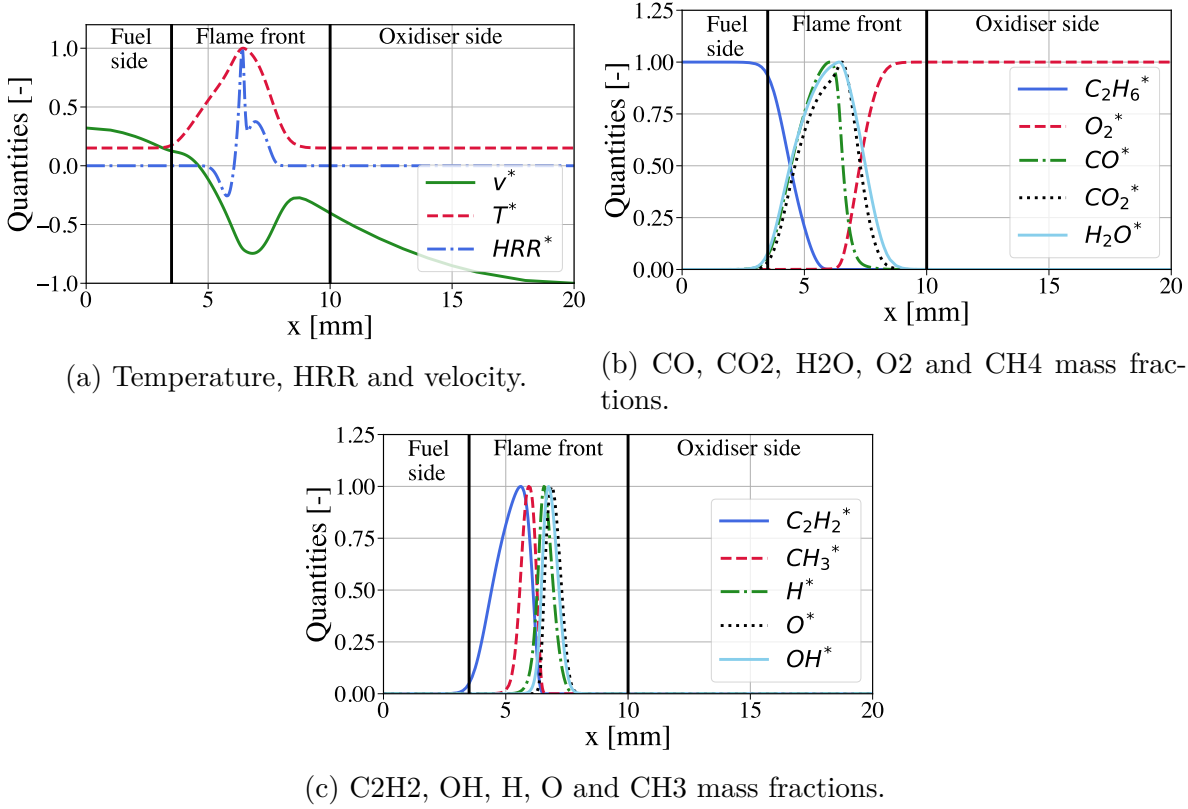


Figure 3.3: Dimensionless profiles for a 1D counterflow diffusion methane-air flame.

line. In the counterflow configuration, it can be approximated as:

$$a = \frac{u_O + u_F}{L} \quad (3.68)$$

with u_O and u_F the oxidiser and fuel injection velocities, respectively, and L the distance between the oxidiser and the fuel injections.

The strain rate quantifies "how hard the fuel and the oxidiser are brought together to burn". There exists a maximum strain rate at which the flame quenches, when the reactant fluxes toward the flame are too high to be fully consumed.

- the **mixture fraction** represents the amount of fuel and oxidiser that would be mixed without burning at a specific location. A classical definition of this quantity is given by:

$$z_{base} = \frac{s_Y Y_F - Y_O + Y_O^0}{s_Y Y_F^0 + Y_O^0} \quad (3.69)$$

with Y_F^0 and Y_O^0 the fuel and oxidiser mass fractions in their respective streams. The mixture fraction is by construction a passive scalar (see [235] for the demonstration) and is equal to 1 in pure fuel and to 0 in pure oxidiser. The mixture fraction can also be computed from the atomic balance, as proposed by Bilger [19]. Here, the formulation is given including C, H and O atoms:

$$z_{Bilger} = \frac{2n_C + \frac{1}{2}n_H - n_O + n_O^0}{2n_C^0 + \frac{1}{2}n_H^0 + n_O^0} \quad (3.70)$$

which can be rewritten as:

$$z_{Bilger} = \frac{\beta - \beta_O}{\beta_F - \beta_O} \quad (3.71)$$

with $\beta = \sum_{i,k} \gamma_i a_{ki} Y_k W_i / W_k$ with a_{ki} the number of atoms i in species k , and γ_i the coefficient for atom i in the balance equation (2 for atom C, 1/2 for atom H and -1 for atom O). In this work, the Bilger definition will be used and simply noted $z = z_{Bilger}$.

The mixture fraction can be interpreted as a local equivalence ratio, as both quantities are directly related:

$$\phi_{loc} = \frac{\frac{z}{1-z}}{\frac{z_{st}}{1-z_{st}}} \quad (3.72)$$

with z_{st} the mixture fraction at stoichiometry.

A change of variable $(x, t) \rightarrow (z, t)$ leads to the flamelet equations, where transport terms have disappeared (meaning that all quantities are transported like z). The flamelet equations are therefore much simpler than the conservation equations, and may be preferred for numerical integration. This was implemented in Cantera, allowing faster and more robust computations. One advantage of solving the equations in the z -space is a better discretisation of the flame zone, which spans over the whole domain. For unity Lewis numbers and constant C_p , the flamelet equations write [231]:

$$\left\{ \begin{array}{l} \frac{\rho\chi}{2} \frac{\partial^2 Y_i}{\partial z^2} = \dot{\omega}_i \\ \rho C_p \frac{\chi}{2} \frac{\partial^2 T}{\partial z^2} = HRR \end{array} \right. \quad (3.73)$$

with the scalar dissipation rate [s^{-1}]

$$\chi = 2D \left(\frac{\partial z}{\partial x} \right)^2 \quad (3.74)$$

More complex expressions may be derived for non-unity Lewis numbers and variable C_p , and may be found in [195]. They remain however simple to integrate.

In a counterflow configuration, the mixture fraction may be analytically formulated with an error function, leading to the following expression for the scalar dissipation:

$$\chi = \frac{a}{\pi} \exp(-2erf^{-1}(1 - 2z)^2) \quad (3.75)$$

In a real combustion chamber, the mixture fraction field allows evaluating the local mixing of reactants but also the local equivalence ratio in the burnt gas. The stretch induced by turbulence is also an important parameter.

In view of the very different features of premixed and diffusion flames, which may co-exist in 3D turbulent burners, it is necessary to identify the local combustion regime. The next paragraph draws a brief state-of-the-art about this question.

3.3.3.3 Flame regime detection

In real combustors, because of the chamber geometry or because of the interaction between turbulence, spray and chemistry, a flame is generally not totally premixed or totally

diffusive. What is occurring is often a collection of the two structures, with more or less probability of occurrence.

To recognise the different flame regimes the Takeno Index, first introduced in [323] is used. It takes the following expression:

$$T = \frac{\nabla Y_F \cdot \nabla Y_O}{|\nabla Y_F \cdot \nabla Y_O|} \quad (3.76)$$

with ∇ the gradient operator.

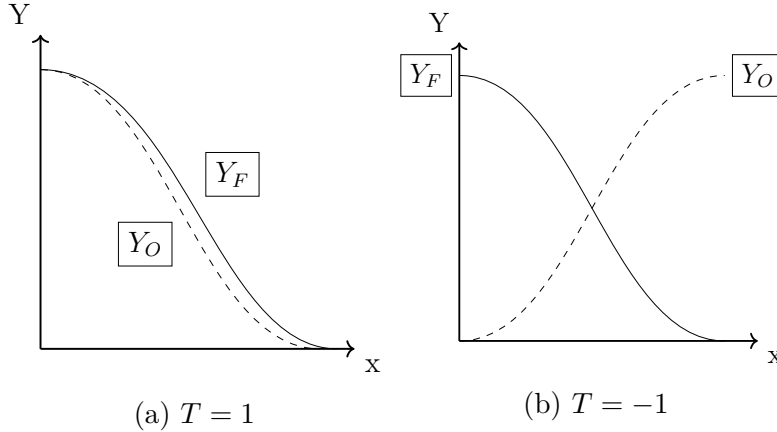


Figure 3.4: Takeno Index for the premixed and diffusion flame cases.

This expression compares the slopes of the fuel and the oxidiser profiles and interprets the result as follows: if both slopes have the same sign, the Takeno Index is positive, and the flame is premixed, as shown in Fig. 3.4. Conversely, if the slopes have opposite signs, then the Takeno Index is negative, the two reactants are not mixed and a diffusion flame structure is identified.

Experimental methods use a similar methodology for recovering the nature of a flame [267]. Several improvements of the Takeno Index expression have been proposed in the literature, such as in [90] where different evaluations of the oxidiser gradient are used to better distinguish between premixed and the diffusion behaviours. In [152], the different contributions to the progress variable source term are used. In [331], several formulations for the Takeno Index are compared for premixed and partially-premixed regimes, leading to the conclusion that the multi-species expression gives better results [90].

When dealing with complex fuels, it is not straightforward to define what is Y_F . As pyrolysis generate molecules which can be oxidised and considered as fuels, these pyrolysis products should be taken into account for a better identification of the flame regime. Therefore, the expression of the Takeno is rewritten:

$$T_{pyro} = \frac{\nabla \sum_{k=1}^{N_{pyro}} Y_k \cdot \nabla Y_O}{|\nabla \sum_{k=1}^{N_{pyro}} Y_k \cdot \nabla Y_O|} \quad (3.77)$$

with N_{pyro} the number of pyrolysis products that are considered. This new definition is in fact a generalisation of the first one.

Since the Takeno Index is of interest only in reactive zones, it is usually conditioned by some reacting variable such as HRR :

$$T^{HRR} = \frac{\nabla Y_F \cdot \nabla Y_O}{|\nabla Y_F \cdot \nabla Y_O|} |HRR| \quad (3.78)$$

or the fuel source term $\dot{\omega}_F$:

$$T^{\dot{\omega}_F} = \frac{\nabla Y_F \cdot \nabla Y_O}{|\nabla Y_F \cdot \nabla Y_O|} |\dot{\omega}_F| \quad (3.79)$$

Both quantities should be interpreted slightly differently:

- when weighted by $\dot{\omega}_F$, the upfront side of the flame is tested, that is to say the way the fuel reacts, which might not be sufficient for some cases.
- when weighted by HRR , the whole reactive zone is enlightened, including the burnt gas side.

Significant difference may be seen between both indicators when the fuel is heavy, i.e., decomposes into lighter hydrocarbons before burning, as the heat release rate profile is often wider and shifted toward the burnt gas compared to the fuel source term profile.

Another difficulty arises for spray flames, where the direct interaction of droplets with the flame front may lead to erroneous values of the Takeno Index. Indeed, not all the fuel vapour is seen if it is immediately burnt after release, and the computed gradient of the fuel mass fraction may be misleading. Similarly, an evaporating droplet in a fuel-air mixture will generate a positive fuel gradient in decreasing air, indicating a diffusion flame, whereas it is a stratified premixed flame. The behaviour of the Takeno Index in spray flames will be investigated in Chapter 9.

Chapter 4

Analysis and reduction of chemical schemes

Contents

4.1	From fuel definition to the reduced mechanism	53
4.1.1	Detailed mechanisms	54
4.1.2	Surrogate fuel model	55
4.1.3	Reduction methods	57
4.2	ARCANE	59
4.2.1	Reduction methods	59
4.2.2	Reduction loop	62
4.2.3	Implementation of ARC schemes in CFD codes	64
4.3	Methods for chemistry analysis	65
4.3.1	Quantitative and qualitative analyses	65
4.3.2	Spatial and time scales	68

The equations developed in the previous chapter include chemical source terms issued from a chemical mechanism. The analysis and reduction of chemical mechanisms are key to obtain a good accuracy and understanding of the combustion process. In Section 4.1, detailed chemical kinetics are described, as well as reduction methods. In Section 4.2, the in-house ARCANE reduction code is presented, together with the implemented methods and algorithms. Finally, analysis methods of chemical kinetics are proposed in Section 4.3, allowing to better understand mechanisms, their major paths and most important species for a target application.

4.1 From fuel definition to the reduced mechanism

Including chemical mechanisms in CFD computations is very recent (end of the 20th century [25]), and started with very simple **global mechanisms**, containing only the main combustion reactants and products. Due to the great increase in computational resource, it is now possible to use more complex mechanisms, implying a higher number of conservation equations, called detailed mechanisms and of which the main characteristics are introduced in Section 4.1.1. However, including detailed, or even skeletal mechanisms in

3D CFD calculations is still not feasible and reduced mechanisms must be used. This implies to first define a surrogate fuel model (Section 4.1.2) before deriving a reduced scheme (Section 4.1.3).

4.1.1 Detailed mechanisms

Detailed mechanisms are the most complete mechanisms that are available today. They are constructed by chemists, using the following methods:

- determination of the coefficients and rates associated to one single reaction, based on the study of the electronic structure, ab-initio calculations and statistical theory.
- measurements in homogeneous reactors or more complex cases. The determination of the rate constants is often done manually; but some automatic codes are emerging [308].

Similar detailed mechanisms are found in numerous domains, in combustion but also atmospheric science, biology, chemical processes, etc. . . Combustion do not only require a good description of the oxidation process, but also a correct prediction of pollutants as well as of the impact of multi-component fuels envisaged for greener aviation. This has led chemists to get more into accurate chemical description of the flow. The available mechanisms show a huge span of different species and reactions as demonstrated in Fig. 4.1.

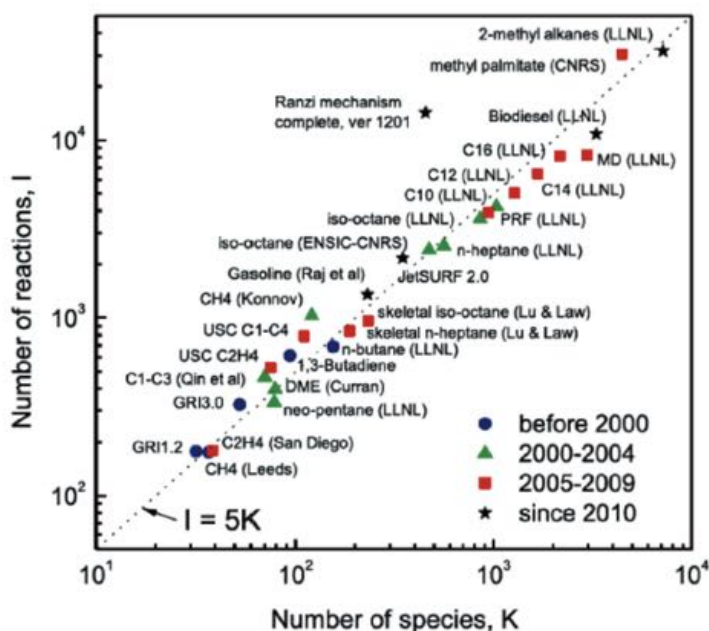


Figure 4.1: Number of reactions vs number of species for mechanisms throughout the time, taken from [57].

As could be expected, the number of species and reactions have increased through the years. One of the first published detailed mechanisms was the models describing ozone [124] in 1953 and hydrazine decomposition [294] in 1956. Models describing hydrogen combustion, methane combustion [280], [290] and methanol combustion [32] followed in

the late 60s and 70s. Several other kinetic developments appeared later [57] and continue to appear. The GRI-Mech 3.0 [106], the first freely available mechanism including NO formation, was tested on several targets. Today's mechanisms have increased in size and include more species such as butane and propane in the USC Mech II [315] for instance, or many more molecules in complex fuels with CRECK mechanisms [126] representing kerosene and oxygenated hydrocarbons.

A well-derived mechanism includes all chemical pathways that are important in the evolution of a mixture for a given target case (reactors or flames, for instance). It is validated by computing the target cases with numerical models such as the Reaction Design's CHEMKIN suite [127], OPENSMOKE [56], FlameMaster [230] or Cantera [103], which all have the capacity to integrate detailed, large size chemical schemes in 0D systems (reactors for instance) and 1D or pseudo-1D systems (flames) as presented in Chapter 3. For the present PhD, the open-source code Cantera has been used, which provides many features as well as a python interface that is easy to handle.

Usually in a CFD code, the time spent on chemistry which implies only local computations, i.e., at each cell or node without using neighbouring values, is short compared to the transport terms in the resolved conservation equations. Therefore, the impact of chemistry on the computational cost of a 3D calculation is directly linked to the number of transported species. In 3D, a CFD code solves 5 conservation equations for non-reactive flows, and $5 + N_S$ equations for reactive flows, at N_x nodes and for N_t time-steps. The most efficient approach to decrease the computational cost is therefore to reduce the number of conservation equations, i.e., number of species. Furthermore, a detailed mechanism may contain very fast species that are very quickly consumed after being produced, leading to very small timescales and therefore high stiffness.

Detailed mechanisms are designed to represent accurately the combustion of most common fuels with their associated pathways towards water and carbon dioxide. For instance, the CRECK mechanism [126] is valid for any hydrocarbon species with 1 to 16 carbon atoms.

4.1.2 Surrogate fuel model

as stated in Section 2.2. Two main categories exist [75], [165]:

- **physical surrogates** reproduce the physical properties of a real kerosene (density, molar mass, distillation curve, etc...)
- **chemical surrogates** reproduce the chemical properties of a real kerosene (cetane number, H/C ratio, lower heating value, auto-ignition delay time, laminar flame speed, etc...)

Surrogates based on both physical and chemical considerations are called **comprehensive surrogates** and are nowadays the most widely built and used. Automatic codes able to build surrogate fuels start to emerge based on optimisation to match the different targeted properties. Depending on their species number, the surrogates are grouped in two categories:

- **mono-component surrogates** such as [59], [186] are based on a single species, usually defined by the general formula of the blend and with properties close to the properties of the real fuel. These fuels can be either an existing species, as $C_{10}H_{22}$ for kerosene, or a fictive species, such as in [94]. Mono-component surrogates have

the advantage of fast computations and simple kinetics. However, when it comes to depicting properties such as preferential evaporation or different H/C ratios in the flame, the next category is preferred.

- **multi-component surrogates** such as [58], [130] are made of several hydrocarbons. The more components, the better the actual fuel, but also the more CPU time it costs. These fuels are interesting as they are able to discretise the different pathways, leading to a better evaluation of pollutants formation as well as flame structure. This representation will be used in Chapter 7 when dealing with the alternative fuels' kinetics.

Usually composed of 3 to 10 species [197], these models are constructed from a chosen set of species with a given subset of reactions that are in the detailed mechanism and are potentially candidates to be surrogates. For the surrogate to be reliable, the chosen species should have accessible thermochemical properties and their associated reactions subset should well reproduce the experimentally measured combustion properties (i.e. auto-ignition delay time, laminar flame speed, intermediate species, products, etc. . .).

Once the surrogate species are chosen and their kinetics developed, their composition is usually determined with the use of an optimisation procedure for some targeted variables. The properties chosen as well as the mixing law applied varies according to the authors [198], [210]. The models are validated against experimentally measurable quantities such as ignition delay time or laminar flame speed if they are available, but the matching of the targeted properties can be considered as satisfactory when no experimental data are available.

The paper of Dryer [68] summarises the progress in fuel surrogate development, from jet fuels [58], [311] to renewable jet fuels [66] through natural gases.

For the fuels selected in JETSCREEN project, the surrogate was built by the method described in Mehl et al. [198]. Figure 4.2 (left) shows the subset of species chosen as an input for the optimiser solver. Those species were selected since a reliable kinetic model exists or could be built. A hybrid approach is applied, where the surrogate candidates subset is manually chosen before optimising numerically the species proportions. A scheme showing the optimisation process is shown in Fig. 4.2 (right).

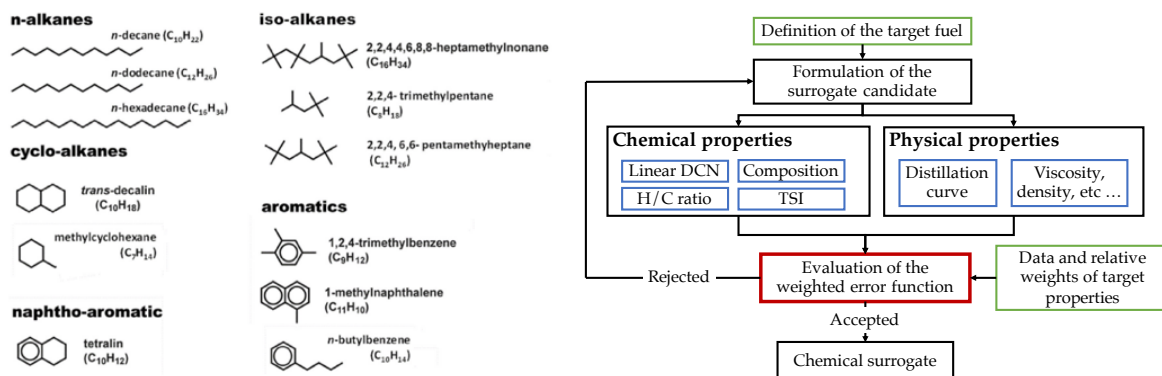


Figure 4.2: Surrogate candidates (left) and methodology (right) for the three fuels [198].

The optimiser, inspired by a previous work of Narayanaswamy et al. [209], is based on the optimisation package of Matlab algorithms, from which home-made algorithms are added such as local optimisation or genetic algorithm. The targeted properties are

the Derived Cetane Number (DCN), the distribution inside the different families, the H/C ratio, the Threshold Sooting Index (TSI) for chemical properties and the distillation curve, the density and the liquid viscosity for the thermochemical properties.

At the end of the process, small variations are applied to build a more accurate chemical scheme, adding or deleting small amounts of a given family that could influence the pollutant creation, for instance.

The development of multi-component surrogates enables the description of different combustion behaviours [74]. The impact on the flame stabilisation, shape and regime however was never studied in detail and will be investigated in Section 9.

Knowing the fuel composition, the following section now details the state-of-the-art in chemistry reduction strategies, with their respective advantages and drawbacks. Finally, the choices made by CERFACS are highlighted and the methods used for the in-house reduction code ARCANE [40] are summarised.

4.1.3 Reduction methods

Figure 4.3 summarises the different methods that are used to reduce mechanisms.

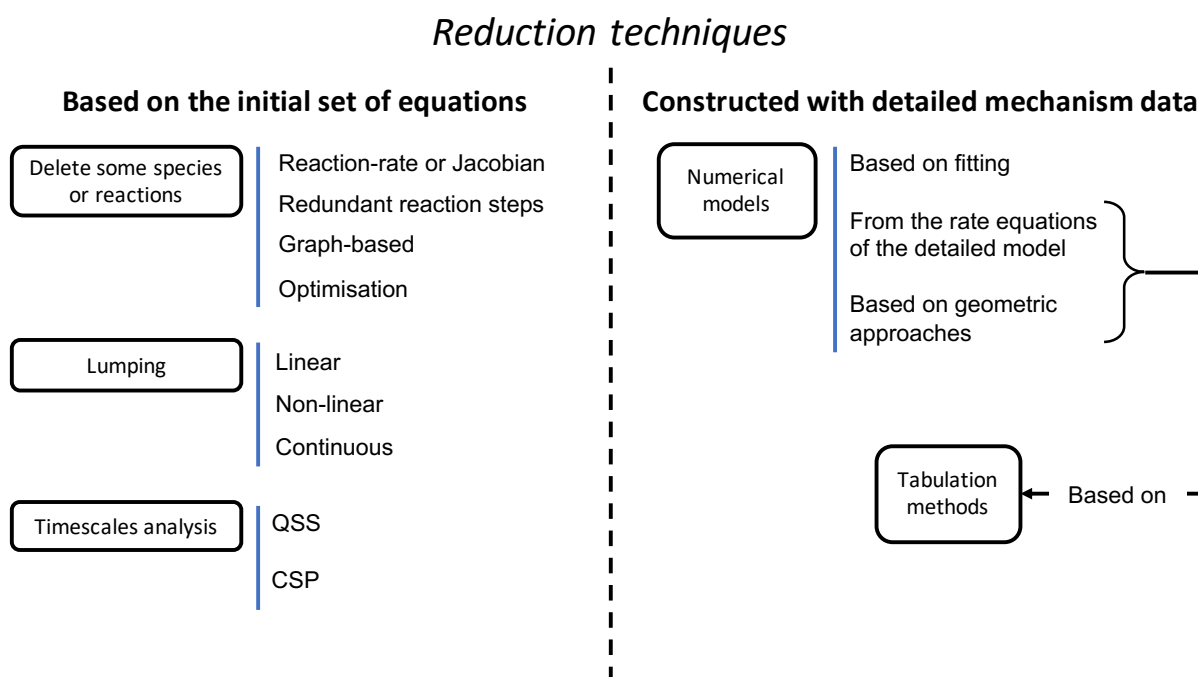


Figure 4.3: Summary of the different main categories of mechanism reduction found in the literature, based on [308].

Two main methodologies are used to build a reduced mechanism. The first family of methods starts from the detailed set of species and reactions, and reduce it by deleting unnecessary species or reactions, lumping species or reactions or finding connections between the species or the reactions through simplifications of the source terms. The second family of methods builds the reduced mechanism without taking into account the relations in the detailed mechanism, but as a system that correlates the inputs with the outputs according to the results given by the detailed mechanism. For this second category, several methods are classified:

- very simple mechanisms containing only a few representative species and reactions that lead to the right equilibrium temperature and species mass fractions are built by hand and fitted on data. They can be global one-step mechanisms, written as a mass balance equation, or two-step mechanisms, for instance in [94], which adds to the global reaction a CO/CO_2 equilibrium reaction. The reaction rates are usually expressed with an Arrhenius formulation, of which coefficients are fitted on the flame temperature and flame speed curves. Note that these coefficients are not constant, but must be varied with the equivalence ratio to get the curve shapes back. As well, four-steps mechanisms also exist, that add H_2 in the list of species [137] which plays an important role in the oxidation of most hydrocarbons [96].
- **numerically reduced models** are built from the detailed mechanism. A numerical relationship is then found between the state variables (the input of the model) and the kinetic variables (the output of the model). Several sub-categories exist, such as:
 1. **parameters fitting** (temporal concentration [70], fitting polynomials [61], [98], [306], high-dimensional model, artificial neural networks [44], [49], etc. . .). This leads to very simple models with low memory requirements, but at the cost of range of validity and accuracy, which will highly depend on the ability of the model to achieve an accurate fitting on the chosen domain.
 2. **low-dimensional manifold** (Rate-Controlled Constrained Equilibrium methods [144], slow manifold methods [268], intrinsic low-dimensional manifolds (ILDM) methods [190]). By recognising that chemical systems evolve in low-dimensional manifold in the phase space, these methods identify the corresponding subspace and record the system evolution in this subspace. The disadvantage of such methods is that the recorded subspace may not contain all possible states encountered in 3D flames.
 3. **geometric approaches** (slow invariant manifolds such as the Invariant Constrained Equilibrium edge Pre-Image Curve (ICE-PIC) method [60], minimal entropy production trajectory method [167], temporal concentration changed based on the self similarity method [118]).

In the two last cases, the subspace is stored in look-up tables, where the mass fractions, temperature or source terms are written as functions of a reduced number of variables. This leads to the **tabulation methods**, where the table is used in 3D calculations, avoiding the integration of the chemical system, which significantly reduces the computing time, although the search and the retrieval of a quantity may take a certain time if the table is large. The accuracy of the result also depends on the interpolation scheme between the stored points. Tabulation methods started to be used in the 90s [302], but at that time suffered from their storage requirements. To overcome this issue, in-situ tabulation was created [182], enabling the table filling during the 3D simulation and only with the accessed regions of the composition space (ISAT (In Situ Adaptive Tabulation [238])). Note that as the chemical system is not integrated in the 3D simulation, tabulation methods allow the use of detailed and skeletal mechanisms.

All the above reduction methods are efficient, but the validity of the chemistry outside the range of derivation and in complex 3D flows with different transport phenomena is not

guaranteed. Moreover, the information about the chemical pathways is completely lost, preventing any chemical analysis in the 3D reactive flows.

In order to keep the most important chemical features of the detailed mechanism, several methods reduce it via a detailed analysis of the kinetics:

- Unnecessary species and reactions may be **removed from the mechanism**. Lots of methods are used to identify them, based on reaction rates [97], [207], [305], [307], on the Jacobian matrix, on sensitivity analysis [310], or on optimisation strategies and graph-based methods, such as Path Flux Analysis (PFA) [301] and DRG (Direct Relation Graph) [184], which consider species as the nodes and reactions as the links. The resulting reduced mechanism is then a subset of the initial group of species and reactions. In ARCANE, the DRGEP (Direct Relation Graph with Error Propagation) [225] has been chosen because of its coding simplicity and its quickness.
- Isomers may be then **lumped together**. Several methods exist such as the linear [65], [215], [317], non-linear [27], [304] and continuous lumping [6]. In ARCANE, a simple linear method has been used [225].
- Species may finally be **separated on a timescale basis**, with a specific treatment of the very fast species. Indeed, species can be defined in **Quasi Steady State (QSS)** when they have a fast destruction timescale. Therefore, as their creation is quickly balanced by their destruction, the contribution of their net production rate is negligible and the species source term can be approximated to 0. The concentration of QSS species can then be expressed as a function of other species concentrations and its transport equation can be discarded. Not only this decreases the CFD computation cost, but it also reduces the stiffness of the scheme by taking away the smallest timescales of the chemical system. To detect these QSS species, two main methods have been developed: the Computational Singular Perturbation (CSP) [154] and the Level Of Importance (LOI) [180]. In ARCANE, calculation time considerations oriented the choice to a modified LOI.

The next section details the three selected reduction methods and their implementation in ARCANE.

4.2 ARCANE

ARCANE (Another Reduction Code: Automatic, Nice and Efficient) is a reduction code co-created by Cornell University (by Perrine Pepiot) and CERFACS [40]. The goal of this section is not to be fully exhaustive in the code description, but to provide a quick overview on the main code features. For more details, please refer to the PhD of Quentin Cazerès [39].

Section 4.2.1 details precisely how each of the reduction methods is working. Then, Section 4.2.2 summarises how the reduction is implemented and optimised. Finally, Section 4.2.3 explains how the reduced mechanisms may be used in CFD codes.

4.2.1 Reduction methods

As explained in the previous section, ARCANE performs three methods of reduction, which are detailed in the following paragraphs:

- the **Direct Relation Graph with Error Propagation (DRGEP)** [225] which is applied to species (DRGEP-S) and to reactions (DRGEP-R) to generate a subset of the chemical system.
- the **linear lumping method** [225] working on isomers to lump them into one single species
- the **Level Of Importance (LOI)** [180], to find QSS species and reduce the stiffness of the final scheme.

4.2.1.1 Direct Relation Graph with Error Propagation (DRGEP)

The initial Direct Relation Graph (DRG) method has been introduced by Lu and Law [181], [185]. They suggested that looking at chemical mechanisms as graphs is suitable for observing the coupling between the species (the nodes) through the reactions (the links).

In practice, the graph is used to determine the connection weights, i.e., how strong each species or reaction is connected to a user-specified **target species** to be kept in the reduced mechanism. The original expression of this weight is:

$$r_{AB} = \frac{\sum_j |\nu_{A,j} \omega_j \delta_B^j|}{\sum_j \nu_{A,j} \omega_j} \quad (4.1)$$

with $\nu_{A,j}$ the stoichiometric coefficient of species A in reaction j . The coefficient δ_B^j is 1 if B is in reaction j and 0 otherwise. Another definition was proposed by Luo et al. [189] to better estimate the part of the consumption and of production of the target species:

$$r_{AB} = \frac{\sum_j |\nu_{A,j} \omega_j \delta_B^j|}{\max(P_A, C_A)} \quad (4.2)$$

with P_A and C_A the production and consumption rates of species A , and computed as:

$$\begin{aligned} P_A &= \sum_{j=1, n_R} \max(0, \nu_{j,A} \omega_j) \\ C_A &= \sum_{j=1, n_R} \max(0, -\nu_{j,A} \omega_j) \end{aligned} \quad (4.3)$$

In the initial DRG method, the coefficient of the path p linking species A and B is then defined as:

$$r_{AB,p}^{DRG} = \min_{i=1}^{n-1} r_{S_i S_{i+1}} \quad (4.4)$$

where S_i , $i = 1, n$ are the species involved in the path, and the final DRG coefficient is:

$$r_{AB}^{DRG} = \max_{\text{all paths } p} r_{AB,p}^{DRG} \quad (4.5)$$

Several improvements of the DRG method exist, such as the DRG-ASA (Direct Relation Graph - Aided Sensitivity Analysis) [329] and the method used in ARCANE, the DRG with Error Propagation (DRGEP) [226]. The main difference with the method of Luo is that, as stated in the name, errors propagate along the graph and all species are not considered equally important anymore. As a consequence, the coefficient was defined to take into account the error propagation:

$$r_{AB,p}^{DRGEP} = \prod_{i=1}^{n-1} r_{S_i S_{i+1}} \quad (4.6)$$

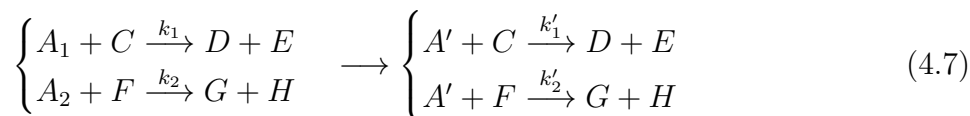
which constitutes an important change compared to the original method. This approach is combined with a scaling of the target species contributions and an integrity check to avoid truncated chemical pathways. In ARCANÉ, DRGEP was also coupled with a sensitivity analysis to build the DRGEP-ASA.

4.2.1.2 Linear lumping

Lumping is another method to be used for reducing the number of species in the mechanism and consists in:

- finding the isomers that are going to be lumped.
- estimate the kinetic parameters of the new links that are created.

To put it simple, if species A_1 and A_2 are isomers in the following system of reactions, they may be both replaced by an equivalent **lumped species** A' :



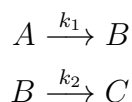
Both reaction rates must be changed accordingly, by fitting the Arrhenius coefficients through the least square method, depending on the composition of the isomers. The thermodynamic coefficients of A' are also adapted if those of A_1 and A_2 are different.

In ARCANÉ, the method chosen is a simple direct lumping [225], according to the following algorithm:

1. look for isomers that present the exact same NASA thermodynamic coefficients. They are all selected together (it could be two species, or three, or four, etc. . .) and lumped. The resulting scheme is then tested.
2. look for isomers that do not necessarily present the same NASA coefficients. They are all selected together (it could be two species, or three, or four, etc. . .) and lumped. The resulting scheme is then tested.
3. inside each group of isomers, look for the capability to lump species two by two: if the error between both C_p and both enthalpy coefficients is below 50%, then both species are lumped together and species are then tested.

4.2.1.3 Quasi-Steady State Assumption (QSSA)

After the DRGEP and the lumping steps, a skeletal mechanism is obtained which generally remains too stiff for a use in CFD. The Quasi-Steady State Assumption enables to find relations between species that are considered as fast reacting species. Let's consider the following system:



If $k_1 \ll k_2$, that is to say, that the second reaction is very fast compared to the first one, the species B is considered in Quasi-Steady State. As a consequence, the following equation can be written:

$$\frac{\partial[B]}{\partial t} = 0 = -k_1[A] + k_2[B] \quad (4.8)$$

Finally, $[B]$ can be calculated from $[A]$ with the following relation:

$$[B] = \frac{k_1}{k_2}[A] \quad (4.9)$$

The conservation equation for B is not more useful and can be discarded. Another consequence is that the stiffness of the system is reduced, since QSS species are the stiffest ones.

In real complex chemical mechanisms, species may be linked with many reactions and the calculation of QSS species concentrations may involve a system with more than two equations. The resolution is then performed with a LU decomposition of the matrix representing the system. Two QSS species lying on the same side of a reaction lead to a non-linear system of equations; in this case, reactions may simply be discarded.

To rank the species that could potentially be QSS species, the **Level Of Importance (LOI)** method, is used. It is based on the characteristic lifetime of a species:

$$\tau_i = \frac{1}{J_{ii}} \quad (4.10)$$

with J_{ii} the diagonal term of the Jacobian matrix of the system:

$$J = \left(\frac{\partial \dot{\omega}_k}{\partial [S_i]} \right) \quad (4.11)$$

and the LOI coefficient then writes:

$$LOI_i = S_{Q,i}[S_i]\tau_i \quad (4.12)$$

with $S_{Q,i}$ the sensitivity coefficient of species i associated to the variable Q (laminar flame speed, auto-ignition time, etc. . .). In ARCANE, the sensitivity coefficient is replaced by the DRGEP coefficient, which has shown to give good results and less calculation time.

4.2.2 Reduction loop

In ARCANE, the organisation of the different reduction steps, from a detailed mechanism to the reduced, so-called Analytically Reduced Chemistry (ARC) mechanism, is fully automatic. Figure 4.4 displays the complete reduction loop.

As the QSS step requires modifying the relation between the species and do not delete any of them, the *LOI* is applied only once at the end of the algorithm, and after all the species have been removed with the DRGEP or lumped. The general order is then the following.

1. A DRGEP-S step is applied. When the step is finished, another DRGEP-S is launched until no further species can be removed.
2. The DRGEP-R is started and continues similarly to the DRGEP-S, i.e. until no more reaction can be removed.
3. Another DRGEP-S is applied, and this alternation between the DRGEP-S and the DRGEP-R continues until no further reaction and species can be removed from the mechanism.
4. A lumping step is applied.

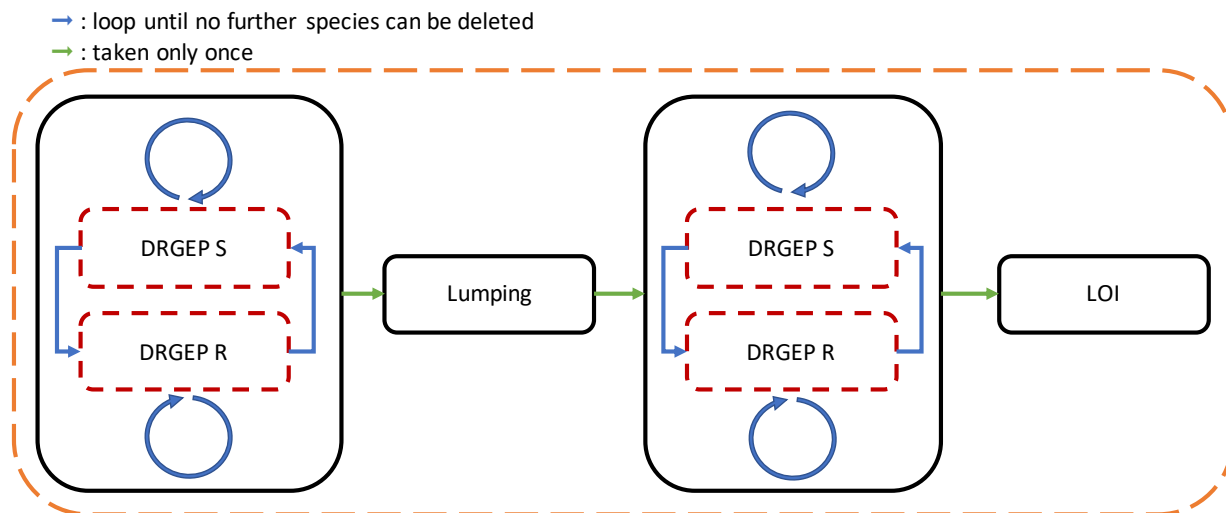


Figure 4.4: Scheme representing the organisation of the different reduction strategies in ARCANE.

5. DRGEP-S and DRGEP-R are repeated as described at point 3. until no further reaction and species can be removed from the mechanism. At the end of this step, a skeletal mechanism is obtained.
6. Finally, the QSSA step is applied and the final ARC mechanism is obtained.

Figure 4.5 represents the general loop which is the same for each reduction method (DRGEP, lumping or LOI).

The different steps in the loop are the following:

1. User-defined reference values of interest are calculated on the selected 0D and 1D cases.
2. Coefficients are evaluated according to the given methodology (DRGEP-S, DRGEP-R, Lumping, QSSA) and ranked. A threshold is calculated based on this ranking, which prevents the reduction from going through important species (or reactions) such as the reactants, the products or important intermediate species that should not be eliminated, lumped or set as QSS species.
3. The loop starts here. The entity, species or reaction, with the lowest coefficient is either erased from the scheme (DRGEP), lumped with an isomer (lumping) or calculated via an algebraic assumption (QSSA).
4. The new mechanism with the modifications above is built, and the same values of interest as in step 1 are calculated.
5. Error is calculated. If the error is weaker than a threshold given by the user, the mechanism is kept and another species or reaction is removed, lumped or put in QSS mode. If the error is larger, the mechanism is not valid and the previous one is kept instead.
6. The loop is repeated until the coefficients of the removed entity is above the threshold calculated at 1.

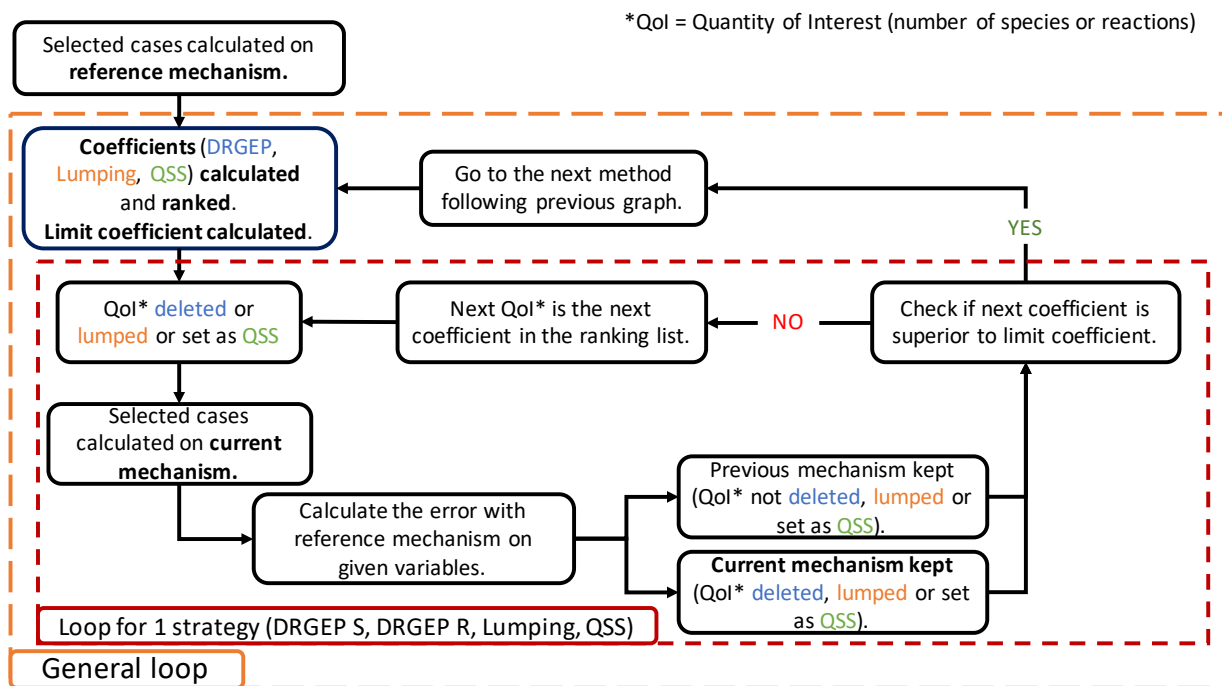


Figure 4.5: Scheme representing the loop, same for all methods (DRGEP, lumping or LOI) in ARCANE.

This methodology enables to greatly reduce the mechanism in a reasonable computing time, which depends on the number of cases and the size of the detailed mechanism.

4.2.3 Implementation of ARC schemes in CFD codes

Due to the QSS species which must be computed from algebraic relations between concentrations, the implementation of ARC chemistry in CFD codes such as Cantera or AVBP require a specific module containing these relations. Therefore, ARCANE has the capability to create Fortran 90 program files which describe the chemistry, including both standard reactions and QSS relations.

To assess the right integration of the mechanism into the CFD solver, the following procedure is applied:

1. the ARC mechanism written in the Fortran program file is compared to the detailed mechanism using Cantera, all calculations with mix transport.
2. the ARC mechanism with simple transport (implemented in the CERFACS version of Cantera) is compared with mix transport using Cantera. This step is important to fit the coefficients of the simple transport model.
3. the ARC mechanism with simple transport is compared in Cantera and in AVBP to assess the implementation in AVBP.

4.3 Methods for chemistry analysis

Chemical systems are non-linear and therefore difficult to analyse, in particular when many species and reactions are involved. In this section, several methods for chemistry analysis are proposed:

- knowing how the “story of the canonical case” occurs, i.e., knowing the order of appearance of the different species, their contribution to heat release as well as their influence on the mechanism is useful to explain the flame structures in 3D cases. Methods to get this knowledge are explained in Section 4.3.1.
- looking at the characteristic timescales and lengths is interesting to see if the mechanism is adapted to CFD constraints (i.e., the mesh and the timestep). Methods to get characteristic timescales and methods to get the number of points needed for an ARC flame are presented in Section 4.3.2.

4.3.1 Quantitative and qualitative analyses

Simple processes such as 0D or 1D cases may be further analysed in terms of influence of species or reactions, qualitatively and quantitatively, to give a better view of the mechanism itself. This section presents three types of analysis that have been developed in ARCANE: the **heat release rate analysis**, the **sensitivity analysis** and the **graph analysis**.

4.3.1.1 Heat-release rate analysis

The identification of the species or reaction that reacts the most gives crucial information on the flame structure. The *HRR* analysis computes the contribution of all the reactions or all the species at all locations (spatial or temporal) of a case, and integrate it along the given axis or not. An example of this method is provided Fig. 4.6a with the location of the analysis Fig. 4.6b.

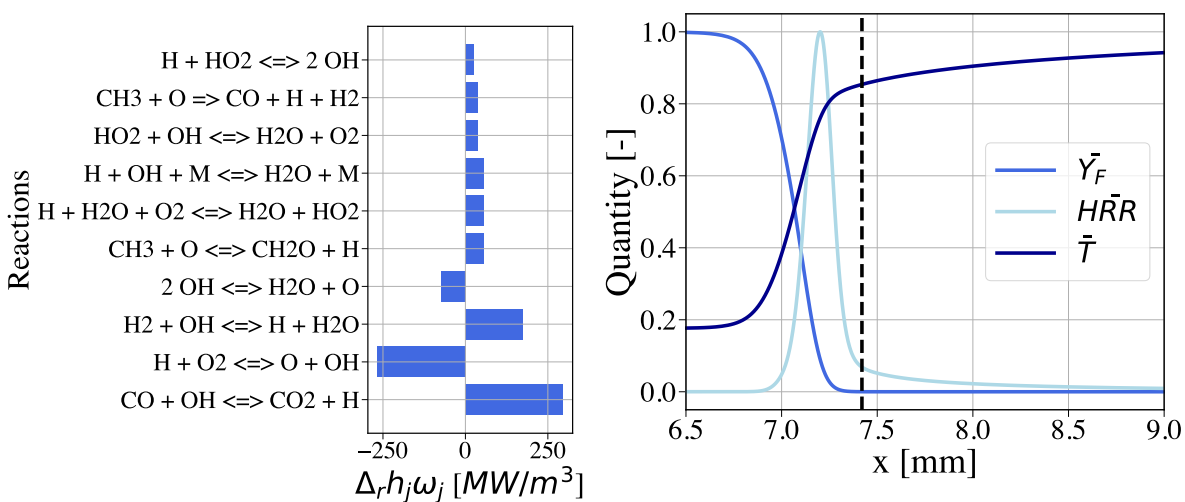


Figure 4.6: Heat-release rate analysis for methane/air flame at $T = 400$ K, $P = 1$ bar and $\phi = 1.0$.

The graph on the right shows the profiles of flame key quantities non-dimensionalised with their maximum value. The heat release rate analysis is then realised in the post-flame zone for this example.

On the graph displayed on the left, the contributions of the reactions are shown in increasing order from top to bottom. In this example, the reaction releasing the most heat is $CO + OH \longleftrightarrow CO_2 + H$, which is expected at this location in the post-flame zone.

4.3.1.2 Sensitivity analysis

A general form of the chemical system can write [308]:

$$\frac{dq}{dt} = f(q, x), \quad q(t_0) = q_0 \quad (4.13)$$

with q the vector of species concentrations and x a vector containing m elements associated to the reactions (rate coefficients) which are used to calculate the evolution of the vector q . A Taylor expansion in x gives the following:

$$q_i(t, x + \Delta x) = q_i(t, x) + \sum_{j=1}^m \frac{\partial q_i}{\partial x_j} \Delta x_j + \frac{1}{2} \sum_{k=1}^m \sum_{j=1}^m \frac{\partial^2 q_i}{\partial x_k \partial x_j} \Delta x_k \Delta x_j + \dots \quad (4.14)$$

The partial derivative $\partial q_i / \partial x_j$ is called the first-order local sensitivity coefficient. All coefficients are normalised to be comparable to each other, which give the **normalised sensitivity coefficients** definition:

$$s_i = \frac{x_j}{q_i} \frac{\partial q_i}{\partial x_j} \quad (4.15)$$

These coefficients may be calculated with a brute force method, but other methods are available such as the Green function method [247], the decoupled direct method [69], the automatic differentiation [21], etc ... In this work, only the brute force method is used: the same perturbation Δx_j is applied to all A_j the pre-exponential Arrhenius coefficients, and the resulting absolute error between the reference and the perturbed solutions Δq_i is calculated.

The only advantage of this method is its simplicity and easy implementation. On the other side, it requires integrating $(m + 1)$ systems. Furthermore, the result may depend on the perturbation value Δx_j : too small values may not allow computing the sensitivity whereas to high values may be out of range of validity of the first order approximation.

A species sensitivity analysis can be conducted by restricting the perturbation to the reactions involving the targeted species. An example of output, comparing the most important reactions in GRI-Mech 2.11 and 3.0 [106], is given in Fig. 4.7.

As expected, the most sensitive reactions are nearly the same for GRI-Mech 2.11 and 3.0 for with the same order of magnitude, except for the two most important reactions which seem to be slightly more sensitive in the GRI-Mech 2.11 than in the 3.0 version.

Sensitivity analysis is useful to know which reaction is driving the system, and for uncertainty quantification of the system.

4.3.1.3 Graph analysis

The above quantitative analyses do not provide a global view of the mechanism with the various chemical paths and their interactions. This information is proposed here in the form of graphs, built to visualise the mechanism structure.

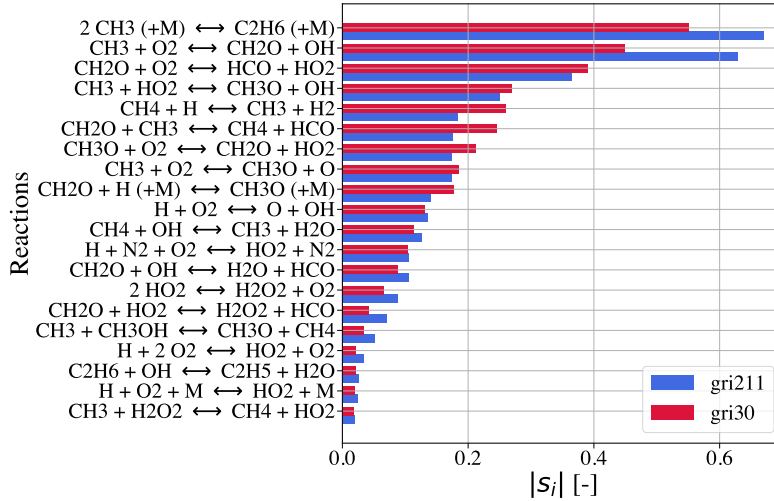


Figure 4.7: Sensitivity analysis of GRI-Mech 2.11 and 3.0 on τ_{ig} for methane/air reactor at $T = 1000$ K, $P = 1$ bar and $\phi = 1.0$.

The amount of each element contained in the mechanism is a conserved quantity and is used to build such graphs. The flux of element A from species i to species k via reaction j may be written:

$$A_{ikj} = \frac{n_{A,i}n_{A,k}r_j}{N_{A,j}} \quad (4.16)$$

with $n_{A,i}$ and $n_{A,k}$ the number of atoms A in species i and k , respectively, r_j the reaction rate of reaction j and $N_{A,j}$ the sum of the number of atoms A . This quantity can be computed at any location of the flame or at any time of the reactor evolution. By summing all the contributions at all locations, an integrated graph of the pathways can be drawn. Finally, only the main paths are shown, based on a given threshold.

This method has been implemented in ARCANE, with an algorithm browsing the different pathways. First, the child species that are directly linked to a given species are determined. Second, the algorithm looks at each child species, and starts the analysis again, until ten generations have been browsed. This enables the drawing of graphs, which can then be analysed to understand how the molecules are converted. An example for methane is given in Fig. 4.8, tracking the carbon atom C . Red colour corresponds to pyrolysis, blue is for the core of the flame (oxidation) with highly reactive species and green represent the carbon-containing products of the flame: CO and CO_2 . The size of the arrow is proportional to the atomic flux. Data were taken from ARCANE and post-processed with Gephi [16].

As shown on this graph, methane is first pyrolysed into CH_3 and then oxidised in multiple species before creating the final products of combustion, CO and CO_2 . Another interest of such graphs is the comparison of the mechanism behaviour of a reactor or a flame facing different operating conditions [227] targeting low pressure.

This method is used in this work to check the different pathways between the species present in fuel blends, as described in Chapter 10.

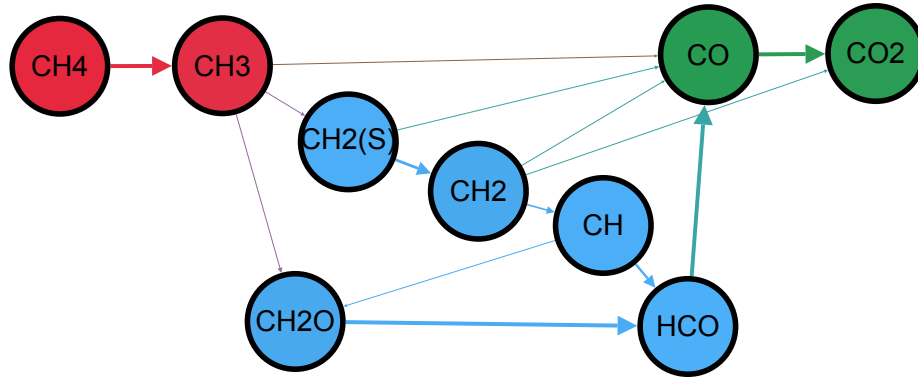


Figure 4.8: Graph analysis for CH_4 /air flame at $T = 400$ K, $P = 1$ bar and $\phi = 1.0$.

4.3.2 Spatial and time scales

The space and time discretisation of the flame must be set in accordance with its space and time scales, which are determined in the following.

4.3.2.1 Timescale analysis

As defined previously, the chemical timescale of a species i is approximated by the inverse of the Jacobian matrix diagonal term:

$$\tau_i^{ch} = \frac{1}{J_{ii}} = \frac{\partial[S_i]}{\partial\dot{\omega}_i} \quad (4.17)$$

To evaluate this timescale, the procedure is usually to perturb the concentration of the species and see the impact on the species source term in a 1D flame. An example is given for GRI-Mech 3.0 Fig. 4.9.

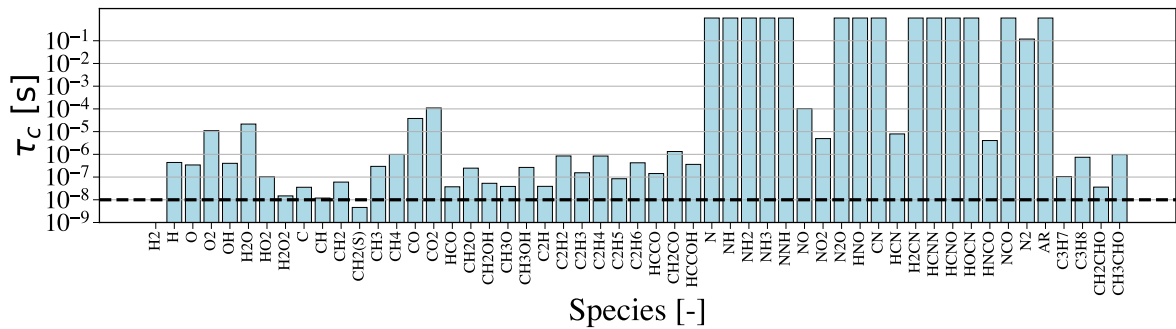


Figure 4.9: Timescales for methane/air flame with GRI-Mech 3.0 at $T = 400$ K, $P = 1$ bar and $\phi = 1.0$. The dotted line is the typical compressible CFD time-step for explicit time integration.

In the example, most species have a timescale between 10^{-9} s and 10^{-3} s. This timescale can be compared to other characteristic timescales, such as the evaporation and the convective timescales, to characterise the flame structure. But it is crucial to compare it to the explicit CFD solver timestep Δt , to ensure $\Delta t < \tau_i^{ch}$. For instance, in the example, $CH_2(S)$ is below the CFD timestep and may lead to numerical instability. Note that the

CFD timestep used here is for a compressible code, i.e., quite small and therefore close to the shortest chemical timescale.

In case the ARC scheme still contains too stiff species, several solutions may be used to overcome the problem:

- try to put the stiff species in QSS mode without increasing the error of the reduced mechanism.
- make the species semi-implicit [134] or an exponential integration [24] which forces positive species concentrations.
- sub-cycle the chemical integration to reach an effective timestep compatible with the chemical timescales.

In practice, simple mechanisms with few species (between 1 and 4) and no intermediate species usually have large chemical timescales. This is not the case for more detailed schemes which contain intermediate short-life species, just a few in ARC but significantly more in skeletal mechanisms and even more in detailed schemes.

4.3.2.2 Space-scale analysis

The flame spatial resolution is driven by the flame thickness. If this quantity is well known a priori for premixed flames, it depends on the flow for diffusion flames and is therefore not known a priori. However, the diffusion flame also adapts to the mesh, and its thickness spontaneously increases on coarse meshes, avoiding numerical resolution issues [55]. Thus, the simulation of a diffusion flame is very robust whatever the mesh, which does not however guarantee that an obtained solution is correct. On the contrary, insufficient spatial resolution of a premixed flame thickness will always lead to numerical instability or even crash.

The spatial discretisation of a premixed flame may be characterised by the **Zeldovich number** [326], expressed for one-step chemistry by:

$$Ze = \frac{T_2 - T_1}{T_2} \frac{E_a}{R} \quad (4.18)$$

The Ze number is a non-dimensional parameter controlling the flame thickness. Following [235]), $Ze/2$ can be interpreted as the multiplication factor of the required resolution between a non-reactive and a reactive case. Typical values for Ze are in the range between 10 and 20, so that the mesh resolution must be increased by at least 5 to 10 times to discretise correctly a single step chemistry.

The problem of mesh requirement is addressed in Chapter 7 for more complex kinetic schemes, for which the intermediate species imply stronger resolution constraints.

Chapter 5

Liquid phase modeling for reactive flows

Contents

5.1 Euler-Lagrange formulation and modelling	71
5.1.1 Spherical droplet model	72
5.1.2 Liquid injection	79
5.1.3 Spray-wall interactions	83
5.1.4 Combustion variables in spray flames	86
5.2 Two-phase combustion regimes	87
5.2.1 Group number	87
5.2.2 Single droplet burning: the MustARD model	89

Aeronautical engines are fed with liquid fuels, which are preferred to gaseous hydrocarbons (up to butane, i.e., 4 C atoms) for their higher density. The liquid fuel is then atomised into small droplets before vaporising. This transformation of the liquid fuel into a gaseous vapour that mixes and burns with air in the combustion chamber needs to be accurately modelled because the impact on the flame is very important. The coupling between the spray and the gas involves mass, momentum and energy exchanges and is two-way, i.e., exchanges are in both directions between the phases.

To simulate sprays in CFD, three classes of approach have been developed throughout the years:

- the **Locally Homogeneous Flow (LHF)** model developed in 1986 [85] is very simple in its derivation and numerical integration. The exchanges of mass, momentum and energy between the liquid and the gas phases is supposed to be infinitely fast, which implies thermodynamic and kinematic equilibrium. The two-phase flow is then represented as one single continuum. A major drawback of this model is the common velocity and the temperature for both phases, which makes it suitable only for very tiny droplets.
- the **Euler-Euler (EE)** approach represents each liquid and gaseous phase as one continuum, with exchanges between the two. Conservation equations are built for both phases, which require closure models [258]. Advantages are that this method

is not computationally costly and easy to implement in a HPC framework. However, the extension to locally polydispersed sprays, i.e., the possibility of having a droplet size distribution at each location and each time instead of only a mean size, is not straightforward. First models have been proposed in the early 2000s [161] by discretising the droplet size distribution in classes and solving independently a continuum for each class. Other approaches have been published later [92]. All these models require complex modelling and significantly increase the computing time.

- the **Euler-Lagrange (EL)** technique methodology, used in this PhD, tracks each droplet individually, thus ensuring the complete spray representation. Exchanges with the gaseous phase then require interpolation operations. The main disadvantages of this method is the computational effort which may greatly increase in some cases, notably in non-reacting cases, as well as the coding complexity.

In AVBP, both the EE and EL methods are available. However, only the EL method is used in this work, to allow a polydisperse spray representation. Section 5.1 thus explains EL equations implemented in AVBP as well as the modelling associated to the two-phase flow. In Section 5.2, the combustion regimes of spray flames are described.

5.1 Euler-Lagrange formulation and modelling

First, the equations of the EL formulation are recalled in Section 5.1.1. Injection and wall interaction modellings are then described, respectively, in Section 5.1.2 and in Section 5.1.3. Finally, some flame key quantities are adapted to the presence of the spray, as explained in Section 5.1.4.

Lagrangian particle tracking obeys simple trajectory equations:

$$\begin{aligned}
 \frac{Dx_{p,i}}{Dt} &= u_{p,i} \\
 \frac{Dm_p u_{p,i}}{Dt} &= F_{p,i}^{ext} \\
 \frac{Dm_p}{Dt} &= \dot{m}_p \\
 \frac{Dm_p h_{s,p}}{Dt} &= \dot{\Phi}_p
 \end{aligned} \tag{5.1}$$

where p is the particle index, i the spatial coordinate, x the position, and F_p^{ext} , \dot{m}_p and $\dot{\Phi}_p$ are corresponding respectively to external forces acting on the droplet, mass variation and internal droplet energy.

The coupling with the gas phase is made through a set of source terms that add to the conservation equations:

$$\begin{aligned}
 mass : S_{mass}^{l \rightarrow g} &= \frac{1}{\Delta V} \sum_{n=1}^N \left(\frac{dm_p}{dt} \right)_n \\
 momentum : S_{mom}^{l \rightarrow g} &= \frac{1}{\Delta V} \sum_{n=1}^N (F_{p,i})_n = \frac{1}{\Delta V} \sum_{n=1}^N m_p \frac{u_i - u_{p,i}}{\tau_p} \\
 energy : S_E^{l \rightarrow g} &= \frac{1}{\Delta V} \sum_{n=1}^N (\phi_g^{cond} + \phi_g^{ev})
 \end{aligned}$$

where ΔV is the local control volume where the N droplets are located.

The next section explains the formulation of these exchange terms with the gas.

5.1.1 Spherical droplet model

The system of equations derived for the liquid phase is constructed for the simple problem of an individual droplet moving in a hot flow, and represented by its time-dependent size, velocity and temperature as represented in Fig. 5.1.

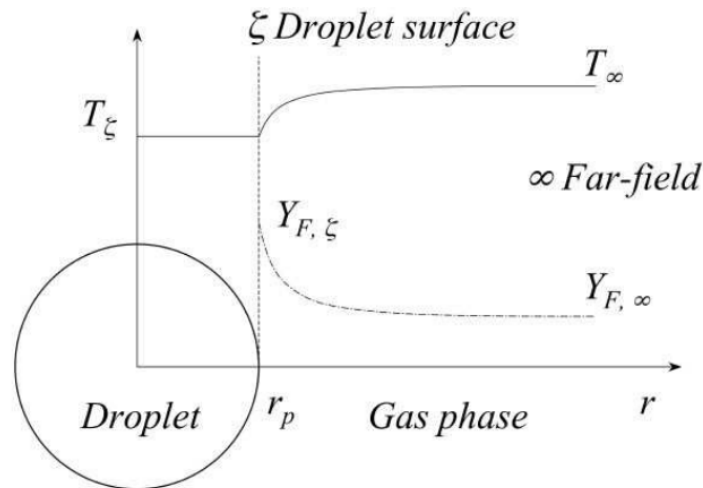


Figure 5.1: Scheme of the spherical droplet problem, taken from [134]

The quantities associated to the surface of the droplet are denoted with ζ index, and the quantities associated to the gaseous far-field with ∞ index. As the droplet is small (droplet radii range from μm to mm), gravity is not taken into account. The droplet is therefore submitted to dynamic forces, heating and evaporation as described in the next paragraphs.

5.1.1.1 Dynamic forces

Different dynamic forces act on a spherical droplet, as expressed by the generalised Basset-Boussinesq-Oseen equation:

- the drag force is a stationary force coming from the momentum difference between the phases and writes:

$$F_{D,i} = \frac{m_p}{\tau_p} (u_i - u_{p,i}) \quad (5.2)$$

with the relaxation time of the particle:

$$\tau_p = \frac{\rho_l d_p^2}{18\mu(1 + 0.15Re_p^{0.687})} \quad (5.3)$$

and Re_p the particle Reynolds number:

$$Re_p = \frac{|u - u_p| d_p}{\nu} \quad (5.4)$$

This relaxation time is an empirical correlation from Schiller and Naumann [279] and the drag coefficient takes the following expression:

$$C_D = \frac{24}{Re_p}(1 + 0.15Re_p^{0.687}) \quad (5.5)$$

- the stationary pressure force, which represents a local hydrostatic pressure gradient, can be neglected because the density of the droplet is much higher than the gas density.
- the virtual mass, and Basset forces are also neglected as the difference in density is.

Stokes number

The droplet motion in the flow under the action of the drag force is characterised by the Stokes number [298] which compares the characteristic motion time of the droplet to the characteristic motion time of the flow:

$$St = \frac{\tau_p}{\tau_{flow}} \quad (5.6)$$

- if $St < 1$, the droplet characteristic time is small compared to the flow and the droplet velocity rapidly equilibrates with the flow velocity. The droplet behaves then as a tracer.
- if $St > 1$, the characteristic time of the droplet is high compared to the flow, and the droplet tends to keep its trajectory independent of the flow.
- if $St \approx 1$, both time scales are comparable and the phenomenon of droplet segregation appears, i.e., preferential concentrations in low-vorticity regions.

5.1.1.2 Evaporation

The spherical model developed by Spalding [292] requires three main assumptions:

1. the spherical droplet is supposed to be **isolated**, therefore no interaction exists between the droplets.
2. the **temperature is uniform** inside the droplet, which means that the liquid conductivity is infinite.
3. the droplet is considered in **quasi-steady state**, that is to say that the liquid phase is always at equilibrium with the gaseous phase.

The third hypothesis implies that the system of equations describing the evolution of the gas around an evaporating droplet, the **Spalding system of equations**, is independent of time and writes in spherical coordinates:

$$\left\{ \begin{array}{l} \rho u r^2 = \text{constant} = \rho_\zeta u_\zeta r_p^2 = \frac{\dot{m}_F}{4\pi} \\ \rho u r^2 \frac{dY_F}{dr} = \frac{d}{dr} \left(r^2 \rho D_F \frac{dY_F}{dr} \right) \\ \rho u r^2 C_p \frac{dT}{dr} = \frac{d}{dr} \left(r^2 \lambda \frac{dT}{dr} \right) \end{array} \right. \quad (5.7)$$

with r the radial coordinate, D_F the fuel diffusion coefficient and \dot{m}_F the fuel vapour mass flow rate.

Mass transfer

By integrating between the droplet surface and the far-field the second equation of the system 5.7, and using the equality of the mass flux between the liquid and the gas side, an expression for the fuel mass transfer $\dot{m}_F = -\dot{m}_p$ is found:

$$\dot{m}_p = -4\pi r_p \rho D_F \ln(B_M + 1) \quad (5.8)$$

with B_M the **Spalding mass number**:

$$B_M = \frac{Y_{F,\zeta} - Y_{F,\infty}}{1 - Y_{F,\zeta}} \quad (5.9)$$

The fuel mass fraction at the interface $Y_{F,\zeta}$ is calculated thanks to the equilibrium hypothesis, considering that the interface is thermodynamically stable and using the **Clausius-Clapeyron relation**:

$$P_{F,\zeta} = P_{cc} \exp\left(\frac{W_F L_v(T_{ref})}{R}\right) \left(\frac{1}{T_{cc}} - \frac{1}{T_\zeta}\right) \quad (5.10)$$

with T_{cc} and P_{cc} values of temperature and pressure on the saturation curve. Due to infinite liquid conductivity, the droplet surface temperature T_ζ is equal to the droplet temperature T_p . L_v the latent heat of evaporation, defined by:

$$L_v = h_{s,F}(T_{cc}) - h_{s,p}(T_{cc}) \quad (5.11)$$

with $h_{s,F}(T)$ the sensible enthalpy of the gaseous fuel species and $h_{s,p}(T)$ the particle sensible enthalpy. Finally, the molar fraction is written:

$$X_{F,\zeta} = \frac{P_{F,\zeta}}{P} \quad (5.12)$$

leading to the mass fraction expression:

$$Y_{F,\zeta} = \frac{X_{F,\zeta} W_F}{X_{F,\zeta} W_F + (1 - X_{F,\zeta}) W_{nF,\zeta}} \quad (5.13)$$

with $W_{nF,\zeta}$ the mean molar mass of the mixture without the fuel at the interface. As the molar mass is supposed to be the same at the far-field, it gives:

$$W_{nF,\zeta} = W_{nF,\infty} = \frac{1 - Y_{F,\infty}}{1 - Y_{F,\infty} \frac{W}{W_F}} \bar{W} \quad (5.14)$$

A more advanced model, from Abramzon and Sirignano [1], is used here with:

$$\dot{m}_p = -Sh\pi d_p \rho D_F \ln(B_M + 1) \quad (5.15)$$

with Sh the modified Sherwood number:

$$Sh = 2 + (Sh^0 - 2)/F_M \quad (5.16)$$

with

$$F_M = (1 + B_M)^{0.7} \frac{\ln(1 + B_M)}{B_M} \quad (5.17)$$

and

$$Sh^0 = 2 + 0.55Re_p^{1/2}Sc_F^{1/3} \quad (5.18)$$

The **Sherwood number** Sh^0 expression is the Ranz and Marshall approximation [250]. It represents the ratio between convective and diffusive mass transfer. This model includes a correlation to correctly represent the heat due to the convective layer that is developing at the surface of the droplet, which increases the temperature and therefore the mass transfer.

Droplets are known to follow a d^2 **law** when evaporating. From the expression for \dot{m}_p [292] obtained in the previous paragraph, and expressing the mass flux as:

$$\dot{m}_p = \frac{4}{3}\pi\rho_l\frac{\partial r^3}{\partial t} \quad (5.19)$$

the evolution of the diameter of the droplet is obtained:

$$d_p^2 = d_{p,0}^2 - \frac{8\rho D_F}{\rho_l} \ln(1 + B_M) t \quad (5.20)$$

with $d_{p,0}$ the initial droplet diameter, and ρ_l the liquid density.

A characteristic number can be given from this definition, namely:

$$\tau_{ev} = \frac{\rho_l d_{p,0}^2}{8\rho D_F \ln(1 + B_M)} \quad (5.21)$$

Vaporisation number

The vaporisation number is given in equation 5.22:

$$\Psi = \frac{\tau_{ev}}{\tau_{flow}} \quad (5.22)$$

where τ_{flow} is here the travel time between the injection and the flame.

- if $\Psi < 1$, the evaporation time of the droplet is less than the flow time: the droplet fully evaporates before reaching the flame front.
- if $\Psi > 1$, the evaporation time of the droplet is more than the flow time: the droplet reaches the flame front and evaporates while burning.

Heat transfer

Similarly to the mass transfer, integrating between the droplet surface and the far-field the third equation of the system 5.7 a first time leads to:

$$\dot{m}_F C_p (T - T_\zeta) = 4\pi\lambda r^2 \frac{dT}{dr} - 4\pi\lambda \left(r^2 \frac{dT}{dr} \right)_\zeta \quad (5.23)$$

Using the boundary condition at the droplet surface for the temperature and its gradient, and integrating a second time, another expression for the fuel mass transfer may be found:

$$\dot{m}_F = 4\pi r_p \frac{\lambda}{C_p} \ln(B_T + 1) \quad (5.24)$$

with the thermal Spalding number:

$$B_T = \frac{C_p(T_\infty - T_\zeta)}{L_v} \quad (5.25)$$

Comparing with the expression of \dot{m}_F with B_M gives:

$$1 + B_T = (1 + B_M) \frac{D_F C_p}{\lambda} \quad (5.26)$$

The boundary condition at the droplet surface may be written:

$$\dot{m}_p L_v(T_\zeta) = \lambda \left(\frac{dT}{dr} \right)_\zeta = Nu \frac{\lambda}{d_p} (T_\zeta - T_\infty) \quad (5.27)$$

Finally, an expression for ϕ_g^{cond} may be found:

$$\phi_g^{cond} = 4\pi r_p \lambda Nu (T_\zeta - T_\infty) \frac{\ln(B_T + 1)}{B_T} \quad (5.28)$$

introducing Nu the modified Nusselt number:

$$Nu = 2 + (Nu^0 - 2)/F_T \quad (5.29)$$

with

$$F_T = (1 + B_T)^{0.7} \frac{\ln(1 + B_T)}{B_T} \quad (5.30)$$

and

$$Nu^0 = 2 + 0.55 Re_p^{1/2} Sc_F^{1/3} \quad (5.31)$$

the Nusselt number from the Ranz and Marshall approximation [250]. Similarly to the Sherwood number, the Nusselt number represents the ratio between the convection and the heat conduction and is introduced to correct the original expression.

The heat exchange terms may then be computed as:

- gaseous evaporation flux ϕ_g^{ev} :

$$\phi_g^{ev} = \dot{m}_F h_{s,F}(T_\zeta) \quad (5.32)$$

- liquid evaporation flux ϕ_l^{ev} :

$$\phi_l^{ev} = \dot{m}_p h_{s,p}(T_\zeta) = -\phi_g^{ev} - \dot{m}_p L_v(T_p) \quad (5.33)$$

- gaseous conductive flux ϕ_g^{cond} :

$$\phi_g^{cond} = 4\pi r_p \lambda Nu (T_\zeta - T_\infty) \frac{\ln(B_T + 1)}{B_T} \quad (5.34)$$

- liquid gaseous conductive flux ϕ_l^{cond} :

$$\phi_l^{cond} = \left(4\pi r^2 \lambda \frac{dT_p}{dr} \right)_{\zeta^-} = -\phi_l^{ev} - \phi_g^{ev} - \phi_g^{cond} = +\dot{m}_F L_v - \phi_g^{cond} \quad (5.35)$$

using the enthalpy balance:

$$\phi_l^{ev} + \phi_l^{cond} + \phi_g^{ev} + \phi_g^{cond} = 0 \quad (5.36)$$

The temperature evolution of the droplet given with an enthalpy balance:

$$\frac{d}{dt}(m_p h_{s,p}(T_p)) = \phi_l^{ev} + \phi_l^{cond} \quad (5.37)$$

then takes the following form:

$$\boxed{m_p C_{p,p} \frac{dT_p}{dt} = \dot{m}_p L_v(T_p) - \pi d_p Nu \lambda (T_p - T_\infty) \frac{\ln(B_T + 1)}{B_T}} \quad (5.38)$$

Multi-component modelling

Multi-component evaporation models can be divided into two categories.

At first, based on the distillation curves, one approach is to adjust the droplet composition to reproduce the evolution of droplet properties when looking at the fuel surrogate. The liquid fuel components are then tracked through the droplet lifetime while evaporating each species differently. This model is called the **Discrete Multi-Component model (DCM)** [246], [273], which is easy to implement, but would be costly when considering all the species (several hydrocarbon families and carbon numbers) that are represented for a given blend.

Another approach is then the **Continuous Multi-Component model (CMC)** suggested by [303] and improved by others [243]. The principle of continuous models is to determine the droplet properties by considering the mixture to depend on a probability density function of the molar weight. The preferential evaporation is then recovered and the coding more efficient, as it does not require an equation per species. However, such model was at first restricted to one family of compound before Yang [324] introduced the **discrete continuous multi-component model** [164]. This model represents each family by a distribution function. An issue with the continuous multi-component models is the link with the gaseous phase, which is not straightforward. Indeed, even if for DNS of droplets, a wide range of species may be considered, the calculation of a 3D turbulent burner is limited in terms of species and therefore the species class represented in the liquid phase has to be limited to one species representing the whole class in the gaseous phase, such as in [74]. Furthermore, the continuous model might not be adapted for every fuel blend, as some of them contain only some given species and thus cannot be approximated as a PDF function.

In this work, multi-component fuels are studied, represented with a simple discrete multi-component model [286]. The associated multi-component evaporation model is detailed in [282] and is similar to the mono-component liquid-phase model. Each fuel component in the droplet is defined by its mass fraction Y_i^{liq} . The diffusivity of the species inside the liquid phase is supposed to be infinite, meaning a uniform droplet composition.

The Spalding mass number is the same for the entire fuel and for each fuel species, and it takes the following expression:

$$B_M^{multi} = \frac{\sum_{i=1}^{N_{s,F}} Y_\zeta^i - \sum_{i=1}^{N_{s,F}} Y_\infty^i}{1 - \sum_{i=1}^{N_{s,F}} Y_\zeta^i} = \frac{Y_\zeta^i - Y_\infty^i}{\epsilon_i - Y_\zeta^i} \quad (5.39)$$

with ϵ_i the fraction of vapour of component i and $N_{s,F}$ the number of species in the fuel.

The vapour pressure is calculated from the component molar fractions:

$$X_{i,\zeta} P = X_{i,liq} P_{i,\zeta} \quad (5.40)$$

with $X_{i,\zeta}$ the molar fraction of fuel component i at the droplet surface, P the pressure of the gaseous phase, $X_{i,liq}$ the liquid molar fraction of fuel component i and $P_{i,\zeta}$ its vapour pressure. This relation is valid for atmospheric pressure cases as, when going to higher pressure cases, a fugacity coefficient is appearing.

The total evaporation rate of the droplet \dot{m}_p and the fraction of vapour created ϵ_i are used to calculate the evaporation rate of each component \dot{m}_p^i :

$$\dot{m}_p^i = \epsilon_i \dot{m}_p \quad (5.41)$$

Transport properties

The transport properties in the gas layer around the droplet may significantly differ from the values in the combustion chamber, with a non-negligible impact on the evaporation rate.

First, the temperature and composition of the gas in this thin film must be determined. This is often calculated with the third rule, which states that approximately all quantities are a mix of far-field and droplet surface values, at a rate of 1/3 and 2/3 respectively:

$$\begin{aligned} T_{film} &= T_\zeta + \frac{1}{3}(T_\infty - T_\zeta) \\ Y_{k,film} &= Y_{k,\zeta} + \frac{1}{3}(Y_{k,\infty} - Y_{k,\zeta}) \end{aligned} \quad (5.42)$$

These values are taken as inputs to calculate transport properties around the droplet:

- a first methodology consists in taking the constant Schmidt and Prandtl numbers defined for the mixture. This may lead to important errors in the predicted evaporation droplet time, as shown in [274].
- a second methodology consists in calculating second values of the Schmidt and Prandtl numbers, more representative of the film mixture. These calculations may be performed with Cantera or any other equivalent code, using the complex transport model. These optimised Schmidt and Prandtl values give more accurate results of evaporation [274] and this method is used in this work for mono-component fuels.
- for multi-component fuels, polynomials taken from [325] are used. They write:

$$\begin{aligned} D_F &= A_{D_F} + B_{D_F}T + C_{D_F}T^2 \\ \mu &= A_\mu + B_\mu T + C_\mu T^2 + D_\mu T^3 \\ \lambda &= A_\lambda + B_\lambda T + C_\lambda T^2 + D_\lambda T^3 \end{aligned} \quad (5.43)$$

where A , B , C and D are coefficients specific to each fuel. To estimate the coefficient of the multi-component fuel, standard mixing laws are finally applied.

5.1.1.3 Point-source approximation

As in most EL models, one main principle of the Lagrangian methodology implemented in AVBP is to represent the droplet as a point and to consider the surrounding gas as the far-field. This avoids describing the volume of each droplet, which would be unfeasible in 3D cases, and is a reasonable approximation for dilute sprays with small droplets. However, if the mesh cell size is comparable or smaller than the droplet size, this approximation may

not be valid anymore. In addition, as the exchange terms in the gas phase are inversely proportional to the cell volume, too small cells may lead to numerical stiffness.

The point-source error increases with smaller mesh size, but effects are already visible for a droplet only ten times smaller than the mesh size, as shown in [222]. Two different methods exist to limit this error:

- the **global method** applies a global filter on the source terms everywhere in the computational domain. It will not be used here, since it may deteriorate the solution at locations without droplets.
- the **local method** spreads the source terms over several surrounding cells to limit the local perturbation induced by the source terms. From 0D isolated droplet evaporation cases, the optimum number of neighbours to be used for spreading the source term corresponds to a volume that is 17 times larger than the droplet [222]. This methodology is more costly than the previous one as cell neighbours need to be found, but it is applied only when necessary.

5.1.2 Liquid injection

Injection controls the spray, which in turn influences the combustion through droplets velocity and diameters. Generally, liquid fuel is going out of the feeding line through the **nozzle** of the **injector**. Droplets are formed and enter the combustion chamber through the **atomiser**, represented in Fig. 5.2. Three physical principles are mainly used to atomise the liquid [171]:

- **pressure atomisers** work on the principle that pressure in the small aperture is converted into velocity when the liquid is thrown into the combustion chamber. As a consequence, the droplets are atomised.
- in **air-assisted or airblast atomisers**, the air flow applies shear forces to the liquid flow which atomises the droplets.
- in **rotary atomisers** the liquid fuel is thrown from a rotating disk with holes at the edges.

The spray coming out of the injector can prefilm on the surrounding walls to re-atomise at the tip in smaller droplets. The air flow can also be divided to increase the number of shear flows and better atomise the fuel. This description is not exhaustive and for more information, please refer to [171].

5.1.2.1 Atomisation

The modelling of liquid injection and atomisation is a field of study on its own, and remains currently a challenge in combustion applications. The complete transformation of a continuous liquid phase to an atomised spray is known to go through two distinct phases:

- the **primary atomisation** [171], [193], [296] (or **liquid breakup**) appears when the liquid sheet or jet is submitted to instabilities such as Rayleigh-Taylor [259], leading eventually to detachment of liquid pockets and breakup. The numerical simulation of this phenomenon is complex [166] and computationally costly since it requires very fine meshes capturing the interface between the liquid and the gas.

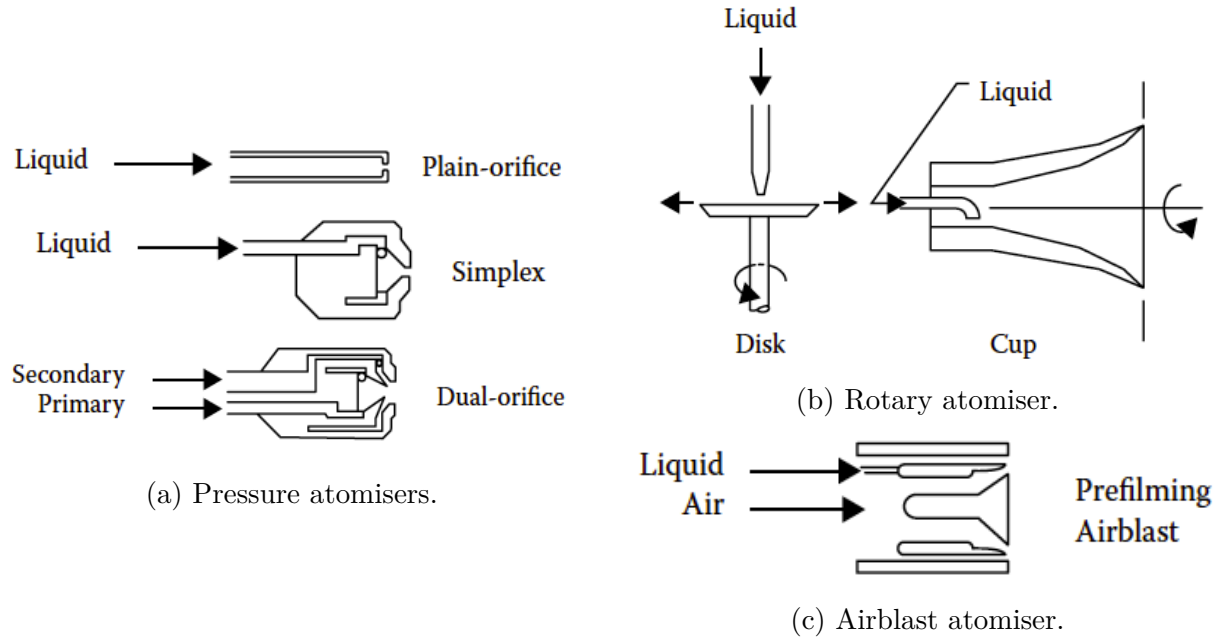


Figure 5.2: Sketches of different atomiser types from [171].

Numerical methods for such computations include interface tracking with the Level-Set method [217] and the Volume of Fluid (VoF) [125] method, but their cost limits their application to low Reynolds numbers and simple geometries. Therefore, primary atomisation is usually not simulated in large 3D calculations but approximated with phenomenological modelling.

The phenomenological model used in AVBP is called **FIM-UR** (Fuel Injection Method by Upstream Reconstruction) [275] and defines injection profiles for a spray produced by the various types of atomisers. A sketch of the model is represented in Fig. 5.3 for a pressure-swirl atomiser, mostly used in aeronautical engines.

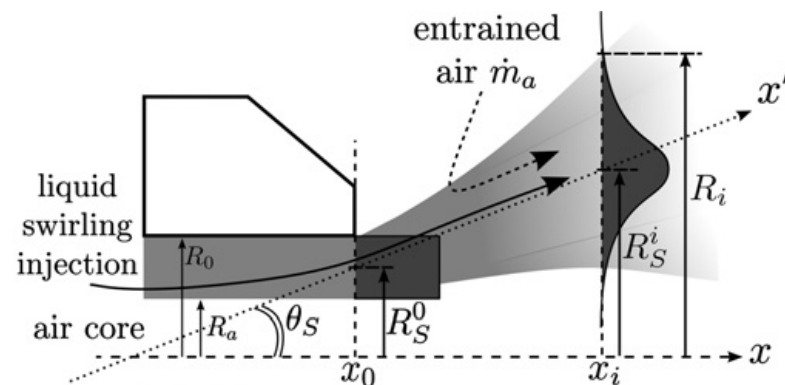


Figure 5.3: Sketch of the FIM-UR modelling for primary atomisation taken from [275].

This scheme illustrates the internal geometry of a simplex atomiser [17]. The liquid comes out in a hollow cone thin liquid sheet of half angle θ_S and radius R_0 . The

following expression [262] relates the half angle to the contraction factor X :

$$X = \frac{A_{air}}{A_{exit}} = \left(\frac{R_a}{R_0}\right)^2 = \frac{\sin^2 \theta_S}{1 + \cos^2 \theta_S} \quad (5.44)$$

From this contraction factor, the velocity of the droplets is expressed at the injector nozzle:

$$\begin{aligned} u_{l,r}^0(\theta, r_0) &= 0 \\ u_{l,\theta}^0(\theta, r_0) &= \frac{\dot{m}_l}{\rho_l A_p} \frac{r_0}{R_S^0} \\ u_{l,x}^0(\theta, r_0) &= \frac{\dot{m}_l}{\rho_l \pi R_0^2 (1 - X)} \end{aligned}$$

with $A_p = 20.73 C_d^2 A_0$ and $C_D = 1.17 \sqrt{\frac{(1-X)^2}{(1+X)}}$ thanks to the correlation of Lefebvre [171]. This model provides an approximate spray injection velocity with on only two user-input parameters: the half-angle of the spray and the radius of the injector tube. It must be achieved by a droplet size distribution, which is described in the next section.

- the **secondary atomisation (or secondary breakup)** occurs when the droplets issued from the primary breakup are subjected to outside forces that are greater than their inside forces, mainly the surface tension. The droplets then further fragment into smaller droplets, reducing the mean spray diameter. This breakup is much more characterised than the primary breakup and easier to model. The secondary breakup model of Gorokhovski et al. [104] is implemented in AVBP [281] but it is not used in this work and is not further detailed.

5.1.2.2 Injection size distribution

Knowing the liquid density, the mass flow rate and the droplet velocity, the droplet size distribution must now be determined. It is described with Probability Density Functions (PDF), which can be defined by either targeting the number of droplets (**numerical** injection) or the volume of droplets (**volume** injection). Examples of both distributions are shown on Fig. 5.4 (left). The various moments of the PDF give characteristic diameters,

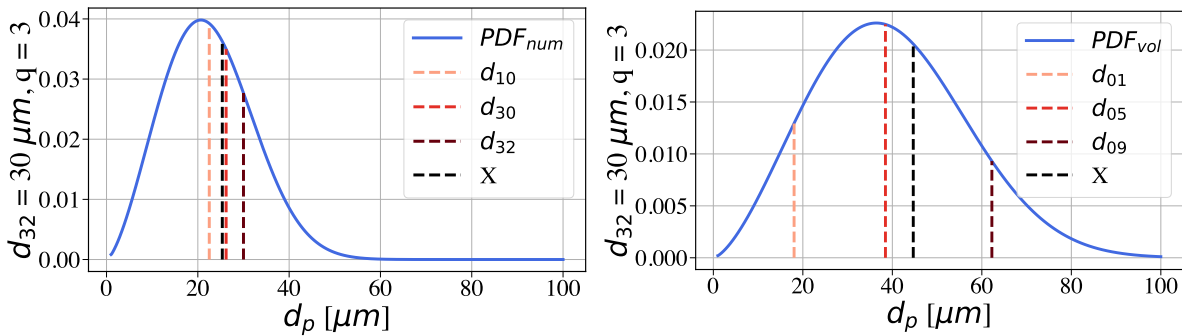


Figure 5.4: Number and volume Probability Density Functions (PDF) with their characteristic diameters.

defined as:

$$d_{ab} = \left[\frac{\int_{d_{p,min}}^{d_{p,max}} d_p^a \frac{dN}{dd_p} dd_p}{\int_{d_{p,min}}^{d_{p,max}} d_p^b \frac{dN}{dd_p} dd_p} \right]^{\frac{1}{a-b}} = \left[\frac{\sum_i d_{p,i}^a N_i}{\sum_i d_{p,i}^b N_i} \right]^{\frac{1}{a-b}} \quad (5.45)$$

with dN/dD the particle numerical distribution and N_i the number of particles within the class diameter $d_{p,i}$. Several mean diameters can thus be defined with varying a and b . Figure 5.4 (right) represents various characteristic diameters. The mean diameters that are mainly used are:

- d_{10} , the mean droplet diameter, which represents a simple arithmetic mean.
- d_{30} , the mean droplet diameter, which represents the arithmetic mean of the diameter weighted by the volume.
- d_{32} , the **Sauter Mean droplet Diameter (SMD)** [278], which represents the mean of the ratio between the volume over the surface of the droplet. The SMD is usually interpreted as the capability of the droplet to evaporate fast or not.

Diameters representing the volume of the liquid injected are measured with d_{0N} , with N an integer, which defines the diameter below which the cumulative PDF represents $N0\%$ of the volume of the spray. The D_{05} , called the **Mass Median Diameter (MMD)**, defines the area containing 50% of the total volume.

Because the droplet size distribution is not always measured, several assumed-shape PDFs exist in the literature (logarithmic distribution, Rosin-Rammler, Chi, etc...) to model it with only a few parameters. In this case, all assumed PDFs are Rosin-Rammler PDFs, detailed next.

The **Rosin-Rammler distribution** is specified through the SMD d_{32} parameter and a spread parameter q . It takes the following expressions:

- if the Rosin-Rammler distribution is volume-based:

$$1 - Q(d_p) = \exp\left(-\left(\frac{d_p}{X}\right)^q\right) \quad (5.46)$$

with X the characteristic diameter:

$$X = d_{32} \Gamma\left(1 - \frac{1}{q}\right) \quad (5.47)$$

$Q(d_p)$ represents the total volume fraction of the liquid phase contained in a volume for diameters less than d_p .

- if the Rosin-Rammler distribution is number-based:

$$1 - n(d_p) = \exp\left(-\left(\frac{d_p}{X}\right)^q\right) \quad (5.48)$$

with X the characteristic diameter:

$$X = d_{32} \frac{\Gamma\left(1 + \frac{2}{q}\right)}{\Gamma\left(1 + \frac{3}{q}\right)} \quad (5.49)$$

$n(d_p)$ is the total numerical fraction of the liquid phase contained in a volume for diameters less than d_p .

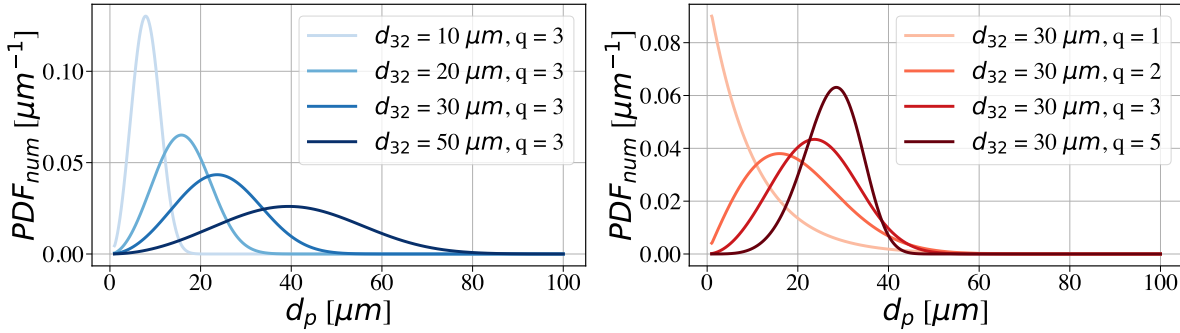


Figure 5.5: Numerical Rosin-Rammler PDF varying the SMD (left) and the spread parameter q (right).

The Rosin-Rammler is the most common distribution representative of industrial cases. Figure 5.5 represents the sensitivity of the Rosin-Rammler distribution shape to the SMD and the spread parameter q .

The higher the SMD d_{32} , the higher the mean diameter d_{10} of the distribution. The higher the spread parameter q , the higher the distribution shifted to the right. Typically, $d_{32} \in [1, 100]$, $d_{10} \in [1, 100]$ and $q \in [1, 3]$.

The numerical injection procedure is then to determine how many droplets should be injected at each time-step in order to reach the targeted mass flow rate.

5.1.3 Spray-wall interactions

The interaction between the walls and the droplets should not be neglected, especially inside the atomisers. Different droplet/wall interaction modes have been observed experimentally [254], that were simplified by [99], namely a droplet can either rebound, film or splash on a wall. The interaction depends on the energy of the droplet when impacting, the wall temperature, the wall roughness and the presence of a liquid film.

In AVBP several options are available:

- the particle can **rebound** on the wall without any loss of energy.
- the particle can **slip** on the wall, that is to say, move along the wall without detaching from it.
- the particle can **film** on the wall, which is detailed in the next paragraph. The main difference between slipping and filming is that in the latter case, the particle motion is the one of the liquid film.
- the particle can **splash** on the wall, that is to say that it is fragmented into particles with lower diameter when hitting the wall.

The two following paragraphs detail the film modelling implementation in AVBP and the model used to handle wall interactions, developed initially by [42] and validated by [131]. These models have been used in the SSB combustion chamber of Chapter 9 and Chapter 10.

Liquid film modelling

When droplets enter the liquid film, i.e., cross the film height, their behaviour is changed to describe the behaviour of a liquid film. In particular, they take the liquid film velocity.

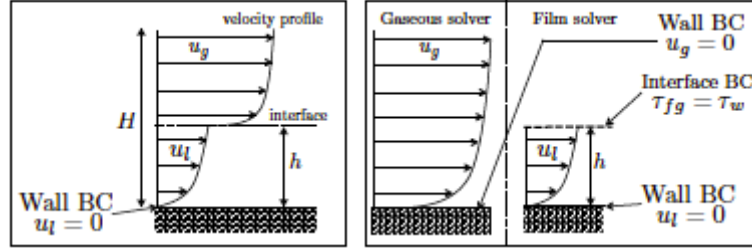


Figure 5.6: Velocity profiles associated to the liquid modelling from [42]

As shown in Fig. 5.6, the thin film hypothesis allows keeping the velocity of the gaseous phase unchanged. The velocity of the liquid film, i.e., of the droplets that are trapped inside the film, writes:

$$u_{fg} = \tau_{fg} \frac{h}{\mu} + \left(\rho g \sin \gamma - \frac{dP}{dx} \right) \frac{h^2}{\mu} \quad (5.50)$$

with τ_{fg} the shear stress at the film/gas interface, u_{fg} the axial velocity, γ the angle of the wall, h the height of the film and μ the viscosity.

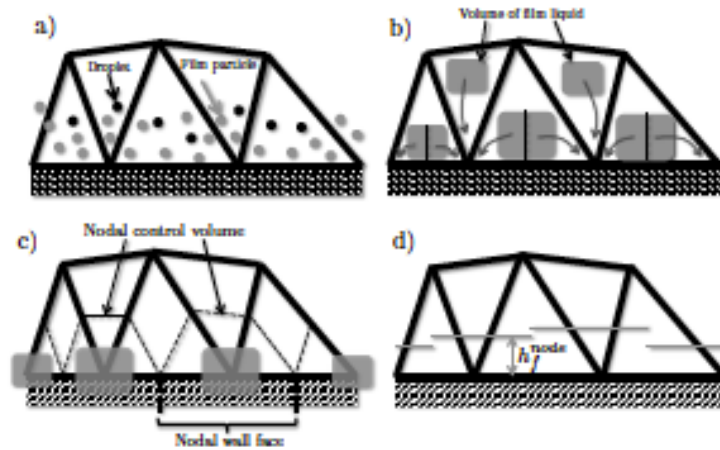


Figure 5.7: Calculation method of the film height.

Finally, the height of the film is calculated by an Eulerian projection of the total liquid volume at the cell nodes located on the wall. Figure 5.7 explains the methodology. The droplets located at a wall distance lower than h form a certain volume of liquid. This volume is then scattered among the nodes of the wall and used to evaluate the film height at each node.

Complex interaction model

Different interaction regimes can be found depending on the wall and the droplet conditions [115]. As shown in Fig. 5.8, the different regimes are simplified in three main regimes, depending on the Weber number and the wall temperature. The Weber number is introduced as:

$$We = \frac{\rho_l |u - u_p|^2 d_p}{\sigma} \quad (5.51)$$

with u_p the droplet velocity and σ the surface tension. This number characterises the ratio of the droplet drag force over the droplet surface force. Large Weber numbers correspond to low surface tension and small droplets. In cold conditions, if the impact energy of the droplet is large enough, the droplet splashes, i.e., the spray is fragmented into finer droplets and a part of the liquid is filming on the wall. Otherwise, the droplet completely films on the wall. For hot conditions, if the impact energy of the droplet is large enough, the droplet splashes, otherwise it rebounds.

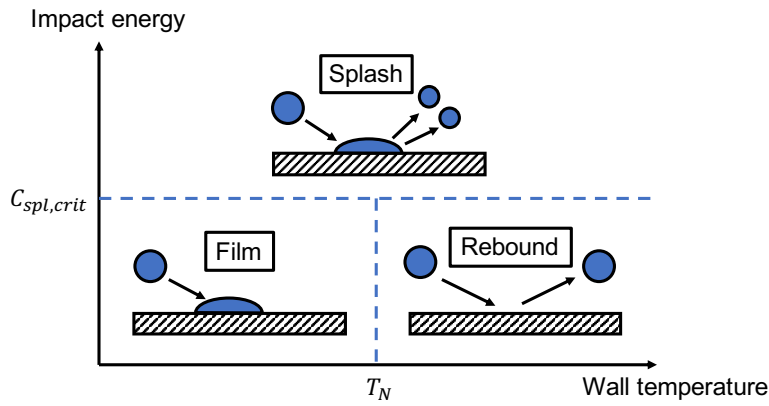


Figure 5.8: Complex wall/particle interaction, adapted from [42].

The transition temperature between the hot and the cold regime is defined as [115]:

$$T_N = \frac{T_{sat} + T_p}{2} \quad \text{with } T_p = \frac{27}{32} T_c \quad (5.52)$$

with T_{sat} the saturation temperature and T_c the critical temperature of the liquid species. For hot conditions, the threshold Weber number is defined from experimental observations [206], [313] as:

$$We_{c,dry} = 30 \quad (5.53)$$

In cold conditions, the critical Weber number depends on the roughness of the wall and the droplet Reynolds number. When taking into account the film thickness, it leads to the following formula:

$$We_{c,wet} = \frac{C_{spray}}{\sqrt{Re_{imp}}} (1500 + 650 \left(\frac{d_p}{R_a}\right)^{0.42}) \quad (5.54)$$

with C_{spray} a constant calibrated in [113], R_a the surface roughness and Re_p the Reynolds number at the droplet impact. To determine if the particle films or splashes, a correlation has been found [114] between the mass of liquid that is ejected m_{splash} and the total mass of liquid impacting the walls m_{impact} :

$$\frac{m_{splash}}{m_{impact}} = \min(2.910 \cdot 10^{-4} \sqrt{Re_{imp}} (We_{imp} - We_{c,f}), 0.75) \quad (5.55)$$

This ratio is then compared to a random number that is comprised between 0 and 1 to determine if the droplet splashes or films. The expression of the diameter of the splashed droplet as well as the velocity after the impact can be found in [131].

5.1.4 Combustion variables in spray flames

In spray flames, a part of the fuel may be hidden from the calculation due to fast combustion after evaporation. This has direct consequences on the combustion variables, such as the mixture fraction, for example. Therefore, these variables must be redefined to take into account the liquid part. It should be noted that gaseous variables still hold in two-phase flames and can still be used, but with special care for interpretation.

Liquid loading

The liquid phase represents a reservoir of fuel which can react after evaporation. This fuel quantity is measured with the **liquid loading**, α_l , which takes the following expression:

$$\alpha_l = \frac{V_{liq}}{V_{liq} + V_{gas}} \quad (5.56)$$

where V_{liq} and V_{gas} are respectively the liquid and gaseous volumes. The liquid loading can also be defined as a mass ratio, introducing the liquid mass fraction:

$$Y_{F,l} = \frac{m_F^l}{m_{tot}} \approx \frac{\rho_l \alpha_l}{\rho} \quad (5.57)$$

This relation is valid for $V_{liq} \ll V_{gas}$.

Liquid equivalence ratio

As a consequence, the equivalence ratio can be redefined to take into account the liquid fuel loading. The resulting equivalence ratio is called ϕ_{tot} and is defined as:

$$\phi_{tot} = \phi_g + \phi_l = s_Y \frac{Y_F}{Y_O} + s_Y \frac{1}{Y_O} \frac{\rho_l \alpha_l}{\rho} \quad (5.58)$$

As in Chapter 3, a local equivalence ratio is defined, as stated in [39]:

$$\phi_{loc,tot} = \phi_g + \phi_l = \frac{2n(C) + \frac{1}{2}n(H)}{n(O)} + \frac{2n_l(C) + \frac{1}{2}n_l(H)}{n(O)} \quad (5.59)$$

Liquid mixture fraction

The liquid mixture fraction has been introduced by Bilger [20] and takes the following form:

$$z_{Bilger,liq} = \frac{\beta - \beta_O}{\beta_F - \beta_O} + Y_{F,l} \quad (5.60)$$

with $\beta = \sum_i \gamma_i \sum_k a_{ki} \frac{W_i}{W_k} Y_k$ and $Y_{F,l}$ the liquid mass fraction of fuel. As well, the liquid mixture fraction may be defined as a function of the different molar quantities:

$$z_{Bilger,liq} = \frac{2n_c + \frac{1}{2}n_H - n_O + n_O^0}{2n_C^0 + \frac{1}{2}n_H^0 + n_O^0} + Y_{F,l} \quad (5.61)$$

For multi-component fuels, the relation above is not valid because the initial quantities (n_C^0 , n_O^0 and n_H^0) may not represent the local blend. To overcome this issue, it is possible to determine the local hydrogen/carbon ratio for the different fuels and deduce the local mixture fraction. Indeed, at first, a relation between s_Y and the molar ratio $H/C = \frac{n_H}{n_C}$ is:

$$s_Y = s_X \frac{W_{O_2}}{W_F} = (x + \frac{y}{4}) \frac{2W_O}{xW_C + yW_H} = 2W_O \frac{1 + \frac{H/C}{4}}{W_C + H/CW_H} \quad (5.62)$$

Then, the stoichiometric mixture fraction is considered, and the local H/C ratio is supposed to be the same as in the initial blend, that is to say at $Y_F^0 = 1$ and $Y_{O_2}^0 = 0.233$, the air composition. As a result, z_{st} can be written:

$$z_{st,loc} = \frac{1}{1 + s_Y \frac{Y_F^0}{Y_{O_2}^0}} = \frac{-\beta_O}{\beta_F - \beta_O} \quad (5.63)$$

By simplifying this expression, the initial fuel of β takes the following expression:

$$\beta_F = -s_Y \frac{Y_F^0}{Y_{O_2}^0} \beta_O \quad (5.64)$$

Therefore, by knowing locally the coefficient s_Y , the proportion of hydrogen and carbon that are burning are known, enabling to construct the local mixture fraction.

As this expression gives the same analysis as the local equivalence ratio, ϕ_{loc} is preferred in this work. However, this mixture fraction could be an interesting parameter for tabulation methods, allowing to give one table instead of three in the multi-component case [328].

5.2 Two-phase combustion regimes

As stated in Section 2.1.3, the combustion mode of the droplets is characterised by the non-dimensional number called the **group number G** and detailed in Section 5.2.1. In Section 5.2.2, the focus will be made on the isolated droplet combustion model.

5.2.1 Group number

Chiu et al. [45], [46] have been the first to classify combustion modes by analysing the evolution of a flame propagating in a droplets cloud in a hot environment. They introduced the group number G , which compares the evaporation characteristic time to the molecular diffusion characteristic time. In Chiu et al. [45], the group number takes the following definition:

$$G_{chiu} = (1 + 0.276Re^{1/2}Sc_F^{1/3})Le_F N^{2/3}(d_f/S) \quad (5.65)$$

where Re_p is the particle Reynolds number, N the total number of droplets in the cloud, d_f the averaged radius of the droplet flame diameter and S the average spacing between the centres of the droplets. The different combustion regimes associated to the different group numbers are represented in Fig. 5.9 in a $S-N$ diagram.

The different flame types are characterised in the following:

- in the **isolated droplet combustion**, a flame stabilises around each single droplet. The group number is less than 0.01.

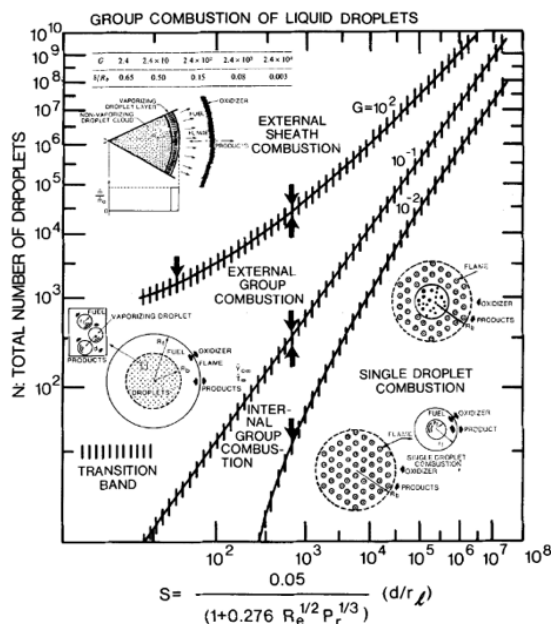


Figure 5.9: Group combustion according to [45].

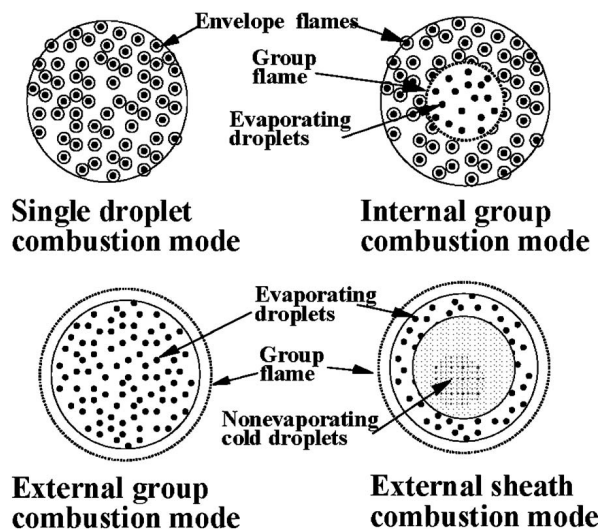


Figure 5.10: Combustion regime diagrams according to [208].

- the **internal group combustion** represents a kernel within the droplet cloud where the droplets are vaporised. The group number is between 0.01 and 1.
- the **external group combustion** corresponds to a flame that encloses the droplets. This is the most common combustion regime in many industrial applications. The group combustion number is found to be between 1 and 100.
- the **external sheath combustion** corresponds to the cloud of droplets burning in a thin sheet of fuel vapour. The group number here is over 100.

Candel [37] showed that in most cases for large Peclet number (i.e. convective characteristic time larger than diffusion characteristic time), the group number can be expressed as:

$$G_{candel} = 5N^{2/3}d_f/S \quad (5.66)$$

Finally, to check the group number in flames, a macroscopic approach [4] has led to the following expression:

$$G_{annamalai} \simeq \alpha_L \frac{d_{cloud}^2}{d_p^2} \quad (5.67)$$

with d_{cloud} evaluated as the mean thickness of the flame spray sheet. This expression was used in [222].

Single droplet combustion and group combustion are very different in terms of local intensity and flame structure. In principle, the flame around a droplet is non-premixed. However, the point source approximation does not allow describing this diffusion flame and in practice the fuel vapour issued from the droplet mixes with the gas and burns in the cell in premixed mode. The evaporation rate and heat release rate are then erroneous and may lead to a wrong shape of the flame. Therefore, a specific model must be used for single droplet burning, presented in the next section.

5.2.2 Single droplet burning: the MustARD model

The MustARD (Multi-state Algorithm for Reactive Droplets) model, which was developed by Paulhac [222], describes the various single droplet combustion regimes and is summarised here. The model is illustrated in Fig. 5.11.

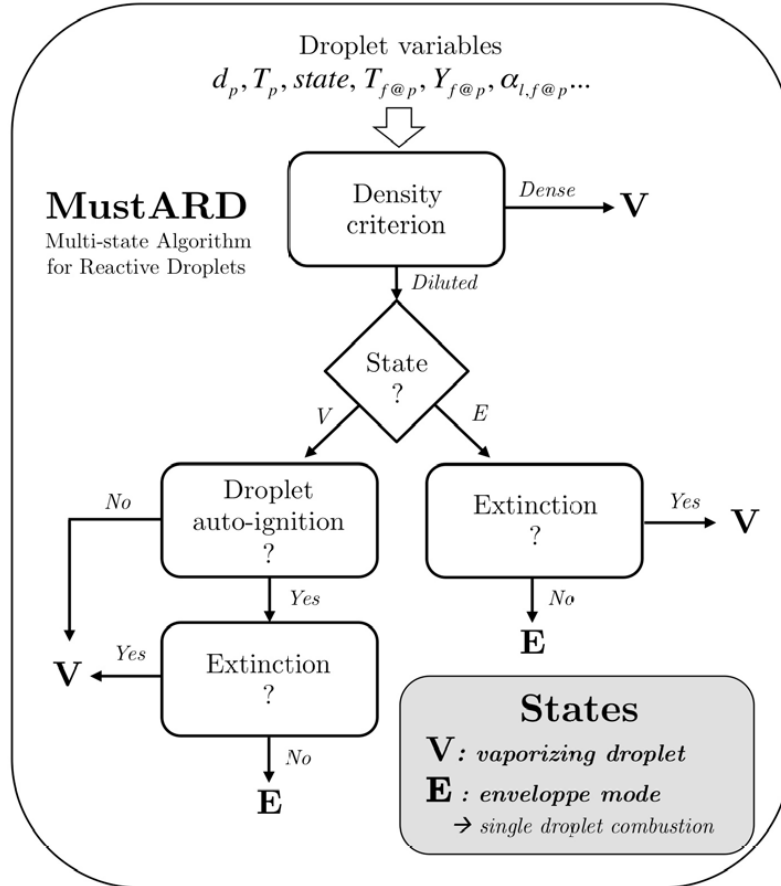


Figure 5.11: MustARD model as shown in [222].

First, at every iteration, a number density criterion is applied to see if the droplets are far enough to burn individually. On the one hand, if this criterion is verified, the occurrence of extinction is tested. If the droplet is quenched, and not able to auto-ignite, the normal vaporising model applies, otherwise an envelope combustion model is used. On the other hand, if the density criterion is not verified, the vaporising mode is activated. The three criteria: number density, auto-ignition and extinction are detailed in the following paragraphs as well as the equations for single droplet combustion.

Number density criterion

First, if the spray is too dense, the droplets cannot burn individually. Therefore, a criterion can be derived to estimate the **inter-droplet distance**:

$$S = \left(\frac{\pi}{6\alpha_l} \right)^{\frac{1}{3}} d_p \quad (5.68)$$

This distance is then compared to the flame diameter d_f , of which the expression will be given later:

- if $d_f < S$, the flame diameter is below the inter-droplet distance and if the conditions allow it, the droplet burns individually (E).
- on the contrary, if $d_f > S$, the space between the droplets is too small to enable the flame to sustain, thus the droplet burns in a group mode and the individual droplet only evaporates (V).

Equations for the envelope mode

The model derived here uses the same assumptions as for the Spalding evaporation model:

- Droplets are supposed to be spherical and isolated.
- The liquid thermal conductivity is supposed to be infinite.
- The droplet is considered to be in a quasi-steady state with the gaseous flame.

The new system of equations, taking into account the chemical reactions, is then the following:

$$\begin{cases} \rho u r^2 = \frac{\dot{m}_F}{4\pi} \\ \rho u r^2 \frac{dY_k}{dr} = \frac{d}{dr} \left(r^2 \rho D_k \frac{dY_k}{dr} \right) + \dot{\omega}_k \\ \rho u r^2 C_p \frac{dT}{dr} = \frac{d}{dr} \left(r^2 \lambda \frac{dT}{dr} \right) + \dot{\omega}_T \end{cases} \quad (5.69)$$

The only difference here is that the combustion occurring at the vicinity of the droplet needs to be taken into account. The chemistry is supposed to be a global one-step reaction, so that:

$$\dot{\omega}_F = s_Y \dot{\omega}_O \dot{\omega}_T = Q \dot{\omega}_F \quad (5.70)$$

with Q the heat of combustion.

Kuo [156] defines two parameters:

$$b_Y = \frac{Y_F - Y_{O,s_Y}}{(Y_{F,\zeta} - 1) - Y_{O,\zeta}/s_Y}$$

$$b_T = \frac{Q Y_{Ox}/s + C_p(T)T}{L_v + Q Y_{Ox,\zeta}/s_Y}$$

and by combining the species conservation equations for the two reactants, the following equation is obtained:

$$r^2 \rho u \frac{db_Y}{dr} = \frac{d}{dr} \left(r^2 \rho D \frac{db_Y}{dr} \right) \quad (5.71)$$

As well, a similar equation can be obtained for b_T and by integrating twice these equations, the same evaporation terms as for the Spalding model are obtained:

- the **mass transfer** is:

$$\dot{m}_p = -4\pi r_\zeta \rho D \ln(1 + B_M^{comb}) \quad (5.72)$$

with

$$B_M^{comb} = \frac{Y_{F,\zeta} + Y_{O,\infty}/s_Y}{1 - Y_{F,\zeta}} \quad (5.73)$$

These expressions are very similar to those obtained for the non-reactive droplet, except that $-Y_{F,\infty}$ is replaced here by $Y_{O,\infty}/s_Y$. The spherical flame radius can then be approximated by equating the mass flow rates at the droplet and at the flame locations:

$$r_f = r_\zeta \frac{\ln(1 + B_M^{comb})}{\ln(1 + Y_O^\infty/s_Y)} \quad (5.74)$$

- the **heat transfer** equations are re-written as well. The time evolution of the droplet temperature writes:

$$\frac{dT_p}{dt} = \frac{1}{m_p C_{p,p}} (-\phi_g^{cond} + \dot{m}_p L_v(T_p)) \quad (5.75)$$

and by applying the same balance between the conductive and evaporation fluxes going in and out of the droplet, the expression of ϕ_g^{cond} may be approximated:

$$\phi_g^{cond} = 4\pi\lambda r_\zeta \ln(1 + B_T) \frac{T_f - T_\zeta}{\frac{1+B_T}{(1+Y_O^\infty)^{1/Le_F}}} - 1 \quad (5.76)$$

with

$$B_T^{comb} = (1 + B_M^{comb})^{1/Le_F} - 1 \quad (5.77)$$

When using MustARD, all the evaporated fuel should burn completely because the chemistry is supposed to be infinitely fast and the relation $\dot{m}_p = \dot{\omega}_F$ is then correct for steady configurations.

V mode: Auto-ignition ?

If the inter-droplet distance S is large enough compared to the flame diameter to enable individual burning, a criterion needs to be set to assess that the flame effectively ignites. By integrating the energy equation of system 5.69 between the droplet surface and the stoichiometry, a chemical timescale may be estimated. Then, to estimate the ignition of a droplet, the **Livengood-Wu** index [178] is used:

$$I_{LW} = \int_0^t \frac{1}{\tau_{chem}(T_{st}(t))} dt \quad (5.78)$$

with τ_{chem} the chemical time used in MustARD and T_{st} the stoichiometric temperature. The integral form of the Livengood-Wu index enables to take into account the unsteady effects during ignition, by accumulating the contributions to the ignition through the droplet lifetime. The ignition and the mode (E) are activated when $I_{LW} = 1$. The model was validated in [222] with some heptane and iso-octane measurements.

E mode: Extinction ?

Extinction of a droplet can occur either by radiative heat loss, by large relative velocity or for too small droplet diameter. The first mechanism is not considered in this study, as droplets are small enough. Thus, both last mechanisms are explained and modelled:

- for **diameter extinction**, the extinction diameter of a burning droplet is evaluated [162]:

$$d_{ext}^2 = 2\tau_{chem,linan}^{ext} D_M \frac{\ln^4(1 + Y_O^\infty/s)}{\ln^2(1 + B_T)} \quad (5.79)$$

with $\tau_{chem}^{ext,linan}$ the chemical timescale valid near extinction and estimated with Linan's asymptotic theory [176]:

$$\tau_{chem}^{ext,linan} = \frac{W_F}{A\rho_M\left(\frac{C_{p,M}T_f^2}{T_a}\right)^3} \frac{L_v}{Q} \frac{1+B_T}{1+Y_O^\infty/s_Y} e^{1+T_a/T_f} \quad (5.80)$$

and

$$B_T = \frac{QY_x^\infty/s + C_p(T - T_p)}{L_v} \quad (5.81)$$

The index M denotes values evaluated at $T_M = \frac{T_f+T}{2}$.

- for **velocity extinction**, a convective time-step $\tau_{conv}^{MustARD}$ can be calculated based on potential flow theory around a sphere:

$$\tau_{conv}^{MustARD} = \frac{d_p}{6||u_p - u||} \quad (5.82)$$

as well as a chemical time-step;

$$\tau_{chem}^{ext} = A^{-1}(\rho Y_O^\infty)^{1-\nu_O-\nu_F} (s_Y W_F)^{\nu_F-1} (W_O)^{\nu_O} e^{\frac{-E_a}{RT}} \quad (5.83)$$

An extinction velocity, relative to this chemical timescale, can then be defined:

$$u_{ext} = \frac{d_p}{6\tau_{chem}^{ext}} \quad (5.84)$$

Therefore, the conditions of the extinction of a droplet are the following:

$$\begin{cases} ||u_p - u|| > u_{ext} \\ d_p < d_{ext} \end{cases} \quad (5.85)$$

If one of the condition is verified, the droplet is quenched. The model is tested in Paulhiac's thesis [222] and results agree well with DNS on n-heptane extinction but differ by one order of magnitude on the droplet extinction velocity, meaning that the auto-igniting droplet extinguishes faster than expected.

Model validations

This single droplet model was validated with several experimental results and applied to a spray counter-flow diffusion flame and to a real burner in Paulhiac's thesis [222]. Good comparisons with experiments were achieved using single droplets combustion. In the counter-flow diffusion flame case, results exhibit a significant part of the droplets burning in single droplet mode, leading to a slightly different flame shape. The combustion chamber analysed that 17.2% of the flame power was given by the single droplet regime. Thermal profiles were not analysed.

This model is used in this PhD to further see its applicability to the SSB combustion chamber, where single droplet burning was found.

Chapter 6

Modelling turbulence in reactive flows

Contents

6.1	Turbulence	93
6.2	LES concept and equations	95
6.3	Combustion/turbulence interaction	97
6.3.1	Turbulent flame regimes	97
6.3.2	Turbulent combustion models	99

Turbulence is defined as an unsteady chaotic motion of a fluid and is characterised by a wide range of time and space scales. It may be seen as a collection of vortices which enhance mixing and induce strong local shear and vorticity.

In Section 6.1, mathematical tools are introduced to characterise the flow and the different numerical methods to take this phenomenon into account are listed. Equations for modelling are then presented in Section 6.2. Finally, the physical interactions between turbulence and combustion as well as their numerical modelling are explained in Section 6.3.

6.1 Turbulence

Turbulence when inertial forces take over viscous forces, as expressed by the **Reynolds number**:

$$Re = \frac{\rho u L}{\mu} = \frac{u L}{\nu} \quad (6.1)$$

with u the characteristic velocity of the flow, L the characteristic length, ρ the density, μ the dynamic viscosity and ν the cinematic viscosity. The flow transitions from a **laminar flow** to a **turbulent flow** for a Reynolds number between 10^3 and 10^4 . When a flow is considered turbulent, the eddies are characterised by two limit sizes:

- the largest eddies are of the order of the **integral length scale** l_T .
- the smallest eddies are of the order of **the Kolmogorov length scale** η_K .

The ratio between both length scales, when considering homogeneous isotropic turbulence, can be related to the turbulent Reynolds number:

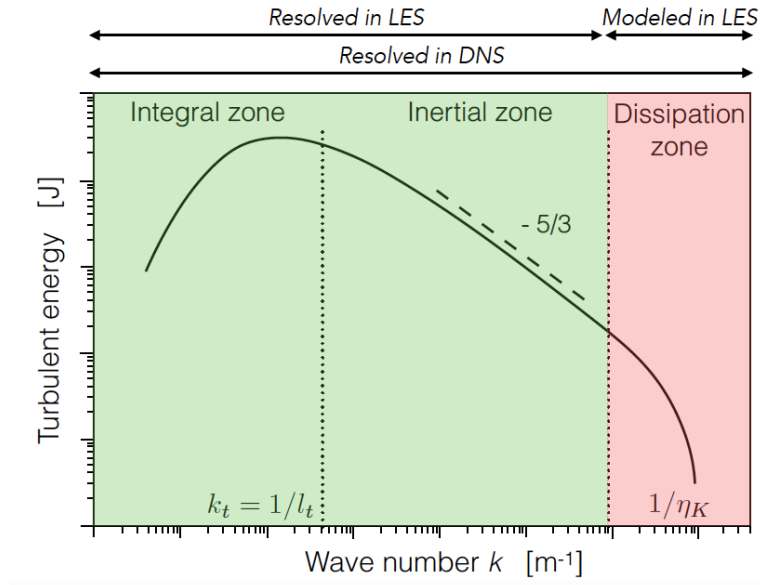


Figure 6.1: Kolmogorov cascade [153] in the kinetic energy spectrum, from [87].

$$\frac{l_T}{\eta_K} = (Re_T)^{\frac{3}{4}} = \left(\frac{\rho u_T l_T}{\mu} \right)^{\frac{3}{4}} \quad (6.2)$$

with u_T the turbulent velocity. This expression is related to the Kolmogorov cascade [153], which states that in-between the two limit length scales, multiple vortex sizes exist and energy is going down from the bigger eddies to the smaller ones before being dissipated in thermal energy by viscous friction.

The multiscale turbulent kinetic energy can be described with a frequency spectrum, which clearly illustrates the Kolmogorov cascade in Fig. 6.1. In the inertial range, the kinetic energy scales like:

$$E(k) \propto k^{-5/3} \quad (6.3)$$

with k the wave number. As explained in the introduction, solving directly the Navier-Stokes equations fails if the grid is not sufficiently refined to take into account the smallest size of the turbulent eddies. Solving the Navier-Stokes equations without any modelling is called a **Direct Numerical Simulation (DNS)** approach.

When the use of refined meshes is not affordable, the **Reynolds Averaged Navier-Stokes (RANS)** approach may be applied, where only the flow statistical moments, and majorly mean quantities \bar{U}_i and RMS quantities u'_i , are computed:

$$\begin{aligned} u_i &= \bar{U}_i + u'_i \\ \bar{u}'_i &= 0 \end{aligned} \quad (6.4)$$

The mean velocity is resolved as the solution of a transport equation, while the RMS quantity is approximated with a model. In most cases, the statistical mean is computed as a time-average.

Because the averaging erases the fluctuations, the spatial scales disappear allowing to use coarse meshes, making RANS methodology a very fast method. However, the non-linear unsteady phenomena can not be well reproduced, in particular the energy production processes, which strongly limits the prediction capability of RANS.

In order to reproduce the main features of turbulence at a reasonable computational cost, the **Large Eddy Simulation (LES)** method discussed here is an in-between solution where the largest scales are directly computed while the smallest scales are modelled. This methodology is used for all 3D computations in this work, and equations are detailed in the next section.

6.2 LES concept and equations

The derivation and the formalism described here come from [235]. The idea of Large-Eddy Simulations is to apply a spatial filter (6.5) on the flow variables to separate larger scales from small ones, such as defined below:

$$\bar{f}(x) = \int f(y)F_{\Delta}(x-y)dy \quad (6.5)$$

where F_{Δ} is the filter kernel and Δ the filter width. For variable density flows, a mass-weighted Favre filter [86] is introduced:

$$\bar{\rho}\tilde{f} = \int \rho f(y)F_{\Delta}(x-y)dy \quad (6.6)$$

With these assumptions, the filtered reactive flow equations are then the following (6.7):

$$\left\{ \begin{array}{l} \frac{\partial \bar{\rho}\tilde{u}_j}{\partial t} + \frac{\partial \bar{\rho}\tilde{u}_i\tilde{u}_j}{\partial x_i} = -\frac{\partial \bar{P}}{\partial x_j} + \frac{\partial}{\partial x_i} (\bar{\tau}_{ij} - \bar{\rho}(\tilde{u}_i\tilde{u}_j - \tilde{u}_i\tilde{u}_j)) \\ \frac{\partial \bar{\rho}\tilde{Y}_k}{\partial t} + \frac{\partial \bar{\rho}\tilde{u}_i\tilde{Y}_k}{\partial x_i} = \frac{\partial}{\partial x_i} (\bar{V}_{k,i}\tilde{Y}_k - \bar{\rho}(\tilde{u}_i\tilde{Y}_k - \tilde{u}_i\tilde{Y}_k)) + \bar{\omega}_k \\ \frac{\partial \bar{\rho}\tilde{h}_s}{\partial t} + \frac{\partial \bar{\rho}\tilde{u}_i\tilde{h}_s}{\partial x_i} = \frac{\partial}{\partial x_i} \left(\lambda \frac{\partial \bar{T}}{\partial x_i} - \bar{\rho}(\tilde{u}_i\tilde{h}_s - \tilde{u}_i\tilde{h}_s) \right) + \frac{\partial \bar{p}}{\partial t} + \overline{u_i \frac{\partial P}{\partial x_i}} \\ \quad + \overline{\tau_{ij} \frac{\partial u_i}{\partial x_j}} - \frac{\partial}{\partial x_i} \left(\overline{\rho \sum_{k=1}^N V_{k,i} Y_k h_{s,k}} \right) + \overline{HRR} \end{array} \right. \quad (6.7)$$

with viscous fluxes approximated by suppressing high-order crossed terms:

$$\begin{aligned} \bar{\tau}_{ij} &= \mu \left(\frac{\partial \bar{u}_i}{\partial x_j} + \frac{\partial \bar{u}_j}{\partial x_i} \right) - \frac{2}{3}\mu \left(\frac{\partial \bar{u}_k}{\partial x_k} \delta_{ij} \right) \simeq \bar{\mu} \left(\frac{\partial \bar{u}_i}{\partial x_j} + \frac{\partial \bar{u}_j}{\partial x_i} \right) - \frac{2}{3}\bar{\mu} \left(\frac{\partial \bar{u}_k}{\partial x_k} \delta_{ij} \right) \\ \bar{J}_{k,i} &= \overline{\rho Y_k (V_{k,i} + V_i^c)} \simeq -\bar{\rho} \bar{D}_k \frac{W_k}{W} \frac{\partial \bar{X}_k}{\partial x_i} - \bar{\rho} \bar{Y}_k \bar{V}_i^c \\ \text{with } \bar{V}_i^c &= \sum_{k=1}^N \bar{D}_k \frac{W_k}{W} \frac{\partial \bar{X}_k}{\partial x_i} \quad \text{and} \quad \bar{D}_k \simeq \frac{\bar{\mu}}{\bar{\rho} S c_k} \\ \bar{q}_i &= -\lambda \frac{\partial \bar{T}}{\partial x_i} + \sum_k \overline{J_{k,i} h_k} \simeq -\bar{\lambda} \frac{\partial \bar{T}}{\partial x_i} + \sum_k \bar{J}_{k,i} \bar{h}_k \\ \text{with } \bar{\lambda} &\simeq \frac{\bar{\mu} \bar{C}_p(\bar{T})}{Pr} \end{aligned} \quad (6.8)$$

In combustion applications, a major difficulty is the **filtered chemical reaction rate** $\bar{\omega}_k$ which needs to be modelled, as will be described in the next section.

The following terms are not unknown in the filtered equations above and need to be modelled with a **subgrid-scale turbulence model** (SGS):

- **Reynolds stresses** $\overline{\tau_{ij}^T} = \overline{u_i u_j} - \tilde{u}_i \tilde{u}_j$. are modelled with a turbulent viscosity:

$$\overline{\tau_{ij,T}} = \bar{\rho} \nu_T \left(\frac{\partial \bar{u}_i}{\partial x_j} + \frac{\partial \bar{u}_j}{\partial x_i} \right) - \frac{2}{3} \bar{\rho} \nu_T \left(\frac{\partial \bar{u}_k}{\partial x_k} \delta_{ij} \right) \quad (6.9)$$

with ν_T , the SGS viscosity, calculated from a turbulence model.

- **species fluxes** $\overline{J_{i,k}^T} = u_i \tilde{Y}_k - \tilde{u}_i \tilde{Y}_k$ are approximated as:

$$\bar{J}_{k,i} \simeq -\bar{\rho} \bar{D}_k \frac{W_k}{W} \frac{\partial \bar{X}_k}{\partial x_i} - \bar{Y}_k \bar{V}_{i,T}^c \quad (6.10)$$

$$\text{with } \bar{V}_{i,T}^c = \sum_{k=1}^N \bar{D}_{k,T} \frac{W_k}{W} \frac{\partial \bar{X}_k}{\partial x_i} \quad \text{and} \quad \bar{D}_{k,T} = \frac{\bar{\mu}}{\bar{\rho} S_{cT}} \quad (6.11)$$

with S_{cT} the turbulent Schmidt number, fixed at 0.6.

- **enthalpy fluxes** $\overline{q_{i,T}} = u_i \tilde{h}_s - \tilde{u}_i \tilde{h}_s$ are similarly approximated as:

$$\bar{q}_i \simeq -\bar{\lambda}_T \frac{\partial \bar{T}}{\partial x_i} + \sum_k \bar{J}_{k,i} \bar{h}_k \quad (6.12)$$

$$\text{with } \bar{\lambda}_T = \frac{\bar{\mu} \bar{C}_p(\bar{T})}{Pr_T} \quad (6.13)$$

with Pr_T the turbulent Prandtl number being fixed at 0.6.

To calculate the SGS viscosity, two models are described here:

- the **Smagorinsky** model [287] defines the turbulent viscosity as:

$$\nu_T = (C_S \Delta)^2 \sqrt{2 \tilde{S}_{ij} \tilde{S}_{ij}} \quad (6.14)$$

where C_S is a model constant varying between 0.1 and 0.18. This model has been developed in the sixties and has been used for a wide variety of configurations. One drawback is that the Smagorinsky model is known to be very dissipative.

- the **WALE** model [93] expresses the turbulent viscosity as:

$$\nu_T = (C_\omega \Delta)^2 \frac{(s_{ij}^d s_{ij}^d)^{\frac{3}{2}}}{(\tilde{S}_{ij} \tilde{S}_{ij})^{\frac{5}{2}} + (s_{ij}^d s_{ij}^d)^{\frac{5}{4}}} \quad (6.15)$$

with

$$s_{ij}^d = \frac{1}{2} (\tilde{g}_{ij}^2 + \tilde{g}_{ji}^2) - \frac{1}{3} \tilde{g}_{kk} \delta_{ij} \quad (6.16)$$

where $C_\omega = 0.5$ is a model constant and \tilde{g}_{ij} the resolved velocity gradient. This model is of particular interest when dealing with wall bounded flows, since it was formulated to recover the correct scaling in boundary layers.

The modelling of the chemical source terms is linked to the turbulence modelling. It is a difficult question and various models have been proposed in the literature, as explained in the next sections.

6.3 Combustion/turbulence interaction

As turbulence and chemistry interact with each other at different timescales and length scales, different combustion regimes may appear and must be identified to apply the correct modelling.

Section 6.3.1 explains how the combustion/turbulence interaction changes with the flame type, namely premixed or diffusion flame. Section 6.3.2 then gives a general insight on the models proposed in the literature for the combustion/turbulence interaction, and finally describes the implementation in AVBP used in this work.

6.3.1 Turbulent flame regimes

Premixed flames

A typical timescale for the premixed flame is:

$$\tau_c = \frac{\delta_l}{s_l^0} \quad (6.17)$$

with δ_l the laminar flame thickness and s_l^0 the unstretched laminar flame speed. To compare the time of the turbulent eddies that were defined in Section 6.1 and the chemical characteristic time, two non-dimensional numbers are used:

- the **Damkhöler number** expressed as:

$$Da = \frac{\tau_T}{\tau_c} = \frac{l_T s_l^0}{u_T \delta_l} \quad (6.18)$$

represents the ratio between the time taken by the biggest eddies associated to the integral scale and the chemical time.

- the **Karlovitz number**, expressed as:

$$Ka = \frac{\tau_c}{\tau_K} = \frac{\delta_l u_K}{s_l^0 \eta_K} \quad (6.19)$$

represents the ratio between the time taken by the chemical time and the smallest eddies associated to the Kolmogorov scale.

These numbers allow determining the turbulent combustion regimes, which can be placed in the Borghi diagram [30] in Fig. 6.2 (left) in terms of length and velocity ratios.

- When $Re_T < 1$, the flame is considered as laminar.
- For small Damkhöler numbers, $Da \ll 1$, the chemical time is larger than the biggest eddies. Therefore, the flow has enough time to mix before the chemistry comes into play, leading to a well-stirred reactor.
- For higher Damkhöler numbers, $Da \gg 1$, the chemical time is smaller than the biggest eddies. The reactants mixing is much slower than their consumption. Then, the combustion regime depends on the Karlovitz number:

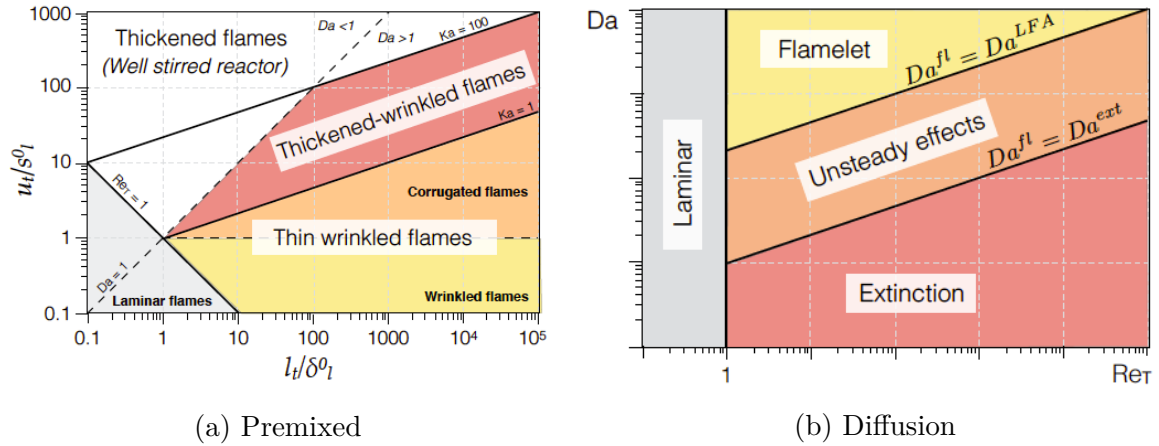


Figure 6.2: Borghi diagram [30] from [87].

- If the Karlovitz number is small $Ka \ll 1$ (and $Da \gg 1$), the time associated to the smallest eddies is also larger than the time associated to the chemistry. Chemistry is then faster than all flow timescales and therefore a **thin wrinkled** flame regime is found. If the velocity ratio u_T/s_l^0 is high, the flame front is said to be **corrugated** (eddies have a stronger impact on the flame front).
- if the Karlovitz number is large $Ka \gg 1$ (and $Da \gg 1$), that is to say $\tau_K < \tau_c < \tau_T$, only the small eddies are faster than the chemical timescale. The flame front is consequently internally stirred, and the flame becomes **thick**. When $Ka \gg 100$, the Kolmogorov scale is much smaller than the chemical scale, and the flame tends to behave as a perfectly stirred reactor.

Diffusion flames

As diffusion flames are driven by the flow strain-rate, the Damkhöler number is modified as:

$$Da^{fl} = \frac{\tau_f}{\tau_c} \quad (6.20)$$

with $\tau_f = 1/\chi_{st}$ the characteristic flow timescale at the flame front, expressed as the inverse of the scalar dissipation rate. Figure 6.2 (right) shows the different regimes for a turbulent diffusion flame:

- for $Re_T < 1$, as for premixed flames, the flame is laminar.
- for $Da^{fl} > Da_{LFA}$, with Da_{LFA} a critical Damkhöler number depending on the flame chemistry, the steady Laminar Flame Assumption (LFA) applies, i.e., the turbulent flame front behaves locally like a laminar flame.
- for $Da_{ext} < Da^{fl} < Da_{LFA}$, where Da_{ext} is the extinction Damkhöler number, the chemical time is non-negligible compared to the flow time and the flame is subject to unsteady chemical effects.
- finally, for $Da^{fl} < Da_{ext}$, the chemistry is too slow compared to the flow timescale and can not sustain a flame anymore.

6.3.2 Turbulent combustion models

It has been seen in the previous section that, depending on the Damkhöler number Da and the Karlovitz number Ka , the flame front may interact with the subgrid-scale turbulence. Moreover, as the reaction thickness is between 0.1 mm and 1 mm for usual fuels, the LES mesh size is generally too coarse to resolve the flame front. As a consequence, a turbulent combustion model must be used to address both issues of subgrid-scale flame-turbulence interactions and flame resolution on the LES grid. A brief overview of today's available methodologies is provided in Section 6.3.2.1 and methods implemented in AVBP are then detailed in Section 6.3.2.2.

6.3.2.1 General overview

The development of turbulent combustion models started in the context of RANS with the work of Spalding and its Eddy Break Up (EBU) model [293] which states, by assuming high Reynolds and Damköhler numbers, that vortices control the reaction rate and that the reaction zone is made of fresh and burnt gaseous pockets transported by those eddies. Other RANS approaches include PDF-based models with either assumed-shape PDFs or computed PDFs (from a transport equation with modelled closure terms) [187], flame front-tracking methods with the transport equation for the flame surface density or with a level-set method [192], [237], and Conditional-Moment-Closure (CMC) methods where equations for the moments of the flame variables, conditioned on mixture fraction or progress variables, are written and solved [18], [150].

The RANS models were later adapted to LES, with more or less success. The EBU model for example was not successful with LES, which increased some problems already present in RANS [236]. PDF-based methods have given good results ([204], [223]), introducing the concept of filtered PDF [53], [54]. Flame front tracking was also successfully applied, in particular with the level-set approach (G-equation model) [35], [146] the Gaussian filtering of the flame, with a filter size larger than the mesh size.

One method specifically designed for LES is the artificial thickening of the flame [36] (TFLES model). From the expressions of the laminar flame speed s_l^0 and reaction thickness δ_l^0 as functions of the thermal diffusivity D_{th} and reaction rate coefficients A [235]:

$$\begin{aligned} s_l^0 &\propto \sqrt{D_{th}A} \\ \delta_l^0 &\propto \sqrt{\frac{D_{th}}{A}} \end{aligned} \tag{6.21}$$

dividing the reaction rate by a factor F the **thickening factor** and multiplying the diffusion coefficients by the same factor F , the flame thickness is multiplied by F while the flame speed is conserved. With this operation and a sufficiently high F , the flame becomes resolvable on the LES grid and may be directly computed. The introduction of the thickening factor has multiple consequences:

- as $HRR = \sum h_k \dot{\omega}_k$, $HRR \longrightarrow \frac{HRR}{F}$.
- as the chemical time $\tau_c = \frac{\delta_L^{th}}{s_L}$ remains unchanged, $\delta_L^{th} \longrightarrow \delta_L^{th} F$.

However, this operation also divides the Damköhler number by F , making the flame less sensitive to turbulence. To recover the correct flame speed, an **efficiency function** is

applied, which depends on the velocity ratio u_T/s_l^0 and the length scale ratio $\Delta/F\delta_l^0$ with Δ the filter size.

The most popular approaches for LES turbulent combustion modelling found in the literature are the PDF-based models and the CMC approach, followed by the TFLES model. They all have their advantages or drawbacks in terms of accuracy, computing cost, complexity and range of validity. Because the TFLES model is the most simple and versatile approach, adapting automatically to any flow and configuration complexities, and because it proved to be accurate in many 3D cases, it is chosen for the present work and further detailed in the next section.

6.3.2.2 The TFLES model in AVBP

The concept of flame thickening is simple, but its implementation raises a number of questions that are addressed here. The first question is the determination of F . To make the flame resolvable on the LES mesh, the cell size is compared to the flame thermal thickness to calculate the number of cells that are located in this zone. If this number is too small, the thickening factor F should be increased until the thickened flame spans over the minimum required number of cells N_c . This minimum number of course depends on the numerical integration scheme and is higher for lower numerical order, but is usually between 5 and 10 as stated earlier. This can be expressed as:

$$F = N_c \frac{\Delta x}{\delta_l^{th}} \quad (6.22)$$

with Δ_x the cell size.

Another issue is the extension of TFLES to non perfectly premixed cases, which are the vast majority of applications. In such case, applying a constant thickening factor over the entire domain results in over-diffusion in non-reactive zones, i.e., a wrong mixing prediction. Therefore, F must be applied only in the flame zone, using a flame sensor, so that:

$$F = 1 + (F_{max} - 1)S \quad (6.23)$$

where S is a flame sensor: $F = F_{max}$ where $S = 1$ and $F = 1$ where $S = 0$ [220]. Two possibilities exist for calculating S in AVBP, detailed below.

Relaxation sensor

The relaxation sensor writes:

$$S = \tanh \left(\beta' \frac{\Omega_{irr}}{\Omega_{1D,irr}} \right) \quad (6.24)$$

with

$$\Omega_{irr} = Y_F^{\nu_F} Y_O^{\nu_O} \exp \left(-\Gamma \frac{E_a}{RT} \right) \quad (6.25)$$

where Γ and β' are constant. The quantity Ω_{irr} is evaluated and compared to its value in premixed flames $\Omega_{1D,irr}$ to trigger the thickening. It can theoretically be based on the heat release rate or on the fuel source term, as in previous works where it yielded better results [134].

Generic sensor

The relaxation sensor suffers from three weaknesses:

- it requires properties of a reference flame, in the form of a table.
- the reference flame may not be representative of the whole 3D turbulent flame, in particular in the case of spray flames.
- thickening may occur even in zones where there is no need to, for instance in the post-flame zone, as chemical activity is still present there.

To overcome these issues, a generic thickening approach [266] which detects the flame front and automatically determines F without any reference flame has been developed. The general methodology is described in [266] and only the main steps are recalled here:

1. **The front is detected.** The function $f(\vec{x})$ chosen for the detection of the flame front is the heat release rate. Note $f'(\vec{x}) = \partial f / \partial x_i$ the gradient vector of f and $f''(\vec{x}) = \partial^2 f / \partial x_i^2$ the hessian matrix of f . If f'' is symmetric and real, then it is diagonalisable with eigenvalues $\lambda_i(\vec{x})$ (Schwartz theorem):

- if the eigenvalues are all positive, f is strictly convex and has a local minimum.
- if the eigenvalues are all negative, f is strictly concave and has a local maximum.
- if both positive and negative eigenvalues exist, a saddle point exists with a change of curvature.

The heat release rate peak having a concave shape, the front is detected at the highest negative eigenvalues and the ridge line is stored in \vec{x}_{line} .

2. **The flame thickness is estimated.** Following the coordinate perpendicular to the ridge line:

$$y = \vec{n}_{line} \cdot (\vec{x} - \vec{x}_{line}) \quad (6.26)$$

with \vec{n}_{line} the normal vector to the ridge line, the function f may be approximated the following way:

$$f(y) = f(\vec{x}_{line}) + f'(\vec{x}_{line}) \vec{x}_{line} + \frac{f''(\vec{x}_{line})}{2} \vec{x}_{line}^2 \quad (6.27)$$

This expression is equal to zero when the coordinate is equal to:

$$y_{\pm} = \frac{-f'(\vec{x}_{line}) \pm \sqrt{f'(\vec{x}_{line})^2 - 2f''(\vec{x}_{line})f(\vec{x}_{line})}}{f''(\vec{x}_{line})} \quad (6.28)$$

The estimated thickness is then equal to:

$$\delta = y_+ - y_- \quad (6.29)$$

This thickness is the thickness of the thickened flame with the current F . Its ratio with Δx is compared to a user-given value of required numbers of cells in the flame front, and modified accordingly to reach this value.

3. **The front is thickened.** To apply F over the whole flame thickness, the neighbouring cells of the ridge line must be identified. With unstructured meshes, an efficient method is to use virtual Lagrangian particles that can propagate F along the normal at each point of the ridge line up to a given distance. The applied thickening function then writes:

$$tf(\vec{x}) = 1 - \tanh\left(\frac{(\vec{x} - \vec{x}_{line}) \cdot \vec{n}_{line}}{N_c \Delta x}\right) \quad (6.30)$$

with \vec{x} the coordinate of the particle. As thickening might not be the same on both sides of the flame front, a parameter α is added on the denominator of the tf function to introduce a difference: tf is divided by $\alpha N_c \Delta x$ in the fresh gas side and by $(1 - \alpha) N_c \Delta x$ in the burnt gas side. The value of α is fixed to $\frac{2}{3}$ in the present work.

TFLES for spray flames: TP-TFLES

In the case where droplets do not fully pre-evaporate, the flame thickness changes and the thickened flame model must be adapted. The evaporation Damkhöler number is expressed as:

$$Da_{ev} = \frac{\tau_{evap}}{\tau_c} \quad (6.31)$$

This Da_{ev} should be kept constant through the thickening operation, so that mass and heat transfer values must be also divided by the F factor. In principle, the Stokes number should also be adapted to maintain the correct drag force through the flame front.

No specific modelling is provided to take into account the missing information due to the fact that one solves the filtered gaseous set of transport equations.

Diffusion flames

Applying the thickening factor only on reactive area is tantamount to the right detection of the flame front. The thickening factor is only applied on premixed area, as the impact on stratified premixed flames is supposed to be low [55]. This topic remains however an open question and may require modelling for high pressure, oxy-combustion and highly turbulent cases.

As a consequence, for this study, the Takeno sensor introduced in Section 3.3.3.3 is used to apply the TFLES model only on premixed area. The Takeno expression applied for the calculation is discussed in Section 9.2.4.3.

6.3.2.3 The efficiency function

As explained in the previous section, an **efficiency function** E is used to recover the subgrid-scale wrinkling of the turbulent flame, so that: $\dot{\omega}_k \rightarrow E\dot{\omega}_k/F$ and $D \rightarrow EFD$. This leads to an enhanced flame speed ES_l^0 , hopefully close to the subgrid-scale turbulent flame speed.

E is a function of the local turbulence, of the flame characteristics (flame speed and thickness) and of the thickening factor. It is defined as the ratio between the wrinkling of the unthickened flame and that of the thickened flame:

$$E = \frac{\Xi(\delta_l)}{\Xi(F\delta_l)} \quad (6.32)$$

In the following, only the models available in AVBP are described.

Static Colin model

The Colin static model [50] expresses wrinkling as:

$$\Xi^{Co} = 1 + \alpha \Gamma \left(\frac{\Delta}{\delta_L^0}, \frac{u'_\Delta}{s_L^0} \right) \frac{u'_\Delta}{s_L^0} \quad (6.33)$$

with Γ a function taking into account the subgrid-scale strain rate of all length scales smaller than Δ .

Static Charlette model

The Charlette static model [41] wrinkling is expressed as:

$$\Xi_\Delta^{Ch} = \left(1 + \min \left[\frac{\Delta}{\delta_L^0}, \Gamma \left(\frac{\Delta}{\delta_L^0}, \frac{u'_\Delta}{s_L^0} Re_\Delta \right), \frac{u'_\Delta}{S_L^0} \right] \right)^{\beta_{Ch}} \quad (6.34)$$

with $\beta_{Ch} \sim 0.5$. Unlike the Colin model, the Reynolds number based on the filter scale avoids the calculation of the integral length scale.

The Charlette model also exists in a dynamic formulation, allowing to determine the exponent β which is not anymore constant but automatically adjusts to the resolved flow by equating the flame surface densities at filtered and test-filtered levels [100]. As β is not changing much with location and time for the SSB configuration in Chapter 9 and Chapter 10, the static Charlette efficiency function is used in this work.

Part III

Chemical and two-phase canonical cases

Chapter 7

Analysis of gaseous chemical processes

Contents

7.1	Reduced chemical scheme for multi-component surrogates	106
7.1.1	Blend composition	106
7.1.2	Mechanism reduction	108
7.2	ARC validation and discussion	110
7.2.1	Net heat of combustion	111
7.2.2	Auto-ignition delay time	115
7.2.3	Laminar flame speed accuracy	118
7.2.4	Pollutants emissions	120
7.2.5	Characteristic species chemical timescales	123
7.2.6	Conclusion	124
7.3	Spatial discretisation for complex kinetics	126
7.3.1	Impact of the discretisation on laminar flame speed	126
7.3.2	Effect of the mesh discretisation on the flame structure	130
7.3.3	Conclusion	137

The accurate modelling and reduction of alternative fuel kinetics is complex, since their chemical properties vary according to their composition. On the one hand, the surrogate model should respect the most accurately the real fuel, for instance the proportion of alkanes, cyclic and aromatic species may influence the H/C ratio, the molar mass, the ignition time, the flame speed, the flammability limits or the lower heating value [171]. On the other hand, the kinetic scheme created should accurately represent the pyrolysis and the oxidation parts. Both the modelling of the fuel surrogate created, and the chemical reduction should account for those key parameters.

Surrogates for the SSB were selected within the JETSCREEN project and their description as well as the mechanism reduction are described in Section 7.1. Section 7.2 employs the different tools presented in Section 3.3 to validate the accuracy of the reduced mechanism compared to the detailed mechanism and to investigate the impact of the variation in the composition on key combustion quantities. Pollutant emissions (NO_x and CO) are also investigated. Finally, the flame structure of ARC mechanisms in general is

analysed in Section 7.3 to exhibit the link between the number of points used to discretise the flame front and the accuracy of the results.

7.1 Reduced chemical scheme for multi-component surrogates

In section 7.1.1, Comprehensive Two-Dimensional Gas Chromatography (GCxGC) experimental results, introduced in Section 4.1.2, are presented and the resulted surrogate model is shown. This results in the mechanism reduction Section 7.1.2 of the three fuels.

7.1.1 Blend composition

First, as the multi-component evaporation model used in this work is discrete, a surrogate model needs to be defined for the different fuels. In JETSCREEN, POLIMI was in charge of modelling the surrogate fuels based on the work of [209], with the GCxGC data shown Fig. 7.1. These bar plots represent the quantity of the five main families of hydrocarbon fuels: n-alkanes, iso-alkanes, cycloalkanes, mono-aromatics and di-aromatics versus the molecule carbon number for the three fuels studied: Jet-A1 (named A1), AtJ (named B1) and a high aromatic fuel (named C1).

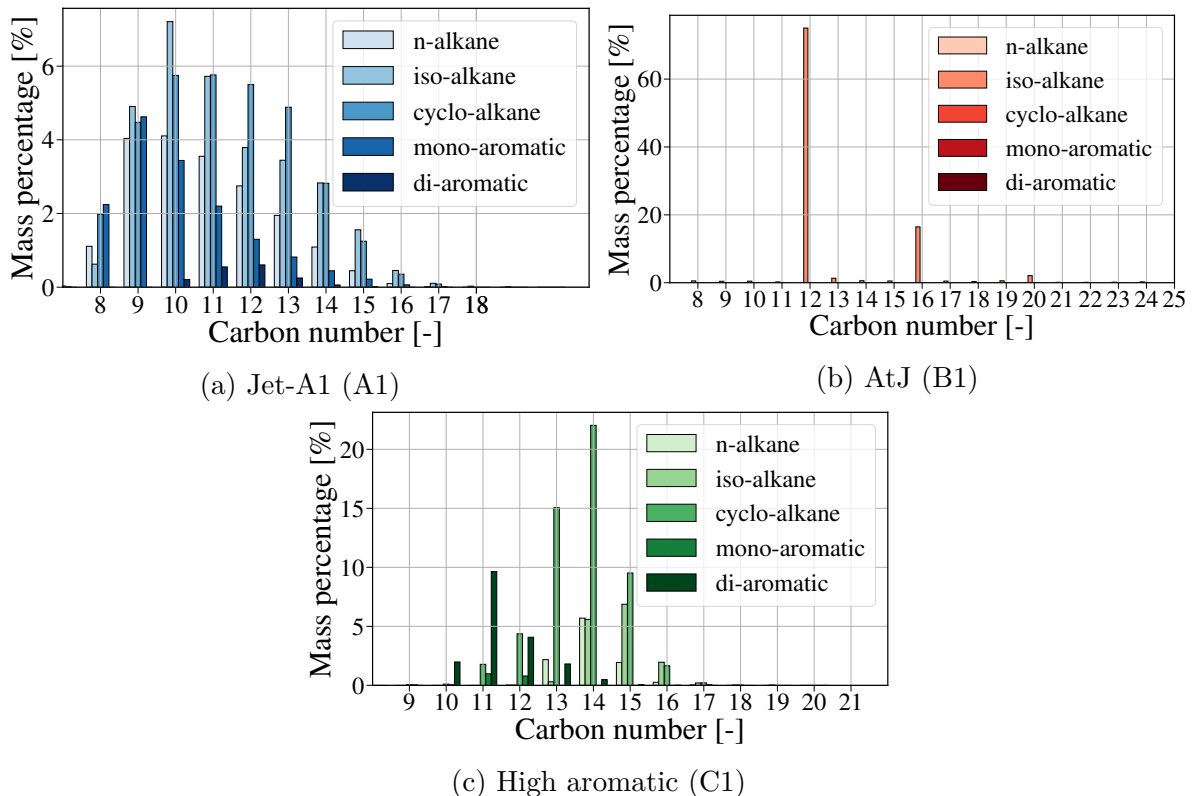


Figure 7.1: Results of the GCxGC experiment for A1, B1 and C1 fuels [91].

On the one hand, B1 mainly contains $IC_{12}H_{26}$ and $IC_{16}H_{34}$ and is therefore the easiest surrogate to model. On the other hand, A1 and C1 fuels show a much more diverse spread in terms of family and carbon number. C1 carbon number range extends from 9 to 17

with a higher di-aromatic contents around 11-12 carbons and alkanes (linear, branched and mostly cycled) around 13 to 15 carbons.

Given these experimental GCxGC results, surrogates were formulated by POLIMI, using the methodology introduced in Section 4.1.2. Table 7.1 first shows the H/C ratio, molar mass W and liquid density ρ_l for the real fuel [197] and surrogates created.

Quantity		A1	B1	C1
ρ_l [kg/m^3]	Real fuel	786.8	756.4	858.1
	Surrogate	775	749	882
W [$kg/kmol$]	Real fuel	150	180	182
	Surrogate	151	173	147
H/C [-]	Real fuel	1.94	2.152	1.718
	Surrogate	2.0	2.17	1.7

Table 7.1: Resulting liquid density, molar mass and H/C for the three fuels.

As the priority was given to H/C ratio during the surrogate formulation, the sensitivity of the fuels are well-matched in the surrogate compositions. The same conclusion can be drawn for the liquid density ρ_l where, despite some bigger errors compared to the real fuel, especially for C1, the fuel sensitivities are well captured. For the molar mass, the real fuel properties are well targeted by the surrogates A1 and B1, but show a larger error when the C1 surrogate is compared to the real fuel. An error is tolerated for C1 since it exhibits a different composition as it is mainly made of cyclic compounds and is therefore interesting for theoretical modelling and combustion.

Figure 7.2 shows the distillation curves (left) and the laminar flame speed (right) for A1, B1 and C1 compared to the measured data on the real fuel.

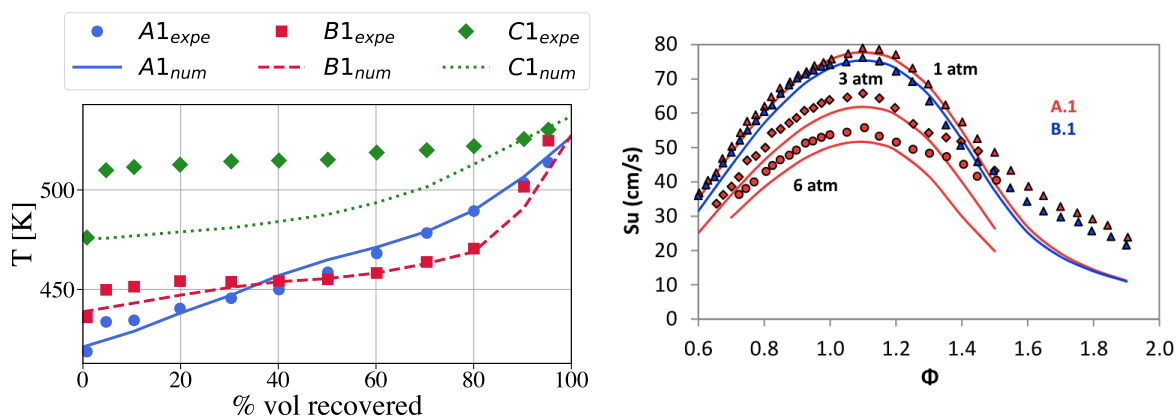


Figure 7.2: Resulting distillation curve (left) and laminar flame speed (right) for the three fuels [198] compared to the measured values for the real fuel.

For the distillation curve results, the agreement is very good for A1 and B1 but the difference increases for C1. Kinetics were then validated on flow reactor simulations and on 1D premixed flames, of which the result is presented in Fig. 7.2 (right) for A1 and B1. Agreement is good and could depict the small difference between A1 and B1 as well as the pressure sensitivity. No data existed for C1 to validate the laminar flame speed.

The final fuel species, composition and molecular structures are summarised in Table 7.2.

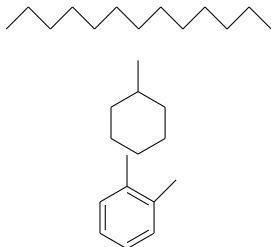
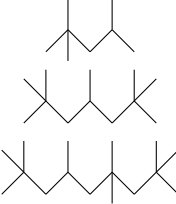
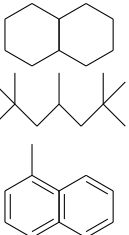
Fuel	Condensed formula	Full name	H/C	X [mol/mol]	Y [kg/kg]	Molecule
A1	$C_{10.2}H_{20.4}$	Jet-A1	2.00	1	1	
	$C_{12}H_{26}$	N-dodecane	2.17	0.60	0.7143	
	C_7H_{14}	Methyl-cyclohexane	2.00	0.20	0.1373	
	C_8H_{10}	Xylene	1.25	0.20	0.1484	
B1	$C_{12}H_{26}$	AtJ	2.17	1	1	
	C_8H_{18}	Iso-octane	2.25	0.08	0.0536	
	$C_{12}H_{26}$	Iso-dodecane	2.17	0.84	0.84	
	$C_{16}H_{34}$	Iso-cetane	2.13	0.08	0.1064	
C1	$C_{10.6}H_{18}$	High Aromatic	1.70	1	1	
	$C_{10}H_{18}$	Decalin	1.80	0.60	0.5703	
	$C_{12}H_{26}$	Iso-dodecane	2.17	0.20	0.1955	
	$C_{11}H_{10}$	Methyl-naphthalene	1.10	0.20	0.2342	

Table 7.2: Surrogate description for A1, B1 and C1 with condensed formula, full name, H/C ratio, molar and mass fractions and molecular structures by POLIMI used in JETSCREEN.

- A1 fuel surrogate is composed of a linear alkane, n-dodecane (NC12H26), a cyclic molecule, methyl-cyclohexane (MCYC6) and an aromatic molecule, xylene (XYLENE).
- B1 fuel surrogate is only composed of branched alkane: iso-octane (IC8H18), a majority of iso-dodecane (IC12H26) and iso-cetane (IC16H34).
- C1 fuel surrogate is mainly composed of cyclic species: mainly decalin (DECALIN), a branched alkane, iso-dodecane (IC12H26) and a double aromatic methyl-naphthalene (C10H7CH3).

These surrogates were built using simple targets; it could have been thought of including some isolated droplet evaporation cases for instance in order to check the accuracy of the surrogate. Finally, once the surrogate model is built, the detailed mechanism can be reduced for the three surrogates.

7.1.2 Mechanism reduction

The detailed mechanism is the CRECK_1909_TOT_HT¹ which contains 368 species and 14323 reactions. Only high temperature paths are included and no NO_x or soot species

¹<http://creckmodeling.chem.polimi.it>

pathways are included. This detailed mechanism selected was successfully compared to experimental data in [251], [252] for each component of surrogate chosen previously and was therefore chosen as a reference to accurately account for the fuel species combustion.

This detailed mechanism was reduced with ARCANE to obtain ARC mechanisms for the three fuels. As stated in Section 4.2, the classical methodology is used, meaning that first a DRGEP and a lumping step are applied to create the skeletal mechanism. Second, the ARC mechanism is created by applying the LOI step, that is to say to set some species in QSS and reduce the stiffness of the mechanism. The operating conditions and the different cases computed are described in Table 7.3. Targets for the DRGEP step were the heat release rate, and the mass fractions of fuel components, CO and CO_2 .

Case type	T_{init} [K]	P [bar]	ϕ [-]	Relative error [%]
0D isochoric reactor	1200 - 1500	1.0	1.0	τ_{ig}^2 : 5
1D premixed flame	400	1.0	0.6 - 1.0 - 1.4	s_L^2 : 5 T_{end} : 1

Table 7.3: Cases and associated errors for ARCANE reduction for ARCANE reduction for A1, B1 and C1.

At the end of the process, three mechanisms were obtained. Their storage as well as their full validation is shown here³ and part of it is presented in the next sections. The nomenclature used for these mechanisms can be summarized through the following pattern: **Fuel_NS_NREAC_NQSS_AUTHOR** with **Fuel** the fuel used, **NS** the number of species, **NREAC** the number of reactions, **NQSS** the number of QSS species and **Author** the author of the mechanism. These mechanisms are the following:

- the Jet-A1 mechanism, called ARC A1 and named A1_36_543_16_QC presented in [39], contains 36 species, 17 QSS species and 543 irreversible reactions.
- the AtJ mechanism, called ARC B1 and named B1_31_386_24_JW, contains 31 species, 26 QSS species and 349 irreversible reactions.
- the high aromatic fuel mechanism, called ARC C1 and named C1_35_299_29_JW, contains 35 species, 20 QSS species and 479 irreversible reactions.

Results of the mechanisms can already be analysed when looking at the atom path flux diagrams following C atom for the skeletal mechanisms are displayed for ARC A1 in Fig. 7.3 with the methods explained in Section 4.3.1.3.

A1, n-dodecane and methyl-cyclohexane are converging towards a similar pathway when reaching $C_7H_{13}(L_1)$ while xylene shows a completely different pathway, explaining the higher number of species.

Pathways for ARC B1 and ARC C1 are shown similarly in Appendix B for the sake of concision. ARC B1 components (IC8H18, IC12H26 and IC16H34) are taking very big common pathways (IC8H17 is a common species for every fuel), enabling the skeletal mechanism to contain fewer species and being much reduced.

Finally, ARC C1 shows three completely different pyrolysis pathways for heavier species, leading to a bigger skeletal mechanism. Note that to keep this reduced mechanism scheme usable for CFD, higher targeted errors have been imposed for C1 compared to A1 and B1.

²For C1, the error of τ_{ig} and s_L was doubled, otherwise the expected threshold could not be reached.

³chemistry.cerfacs.fr

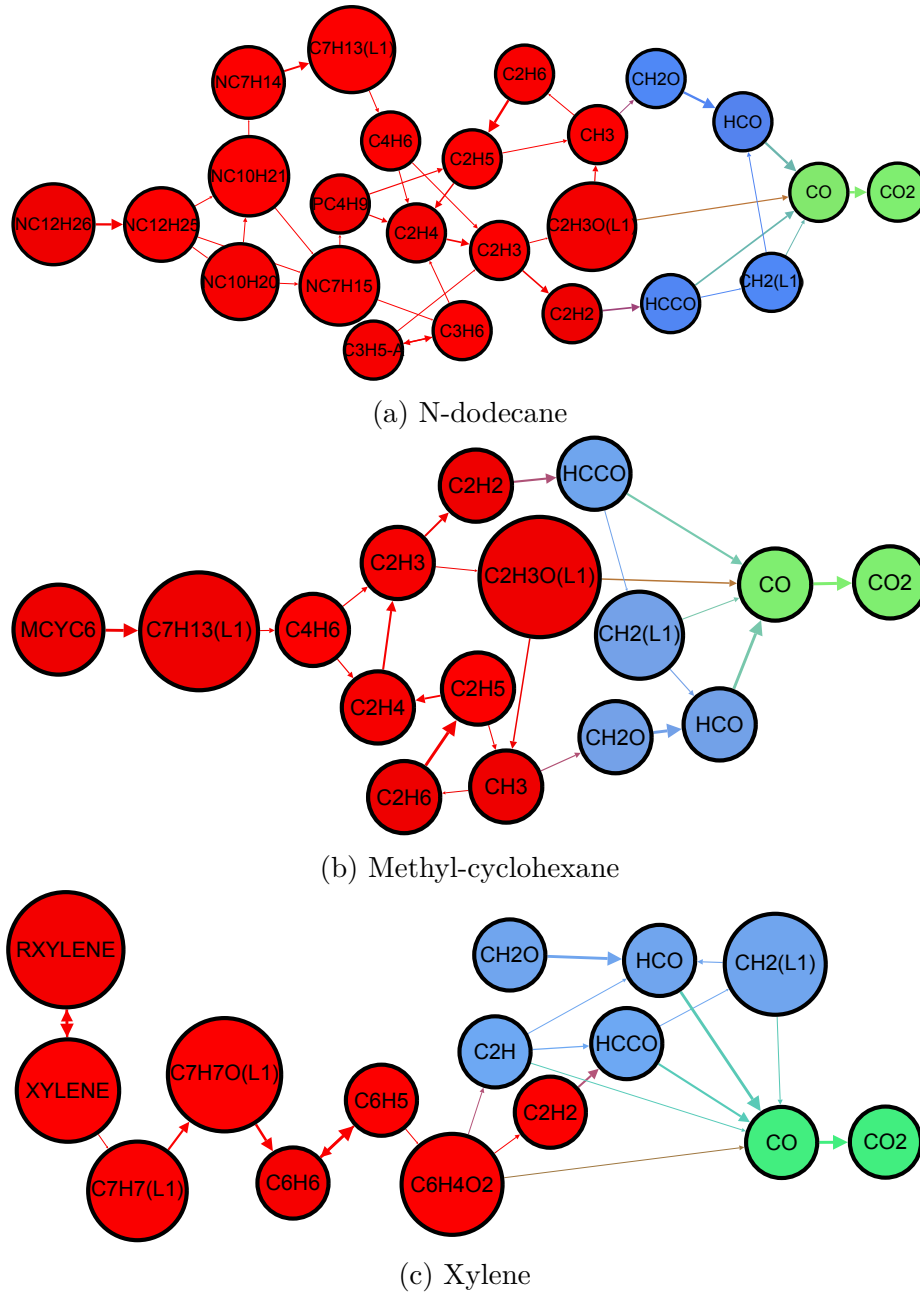


Figure 7.3: Chemical pathways for ARC A1 components at $T = 400K$, $P = 1$ bar and $\phi = 1.0$ with the method introduced in Section 4.3.1.3. Red colour represents pyrolysis products, green colour CO and CO_2 and blue colour the other species.

7.2 ARC validation and discussion

Equilibrium calculations, reactors and 1D premixed flames are calculated and compared to the detailed scheme to assess the validity of the schemes. Furthermore, for each of these canonical cases, the analysis is extended to understand how the multi-component fuel behaviour affects each canonical characteristic quantities.

To investigate the link between the initial composition and the results, one may consider

the H/C ratio, defined as:

$$H/C = \frac{n_H}{n_C} = \frac{X_H}{X_C} \quad (7.1)$$

where n_e is the molar quantity of element e and X_e is the molar fraction of element e, defined as:

$$X_e = \sum_{k=1}^{N_{species}} a_{e,k} X_k \quad (7.2)$$

with X_k the molar fraction of species k and $a_{e,k}$ the number of atoms e in species k as defined in Section 3.1.1. At first glance, the H/C ratio gives an idea of the molecule structure:

- if the molecule is linear or branched, the average number of H atoms per carbon is maximised.
- if the molecule is unsaturated (double or triple C-C bond), the average number of H atoms per carbon is reduced.
- if the molecule is cyclic, results are the same: the average number of H atoms per carbon is reduced.

7.2.1 Net heat of combustion

The LHV measures the quantity of energy required to completely transform the fuel and the oxidiser in stoichiometric proportions into water and carbon dioxide at standard pressure and temperature. The LHV is directly linked to the laminar flame speed of the fresh gas mixture, as it is directly proportional to the integral of heat release rate:

$$LHV = \dot{m}_F * \int_{v=0}^V HRR dv \quad (7.3)$$

Experimental vs numerical net heat of combustion

First, the **net heat of combustion** or lower heating value (LHV) are compared with the experimental values in Table 7.4.

Blend	Reduced [MJ/kg]	Experimental [MJ/kg]	Relative error [%]
A1	43.869	43.375	1.14
B1	44.411	44.159	0.57
C1	42.621	42.597	0.56

Table 7.4: Lower Heating Value (LHV) for A1, B1 and C1 surrogate fuels.

There are some discrepancies with the experimental measurements, but overall the agreement is good. B1 mechanism has a higher LHV than A1 and C1 a lower one.

For the simulations in the SSB configuration (Chapter 9 and Chapter 10), the fuel mass flow rate \dot{m}_F has been adapted for the three fuels so that the integral of heat release rate remains constant and equals 10.2 kW. The correct prediction of the LHV is then essential to get the right heat of combustion.

Figure 7.4 presents the effect of surrogate composition on Lower Heating Value (LHV) depending on the composition, calculated with Cantera. This triangular plot representation will often be used in this work, as it proposes a clear cartography of the effect of fuel composition. Indeed, as the three surrogates are composed of three components, only two components are moving, the third one being calculated from the two others. The three axis represents the molar fraction of each surrogate component. Every triangular plot is calculated with a molar fraction step of 0.1.

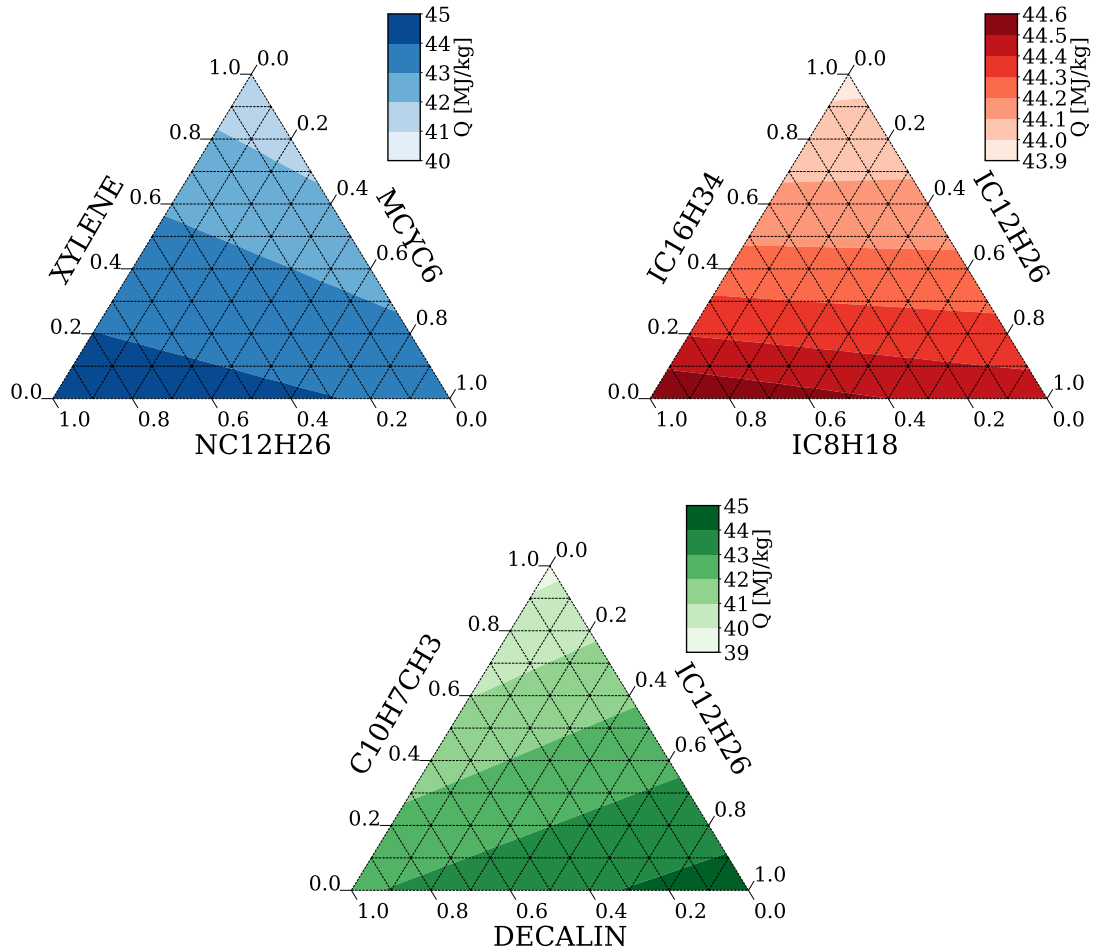


Figure 7.4: LHV triangle plots depending on the fuel composition.

Xylene and methyl-naphthalene ($C_{10}H_7CH_3$) show a lower LHV than linear alkanes. Cyclic molecules can be found in-between the aromatic molecules and the branched alkanes, but closer to alkane reactivity. The LHV of a multi-component mixture is mathematically equivalent to the sum of the pure LHVs balanced by the fuel mass fractions.

The link between the LHV and the H/C ratio is now investigated. The general formula for a hydrocarbon fuel can be written $C_xH_{2[x-d+1-r-2t]}$ with x the number of carbons, d the number of double bonds, t the number of triple bonds and r the number of cycles. Therefore, at reference temperature $T_0 = 298.15$ K, the LHV may be approximated by (Demonstration is provided in Appendix B):

$$LHV_{mol} = 407x + 100y + 82d + 205t \quad (7.4)$$

and by developing y from the general formula for hydrocarbon fuels:

$$LHV_{mol} = 607x + 200 - 118d - 200r - 195t \quad (7.5)$$

The mass LHV can be then deduced:

$$LHV_{mass} = \frac{LHV_{mol}}{W_F} \quad (7.6)$$

where W_F is the molar mass defined as $W_F = xW_C + yW_H$. Two main conclusions may be drawn:

- Equation 7.4 shows that the molar LHV is not only dependent on the number of C and H but also depends on the molecular structure.
- Equation 7.5 shows that a double bond (d) has less impact on the LHV than a cycle (r) and a triple bond (t).

Table 7.5 compares the approximate LHV value with the real one for different fuels and estimates the resulting absolute error. Globally it appears that Equations 7.4 and 7.5 approximate well the real LHV, and that LHV is not linear with H/C (error lower than 5%) for all species.

Species	Cantera LHV [MJ/kg]	Formula LHV [MJ/kg]	Absolute error [%]
NC12H26	44.46	43.94	1.18
MCYC6	43.72	43.27	1.03
XYLENE	41.21	42.40	2.91
IC8H18	44.61	44.26	0.785
IC12H26	44.46	43.94	1.18
IC16H34	43.98	43.77	0.472
DECALIN	42.87	42.46	0.954
C10H7CH3	39.75	41.40	4.14

Table 7.5: LHV of the fuel components determined by POLIMI for A1, B1 and C1 components. Comparison between the real value and the approximated expression from Equations 7.4 and 7.5.

In details, the approximated formula performs very well for alkanes and cyclic molecules. However, it over-estimates LHV for aromatic species for instance, which is the limit of the method. Indeed, a constant value for all the bonds is a strong approximation as the bond energy also depends on the molecular structure. For instance, aromatic species are a very stable configuration and such structure then influences the bond value compared to the tabulated value one can find in the literature.

Final state

Equilibrium calculations with constant pressure and enthalpy have been performed for $T = 323.15$ K, $P = 1$ bar and $\phi = 0.8$. The equilibrium temperature and species mass fractions are compared for the ARC schemes in Table 7.6.

For the equilibrium temperature, A1 has a higher equilibrium temperature than B1 but a lower one than C1. For the burnt gas composition, B1 shows a higher water content and

Fuel	T_{ad}	Y_{H_2O}	Y_{CO}	Y_{CO_2}	Y_{O_2}
A1	2084.54	0.0654	0.00133	0.160	0.0443
B1	2076.34	0.0691	0.00122	0.156	0.0443
C1	2092.96	0.0583	0.00148	0.168	0.0444

Table 7.6: Equilibrium state for the three fuels A1, B1 and C1 at $\phi = 0.8$, $T = 323.15$ K and $P = 1$ bar.

a lower carbon mono- and di-oxide content than A1. For C1, the opposite conclusion can be drawn. The nitrogen and oxygen levels remain approximately the same for the three fuels.

Figure 7.5 displays the equilibrium temperature lines versus equivalence ratio at $T = 323.15$ K and $P = 1$ bar for the three surrogates and their components.

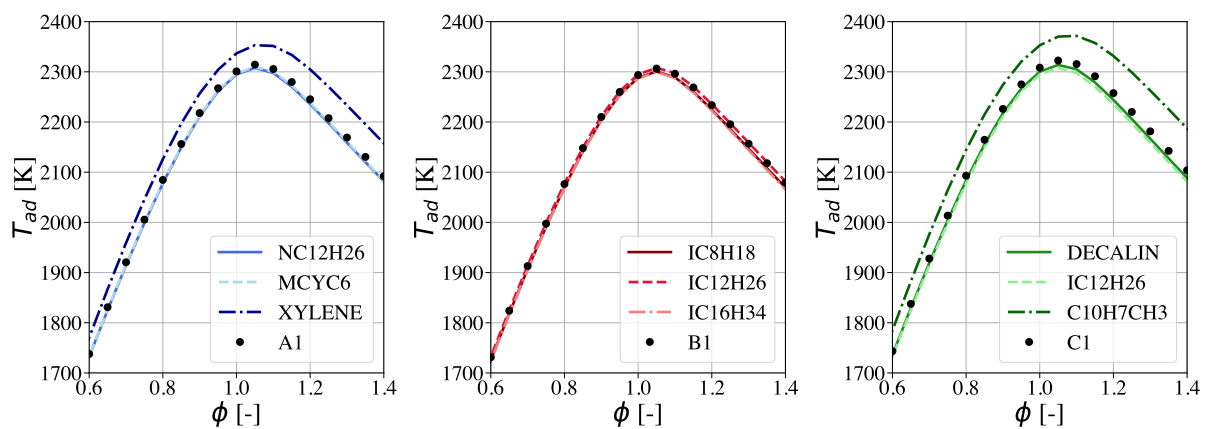


Figure 7.5: Equilibrium temperatures versus equivalence ratio for the three surrogates and their components for $T = 323.15$ K and $P = 1$ bar

The equilibrium temperature depends on the fuel considered. It is higher for low H/C ratio species such as xylene and methyl-naphthalene. As a consequence, A1 and C1 have a slightly higher equilibrium temperature than the main blend component. For B1, every component has a similar H/C ratio, leading to the same adiabatic temperature.

The link between the H/C ratio and the final state is now investigated. The equilibrium temperature can be estimated by:

$$Cp_2T_2 - Cp_1T_1 = \frac{LHV_{kg} \cdot \phi \cdot Y_{O_2}}{s_Y} \quad (7.7)$$

if LHV_{mass} is known for the given blend. The blend equilibrium temperature is not perfectly equal to the sum of the pure species equilibrium temperatures, balanced with their composition in the blend.

The only unknown parameter in this equation is the mass stoichiometric ratio s_Y , which can be linked to the H/C ratio and is defined as:

$$s_Y = 32 \frac{1 + \frac{1}{4}H/C}{W_C + H/CW_H} \quad (7.8)$$

with W_C the atomic carbon molar mass and W_H the atomic hydrogen molar mass. s_Y is generally not linear with respect to H/C , but in the given range of H/C ratio ($1.5 < H/C < 2.5$), it can be considered as such.

From equation 7.8, the final water and carbon dioxide for lean mixtures can be inferred doing an advancement calculation (Demonstration in Appendix B):

$$X_{H_2O,lean} = \frac{\frac{H/C}{2}}{\frac{H/C}{4} + 4.76 \frac{1+H/C}{\phi_{lean}}} \quad (7.9)$$

$$X_{CO_2,lean} = \frac{1}{\frac{H/C}{4} + 4.76 \frac{1+H/C}{\phi_{lean}}} \quad (7.10)$$

To understand the relation between T_{eq} and H/C , scatter plots representing the equilibrium temperature as a function of the H/C ratio are displayed in Fig. 7.6 for the surrogate components for different surrogate composition at $T = 323.15$ K, $P = 1$ bar and $\phi = 1.0$.

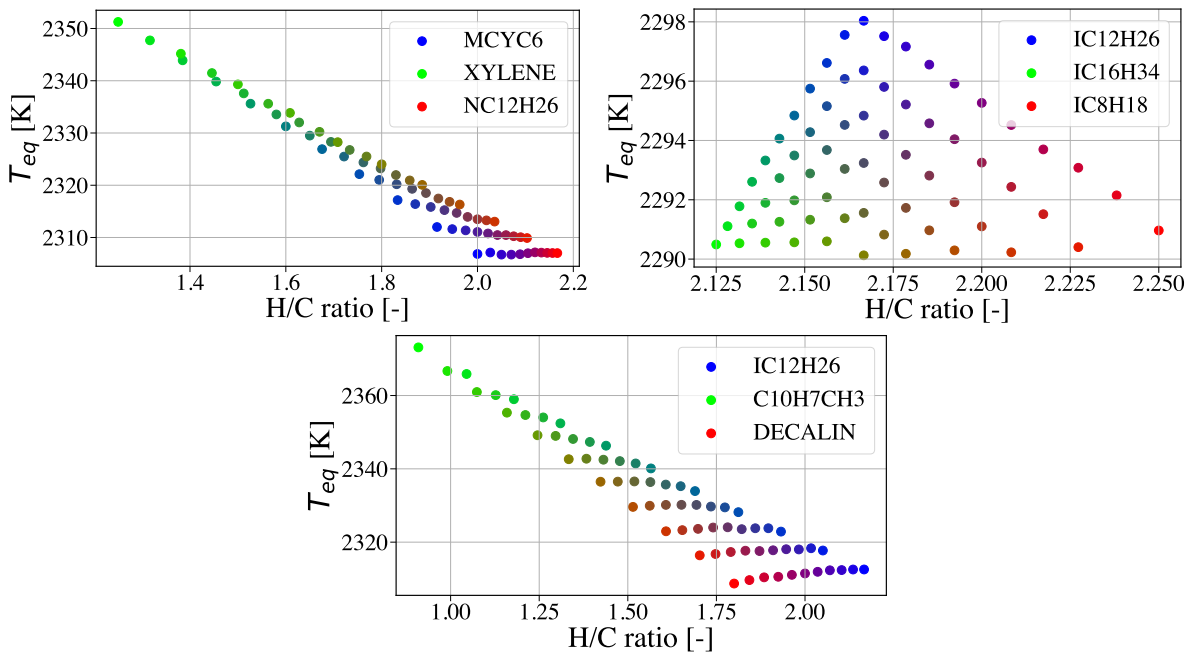


Figure 7.6: Temperature difference T_{eq} as a function of H/C ratio for different compositions from A1 (upper left), B1 (upper right) and C1 (lower) fuel species for $T = 323.15$ K, $P = 1$ bar and $\phi = 1.0$.

At first glance, there is a rough link between the equilibrium temperature and the H/C ratio: the equilibrium temperature is higher for fuels with a lower H/C ratio. This is mainly due to the lower hydrogen amount in the burnt gases, which reduces the heat capacity and therefore increases the equilibrium temperature. For B1 components, such a relation is not strictly valid. However, the spread range is very narrow and the global statement saying that aromatics have a higher adiabatic temperature because of a lower H/C ratio remains valid.

7.2.2 Auto-ignition delay time

The accuracy of the reduced mechanisms is now evaluated by comparison with the detailed mechanism. Figure 7.7 shows the auto-ignition time as a function of the initial temperature for $P = 1$ bar and $\phi = 1$.

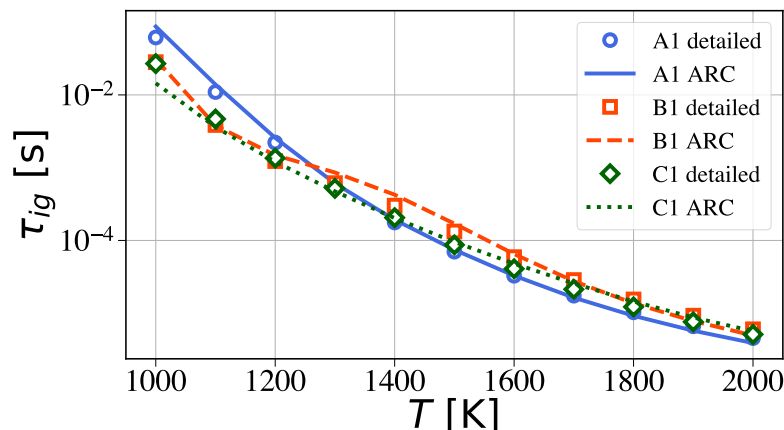


Figure 7.7: Auto-ignition time versus initial temperature for A1, B1 and C1 fuel for $P = 1$ bar and $\phi = 1$. Comparison between detailed mechanism and reduced mechanism.

Results show a good agreement within the whole temperature range and for the three surrogates, especially at high temperature. For lower temperature, very small discrepancies can be seen for A1 and C1 between the ARC mechanism and the detailed one.

Differences between the fuels remain below 50% of relative differences. A1 seems to take more time to ignite for low temperatures than B1 and C1, but shows the opposite behaviour for higher initial temperatures. B1 and C1 exhibit roughly the same levels of auto-ignition time, except for temperature between 1200 K and 1600 where B1 mechanism exhibits a slight change of slope.

0D isochoric reactors have been computed for the ARC schemes for $T = 1200$ K, $P = 1$ bar and $\phi = 1.0$ for all the fuel compositions available to have an insight on how the kinetic mechanism is behaving. Triangle plots with different fuel compositions are computed showing the ignition delay time (Fig. 7.8) for A1, B1 and C1.

The auto-ignition time represents the time required by a given mixture to ignite at a certain temperature.

ARC A1 shows a great disparity in terms of auto-ignition times. Pure xylene (aromatic species) shows an auto-ignition time near 16 ms, pure methyl-cyclohexane (cyclic species) around 9 ms and pure n-dodecane around 2 ms.

ARC C1 also exhibits great disparity. As for ARC A1, the pure aromatic species (methyl-naphthalene) shows the largest auto-ignition time (6.5 ms), followed by Decalin and iso-dodecane.

Auto-ignition timescales for mixtures composed of B1 composition do not vary so much. Iso-dodecane is the fastest to ignite, followed by iso-octane and iso-cetane. Again, the shape of the molecule has a strong impact on the key quantity, but the auto-ignition time can not be directly linked to the H/C ratio of the molecule.

To go deeper into the analysis of the flame structure, an interesting quantity to evaluate is the non-dimensional effective equivalence ratio, defined as:

$$\phi_k^{eff} = \frac{s_{Y,k} Y_k}{\sum_k s_{Y,k} Y_k} \quad (7.11)$$

with $s_{Y,k}$ the individual mass stoichiometric ratio of the pure species k of the fuel and Y_k the mass fraction of species k . ϕ_k^{eff} gives an insight on which species in the fuel is dominant for the combustion process. The non-dimensional effective equivalence ratio and the heat

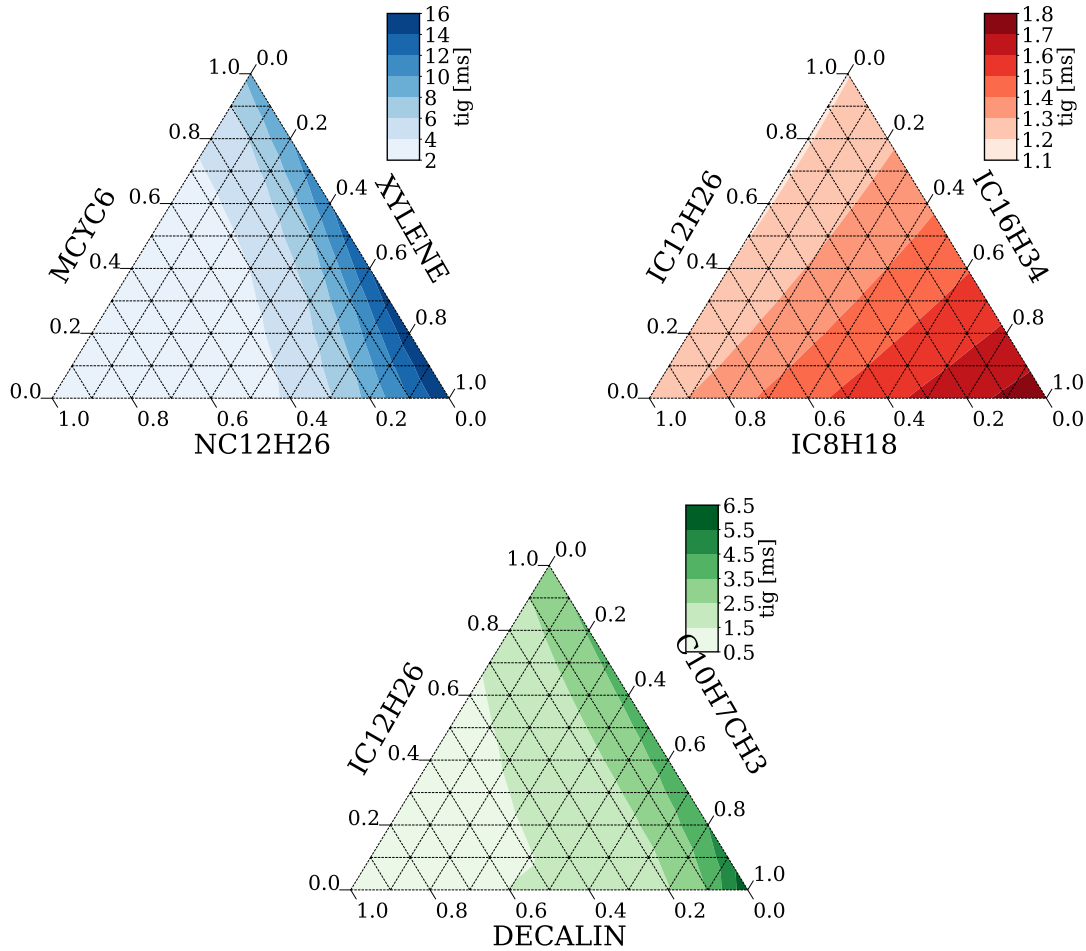


Figure 7.8: Auto-ignition time τ_{ig} triangle plots for $T = 1200$ K, $P = 1$ bar and $\phi = 1$ depending on the fuel composition.

release rate (HRR) curves are displayed Fig. 7.9 as function of time for ARC A1, ARC B1 and ARC C1.

For ARC A1, n-dodecane reacts quickly, followed by methyl-cyclohexane. Between the initial and the reactive time, xylene is largely dominant among the three fuel species. For ARC C1, iso-dodecane is immediately pyrolysed, followed by decalin and finally methyl-naphthalene. ARC B1 behaviour differs from the two other fuels. Indeed, the three branched alkanes are quickly consumed, but the auto-ignition happens later on compared to ARC A1 and ARC C1. This testifies that other transformations are occurring in the mixture before the fuel completely burns.

The profiles shown here display mostly the same order of consumption than what the auto-ignition timescale triangle plots suggest, that is to say that aromatic species take more time as cyclic species which take more time than alkane species. The negative heat release rate at the beginning, visible in the three plots, is due to the direct pyrolysis of the fuel that extracts energy from the mixture and releases it afterwards.

Looking back at A1 triangle plot, when looking at the $Y_{MCYC6} = 0$ isoline at the bottom of the triangle, one can notice that the auto-ignition time remains low and sharply increases around $Y_{NC12H26} = 0.5$. This limit corresponds to the LBO limit of n-dodecane ($\phi_{LBO} = 0.5$ at atmospheric pressure and temperature). Consequently, the amount of

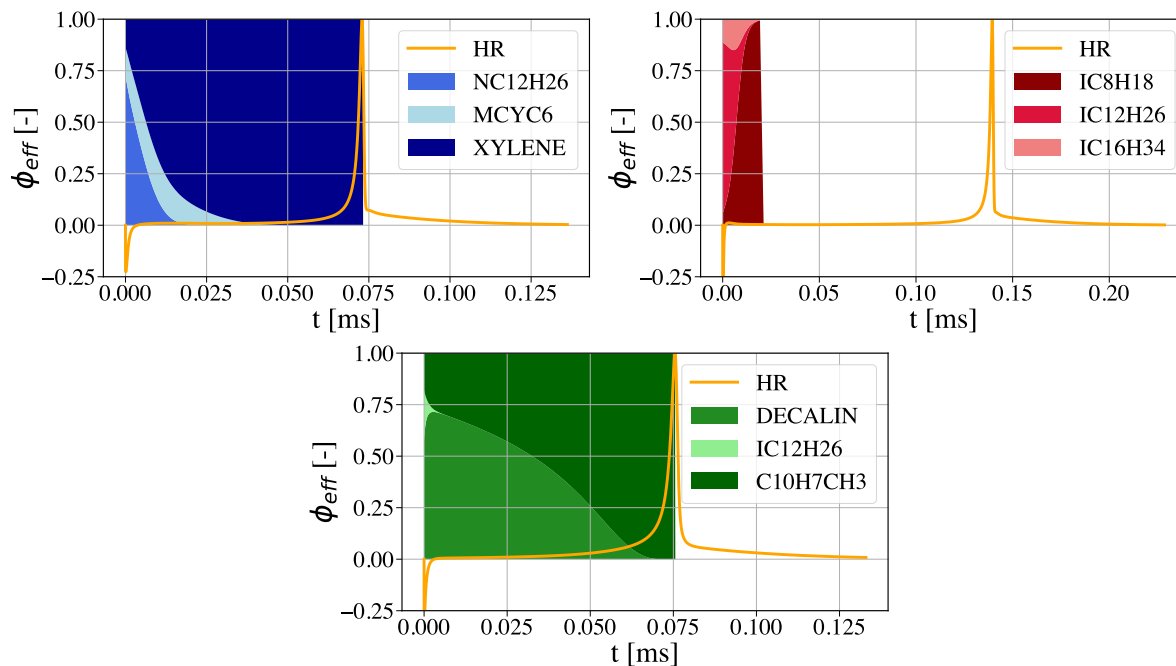


Figure 7.9: Effective equivalence ratio and HRR as a function of time for A1, B1 and C1 reduced mechanisms for $T = 1500$ K, $P = 1$ bar and $\phi = 1$.

n-dodecane in the mixture controls the auto-ignition time. In other words, if not enough n-dodecane is present in the mixture for combustion, the mixture needs to wait for xylene to be pyrolysed before igniting. The same conclusion can be drawn for the other fuel species, where the pyrolysis time is the interesting process to explain the differences in terms of ignition times.

7.2.3 Laminar flame speed accuracy

The accuracy of the reduced mechanisms has then been evaluated in 1D gaseous laminar premixed flames at fresh gas $T = 400$ K and atmosphere pressure, for a wide range of equivalence ratio. Figure 7.10 compares the detailed and ARC mechanisms for the three surrogates in terms of laminar flame speed.

Good agreements between the detailed and the ARC schemes are found for A1 and C1. For B1, the ARC mechanism slightly overestimates the laminar flame speed compared to the detailed scheme, but still remains under the target error limit (5%). This reduces the difference in laminar flame speed predicted by the ARC schemes between A1 and B1, especially in the range $\phi \in [0.9, 1.3]$. ARC A1 exhibits a larger laminar flame speed on the whole range, compared to ARC B1, and ARC C1 shows the lowest flame speed. Experiments [271] on laminar flame speed for the three fuels were conducted by the DLR at $T = 473$ K, $P = 1$ bar and $\phi = 0.8$. Comparison between ARC prediction and measurements is provided in Table 7.7.

The discrepancies are small between ARC A1 and ARC B1 and the experimental results, showing that the over-estimation for ARC B1 shown in Fig. 7.10 is reasonable. On the contrary, both the detailed and the ARC schemes underestimate the measurements for ARC C1. This means that the detailed mechanism lacks agreement for C1, as no data of the high aromatic fuel were available to validate the kinetic mechanism.

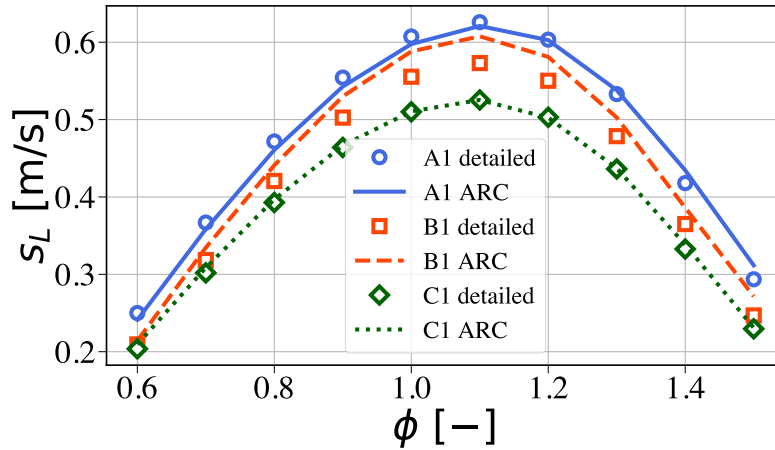


Figure 7.10: Laminar flame speed s_L versus equivalence ratio for A1, B1 and C1 surrogates for $T = 400$ K and $P = 1$ bar between detailed POLIMI and ARC mechanisms.

Fuel	Experiments	Detailed	ARC	Exp/ARC relative error [%]
A1	0.6200	0.648	0.6361	2.6
B1	0.6041	0.605	0.60139	0.45
C1	0.6095	0.5684	0.54537	10.5

Table 7.7: Experimental versus numerical laminar flame speed predicted by ARC schemes at $T = 473$ K, $P = 1$ bar and $\phi = 0.8$.

Triangle plots varying the composition of the blends have been plotted for the three cases in Fig. 7.11 using the ARC scheme.

The different laminar flame speeds are compared:

- for ARC A1, *n*-dodecane $n\text{-C}_{12}\text{H}_{26}$ shows the largest laminar flame speed. Conversely, xylene C_8H_{10} exhibits a laminar flame speed which is lower by 0.1 m/s and is the latest to react. Methyl-cyclohexane C_7H_{14} lies in between the two other components. This behaviour can be explained by the shape of the three molecules. Indeed, as xylene is an aromatic, it reacts very badly compared to a linear molecule which can break more easily, even if the chain length is lower.
- for ARC B1, on the contrary, all the components belong to the same type of molecules, namely branched alkanes. The difference between the three components is however not linked to the chain length: *i*- $\text{C}_{12}\text{H}_{26}$ shows the smallest timescale, followed by *i*- C_8H_{18} and finally *i*- $\text{C}_{16}\text{H}_{34}$. Varying the fuel composition only slightly affects the flame speed, with values between 0.55 and 0.6 m/s.
- for ARC C1, methyl-naphthalene $\text{C}_{10}\text{H}_7\text{CH}_3$ has the lowest laminar flame speed because of its double aromatic wing that is difficult to break. Iso-dodecane *i*- $\text{C}_{12}\text{H}_{26}$ shows the quickest reacting behaviour followed by decalin $\text{C}_{10}\text{H}_{18}$, which is cyclic.

As for the auto-ignition time, a direct correlation between the laminar flame speed and the H/C ratio is difficult to draw.

The effective equivalence ratio and the Heat Release Rate are plotted in Fig. 7.12 for the three fuels and for $T = 400$ K, $P = 1$ bar and $\phi = 1$.

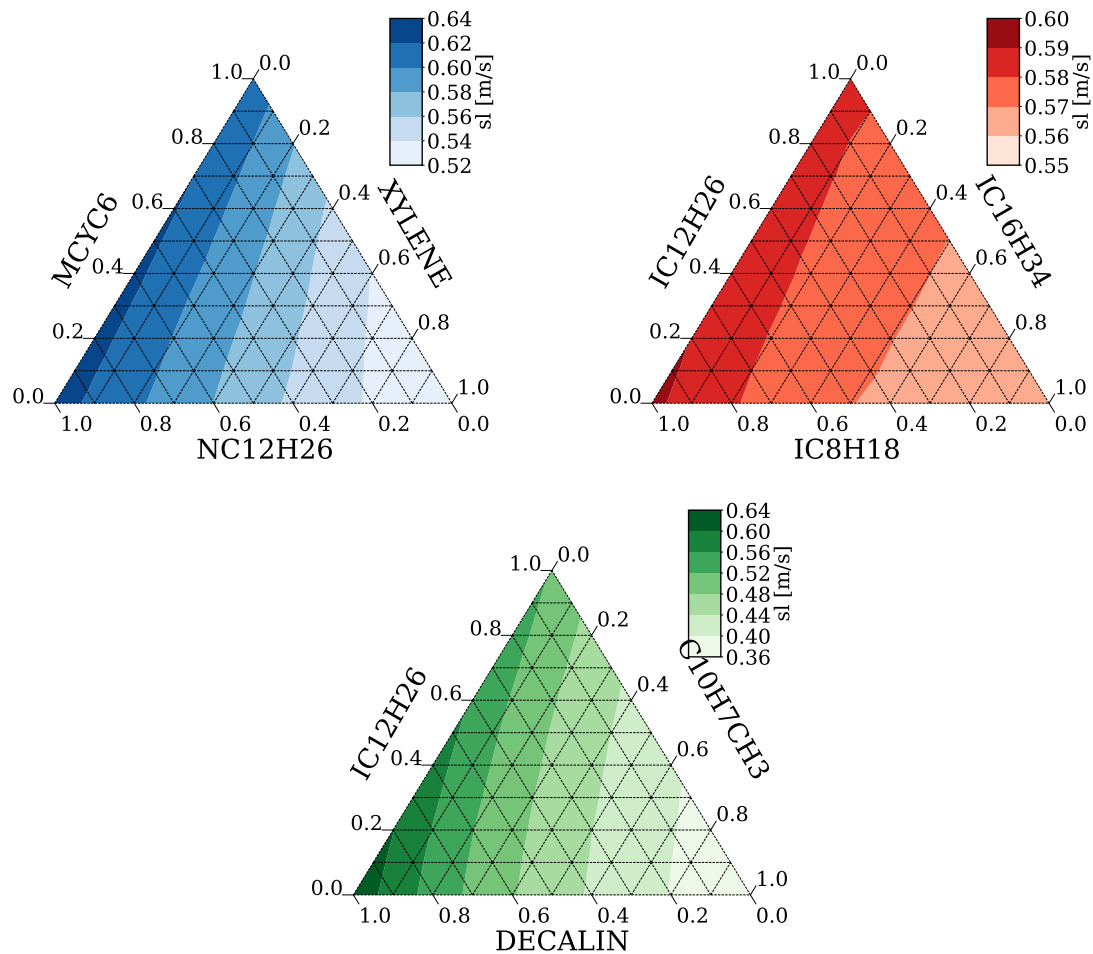


Figure 7.11: Laminar flame speed triangle plot $T = 400$ K, $P = 1$ bar and $\phi = 1$ depending on the fuel composition.

For the three fuels, the order of the species being consumed is maintained compared to the 0D case. For B1, the three components seem not to penetrate much in the flame front compared to A1 or C1 where XYLENE and $C_{10}H_7CH_3$ respectively are being consumed much later than the two others components, due to their unsaturated molecule structure.

The different proportions of the reaction rate $\nu_k \omega_k$ are given for the three fuels in Fig. 7.13 for ARC A1 and in Appendix B for ARC B1 and ARC C1.

The striking positive reaction rate for xylene is a demonstration of the stability of the double links and of the difficulty to decompose such species into combustion products. For alkanes, reactions with diffusive intermediate species (O , OH and H) enhance the combustion because of a higher Arrhenius coefficient as shown in [9], and at higher temperature, the direct fuel species decomposition is taking place.

7.2.4 Pollutants emissions

CO , CO_2 , NO_x have been focused on in this study. The prediction of soot precursors and soot particles are not of the scope of this work but has been worked on by other groups within JETSCREEN as it would involve a much more complicated setup and calculation. Indeed, C_2H_2 mass fraction was thought at first to evaluate the sooting impact of the three

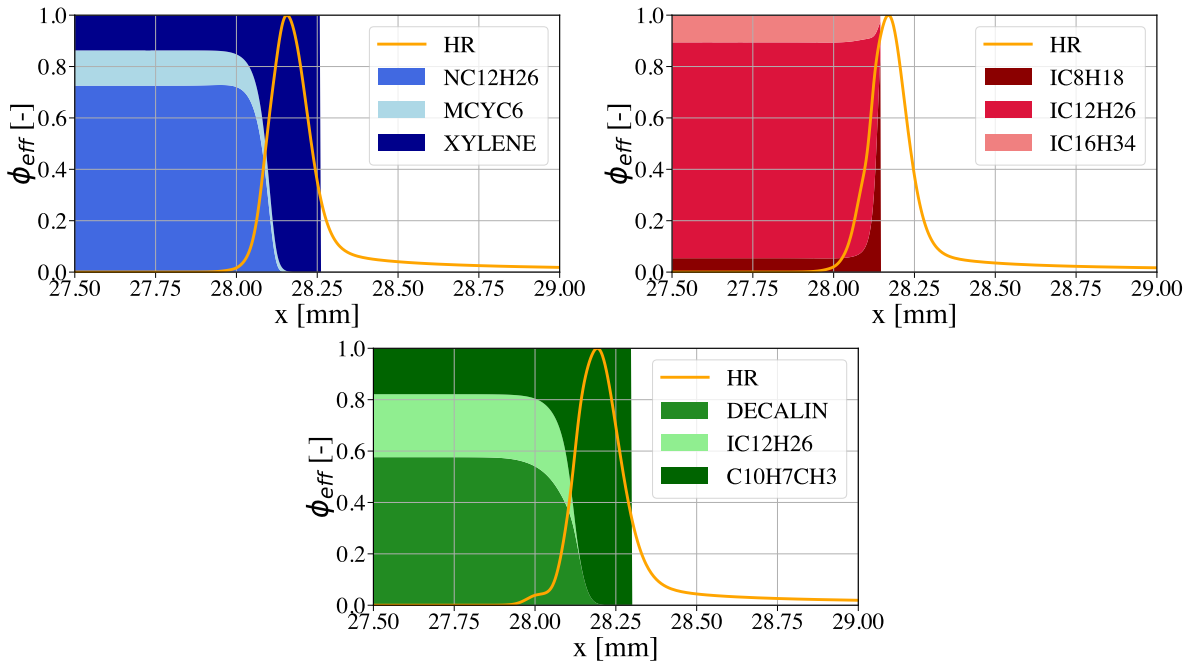


Figure 7.12: Spatial profiles of effective equivalence ratio and HRR for A1, B1 and C1 reduced mechanisms for $T = 400$ K, $P = 1$ bar and $\phi = 1$.

fuels. However, C1 is supposed to release more soot due to the high content of aromatics, which is not the case here, as other intermediate species are prone to create soot. Indeed, the idea to check the fuel influence on soot emissions would be to reduce a scheme from a detailed mechanism that is taking into account the soot creation pathways. Once done, a 1D premixed flame may be simulated. Finally, the soot volume fraction and particle density for particles over a given size are obtained by running the Cantera soot solver, CERFACS modified version of Cantera⁴.

As CO and CO_2 are targeted variables, their concentrations can be directly evaluated from the reduced mechanisms. NO_x pathways are not included in the detailed mechanism, chosen for this work. The POLIMI mechanism, named CRECK_2003_TOT_HT_NOX, has been used to evaluate the NO_x concentration, presented in Fig. 7.14 with CO and CO_2 .

For the three fuels, the global trend for the different pollutants is the following:

- CO_2 increases for lean mixtures and decrease for the rich ones. A peak is reached around stoichiometry. Differences between the three fuels are coherent with the equilibrium calculations: C1 exhibits a higher level of CO than A1 and B1, in agreement with the larger equilibrium temperature (see Section 7.2.1).
- CO mass fraction increases as the equivalence ratio increases. C1 shows a slightly higher maximum level than A1 and B1. The differences between the fuels are less significant than the effect of operating point changing.
- NO_x increase from lean mixtures to stoichiometric ones, then show a plateau and decreases rapidly around $\phi = 1.4$. A1 and B1 depict roughly the same levels of NO

⁴chemistry.cerfacs.fr

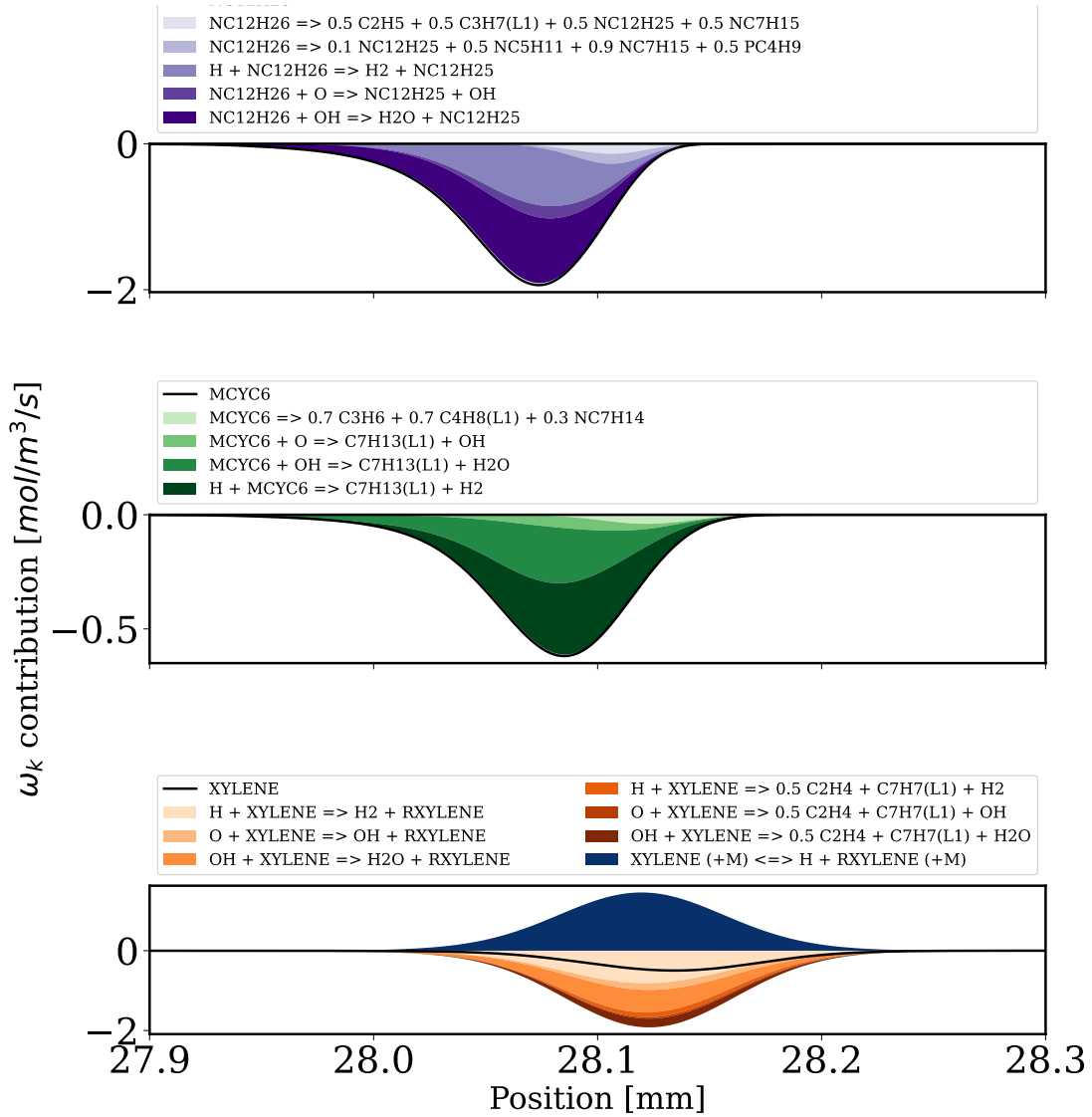


Figure 7.13: Source term for the A1 components and their reaction contributions for $\phi = 1$, $P = 1$ bar and $T = 400$ K.

mass fraction whereas NO from C1 is much higher, except in the rich zone, where C1 seems to produce slightly less NO than A1 and B1 around $\phi = 1.5$.

To further extend the results to the 3D simulations, NO_x pathways are investigated. According to the literature [134], five different routes promote the formation of NO_x :

- the **thermal route**, triggered by $O + N_2 \rightleftharpoons NO + N$ reaction. This reaction initiates the Zeldovich mechanism and is mainly dependent on temperature. The thermal route is significant for temperatures above 1800 K. It is a slow process and mainly occurs in the post-flame zone.
- the **prompt route**, triggered by $N_2 + CH \rightleftharpoons NCN + H$ reaction. This reaction occurs in the reaction zone and is dominant for rich conditions.

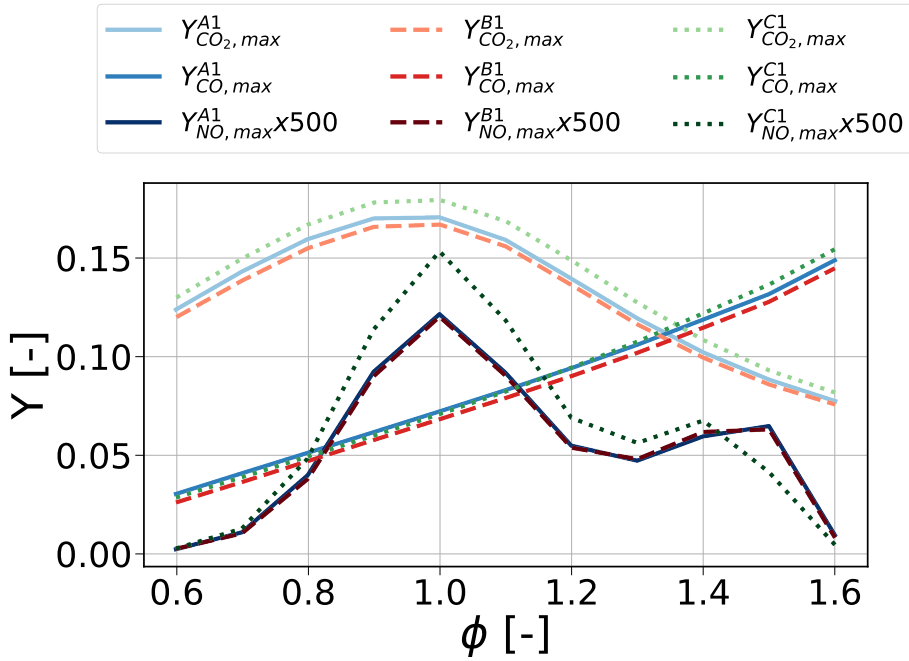


Figure 7.14: Final CO_2 , maximum CO and maximum NO mass fractions as a function of the equivalence ratio for A1, B1 and C1 fuel for $T = 400$ K and $P = 1$ bar.

- the **N_2O route**, triggered by $N_2 + O(+M) \rightleftharpoons N_2O(+M)$ reaction. It is usually found in lean premixed high pressure conditions.
- the **NNH pathway**, triggered by $N_2 + H \rightleftharpoons NNH$ reaction. It is promoted for low temperature kinetic pathways.
- the **fuel pathway**, activated when the fuel contains nitrogen, which is not the case here.

To check the dominant pathways, Fig. 7.15 represents the different pathways for $P = 1$ bar and $T = 400$ K versus the equivalence ratio. As many reactions occur from NNH to nitrogen and N_2O to nitrogen, they have been summed up and brought together with the name NNH-N2 and N2O-N2.

For lean stoichiometric mixtures (between 0.6 and 1.2), the thermal route is by far the predominant pathway. For richer conditions, the prompt route becomes dominant. N_2O and NNH routes remain very negligible. However, the NNH pathway seems to be slightly less important for A1 than for B1 and C1 and compensates the higher A1 thermal route, leading to the same NO_x level as for B1. Of course, such analysis may also depend on the operating conditions (higher pressure or temperature) and the flame structure (diffusion or premixed). This is however a start for further interpretation in more complex flame structures.

7.2.5 Characteristic species chemical timescales

Characteristic timescales for the three reduced mechanisms have been computed for $T = 323.15$ K, $P = 1$ bar and $\phi = 0.8$ to ensure that the stiffness is manageable in such a code as AVBP and are shown in Fig. 7.16. The typical timestep of the non-reacting simulation in the SSB configuration ($\Delta t_{non-reac} = 10^{-8}$ s) is added for reference.

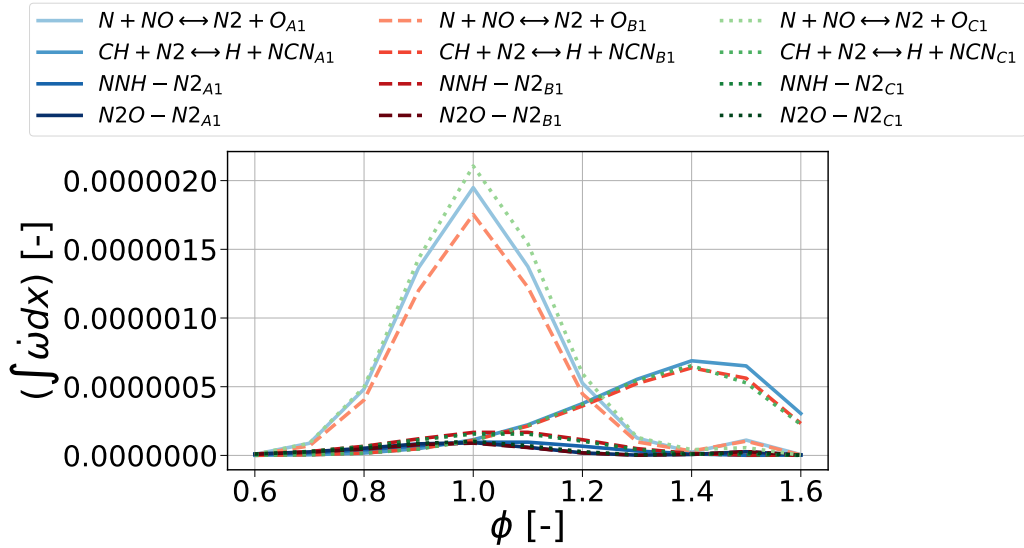


Figure 7.15: Integral of reaction rates relative to the NO_x creation pathways at $P = 1$ bar and $T = 400$ K.

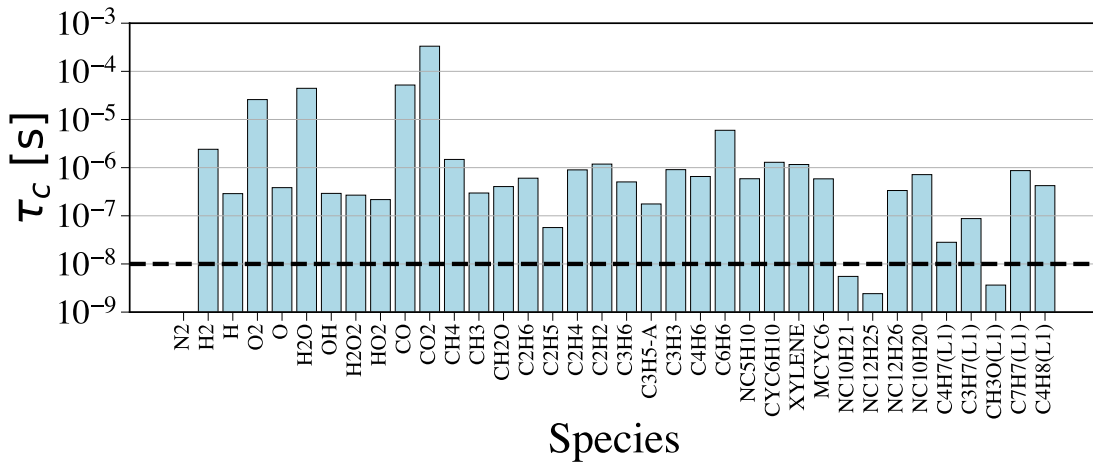
Results show that B1 reduced mechanism is less stiff than A1 and C1 reduced ones. Indeed, for AtJ, no species is found to be below the explicit time-step of the computation, whereas for A1 three intermediate species ($n-C_{10}H_{21}$, $n-C_{12}H_{25}$ and $CH_3O(L_1)$) are found to be stiff. For ARC C1, only $CH_3O(L_1)$ is problematic. To overcome this issue and to avoid wasting computational time, 3 sub-cycling iterations through the chemical routine are performed for the ARC A1 and the ARC C1 calculations. In other words, for one iteration, based on the acoustic CFL, the chemical routine is activated three times and chemical source terms are successively applied to the Navier-Stokes equations. This avoids going through every advection/diffusion routines three times and thus spares calculation time. Chemistry is then ready to get properly integrated into the CFD calculation.

7.2.6 Conclusion

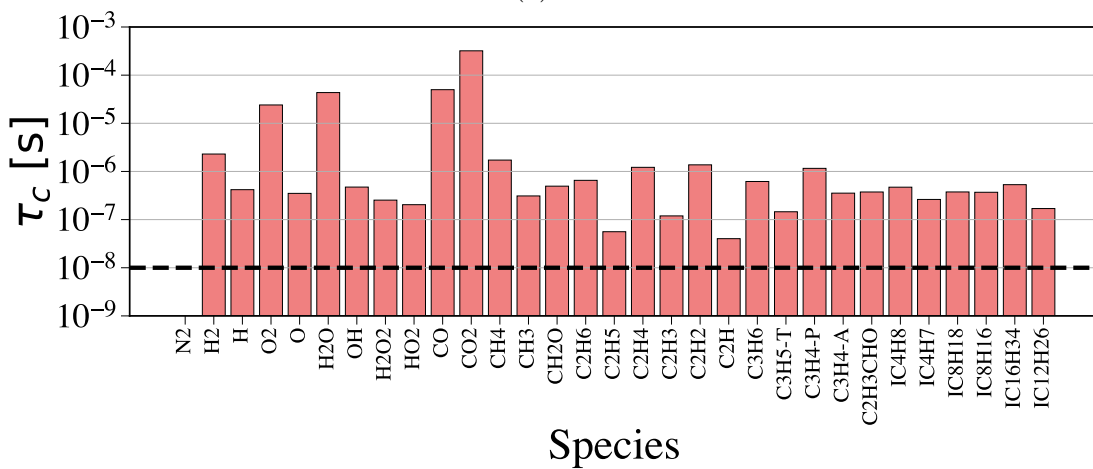
The objective of this section was to determine the fuel dependencies on the chemical properties in canonical case prior to perform 3D simulations, as well as to provide the tools to analyse the numerical results.

Chemistry for blends from POLIMI surrogates were reduced with ARCANE, giving good accuracy on the main characteristic quantities. As well, the blends exhibit different sensitivities to the different pure species, even if the condition of the fuel chosen for reduction is the blend. Linear molecules perform better than cyclic and aromatics ones in terms of combustion power and reaction speed, as cycles and doubles bonds add stability to the species, making them more difficult to transform. A relation between the different properties and the H/C ratio could not be mathematically stated. Pollutants emissions were also studied (CO , CO_2 , NO_x but not soot for this case), showing a very small impact on CO and on CO_2 , but a larger one on NO_x for C1 compared to A1 and B1.

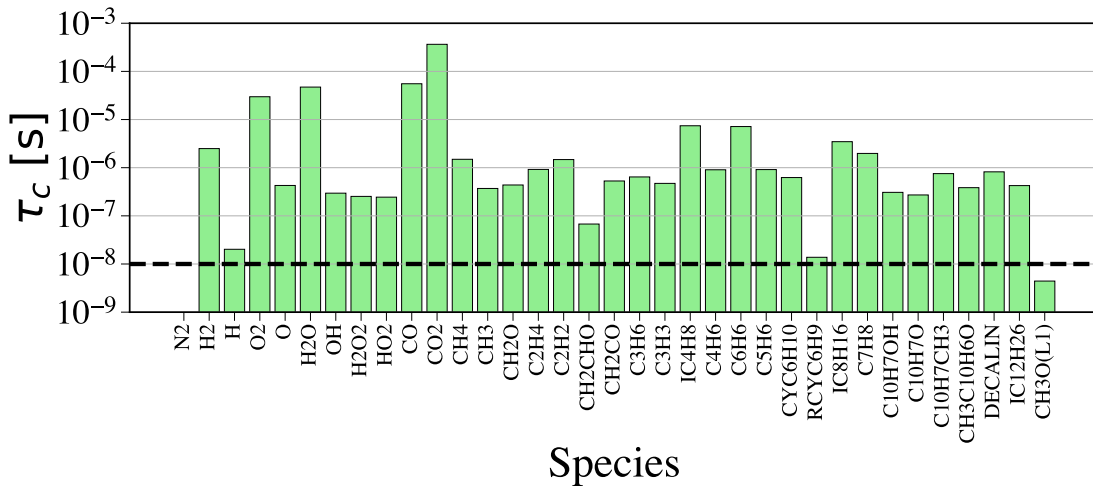
Before studying the two-phase flow properties of those fuels, the discretisation of complex kinetics should be ensured. As mentioned in Chapter 4, the temporal stiffness linked to the development of complex kinetic mechanisms has already been documented [308] and the problem has been resolved by different methodologies to enable the computation of 1D



(a) A1



(b) B1



(c) C1

Figure 7.16: Species timescales for A1, B1 and C1 reduced mechanisms at $T = 323.15$ K, $P = 1$ bar and $\phi = 0.8$.

premixed flames with complex kinetics [24], [87], [134]. However, the spatial discretisation of a complex fuel remains an open question for ARC schemes that is investigated in the next section.

7.3 Spatial discretisation for complex kinetics

The spatial discretisation of a 1D premixed flame has already been tackled rigorously by Roache [263], concluding that the convergence of global quantities such as laminar flame speed is not sufficient to assess if the solution is fully resolved or not. Indeed, some quantities may be insensitive to the error of others. For example, correctly predicting the laminar flame speed does not ensure that all the species mass fractions profiles are correctly reproduced. This is also assessed by [239], that the grid size must be smaller than the minimal reaction length to fully converge the flow. To resolve a hydrogen/air flame at $T_{init} = 800$ K and $P = 1$ bar, Al Katheeb et al. [147] conclude that the micro-metre scale level is needed. They also found that the length-scales predicted do not depend on the numerical method used, but on the advection-diffusion mechanism of the flame. And, as stated by Roache, the mesh cell size should be narrower than what is commonly used to compute CFD calculations.

However, for CFD applications, refinement at the order of the microscale is most of the time computationally not affordable, leading to enormous time-resolving calculations. ARC schemes may be of interest since the reduction methodology enables to set the very stiff species as QSS when they are not necessary to accurately predict the flame stabilisation. This enables to correctly predict reaction intermediates with only a few points in the flame front. Applying a rule with Zeldovic number (introduced in Section 3.3) valid for a one-step global chemistry, which states that 5 to 10 points are needed in the flame front [235], works empirically valid for ARCs. Why does such a rule work for complex kinetics ? What is the impact of the mesh discretisation on the laminar flame speed and the convergence of species mass fractions profiles ? What are the main metrics defining if an error is going to be important or not ?

To answer those questions, 1D premixed flames are performed, varying the fuel and the operating parameters in Section 7.3.1 to determine if 5 to 10 points in the flame front are indeed sufficient. Second, key quantity profiles are studied in detail in Section 7.3.2 to understand how the flame adapts to a coarse grid and how the reaction/diffusion mechanisms takes place.

7.3.1 Impact of the discretisation on laminar flame speed

To verify if 5 to 10 points are sufficient to describe the flame structure, the behaviour of flame spatial convergence with varying operating conditions is compared to the one of a reference flame. The reference case and the methodology to assess the errors are described in Section 7.3.1.1 and results are discussed in Section 7.3.1.2.

7.3.1.1 Reference case and methodology

The reference case chosen for this study is a fuel/air premixed flame taken at fresh gas temperature $T = 400$ K, atmospheric pressure and at stoichiometry as shown in Table 7.8. Two fuels are studied, namely methane and n-dodecane, and two ARC schemes are employed. The 1D domain is 8 cm long.

Simulations are performed with Cantera open-source kinetics solver. Figure 7.17 summarises the Cantera parameters used to compute the refined reference case and displays the spatial profiles of local grid refinement.

Such parameters result in a domain comprising about 10 000 points, with a local refinement in the flame front: about 5000 points in the flame front for CH_4 and 7000

Fuel	ARC name	Oxidiser [-]	Fuel composition [-]	P [Pa]	T [K]	ϕ [-]
CH_4	CH4_15_256_9_AP,	$X_{O_2} = 0.21$	$X_F = 1.0$	10^5	400	1.0
$C_{12}H_{26}$	C12H26_27_260_15_JW	$X_{N_2} = 0.79$				

Table 7.8: Operating conditions of the reference case.

Cantera refinement parameters	
ratio	2.0
slope	0.001
curve	0.01
prune	-0.1
grid_min	$1e^{-10}$
max_grid_points	10000

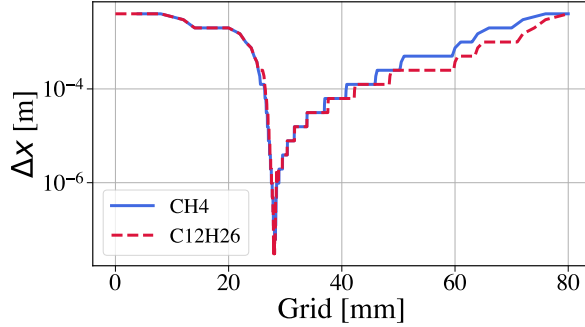


Figure 7.17: Cantera refinement parameters for the reference cases (left) and spatial profiles of local grid refinement (right).

for $C_{12}H_{26}$.

Several parameters have been varied: the mechanism, the fuel, the pressure P , the initial temperature T_{init} and the global equivalence ratio ϕ_g . The methodology employed in the following can be summarised as follows:

1. A chosen parameter is varied from the reference case. For instance, the initial temperature is increased to 800 K.
2. For parameter variation, the reference laminar flame speed (s_L^0) (calculated with the source term integral expression introduced in Section 3.3.3.1) and the associated thermal thickness ($\delta_L^{th,0}$) (of which the expression is given in Section 3.3.3.1) are evaluated. The 0 index stands for the reference case.
3. For each parameter variation, on a fine grid automatically computed by Cantera, several coarser simulations are then performed, varying the grid resolution but keeping it uniform. The thermal thickness ($\delta_L^{th,1}$) and the laminar flame speed (s_L^1) are evaluated. Knowing the cell size Δx , the number of points N_c in the flame front is evaluated for each case:

$$N_c = \frac{\delta_L^{th,1}}{\Delta x} \quad (7.12)$$

As a consequence, the computed number of points in the flame front is not necessarily an integer but may vary according to the thermal thickness estimation of the coarse case.

4. Eventually, the relative error ϵ_{s_L} between the laminar flame speed of the coarse and reference cases is evaluated:

$$\epsilon_{s_L} = \frac{s_L^1 - s_L^0}{s_L^0} \quad (7.13)$$

This relative error is then computed as a function of the number of points N_c in the flame front for each different operating condition.

This methodology enable to determine the number of points needed in the thermal flame front to keep an error on laminar flame speed lower than 5%.

7.3.1.2 Analysis of the results

Figure 7.18 displays for the methane case the evolution of the relative error ϵ_{s_L} with the number of points in the flame front N_c varying the chemical scheme, initial temperature, pressure, equivalence ratio and

The results of this study are shown in Fig. 7.18 and are described afterwards. Each graph is scaled for a maximum error on s_L of 30 % and between 3 and 12 points, except when the fuel is varied.

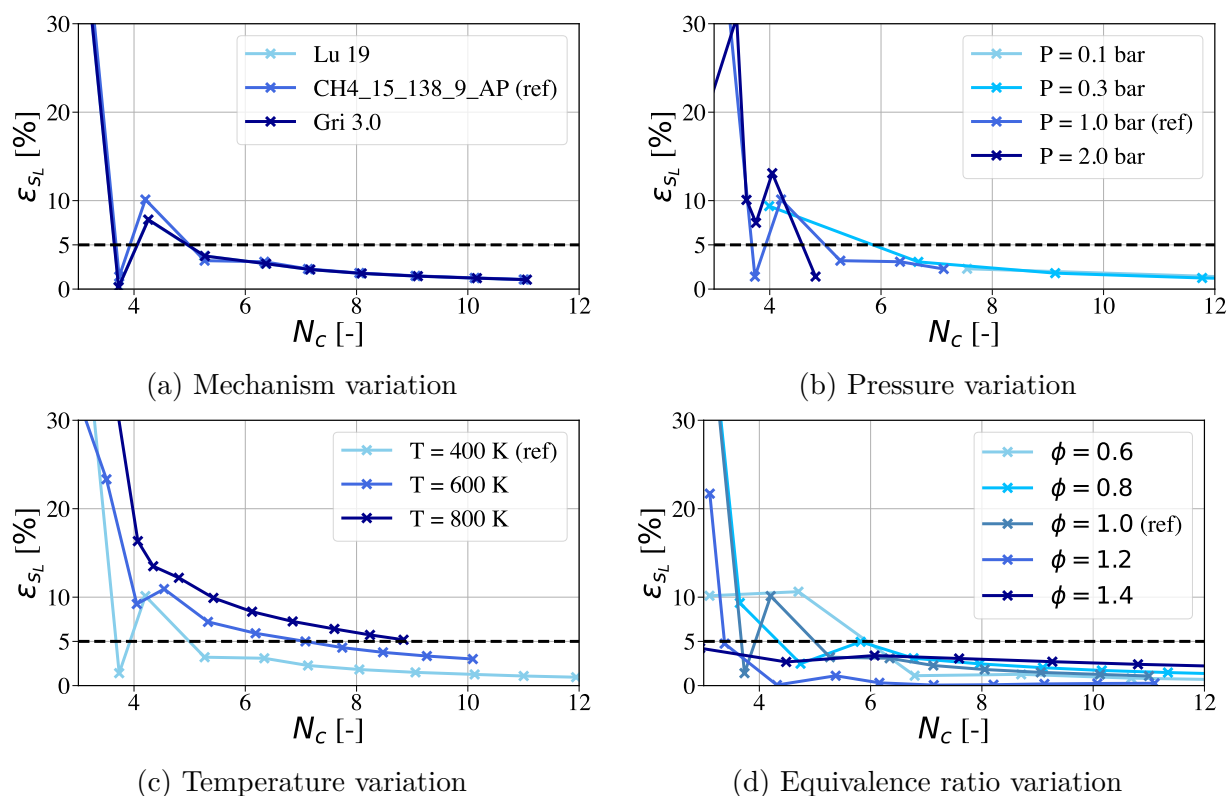


Figure 7.18: Relative error on the laminar flame speed ϵ_{s_L} versus number of points in the flame front N_c for several variations around reference case for methane.

It is observed that a minimum of 3 points in the flame front is required to obtain a reasonable error ($\epsilon_{s_L} < 15\%$). On every plot, before a threshold for N_c , the error on laminar flame speed fluctuates and may even be lower than the targeted error of 5 % for some cases. This does not mean that convergence is reached, but is a lucky guess, as the flame structure might be very different from the reference solution in these cases. After this threshold for N_c , the evolution of the error seems to be monotonous, and the flame structure remains the same. The reference case for methane in Table 7.8 reaches an error ϵ_{s_L} lower than 5% error for $N_c \sim 5$. Each parameter is analysed hereafter.

- **Chemical mechanism variation**

The ARC_15_138_9_AP mechanism, the ARC Lu 19 from [183] and the detailed Gri-30 [106] mechanisms are compared to evaluate if the scheme or the level of chem-

ical reduction influences the convergence. The results are unequivocal: changing the mechanism or the degree of reduction does not affect much the results, as the reduced schemes contains by construction the main pathways for the flame stabilisation.

- **Pressure variation**

Pressure varies between 0.1 bar and 2 bar. The higher the pressure, the fewer number of points in the flame front are needed for the flame to be converged. This parameter is influencing very much when going towards lower pressure, which is rarely happening for standard aeronautical field operating points.

- **Temperature variation**

Temperature varies between 400 K and 800 K. This graph shows that the higher the temperature, the higher the error is for a given number of points in the flame front. Indeed, for an initial temperature of 400 K, 5 points are needed whereas for $T_{init} = 800$ K, 9 points in the flame front barely reach this limit. This variation is strong, and the initial temperature may be considered as an important influencing parameter.

- **Equivalence ratio variation**

The equivalence ratio varies from lean to rich mixtures. The leaner the equivalence ratio, the more points in the flame front it needs (approximately 6 here) to make the error lower than the $\epsilon_{s_L} = 5\%$ horizontal line, against 5 for the stoichiometric point and less than 3 for the richer operating point.

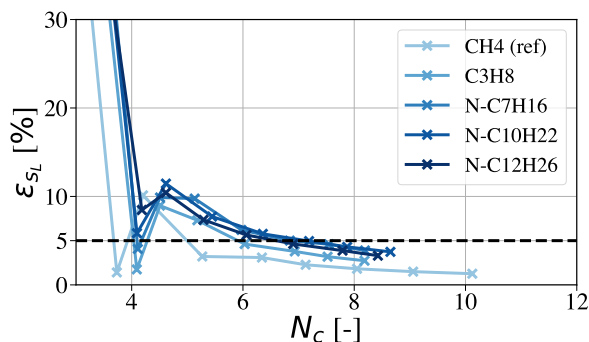
Eventually, different fuels are studied. The associated reduced mechanisms used are listed in Table 7.9. All the reduced mechanisms are available on: <https://chemistry.cerfacs.fr>.

Fuel species	Associated mechanism	T_{ad} [K]	s_L^0 [m/s]	$\delta^{th,0}$ [mm]
CH_4	<i>CH4_15_256_9_AP</i>	2278	0.58411	0.39359
C_3H_8	<i>C3H8_22_173_12_FC</i>	2363	0.64890	0.31032
C_7H_{16}	<i>NC7H16_25_210_27_FC</i>	2396	0.64561	0.31068
$C_{10}H_{22}$	<i>C10H22_26_255_16_PP</i>	2331	0.59168	0.33404
$C_{12}H_{26}$	<i>C12H26_27_260_15_JW</i>	2328	0.64236	0.31762

Table 7.9: Fuel, associated reduced mechanisms and key properties for the reference operating points: adiabatic temperature T_{ad} , laminar flame speed s_L^0 and thermal thickness δ_L^0 .

The results displayed Fig. 7.19 show that light hydrocarbons such as methane requires approximately 5 points in the flame front to reach the $\epsilon_{s_L} = 5\%$ target value, 6 points are needed for medium fuels such as n-propane and 7 points are required for heavy fuels such as n-heptane, n-decane and n-dodecane.

To summarise, for all the cases performed, the flame converges for N_c between 5 and 10 points in the flame front. This extends the statement of Zeldovic at ARC schemes. To understand why so complex kinetics only require 5 to 10 points to correctly reproduce the laminar flame speed, chemistry needs to be studied more in details.



(a) Fuel variation

Figure 7.19: Relative error on the laminar flame speed ϵ_{s_L} versus number of points in the flame front N_c for several hydrocarbon fuels around the reference case for methane.

7.3.2 Effect of the mesh discretisation on the flame structure

First, spatial profiles of HRR, temperature and species profiles for different grid refinement levels are compared in Section 7.3.2.1 to analyse the impact of the refinement on such profiles. The reaction/diffusion mechanism is then introduced 7.3.2.2 before focusing on the reaction sensitivity 7.3.2.3. Finally, the impact of the different reactions with the fuel on the laminar flame speed is explained in Section 7.3.2.4.

7.3.2.1 Spatial profiles of global variables and final state

Figure 7.20 displays spatial profiles of heat release rate, temperature, CH_4 , CO , CO_2 and velocity for a methane-air flame in the reference case of Table 7.8, varying the number of points with the flame front N_c .

The adiabatic temperature is reached whatever the N_c used, which means that the power released by the chemical scheme is the same whatever the N_c used. For low N_c values, the heat release rate profile is thickened than for the refined case. This leads to a larger flame thickness and therefore slopes in the flame front are smoothed for temperature, reactants and products profiles. CO shows the same trend. The final composition is very close in-between every case (less than 0.1 % of error). This means that the final state and what is happening in the burnt gases' region is not very important for the stabilisation of the flame. To investigate that, additional variables are plotted as a function of the number of points N_c in Fig. 7.21.

The final state, namely the adiabatic temperature and final water and carbon dioxide mass fractions, converge more quickly than the laminar flame speed, which confirms what was stated previously, i.e. that the final state is not controlling the flame convergence. The heat release rate integral follows of course the same trend as the laminar flame speed s_L since they are directly proportional. The same conclusion can be drawn for the fuel source term, not shown here. The maximum of CO mass fraction converges as quickly as the laminar flame speed. The maximum of C_2H_2 , an example of pyrolysis product, shows an error slightly higher than the laminar flame speed one but remains acceptable. The flame thickness shows the maximum error with the reference case. This is explained by the dependency of the thermal thickness to the maximum of the temperature gradient, which is very sensitive to the peak discretisation and is underestimated in coarser meshes (as shown in Fig. 7.20).

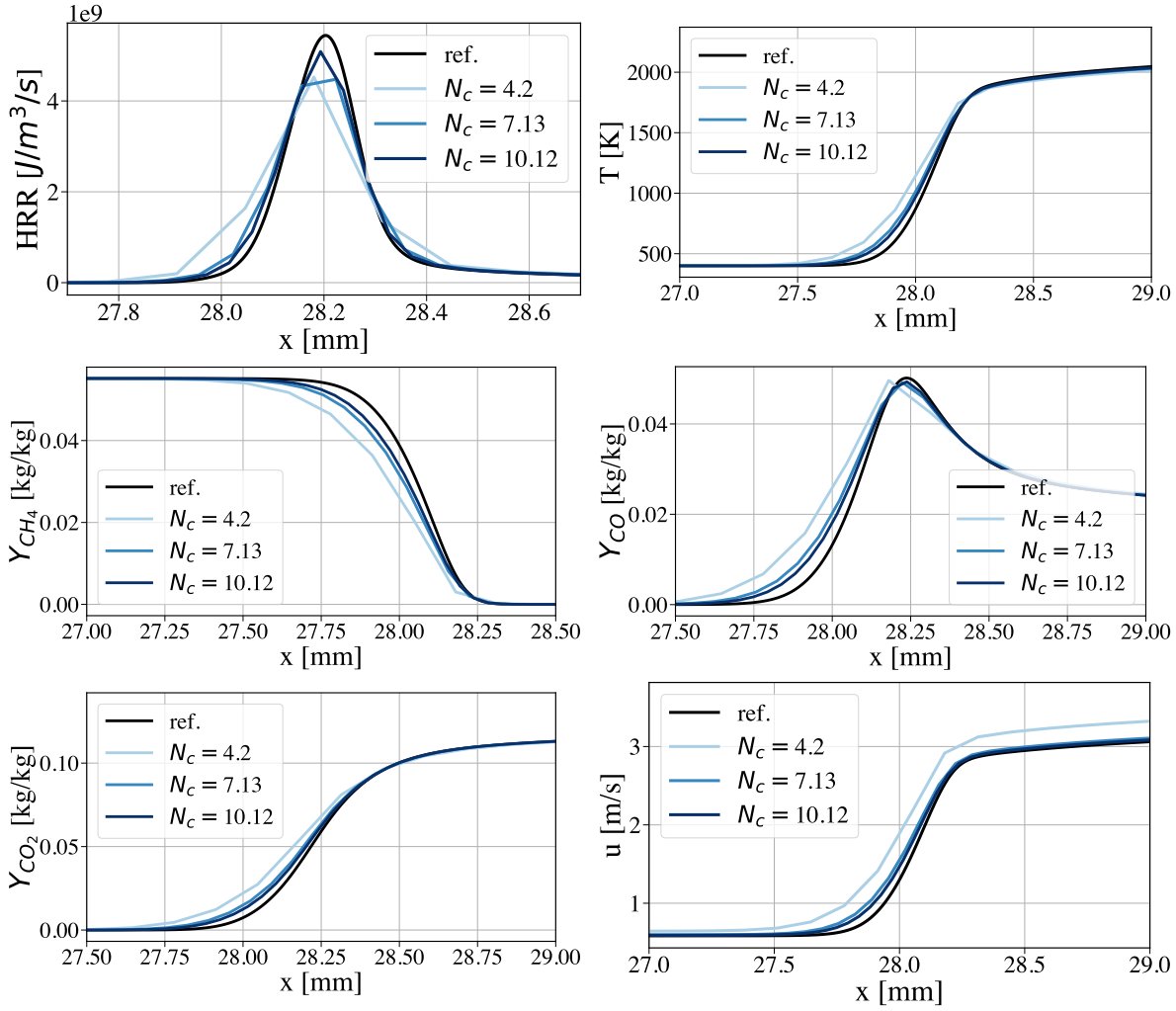


Figure 7.20: Methane/air flame key quantities spatial profiles for different number of points N_c in the flame front for the reference case (Table 7.8).

7.3.2.2 The reaction/diffusion mechanism

Mathematically, the overall flame structure depends on the flame source term consumption. By integrating the Navier-Stokes system of equations applied on the 1D domain of a premixed flame, the following relations are found [235]:

$$\begin{aligned} \rho_{fresh} s_L (Y_{burnt,i} - Y_{fresh,i}) &= \int_0^{L_{domain}} \dot{\omega}_i dx \\ \rho_{fresh} s_L \int_0^{L_{domain}} c_p dT &= \int_0^{L_{domain}} HRR dx \end{aligned} \quad (7.14)$$

for any species i . Combining the two relations of Eq. 7.14 and applying it to the fuel for a lean premixed flame leads to:

$$\int HRR dx = \frac{\int c_p dT}{Y_{F,burnt} - Y_{F,fresh}} \int \dot{\omega}_F dx \quad (7.15)$$

Thus, the integral of heat release rate depends on the fuel consumption rate, on temperature and on the final fuel mass fraction.

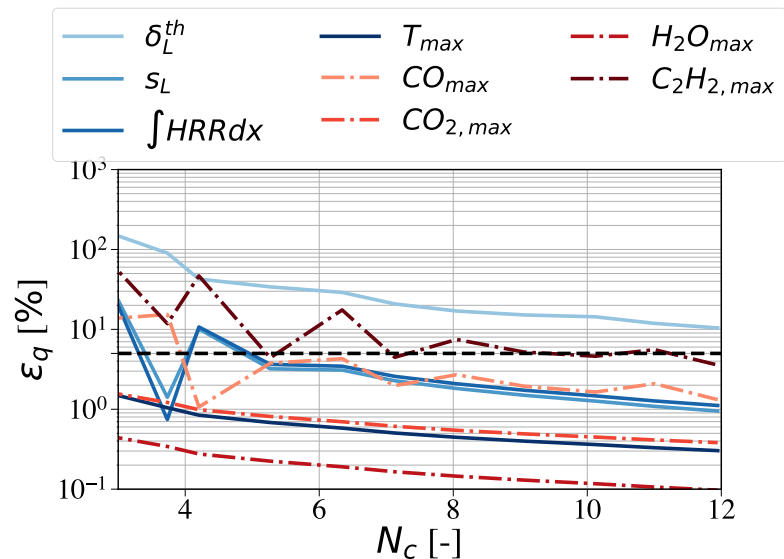


Figure 7.21: Relative error of different flame quantities as a function of the number of points in the thermal thickness N_c for the reference case.

The key reactions for the flame stabilisation are then the fuel reactions. What happens downstream is then just a consequence of the reaction zone, triggering important intermediate species to burn and form the combustion products. Those intermediate species are interacting with the foot of the flame through a reaction/diffusion mechanism to enhance the combustion process. To confirm this statement, the error made on the mass fraction integrals between the coarse mesh and the reference refined case, defined as:

$$\epsilon_{\int Y_k} = \frac{\int_0^{L_{domain}} Y_k dx - \int_0^{L_{domain}} Y_k^{ref} dx}{\int_0^{L_{domain}} Y_k^{ref} dx} \quad (7.16)$$

is plotted as a function of the number of point in the flame front N_c for methane and n-dodecane at the reference conditions using the two ARCS (CH4_15_138_9_AP and C12H26_27_260_15_JW) Fig. 7.22. Colours are defining sub-spaces of all the species in the mechanism, namely:

- green with a cross symbol represents the major reactants and products of combustion.
- grey, red and purple colours with triangle, diamond and square symbols represent light, medium and heavy pyrolysis products respectively.
- blue with circles represents other species.

The major species (green crosses) show the smallest error because their mass fraction profile shows a step and not a peak. Intermediate species mass fractions are zero at the beginning, are zero or very small in the burnt gases, and display a strong peak in the flame front. The species that display the maximum of error are the pyrolysis products for both cases. For n-dodecane, pyrolysis products seem to have a higher error compared to light and medium pyrolysis products. Thus, the hypothesis made previously is reinforced: the flame is mainly controlled by the direct fuel pyrolysis and that what is happening afterwards is only a consequence of it.

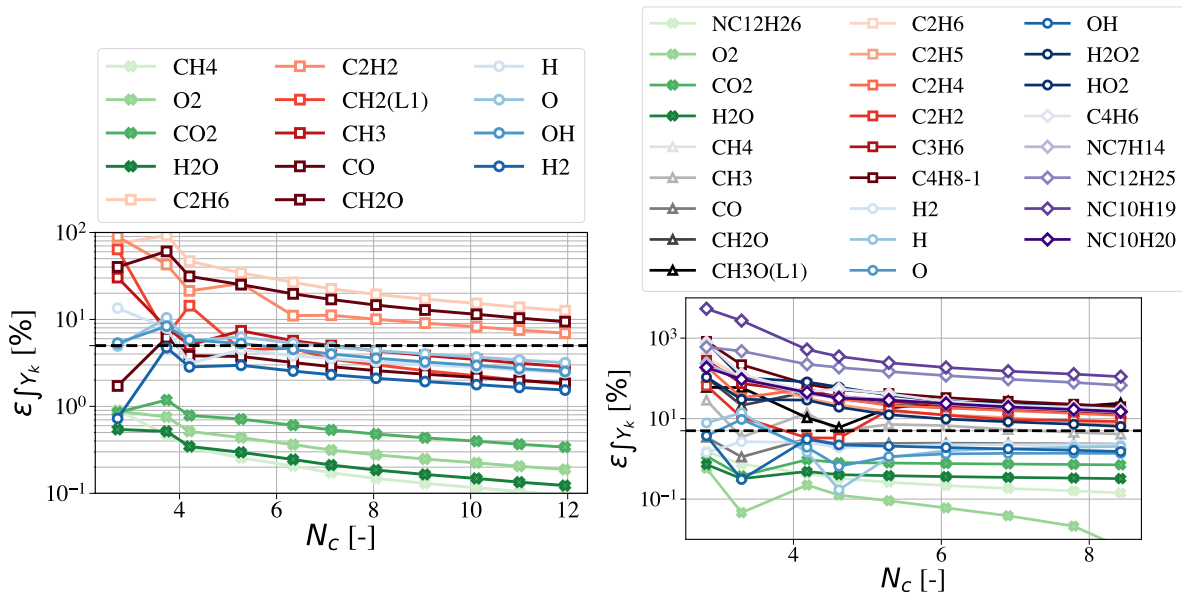


Figure 7.22: Error on mass fraction integrals versus N_c for CH₄/air (left) and C₁₂H₂₆/air (right) at $P = 1$ bar, $T = 400$ K and $\phi = 1.0$ displaying main reactants and products (green crossed), pyrolysis products (grey triangles, red squared and purple diamonds) and other species (blue circles).

For both cases, other species seem to fluctuate more than others in terms of convergence. Indeed, as those depend on how pyrolysis occurs, the different contributions might compensate, giving the right integral but for wrong reasons.

The next step to analyse in more details the influence of the discretisation is to look at the species source terms. However, species source terms are difficult to analyse, because they are per definition a composition of reaction rates, which can lead to a very wide variety of profile types. Moreover, as most of the species are intermediate species, the energy balance is neutral, making a power analysis useless. On the contrary, the reaction source terms can be easily analysed, as reaction rate thicknesses are defined for each peak and show only one peak because backward and forward reaction source terms are separated, as defined in Section 3.3.3.1. Therefore, a sensitivity analysis is performed in the next section.

7.3.2.3 Sensitivity analysis

Looking at the width of the reaction rates gives a first insight on the stiffness of the system. One can wonder if the narrowest reaction rate peaks are creating the highest flame error, as these peaks might not be fully discretised when the grid is coarse. To answer this question, a sensitivity analysis (SA) is performed on the two ARCs mechanisms to determine if a link exists between the error induced by a given reaction and its width for a light fuel (CH₄) and a heavier one (C₁₂H₂₆).

Figure 7.23a compares the relative error of the laminar flame speed compared to the refined case obtained by the SA as a function of the width of the different reactions for methane. Each point represents the SA applied on a given reaction, and both axis scales have been set to a logarithmic scale for better visualisation. The thermal thickness and the HRR thickness of the reference case have been plotted as well. The same plot is displayed for n-dodecane in Fig. 7.23.

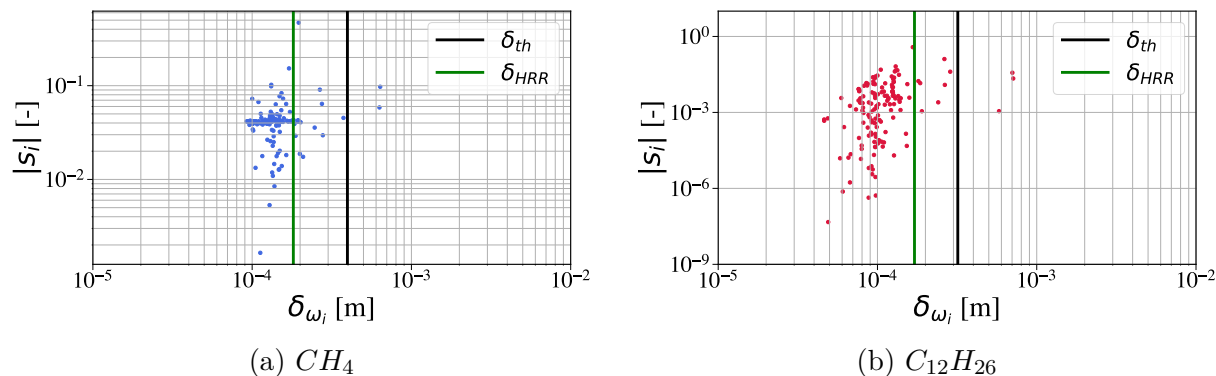


Figure 7.23: Sensitivity analysis: error of the laminar flame speed for each perturbed reaction rate as function of the width of the reaction considered, each point represents a given reaction.

Several conclusions can be drawn from this graph concerning the influence of the reactions on the laminar flame speed:

- The error of the laminar flame speed induced by the sensitivity analysis and the width of each reaction rate are not correlated. Therefore, the smallest reaction rates do not influence much the flame and the flame speed accuracy does not depend on the spatial discretisation only.
- The HRR thickness shows a very close value compared to the biggest amount of points on the graph, meaning that it is representative of the width of most of the reactions occurring in an ARC flame. The thermal thickness is slightly bigger, but still remains within the same order of magnitude. Moreover, only a few reaction rates have a width that goes below 1/10 mm.
- Reactions that are very sensitive are found to have a width closer to the thermal thickness, which would explain why with a few points in the flame front (like 3 or 4), the simulation does not crash even if giving very large error in terms of laminar flame speed occur.

When comparing both graphs, they look very similar, except that some reaction rates exhibit an even smaller width. They mainly correspond to direct fuel decomposition steps, as shown in Table 7.10.

Thus, predicting small reaction rates accurately is not the monitoring parameter for the 1D premixed flame spatial stabilisation, explaining why the laminar flame speed and other quantities are not incoherent when having between 5 and 10 points in the flame front.

In other words, there exists a ranking in the reactions that influence the flame stabilisation and this ranking is not necessarily depending on the flame width. Besides, the sensitivity analysis performed here is not the right indicator to show which reactions are influencing the flame convergence. Indeed, varying one reaction without considering its impact on other reactions does not enable to rebuild the causal interaction between the species and thus only answers part of the question. A better suited methodology has been developed in the following section.

Reaction	Width [μm]
$n\text{-C}_{12}\text{H}_{26} \longrightarrow 0.5\text{C}_2\text{H}_5 + 0.5\text{C}_3\text{H}_7(L_1) + 0.5n\text{-C}_{12}\text{H}_{25} + 0.5n\text{-C}_7\text{H}_{15}$	46.29
$n\text{-C}_{12}\text{H}_{26} \longrightarrow 0.1n\text{-C}_{12}\text{H}_{25} + 0.5n\text{-C}_5\text{H}_{11} + 0.9n\text{-C}_7\text{H}_{15} + 0.5p\text{-C}_4\text{H}_9$	46.29
$n\text{-C}_{10}\text{H}_{20} \longrightarrow 0.5\text{C}_3\text{H}_5\text{-A} + 0.5\text{C}_4\text{H}_7(L_1) + 0.25n\text{-C}_5\text{H}_{11} + 0.75n\text{-C}_7\text{H}_{15}$	48.79
$n\text{-C}_5\text{H}_{11} \longrightarrow 0.25\text{C}_2\text{H}_4 + 0.55\text{C}_2\text{H}_5 + 0.55\text{C}_3\text{H}_6 + 0.25\text{C}_3\text{H}_7(L_1) + 0.2\text{C}_4\text{H}_8\text{-1} + 0.2\text{CH}_3$	49.05
$\text{C}_4\text{H}_7(L_1) \longrightarrow \text{C}_4\text{H}_6 + \text{H}$	58.25
$n\text{-C}_7\text{H}_{14} \longrightarrow 0.5\text{C}_2\text{H}_5 + 0.5\text{C}_3\text{H}_7(L_1) + 0.5\text{C}_4\text{H}_6 + 0.5\text{C}_4\text{H}_7(L_1) + 0.5\text{CH}_3$	59.25
$\text{C}_4\text{H}_8\text{-1} + \text{H} \longrightarrow p\text{-C}_4\text{H}_9$	60.56
$\text{C}_4\text{H}_7(L_1) \longrightarrow \text{C}_4\text{H}_6 + \text{H}$	61.68
$\text{C}_3\text{H}_6 + \text{H} \longrightarrow \text{C}_3\text{H}_7(L_1)$	65.73
$n\text{-C}_{10}\text{H}_{20} + \text{OH} \longrightarrow \text{H}_2\text{O} + n\text{-C}_{10}\text{H}_{19}$	67.19
$n\text{-C}_{10}\text{H}_{19} \longrightarrow 0.6\text{C}_2\text{H}_4 + 0.5\text{C}_3\text{H}_5\text{-A} + 0.6\text{C}_3\text{H}_6 + 0.5\text{C}_4\text{H}_7(L_1) + 0.5n\text{-C}_7\text{H}_{14}$	67.19
$\text{C}_4\text{H}_8\text{-1} + \text{H} \longrightarrow p\text{-C}_4\text{H}_9$	67.87

Table 7.10: Reactions showing the smallest width for $\text{C}_{12}\text{H}_{26}$ /air flame, less than $70 \mu\text{m}$.

7.3.2.4 Reaction analysis

Looking at how the important intermediate species influence the flame front, the relative error of the laminar flame speed can be linked to the relative error of the reaction rate integral, by using:

$$s_L = \frac{1}{\rho_{fresh}(Y_{F,burnt} - Y_{F,fresh})} \int \dot{\omega}_F \quad (7.17)$$

the relative error of the laminar flame speed is equal to the error of the fuel source term ($\epsilon_{s_L} = \epsilon_{\int \dot{\omega}_F}$) since ρ_{fresh} and $Y_{F,fresh}$ do not depend on the flame resolution. Furthermore, by expressing the fuel source term as a function of its reaction source term:

$$\dot{\omega}_F = \sum_{j=1}^{N_r} \nu_j \omega_j \quad (7.18)$$

and by introducing the relative error of the reaction j :

$$\epsilon_{\int \omega_j} = \frac{\int \omega_j - \int \omega_{j,0}}{\int \omega_{j,0}} \quad (7.19)$$

The error of the reaction rate then becomes:

$$\epsilon_{s_L} = \sum_{j=1}^{N_r} \nu_j \frac{\int \omega_{j,0}}{\int \dot{\omega}_{F,0}} \epsilon_{\int \omega_j} = \sum_{j=1}^{N_r} \epsilon_{s_{L,j}} \quad (7.20)$$

with ν_k the stoichiometric coefficient in front of the fuel in reaction j , $\int \omega_{j,0}$ the exact value of the reaction rate of reaction j , $\int \dot{\omega}_{F,0}$ the exact value of the fuel source term and $\epsilon_{\int \omega_j}$ the relative error of the reaction rate k . $s_{L,j}$ is then defined as the part of the rate of reaction j that contributes to the laminar flame speed and $\epsilon_{s_{L,j}}$ the associated relative error. By computing the values of $\nu_j \frac{\int \omega_{j,0}}{\int \dot{\omega}_{F,0}} \epsilon_{\int \omega_j}$ for each reaction rate, the reactions that influence the flame by having the greatest errors can be determined. Figure 7.24 shows the laminar flame speed relative error and the part of the error coming from reaction j $\epsilon_{s_{L,j}}$.

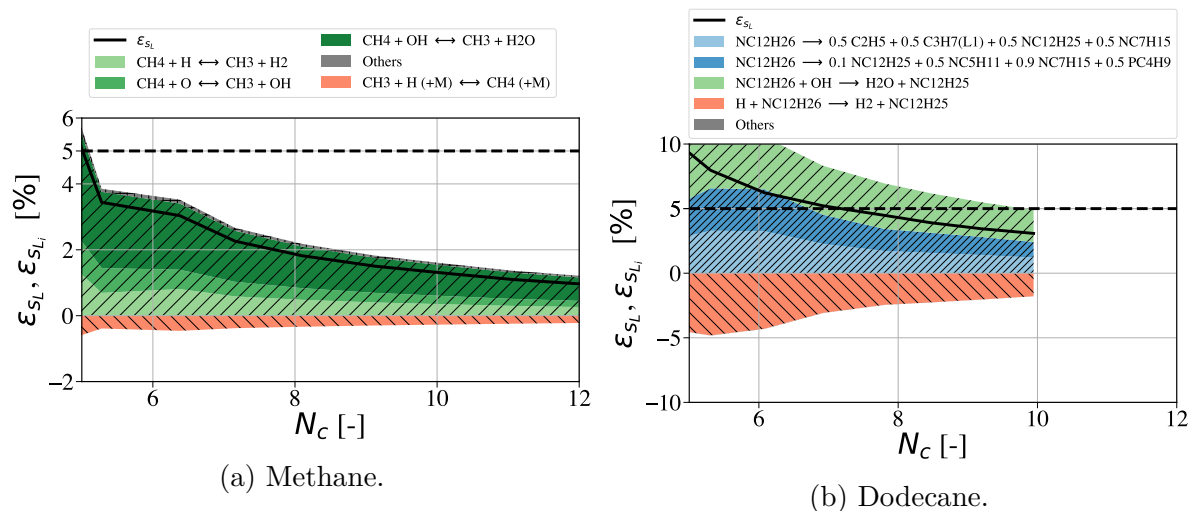


Figure 7.24: Relative error of the laminar flame speed ϵ_{s_L} and part of the error coming from reaction j $\epsilon_{s_{L,j}}$ versus N_c in the thermal thickness at $T = 400$ K, $\phi = 1.0$ and $P = 1$ bar.

Those graphs show that the reactions that are more prone to generate some errors on the laminar flame speed are the one depending on the most diffusive intermediate species (O , H and OH) because of their small weight. This is coherent with O , OH and H being the species that are the most sensitive in the scheme (Fig. 2 in Appendix A). This also shows that the diffusion mechanism influences the flame root, namely the fuel consumption, which influences the whole flame and determine the laminar flame speed error. Moreover, the error on the laminar flame speed is not determined by one reaction, but by several reactions.

Direct n-dodecane decomposition reactions takes a smaller part of the error at the beginning but become more important at the end in terms of proportion, as shown in Appendix A. Indeed, their small thickness leads to a high level of error. Those direct fuel decomposition reactions have the same relative error because their Arrhenius coefficients are strictly identical.

When equation 7.20 is investigated, the expression may be divided into two sub-terms:

- The first component of equation 7.20, $\frac{\int \omega_{j,0}}{\int \dot{\omega}_{F,0}}$, is easy to determine and represents the influence of the reaction rate j in the fuel source term.
- The second term, $\epsilon_{\int \omega_j}$, is expected to depend on the reaction rate discretisation.

To confirm this, Fig. 7.25 displays the error of the reaction rate compared to refined case as a function of N_c used.

The reaction rate accuracy clearly depends on the number of points used. The least discretised equations are then not obviously the one that impacts the most the laminar flame speed. For instance, reaction $CH_3 + HCO \longleftrightarrow CH_4 + CO$ displays one of the highest error in terms of integral of reaction rate but is completely invisible in the contributions to the laminar flame speed final error. Every reaction linked to the fuel then influences the flame accuracy in the following way:

- the more a reaction takes part in the energetic balance of the fuel source term, the more this reaction influences the laminar flame speed.

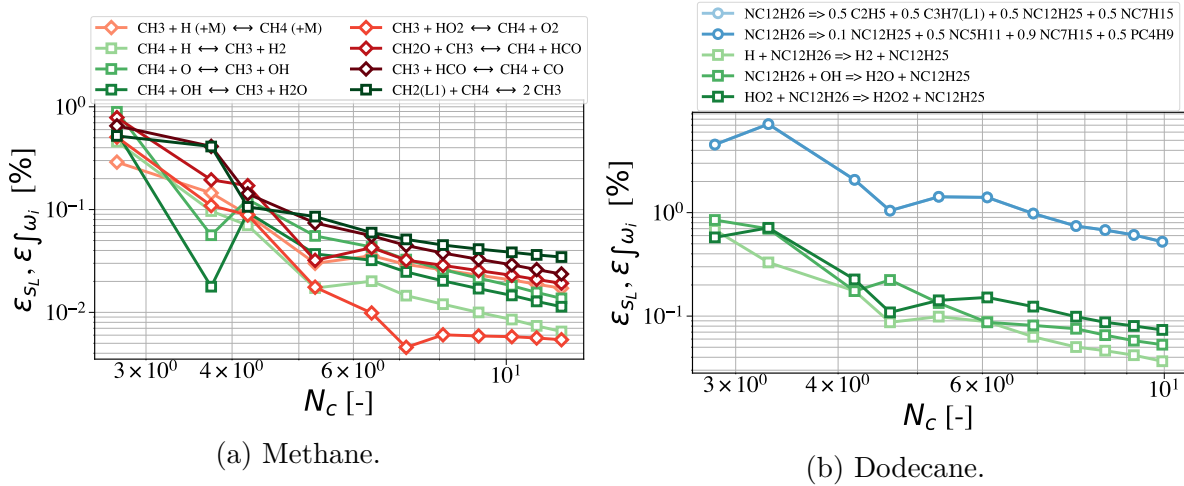


Figure 7.25: Relative error of the reaction rates ϵ_{ω_j} as a function of the number of points at $T = 400$ K, $\phi = 1.0$ and $P = 1$ bar.

- the thinner a reaction rate is and the fewer number of points it contains, the biggest error this reaction rate has and the more it influences the laminar flame speed.

A direct consequence of this result is the need for intermediate species to be present in the mechanism. Indeed, species such as OH, H or O influence the flame because of their diffusion properties.

7.3.3 Conclusion

The spatial discretisation of 1D premixed flames with ARC schemes has been investigated. First, the parametric study on the error on the laminar flame speed as a function of the number of points in the flame front shows that the temperature and the fuel composition are the parameters that require the higher number of points in the flame front. The Zeldovich statement, that 5 to 10 points in the flame front are sufficient to accurately reproduce the laminar flame speed, can be extended to ARC.

Characteristic quantity profiles demonstrate that the final state of the flame does not change much with the spatial discretisation and that the laminar flame speed is a fairly good indicator of the overall flame convergence, even though all the species could not be well-discretised. The flame is controlled by a reaction/diffusion mechanism, depending on the fuel decomposition. The reaction rate quantity was suggested as the most practical quantity to be looked at, showing that the reactions influencing the flame were either the narrowest ones or the most powerful ones.

Now that the convergence of the flame with complex kinetics is ensured temporally and spatially, the two-phase flow properties of the fuels may be analysed.

Chapter 8

Analysis of laminar spray flames

Contents

8.1	Evaporation properties of the surrogates	138
8.1.1	Two-phase flow properties	139
8.1.2	Evaporation properties	140
8.2	Multi-component spray flame structure	142
8.2.1	Setup for a 1D spray flame	142
8.2.2	Flame dynamics	144
8.2.3	Influence of the liquid phase on pollutants prediction	148
8.2.4	Conclusion	150
8.3	Spray counterflow diffusion flame	150
8.3.1	Presentation of the configuration and numerical set-up	151
8.3.2	Polydisperse spray flame	154
8.3.3	Flame structural analysis	155
8.3.4	Single droplet modelling	165
8.3.5	Conclusion	167

As stated in Chapter 5, hydrocarbon fuels are liquid when containing more than four atoms of carbon, which is the case for JETSCREEN fuels. Thus, the accurate description of the evaporation properties is needed to characterise properly the different fuels and is done in Section 8.1. As stated in Section 2.1, the interaction between the spray and the flame is important for the flame structure, even more when dealing with multi-component fuels. As a consequence, spray flame structures have to be studied. A 1D spray flame is then investigated in Section 8.2. Finally, a spray counterflow diffusion flame is introduced in Section 8.3 and analysed.

8.1 Evaporation properties of the surrogates

The droplet lifetime is monitored by its liquid properties, indicating how the droplet atomises and evaporates before being consumed by the flame. First, fuel liquid properties are compared in Section 8.1.1 for the three fuels A1, B1 and C1. Second, the multi-component evaporation model is evaluated for A1, B1 and C1 by comparison with the DLR measurements in Section 8.1.2 as well as the preferential evaporation behaviour phenomenon.

8.1.1 Two-phase flow properties

As no atomisation model is used in AVBP, only the properties concerning the vaporisation processes are compared.

First, the liquid density remains constant in AVBP because the conductivity is supposed to be infinite, which is equivalent to no diffusion inside the droplet. The density is considerably higher for C1 ($\rho_L = 882 \text{ kg/m}^3$) than for A1 ($\rho_L = 756 \text{ kg/m}^3$) and for B1 ($\rho_L = 751 \text{ kg/m}^3$). The density impacts the number of droplets generated during the atomisation process, namely C1 gives a lower droplet number than A1 and B1. Nevertheless, density is known to have a lower impact on the atomisation process than the other parameters [109].

Figure 8.1 compares the vapour pressure and the specific enthalpy of vaporisation as a function of the droplet temperature for the three fuels.

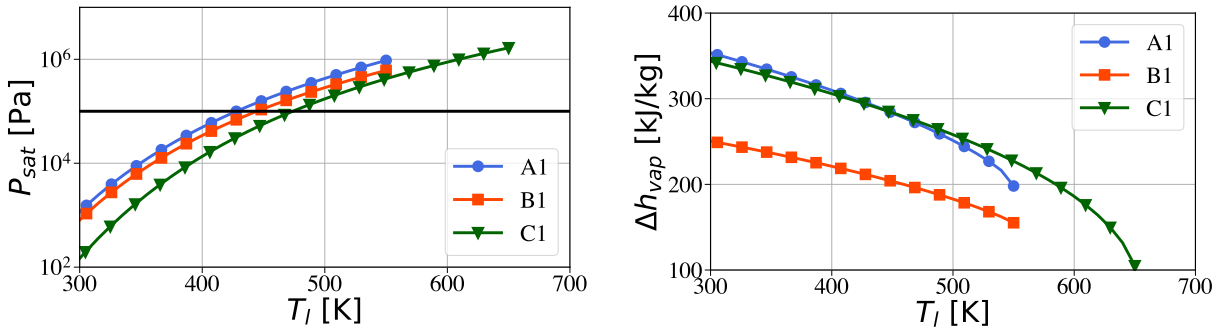


Figure 8.1: Comparison of vaporisation properties between A1, B1 and C1.

The vapour pressure $P_{sat,i}$ represents the pressure at which the species i in the droplet is supposed to be vaporised. Using Raoult's law [253], if $X_{i,liq}P_{sat,i} > X_iP$, with P the pressure around the droplet, $X_{i,liq}$ the liquid molar fraction and X_i the gaseous molar fraction then the fuel remains liquid. On the contrary, if $X_{i,liq}P_{sat,i} < X_iP$, the droplet changes of state and evaporates. For a multi-component fuel, the saturation pressure is calculated through:

$$P_{sat} = \sum_i X_{i,liq}P_{sat,i} \quad (8.1)$$

Figure 8.1 shows that the saturation pressure is higher for A1 and B1 than for C1 for a given liquid temperature. Therefore, the droplets are evaporating at a higher temperature for C1 than for B1 and A1.

The vaporisation enthalpy represents the energy needed for a fuel to switch from the liquid state to the gaseous state. Vaporisation enthalpy is considerably lower for B1 than for A1 and C1, which indicates that B1 should evaporate faster than A1 and C1, when considering only this parameter.

To conclude, after the vaporisation step, A1 and C1 are expected to produce larger droplets than B1 because the vapour pressure of the three fuels is similar, but its vaporisation enthalpy is much smaller. C1 droplets are expected to sustain longer in the flame because of the higher boiling temperature. The differences in evaporation are studied in 8.1.2.

8.1.2 Evaporation properties

The multi-component evaporation Spalding model described in Chapter 5.1.1 can be evaluated for A1, B1 and C1 by comparison with measurements conducted at DLR [297]. The aim of this paper was to compare numerical and experimental simulations of the droplet diameter evolution for some fuels. The experimental setup is shown Fig. 8.2.

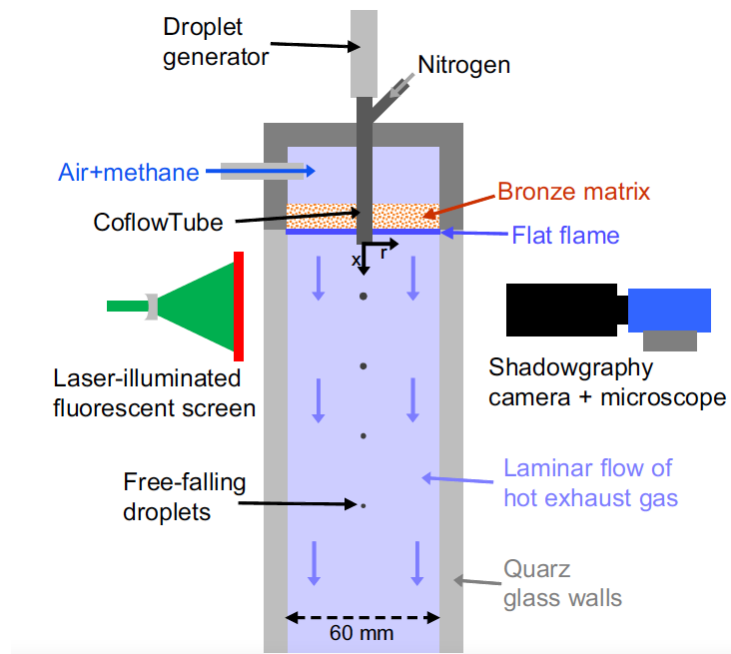


Figure 8.2: Experimental setup from DLR measuring droplet diameter temporal evolution from [297].

A methane flat flame is stabilised in the domain. A duct is then introduced in the hot gases, and the cold droplets are injected through this duct with gaseous nitrogen. The droplet diameter is followed using microscopic double-pulse shadowgraphy technique. Gas temperature profiles could not be measured, but DLR computed, with their in-house code THETA, the configuration numerically, to provide both the gaseous temperature and the gaseous mass fraction fields encountered by the droplets, see Fig. 8.3. The numerical results from DLR in terms of evaporation were in good agreement with the measurements for the 3 fuels considered in this work.

To assess the evaporation capability of AVBP for A1, B1 and C1, the DLR numerical gaseous temperature and species profiles (shown in Fig. 8.3 (left)), were used to compute the evaporation of a single droplet of diameter size $d_0 = 80 \mu\text{m}$. Note that measurements are available for A1 and B1 only. Results for C1 are added to Fig. 8.3 (right) for comparison.

Figure 8.3 represents the temporal evolution of the non-dimensional diameter squared divided by the initial diameter d_0 squared for better comparison between the fuels. The multi-component evaporation model is capable to reproduce the differences between the fuel droplet evaporation time. However, the behaviour at low gaseous temperature is not correctly reproduced for two main reasons:

- the Spalding model does not include liquid density variation inside the droplet as the droplet is considered to be in a quasi-equilibrium mode. Therefore, the droplet cannot become larger than the initial diameter, which is seen experimentally.

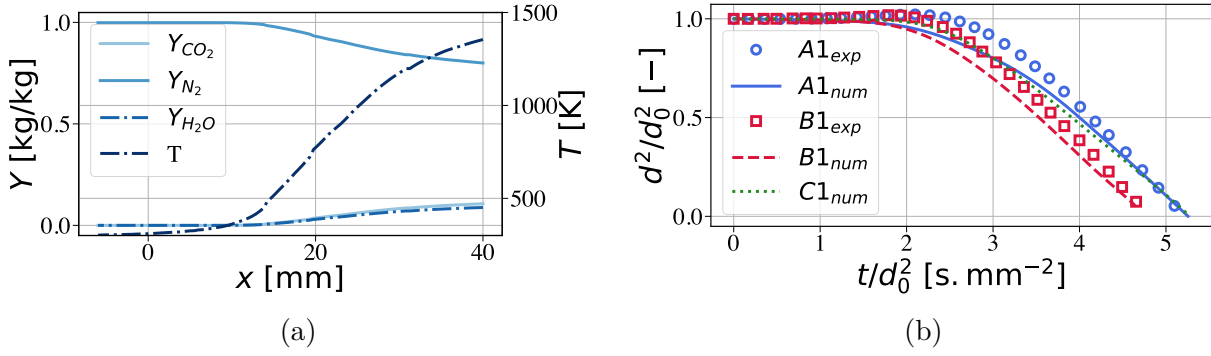


Figure 8.3: Numerical gaseous profiles from DLR for gaseous temperature and mass fractions (a) and comparison of the experimental and numerical diameter temporal evolution for A1, B1 and C1 (b).

- the temperature and species mass fraction profiles that have been taken from the DLR numerical simulation have not been compared to experimental measurements. Thus, assessing the accuracy of the droplet environment is not entirely possible.

As expected in Section 8.1.1, B1 evaporates quicker than A1 and C1. The next step is to study the impact of preferential evaporation due to the multi-component surrogates considered. Figure 8.4 shows the temporal evolution of the liquid mass fractions of the three components for A1, B1 and C1.

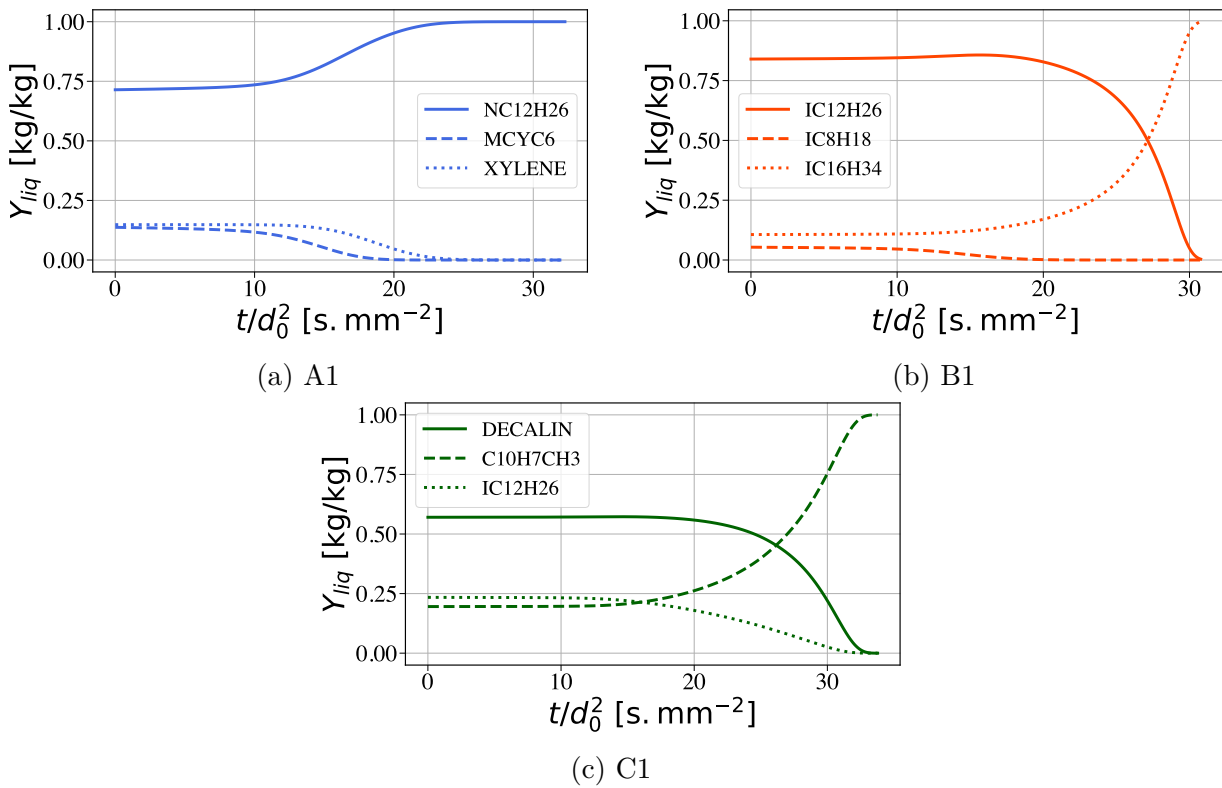


Figure 8.4: Temporal evolution of liquid mass fractions in the droplets for A1, B1 and C1.

Preferential evaporation is observed for the three fuels:

- for A1, methyl-cyclohexane is found to evaporate first, followed by xylene and n-dodecane.
- for B1, iso-octane evaporates faster than iso-dodecane and iso-cetane.
- for the high aromatic fuel C1, iso-dodecane evaporates the fastest, followed by decalin and methyl-naphthalene.

Such preferential evaporation may notably affect the 1D flame structure, as shown in Section 8.2.

8.2 Multi-component spray flame structure

Evaporation affects key quantities of the flame, such as the laminar flame speed and the final temperature, as shown in [265]. Therefore, two-phase multi-component flames need to be studied in terms of structure. This work at CERFACS started in the PhD of Cazerès [39] and Shastry [283]. Three main topics need to be pushed forward:

1. the **comparison of the 1D two-phase flame with the corresponding 1D gaseous flame** was not performed, especially in terms of effective equivalence ratio and predominant reactions.
2. when **the fuel has slightly pre-evaporated before entering the flame front**, as it is the case in the SSB configuration, the pre-evaporation should not be considered as uniform for every component., This influences the flame structure depending on which species evaporates the first.
3. the two-phase flow structure impacts **the pollutant productions**, which was not analysed in the previous works.

To investigate those complex spray flame structures, the setup of two-phase premixed flame structure is necessary, as described in Section 8.2.1. In Section 8.2.2, the spray flame dynamics are analysed. Finally, in Section 8.2.3, the influence of the liquid fuel on the pollutant production is investigated.

8.2.1 Setup for a 1D spray flame

The setup of the 1D spray flames are displayed in Fig. 8.5.

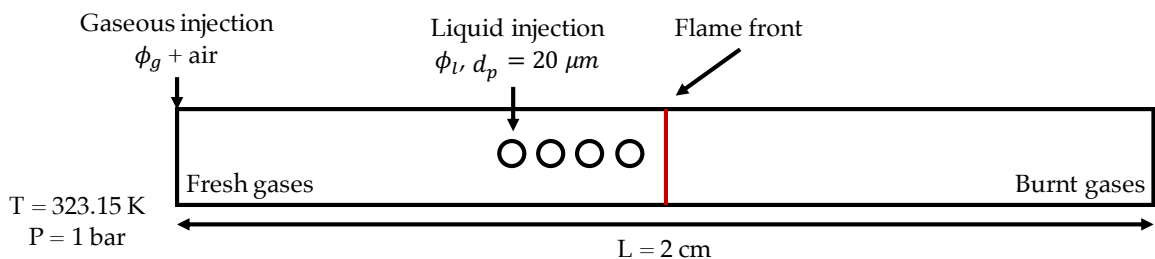


Figure 8.5: Sketch of the 1D spray flame configuration.

A gaseous premixed flame with equivalence ratio ϕ_g is first set up at atmospheric pressure and ambient temperature. Then droplets are injected just before the flame front in order to avoid any evaporation prior to the flame front and control the droplet state before evaporation and combustion. The diameter is constant ($d_p = 20 \mu\text{m}$). Three cases are compared, all shows the same total equivalence ratio $\phi_{tot} = \phi_G + \phi_L = 0.8$:

- the gaseous premixed flame ($\phi_G = 0.8, \phi_L = 0.0$).
- the semi-gaseous flame ($0 < \phi_G < 0.8, 0 < \phi_L < 0.8$).
- the fully liquid flame ($\phi_G = 0.0, \phi_L = 0.8$).

For the semi-gaseous case, preferential evaporation must be evaluated to determine the fuel gaseous and liquid compositions. As the fuel is composed of three different species, the mass fraction of one component over the total mass of interest:

$$Y_{F_k}^{eff} = \frac{m_{F_k}}{m_F} = \frac{Y_{F_k}}{Y_F} \quad (8.2)$$

with $m_{F,k}$ the mass of the component k and m_F the total liquid mass defines as

$$\begin{aligned} m_F &= \sum_{F_i} m_{F_i} \\ Y_F &= \sum_{F_i} Y_{F_i} \end{aligned} \quad (8.3)$$

To evaluate the pre-evaporated fuel quantities, the setup of the single droplet evaporation case in Section 8.1.2 is used. Figure 8.6 displays the gaseous and liquid equivalence ratios (left) and the given composition of the single components (right) as a function of the time divided by the squared diameter for the three fuels A1, B1 and C1.

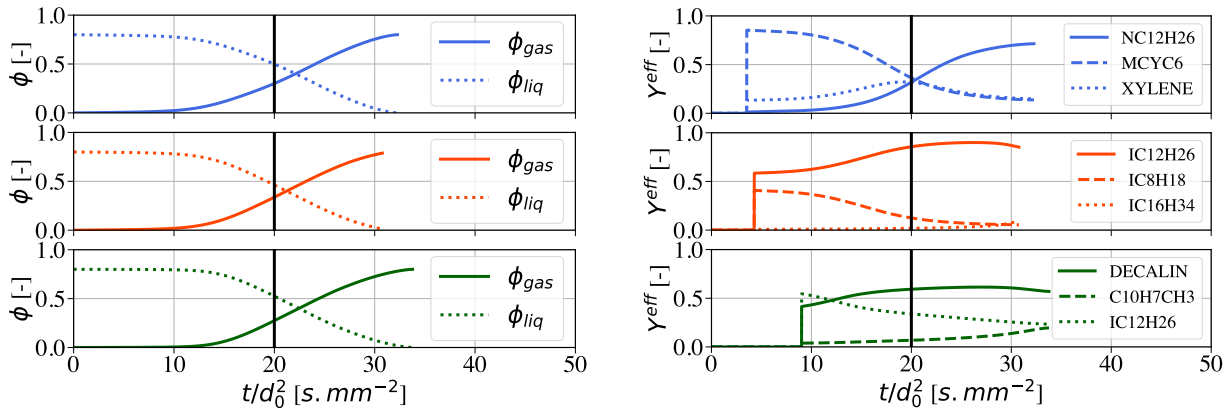


Figure 8.6: Equivalence ratios (left) and fuel gaseous mass fractions (right) as a function of the time divided by the initial diameter squared for A1 (top), B1 (middle) and C1 (bottom).

As expected, the gaseous equivalence ratio is increasing and the liquid one decreasing through time. For the species mass fractions, the gaseous mass fractions at the end of the computation are the same as the initial liquid ones, since the whole liquid fuel was turned into vapour. However, before totally pre-evaporating, they face preferential evaporation which will affect the flame structure. Values corresponding to the vertical line at $t/d_0 =$

Fuel		Liquid phase	Gaseous phase	Reference value
A1	ϕ	$\phi_L = 0.3$	$\phi_G = 0.5$	$\phi_G = 0.8$
	$Y_{NC_{12}H_{26}}^{eff}$ [%]	95.23	31.9	71.4
	$Y_{MCYC_6}^{eff}$ [%]	0.13	36.3	13.75
	Y_{XYLENE}^{eff} [%]	4.64	31.8	14.85
B1	ϕ	$\phi_L = 0.34$	$\phi_G = 0.46$	
	$Y_{IC_8H_{18}}^{eff}$ [%]	0.16	12.5	5.5
	$Y_{IC_{12}H_{26}}^{eff}$ [%]	82.81	85.6	84
	$Y_{IC_{16}H_{34}}^{eff}$ [%]	17.03	1.9	10.5
C1	ϕ	$\phi_L = 0.275$	$\phi_G = 0.525$	
	$Y_{DECALIN}^{eff}$ [%]	55.86	59.3	57
	$Y_{IC_{12}H_{26}}^{eff}$ [%]	17.94	33.9	19.5
	$Y_{C_{10}H_7CH_3}^{eff}$ [%]	26.2	6.8	23.5

Table 8.1: Mass composition of the three components for the semi-gaseous and the reference cases for A1, B1 and C1.

20 s.mm⁻¹ are summarised in Table 8.1 for the liquid and gaseous equivalence ratios, as well as for the mass fractions in the different phases. The reference value of the fuel compositions in the pure gaseous case are also given.

Two differences of this setup with the experimental work can be highlighted:

- the experiment was realised with $d_p = 80 \mu\text{m}$ and the 1D flame is simulated with $d_p = 20 \mu\text{m}$.
- the resulted simulation was made up with temperature and species profiles that are not the same as the ones in the 1D premixed flame.

Preferential evaporation does not depend on the initial diameter because of the infinite diffusion of the fuels inside the droplet.

However, preferential evaporation depends on the gaseous temperature, since the estimated molar fraction at the droplet interface $X_{i,\zeta}$ depends on the saturation pressure, which is dependent on the temperature. When the droplet temperature is reaching its maximum temperature, the saturation pressure ratio is fixed and therefore the preferential evaporation does not depend on the temperature anymore.

Finally, these values have been set as inputs of the gaseous and liquid inlets of the spray flames. The speed at the inlet of the domain is set to the gaseous flame speed and is evaluated afterwards through the species source term for post-processing. The multi-component model presented in Section 5.1.1.2 is used.

8.2.2 Flame dynamics

To compare the fuel consumption structure with the 1D gaseous flame, the total effective equivalence ratio presented in Section 7.2.2 of the different species for the three fuels is represented in Fig. 8.7.

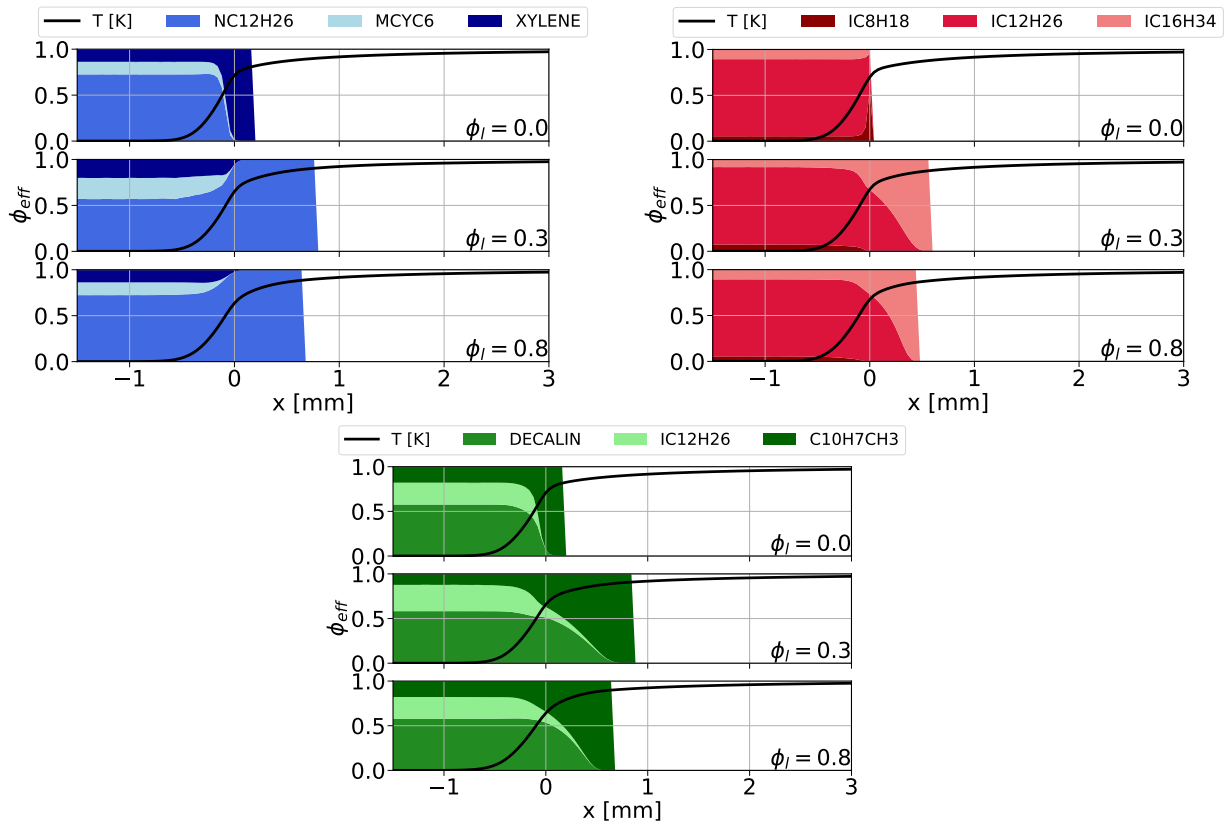


Figure 8.7: Effective equivalence ratio of the gaseous, semi-gaseous and liquid cases for A1, B1 and C1.

The conclusions are very different for the three fuels:

- for A1, the effective equivalence ratio shows that the reacting species order is very different for a 1D flame and a 1D two-phase flame. Indeed, for the gaseous flame, NC12H26 is the first species to react, followed by MCYC6 and XYLENE. In the two other cases, NC12H26 is the last species remaining in the medium because it is the last species to evaporate. Furthermore, the relative importance of the different species is slightly different for the semi-gaseous and liquid case. Indeed, methylcyclohexane in A1 and xylene in C1 seem to be present in higher proportion than in the initial blend for the semi-gaseous case.
- for B1, the order of the species is also very different. In the pure gaseous case, IC16H34 is the first to react, followed by IC12H26 and IC8H18, the last species remaining in the domain. For the other cases, this order is inverted because IC8H18 is the first to evaporate, followed by IC12H26 and IC16H34. No difference is clearly visible between the three cases.
- for C1, the order remains the same between the pure gaseous flame and the liquid flames. Indeed, the chemical reactivity goes along the evaporation characteristic timescale for this fuel. For the semi-gaseous case, IC12H26 seems to have a higher effective equivalence ratio and C10H7CH3 a lower one in comparison to the full liquid case.

Of course, preferential evaporation (and thus reactivity) influences the flame structure. In order to analyse the impact of the pre-evaporation, Fig. 8.8 represents the heat release rate and the species source terms for the three fuels A1, B1 and C1 and each case: gaseous, semi-gaseous and liquid.

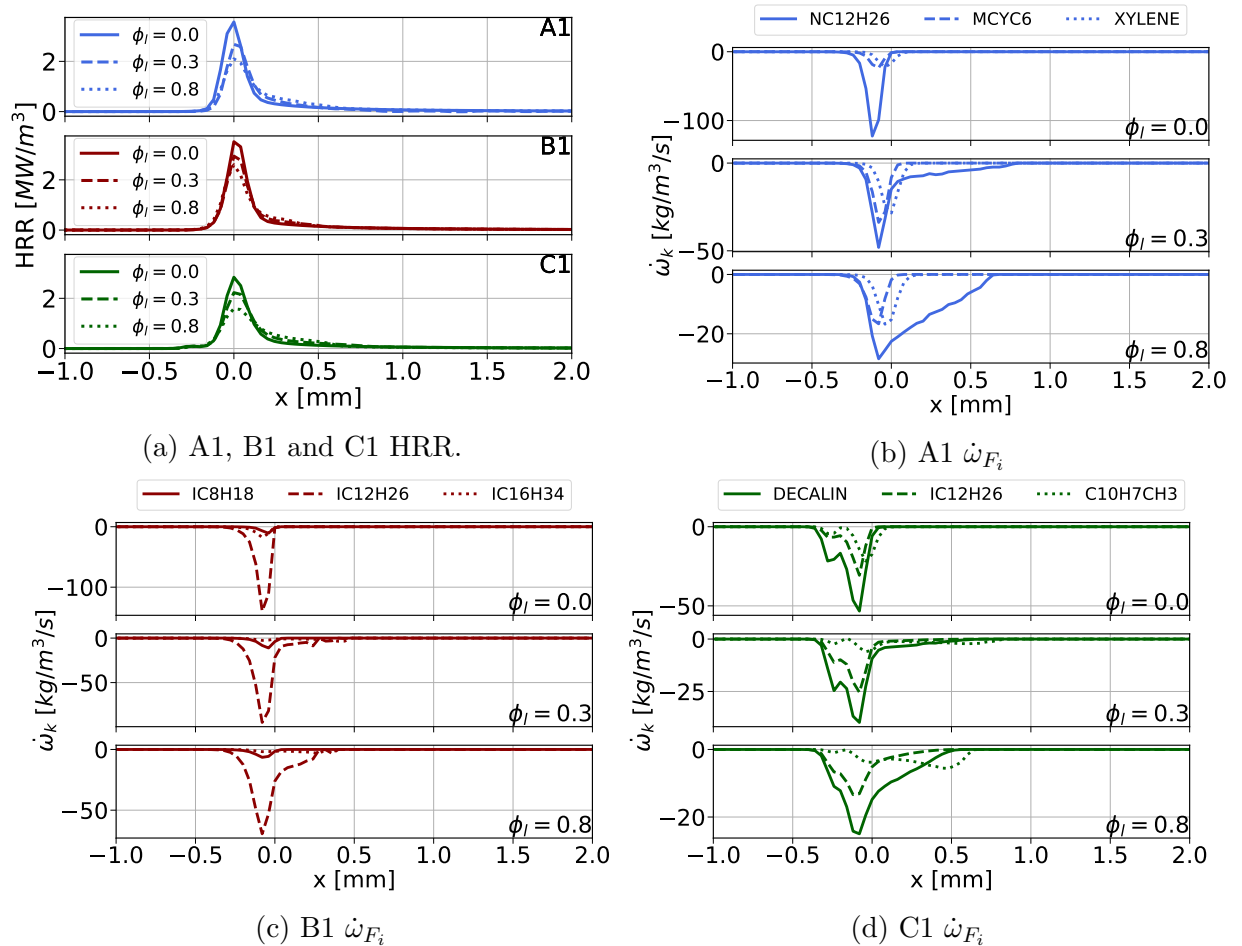


Figure 8.8: Heat release rate and species source terms for the three fuels and each liquid equivalence ratio.

As depicted in [39], increasing the liquid equivalence ratio is tantamount to a lower maximum heat release rate (or species source term) and an increase of its spread in the burned gases area.

- in the A1 case, the proportion of fuel reacting as pre-evaporation and the one reacting in the burnt gases is very different depending on the three cases. For the pure gaseous case, NC12H26 source term is 10 orders of magnitude above the two other species source term whereas for the two-other cases, it exhibits roughly the same order of magnitude. The only fuel that seems to contribute to the heat release rate for the semi-gaseous and fully liquid cases in the burnt gases area is n-dodecane.
- in the B1 case, as IC12H26 is the greatest in proportion, this fuels species is dominant in the three simulations compared to the two others. All the fuels do not enter deeply in the burnt gases area.

- in the C1 case, DECALIN shows the greatest peak in front of IC12H26 and C10H7CH3. In the semi-gaseous case, DECALIN becomes low compared to IC12H26. C10H7CH3 for the same case is very reduced and burns mostly in the burnt gases area.

This reveals that every fuel is not giving the same contribution to the total species source term, which could influence how the laminar flame speed is actually evolving with the liquid equivalence ratio. For that reason, Fig. 8.9 presents the evolution of the laminar flame speed. As well, the effective source term integral for the three fuels is shown and each case as a function of the liquid equivalence ratio, defined as:

$$\left(\int \dot{\omega}_{F_k} dx\right)^{eff} = \frac{\int \dot{\omega}_{F_k} dx}{\int \dot{\omega}_F dx} \quad (8.4)$$

with $\dot{\omega}_{F_k}$ the source term of species F_k and $\dot{\omega}_F$ the total fuel source term.

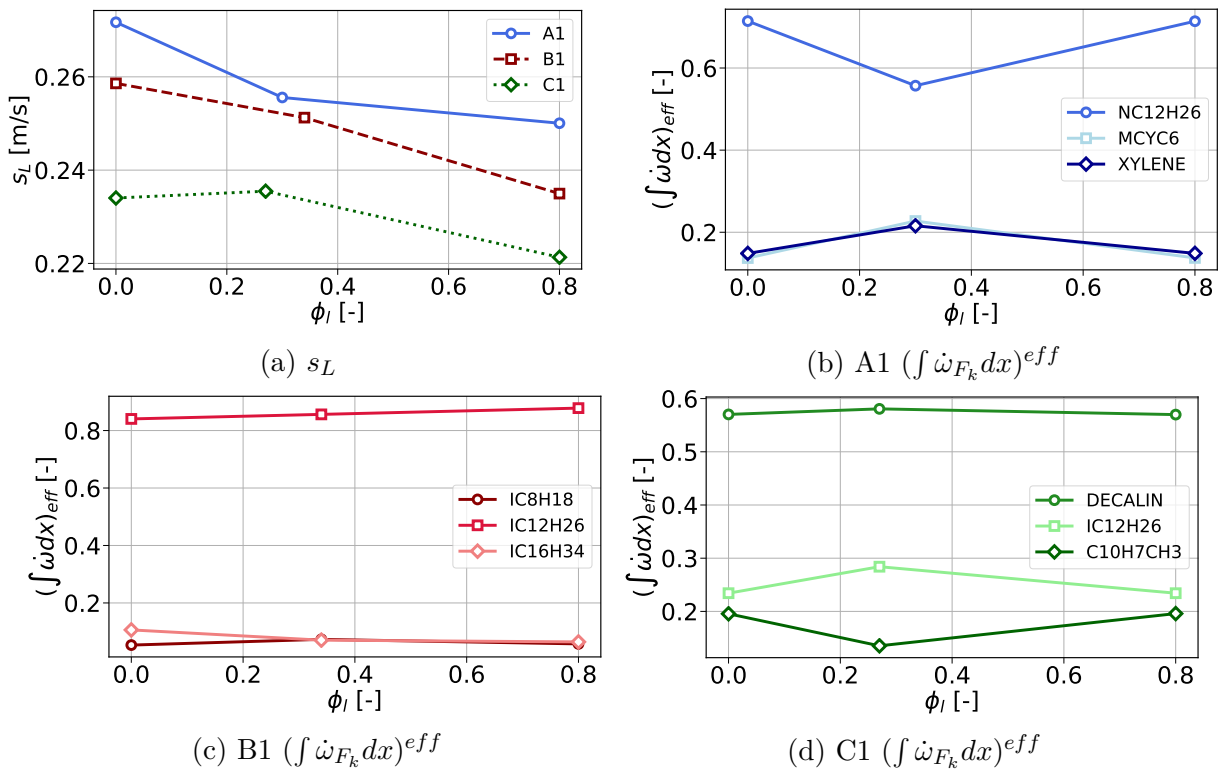


Figure 8.9: Laminar flame speed and effective source term integral for A1, B1 and C1 versus the liquid equivalence ratio.

For every case, the contribution of the species source terms is the same for the edges, namely a totally gaseous flame and a totally liquid flame, except for B1 flame. In-between however, the preferential evaporation has an impact on the value of the laminar flame speed:

- for A1, as shown on the species source term graph, the contribution of n-dodecane is lowered for the pre-evaporation part of the species source term, leading to a strong decrease of the laminar flame speed.
- for B1, the quantities are not evolving much and the contribution of the species is nearly the same, therefore the laminar flame speed decreases normally.

- for C1, the laminar flame speed is going up for the semi-gaseous case. Indeed, as IC12H26 source term increasing and as it has a better efficiency than methyl-naphthalene, the laminar flame speed is rising.

Concerning the laminar flame speed evolution, as explained in [283] and in [39], the curves are decreasing because the two-phase flow is reducing the flame dynamic properties. Moreover, the global equivalence ratio is lean and can not go through a stoichiometric reaction near the flame front, the only case where the laminar flame speed can increase with a higher liquid loading [283]. The order between the three curves is not changed with increasing the liquid equivalence ratio. The three curves are decreasing very differently and this can be correlated with the amount of fuel component burning through the formula:

$$s_L = -\frac{1}{\rho_1 Y_{tot,1}} \sum_{k=1}^{N_{fuel}} \int_{x=0}^L \dot{\omega}_k dx \quad (8.5)$$

with ρ_1 the cold flow density, $Y_{tot,1}$ the total fuel mass fraction and $\int_{x=0}^L \dot{\omega}_k dx$ the fuel source term of the species k. Indeed, the laminar flame speed is evolving with the fuel source term. When dealing with multi-component, there is then a competition between the different fuels and their contribution to the laminar flame speed, and the semi-gaseous case is interesting to highlight the differences between the blends:

- A1 fuel laminar flame speed is decreasing very sharply, i.e. more than if the decrease was linear between $\phi_g = 0.0$ and $\phi_l = 0.8$. As xylene and methyl-cyclohexane are contributing more to the overall source term than the extreme cases, the laminar flame speed is then decreased.
- B1 fuel shows a slightly higher laminar flame speed than the linear curve, due to the increase of iso-octane compared to iso-cetane.
- C1 fuel is the most interesting case, as the laminar flame speed is increasing for the semi-gaseous case and then decreases towards the fully liquid fuel. The strong increase of iso-dodecane combustion in the effective fuel source term is the answer. Indeed, as methyl-naphthalene is very poorly reactive, the strong reactivity of iso-dodecane enhances the flame dynamics.

To sum-up, the two-phase flame structure is influencing the combustion in two ways:

- generally, the more liquid the flame is, the lowest the flame burning properties are, since the flame is lean.
- if a species is likely to be more present in terms of proportion because of the preferential evaporation, conclusions stated in the previous point may change.

Next section underlines the impact of the flame structure on pollutants' production.

8.2.3 Influence of the liquid phase on pollutants prediction

The flame structure can explain how quantities of interest evolve with preferential evaporation. One can also wonder how the pollutants concentration rises for the fuels and if their release is drastically different or not for two-phase flow flames. The mechanism that was developed for this study does not contain any NO_x and soot pathways in it. However, several variables might be evaluated:

- CO and CO_2 concentrations are directly accessible from the species in the mechanism.
- for NO_x , as the fuel burning is a heavy hydrocarbon in lean conditions, the pathway is mostly the thermal one. Therefore, the final temperature of the flame should be an indicator of the NO_x production.

Figure 8.10 represent those different quantities. As well, the maximum equivalence ratio in the flame was plotted for the three fuels.

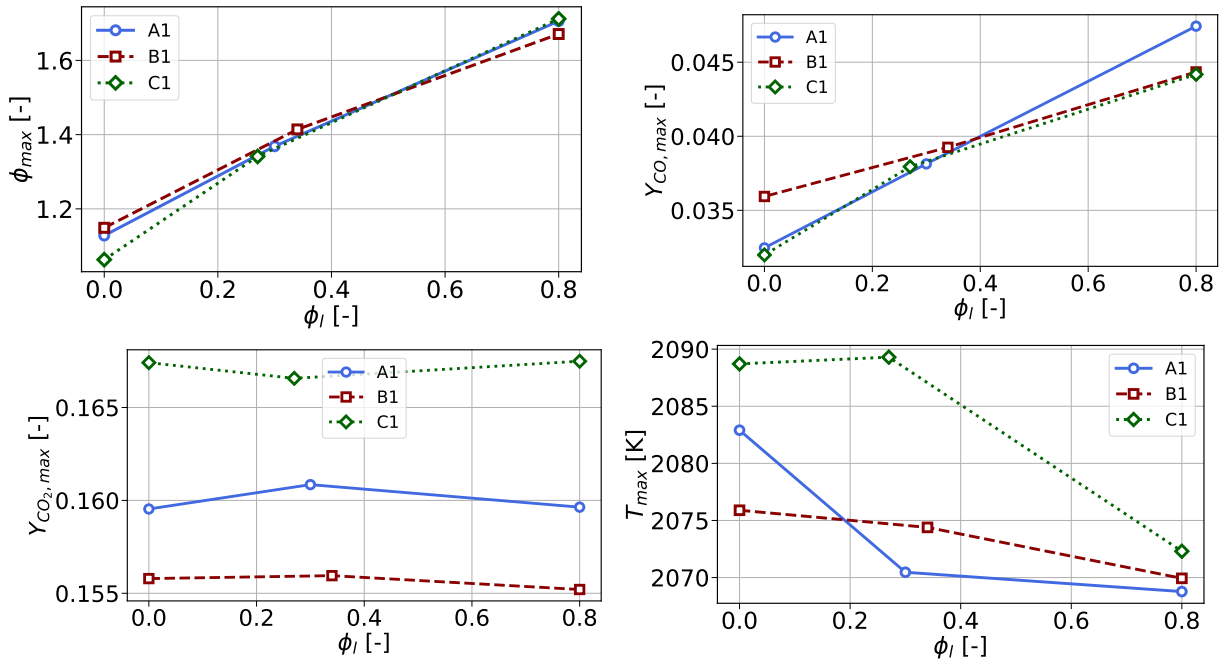


Figure 8.10: Maximum of equivalence ratio, temperature, CO and CO_2 mass fractions for the A1, B1 and C1 fuels and varying the liquid equivalence ratio.

The evolution of the different pollutant species for the three fuels may be analysed:

- first, CO_2 mass fraction maximum remains the same when considering the fully gaseous and the fully liquid cases. However, when looking at the intermediate case, small differences appear. C1 has a slightly lower CO_2 emissions because of iso-dodecane is more consumed in the premixed mode than the initial composition. For A1, however, the opposite is happening because xylene is more present in the gaseous consumption, creating more carbon dioxide. B1 does not show great disparities compared to the initial case.
- CO mass fraction maximum increases when going towards full liquid fuel for every fuel. A1 and C1 CO levels seem to be lower at full gaseous fuel, but a shift is occurring and A1 is higher at full liquid fuel than B1 and C1. Overall, the differences between the three fuels are very small and optimisation of the system would better performed by working on the evaporation, the atomisation and on the operating point than on the fuel itself for CO emissions.
- the maximum temperature graph testifies that the final temperature of C1 remains a lot higher than the two other temperatures. C1 would then be more prone to

NO_x creation than A1 and B1. However, the maximum temperature is a too simple criterion to compare the three fuels, as the temperature differences between the three fuels does not reflect at all the strong difference in terms of NO_x production.

Overall, the graph displaying the maximum of equivalence ratio displays the same trend for the three fuels: if the fuel is less pre-evaporated when reaching the flame front, the local equivalence ratio tends to be higher and the emissions are rising.

8.2.4 Conclusion

The aim of this section was to list the fuel dependencies on the two-phase flow properties, to have an idea on the 3D calculation output as well as to give the tools to analyse it.

Evaporation was well-discretised between the fuels due to the two-phase flow properties that occur during the atomisation and the vaporisation processes. This last process is influencing the diameter reduction the most as B1 was found to have a lower reactivity than A1 and C1. Preferential evaporation could be well retrieved, influencing the location of the fuel combustion, as shown in the last section.

Indeed, the two-phase flow 1D premixed flame setup has shown that flame structure is completely reshaped when the evaporation is taken into account, especially when the fuel evaporation is contradictory with the combustion behaviour. Main reacting properties are found to be decreased when increasing the liquid phase proportion at injection, except when fuel proportion is changed, leading to enhanced combustion properties (C1 case for instance). Increasing the liquid loading slightly changed the CO_2 mass fraction, but levels remain slightly the same. CO mass fraction however increased with higher liquid loading. As the maximal temperature is reduced when burning more liquid fuel, the NO_x levels are expected to decrease along with ϕ_l .

When the fuel is injected as a two-phase flow in 3D real burner, the flame structure is very important to detect how the fuel is consumed by the flame. Configurations with premixed, diffusion, two-phase premixed and two-phase diffusion modes may be found as well as more stratified fields. Two-phase diffusion flames, especially with polydisperse fields, exhibit a very complex flame structure and the next chapter analyses it in comparison with experimental visualisations. This also introduces more complex evaporation analysis and modelling, used in the 3D configuration Chapter 9.

8.3 Spray counterflow diffusion flame

The Counterflow Diffusion Flame (CDF) is a canonical case for non-premixed combustion and is the subject of many studies. When fuel is injected in an atomised liquid state in the counterflow, the resulting spray flame structure is not known a priori. Studies on counterflows comprising an inert gas and droplets of fuel on one side and an oxidiser on the other side are flourishing [43], [245]. Objectives are to characterise the response [174] of the flame to the droplet characteristics, to a perturbation [95] or near extinction [71]. Counterflow spray flames are also useful for flamelet models, which assume a priori a flame regime and structure [216].

Flames featuring several reaction zones have already been observed in partially premixed cases [105]. For pure counterflow flames, the structure depends on whether the droplets pre-evaporate or interact directly with the flame. In the latter case, various combustion regimes may occur, from a single droplet combustion to an external sheath group

combustion [256]. Spray counterflow flames are therefore very sensitive to the droplet diameter, the global equivalence ratio and the strain rate. Such flames have largely been characterised in the literature, using monodisperse and bidisperse size-distributions of the spray [112], stating that the flame temperature increases with the droplet diameter due to the longer residence time in the flame [72]. The next question is therefore to know how polydispersion size impacts the flame structure. This is the objective of the present chapter.

To do so, the experimental configuration of Mikami [201], a polydisperse heptane-oxygen spray flame, is chosen. The chemistry is modelled with an Analytically Reduced Chemistry (ARC) for a better cost/accuracy trade-off. The chapter is organised as follows. In Section 8.3.1, the experimental case, mesh and main parameters of the numerical set-up are described. Results are presented in Section 8.3.2 for the polydisperse case and analysed with the help of monodisperse case in Section 8.3.3. Finally, the single droplet modelling is tackled in Section 8.3.4. Most of the results presented here have been presented at the 38th combustion symposium [319].

8.3.1 Presentation of the configuration and numerical set-up

The aim of this section is to show how the experimental work of Mikami was converted to a numerical simulation in order to analyse the flame structure. Section 8.3.1.1 sums up the experimental case and main findings of Mikami. Based on this configuration, Section 8.3.1.2 details the numerical setup built to simulate the counterflow flame. Finally, the chemical scheme development is explained in Section 8.3.1.3.

8.3.1.1 Experimental case

The configuration is the same as Mikami's et al. [201], where a complex flame resulting from the direct interaction of droplets with the flame was observed. A sketch of this configuration is presented in Fig. 8.11. Two opposed streams, pure oxygen on one side and fuel droplets with nitrogen on the other side, lead to a counterflow flame. The inner ducts (diameter $d_{in} = 23$ mm and length 700 mm) containing the oxidiser and fuel streams are placed inside outer ducts (diameter $d_{out} = 40$ cm and length 300 mm) containing nitrogen flow to avoid the shearing of the reactant stream flows by the ambient air. N-heptane is used as liquid fuel. Both inner gaseous streams are set to $q_{N_2} = q_{O_2} = 20$ L/min, while the fuel stream is set to $q_F = 6$ mL/min, leading to a lean configuration of global equivalence ratio:

$$\phi_g = s \frac{\rho_F q_F \dot{m}_2}{\rho_{O_2} q_{O_2} \dot{m}_1} = 0.55 \quad (8.6)$$

with s being the stoichiometric ratio, ρ the density and m_1 (respectively m_2) the mass flow rate of the upper (respectively lower) stream. The distance between the two injectors is $h = 10$ mm. The global strain rate was maintained at $a_{exp} = 320$ s⁻¹, defined by the following formula:

$$a_{exp} = \frac{2}{h} \left(v_1 + v_2 \sqrt{\frac{\rho_1}{\rho_2}} \right) = 320 \text{ s}^{-1} \quad (8.7)$$

with v_1 (respectively v_2) the velocity magnitude and ρ_1 (respectively ρ_2) the gas density of the upper (respectively lower) stream. This strain-rate, called the oxidiser side theoretical strain rate, corresponds to the theoretical gradient of the stagnation point of the plug flow

[214], i.e. neglecting the viscosity. As many theoretical analyses are given with the strain rate defined in Chapter 3, the equivalent strain rate used numerically is the following:

$$a_{num} = \frac{|v_1| + |v_2|}{h} = 160 \text{ s}^{-1} \quad (8.8)$$

As the densities of both incoming fields look similar, the only difference between the two values is a factor 2 that comes from the derivation of the formula.

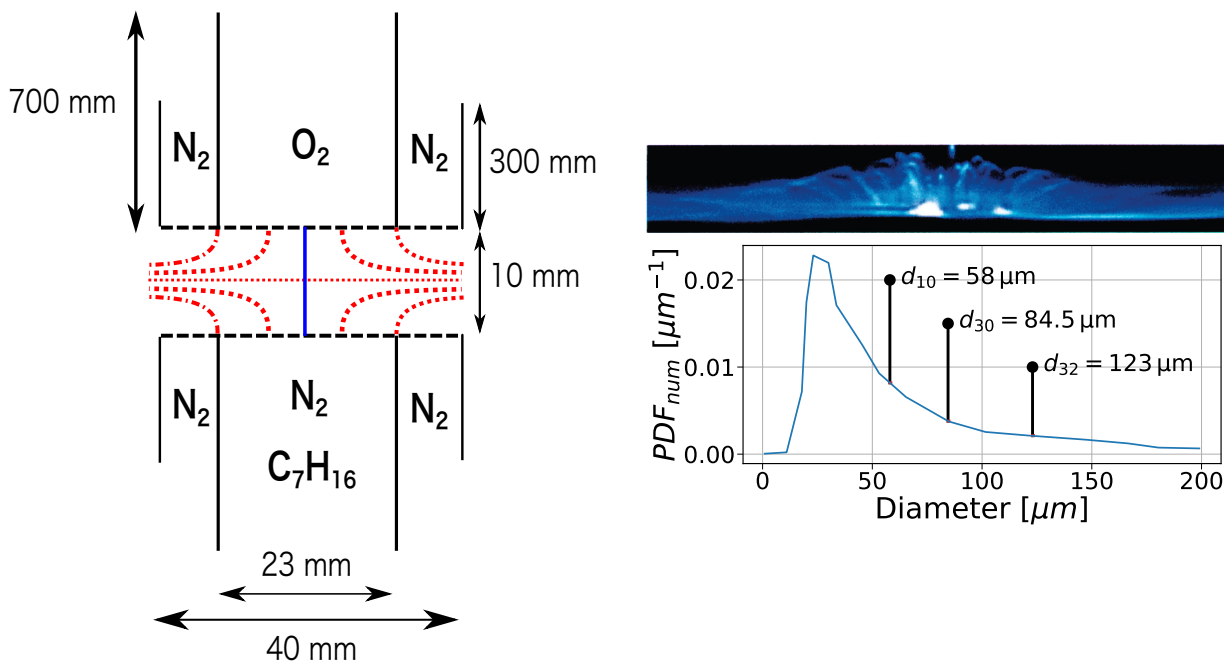


Figure 8.11: Experimental setup (left), flame visualisation (upper right) and numerical PDF (lower right) from [201] of the studied spray counterflow diffusion flame.

The size distribution of the droplets is shown in Fig. 8.11 and was taken from Mikami et al.. Mikami presented several cases, among which one was illustrated with a direct visualisation of the reactive area, showing a large reaction zone with burning droplets passing through. This case was then chosen for the present study.

8.3.1.2 Numerical setup

The axisymmetric configuration was transformed into an equivalent planar two-dimensional geometry shown Fig. 8.12. The surrounding nitrogen side flows have been included. The mesh contains around 500 000 triangles and is refined at the centre of the domain to reach a cell size of 20 μm, while it is 100 μm at injection. With injection velocities of $v_1 = v_2 = 0.8 \text{ m/s}$, the Reynolds number is approximately 2.10^3 , which means a fully laminar flow.

Simulations were performed with the in-house code AVBP¹. Convection is computed with the Lax-Wendroff [163] scheme of order 2 and a finite element of order 2 is used for diffusion. Droplets are tracked with a Lagrangian methodology and are considered as source points that interact with the gaseous field via source terms for mass, momentum and energy transfer. The drag model is Schiller and Naumann's [279] and the evaporation model

¹<https://www.cerfacs.fr/avbp7x/>

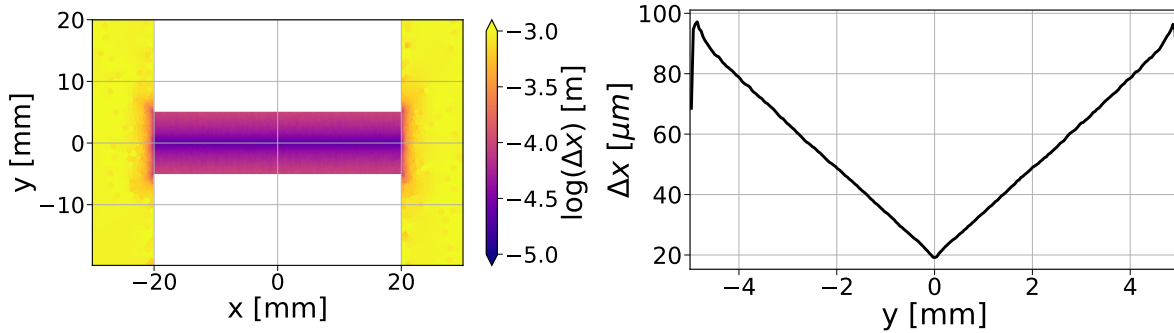


Figure 8.12: Characteristic cell length field (left) and plot (right) at the central axis.

Numerical models	
Convective scheme	Lax-Wendroff [163] of order 2
Diffusive scheme	Finite element of order 2
Artificial viscosity model	Colin based on ρu and ρY
Liquid properties	
Modelling	Lagrangian
Evaporation model	Abramzon & Sirignano [1]
Drag model	Schiller & Naumann [279]
Injection type	Line
Distribution type	User-defined
Walls	
Gaseous	Adiabatic.
Liquid	Elastic rebound.

Table 8.2: Numerical setup of the spray counterflow diffusion flame.

from Abramzon and Sirignano (AS) [1]. The distribution is taken from the experimental work and injection on a line on the patch representing the nitrogen flow. Walls that are not inlet or outlet are all adiabatic for the gas and have no influence on the counterflow diffusion flame structure. Droplets are supposed to elastically rebound on the walls.

For an accurate description of the combustion chemistry, the Analytically Reduced Chemistry (ARC) methodology was used to develop a reduced mechanism for heptane oxy-combustion. Such reduced schemes have already shown good results [87], [134] while being still computationally affordable. Reduction parameters and results are presented in the next section.

8.3.1.3 Chemical scheme

The reduction code ARCANE [40], based on the methodology of [225] for chemistry reduction and jointly developed at CERFACS and Cornell University, has been used to reduce the detailed mechanism of Jerzembeck [135]. Fuel, CO , CO_2 and the heat release have been set as targets for a maximum error below 7% for the heat release rate and 1% for the maxima of the species mass fractions and temperature. The ARC scheme finally comprises 29 transported species, 90 reactions and 7 QSS species.

Results are provided in Fig. 8.13. As the auto-ignition time was not a major issue in this work and was found to be a limit in terms of reduction, its error was set high, which lead to

Case type	a [s^{-1}]	T [K]	P [Pa]	ϕ [-]	Error [%]
0D isochoric reactor		1000	1e5	1.0	tig: 30
1D diffusion flame	160	400	1e5	0.6 - 1.0 - 1.4	$\int HRR$: 7 T: 1

Table 8.3: Reduction cases for C_7H_{16}/O_2 .

an ARC mechanism that reacts faster than the corresponding detailed mechanism. Indeed, as combustion of the droplet is occurring mainly because of the temperature diffusion, the ignition of the mixture is not an issue to start combustion.

Second, the premixed laminar flame speed was plotted as a function of the equivalence ratio. As only diffusive cases were targeted for the reduction, paths can be missing and lead to a high error around $\phi = 1$ (approximately 20%). No premixed cases were targeted for being able to reach an acceptable number of species for the reduction. For very lean and rich equivalence ratios, the reduction is performing well, even for cases that were not targeted.

Finally, for diffusion flames, the quantity of interest is the integral of the heat release rate [284]. This quantity is performing well on the whole domain and is very close to the detailed mechanism behaviour. Profiles at $\phi_g = 0.55$ are presented on the right of Fig. 8.13 and also show a good agreement between the obtained ARC mechanism and the detailed mechanism for a laminar diffusion flame at $\phi_g = 0.55$. The endothermic peak of the heat release rate is slightly underpredicted, but the flame structure is captured, even for intermediate species. The final state as well as the intermediate species profiles are very well captured.

Chemical timescales of the transported species are shown in Fig. 8.14. The shortest timescale of approximately $2 \cdot 10^{-8}$ s, which is above the convective time-step, ensuring the proper integration of the chemistry in the numerical work.

8.3.2 Polydisperse spray flame

Figure 8.15 shows the computed heat release rate field for the polydisperse case along with examples of computed particle trajectories.

The flame shows two continuous reaction zones, separated by a zone of discrete particle burning, as observed in the experiment. As expected, the droplet trajectories are much correlated to their diameter. Small particles evaporate quickly and follow the gas flow, whereas larger particles persist longer along more straight lines, even crossing the entire flame front for the largest ones.

Thermal and velocity profiles are shown in Fig. 8.16. The temperature profile is very wide and encapsulates the heat release rate profile, exhibiting two distinct peaks with a highly fluctuating area in-between. The velocity profile is very strong in the oxidiser region.

Mass fraction profiles obtained for the reactants (C_7H_{16} and O_2), the major products (CO , CO_2 and H_2O) and N_2 in the centre line of the configuration are given as well Fig. 8.16. The two reaction zones of Fig. 8.15 are linked to the two fuel peaks seen in Fig. 8.16. The main flame front stabilises on the fuel side, as dictated by the lean global equivalence ratio of the configuration. Note that oxygen and heptane do not react directly with each other but first decline in other species which then enter the oxidation process, as described in the ARC scheme.

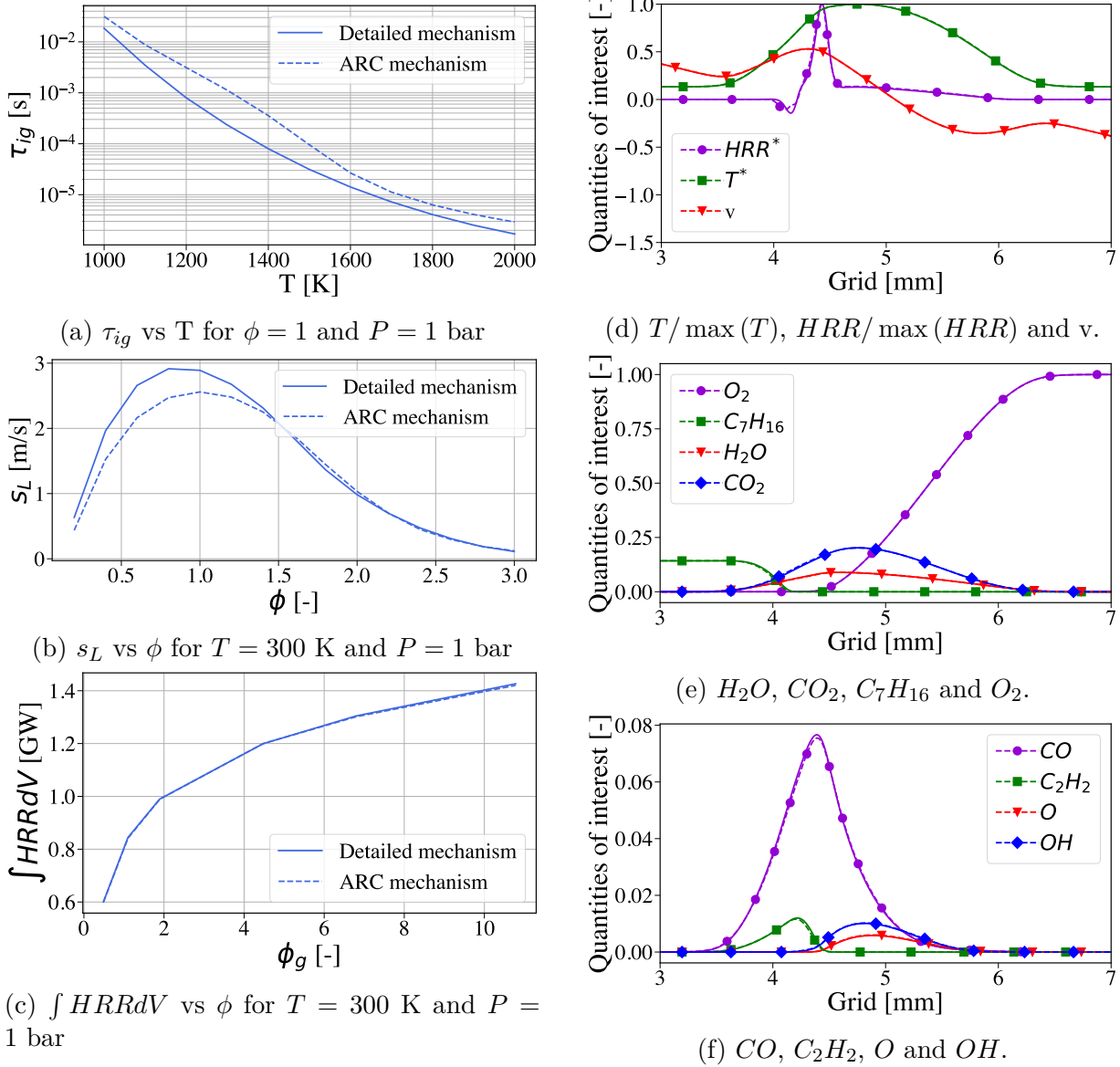


Figure 8.13: Scheme validation (left) on 0D isochoric reactors (top), 1D premixed flames (middle) and 1D counterflow diffusion flames (bottom) and gaseous diffusion flame structure accuracy (right) between detailed mechanism (full lines) and ARC mechanism (dashed lines) for $T = 300$ K and $P = 1$ bar.

A secondary flame appears on the oxidiser side, where a second heptane peak is formed. This results from large droplets which are able to cross the double flame front and still evaporate in the oxidiser stream. The fuel vapour then mixes with the oxygen, sustaining a lean secondary premixed flame.

This flame structure is unusual and is being analysed in Section 8.3.3.

8.3.3 Flame structural analysis

To better illustrate the effect of polydispersity on the flame structure, several monodisperse cases have also been computed, namely with droplet diameters of $5 \mu m$, $25 \mu m$, $75 \mu m$, $175 \mu m$ and $123 \mu m$. This latter corresponds to the SMD of the distribution.

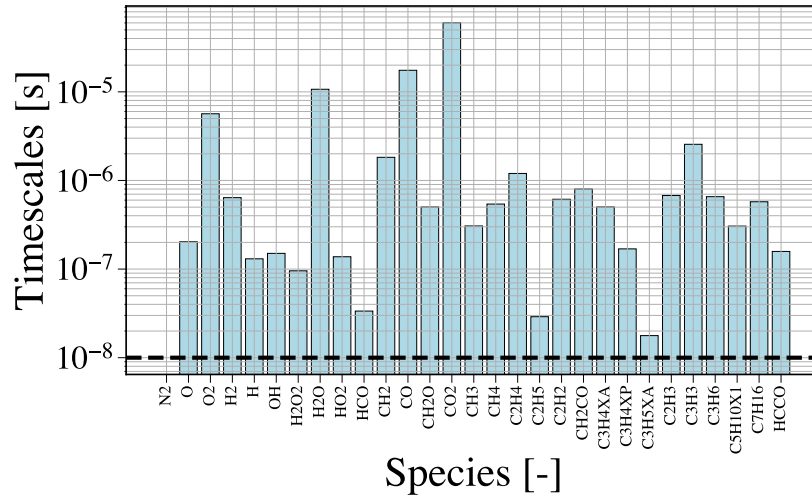


Figure 8.14: Chemical timescales of the reactive species from the ARC mechanism.

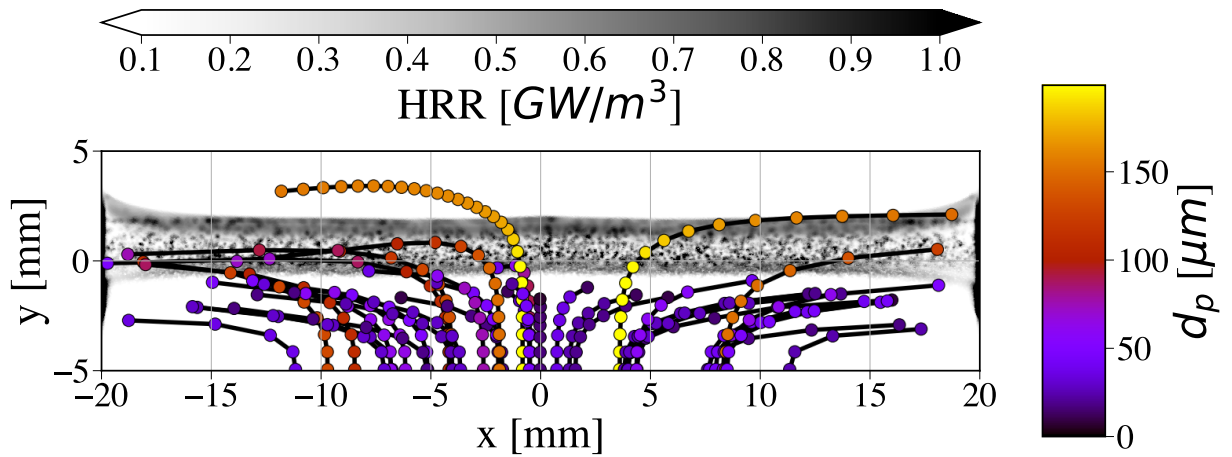


Figure 8.15: Heat release rate field for the polydisperse computation, along with computed droplets trajectories coloured by their diameters.

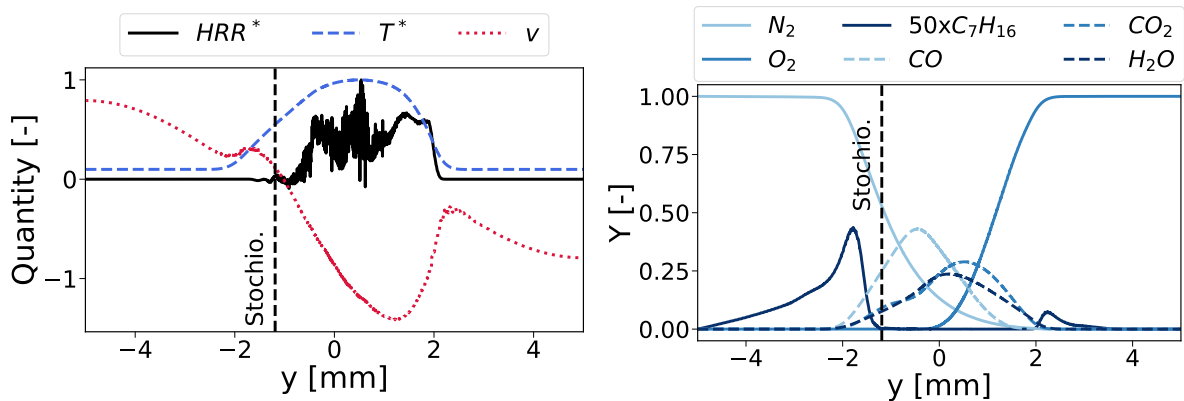


Figure 8.16: Main quantities (left) and species mass fractions (right) on the axial line for the polydisperse case.

These different diameter values correspond to cases where pre-evaporation of the droplets before the flame zone is total ($5 \mu\text{m}$), partial ($25 \mu\text{m}$, $75 \mu\text{m}$ and $123 \mu\text{m}$) and nearly non-existent ($175 \mu\text{m}$). The droplet motion is controlled by both the Stokes number St and the vaporisation number Ψ , defined for a counterflow diffusion flame as:

$$St = \frac{\tau_p}{\tau_{flow}} = \frac{\rho_l d_p^2 a}{18 \rho_g \nu_g} \quad (8.9)$$

with ρ_l the liquid density, d_p the droplet diameter, ρ_g the gaseous density and ν_g the gaseous kinematic viscosity, and:

$$\Psi = \frac{\tau_{evap}}{\tau_{flow}} = \frac{d_p^2 a}{K} \quad (8.10)$$

where $K = 8 \rho_g D_F / \rho_l \ln(B_M + 1)$ where D_F is the fuel diffusivity and B_M the Spalding mass number is the vaporisation rate constant.

The Stokes number compares the relaxation time of the particle τ_p with the characteristic time of the flow τ_{flow} , which is defined as $1/a$ with a the flame strain rate in this configuration. Conversely, the vaporisation number compares the evaporation characteristic time τ_{evap} with the flow characteristic time. The particle diameter drives both numbers. This has consequences on the particle motion, as shown in Fig. 8.17.

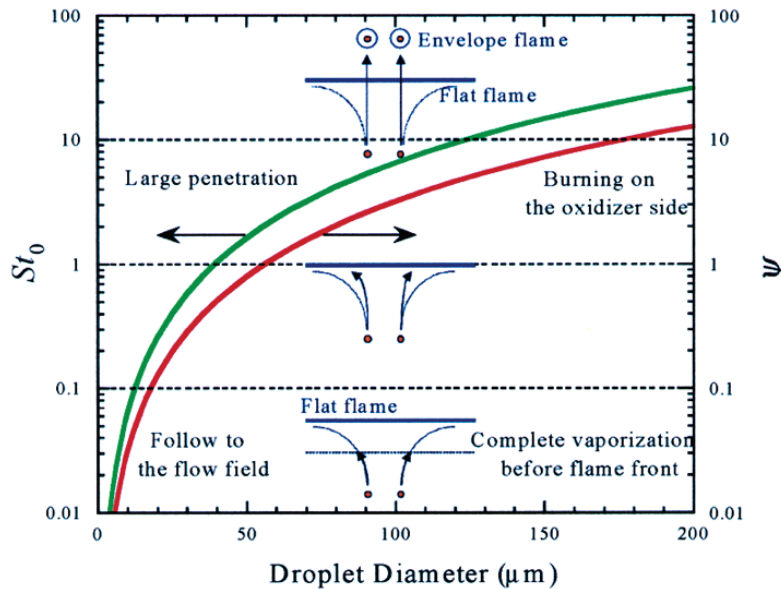


Figure 8.17: Stokes and vaporisation numbers as a function of the diameter size from [201]

This graph represents both non-dimensional numbers, St and Ψ , for varying droplet diameters evaluated and with $K = 1 \text{ mm}^2/\text{s}$. The larger particles, the longer time they stop and evaporate. This explains the strong impact of the droplet diameter on combustion and the expected new flame structures induced by size polydispersion combining various droplets' behaviour.

In the present cases, the relaxation time of the largest droplet is one order of magnitude lower than the flow time through the atomiser. Therefore, the injected droplets are considered mostly in equilibrium with the gas and have mean velocity at injection with only one percent velocity fluctuation.

To start with, monodisperse flame profiles are compared polydisperse ones in Section 8.3.3.1. The origin of the second peak of heat release rate is then explained in Section 8.3.3.2. Finally, the flow regime is detailed in Section 8.3.3.3.

8.3.3.1 Comparison with monodisperse cases

The aim is to give more insights about the polydisperse case compared to several monodisperse cases. First, time-averaged heat release rate and temperature profiles are compared in Fig. 8.18.

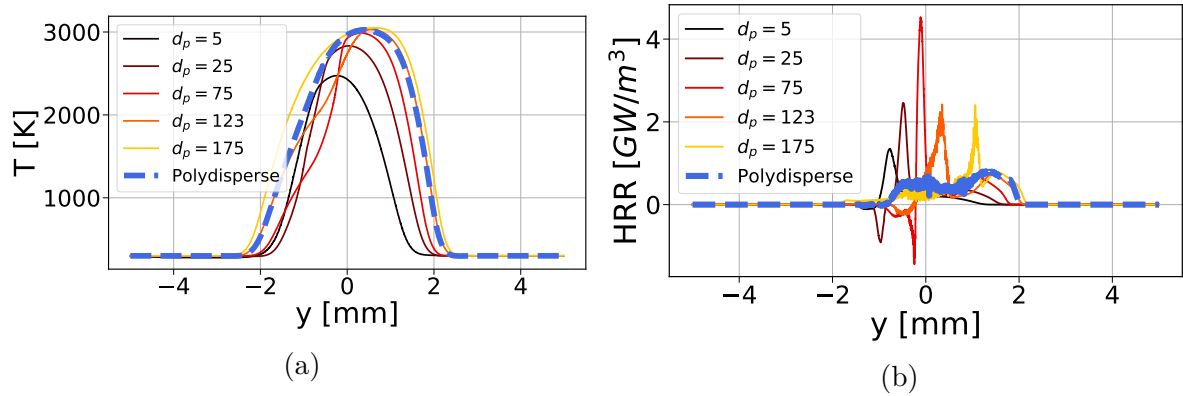


Figure 8.18: Time-averaged temperature (a) and heat release rate (b) profiles on the central line for numerous monodisperse and polydisperse cases.

The more the diameter increases, the more the maximum temperature increases, reaching its maximal value for $d_p = 75$ μm at $T = 3035$ K (the maximum adiabatic temperature is 3150 K for $\phi = 1.1$). Profiles are also more shifted to the right, showing a larger reaction zone. Once the maximum temperature is reached, profiles are expanding on the left side, that is to say the fuel/nitrogen side.

These results are in agreement with the heat release rate profiles. The bigger the diameter, the further right the heat release rate peak occurs. For the polydisperse case, no clear single peak is visible, but only two small peaks with the same intensity seem to appear. The endothermic zone is visible until $d_p = 123$ μm . For $d_p = 175$ μm and the polydisperse case, the flame exhibits no negative heat release rate peak, which is explained by smaller pre-evaporation compared to the other cases. Finally, the bigger the diameter is, the higher a second flame peak appears on the right side of the flame.

To understand better the differences between the temperature profiles, Fig. 8.19 represents the temperature profiles as a function of the Bilger mixture fraction (defined in Section 3.3.3.2) for the different monodisperse cases, the polydisperse case and the gaseous case.

The $d_p = 5$ μm case is very close to the gaseous profile with a bigger difference when going towards the fuel side ($z = 1$), since the fuel vaporisation for the $d_p = 5$ μm lowers at first the temperature (for $0.9 < z < 1.0$).

For larger diameters ($d_p < 75$ μm), the flame seems to extend towards the oxidiser side first, the temperature increasing and the profiles being shifted to the left. For diameters $d_p > 75$ μm , the profiles are not shifted anymore towards the left side, but the temperature on the fuel side increases, as if the profiles inflated. Indeed, as less pre-evaporation occurs, the droplets are only consumed in the flame front, which increases the temperature

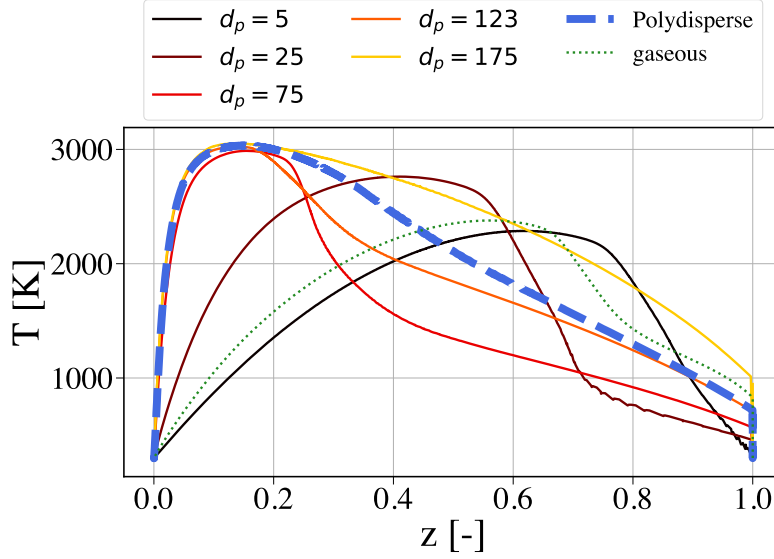


Figure 8.19: Time-averaged temperature versus Bilger mixture fraction for various monodisperse, the polydisperse case and the gaseous case.

for a fixed mixture fraction on the fuel side when the injected diameter increases. This also implies that the stoichiometric mixture fraction z_{st} seen by the flame is different for increasing diameters and stabilises when the droplets are big enough, as the temperature maxima are shifted to lower mixture fractions.

To investigate the diameter impact on the flame structure, the flame thickness is then evaluated. As defined by [284], the thickness of a diffusion flame is usually defined as:

$$\delta_L^{CDF} = \frac{1}{(\partial z / \partial x)_{st}} = \left(\sqrt{\frac{\pi D}{2a}} \right)_{st} \quad (8.11)$$

with D the diffusion supposed to be constant and a the strain rate. However, this definition cannot be used for this case because the value of stoichiometry changes too much and cannot be used properly since wiggles perturb the value. To estimate δ_L^{CDF} in our case, the distance between the location of $T = 400$ K (convenient value to detect the sharp rise of temperature) on both sides is measured and results are reported in Fig. 8.20.

First, the diffusion flame thickness is of the order of the millimetre whatever the case, which is much higher than the thickness corresponding gaseous premixed flame. Second, with the diameter increases, the flame thickness increases due to the longer evaporation time. Linking the flame thickness to the flow properties was performed in the work of Rochette et al. [265], where the evaporation thickness δ_{ev} was estimated to be equal to $\delta_{ev} = u_l \tau_{ev}$. As shown in Section 3.3.3, the thickness evaluation is very different for the premixed and diffusion flame cases. Therefore, the application of the formula of [265] (not shown here) did not lead to satisfactory conclusions.

Eventually, dynamic properties are evaluated for all the cases. Figure 8.21 represents the time-averaged velocity and strain rate profiles on the vertical line for the different monodisperse, the polydisperse and the gaseous cases, with the following definition to evaluate the strain rate:

$$a = \frac{1}{\rho_g} \frac{\partial \rho v}{\partial y} \quad (8.12)$$

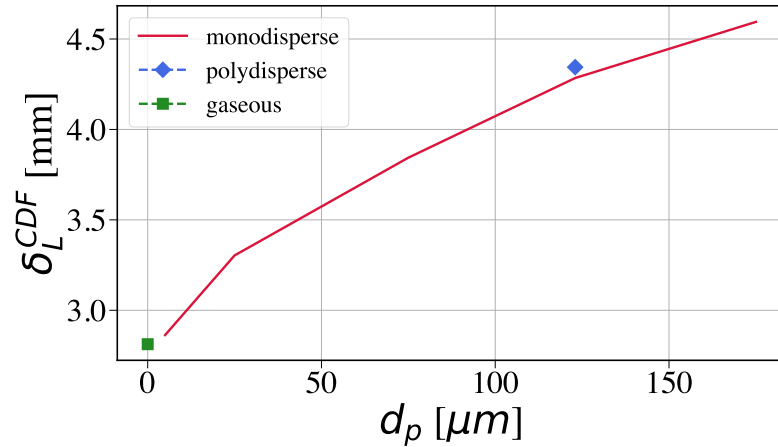


Figure 8.20: Flame thickness δ_L^{CDF} vs diameter d_p for various monodisperse, the polydisperse and the gaseous cases.

with ρ_g the gaseous density, y the axial position and v the axial velocity.

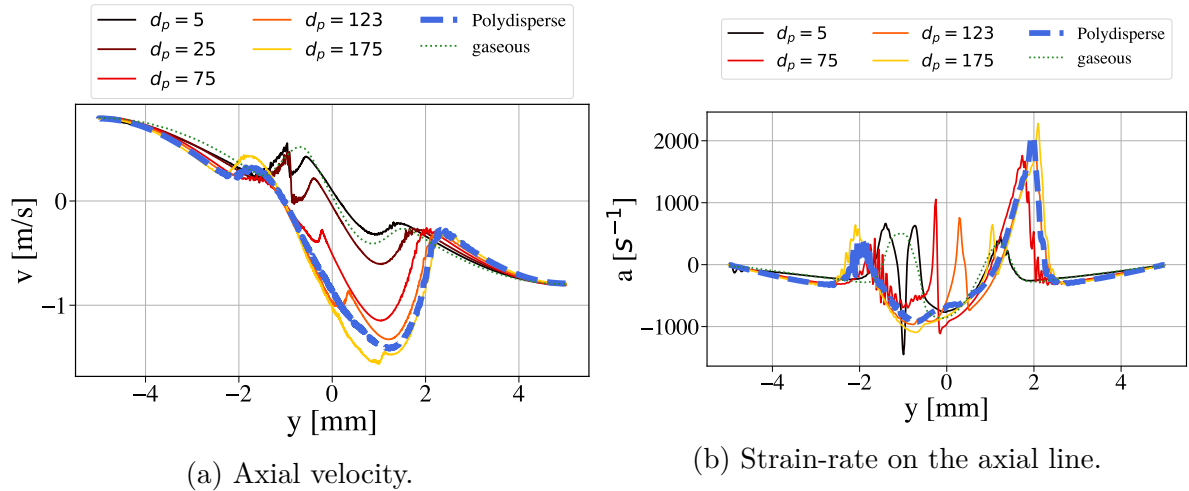


Figure 8.21: Time-averaged velocity (a) and strain-rate (b) versus axial position on the central line for various monodisperse, the polydisperse and the gaseous cases.

The gaseous velocity profile can be explained by the density profiles (shown Fig. 8.22). Indeed, as both flows face each other, the velocity should decrease in intensity when getting closer to $x = 0$ and grow up again on the other side. However, because of the reaction zone in the middle of the domain, the density is there reduced, resulting in an increase of the velocity absolute value on both sides.

For the gaseous case, the profile is almost symmetric on both sides, because the velocity is almost the same on both sides. As the strain rate proportional to the derivative of this axial velocity field, the strain rate for the gaseous case is negative on both edges, then exhibits two positive peaks when getting closer to the reaction zone (corresponding to the increase of velocity) and is finally negative in the reaction zone. There is a slight asymmetry between the oxidiser and the fuel strain rate peaks.

For the $d_p = 5 \mu\text{m}$ case, the velocity profile is very similar to the gaseous profile on the oxidiser side, but exhibits a slight drop on the fuel side. This corresponds to the sudden increase of the fuel mass fraction due to the evaporation of the droplets.

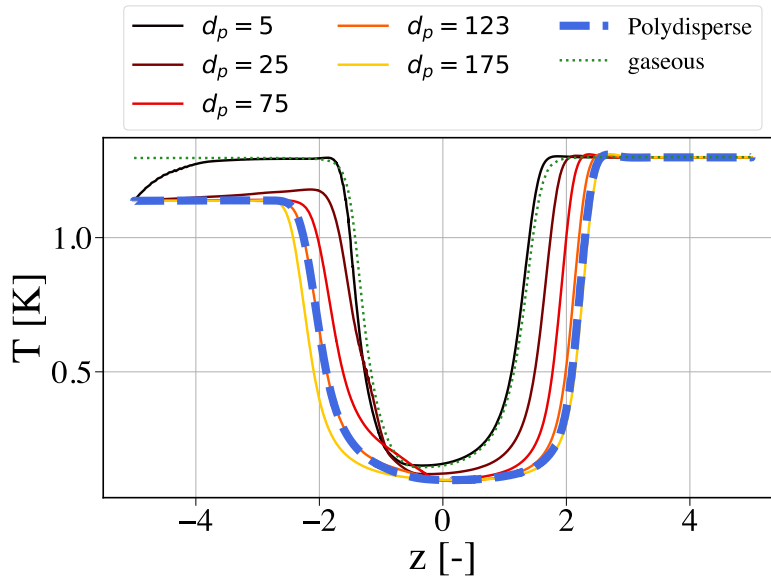


Figure 8.22: Time-averaged density versus axial position on the central line for various monodisperse, the polydisperse and the gaseous cases.

When increasing the droplet size, the velocity becomes higher on the oxidiser side and the peak on the fuel side is less visible. The sudden increase of fuel mass fraction has almost completely disappeared for a very large diameters and for the polydisperse case. This impacts the strain rate profiles, with a three-peaks shape for large diameter cases and the polydisperse case:

- one peak for the fuel entering the burnt gases area as for the gaseous case, almost constant in terms of higher value.
- one on the oxidiser side that become higher when the diameter increases and stabilises at a given diameter.
- one in the hot temperature area, representing the sudden variation of fuel associated to the location where the fuel has almost completely vaporised, which moves to the right with increasing diameter.

To sum up, the monodisperse cases show that the flame burns more intensively along when the droplet diameter increases. Indeed, the temperature rises and the burnt gases area is widened. Moreover, dynamic profiles exhibit higher values, considering either the velocity or the strain rate profiles.

8.3.3.2 Second flame peak

Figure 8.23 gives a comparison of the heat release rate field between the polydisperse and the different monodisperse computations.

As shown earlier, only the polydisperse case shows a double flame front with a comparable amount of heat released in both flames. The two small diameter particle cases give similar flames, having the structure close to a gaseous diffusion flame. However, the late fuel evaporation leads to locally higher fuel mass fraction, i.e., higher equivalence ratio

($\phi = sY_F^0/Y_{O_2}^0$, with Y_F^0 and $Y_{O_2}^0$ respectively the fuel and oxygen mass fractions in the fuel and oxidiser streams) seen by the flame.

As well, Fig. 8.23 shows the Takeno flame index, defined as the Takeno number multiplied by the fuel source term, and expressed as in Chapter 3:

$$T\dot{\omega} = -\frac{\nabla Y_F \cdot \nabla Y_{O_2}}{|\nabla Y_F \cdot \nabla Y_{O_2}|} \dot{\omega}_{C_7H_{16}} \quad (8.13)$$

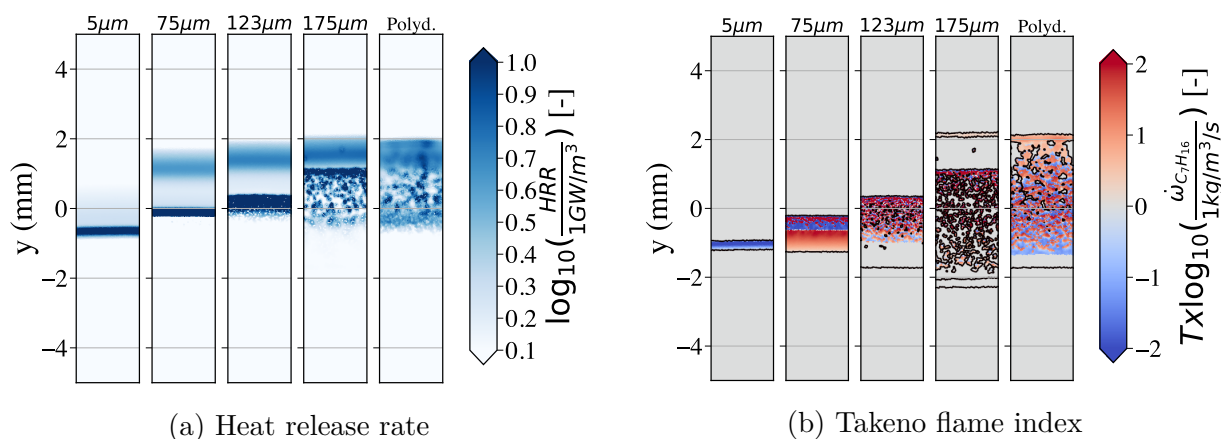


Figure 8.23: Gaseous fields for $d_p = 5 \mu\text{m}$, $d_p = 75 \mu\text{m}$, $d_p = 123 \mu\text{m}$, $d_p = 175 \mu\text{m}$ and the polydisperse configuration.

As the fuel source term is always negative, a positive index means a premixed flame structure and a negative one a diffusion flame structure. The positive Takeno on the fuel side for the $d_p = 75 \mu\text{m}$ case is due to the increasing fuel mass fraction as droplets evaporate while approaching the main reaction zone, and should not be interpreted as a premixed flame. The main flame in the fuel side is non-premixed, resulting from the burning of the fuel vapour with the opposite oxygen stream. When the diameter increases, this diffusion flame gradually weakens, and a premixed flame zone appears on the oxidiser side. In the polydisperse case, both the non-premixed and premixed zones are present in relatively similar proportions. To achieve these plots, the evaporate rate and the source term fields are also given in Appendix C.

To better understand these flame structures, Fig. 8.24 shows the heat release rate profile of gaseous flames at different values of ϕ_g . In globally rich cases, the decomposition of fuel into smaller molecules, in particular the hydrogen radical enhances secondary reactions with oxygen in the oxidiser side such as $H + O_2 \rightarrow HO_2$ (see Fig. 8.25) and the subsequent conversion of intermediates into products of combustion, leading to a secondary peak of heat release.

The counterflow flames obtained with the two smallest diameters have a structure very similar to globally rich gaseous flames, with a secondary heat release zone in the oxidiser side, indicating that they see an effective rich equivalence ratio.

The largest droplet case on the contrary exhibits droplet individual burning prior to a zone of continuous burning in premixed mode. Some droplets cross the flame front, as indicated by local spots of heat release rate. In this case, the spray is not sufficiently dense to sustain a continuous diffusion flame in the fuel side. However, as in the small droplet cases, the equivalence ratio ϕ is modified by evaporation, and the fuel excess similarly leads

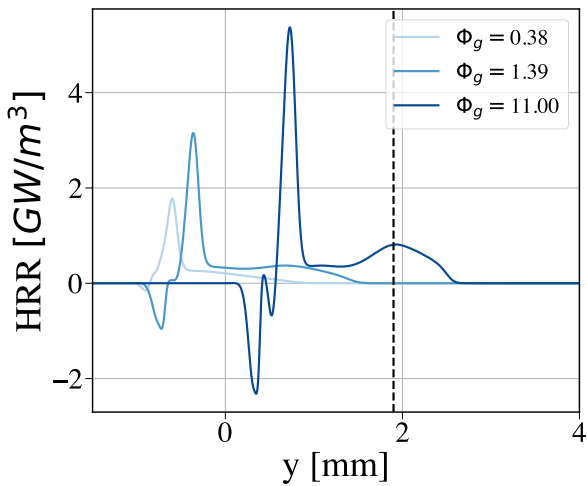


Figure 8.24: Heat release rate profile for gaseous diffusion flames at different global equivalence ratios.

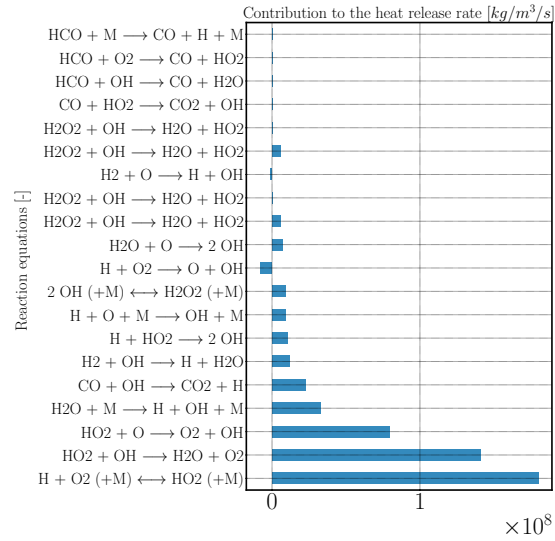


Figure 8.25: Contribution of the most important reactions to the 2nd heat release rate peak.

to a secondary heat release rate zone which adds to the direct burning of the droplets in the oxidiser side.

Interestingly the increase of the flame thickness in the polydisperse case due to slower evaporation of larger droplets, is partly compensated by the small droplets leading to a flame thickness slightly smaller than the largest particle diameter case.

To sum up, three main contributions are leading to the second flame peak:

- the increase of the diameter changes the **flame structure, which is similar to a rich gaseous flame**. The strong dissociation of the fuel and the strong reactivity of pure oxygen enable a secondary reaction peak, monitored by recombinations.
- droplets are not all consumed in the flame front and bigger **droplets are crossing it and evaporating in the oxidiser area, leading to a small amount of fuel that is being consumed in premixed mode**.
- as overall in the high temperature zone, **droplets are evaporating individually**, constituting the third contribution of this second heat release rate peak.

The two peaks on the polydisperse flame being of the same order of magnitude is then unintended and due to the flow polydispersion. To understand why the flame power is increasing with higher diameter, flame regimes are analysed in the coming section.

8.3.3.3 Flame regime

The consumption speed is proportional to the heat release rate integrated across the flame front as combustion is complete, so that both quantities are equally used in the following. The total heat release of the flame is plotted in Fig. 8.26 for gaseous flames as a function of equivalence ratio, and for two-phase flames at $\phi_g = 0.55$ as a function of particle diameter.

According to theory and as observed in Fig. 8.26, at fixed strain rate, the gaseous flame consumption speed increases with the fuel loading up to the maximum reached for a pure fuel stream, following the expression [235]:

$$\dot{\Omega}_F = -\rho_g \frac{Y_F^0}{1 - z_{st}} \left(\frac{a_{num} D_F}{2\pi} \right)^{\frac{1}{2}} e^{-\zeta_f} \quad (8.14)$$

with $\dot{\Omega}_F$ the integral fuel source term, z_{st} the stoichiometric mixture fraction and ζ_f the flame position. This is what is observed in Fig. 8.26, with the maximum reached at $\phi_g = 11$ corresponding to a pure fuel stream.

On the other hand, the consumption speed for two-phase monodisperse cases increases with the particle diameter. Indeed, as already explained, the overall lean diffusion flame burns at an effective equivalence ratio closer to stoichiometry under the effect of evaporation and drag, which concentrate the fuel vapour at the flame front. This effect increases with the droplet size, which leads to straighter trajectories and delayed evaporation, possibly reaching fuel mass fraction in front of the flame far above the equivalent purely gaseous flame. This effect is maximum at saturation, and in theory a plateau is also reached for the two-phase flames, at a lower level than the gaseous plateau because the saturation fuel vapour mass fraction is always less than 1.

However, it is observed in Fig. 8.26 that for droplet diameters above 150 μm approximately, the two-phase flame total heat release rate exceeds the maximum total heat release rate of gaseous diffusion flames. In view of the above discussion, this must be related to a progressive change of combustion regime from pure diffusion to partial premixing.

To highlight this mechanism, Fig. 8.27 presents the contributions to the total integrated fuel source term (defined in Section 3.3.3.3) of the diffusion (subscripted diff) and the premixed (subscripted prem) reacting zones for varying droplet sizes (superscripted d_p) and the polydisperse case (superscripted *polyD*).

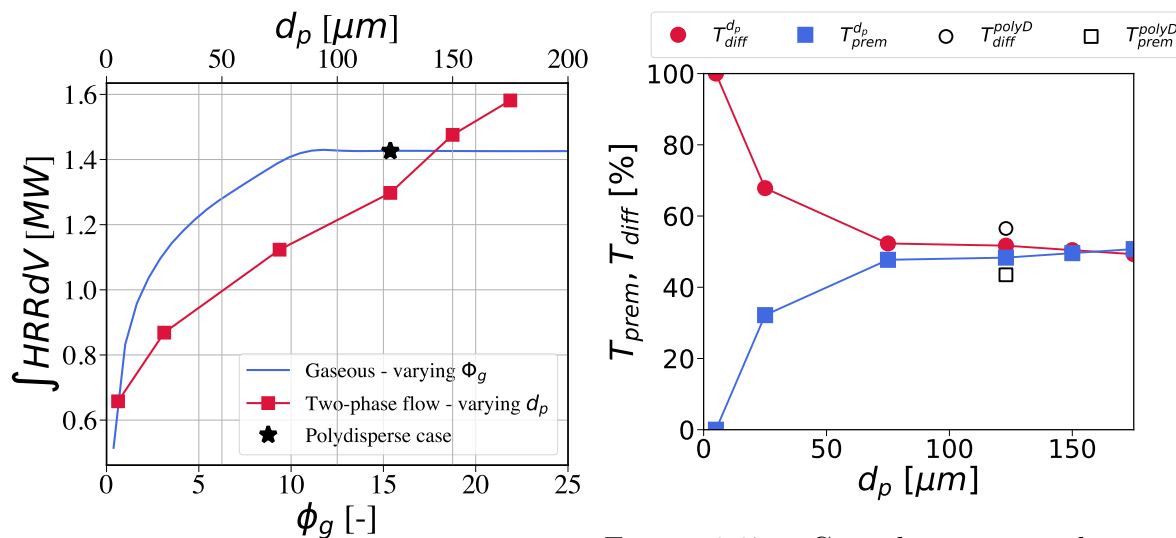


Figure 8.26: Integral of heat release rate for gaseous flames (varying ϕ_g) and two-phase flames (varying droplet size).

Figure 8.27: Contributions to the integrated fuel source term corresponding to the diffusion and the premixed flames as a function of the particle diameter.

For very small monodisperse particle diameters, the flame is purely non-premixed. As the diameter increases, the penetration of the droplets in the flame induces an increasing

premix burning mode. For droplet diameters above $150\ \mu\text{m}$, the premixed mode is prevailing and the total flame burning rate exceeds the maximum for gaseous diffusion flames. The polydisperse case also exhibits a total heat release rate higher than the maximum in diffusion mode. In this case, both the diffusion flame and the premixed flame exist, contributing almost equally to the total source term, and contributing similarly to the flame consumption speed acceleration, which shows that less premixed burning than the equivalent monodisperse case ($d_p = d_{32}$), because small droplets are able to sustain a stronger diffusion flame.

8.3.4 Single droplet modelling

As the different fields shown in section 8.3.3.2 are very spotty, droplets may burn individually. In Section 8.3.4.1, the group number is pre-evaluated to evaluate the droplet combustion regime encountered. Second, the MustARD model presented in Chapter 5 is applied in Section 8.3.4.2 and the observed differences with the simulation without single droplet model (AS) are analysed.

8.3.4.1 Group number

To identify the droplet combustion regime, the group number G is considered. It compares the radius of the flame to the inter-droplet distance around an individual burning droplet. Small values of G indicate a regime of individual burning, while large values of G characterise group burning. The formula of G according to Chiu et al. [45] presented in Chapter 5 is recalled here:

$$G_{chiu} = (1 + 0.276Re_p^{1/2}Sc^{1/3})LeN^{2/3}(d_f/S) \quad (8.15)$$

- $Re_p = \frac{|v_g - v_p|d_p\rho_g}{\mu_g}$ is calculated on the axial line.
- $Sc = 2.3$ and $Le = 3.14$ are calculated from the Schmidt number estimated with the ARC scheme development.
- N is defined as the total number of droplets in the cloud and, here, estimated as the number of droplets in the burning area.
- $d_f = d_p \frac{\ln(1+B_M)}{\ln(1+Y_{O_x}/s)}$ as defined in the MustARD algorithm. This definition diverges in the fuel + nitrogen area and is therefore equal to infinity in this region. As a conclusion, a threshold was set to avoid numerical errors when G exceeds 1000.
- $S = \left(\frac{\pi}{6\alpha_l}\right)^{\frac{1}{3}}d_p$, as introduced in 5.2.1, the characteristic interdroplet distance which represents the mean distance on a given group of particles.

Figure 8.28 shows the axial profiles of the mean group number in the polydisperse case.

The Group number gradually decreases from the fuel side to the oxidiser side, indicating that the droplets are first in a group burning regime, and gradually change to individual droplet burning as the smallest droplets disappear.

Therefore, and as the evaporation around the droplets might be unresolved because they enter a single droplet combustion regime, the MustARD model is applied in Section 8.3.4.2.

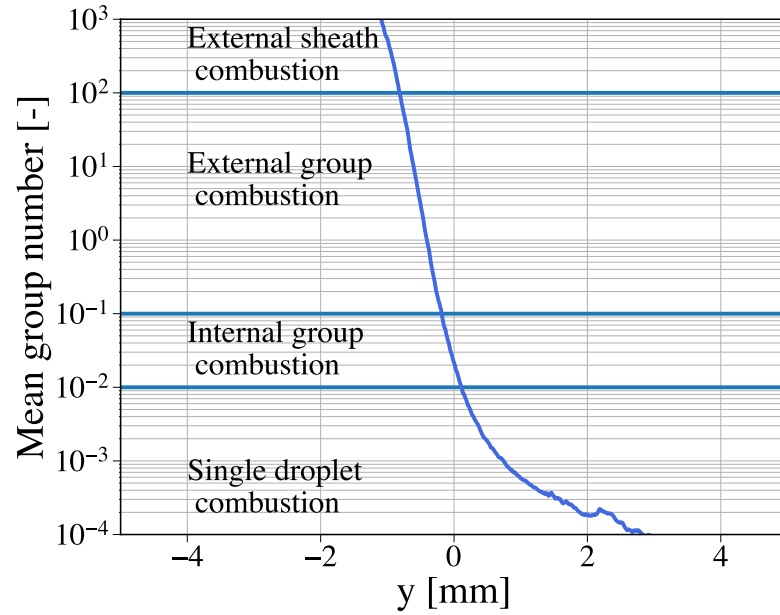


Figure 8.28: Axial profile of the mean transversal group number of the droplets on the central line in the polydisperse case.

8.3.4.2 MustARD

The difference between the heat release rate field with and without MustARD model is displayed in Fig. 8.29. The flame is at the same location in both cases. However, the second peak ($y = 2$ mm) exhibits a stronger droplet evaporation in the MustARD case.

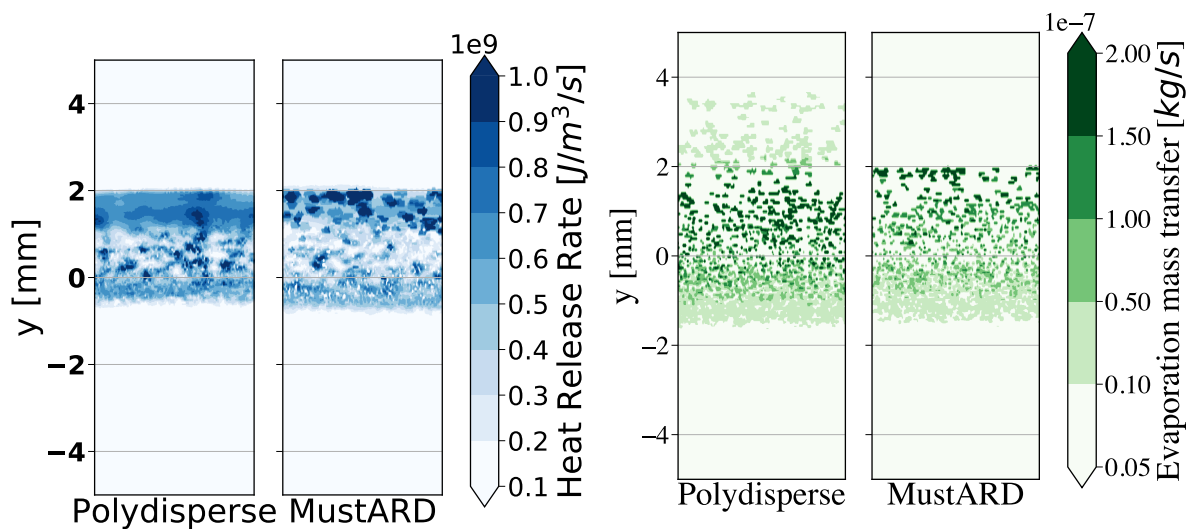


Figure 8.29: Heat Release Rate field for non-MustARD and MustARD cases.

Figure 8.30: Evaporation mass transfer field for non-MustARD and MustARD cases.

Moreover, big diameters are crossing the second flame front in the polydisperse case and bring back a premixed contribution to the flame front. This is not the case any longer

when looking at the MustARD case, as all the droplets have disappeared after the second flame front.

Figure 8.31 displays the time-averaged total heat release rate profiles of the non-MustARD (HRR_{tot}^{AS}) and the MustARD case ($HRR_{tot}^{MustARD}$) on the central line. For the MustARD case, the contributions of the single droplet combustion model ($HRR^{MustARD}$) is detailed.

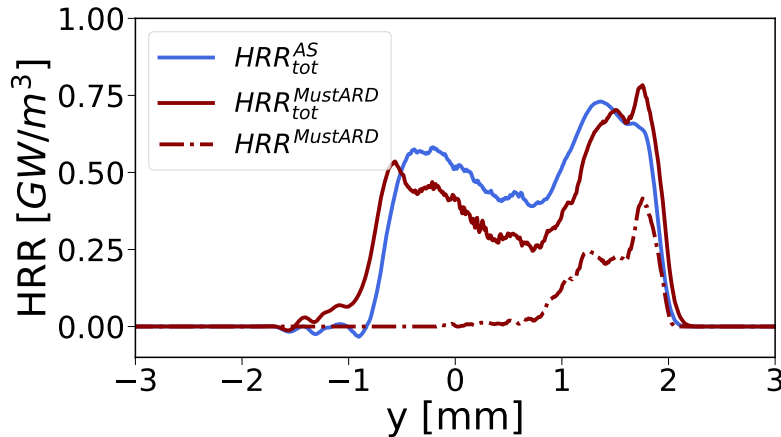


Figure 8.31: Time-averaged heat release rate profiles on the central line for AS and MustARD cases. The contribution of the isolated droplet burning mode is added.

The MustARD model activates roughly in the same region as the second heat release rate peak, showing that the droplets are separated enough and can burn individually. This result is globally in accordance with the group number behaviour. In the second peak, the contribution of the isolated droplet combustion mode to the heat release rate is half the total heat release rate.

Finally, both profiles show the same structure. Indeed, MustARD only impacts the evaporation of the droplets in the second peak, which do not represent the major contribution to the heat release rate at this location. The use of MustARD however seems to slightly shift the profiles to the left and decrease the heat release. Indeed, in the AS case, droplets are accumulating on the other side of the flame, giving a gaseous premixed contribution to the flame contrary to MustARD case which burns every droplet in the second peak area. Consequently, the accumulating particles are giving additional fuel to burn, which displaces the profiles and slightly alters the heat spread along the central line.

8.3.5 Conclusion

Understanding complex two-phase flames associated with complex kinetics mechanisms is the final goal of this PhD. Two-phase diffusion flames were the last final elementary brick to understand the overall phenomena happening in the complex burner. To study this particular flame, the experimental work of Mikami et al. [201] was taken as a starting point and translated into a numerical configuration. A heptane/oxygen mechanism was derived, with a satisfactory number of species, and showed a good agreement with respect to the detailed mechanism.

The two-phase counterflow diffusion flame was then computed, showing a good agreement with the flame visualisation, and exhibiting two distinct almost similar heat re-

lease rate peaks. After computing the corresponding mono-disperse cases, from full pre-evaporation ($d_p = 5 \mu\text{m}$) to higher diameter sizes ($d_p = 175 \mu\text{m}$), the second heat release rate peak could be explained by the higher diameters triggering a second gaseous reaction zone, by some of the particles crossing the flame front and evaporating on the oxidiser side and by droplets evaporating in the second heat release rate peak. Eventually, the higher flame power that is correlated with a higher diameter is a consequence of a change in the flame regime, where the premixed burning mode takes a higher proportion when the diameter gets bigger. Besides, MustARD algorithm was tested on this configuration and slightly changed the location of the evaporation rate, impacting slightly the HRR profiles.

Part 1 of this manuscript was dedicated to the theory used, explaining how combustion, chemistry, turbulence and two-phase flow are modelled in a CFD code. Part 2 that has ended here aimed to use the elemental bricks constructed with part 1 to investigate topics of interest for a two-phase turbulent multi-component burner. This introduces part 3, of which the goal is to apply all this acquired knowledge to understand the flame structures of SAF surrogates and extinction in the academical SSB burner.

Part IV

Alternative fuels combustion in a turbulent combustor

Chapter 9

Simulation of LBO in a swirl spray burner

Contents

9.1	From the geometry to the reactive flow numerical setup . . .	171
9.1.1	Presentation of the burner and experimental data	171
9.1.2	Set-up and cold flow	174
9.1.3	Reactive two-phase flow	177
9.2	Stable spray flame: impact of the chemical modelling for a standard fuel	182
9.2.1	Fuel properties	182
9.2.2	Results: mean solution	185
9.2.3	Flame structure analysis	194
9.2.4	Flame structure: effect of the fuel model	199
9.2.5	Conclusion	202
9.3	Lean Blow-Out calculations	204
9.3.1	Timescales and methodology	204
9.3.2	Towards LBO	207
9.3.3	LBO detection	214
9.3.4	Discussion	216
9.3.5	Conclusions	218

The Spray-Stabilised Burner (SSB) is an optically accessible combustor built at DLR Stuttgart to study the impact of the fuel on the stabilised flame and the lean blow-out phenomenon. In this chapter, Section 9.1 presents the burner and the available experimental data, as well as the process towards the reactive calculation setup. The stabilised flame simulated is then analysed in Section 9.2 and the differences between a mono-component and a multi-component surrogate fuel. Finally, Section 9.3 performs lean blow-out calculations with the mono-component surrogate fuel.

9.1 From the geometry to the reactive flow numerical setup

The aim of this section is to present the workflow from the geometry reception towards the integration set-up in AVBP for reactive simulations. The SSB configuration was experimentally studied at DLR by Grohmann [107]–[111] and Cantu et al. [38] and their results are detailed in Section 9.1.1. Section 9.1.2 then details the mesh, the numerical setup and the results obtained for the non-reactive simulation. Finally, Section 9.1.3 explains the setup for the reactive flow and the methodology employed to determine the injected diameter PDF.

9.1.1 Presentation of the burner and experimental data

The entire SSB geometry is shown in Fig. 9.1a, as well as a sketch of the atomiser in Fig. 9.1b and the two swirler stages in Fig. 9.1c and Fig. 9.1d.

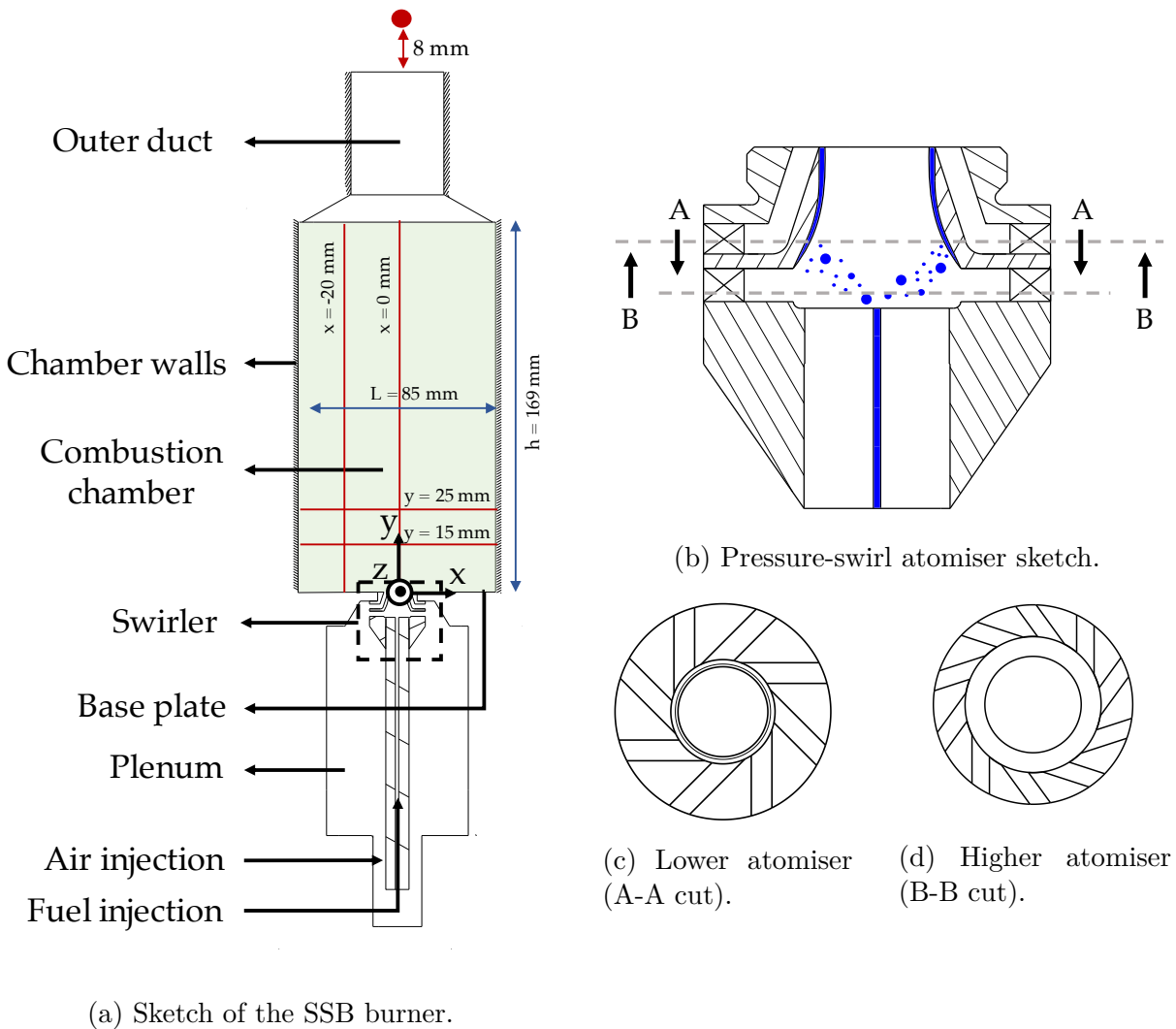


Figure 9.1: SSB geometry.

Air is injected in the plenum, while fuel is injected through a duct and directly atomised in the pressure swirl atomiser. After being mixed with air in the swirler, the atomised fuel

is released in the chamber where it evaporates, mixes with air and starts burning. Exhaust gases are released through a convergent duct.

The diameters of the inner and outer nozzle are respectively 8 and 11.6 mm. The combustion chamber has a square cross-section of 85×85 mm and a height of 167 mm. The pressure-swirl atomiser system shown in Fig. 9.1b is composed of two stages:

- a first lower stage containing 8 vanes injecting air at the atomiser exit plane to fragment the liquid fuel jet into droplets. These droplets then interact with the diffuser walls, and mostly film on it.
- a second higher stage containing 10 vanes is then used to inject air at the diffuser exit and further atomise the droplets.

Several operating conditions were experimentally tested with varying air mass flow rates and temperatures. However, only one condition was computed in this study, detailed Table 9.1. It was chosen because it is the one with most experimental data.

P [bar]	ϕ [-]	P_{th} [kW]	T_{fuel} [K]	T_{air} [K]	\dot{m}_{air} [g/s]
1.0	0.8	10.2	303.15	323.15	4.31

Table 9.1: Operation point of the studied case in the SSB burner.

The chamber operates at atmospheric pressure. It is designed to work at a power of 10.2 kW and at an equivalence ratio of 0.8. Air is injected with a mass flow rate of 4.31 g/s and a temperature of 50° C. The fuel mass flow rate corresponds to the equivalence ratio and is injected at 30°. The **swirl number** measured in the experimental work takes the following definition:

$$S_w = \frac{\int_S r v u_\theta dS}{\bar{r} \int_S v^2 dS} \quad (9.1)$$

with v the axial velocity, u_θ the azimuthal velocity, S the integration surface area and \bar{r} the mean radius:

$$\bar{r} = \frac{1}{S} \int_S r dS \quad (9.2)$$

The experimental swirl number was estimated at $S_w^{exp} = 1.17$ in the centre flow and $S_w^{exp} = 1.22$ in the annular flow.

The experiments on this operating point conducted at the DLR Stuttgart are summarised in Table 9.2 for the three fuels studied in this work. Several other mono-component fuels have also been experimentally tested, which are not detailed in this manuscript but may be found in Grohmann's papers [107]–[111].

The different experimental techniques are briefly recalled below. More details on the experimental techniques and their characteristic values may be found in Grohmann's papers.

- **Particle Image Velocimetry (PIV)**, described for example in [240], measures the three components of the gaseous velocity (u_{gas} , v_{gas} , w_{gas}) on an x-y plane for the non-reactive and Jet-A1 reactive flows. The reactive flow measurements are not available on the whole plane due to problems with the hot gases.
- **Phase Doppler Anemometry (PDA)** measures some characteristic diameters and velocities of the droplets at $y = 15$ mm and $y = 25$ mm for the Jet-A1 reactive

Experimental technique	Location	Quantity measured	Non-reactive	Jet-A1 (A1)	AtJ (B1)	High aromatic (C1)
PIV	XY plane	$u_{gas}, v_{gas}, w_{gas}$	✓	✓	✗	✗
PDA	$y = 15$ mm, $y = 25$ mm	$d_{10}, d_{32}, d_{01}, d_{05}, d_{09}, u_{liq}, v_{liq}, w_{liq}$	✗	✓	✗	✗
Mie scattering	XY plane starting at $y = 15$ mm	α_{liq}	✗	✓	✗	✗
CARS measurements	$y = 15$ mm, $y = 25$ mm, $x = 0$ mm, $x = -20$ mm	$T_{mean}, T_{mp}, T_{05}, T_{95}$	✗	✓	✓	✗
Phosphoric measurements	Base plate and chamber walls	T_{walls}	✗	✓	✓	✗
Chemiluminescence fields	Integrated XY plane	CH^* fields	✗	✓	✗	✗
Flame visualisation	Plane	Luminosity	✗	✓	✓	✗
LBO measurements	/	LBO limits	✗	✓	✓	✓
Exhaust gas measurements	8 mm over the end of the duct	$[CO], [NO], [O_2]$	✗	✓	✗	✗

Table 9.2: Experiments of the SSB burner made at the DLR

flow. Characteristic diameters measured are the mean diameter d_{10} , the Sauter Mean Diameter (SMD) d_{32} and the diameters representing respectively 10% (d_{01}), 50% (d_{05}) and 90% (d_{09}) of the liquid volume. As well, the three components of the liquid velocities are measured (u_{liq} , v_{liq} and w_{liq}) and classified in diameter categories.

- **Mie scattering** is used to measure the conditional liquid loading of the droplets α_l for the reactive Jet-A1 flow on a x-y plane. Measurements could be performed for $y > 15$ mm only because the spray was too dense below that limit.
- **Coherent Anti-stokes Raman Spectroscopy (CARS)** measures temperature distributions on several points on the $y = 25$ mm line in the radial plane and the $x = 0$ mm line in the axial plane for the reactive Jet-A1 and AtJ flows. For Jet-A1 measurements at $y = 15$ mm and $x = -20$ mm have been added. The measured temperatures are the mean gaseous temperature T_{gas} , the most probable temperature T_{mp} i.e. the temperature at which the distribution reaches its peak point, and the temperatures representing 5% (T_{05}) and 95% (T_{95}) of the local distribution, which gives an insight of the spread of temperature values.
- **Phosphoric measurements** are used to get the temperature of the inner walls and

the baseplate for the reactive Jet-A1 flow.

- **Chemiluminescence fields**, deconvoluted with the Abel transformation [241], visualise the CH^* radical fields, which can be related to the averaged heat release rate field integrated through the line of visualisation.
- **Direct flame visualisations** have been given for Jet-A1 and AtJ.
- **Exhaust gas measurements** (CO and NO_x) have been made with a probe located at the end of the exit duct for the reactive Jet-A1 flow.
- **LBO measurements** have been realised by slowly reducing the fuel mass flow rate for the Jet-A1, the AtJ and the C1 cases. The methodology used is explained below.

The experimental procedure for Lean Blow-Out measurement is detailed in [107]. Figure 9.2 (left) summarises the main steps of the LBO procedure, which are detailed below:

1. The experimental procedure starts at the stable operating point $\phi_g = 0.8$. The air mass flow rate is kept constant during the whole procedure.
2. The fuel mass flow rate is then reduced so that the flame reaches an equivalence ratio of $\phi = 0.6$ where the flame is thermally stabilised. The time necessary to stabilise the flame is not specified, so that the time displayed in the graph of Fig. 9.2 (left) is not representative of the experimental procedure.
3. The fuel flow rate is further reduced to 80 g/h above the expected lean blow-out limit. As well, the time taken to stabilise the flame at this point is not specified.
4. From this operating point, the fuel flow rate is finally reduced at a fixed rate of 0.5 g/h/s, which corresponds to a reduction of ϕ_g to the order of 0.001 s^{-1} to 0.0001 s^{-1} , until the flame blows out.

The method was repeated three times per fuel, with overall average deviations from the mean values of 0.6%. LBO was measured for several mono-component fuels (n-hexane, iso-octane, n-dodecane) and multi-component fuels (Jet-A1, AtJ, C1, Readijet, HEFA), for different air mass flow rates and different air temperatures. Two types of blow-out appeared: either the flame completely blows off directly, or it extinguishes and reignites intermittently until complete blow-off. In every case, the last extinguishing event was chosen as the lean blow-out limit. The extinction event was however not described for the three fuels. The A1, B1 and C1 results on the different operating conditions are shown on Fig. 9.2 (right).

For the given air temperature, A1 and C1 show a lower equivalence ratio at LBO than B1. A1 and C1 representing the LBO equivalence ratio versus the air mass flow rate are similar, while the B1 profile is much higher. At the air mass flow rate of the studied operating point, $\dot{m}_{air} = 4.3 \text{ g/s}$, A1 and C1 have the same LBO limit.

9.1.2 Set-up and cold flow

The mesh and the numerical parameters are described and justified in Section 9.1.2.1 for the cold flow simulation. Results are presented in Section 9.1.2.2 with a comparison to the experiments.

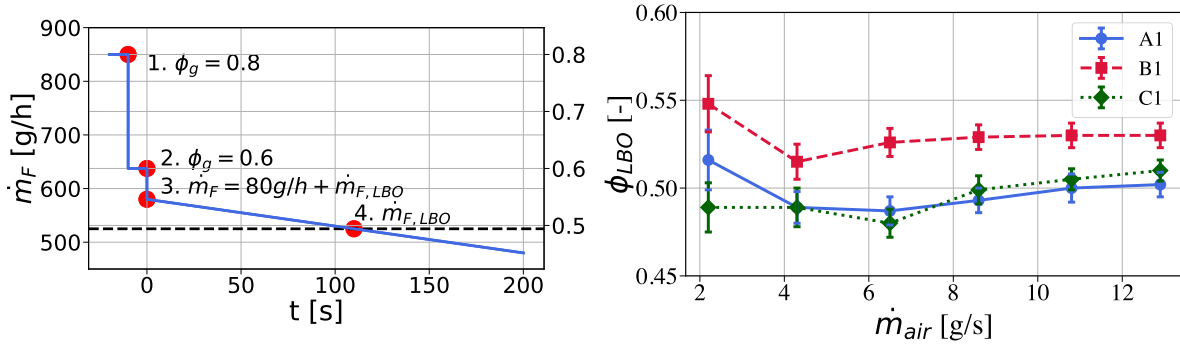


Figure 9.2: Experimental procedure for the LBO detection (left) and LBO limits for A1, B1 and C1 as a function of the fuel mass flow rate for $T_{air} = 323.15$ K (right), given by the DLR.

9.1.2.1 Numerical set-up

The mesh used to compute the SSB was produced with centaur software and comprises 3.2 million nodes and 18 million tetrahedral elements. The mesh in the combustion chamber and in the swirler vanes is displayed in Fig. 9.3.

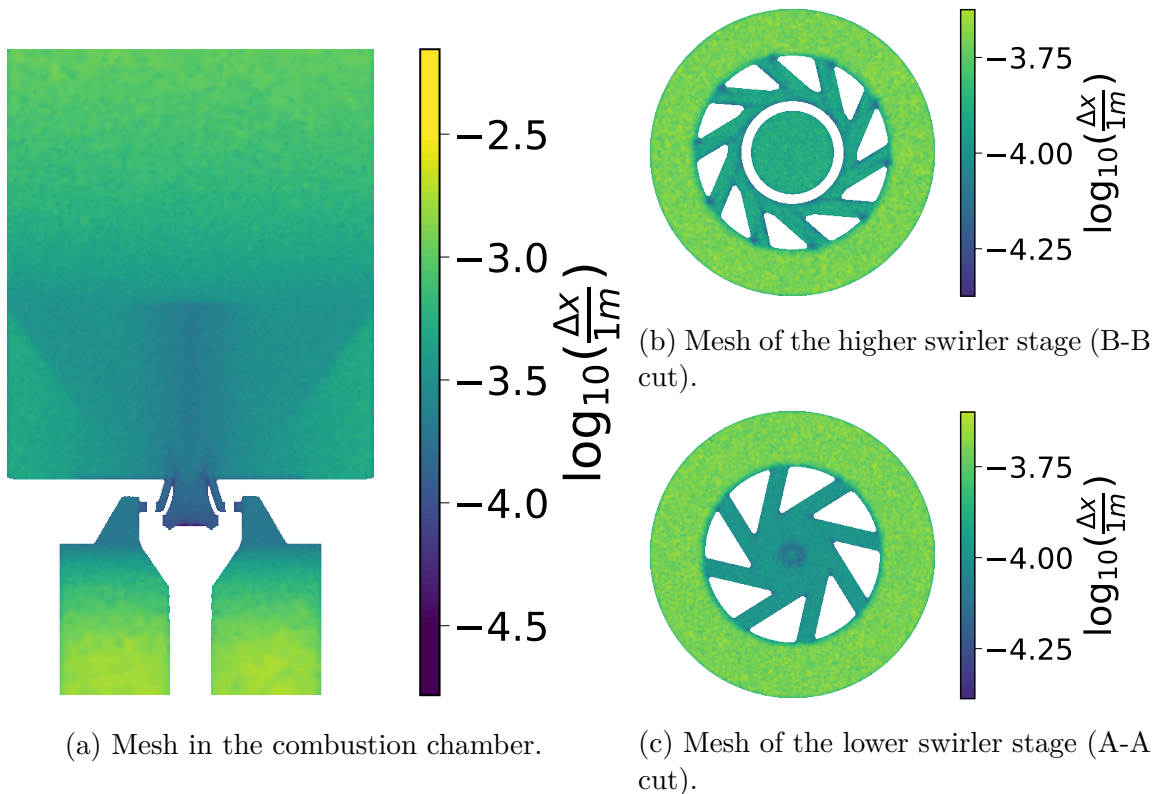


Figure 9.3: Views of the mesh with fields of cell size Δx .

The swirler vanes are refined to get approximately 10 points in a given direction. As well, the vicinity of the flame front is refined to have a cell size of the order of the flame thickness, which was evaluated beforehand to be equal to 0.4 mm for the considered operating point.

Table 9.3 summarises the numerical choices used to compute the SSB.

Numerical models	
Convective scheme	Lax-Wendroff [163] of order 2
Diffusive scheme	Finite element of order 2
Artificial viscosity model	Colin [52] based on ρu and ρY
LES closure	WALE model [93]

Table 9.3: Numerical set-up for the non-reactive flow in the SSB

The convective scheme is a Lax-Wendroff [163] of order 2. A TTGC scheme which has a higher order, is available but was not used because of CPU time considerations. The artificial viscosity model is a Colin-based (see Section 3.2.3.2) on ρu and ρY_k , with a maximum of 0.1 for the second order and 0.05 for the fourth order coefficients. The WALE [93] subgrid-scale model is used, together with wall-laws applied in the swirler. Other walls are treated as no slip walls and all walls are adiabatic. The mesh induces a wall cell size in the combustion chamber in the range $5 < y^+ < 7$, which is close to a resolved flow at the wall.

9.1.2.2 Results

This section provides results of the non-reactive simulation and the comparison to the experimental work of Grohmann [110]. For this simulation, the mixture is air only. The simulation was converged to a mean steady state and then averaged for approximately 85 ms, corresponding to 17 flow-through times, calculated as:

$$\tau_{chamber} = \frac{L_{chamber}}{u_{bulk}} = 5 \text{ ms} \quad (9.3)$$

with

$$u_{bulk} = \frac{\int \rho v S}{\int \rho S} = 33 \text{ m/s} \quad (9.4)$$

S being the area of the section between the swirler and the combustion chamber.

Figure 9.4 compares the time-averaged field of the axial velocity with the experimental PIV.

The flow exhibited is highly turbulent as the air goes out of the swirler with a high velocity (of the order of 100 m/s). The swirl creates a low pressure area at the centre of the flow, leading to the formation of an Inner Recirculation Zone (IRZ). Besides, Outer Recirculation Zones (ORZ) form in the bottom corners of the chamber. The numerical field shows a very good agreement with the experiment. The flow structures are recovered, and the different contour lines are very similar. Maximum axial velocity is the same in both fields. The only differences are a slight upward shift of the centres of the ORZ in the numerical solution, and a slightly wider low pressure zone at $y = 10$ mm in the experiment.

The swirl number is found in the LES at 1.11, close to the 1.17 experimental value. The Reynolds number measured numerically at the outlet diameter gives a value of $Re = 25500$, which is close to the experimental value of 25000 [110].

To compare more precisely the LES results with the PIV results, the time-averaged velocity profiles taken in a $x - y$ plane are displayed in Fig. 9.5 at different heights above the burner ($y = 5$ mm, 10 mm, 15 mm and 20 mm).

A very good agreement is obtained for the three velocity components, both in shape and maxima of the profiles, with a maximum difference much lower than the numerical

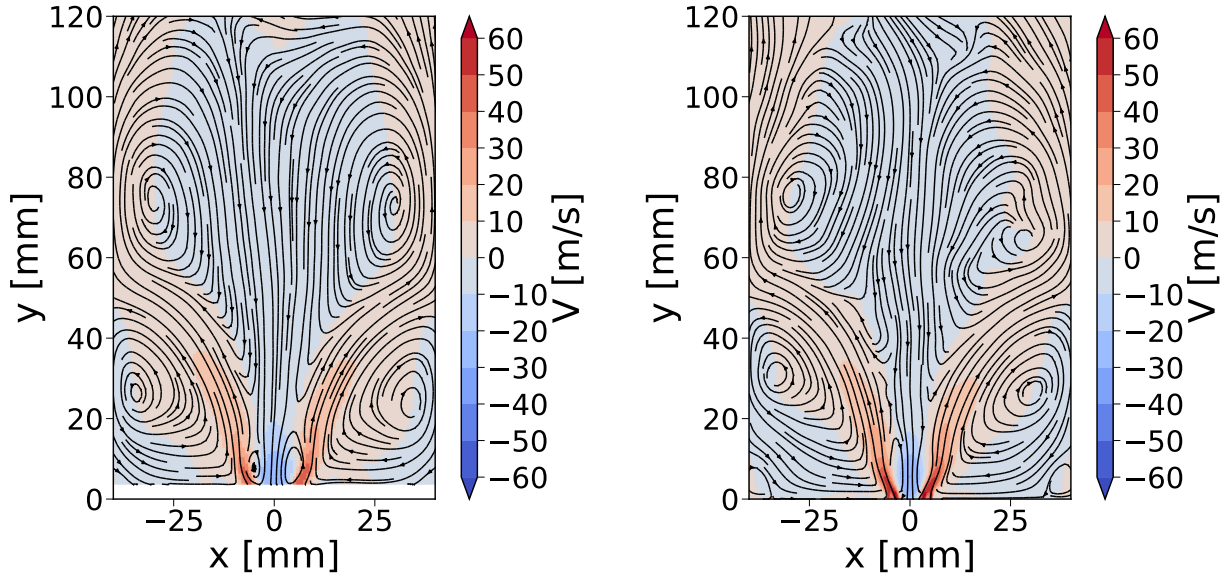


Figure 9.4: Experimental (left) and numerical (right) time-averaged axial velocity fields of the non-reactive flow in the SSB. The PIV data starts at $y = 5$ mm

and experimental uncertainties. The inner recirculation zone is perfectly captured, and is not closed at the height of 20 mm.

Similarly, the time-averaged RMS velocity profiles for the three components are compared to measurements in Fig. 9.6 at the same heights above the burner.

The agreement is here again very good, although showing slightly more difference compared to the mean velocity as a small overprediction is observed.

9.1.3 Reactive two-phase flow

The set-up for the reactive two-phase flow requires additional parameters given in Section 9.1.3.1 and Section 9.1.3.2 details the spray injection.

9.1.3.1 Numerical parameters

The reactive flow computation is started with a two-step chemical scheme (BFER scheme [94]) containing 6 species and 2 reactions to obtain a fast first converged solution. Then the intermediate species of the ARC scheme are added to the gaseous mixture, the droplet composition is changed to introduce several species and the simulation is converged again. The numerical set-up for the 3D reactive flow is summarised in Table 9.4.

The same numerical parameters of the cold flow are kept. In addition, the combustion/chemistry interaction is modelled by a thickening flame model [266] with a global Charlette efficiency model [41].

The spray is described with the Euler-Lagrange formulation, using the evaporation model from Abramzon & Sirignano [1] and the drag model from Schiller & Naumann [279]. The FIM-UR model [274] is used for injection and enables a spatial size-distribution of the droplets. The injection diameter and angle are both from the experiment, but the injection angle was corrected from 30° (measured) to 20° to numerically avoid accumulation of particle in the chamber, which would increase the computational time. Indeed, as the pressure vortex core goes very deep in the swirler, droplets were found to be stuck in the

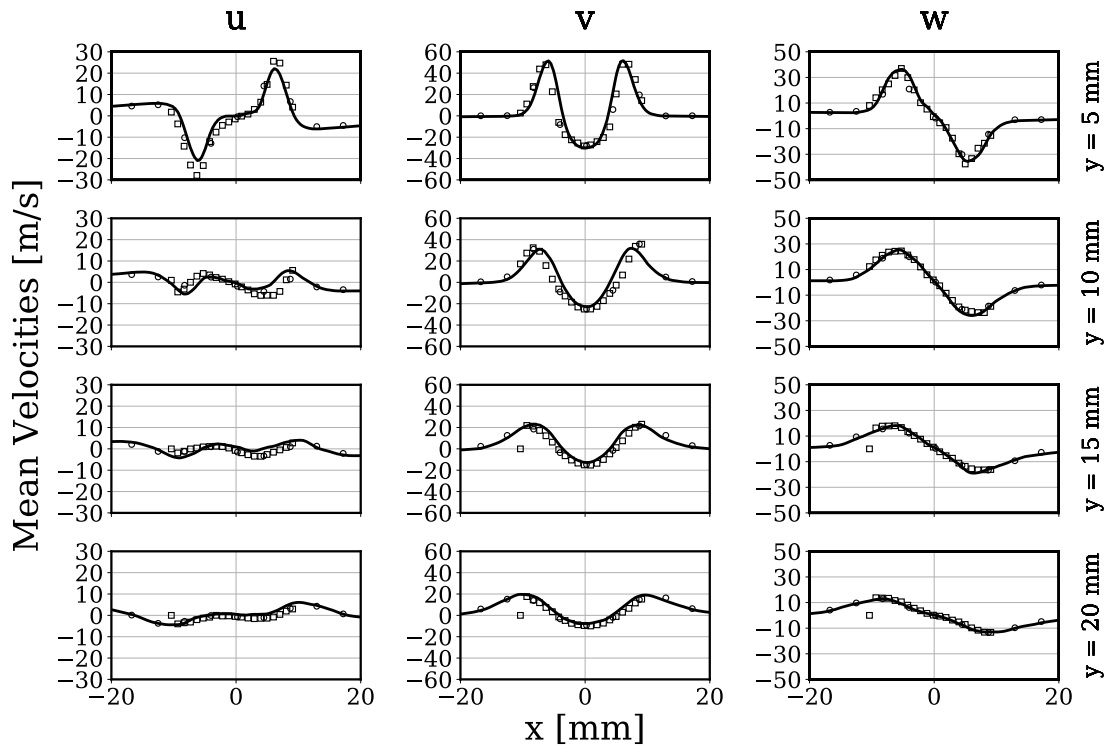


Figure 9.5: Time-averaged mean velocity profiles of the non-reactive flow at different heights above the burner: comparison between LES and PIV.

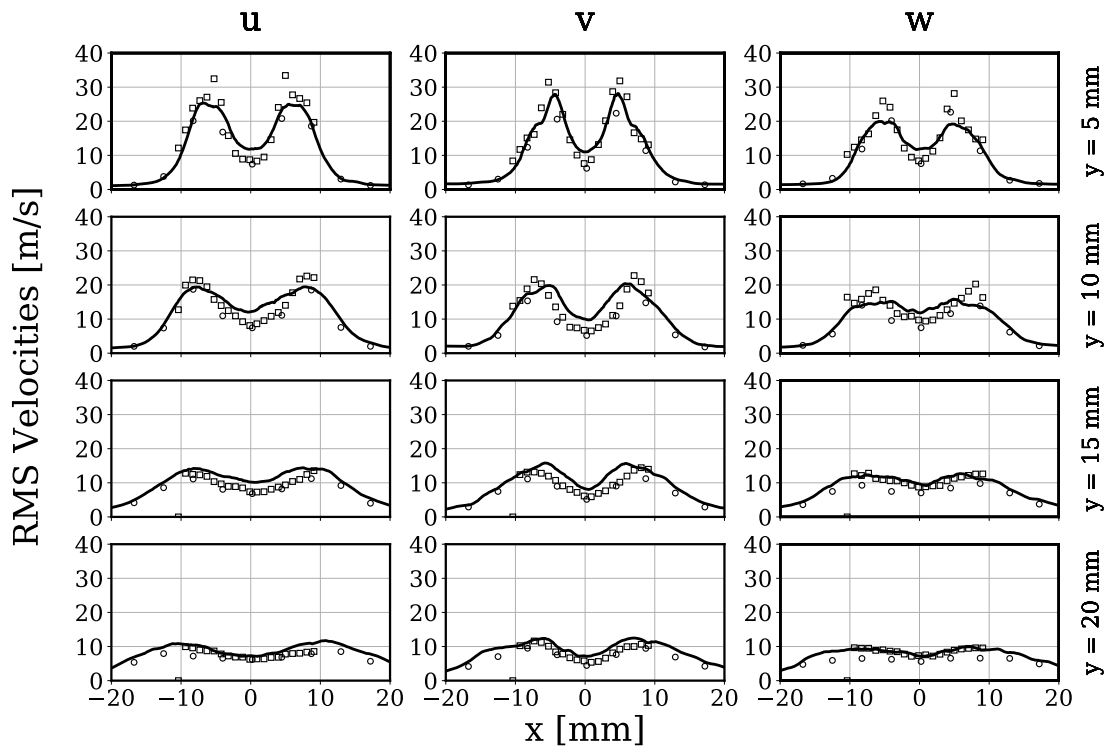


Figure 9.6: Time-averaged RMS velocity profiles of the non-reactive flow at different heights above the burner: comparison of LES with PIV.

Numerical models	
Convective scheme	Lax-Wendroff [163] of order 2
Diffusive scheme	Finite element of order 2
Artificial viscosity model	Colin [52] based on ρu and ρY
LES closure	WALE model [93]
Combustion/chemistry interaction	TF-LES model [36] with Rochette sensor [266] with Charlette efficiency model [41]
Liquid properties	
Modelling	Lagrangian
Evaporation model	Abramzon & Sirignano [1]
Drag model	Schiller & Naumann [279]
Injection type	FI-MUR [274]
Injection diameter	0.35 mm
Injection angle	20
Distribution type	Numerical Rosin-Rammler
Walls	
Gaseous	Experimental temperature profiles for the combustion chamber and the baseplate (see after). Every other wall is adiabatic.
Liquid	Complex interaction on the swirler walls, slip on the rest of the walls and exit at the end of the domain [131]

Table 9.4: Numerical set-up for the reactive flow simulation of the SSB.

swirler vanes and take a long time before going out. Moreover, this slight change of angle was tested and did not have a significant impact on the flame shape, since the droplets' motion in the film region is mostly driven by the surrounding gaseous flow and not the initial velocity. A numerical Rosin-Rammler size distribution is set with $d_{32} = 37 \mu\text{m}$ and $q = 2.1$, determined via an optimisation procedure explained in Section 9.1.3.2.

Gaseous wall temperatures were computed at the baseplate and at the chamber walls from experimental temperature fields for the given operating point (see Fig. 9.7). The isothermal boundary condition is then imposed with a heat flux formulated as a relaxation term, with a relaxation coefficient of 0.9.

Wall conditions for the liquid phase are imposed as slipping particles except on the swirler walls. Indeed, as already mentioned the spray impacts these walls, forms a film and re-atomises at the wall tips. A complex interaction model is therefore used, using the droplet velocity and temperature at impact as explain in Section 5.1.2. The roughness of the wall is set to $1 \mu\text{m}$ (typical value for quartz walls).

9.1.3.2 Droplet diameter distribution at injection

Droplet diameters and velocities have been measured in the experiment at $y = 15 \text{ mm}$ and $y = 25 \text{ mm}$ planes in the hot flow, after the flame was stabilised. Therefore, a methodology must be developed to determine the diameter distribution.

The idea is to optimise the injected spray parameters to recover the observed flame shape. This optimisation uses a surrogate model, built with a Gaussian process, from a set of simulations sampling the parameter space. The following paragraphs explain the

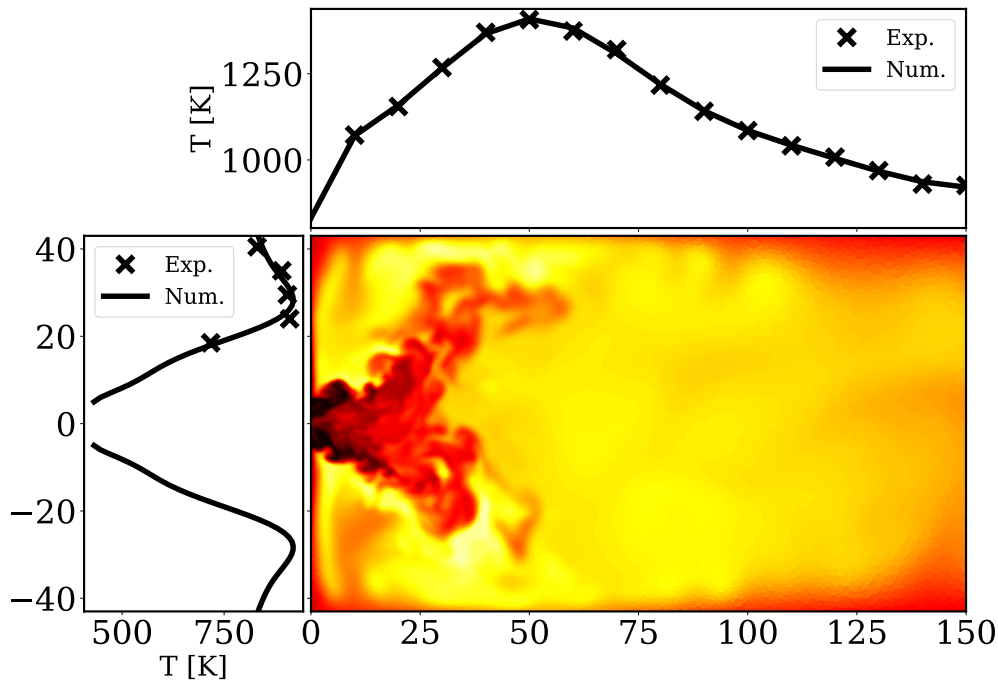


Figure 9.7: Temperature field and profiles at the walls of the SSB combustion chamber.

methodology that was set up and the results obtained that enabled guessing the diameter distribution at the injection.

The two parameters to be optimised are the Sauter Mean Diameter d_{32} and the spread parameters q of the Rosin-Rammler distribution. A **Design of Experiment (DoE)** is first built, which samples the parameter space with 20 simulations in the range $10 \mu\text{m} < d_{32} < 60 \mu\text{m}$ and $1 < q < 20$. The simulations are run for two flow-through times (approximately 10 ms). The DOE samples allow then to build a surrogate model for the error function, which compares the numerical solution to the experiment. The point of the parameter domain which minimises the error function gives the Rosin-Rammler distribution parameters to be used in the LES.

The error function was defined as:

$$Q = R^2 = 1 - \frac{\sum_i (y_i - y_i^{exp})^2}{\sum_i (y_i - \bar{y}_i)^2} \quad (9.5)$$

with y_i the numerically calculated quantity, y_i^{exp} the experimental value, and \bar{y}_i the mean of the chosen quantity. In this study, y_i and y_i^{exp} are taken along a line at a certain height above the burner. This expression of Q corresponds to an evaluation of the **coefficient of determination** or R^2 which assesses if the two sets of data are proportional or uncorrelated:

- if $R^2 = 1$, y_i and y_i^{exp} are proportional and data are matching.
- if $0 < R^2 < 1$, the numerical data follow the same trend as the experimental data, but both are not proportional.
- it can happen that $R^2 < 0$, which means that the two data sets are less correlated than the auto-correlation of the numerical data set.

The BATMAN (Bayesian Analysis Tool for Modelling and uncertainty quaNtification) code [269], [270] was used to perform this optimisation. This python code, developed by CERFACS, allows doing statistical analysis (sensitivity analysis, uncertainty quantification, moments) of any kind of data.

The quantities y_i chosen to build the error function are droplet size and velocity. These quantities indeed react faster to a change of injection parameters than the thermal gaseous fields, such as heat release rate or temperature.

Response surfaces are displayed in Fig. 9.8 for characteristic diameters: the mean diameter d_{10} at $y = 15$ mm (9.8a), the q parameter at $y = 25$ mm (9.8b), and velocities: axial component (9.8c) and transversal component (9.8d) at $y = 15$ mm. Black points represent the DOE sample points on which the surrogate model was built.

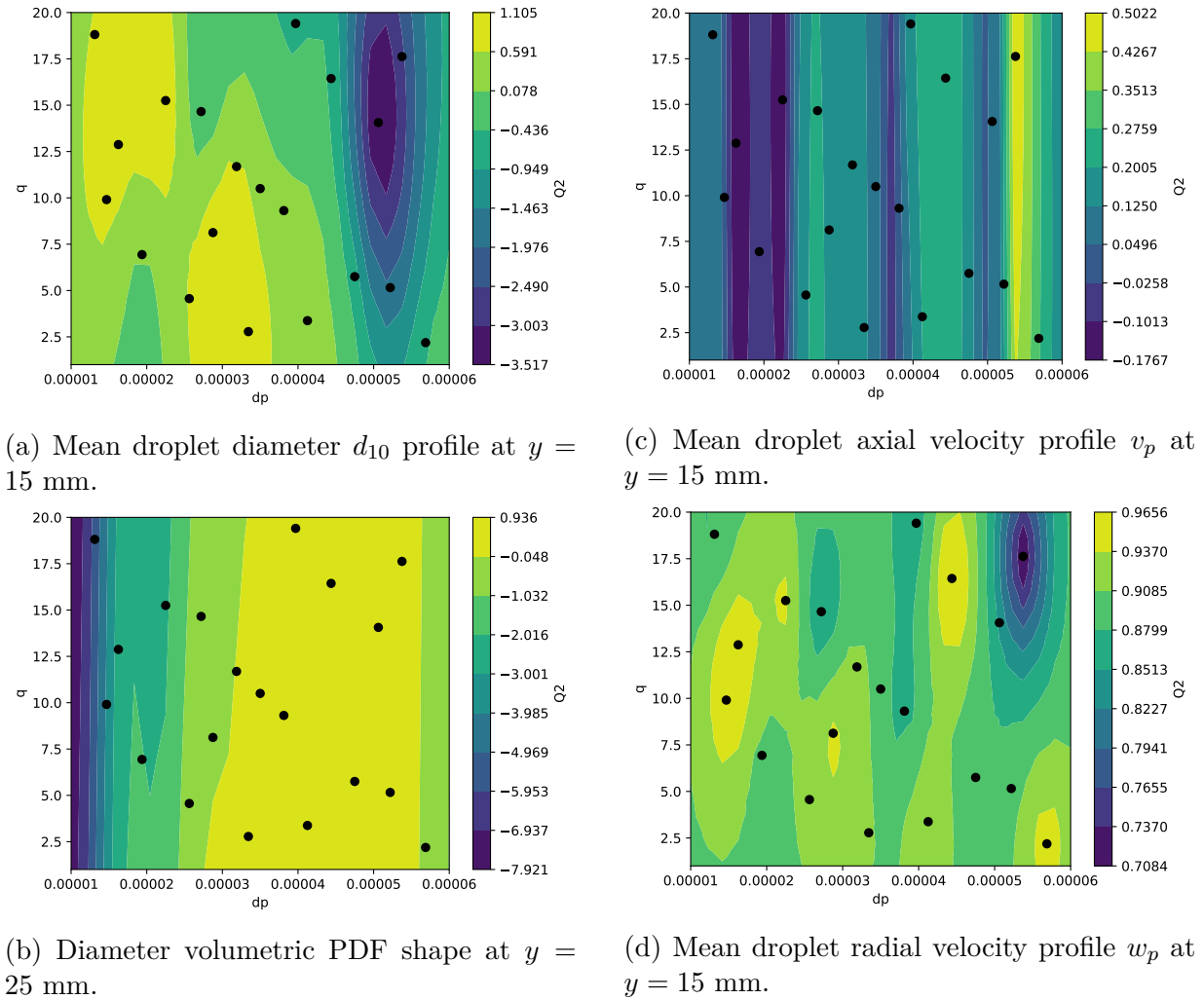


Figure 9.8: Outputs of BATMAN: contour plots showing the DoE (black points) and the response surfaces (colormap)

Such computations are very costly, as 20 computations of 10 ms of physical time are required for every operation point. The corresponding computational time is estimated in Appendix D for one flow-through time (5 ms). As a consequence of the short physical times, u_p (not shown here), v_p and w_p do not reveal significant differences between the results because the flame did not have sufficient time to adapt to the distribution change. This confirms that optimising on the spray properties, when available, is more efficient to

determine the injection spray parameters.

The response surface of d_{10} at $y = 15$ mm, shows that injecting small diameters gives the best results compared to the experiment. Overall, the spread parameter q seems to have very small influence. On the contrary, for the PDF profile error function at $y = 25$ mm, injecting medium diameters gives the best fit with the experimental data. Thus, larger SMDs at injections are most representative of the liquid volume seen by the flame at $y = 25$ mm.

Overall, the chosen set of distribution parameters is the one fitting best the numerical (d_{10}) and volumetric properties (volume PDF): $d_{32} = 32 \mu\text{m}$, $q = 2.7$. Further change of the distribution by trial and error around that point have finally shown that the best point was the following:

$$\boxed{d_{32} = 37 \mu\text{m}, q = 2.7} \quad (9.6)$$

Overall, two main conclusions can be drawn from the methodology:

- computations made with BATMAN are able to determine the best (d_{32} , q) couple.
- the spread parameter has a small effect on the results, and another parameter might be more interesting to be more precise on the selected point.

Note that with this methodology, the size distribution is fitted for a single operating point and may not be valid for another one or for a different fuel. However, in the absence of more data, the same size distribution will be used for all cases studied in this work.

9.2 Stable spray flame: impact of the chemical modelling for a standard fuel

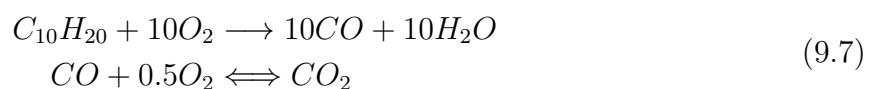
The SSB configuration is first investigated in stable condition at the selected operating point. Both the simple 2-step and the ARC scheme for Jet-A1 are compared. First, the chemical and evaporation properties are presented for both fuel models in Section 9.2.1. Then the time-averaged quantities of the SSB turbulent spray flames are analysed in Section 9.2.2. Finally, Section 9.2.3 investigates the 2-step flame instantaneous structure, and is compared to the ARC flame in Section 9.2.4.

9.2.1 Fuel properties

Fuel properties are presented to highlight chemical differences (9.2.1.1) and liquid phase differences (9.2.1.2) between the two fuel models.

9.2.1.1 Chemical properties

The mono-component surrogate used is the 2-step chemistry (hereafter denoted 2S) based on a kerosene oxidation followed by a $CO-CO_2$ equilibrium [94] and containing six species:



The reaction rates are based on a simple Arrhenius law:

$$\begin{aligned} \omega_1 &= k_{f,1}[C_{10}H_{20}]^{0.55}[O_2]^{0.9}f_1(\phi) \\ \omega_2 &= k_{f,2}[CO][O_2]^{0.5}f_2(\phi) \end{aligned} \quad (9.8)$$

where ω_j are the reaction rates of equation j and $f_j(\phi)$ are the Pre-Exponential Adjustment (PEA) functions [94] used to recover the correct behaviour from lean to rich combustion. To simplify the results, ARC A1 will be called A1 in the following.

This mechanism ($H/C = 2$, $LHV = 43.822$ MJ/kg) has almost the same net heat of combustion than the multi-component surrogate (hereafter denoted A1) used in the ARC chemistry (presented in Section 7.1 $H/C = 2$, $LHV = 43.869$ MJ/kg). Equilibrium quantities at $\phi = 0.8$, $T = 323.15$ K and $P = 1$ bar are compared in Table 9.5:

Fuel	T_{ad}	Y_{H_2O}	Y_{CO}	Y_{CO_2}	Y_{O_2}
2S	2093.64	0.0663	0.00141	0.160	0.0450
A1	2084.54	0.0654	0.00133	0.160	0.0443

Table 9.5: Equilibrium state of the different mechanisms for A1 at $\phi = 0.8$, $T = 323.15$ K and $P = 1$ bar.

For the studied operating point, the adiabatic temperature is $10^\circ C$ higher for the 2-step chemistry. The amount of products is very close, with the ARC case exhibiting slightly lower oxygen O_2 , CO and H_2O levels, due to the presence of other minor species, not displayed in the Table but representing a small but non-negligible fraction of the mass at equilibrium. As the difference between the detailed mechanism and the ARC A1 are small, only the ARC A1 will be considered as reference here and called A1.

Figure 9.9 displays the auto-ignition delay time at $P = 1$ bar as a function of the temperature, and the laminar flame speed at $P = 1$ bar and $T = 323.15$ K as a function of the equivalence ratio. Transport properties follow the simple transport formulation, and the list of Schmidt and Prandtl numbers is given in Appendix B for both fuel models.

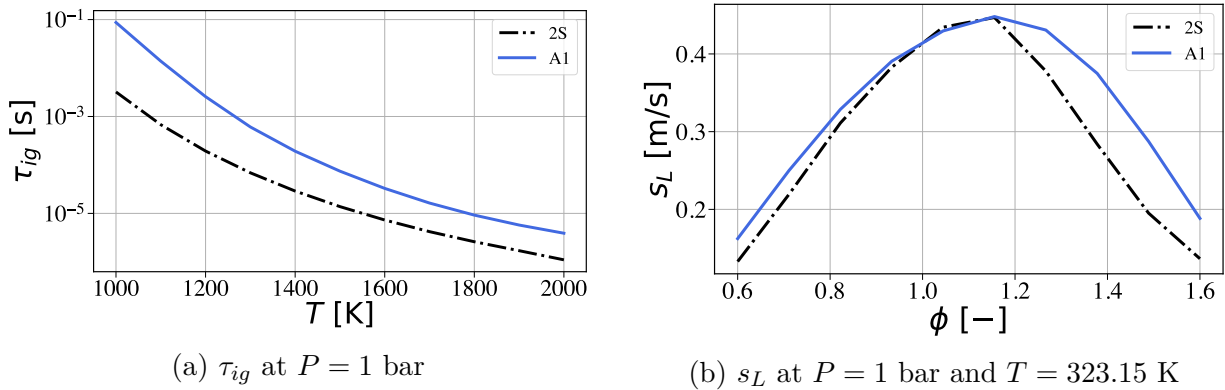


Figure 9.9: Comparison of chemical properties between the 2S and A1 fuel models of A1.

Overall, the 2S mechanism exhibits a higher reactivity compared to the ARC scheme, with an auto-ignition delay time one order of magnitude lower for higher temperatures and two order of magnitude lower for lower temperatures. The laminar flame speed is very close to A1 mechanism in the lean side and near stoichiometry. Higher differences are observed in the rich side, where the 2S laminar flame speed is lower than the ARC one. This is a known error of 2-step schemes [94], usually ignored as engines always operate at a global lean equivalence ratio ($\phi = 0.8$ here). However, spray flames may locally burn at high equivalence ratio, leading to possible local error with the 2S scheme.

Pollutant emissions are shown in Fig. 9.10, namely CO maximum mass fractions and CO_2 final mass fraction for $P = 1$ bar and $T_{fresh} = 323.15$ K as functions of the equivalence ratio.

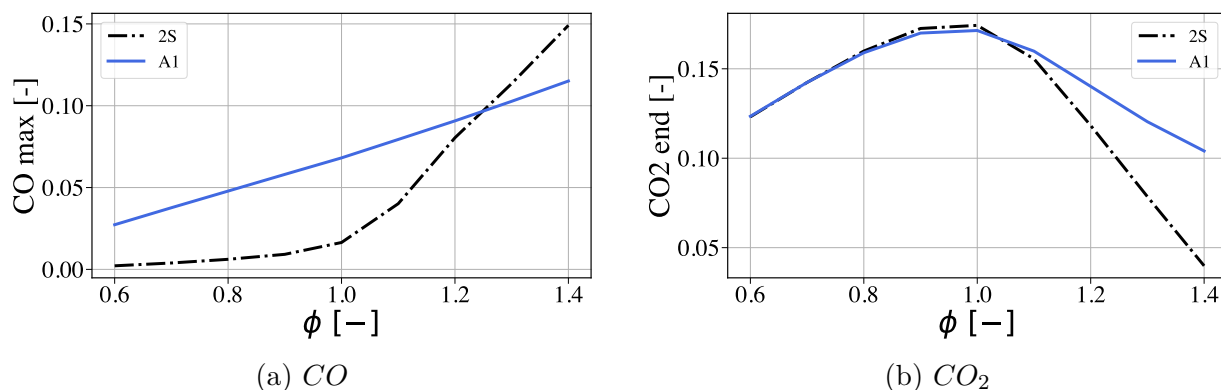


Figure 9.10: Comparison of pollutant emissions in a 1D premixed A1 flame at $P = 1$ bar and $T_{fresh} = 323.15$ K between 2S and ARC schemes: maximum CO and final CO_2 mass fractions as functions of the equivalence ratio.

The 2S scheme strongly under-predicts the production of CO up to $\phi = 1.2$, then over-predicts it. This is the result of a faster CO - CO_2 equilibrium in the 2S scheme, which was design to confine chemical activity in a thin zone [94]. Nevertheless, the final main products (CO_2 and H_2O (not shown)) are well retrieved for lean equivalence ratio. In the rich side, the 2S scheme tends to predict less carbon dioxide than the ARC scheme. This is consistent with the modified CO - CO_2 equilibrium already seen in the left figure of Fig. 9.10.

For the targeted operating point, the ratio of CO between the two schemes is about 5: with such an error, the comparison of CO between the two schemes is meaningless and will not be analysed.

9.2.1.2 Evaporation properties

First, the density differs slightly between the two fuels, with $\rho_{liq}^{2S} = 780$ kg/m³ compared to $\rho_{liq}^{A1} = 775$ kg/m³ (the liquid density is constant in AVBP, see Section 8.1).

The liquid properties important for vaporisation are shown for both fuels in Fig. 9.11, namely the saturation pressure and the vaporisation enthalpy.

The 2S boiling temperature (which is defined as the point where P_{sat} encounters the ambient pressure value) is slightly higher for 2S than for A1 with the given composition. Looking at the latent heat of vaporisation, the 2S case misbehaves above the boiling temperature as it increases, but this part of the diagram is never reached in the simulation and may be disregarded. Below the boiling temperature, the 2S case is found to require less energy to evaporate than the A1 case and is therefore expected to have a higher vaporisation rate. However when looking at Fig. 9.12 where the DLR experimental results (presented in Section 8.1.2) for A1 are compared to the numerical results for both 2S and A1, in terms of droplet diameter and liquid enthalpy, the evaporation of the 2S fuel is surprisingly longer. The reason for it is the liquid enthalpy, displayed on the same figure, which is higher for 2S than for A1.

Overall, it is found that the 2S mechanism leads to slightly slower evaporation and exhibits a faster CO - CO_2 reaction, leading to a wrong prediction of CO . The flame

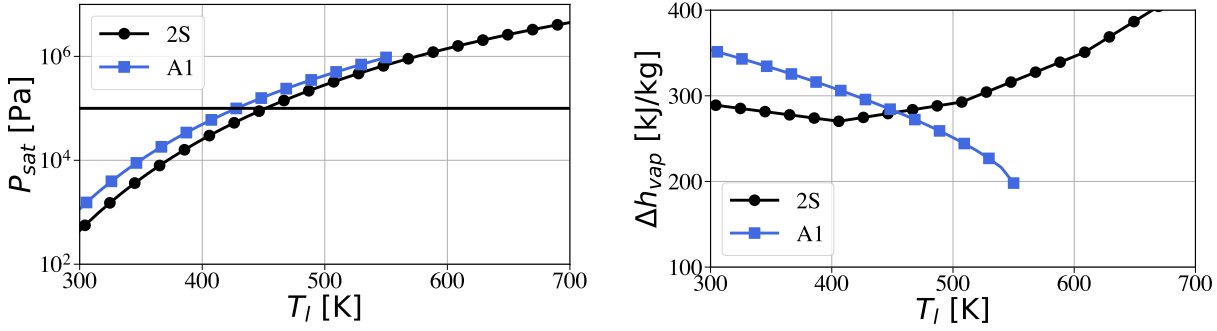


Figure 9.11: Liquid properties as a function of the droplet temperature for both fuels 2S and A1.

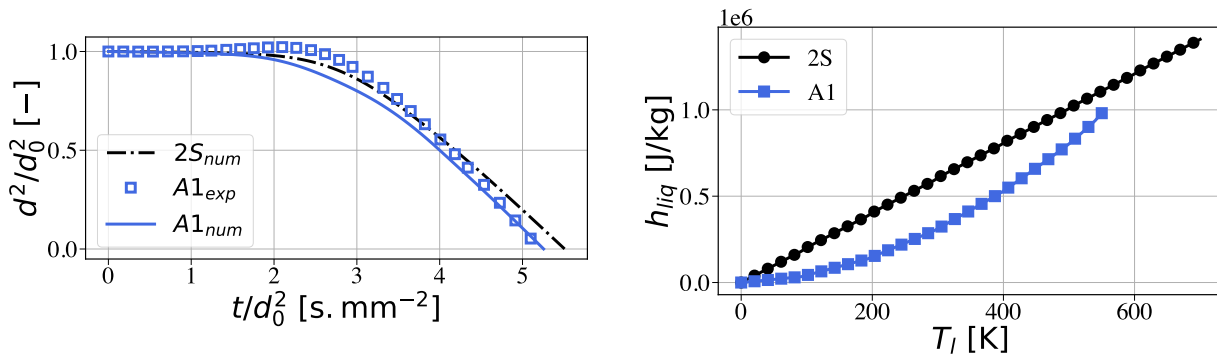


Figure 9.12: Evolution in time of the droplet diameter (left) for the two fuel models and experiment of DLR, and liquid enthalpy as a function of liquid temperature (right) for the two fuel models (right).

characteristic parameters such as the laminar flame speed and the final equilibrium are however valid on the lean side.

9.2.2 Results: mean solution

This section analyses the mean solutions obtained with both fuel models and their comparison to the experiment. Section 9.2.2.1 details the comparisons in terms of two-phase flow properties, Section 9.2.2.2 shows the differences related to flow dynamics. Section 9.2.2.3 compares the end state with equilibrium. Section 9.2.2.4 finally presents the thermal fields.

9.2.2.1 Two-phase flow

Figure 9.13 presents the mean diameter and the Sauter mean diameter profiles at $y = 25$ mm for both fuels. As well, diameters representing 10% (d_{01}), 50% (d_{05}) and 90% (d_{09}) of the total volume are plotted.

All diameter profiles fit well the experimental curves. This confirms that the injected droplet size distribution, determined by optimisation with BATMAN (see Section 9.1.3.2) is correct with the modelling assumptions made for the spray formation (no lip atomisation and no secondary atomisation).

The three droplet velocity profiles (radial, axial and transverse) are now compared to

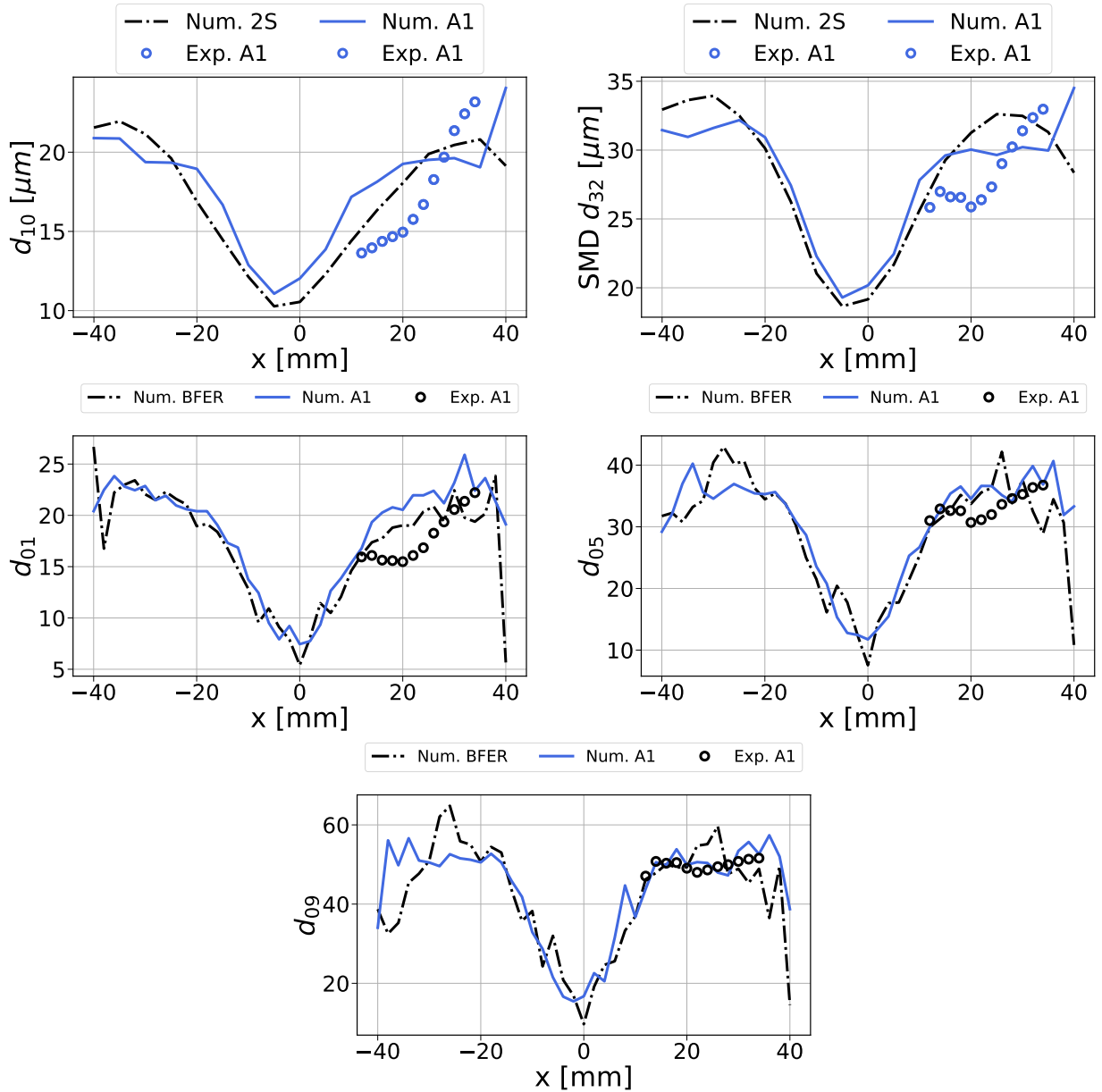


Figure 9.13: Characteristic diameters: d_{10} , d_{32} , d_{01} , d_{05} and d_{09} for A1 in the experimental (o) and in the numerical simulation with 2S (-) and A1 (-) at $y = 25$ mm.

the experimental ones on Fig. 9.14.

Overall, all the velocity components are in very good agreement with the experiment. The axial and radial velocities are slightly underestimated and shifted towards the centre. The pressure drop is well predicted on the axial velocity profile.

The three droplet velocity profiles (radial, axial and transverse) are now separated in diameter classes and compared to the experimental ones on Fig. 9.15.

The sensitivity to the different diameters is very small for the experimental work, for $y = 15$ mm and for $y = 25$ mm. This small sensitivity is well retrieved for the axial velocity v_p and the transversal velocity w_p . For radial velocity profiles u_p , small droplets have a very different behaviour than the experimental velocities, with droplets associated to the lowest diameters showing a lower velocity.

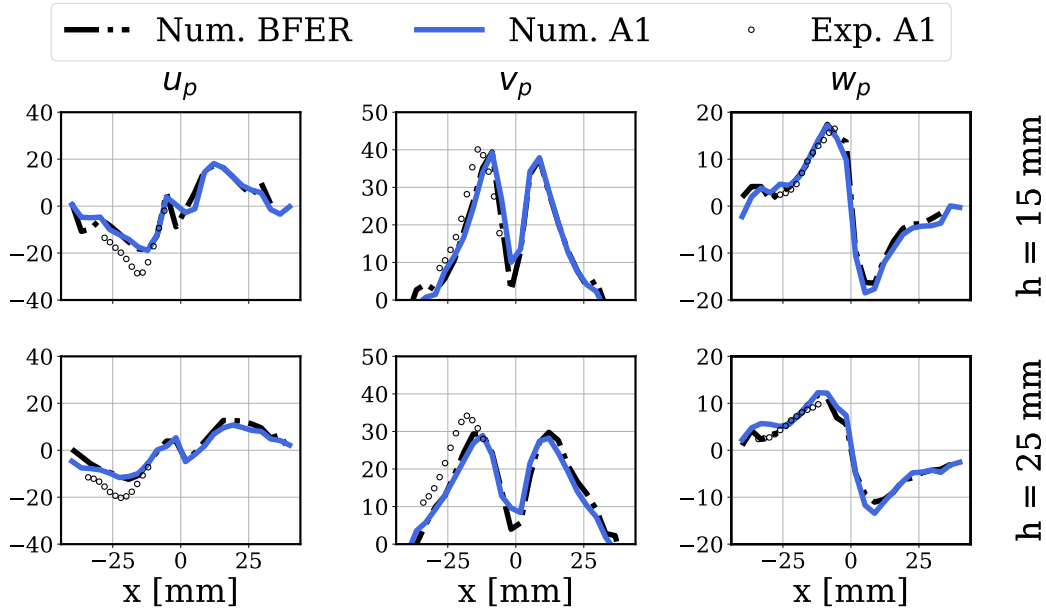


Figure 9.14: Experimental and numerical droplet velocity profiles of A1 at $y = 15$ mm and at $y = 25$ mm: radial u_l , axial v_l and transverse w_l .

Overall, the droplets with the lowest velocity have the smallest diameter, with small Stokes number making them behave like tracers. For the axial velocity profiles, droplets at the centre exhibit a very small velocity compared to the droplets with the highest diameters.

Finally, Fig. 9.16 compares the normalised volume fraction α_l fields. In the experiment, it was measured as a probability of presence, counting each detected droplet at a given location in a control volume. The data is not shown in the region close to the injector exit, where measurements were not possible due to a too dense spray there.

From these results, it may be concluded that the spray angle is about 10° lower in both numerical simulations. For the 2S computation, the droplet relative levels are in fairly good agreement with the experiment, with droplets evaporating closer to the flame. For the A1 case, the droplets evaporate slightly later in the flame but at the same distance from the side combustor walls.

9.2.2.2 Velocity

Numerical time-averaged gaseous velocity profiles as well as the RMS values are compared with the experiment in Fig. 9.17 at different heights over the burner ($y = 20$ mm and 40 mm). No measurement could be realised closer to the swirler exit, where the reactive flow does not allow PIV measurements.

The LES captures very well the reactive gaseous flow in the three directions. Both simulations give very similar results. The inner central recirculation zone is slightly underestimated, but the flow opening angle and swirl are well retrieved. The RMS quantities are also well predicted by the LES, which captures the right profiles in shape and level despite some discrepancies. Axial and radial RMS velocity profiles are overestimated in the numerical work at $y = 20$ mm but show good results at $y = 40$ mm. On the contrary, the transverse RMS velocity is well-captured at $y = 20$ mm but vanishes at $y = 40$ mm

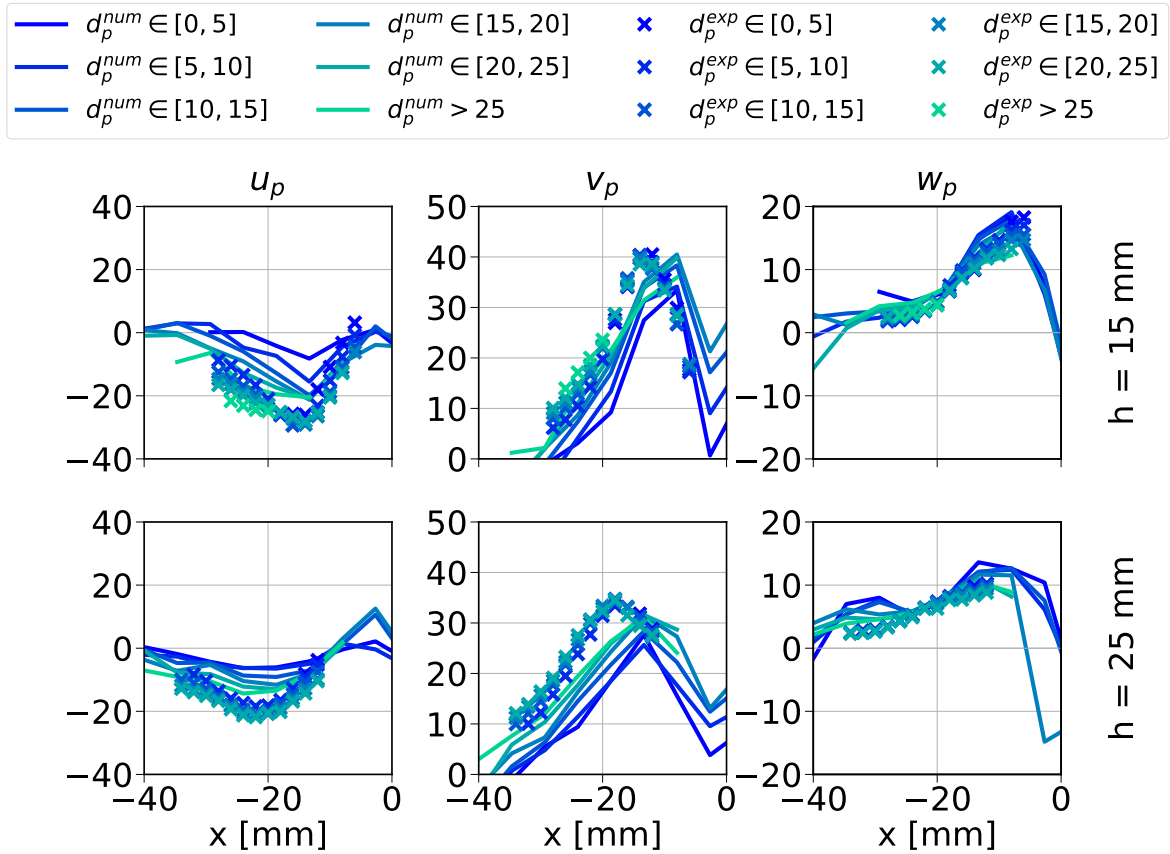


Figure 9.15: Experimental and numerical droplet velocity profiles (radial u_l , axial v_l and transverse w_l) of 2S at $y = 15$ mm and at $y = 25$ mm per diameter class in the left half -40 mm $< x < 0$ mm of the burner.

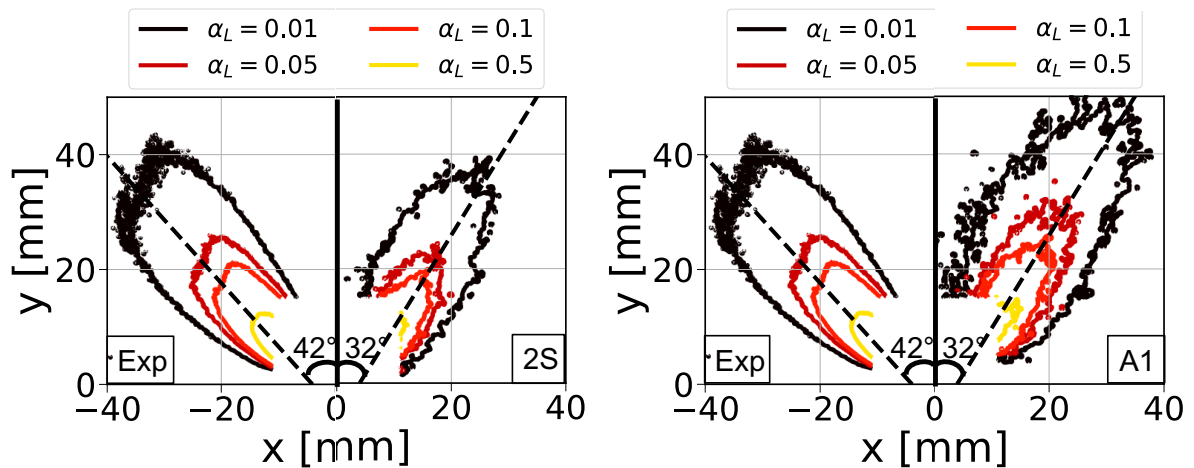


Figure 9.16: Fields of normalised volume fraction α_L : comparison of experiment (left half) with 2S (left figure) and A1 (right figure).

where measurements still see high level. In fact in the experiment no significant change is observed between the two heights, whereas RMS velocities decrease with heights in the simulations. This may be the result of the coarser mesh downstream, as the RMS values only

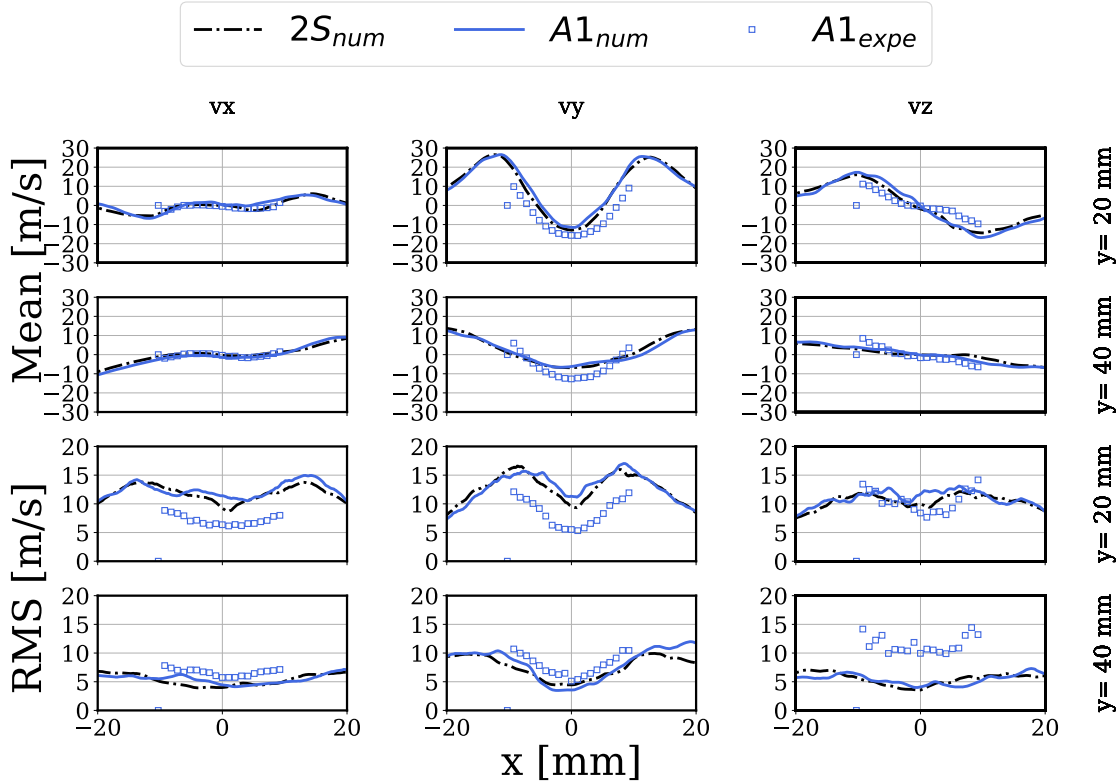


Figure 9.17: Time-averaged mean and RMS gas velocity profiles of the reactive flow for 2S and A1 cases at different heights over the burner and compared to the PIV.

report the filtered fluctuations, missing the sub-grid scale contributions.

9.2.2.3 Wall heat losses & equilibrium

Wall heat losses are reported for the 2S and the A1 simulation in Table 9.6, distinguishing the chamber walls Q_{walls} and the baseplate $Q_{baseplate}$.

Fuel	Q_{walls} [W]	$Q_{baseplate}$ [W]	Q_{tot} [W]
2S	-2815	-1039	-3854
A1	-2928	-993	-3921

Table 9.6: Wall heat losses for 2S and A1.

Overall, heat losses are very close for the two cases, with slightly higher values in the A1 case are explained by more droplets burning along the walls. To check the consistence of the results, a thermal balance calculation is performed, based on the following equation:

$$C_{p_{burnt}}T_{final} = C_{p_{ad}}T_{ad} - Q_{tot} = \int HRRdV + C_{p_{init}}T_{init} - Q_{tot} - \Delta H_{vap} \quad (9.9)$$

with ΔH_{vap} the total enthalpy change due to evaporation, estimated at the boiling temperature. The adiabatic temperature T_{ad} is calculated with a constant enthalpy equilibrium calculation of Cantera. Subtracting the wall losses Q_{loss} obtained in the simulation gives the final temperature $T_{eq,theo}$ that the system should eventually reach at equilibrium. This

Fuel	T_{ad} [K]	$T_{eq,theo}$ [K]	$T_{final,num}$ [K]
2S	2093.54	1287	1385
A1	2084.54	1239	1311

Table 9.7: Final temperatures for 2S and A1.

is to be compared to the time-averaged numerical final temperature at the exit plane in the simulation $T_{final,num}$. Results are summarised in the Table 9.7:

As expected, the difference in adiabatic temperature for both fuel is small (less than 1 % maximum), as both have very close LHV. As heat losses are slightly higher for the 2S computation, the difference in terms of theoretical equilibrium accounting for heat losses is higher (50 K).

The measured final temperature shows roughly the same difference (64 K higher for 2S than for A1). In both cases, the obtained final temperature is significantly higher than the equilibrium temperature. This indicates that the mixture has not yet reached a steady homogeneous state at this location, due to both the non-uniform cooling of the burnt gas and the incomplete reaction process, which must adjust to the decreasing temperature. Moreover, thermal heat losses are applied all along the combustion chamber, which implies that the system is submitted to an enthalpy change and needs time to adapt to the final expected equilibrium.

The distance to equilibrium may be evaluated by comparing the time-averaged main species mass fractions at the exit plane, as shown in Table 9.8.

Fuel	Value	Y_{H_2O}	Y_{CO_2}	Y_{O_2}
2S	Theoretical	0.0663	0.162	0.0441
	Numerical	0.0638	0.1559	0.0514
A1	Theoretical	0.0663	0.162	0.0441
	Numerical	0.0644	0.1589	0.0477

Table 9.8: Comparison between theoretical equilibrium and numerical final fuel mass fractions for 2S and A1.

The final state is very close to the theoretical equilibrium for both cases, slightly closer for A1 than for 2S. In both cases, the oxygen mass fraction is higher than the equilibrium value while the product species values are lower, indicating incomplete combustion with droplets stuck in the swirler vanes. The average fields of CO , H_2O and CO_2 are compared for both cases in Fig. 9.18.

The CO_2 mass fraction fields look alike for both cases, featuring a high mass fraction in the ORZ, close to the value of the equilibrium for $\phi = 1.0$. H_2O fields on the contrary seem to be slightly different between both cases: A1 exhibits a higher content in the ORZ. Finally, CO mass fraction is around 10 times lower with the 2S scheme, as expected from the faster $CO-CO_2$ reaction.

9.2.2.4 Thermal fields

Figure 9.20 displays HRR fields, namely the direct view of the flame annotated with the different lines at which the profiles will be compared, the deconvoluted CH^* field in a vertical cut, to be compared with the simulated heat release rate integrated along the line-of-sight.

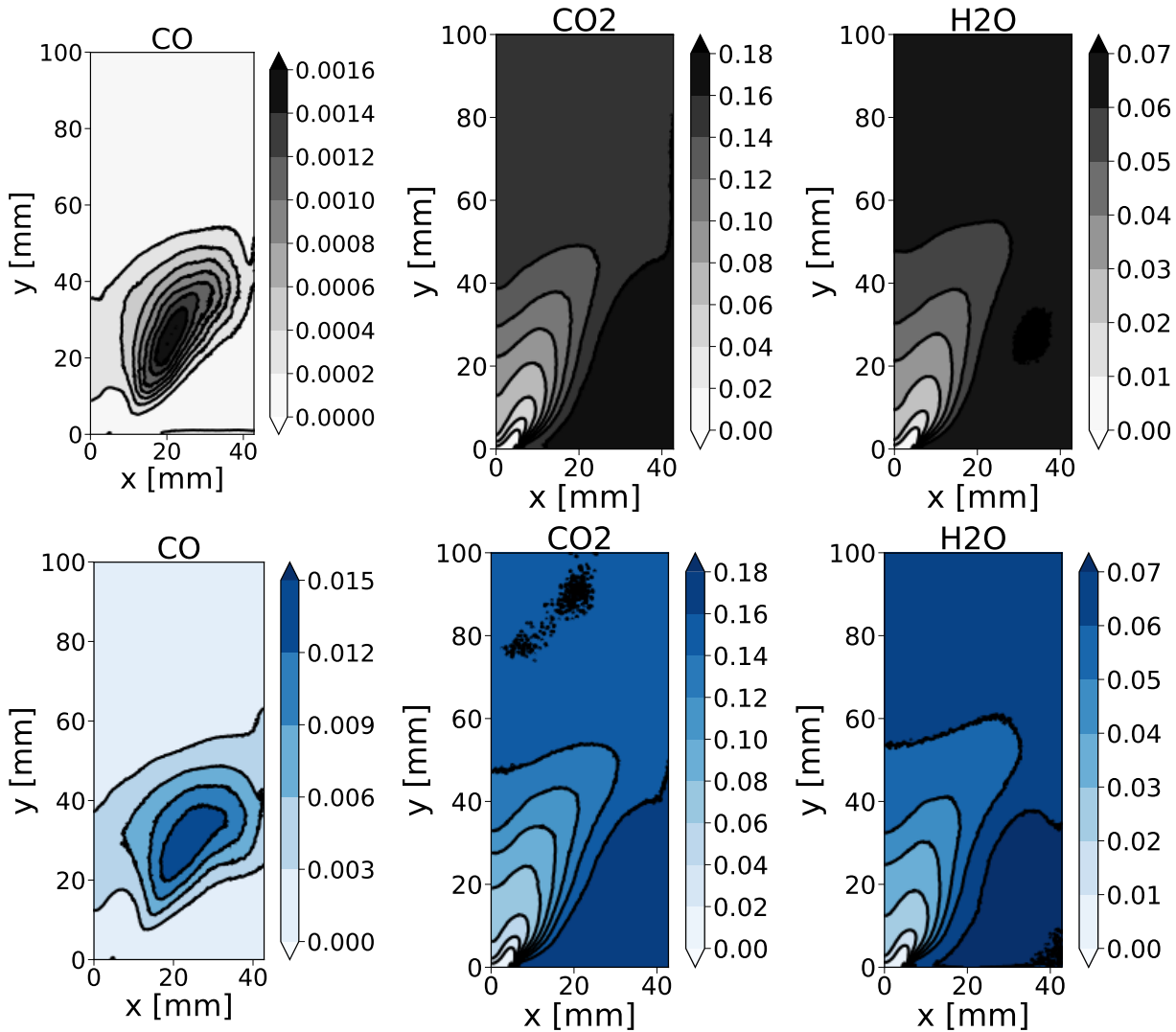


Figure 9.18: 2S (black colormap upper plots) vs A1 (blue colormap lower plots) product species mean fields in a vertical half-plane cut.

Both numerical heat release rate fields exhibit the same levels and the same V-shape. The 2S flame seems less diffuse than the A1 flame. The integrated profiles show that the 2S and A1 flames stabilise at the same location, both shifted toward the burnt gases compared to the experimental flame.

Figure 9.20 represents the cumulative integral of the normalised numerical heat release rate along the y -axis compared with the normalised experimental CH^* mass fraction.

2S and A1 flames are comparable to each other in terms of stabilisation location. However, A1 seems to be less thick and slightly shifted towards the burnt gases.

The above extensive comparison with experiment demonstrates that AVBP is capable of predicting the behaviour of the two-phase reactive flow in the SSB configuration. The comparison of two thermochemical models shows an overall similar behaviour but as could be expected a clear difficulty of simple chemistry to describe complex chemical phenomena such as CO production.

Figure 9.21 represents the resulting mean temperature profiles for the 2S and the A1 fuels along the axial line at $x = -20$ mm and at $x = 0$ mm and along a radial cut at $y = 15$ mm, $y = 25$ mm and $y = 35$ mm.

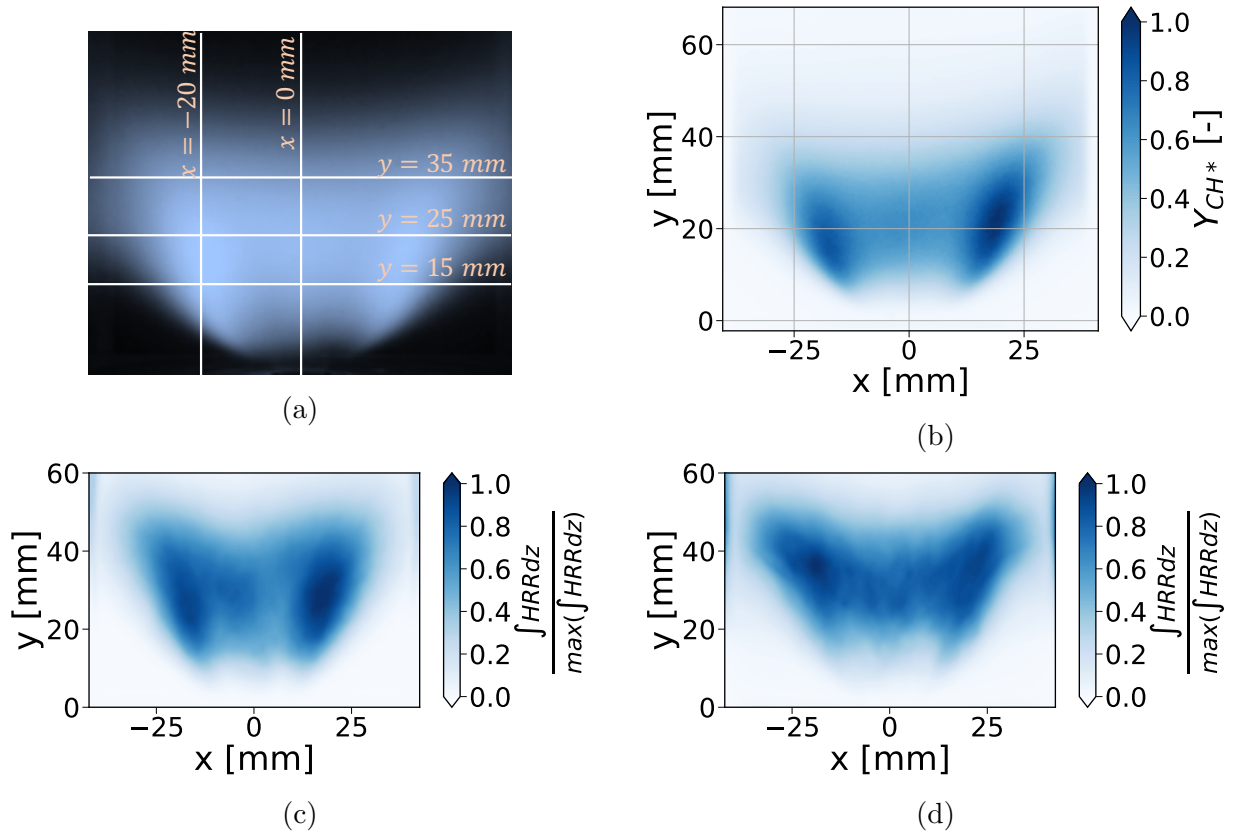


Figure 9.19: Time-averaged experimental profiles showing (a) direct view of the flame; (b) experimental deconvoluted CH^* field; (c) integrated heat release rate field, 2S case; (d) integrated heat release rate field, A1 case.

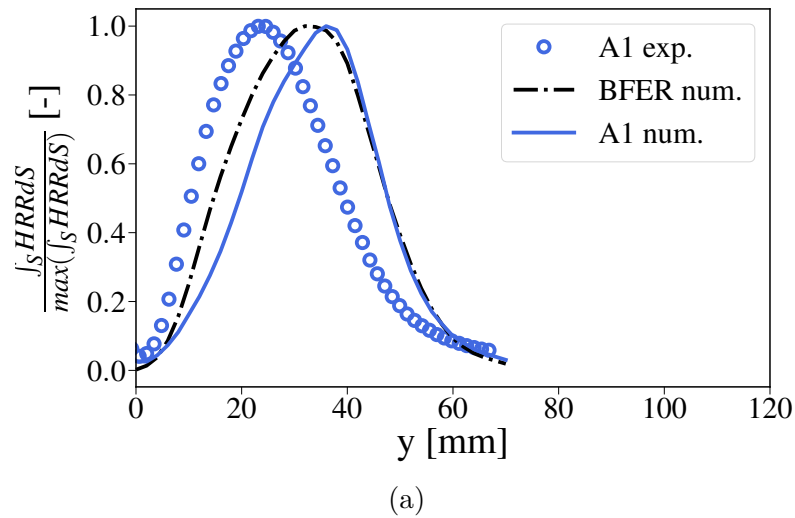


Figure 9.20: Average experimental CH^* , average 2S and A1 heat release rate integrated line along the central axis.

Both mean numerical fields exhibit smaller maximum values than experiment at all locations. At $x = 0 \text{ mm}$, both flames seem to be shifted towards greater y values. The maximum is obtained around $y = 70 \text{ mm}$ as in the experiment, but the value is about

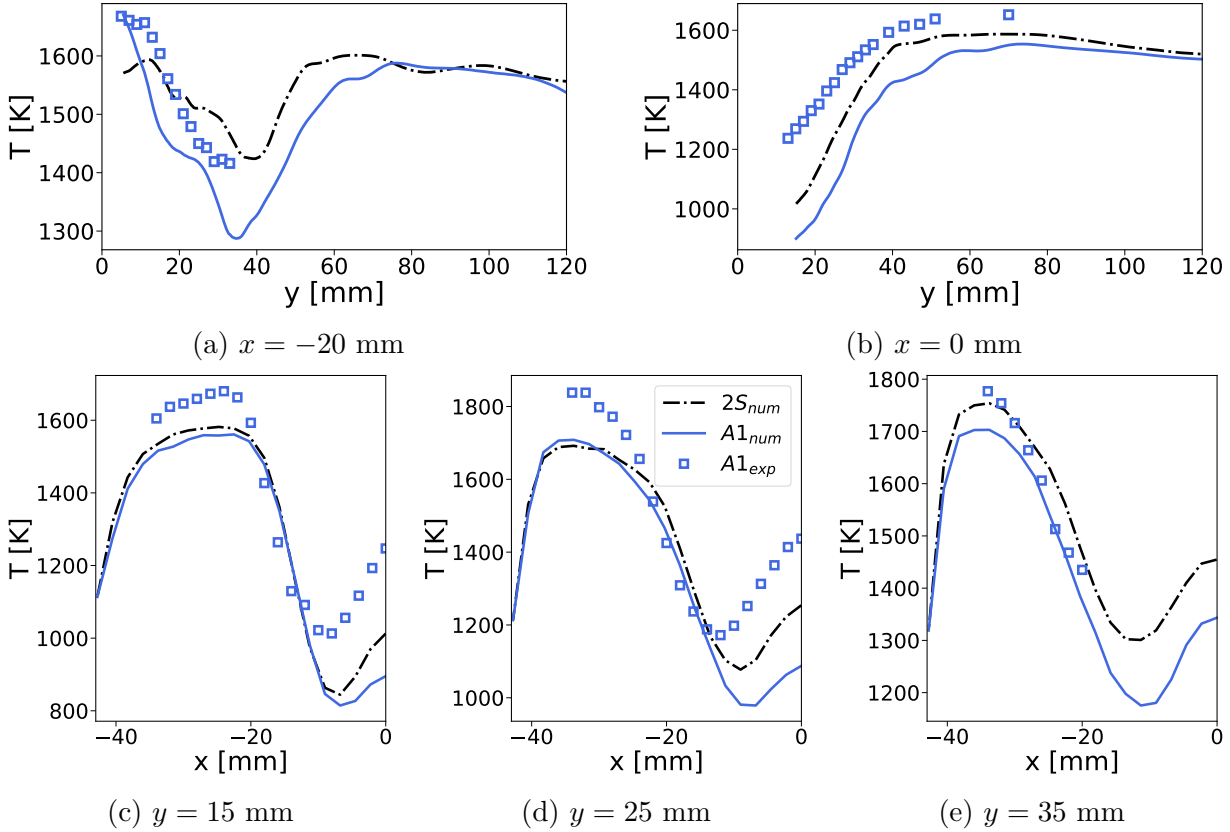


Figure 9.21: Experimental (o) vs numerical (-) 2S and A1 mean temperature profiles in the axial direction ($x = -20$ mm and $x = 0$ mm) and in the radial direction ($y = 15$ mm, $y = 25$ mm and $y = 35$ mm).

100 K lower. For all the radial plots, the temperature in the ORZ is lower for both fuels and the temperature variation in the low pressure zone. (-10 mm $< x < 10$ mm), although well retrieved, is not as pronounced as in the experiment. These differences in temperature can be related to the difference in the angle of the spray, which is lower in the simulation (see Section 9.2.2.1). As a consequence, the flame extends further in the axial direction, leading to a delayed temperature increase.

When comparing both fuels, the 2S flame appears shorter than the A1 flame. The temperature starts increasing closer to the injection plane, as shown in the $x = 0$ mm plot. Temperature in the ORZ seems to be the same for both fuels, except at $y = 35$ mm. This difference might be explained by the faster and stronger reacting behaviour of the 2S scheme, since the evaporation characteristics are nearly the same for both fuels.

To further investigate why the temperature profiles are different between both fuels, Fig. 9.22 compares the CARS measurements of DLR [38] at $y = 25$ mm to both simulations. The mean temperature (continuous line), as well as the T_{mp} (dotted line) the T_{05} and T_{95} (surface colour) introduced in Section 9.1.1 are plotted.

First, both the experimental and the numerical results exhibit a wide range of temperature, whether near the centre of the flow or towards the chamber walls. The temperature near the centre is found to vary between 1100 K and 1700 K in the experiment, between 900 K and 1520 K in the 2S case and between 850 K and 1350 K in the A1 case. Temperatures reached near the walls are lower in the computations than in the experiment.

The transition between the cold gases to the burnt gases seems to occur closer to the

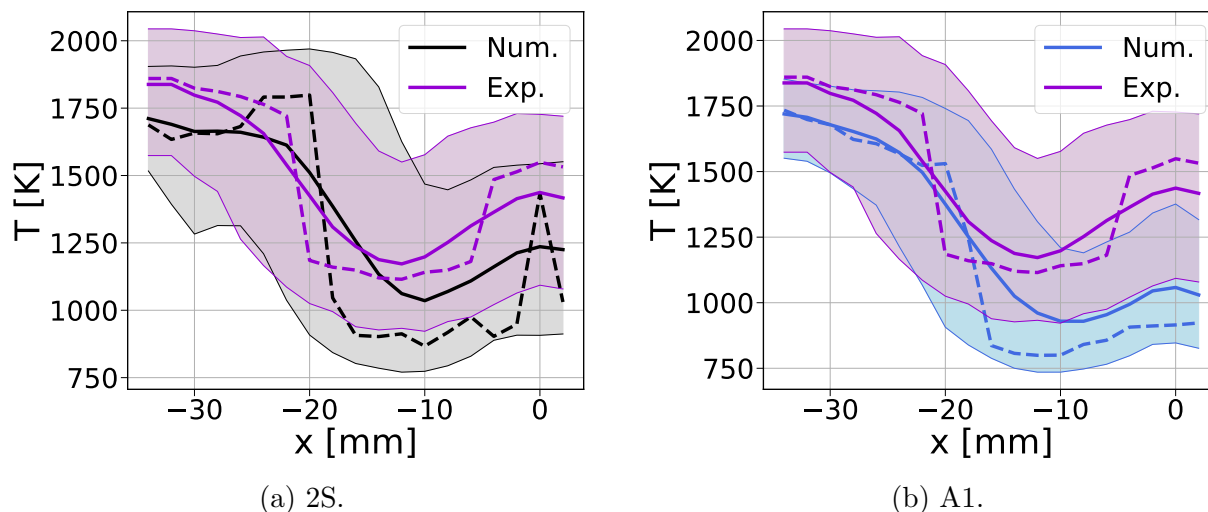


Figure 9.22: Profiles at $y = 25$ mm of the experimental and numerical mean temperature (-), most probable temperature T_{mp} (- -) and T_{05} and T_{95} intervals, for 2S case (left) and A1 case (right).

centre in the simulations than in the experiment. The measured most probable temperature is higher than the numerical one in the central zone.

The aim of the next section is double: on the one hand, some of the models used for combustion and evaporation are described and their relevance for the SSB is debated; on the other hand, the flame structure is further analysed to understand in detail the underlying phenomena.

9.2.3 Flame structure analysis

To underline the sensitivity of the flame to combustion and evaporation parameters, the analysis starts with the flame shape and general features in Section 9.2.3.1. Then the flame index is applied to determine the combustion regime in Section 9.2.3.2. Finally, the possible occurrence of single droplet burning mode, and application of the MustARD model, are tested in Section 9.2.3.3. In all these sections, only the 2S results are analysed.

9.2.3.1 Flame shape

The flame shape is illustrated with the logarithm of an instantaneous heat release rate field, contoured by the thickening factor F in Fig. 9.23a), and an instantaneous temperature field contoured by the local gaseous equivalence ratio in Fig. 9.23b).

The heat release rate field exhibits an overall M-shape, with strong reaction zones between the fresh gases and the ORZs and a weaker central zone. The spotty aspect of HRR shows a non-negligible interaction between the evaporation of the droplets and the combustion zone. Intermittent interaction of the flame with the wall occurs, as visible on the right side of the shown snapshot. The flame base is not attached to the swirler.

The thickening field shows greater values at the top of the flame, which is a direct consequence of the mesh coarsening. This F field is not uniform and depends on the local burning of the flame, but it displays values that remain consistent with the target mesh size, even though they are slightly under the expected F value from gaseous 1D flame

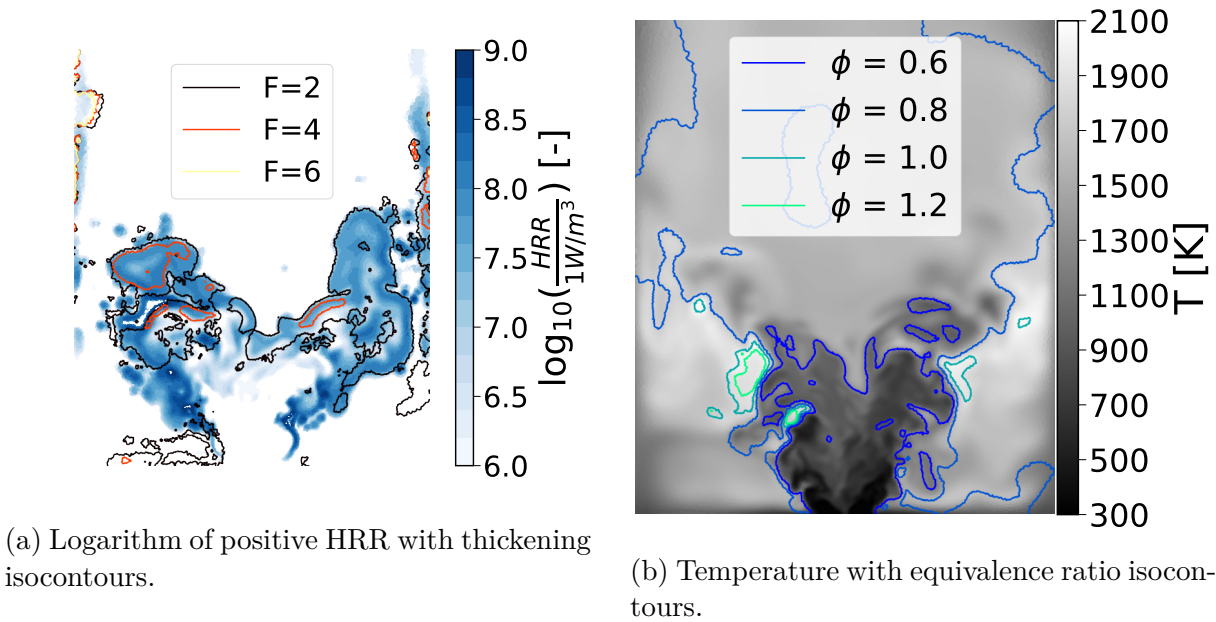


Figure 9.23: Instantaneous fields in a vertical cut plane for the 2S case.

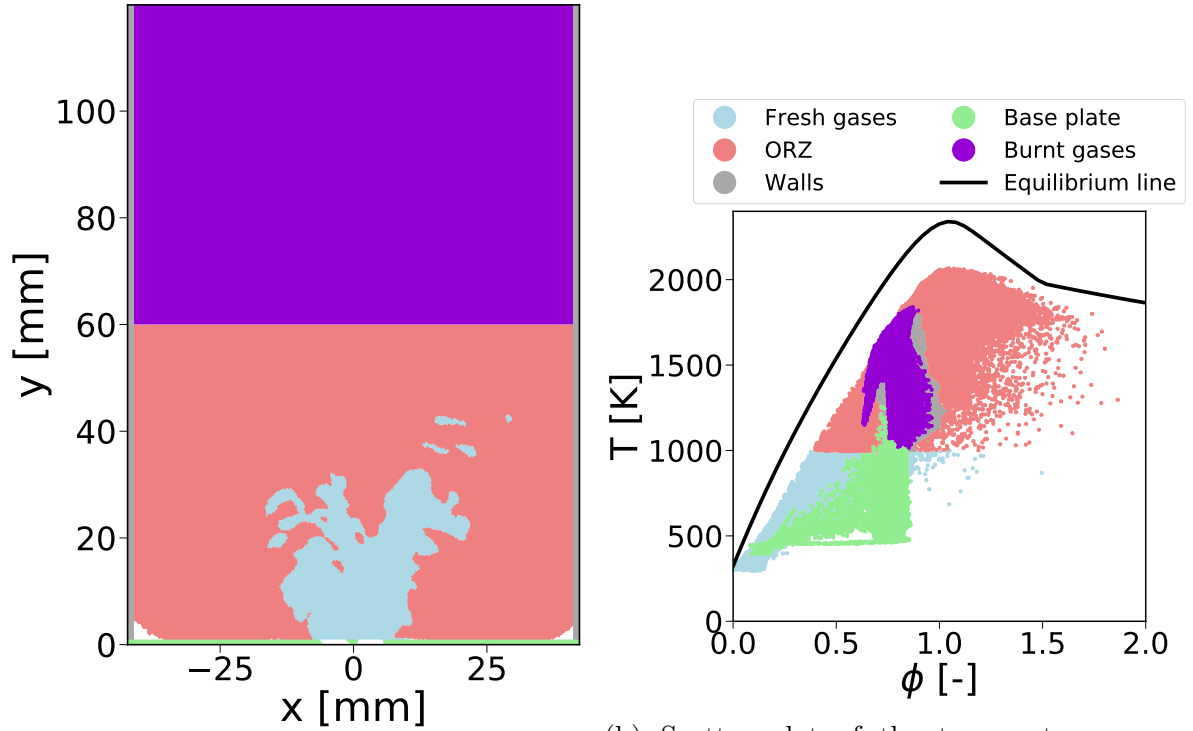
simulations. This is due to the presence of the spray, which tends to extend the reaction zone compared to the purely gaseous case, as shown in Section 8.2.2. Droplets that move along the walls and continue burning there generate a non-unity thickening value.

The temperature is maximum in the ORZs, close to the heat release zone and with little wall cooling and mixing with colder burnt gas. Both the ORZ and IRZ bring back part of the hot gas to respectively the foot and the top of the flame, allowing a continuous igniting of the fresh mixture.

The equivalence ratio contour shows a strongly non-uniform mixture, being a direct consequence of fuel spray evaporation. The gaseous mixture is lean in the spray zone, and becomes more rich through the flame, even locally above stoichiometry, as evaporation accelerates. The ORZs and downstream burnt gases recover the global equivalence ratio of 0.8. The relation between the temperature and the equivalence ratio is further detailed in Fig. 9.24, (right) with a scatter plot of temperature vs gaseous equivalence ratio. The colours refer to several zones inside the burner, presented in Fig. 9.24(left), as was done in [74]. The solid line reports the equilibrium temperature.

The scatter plot shows again that the temperature does not reach the equilibrium values, due to thermal losses through the walls. The equilibrium line should be disregarded for equivalence ratio above 1.5 where the 2S scheme is not able to recover the correct equilibrium state [94]. Few points of the scatter plot lie in the very rich side, but most of the mixture is lean.

The particular structure of the scatter plot can be linked to the flame structure. The unburnt mixture in blue (for $T < 1000$ K) contains the spray, which heats up and slowly evaporates. Droplets and fuel vapour then burn in the ORZ and the IRZ, in red, and stay below the equilibrium line due to thermal losses. The highest temperature for a given equivalence ratio is reached on the axis, where the losses have the smallest impact. Some points reach a rich equivalence ratio when fuel vapour is released massively at one location. Near the baseplate in green, a wide range of temperature can be seen for each mixture fraction value, with both a lower temperature limit and upper equivalence ratio limit. Various mix of these two states of course exist, which is why the scatter plot



(a) Different zones in the SSB burner. Blue: $T < 1000$ K. Green: $y < 1$ mm (base plate). Grey: $|x| < 42$ mm (walls). Purple: $y > 60$ mm. Red: $y < 60$ mm

(b) Scatter plot of the temperature versus equivalence ratio.

Figure 9.24: Temperature vs equivalence ratio scatter plot, associated with different zones in the burner.

associated to this region has a triangle shape. Near the chamber walls in grey, points are as well submitted to strong heat losses, making them fluctuate below the equilibrium curve. Finally, points in the far field in purple are very close around the global equivalence ratio. However, they show various temperatures because thermal losses are still occurring, lowering the temperature in the downstream direction.

9.2.3.2 Flame combustion regime

To get information about the flame regime, the **Takeno Index (T.I)** is used, as defined in Section 3.3.3.3:

$$TI = \frac{\nabla Y_F \cdot \nabla Y_{O_2}}{|\nabla Y_F \cdot \nabla Y_{O_2}|} \quad (9.10)$$

This quantity enables to distinguish between premixed and diffusion zones in the flame, which is important for understanding the flame behaviour as well as applying the thickening model only in the premixed area as discussed in Section 6.3.2. As depicted in Section 3.3.3.3, care needs to be taken when analysing flame index fields, in particular in spray flames [266], [284].

The above Takeno Index field contoured by $HRR = 10 \text{ MW/m}^3$ is represented in Fig. 9.25. To avoid numerical division by 0, a threshold is applied on the gradient values: if $\nabla Y_F < 10^{-6}$ or $\nabla Y_O < 10^{-6}$, $TI = 0$.

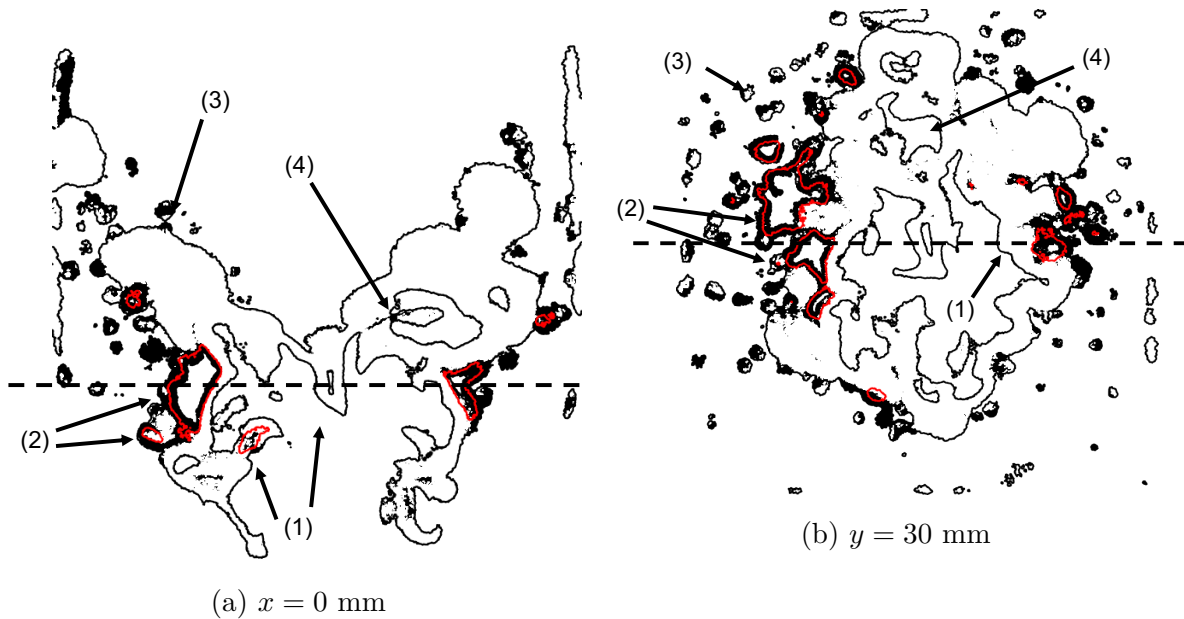


Figure 9.25: Vertical and horizontal cuts of instantaneous Takeno field at $HRR > 10 \text{ MW/m}^3$ for the 2S flame. Premixed zones in white, diffusion zones in black and stoichiometric isocontour in red. The dotted lines represent the location of the cuts.

In this case with 2-step chemistry, premixed and diffusion zones are very well separated, showing mostly premixed combustion and a some local diffusion flames. The pre-evaporated fuel creates a zone, where gases are mostly reacting in a premixed mode, called **the pre-evaporated premixed zone (1)**. To simplify the explanation, the heat release rate associated to this area is called the pre-evaporated HRR zone. Then, the heat release is produced at three other locations:

- directly behind the pre-evaporated flame front, a **gaseous diffusion zone (2)** can be found. It is the consequence of several fuel droplets evaporating at the same time, producing a large amount of fuel in the ORZ which is filled with burned gases, and therefore has not enough oxygen for premixed burning. The vapour then burns with the fresh air containing the spray, in a double flame structure as discussed in [188].
- A group of droplets burn in the upper part of the ORZ in a diffusion mode, as in (2), creating a high local heat release rate amount, that is a **droplet diffusion zone (3)**. Those droplets burning in the hot field may be related to the averaged diameter profiles in Section 9.2.2.1, as higher diameters with high Stokes numbers are not following the flow and entering the ORZ with the same angle as when being released by the spray. Droplets also slip along the wall, leading to a premixed burning mode.
- The premixed burning area extends toward the flow directions (north-west and north-east), in a region called the **extended premixed area (4)**.

Statistics over several instantaneous solutions show that the flame burns at 72% in premixed mode and 28% in diffusion mode, with a standard deviation of 2%.

9.2.3.3 Single droplet burning

To verify the possible occurrence of isolated droplets combustion, MustARD was applied with the 2S fuel model. The two criteria for single droplet burning defined in MustARD (see Section 5.2.2), that is to say the ratio between the inter-droplet distance and the flame radius and the Livengood-Wu ignition index I_{LW} are looked at. Figure 9.26 shows a scatter plot representing the distance between the droplets as a function of the flame radius of the droplets, coloured by $I_{LW} > 1$ in red and $I_{LW} < 1$ in blue.

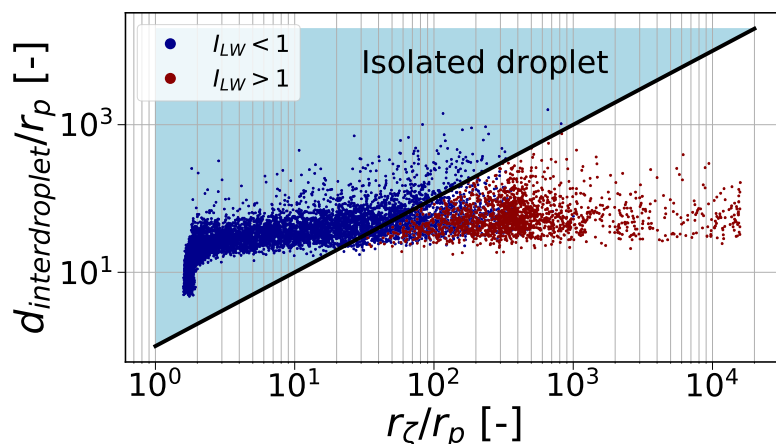


Figure 9.26: Scatter plot of the distance between the droplets as a function of the flame radius of the droplets, coloured by $I_{LW} > 1$ in red and $I_{LW} < 1$ in blue.

A red point is capable of auto-igniting, contrary to a point in blue. A point in the lower right part of the graph shows that the radius of the flame is larger than the distance between two droplets, which means that the droplets are too close to each other to sustain individual diffusion flames around them. As a consequence, points that can ignite must be located in the upper left part of the graph (the droplet is sufficiently far from the others) and be coloured in red (the droplet is capable to ignite). The graph then demonstrates that there are no such points in the SSB configuration. This means that individual droplet burning is not possible in this SSB burner.

When looking at the particle field, most of the droplets that are considered as isolated (in the upper left part of the plot) are located in the cold flow, where they cannot ignite because of the too low temperature. On the other hand, droplets in the ORZ face a sufficient temperature to auto-ignite. Their flame radius may be estimated with the following expression:

$$r_\zeta = r_p \frac{\ln(1 + B_M)}{\ln(1 + Y_{O_2, \infty}/s)} \quad (9.11)$$

The very low oxygen mass fraction in the ORZ then leads to a large flame radius, which can not exist in the small inter-droplet space.

Therefore, and contrary to the spray counterflow diffusion flame case seen in Section 8.3, results show that only very few particles may burn individually, representing a too small amount to contribute to the total heat release.

As a consequence, no single droplet model is used for the SSB flame.

9.2.4 Flame structure: effect of the fuel model

The multi-component and reduced kinetics modelling of the Jet-A1 adds complexity to the flame analysis. As a consequence, both the flame shape and Takeno Index are compared to the 2S case detailed in the previous paragraph.

9.2.4.1 Pre-evaporation

To evaluate the amount of fuel that has pre-evaporated prior to reach the flame front, the gaseous local equivalence ratio is plotted in a vertical cut in Fig. 9.27, for $T < 1000$ K for both the 2S and A1 cases.

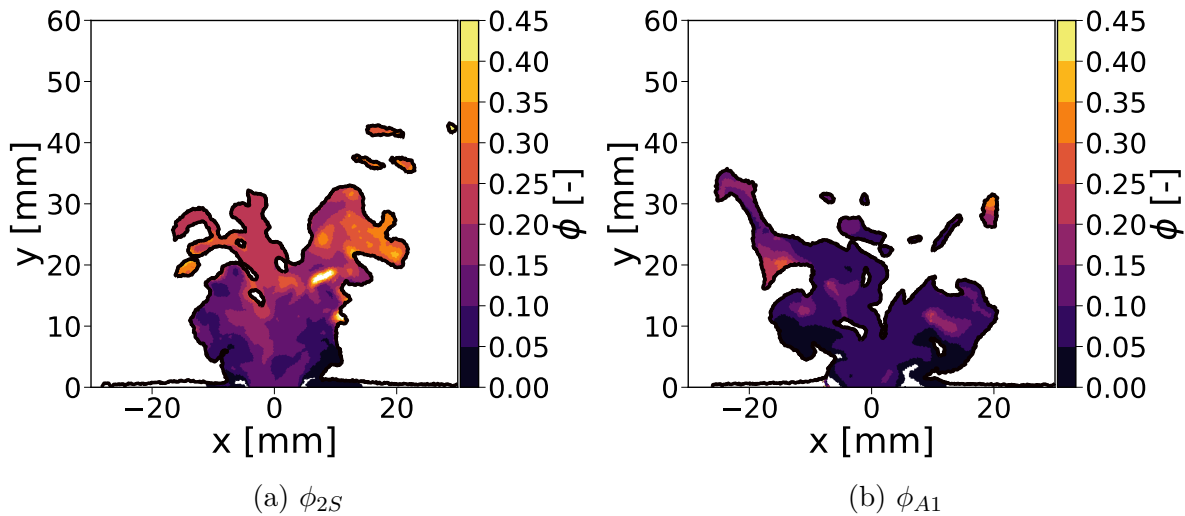


Figure 9.27: Fields in a vertical cut plane of the instantaneous equivalence ratio conditioned on $T < 1000$ K.

In the A1 case, the gaseous equivalence ratio is nearly close to zero, which means that the spray has almost not evaporated and most fuel is in the liquid phase, contrary to the 2S case showing higher fuel vapour content on the top of the zone.

9.2.4.2 Flame shape

As for the 2S case, both the heat release rate field contoured by the thickening factor (Fig. 9.28a) and the temperature field contoured by the gaseous equivalence ratio (Fig. 9.28b) are presented.

The heat release rate field looks much more spread towards the ORZ than in the 2S case. No droplets are burning along the walls as for the 2S case. Dark blue points can be seen on the left of the plot, corresponding to a negative heat release rate due to the droplets' pyrolysis, not visible in the 2S case.

The thickening field is similar to the 2S case, with the same order of magnitude. However, thickening appears on the right side of the chamber, associated to a gaseous fuel mass fraction released and burning in the hot gases.

The temperature field is not much different from the 2S case. However, more regions display a high local equivalence ratio. Scatter plots of temperature as a function of the equivalence ratio weighted by their occurrence in the combustion chamber are displayed in Fig. 9.29.

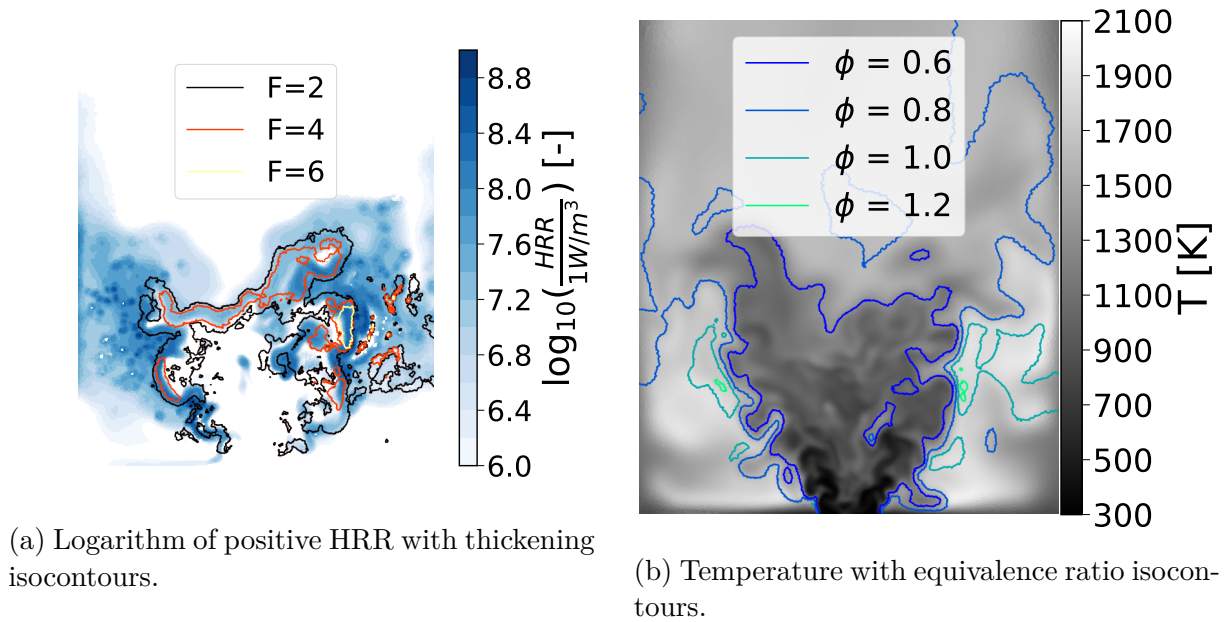


Figure 9.28: Instantaneous fields in a vertical cut of the A1 case.

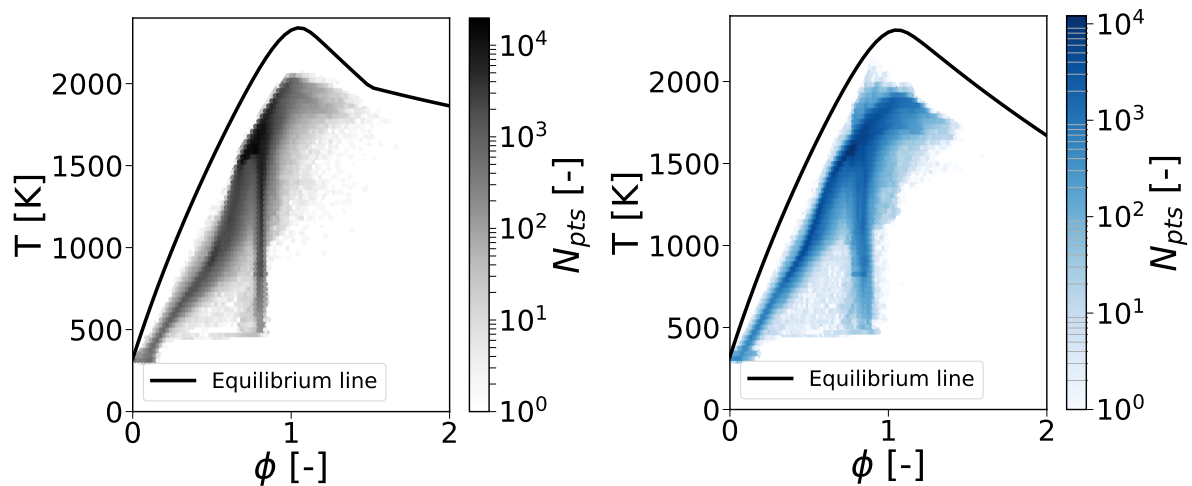


Figure 9.29: Scatter plot of temperature as a function of the equivalence ratio for the 2S (left) and A1 (right) cases.

Both scatter plots are again very similar. Temperature maxima as well as the slopes towards the stoichiometry or the behaviour of points next to the baseplate are not different. However, in the rich region, the A1 case displays more points than the 2S case., indicating a more stratified mixture.

9.2.4.3 Flame regime

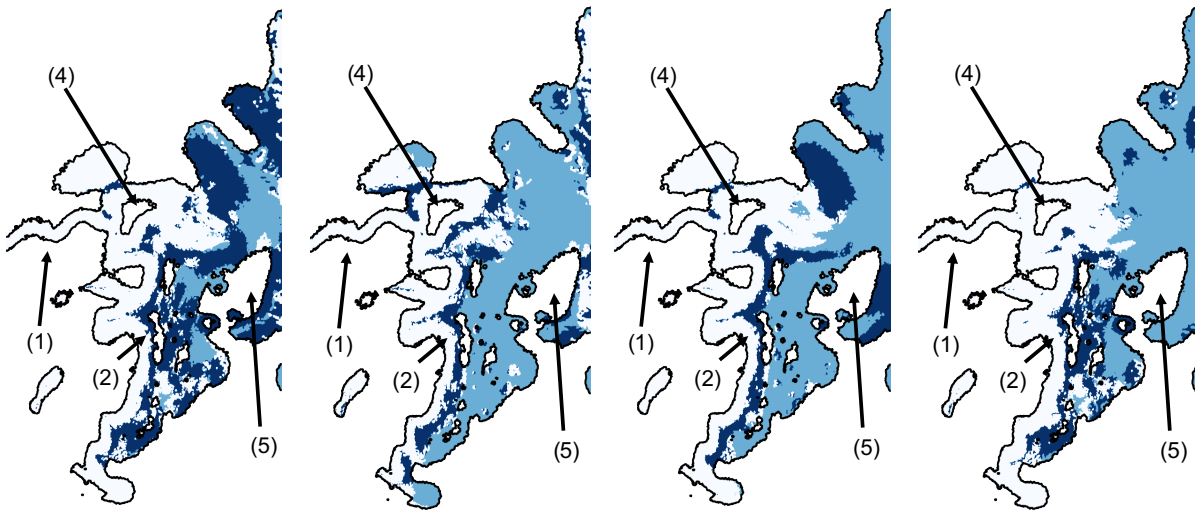
The definition of the Takeno Index is not straightforward for multi-component fuels:

- the Takeno flame index may be technically defined for each component of the fuel or for the sum of all fuel species. The questions are posed, of which definition is the most suitable, or what additional information bring the indices defined for each fuel.
- does the flame index, without taking into account some intermediate species, enable

the correct characterisation of the flame regimes ?

Individual Takeno indices and global Takeno of the sum of all fuels

The individual contributions for each fuel species and of the sum of all fuel species are displayed in Fig. 9.30 for the right wing of the flame.



(a) Based on $\sum_i Y_{F_i}$. (b) Based on $Y_{NC_{12}H_{26}}$. (c) Based on Y_{MCYC6} . (d) Based on Xylene.

Figure 9.30: Cuts in a vertical plane of instantaneous Takeno Index fields at $HRR > 10 \text{ MW/m}^3$ for the A1 flame. Premixed zones in white, diffusion zones in dark blue and no Takeno in light blue.

Zone (5) will be introduced in the next paragraph. For the zone (1), all Takeno definitions are featuring the same result, that is to say a premixed mode. The same conclusion can be drawn for zone (4).

Differences appear in the zone (2), where the mixture is much more stratified and combustion is not occurring at the same time for each fuel. The few differences that one can look at in the stratified area do not overlap, i.e., very few zones depict a diffusion flame for one fuel species and a premixed flame for another fuel species at the same location. The Takeno Index based on the sum of the fuels therefore represent well the overall flame regime and will be used in the following analyses. Note that the conclusion could be different for blends containing lighter fuels, such as hydrogen.

The question now remains on whether to take into account other species than the fuel, namely pyrolysis products which oxidise like a fuel.

Takeno Index, including pyrolysis products

A first guess would be that, as the chemistry is complex, a Takeno Index based on all the species that the fuel contains and all the pyrolysis products could be adequate to

identify the flow regimes in a 3D combustor. Therefore, the Takeno Index fields contoured by $HRR = 10 \text{ MW/m}^3$ are represented for the sum-of-fuel-based Takeno Index and the pyrolysis-containing Takeno Index for A1 fuel in Fig. 9.31. Pyrolysis products are defined as species that can react with oxygen to create sub-products and products of combustion. A threshold on the gradient values has been applied: if $\Delta Y_F < 10^{-6}$ or $\Delta Y_O < 10^{-6}$, $TI = 0$.

Both Takeno Indices lead to the same combustion regime of the overall flame: the flame is mainly premixed and diffusion flame zones only arise in the ORZ. However, the ORZ stratification is better characterised when considering pyrolysis products. Indeed, as the temperature is high in the ORZ, the fuel species very quickly pyrolyse, i.e., they disappear and only pyrolysis products remain. This is a direct consequence of the use of complex chemistry coupled with a polydisperse two-phase flow. Therefore, if the pyrolysis products are not taken into account in the Takeno Index, part of the analysis is missed, leading to zones where the Takeno Index is not defined.

Compared to the 2S case, and as shown in the heat release rate field, the diffusion flame area is much more extended with A1. As a consequence, the (3) combustion mode with droplets igniting is less often occurring.

For A1, the different zones that were depicted for the 2S calculation can be recovered, but the Takeno Index field displays differences:

- the gaseous diffusion zones (2) seem to occur more often than in the 2S case.
- a new combustion mode (5) has appeared, consisting in a second diffusion flame occurring in the ORZ.

Contrary to the 2S case, statistics on the Takeno Index conditioned on the heat release rate show that the flame burns at 51.5% in premixed mode and 48.5% in diffusion mode. The fuel mode is then changing the flame regime, which leads to a difference in terms of flame shape and burning.

9.2.5 Conclusion

In this section, the flame structures of two different fuel models were compared. At first, in terms of time-averaged results, the two-phase flow properties did not show strong differences while reactive velocity fields seemed to be slightly different. Finally, the thermal profiles are slightly different with smaller values for the ARC model, mainly due to the complex structure created in the ORZ.

The 2S flame is a M-shape flame stabilised by two high temperature ORZ, bringing heat to the in-coming flow and evaporating the liquid fuel. The thickening model used for turbulent combustion works well and correctly acts on the solutions. Individual droplets were not observed and the MustARD model was not used. Indeed, the oxygen available in the ORZ was too low to sustain individual droplet flames. The Takeno Index field exhibits a complex stratified premixed structure, with heat provided mostly in premixed mode and controlling the flame.

For A1, the flame seems slightly more complex. While featuring the same overall structure, diffusion flames are more prominent than for the 2S flame, testifying complex reactions coming from the multi-component fuel evaporating (analyse in more details in Chapter 10) and burning in the ORZ. For such configuration, the Takeno Index based on the sum of the fuel species and their pyrolysis product seems to be a good indicator to understand how the flame behaves.

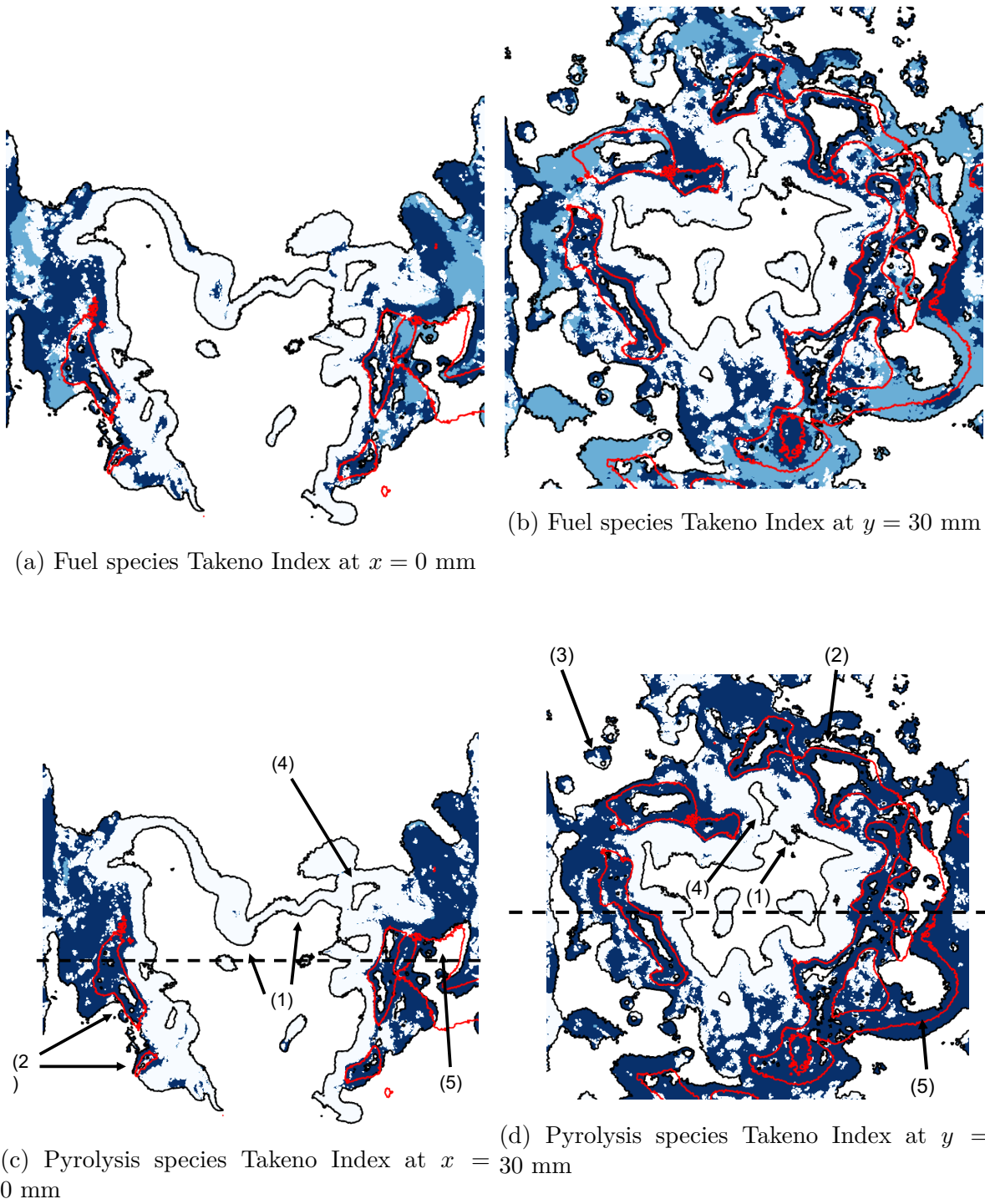


Figure 9.31: Cuts of instantaneous Takeno field for $HRR > 10 \text{ MW/m}^3$ for the A1 flame for the Takeno Index with only fuel species and the Takeno Index including pyrolysis products. Premixed zones in white, diffusion zones in dark blue, not specified zones in light blue and stoichiometric isocontour in red.

9.3 Lean Blow-Out calculations

As mentioned in Section 2.3, the numerical prediction of **Lean Blow-Out** (LBO) remains a research field with questions that have not been, or only partly answered yet, especially for turbulent two-phase flames. Setting the right methodology as well as finding the key indicators of LBO is the objective of this section. For this reason, the LBO computation was only set-up for the 2S scheme and not the multi-component surrogate.

To start with, the characteristic timescales are estimated and a first methodology plan is set up in Section 9.3.1. Afterwards, several computations are performed:

- by changing the stabilisation point, Section 9.3.2 investigates the flame response time and the quantities indicating that LBO is close to happen.
- in Section 9.3.3, the LBO is detected and the important quantities indicating that LBO has occurred are depicted.
- Section 9.3.4 highlights the approximations that were done in these tests and concludes with some perspectives to better predict LBO.

9.3.1 Timescales and methodology

As observed in the previous section, droplets strongly interact with the flame front, introducing new timescales in the flame response to perturbations. Therefore, Section 9.3.1.1 reevaluates the characteristic timescales that are relevant for LBO. Then, Section 9.3.1.2 explains the methodology chosen to evaluate and analyse the flame near and at LBO.

9.3.1.1 Characteristic timescales for LBO

Knowing the complex phenomena occurring in the combustion chamber, timescales are reevaluated to obtain a finer analysis of the transition between two steady states of the flame in the SSB. For that purpose, Fig. 9.32 summarises the different timescales in the SSB burner.

The timescales may be divided into two subcategories: the flow timescales (top half of Fig. 9.32), and the two-phase reactive timescales (bottom half of Fig. 9.32). The definitions are given below.

Flow timescales

- $\tau_{swirl} = u_{radial}\pi/R = 0.7$ ms, is the **swirl characteristic time**, with u_{radial} the averaged radial velocity at the injection system boundary and R the radius of the swirler. This time provides an estimation of the time taken by a particle to do a complete loop in the swirler. Note that this is just an estimation and that this timescale can be higher due to the fact that droplets may be stuck in the swirler and/or do several loops.
- $\tau_{conv}^{half} = L_{conv}/u_{bulk} = 1.8$ ms, is the **convective characteristic time**, with L_{conv} the characteristic convective length (here, half the length of the chamber) and u_{bulk} the bulk velocity estimated by $u_{bulk} = \int \rho v S / \int \rho S$ with v the axial velocity, ρ the density and S the surface of the swirler section area. This time represents the time

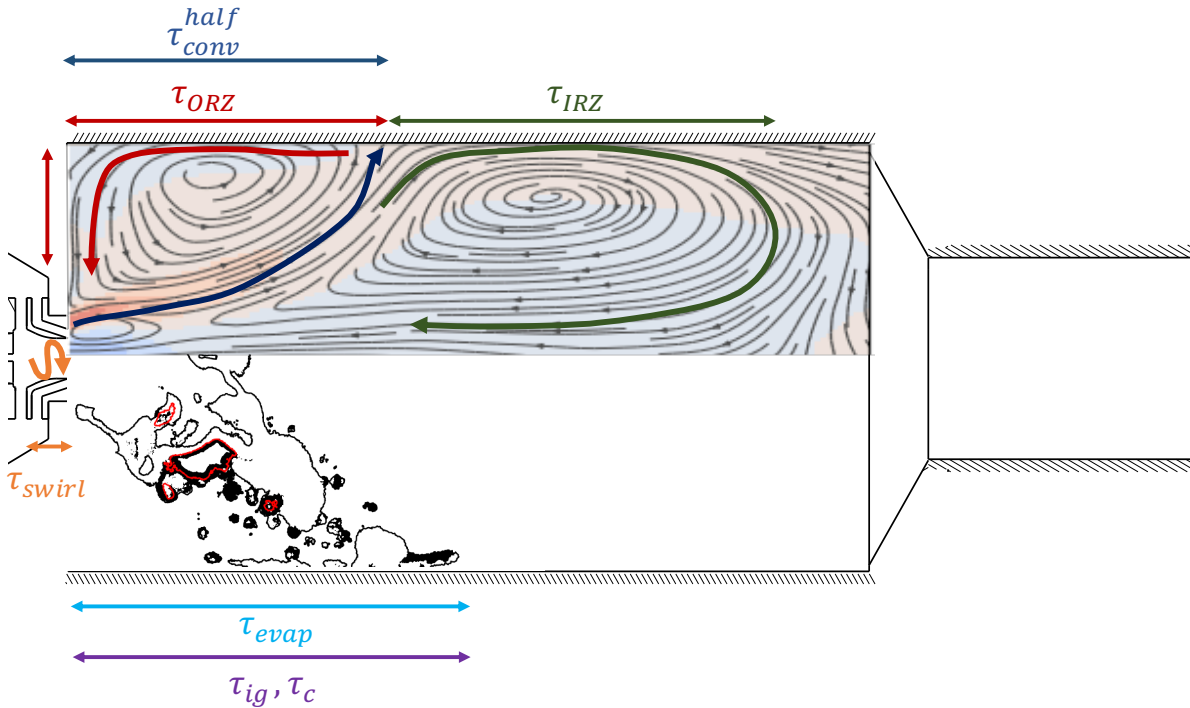


Figure 9.32: Characteristic flow (top half) and two-phase (bottom half) timescales in the SSB burner.

taken by the particle to travel from the exit of the swirler to the tip of the Outer Recirculation Zone.

- $\tau_{ORZ} = 15$ ms, measured with local velocities of the calculation, is the **characteristic ORZ time**, which represents the time taken by a particle to complete an entire loop in the ORZ. An entire loop means that the gas is going from the tip of the ORZ back to the foot of the flame.
- $\tau_{IRZ} = 100$ ms, measured with local velocities of the calculation, is the **characteristic IRZ time**, i.e., the time taken by a particle to complete an entire loop in the IRZ. A complete loop means going from the tip of the ORZ, to the tip of the IRZ and back to the tip of the fresh gases.

Two-phase reactive timescales

- $\tau_{evap} = 0.1 - 10$ ms the **evaporation characteristic time**, is estimated via a 0D evaporation solver for a given gaseous environment and liquid state. This time represents the time taken by the particles to completely evaporate. Of course, this timescale is small when the gaseous temperature surrounding the droplet is high.
- $\tau_{ig} = 0.01 - 10$ ms, the **ignition characteristic time**, is estimated via Cantera or ARCANE and represents the time taken by the premixed mixture to ignite.
- $\tau_c = \partial c / \partial \dot{c} = 1$ ns $- 10$ μ s, the **chemical characteristic time**, is the time taken by a single species to react, estimated via Cantera or ARCANE.

These timescales are used to analyse the flame when converging towards lower equivalence ratio.

The methodology for LBO prediction is now explained.

9.3.1.2 LBO prediction methodology

The experimental ramp presented in Section 9.1.1 is not affordable in a 3D numerical simulation. Indeed, keeping a constant decreasing rate of 5 g/h/s is tantamount to be able to simulate 100 s of physical time, which is not affordable today with LES.

Therefore, a methodology has to be found to enable the LBO simulation. A classical approach is to adapt the experimental flame stabilisation procedure while keeping the same framework as in the real combustor. This is presented in Fig. 9.33 for conditions presented in Section 9.1.1, that is to say Jet-A1 at $T_{air} = 323.15$ K, $T_{fuel} = 303.15$ K and $P = 1$ bar.

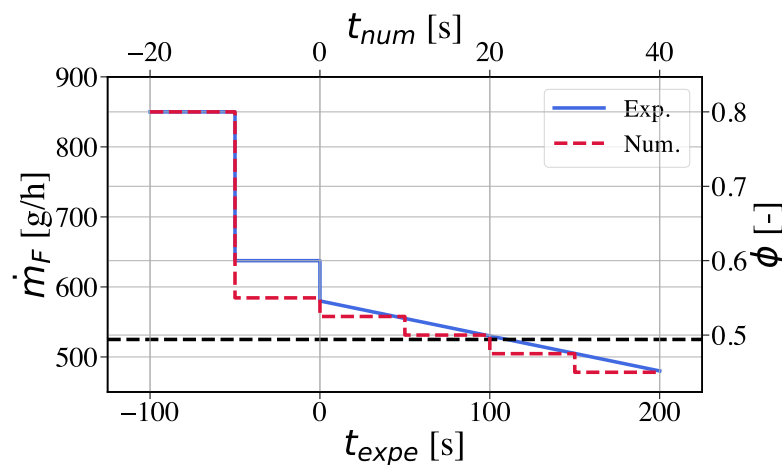


Figure 9.33: Numerical and experimental classical LBO methodologies for Jet-A1 at $T_{air} = 323.15$ K, $T_{fuel} = 303.15$ K and $P = 1$ bar.

The approximations made in the numerical framework are the following:

1. the flame is stabilised slightly above the expected LBO value, at $\phi = 0.55$. The convergence time was expected to be equal to roughly two convective time-steps estimated in Section 9.2, that is to say $2\tau_{conv} = 10.0$ ms.
2. the continuous ramp is converted into small discrete steps towards extinction. The time of these steps depends on the flame convergence typical time. Indeed, the quasi-steady state at each step is necessary to ensure that the right equivalence ratio is injected into the chamber. The time chosen to converge the flame between each step is two convergence time-steps as well.
3. the flame blow-off is then detected with a numerical criterion depending on global or local variables of the chamber. Usually, the heat release rate and the fuel mass fraction are taken.

However, this methodology could not be applied in the SSB burner because of the long converging time requiring lots of computational resources, as explained in next section. Therefore, attempt to find the LBO is first made on steps from $\phi = 0.8$ to lower equivalence ratios. The next section details the results of these steps as well as the tools developed to analyse the transient calculations.

9.3.2 Towards LBO

LBO in the 2S case is supposed to be the same as in the A1 case, that is to say $\phi = 0.49$. Numerically, it was found with this method that $0.35 < \phi_{LBO} < 0.45$. Therefore, starting from the stabilised flame at $\phi = 0.8$, the first step has been to lower ϕ in the 2S calculation towards $\phi = 0.55$ to observe the near blow-out. Aside from this main calculation, several other calculations towards other equivalence ratios were realised, from $\phi = 0.8$ to $\phi = 0.45$, $\phi = 0.35$ and $\phi = 0.10$. The aim of these steps is to evaluate the flame response time as the time needed to stabilise at a new operation point. Besides, they give a first rough idea of the numerical LBO.

The section is then organised as follows:

- the flame response and convergence to steady state is looked at in Section 9.3.2.1 for all the cases to check the agreement with the expected converging time.
- the main results of the flame convergence at $\phi = 0.55$ are presented in Section 9.3.2.2.
- the behaviour of the different quantities during the transient time is looked at and the indicator to detect LBO is investigated in Section 9.3.2.3.

9.3.2.1 Flame response

Integrated quantities, the total mass in the domain and the total heat release rate, are shown in Fig. 9.34.

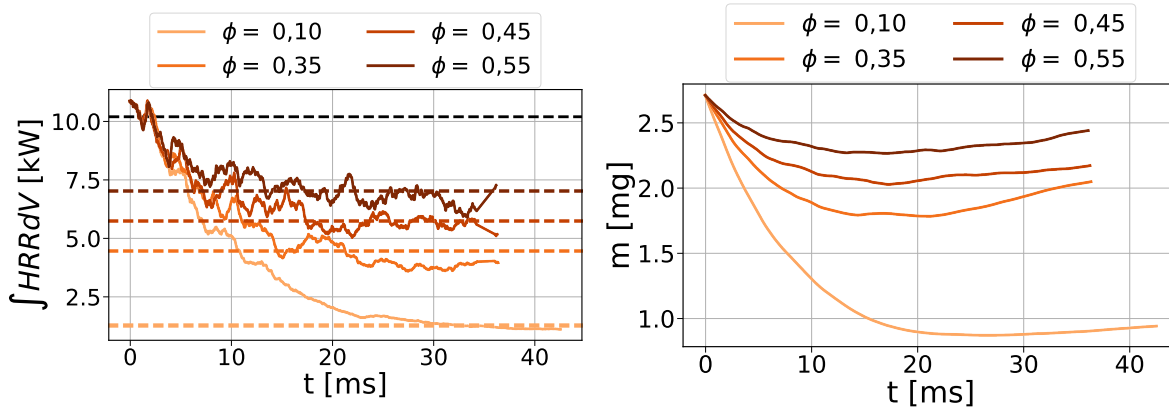


Figure 9.34: Time evolution of the total HRR (left) and total mass (right) in the SSB domain after an abrupt change of equivalence ratio.

The total HRR stabilises again after a time which, based on the LHV, seems to be very similar for each case, at approximately $t = 20$ ms. For all the steps, and even for the cases where the global equivalence ratio is below the expected lean blow-out limit value $\phi = 0.49$, the theoretical heat release is reached. Moreover, the slope taken by the heat release is very different for all the cases, but they seem to reach the theoretical heat release at almost the same time, around $t = 20$ ms. This highlights the dependency of the heat release in the chamber to the convective time of the droplets, which are monitored by the convective timescale τ_{conv}^{half} and the swirling timescale τ_{swirl} , where $\tau_{conv}^{half} + \tau_{swirl} = 2.5$ ms. The flow then takes around 8 times of these timescales to converge.

The second graph represents the total mass in the domain. It always slightly decreases at first and then starts growing again, approximately at $t = 20$ ms. This behaviour is surprising, because the following scenarios were expected:

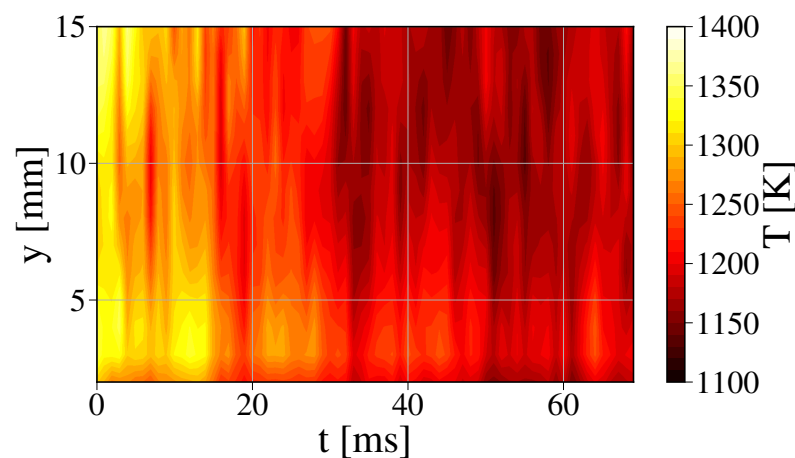
- for a non-quenched case, a first decrease of fuel mass (caused by the decrease of mass flow rate at injection) and then a flat curve (because the fuel mass does not evolve anymore in the chamber when the flame is stabilised).
- for a quenched case, a first decrease of fuel mass (caused by the decrease of mass flow rate at injection) and then an increase due to the accumulation of unburnt fuel.

Table 9.9 shows the final state at $\phi = 0.55$ case measured with a probe at $y = 80$ mm (in IRZ) compared to the equilibrium values at the same equivalence ratio.

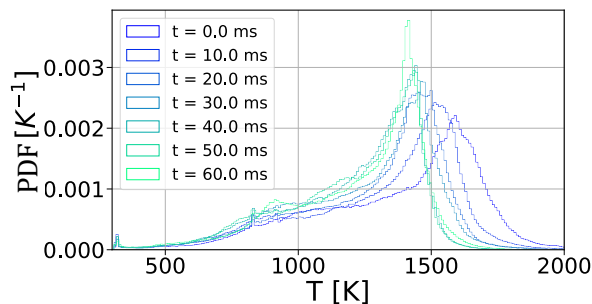
Case	O_2 [-]	CO_2 [-]	H_2O [-]
Theoretical	0.1010	0.113	0.046
Numerical	0.0937	0.119	0.0489

Table 9.9: Comparison of the equilibrium at $\phi = 0.55$ and the simulated values measured with a probe at $y = 80$ mm in the combustion chamber.

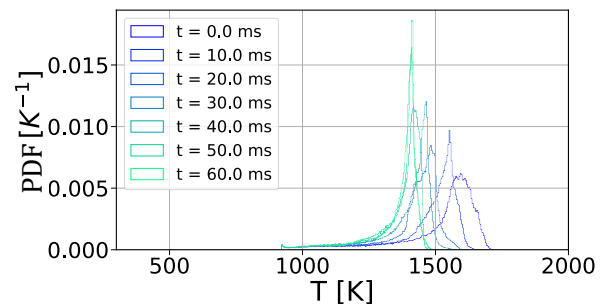
The different species mass fractions are very close to equilibrium, without exactly reaching it. This tells us that the flame has adjusted to the new equivalence ratio. To better see when, how and which regions of the calculation have made the transition, the temperature field evolution should be analysed as it has been demonstrated in previous sections that its response time is larger than the one of the flame. In Fig. 9.35a the graph represents the mean temperature along the axial height of the burner as a function of time.



(a) Axial mean temperature field as a function of time.



(b) Temperature distribution in the ORZ.



(c) Temperature distribution in the IRZ.

Figure 9.35: Temperature distributions in the ORZ and in the IRZ for different times.

The flame temperature in the entire domain seems to stabilise around 50 ms. Of course, as the temperature is fluctuating, a better indicator is to look at a temperature PDF. Therefore, Fig. 9.35 represents the temperature distribution in the ORZ (left) and in the IRZ (right) at different times. Comparing both graphs, as expected, the IRZ presents a lower variation of the temperature as the time taken to fully change the temperature is very long. On the contrary, the ORZ temperature distribution maximum is evolving more quickly. Conclusions are then the same as for the previous representation: the flame is stabilising thermally around $t = 50$ ms.

This leads to the conclusion that the SSB response time to a mass flow rate step, is about 20 ms in terms of flame power and 50 ms in terms of temperature field. The far-field might change, but it has a negligible impact on the reaction zone and is therefore not considered. This response time of the temperature field is approximately three times the ORZ timescale provided in Section 9.3.1.1. The combustion scenario of droplets going through the flame front and evaporating and burning in the ORZ, lead to hot burnt gas trapped in the ORZ, lengthening the convergence time and explaining the long response time of the temperature field. As a consequence, going towards LBO with a series of quasi steady-state steps seems impossible at this time since too many calculations would be required to apply the methodology, which would be too long.

Before going toward LBO, the $\phi = 0.55$ solution is compared to the $\phi = 0.8$ flame.

9.3.2.2 Flame near LBO

To understand more precisely the shape of the flame near LBO, the HRR contoured by the thickening factor are displayed in Fig. 9.36 for both values of the equivalence ratio.

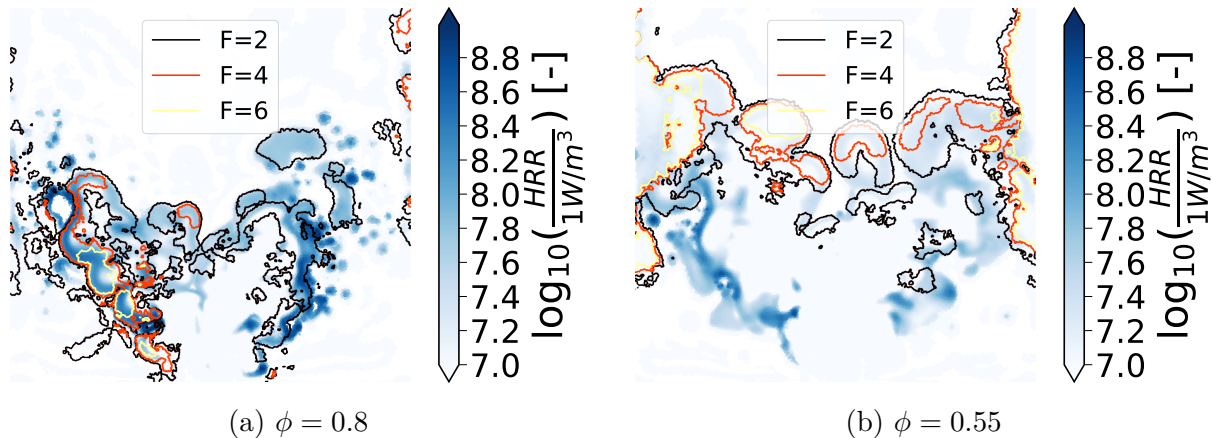


Figure 9.36: HRR field in a vertical cut plane, contoured by thickness factor.

At $\phi = 0.55$, the flame is not extinguished as in the experiment. The combustion mode has slightly changed: fewer droplets are burnt directly in the ORZ, but more are converted to gas before burning. In other words, there is less evaporation/combustion interaction. The combustion is occurring much closer to the walls than for the $\phi = 0.8$ flame. The flame side branches are weaker near LBO and the branch between the IRZ and the cold gases is nearly not existing.

The thickening fields of $\phi = 0.8$ and $\phi = 0.55$ are very different. In the first case, the thickening factor is perfectly placed around the flame and in the latter case, the thickening is mainly located around the walls. This flame extension is a direct consequence of the lower equivalence ratio, leading to lower temperatures in the ORZ and therefore the fuel

mass fraction occupies a bigger zone in the domain at $\phi = 0.55$, as may be seen in Fig. 9.37. Besides, the thickening values seem to be higher for the $\phi = 0.55$ case since the mesh is a lot more coarsen in this region, which could influence the results.

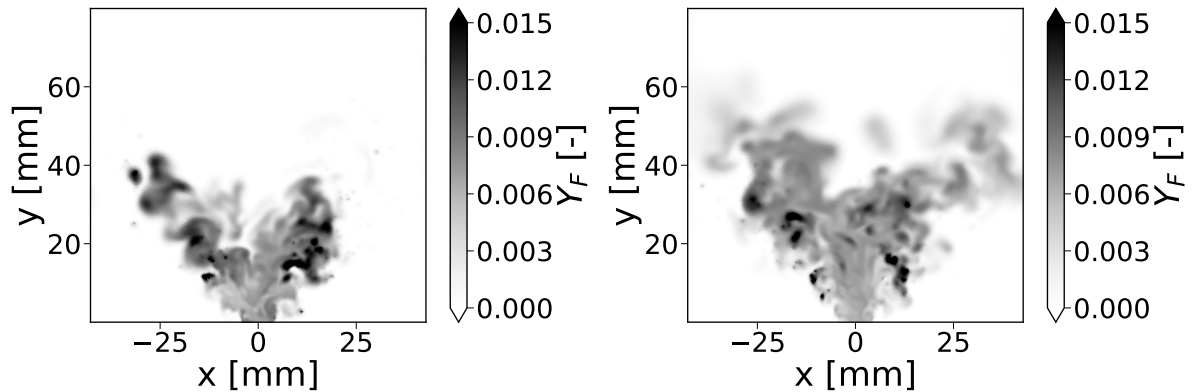


Figure 9.37: 2S fuel mass fraction fields in a vertical cut plane, displayed for $\phi = 0.8$ (left) and $\phi = 0.55$ (right).

The larger cold gas region implies a larger non-evaporating zone, i.e., a larger amount of droplets in the cold area in the leaner case. This may explain the increase of equivalence ratio seen in Fig. 9.34: at first, the flame adjusts to the *HRR* corresponding to the modified mass flow rate. Then in a second step, the decreasing temperature, controlled by the ORZ timescale ($\tau_{ORZ} = 15$ ms) enables the expansion of the fuel in the combustion chamber, leading to an increase of the fuel mass in the domain.

Additional figures showing the other species mass fractions fields and two-phase properties of the two different operating points are shown in Appendix D. This does not provide more information than what has been said, except that the flame is nearly converged at $\phi = 0.55$ because it reaches the same values as for the 1D premixed flame at $\phi = 0.55$.

Finally, to investigate if the flame structure has changed, the Takeno Index field is plotted for $\phi = 0.8$ and $\phi = 0.55$ in Fig. 9.38.

The main difference between both cases is the collapse of the diffusion flames in the $\phi = 0.55$ flame compared to the $\phi = 0.8$ flame. Burning of individual droplets is still occurring on the sides. The Takeno Index conditioned by the *HRR* field shows that for $\phi = 0.55$, 85% of the combustion is occurring in premixed mode and only 15% in diffusion mode. The premixed region is extended in the lower equivalence ratio case, testifying that more evaporation has occurred prior to the flame front.

9.3.2.3 Indicator of LBO

The variables to detect whether the flame is going to quench are looked at. For this purpose, several variables are plotted in Fig. 9.39:

- Mean and integrated variables plotted versus time give information concerning the overall behaviour of the system.
- Minimum and maximum variables of interest versus time give information about the combustion occurring in the middle.

The mean, maximum and minimum values are analysed below $y = 60$ μm since the combustion is occurring in this area in the whole burner. An average on the whole solution

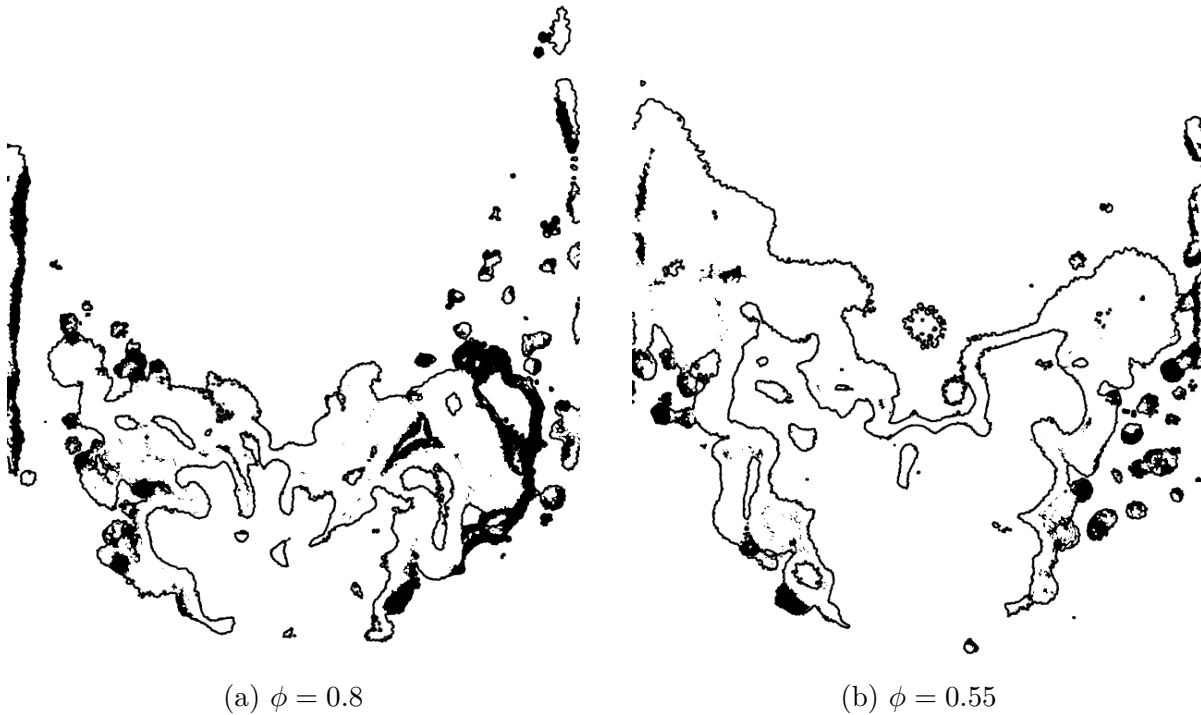


Figure 9.38: Takeno Index fields in a vertical cut plane.

would take a lot of time before converging. To save space, the plots not shown here are given in Appendix E.

LBO is found to be around $\phi = 0.4$ according to these plots. The time evolution of the different variables is explained as followed:

- mean source terms (fuel species and HRR (not shown)) and mean temperature decrease as less fuel enters the chamber. For the extinguishing cases, such as $\phi = 0.10$ and $\phi = 0.35$, the maximum quantities (temperature, CO , HRR) also decrease, whereas they are maintained close to their initial value in the non-quenched cases. As well, the maximum fuel species source term absolute value decreases.
- mean product species (CO_2 and H_2O (not shown)) are expected to fall down because their amount is directly linked to the amount of fuel. Those values are not reaching a plateau, even after 60 ms of calculation, meaning that the calculation does not seem to be fully converged.

The cases that experience blow-off are $\phi = 0.35$ and $\phi = 0.10$, meaning that the extinguishing equivalence ratio could be between $\phi = 0.35$ and $\phi = 0.45$. Mean quantities are not helpful to guess if an LBO event will soon occur. On the contrary, minimums and maximums quantities display a step, enabling to detect the moment where LBO was detected or close to be detected.

The evolution of these different variables is explained by the two-phase characteristic of the flow burning in the ORZ which create higher temperatures locally in the ORZ and the heat losses modifying the temperature in the ORZ. The different temperature scatter plots as a function of the equivalence ratio in the ORZ are then looked at in Fig. 9.40 for all the steps that have been calculated for $t = 30$ ms.

Less combustion is occurring in the rich region, that is to say in diffusion mode, as the equivalence ratio is reduced. For all the cases, the majority of the combustion is

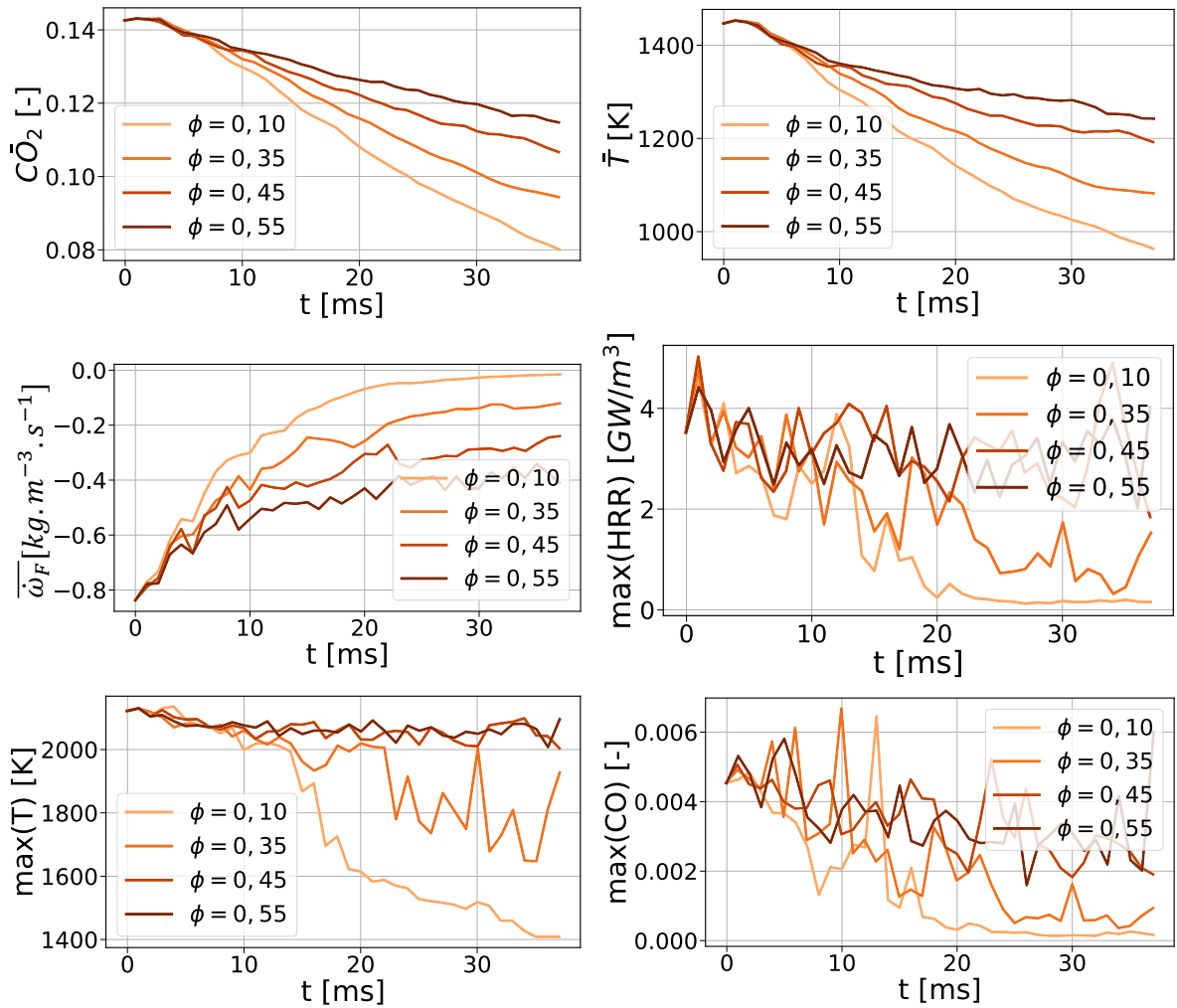


Figure 9.39: 2S mean species and thermo-chemical variables below $y = 60$ mm as a function of the time for the different steps in equivalence ratio.

occurring in premixed mode. The temperature maximum decreases when the equivalence ratio decreases, meaning that all combustion occurs in premixed mode. The vertical line representing the baseplate combustion is shifted towards lower equivalence ratios for lower injection equivalence ratios, testifying the change of composition and temperature in the ORZ at the vicinity of the baseplate.

The flame blows out, not because of strain or because of high diffusion flame zones, but because of fuel depletion that is not feeding the ORZ in a sufficient level. Of course, all plots shown in this section were taken at one instant and fluctuate through the time, as the heat release rate generated by the droplets in the ORZ is unsteady, modifying strongly the maximum temperature through the time.

As the flame studied here is not a purely gaseous flame, but a two-phase flame with heat losses, the equivalence ratio is not the one from the global one but the one that the flame sees at a given time. The previous analyses then suggest that extinction would occur at a given equivalence ratio inside the combustion chamber that would be the same for all cases. To investigate this, the maximum of the absolute value of the fuel source term as a function of the time-evolving mean equivalence ratio $\bar{\phi}$ in a box around the flame ($0 \text{ mm} < y < 80 \text{ mm}$) is plotted in Fig. 9.41. The time-evolving mean equivalence ratio is

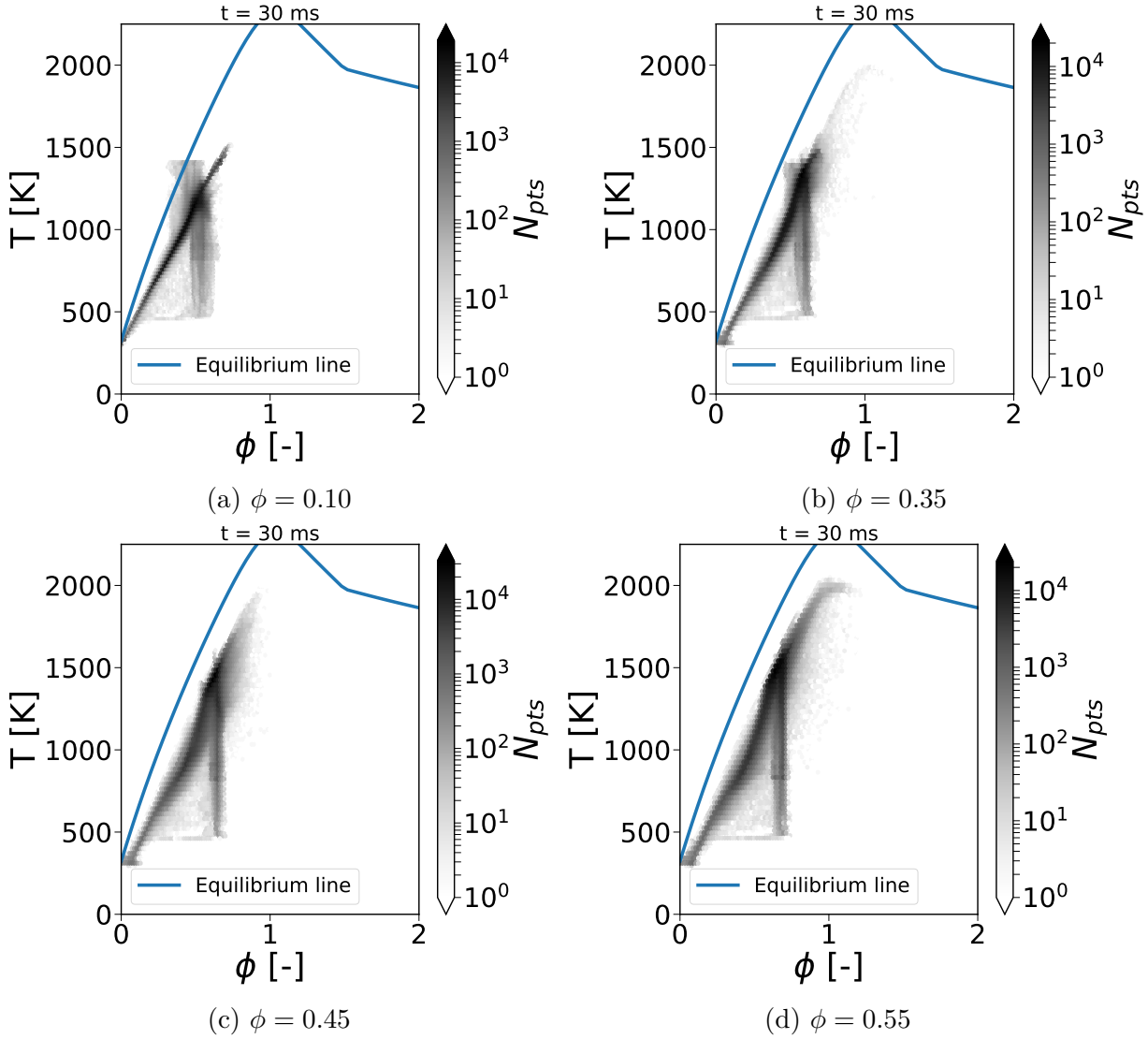


Figure 9.40: Scatter plot of temperature vs equivalence ratio at $t = 30$ ms for the steps towards $\phi = 0.1$, $\phi = 0.35$, $\phi = 0.45$ and $\phi = 0.55$.

calculated as:

$$\bar{\phi} = \frac{\bar{z}/(1-\bar{z})}{z_{st}/(1-z_{st})} \quad (9.12)$$

with

$$\bar{z} = \sum_{domain} z_{Bilger,liq} \quad (9.13)$$

and $z_{Bilger,liq}$ the extended mixture fraction for two-phase flows as introduced in Section 5.1.4.

All curves seem to follow the same trend for $0.6 < \bar{\phi}(t) < 0.8$, with a maximum value stabilising around $|\dot{\omega}_{F,max}| = 120 \text{ kg/m}^3/\text{s}$. For $0.6 < \bar{\phi}(t)$, both non-extinct cases ($\phi_g = 0.45$ and $\phi_g = 0.55$) are going on stabilising around the value with a reducing equivalence ratio, while the two other case ($\phi_g = 0.10$ and $\phi_g = 0.35$) have a maximum value diminishing to reach zero, along with a reduction of their time-evolving mean equivalence ratio $\bar{\phi}(t)$. As a consequence, this reinforces the existence of a given equivalence ratio for which the flame is quenched and that could be used for analysing the extinction of two-phase turbulent flames.

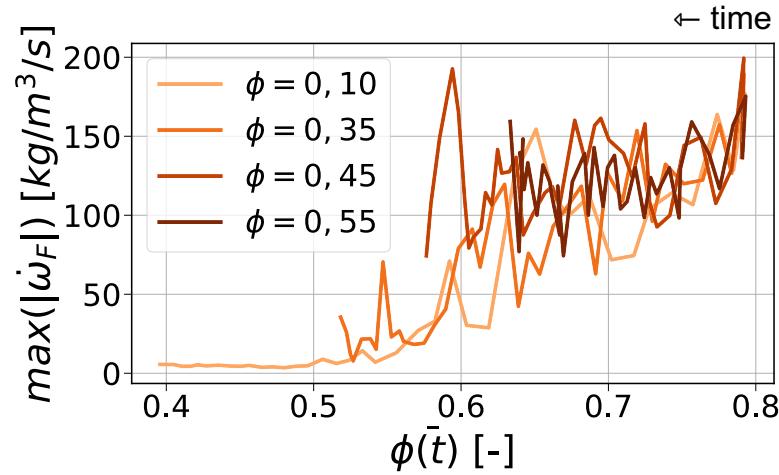


Figure 9.41: Maximum of the absolute fuel species source term $\max(|\dot{\omega}_F|)$ vs the time-evolving mean equivalence ratio $\bar{\phi}(t)$.

9.3.3 LBO detection

From the previous sections, the long flame response time in the SSB is problematic for the application of a fuel ramp, or of a succession of steps, due to too small simulation times. Indeed, the chamber cannot be considered as quasi-steady when the fuel mass flow rate changes.

As a consequence, another approach has been set up to detect the LBO, based on the simulation of ignition and stating that a quenched flame is equivalent to a flame that does not ignite. The ignition is realised by filling the combustion chamber with hot gases at $T = 1660K$ (highest measured temperature for the experimental Jet-A1 temperature profile). The composition of the hot gases is: $Y_{N_2} = 0.7274$, $Y_{O_2} = 0.0449$, $Y_{CO} = 0.0012$, $Y_{CO_2} = 0.1601$ and $Y_{H_2O} = 0.0664$. Two operating points are presented: one at $\phi = 0.45$ and one at $\phi = 0.40$.

As the time taken by the flame to adapt from an equivalence ratio to another one is long, an ignition of the flame from scratch has been computed to look at the flame adaptation. Two equivalence ratios were tested: $\phi = 0.45$ and $\phi = 0.4$, as these are the points where the numerical blow-out is supposed to occur. Figure 9.42 represents the flame temperature distributions up to 50 ms.

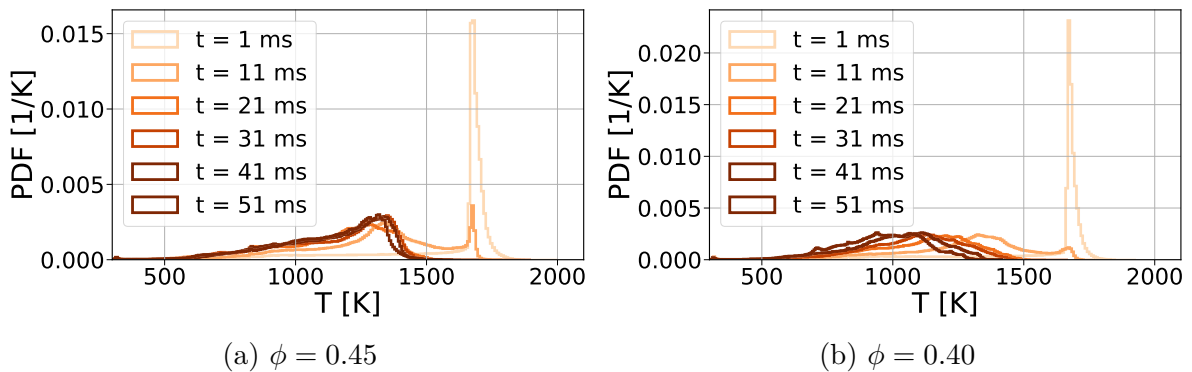


Figure 9.42: Temperature distribution for several times with a gas out.

The flame at $\phi = 0.45$ continues to ignite, compared to the $\phi = 0.4$ flame, which seems to quench. This assumption by some indicators, such as the mean kerosene source term and the fuel mass fraction versus time displayed in Fig. 9.43.

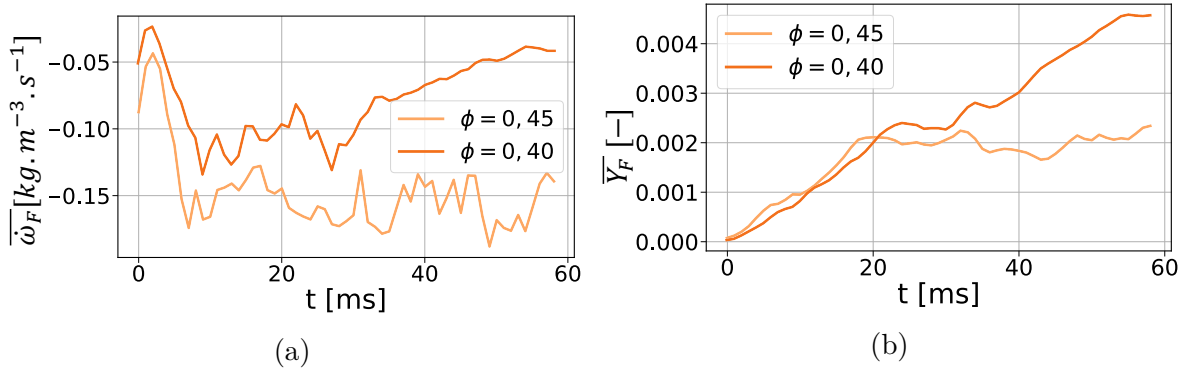


Figure 9.43: Mean kerosene source term (a) and mass fraction (b) versus time for $\phi = 0.40$ and $\phi = 0.45$.

For $\phi = 0.45$, the mean fuel source term is rising before stabilising around $\bar{\dot{\omega}}_F = -0.15 \text{ kg/m}^3/\text{s}$. The mean fuel mass fraction \bar{Y}_F in the domain is rising before stabilising around $\bar{Y}_F = 0.002$.

Conversely, for $\phi = 0.40$, the mean fuel source term is rising, stabilising around $\bar{\dot{\omega}}_F = -0.10 \text{ kg/m}^3/\text{s}$ before decreasing around $t = 30$ ms. The fuel mass fraction is as well rising, reaching a stabilised value for $20 \text{ ms} < t < 30 \text{ ms}$ and rising for $t > 30$ ms. This shows that LBO occurs for $\phi = 0.4$ at $t = 30$ ms. However, the mean fuel source term in the domain decreases slowly and even seems to reach a stabilised value around $t = 50$ ms.

To investigate why it might be the case, the heat release fields are displayed for both equivalence ratios $\phi = 0.45$ and $\phi = 0.40$ Fig. 9.44.

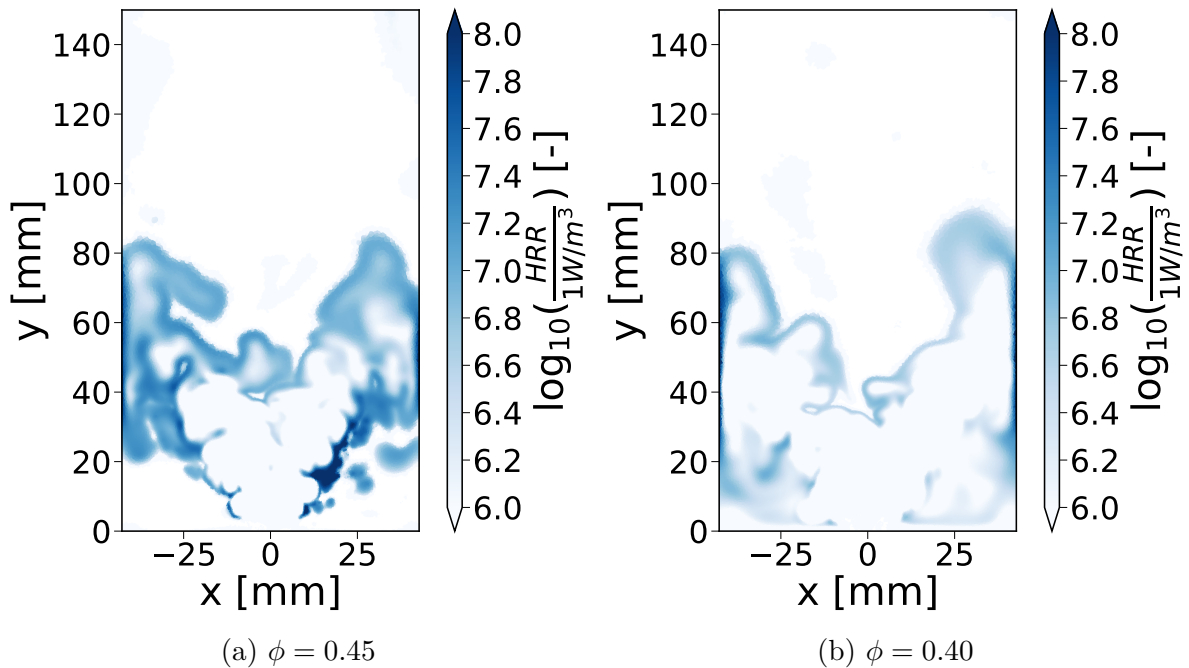


Figure 9.44: Heat Release Rate field in a vertical cut plane for $\phi = 0.45$ and $\phi = 0.40$.

The heat release rate of $\phi = 0.45$ is much stronger than the one at $\phi = 0.40$, leading to an extinction case for the latter case. However, on the $\phi = 0.40$, higher heat release rate can be seen near the walls, especially between $40 \text{ mm} < y < 60 \text{ mm}$.

This shows that the wall temperature influences the flame, giving heat to the system and sustaining a high level of heat release while extinguishing the flame. The question is then raised on the influence of the wall temperatures on retrieving the correct LBO limit.

9.3.4 Discussion

The simulations realised in this section are biased because some elements have been oversimplified. The goal of this section is to explain the assumptions made and how they could be overcome.

9.3.4.1 Chemistry

The chemical scheme might induce an error in terms of extinction prediction. Indeed, at first, the transport parameters are very different for the 2S case ($Sc_F = 0.7$) than for the A1 case ($Sc_F = 2.3$) and could induce a different behaviour when facing local extinction. The chemical behaviour, and in particular some intermediate species, may also play a role.

9.3.4.2 Two-phase flow

The two-phase flow properties of the system have not been modified for the LBO study compared to the stable case, and might have an impact on the final result. The first modification of the two-phase flow properties is the diameter distribution. Indeed, as fewer liquid fuel is injected into the swirler through the atomiser, droplets may be badly atomised, leading to a different interaction with the swirler boundaries. As well, droplets being re-injected at the swirler lips may change angle and atomisation due to a reduction of the pressure loss between the fully-reactive case and the case near LBO.

The evaporation model used, whether mono- or multi-component, might significantly alter the flame stabilisation near LBO. Indeed, the multi-component fuel is evaporating at different levels according to the preferential evaporation, which might lead to a better flame foot stabilisation. Furthermore, the differences in the flame shape induced by the two-phase flow coupled with the kinetics is also critical, as the proportion of diffusion structure in the flame regime might change the flame behaviour near extinction.

9.3.4.3 Turbulence

The efficiency model used is a Charlette model [41] with a beta parameter that is constant. Changing the operating point might create a wide range of structures with a beta parameter that fluctuates more and thus changes the extinction of the turbulent flame.

9.3.4.4 Thermal environment

The wall temperatures have not been adapted for all the cases and temperatures for the stabilised flame have been kept for lower equivalence ratios, creating an error in terms of wall heat loss. The influence of the walls is studied by converging the $\phi = 0.45$ case with an adapted wall temperature. By imagining the burner completely filled with burnt gases

at final temperatures $T_{final}^{0.8}$ for $\phi = 0.8$ and $T_{final}^{0.45}$ for $\phi = 0.45$, the following balance can be estimated:

$$\begin{aligned} C_{p,final}^{0.8} T_{final}^{0.8} &= C_{p,ad}^{0.8} T_{ad}^{0.8} - Q_{wall}^{0.8} \\ C_{p,final}^{0.45} T_{final}^{0.45} &= C_{p,ad}^{0.45} T_{ad}^{0.45} - Q_{wall}^{0.45} \end{aligned} \quad (9.14)$$

By introducing T_{wall} the wall temperature, the ratio $r = T_{ad}^{0.8}/T_{ad}^{0.45}$ can be defined. By assuming that:

$$r = \frac{T_{ad}^{0.8}}{T_{ad}^{0.45}} = \frac{T_{final}^{0.8}}{T_{final}^{0.45}} \quad (9.15)$$

as well as $C_{p,final}^{0.8} = C_{p,final}^{0.45}$, the demonstration in Appendix E shows that:

$$r = \frac{T_{wall}^{0.8}}{T_{wall}^{0.45}} \quad (9.16)$$

Therefore, the new wall temperatures have been adapted, knowing that:

$$T_{wall} = \frac{S_{baseplate} T_{baseplate} + S_{chamber} T_{chamber}}{S_{wall}} \quad (9.17)$$

Therefore, the baseplate temperature has been set to $T_{baseplate} = 400$ K and $T_{chamber} = 700$ K. Results showing the heat release rate variation and the heat release rate fields are displayed in Fig. 9.45.

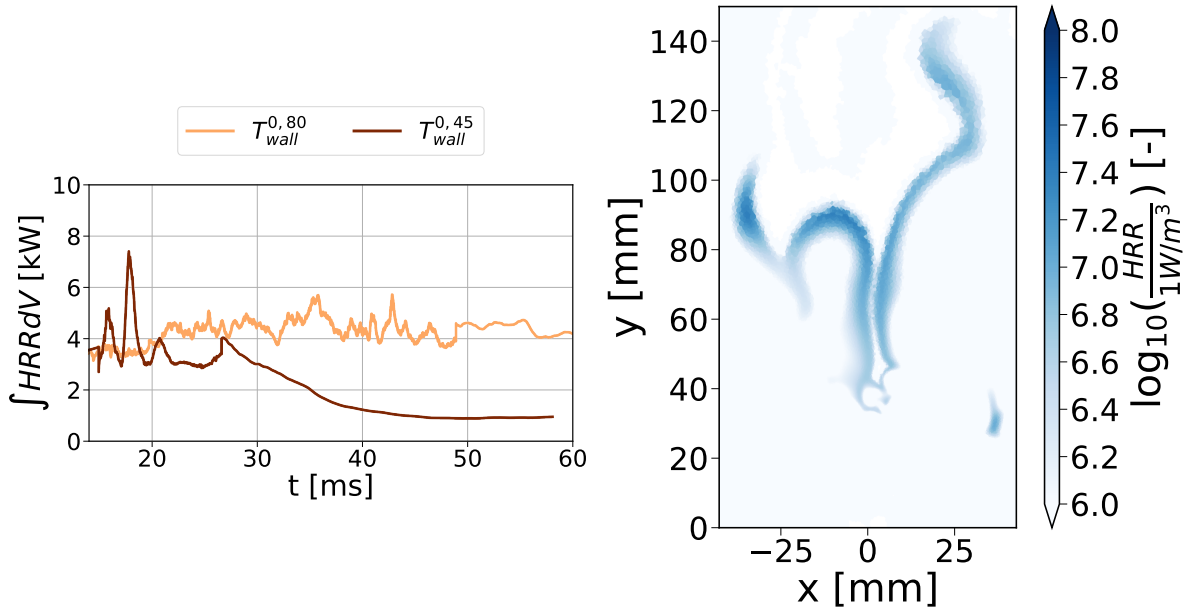


Figure 9.45: Total HRR vs time (left) and HRR field for the adapted wall temperature after 60 ms (right) for $\phi = 0.45$.

Clearly, for $\phi = 0.45$, between the stable case with wall temperatures at $\phi = 0.8$ and the case with the estimated wall temperatures, the first goes on burning whereas the second does not. This justifies that the wall condition is a key value to estimate correctly the LBO limit, and is discussed in the next section.

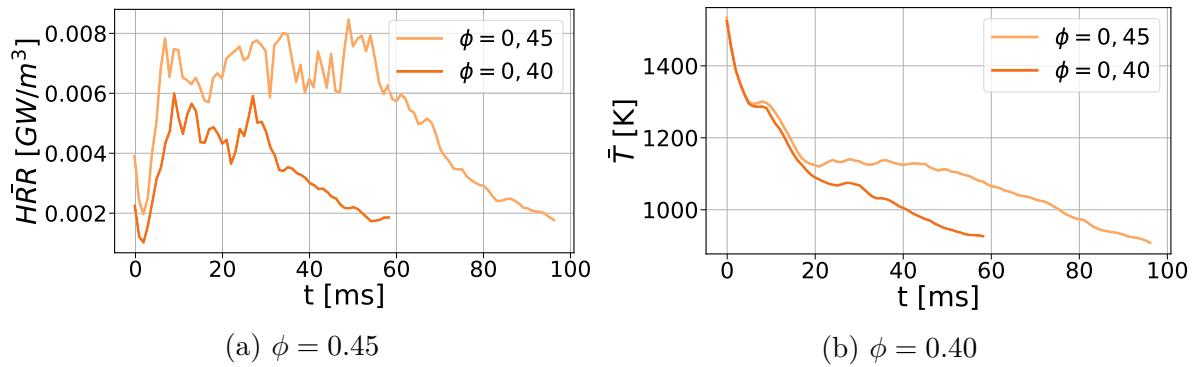


Figure 9.46: Heat Release Rate and temperature fields for $\phi = 0.45$ and $\phi = 0.40$.

9.3.4.5 Timescales

The assumption made at first for which the simulation time would depend on the temperature field may be altered. Indeed, Fig. 9.46 shows results when going further into the computation for $\phi = 0.45$:

As can be seen, the case at $\phi = 0.45$ exhibits a plateau near 40-50 ms, especially visible in the mean temperature plot as a function of time. However, the case is then completely blown-off for a longer simulation time.

This can be explained by the methodology, which surely depends on how the flame is stabilised and then extinguishes. Or it may be due to physical reasons: the IRZ as well as the ORZ compositions are slightly influencing the overall flame stabilisation and could be the reason of such an extinction.

9.3.5 Conclusions

After briefly recalling the main methodologies to simulate LBO, the DLR experimental work was recalled. The LBO procedure was then set up with the 2S mechanism for time considerations. Characteristic timescales of the different zones were as well evaluated.

Firstly, different steps from $\phi = 0.8$ to lower equivalence ratios were applied and calculations were conducted, finding LBO for $0.35 < \phi_g < 0.45$. This revealed that the HRR convergence was reached after approximately 20 ms, the thermal convergence approximately around 50 ms but not the composition convergence. Markers for the extinction were detected, showing that the combustion minima and maxima are strongly varying when extinguishing, suggesting that there exists a global equivalence ratio for which the extinction occurs in the chamber.

From this finding, the step-like approach was dropped down and two cases ($\phi = 0.45$ and $\phi = 0.40$) were enlightened from scratch to see if the convergence time could be reduced and if LBO could be reached. LBO is reached for $\phi = 0.40$, not for $\phi = 0.45$. Key parameters to testify that the flame was extinguished are the heat release consumed by the flame and the gaseous mass fraction released through the time. Finally, several approximations on the setup were pointed out depicting the complex phenomena, namely heat losses, ORZ long residence times and spray/combustion interactions, associated to the simulation of LBO, requiring great precision to account for those effects.

Ending this part on the study of the 2S computation, next chapter will show the main differences between the three fuels targeted from JETSCREEN project, and explain them.

Chapter 10

Effect of fuel on flame structure

Contents

10.1 Time-averaged spray flames	219
10.1.1 Two-phase flow fields	220
10.1.2 Adiabatic temperature equilibrium	221
10.1.3 Reacting fields	222
10.2 Spray flame structures	225
10.2.1 Fuel evaporation	225
10.2.2 Combustion regime	229
10.2.3 Towards optimised SAF	234
10.3 Conclusion	237

The objective in the SSB configuration was to investigate the effect of fuel on flame position and flame structure. Thus, the same numerical method as described in Section 9.1.1 for A1 is used here for the alternative fuels B1 and C1 presented in Chapter 7. First, the time-averaged fuels are analysed in Section 10.1 and compared with the experimental results available. Second, the flame structures for the three fuels are analysed in Section 10.2 to explain the results of Section 10.1 and this analysis is used to estimate what would be the most suited SAF for the SSB. In the entire section, ARC A1, ARC B1 and ARC C1 will respectively be called A1, B1 and C1.

10.1 Time-averaged spray flames

As for A1, LES using B1 was initialised using reactive 2S fields. The LES was performed during 20 ms and before time-averaging it during 50 ms. For C1, its liquid density is much larger than the two other surrogates, it was then useless using the BFER, A1 or B1 simulations because the spray is expected to differ notably. Therefore, for the aromatic C1, only the gaseous field from the BFER case was used to initialise the gaseous field and the spray was initialised from scratch. The same temperature profiles were applied to the chamber walls and the baseplate for all the fuels, although the wall temperatures have been experimentally measured for A1 and B1 only.

Section 10.1.1 compares A1, B1 and C1 in terms of two-phase flow fields. Section 10.1.2 evaluates the impact of fuel on equilibrium temperature. Section 10.1.3 finally compares the fuel in terms of flame position, temperature and heat release

This section shows the different outputs obtained and their comparisons to the experimental work and to the other fuels. Section 10.1.1 details the comparisons in terms of two-phase flow properties. Section 10.1.2 checks the consistency of the calculations. Section 10.1.3 finally presents the temperature and heat release rate fields.

10.1.1 Two-phase flow fields

Figure 10.1 displays the mean diameter (d_{10}) and the SMD (d_{32}) profiles at $y = 25$ mm for the three fuels A1, B1 and C1 and the measurement for Jet-A1. Note that no experimental data are available for B1 and C1 for the two-phase flow characteristic quantities.

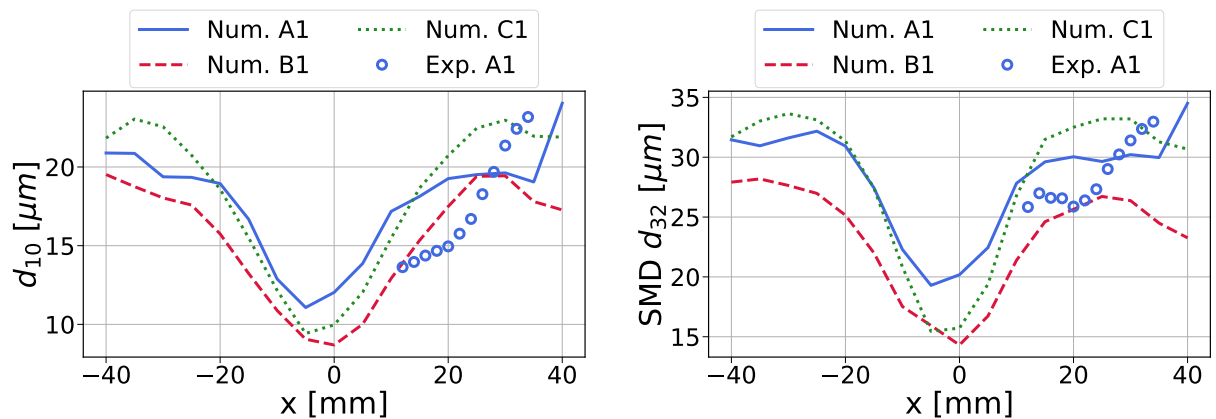


Figure 10.1: d_{10} (left) and d_{32} (right) for A1, B1 and C1 (-) at $y = 25$ mm. Measurements for A1 are added (o) when available.

As expected, B1 evaporates faster than A1 and C1. For every fuel, the pressure loss region is observed and droplet diameter is much lower for C1 than A1. Indeed, C1 shows slightly larger diameters on the sides of the spray and smaller ones on the centre, which could be due to the higher density of C1. Moreover, even though the differences between the fuels are of the same order than the differences between the experiment and the numerical results for A1, the LES show results in agreement with the subprocess analysis made in Section 8.1.2.

Figure 10.1 displays the mean diameter (d_{10}) and the SMD (d_{32}) profiles at $y = 25$ mm and the numerical and volumetric PDF of the three fuels A1, B1 and C1 and the measurement for Jet-A1. Note that no experimental data are available for B1 and C1 for the two-phase flow characteristic quantities.

Looking at the PDF at $y = 25$ mm, A1 and C1 show a similar shape. The PDF for B1 is shifted to the left, showing fewer large droplets than the two other fuels. Besides, the largest diameter is much smaller for C1 ($50 \mu\text{m}$ instead of $70 \mu\text{m}$). Differences between C1 and A1/B1 are larger than experimental and numerical results for A1.

The two-phase flow dynamics is further studied looking at the three droplet velocity component profiles at two positions ($y = 15$ mm and $y = 25$ mm) is further studied looking at Fig. 10.3. The experimental results for Jet-A1 are added as well. Differences between the three fuels are here again lower than the difference between the experimental work and numerical results for A1. Only B1 exhibits a lower velocity in the central region of the flow. The axial and the transverse velocity profiles are very similar for the three fuels. One can only notice a smaller axial velocity and a larger radial velocity in the central region.

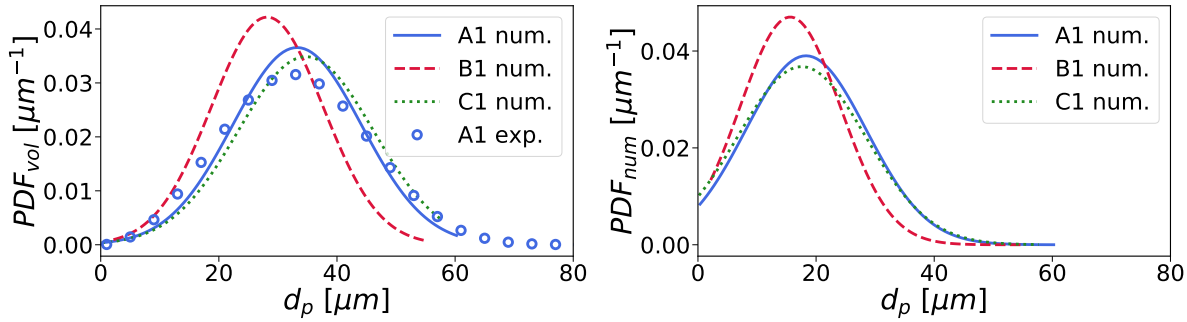


Figure 10.2: PDF for the droplet number (left) and the droplet volume (right) for A1, B1 and C1 (-) at $y = 25$ mm. Measurements for A1 are added (o) when available.

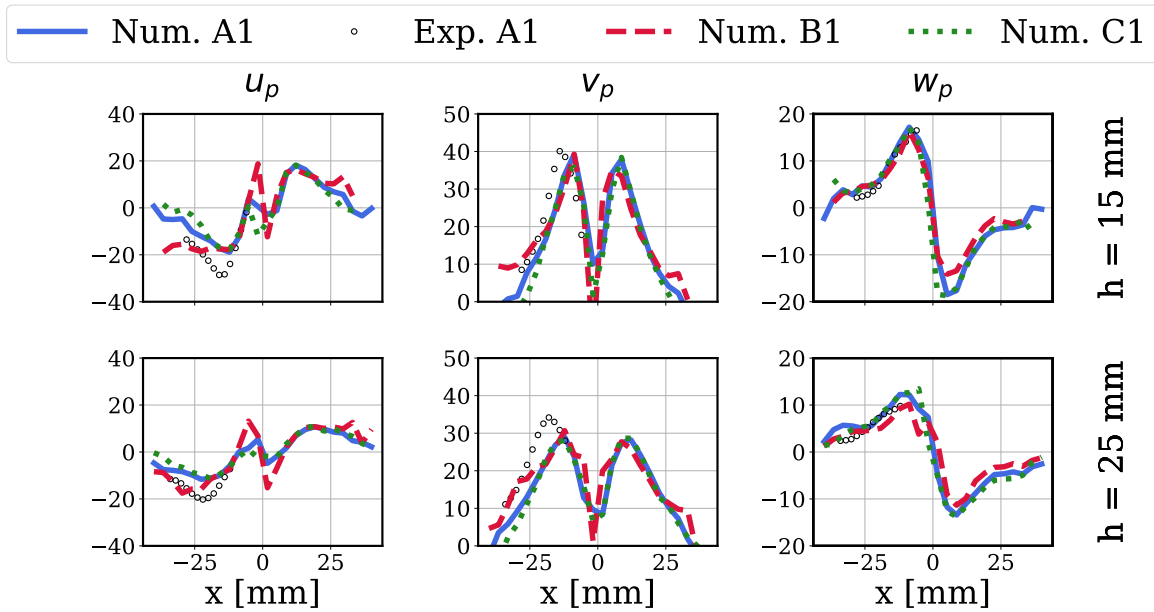


Figure 10.3: Numerical droplet velocity profiles for A1, B1 and C1 at $y = 15$ mm (top) and at $y = 25$ mm (bottom): radial u_p , axial v_p and transverse w_p . Measurements for A1 are added.

Eventually, in Fig. 10.4, the numerical liquid conditional loading are compared. As in Chapter 9, a square masking the data for the numerical results has been applied since measurements have not been performed experimentally as there were too many droplets in this region. No data were available for B1 and C1.

Results clearly show that A1 and C1 sprays are very similar and penetrate in the flame more than the B1 spray. The spray angle does not vary with the fuel tested, thus showing the same error with respect to the measurements.

10.1.2 Adiabatic temperature equilibrium

As in Chapter 9, the theoretical and numerical time-averaged thermal losses are compared in Table 10.1 for the three surrogates.

A1 and C1 show almost the same enthalpy losses, with the same repartition between the chamber walls and the baseplate. The thermal losses for B1 are higher on the chamber

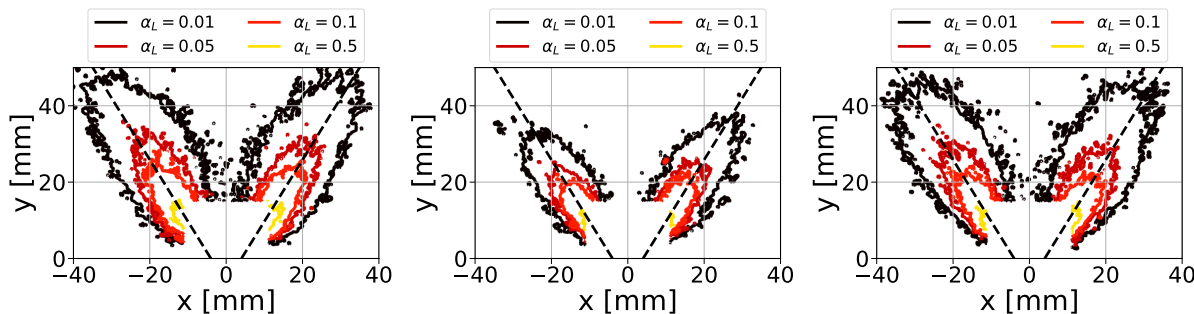


Figure 10.4: Numerical conditional loading for A1, B1 and C1.

Fuel	Q_{walls} [W]	$Q_{baseplate}$ [K]	Q_{tot} [K]
A1	-2815	-1039	-3854
B1	-3152	-1035	-4187
C1	-2827	-1068	-3896

Table 10.1: Enthalpy losses for A1, B1 and C1.

walls, increasing its total thermal losses. As in Section 9.2.2.3, and thanks to the constant enthalpy equilibrium calculation from Cantera, the adiabatic temperature T_{ad} was calculated. Afterwards, the energetic wall losses Q_{tot} were subtracted to the enthalpy to obtain the theoretical temperature $T_{eq,theo}$ that the flow should reach at the chamber exit. These results are compared to the numerical equilibrium temperatures $T_{final,num}$ for the three fuels. Time-averaged results are summarised in the Table 10.2.

Fuel	T_{ad} [K]	$T_{eq,theo}$ [K]	$T_{final,num}$ [K]
A1	2084.54	1239	1311.23
B1	2076.34	1224	1286.4
C1	2092.96	1263	1346.34

Table 10.2: Final temperatures for A1, B1 and C1.

The higher numerical temperature compared to the theoretical equilibrium is attributed to the same cause as in Section 9.2.2.3, that is to say, a delay in the system adaptation towards the enthalpy change due to the heat losses. The theoretical adiabatic temperatures are very close for the three fuels, with a difference of less than 1%. The theoretical equilibrium temperatures exhibit some differences, with C1 having a higher temperature than A1 (a difference of 24 K and especially B1 (a difference of 39 K). This difference is roughly the same as the one shown in the numerical measured temperature.

10.1.3 Reacting fields

Figure 10.5, the first row presents experimental visualisations of A1 and B1 flames. In the lower row, the heat release rate integrated in the z-direction for the three fuels is displayed. No visualisation or data were provided for the C1 flame.

First, the experimental visualisations for A1 and B1 do not show much different in terms of power location. B1 does not seem to be symmetric, with a left bench more intense than the right one. Moreover, for A1, the flame is lifted nearer the injection than

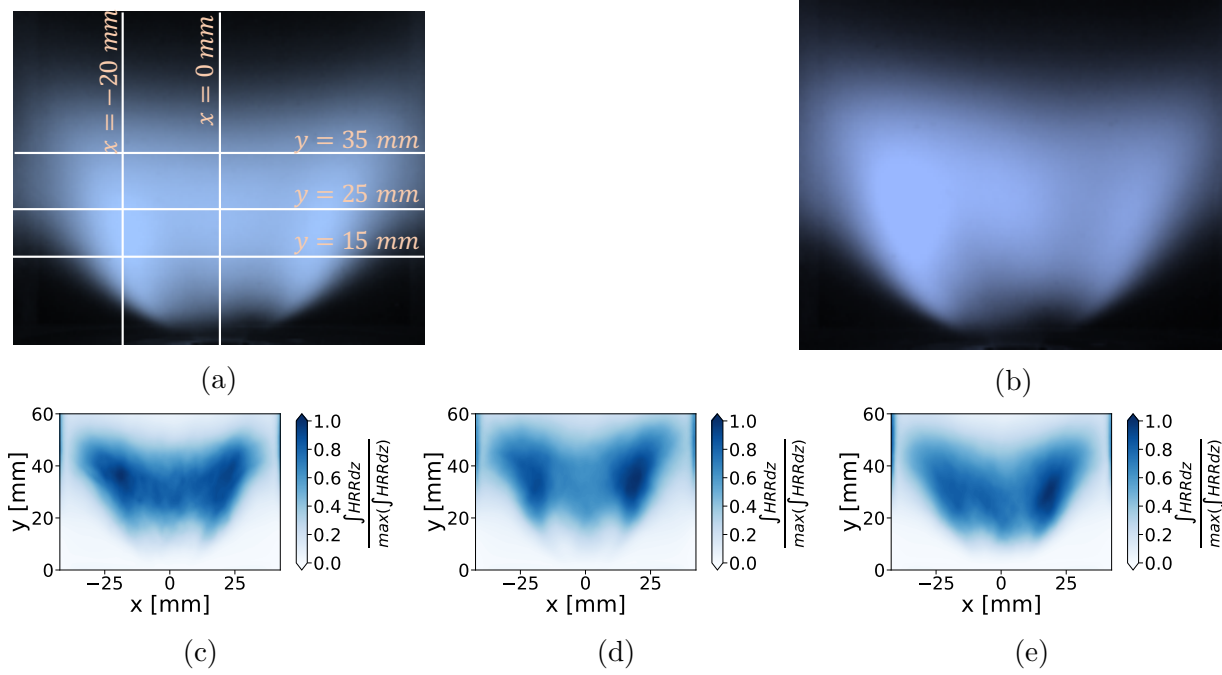
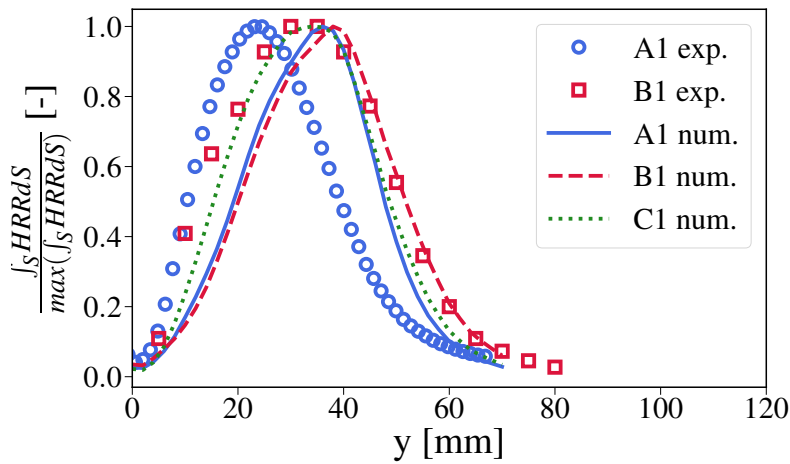


Figure 10.5: (a) Direct view of A1 flame; (b) Direct view of B1 flame; (c) heat release rate field, A1 case; (d) heat release rate field, B1 case; (e) heat release rate field, C1 case.

for B1. A1 experimental HRR profile also shows the different lines at which the profiles will be compared.

Looking at the three numerical fields, the V-shape observed for A1, B1 and C1 is retrieved compared to the measurements. B1 flame lift-off is larger than for A1 and C1 and it shows outer branches more intense than the central zone one. A1 and C1 look similar, but A1 seems to be more active in the central zone ($y = 15$ mm).



(a) HRR profiles

Figure 10.6: Average heat release rate integrated line along the central axis for A1, B1 and C1 fuels.

Finally, the integrated profiles of HRR (displayed in Fig. 10.6) show that B1 and

A1 flames are comparable to each other in terms of stabilisation location. However, B1 seems to be slightly shifted towards the burnt gases, which reproduces the trend of the experiments, although the drift is larger experimentally. Compared to numerical curves for A1 and B1, C1 is shifted towards the injection system with a relatively shorter flame.

Figure 10.7 displays the gaseous temperature profiles at $x = -20$ mm and at $x = 0$ mm and on a radial cut at $y = 15$ mm, $y = 25$ mm and $y = 35$ mm.

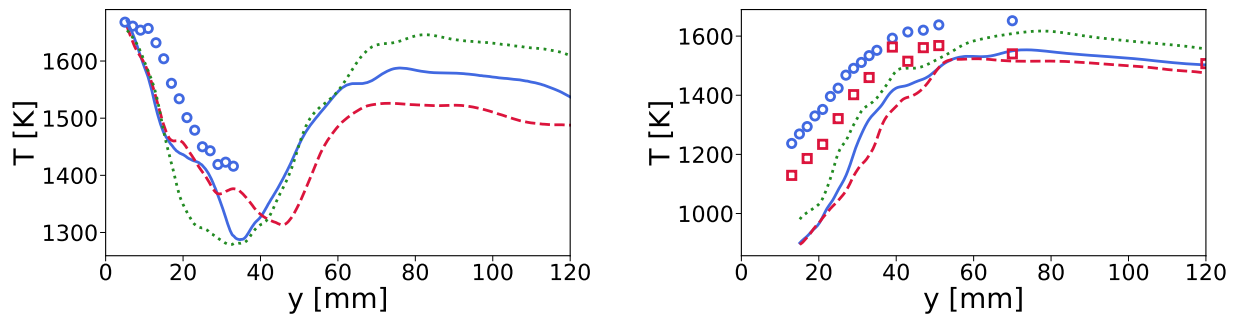


Figure 10.7: Axial temperature files at $x = -20$ mm and at $x = 0$ mm for A1, B1 and C1. Experimental results are added for A1 and B1.

As for A1, LES under-estimates the axial temperature profile compared to measurements. The trend between A1 and B1 is reproduced numerically, theoretical temperature being lower for B1 than for A1. Nevertheless, the difference is smaller in the LES than in the experiments. The main difference for C1 (for which no measurements are available) is a higher temperature in the second half of the chamber ($y > 40$ mm).

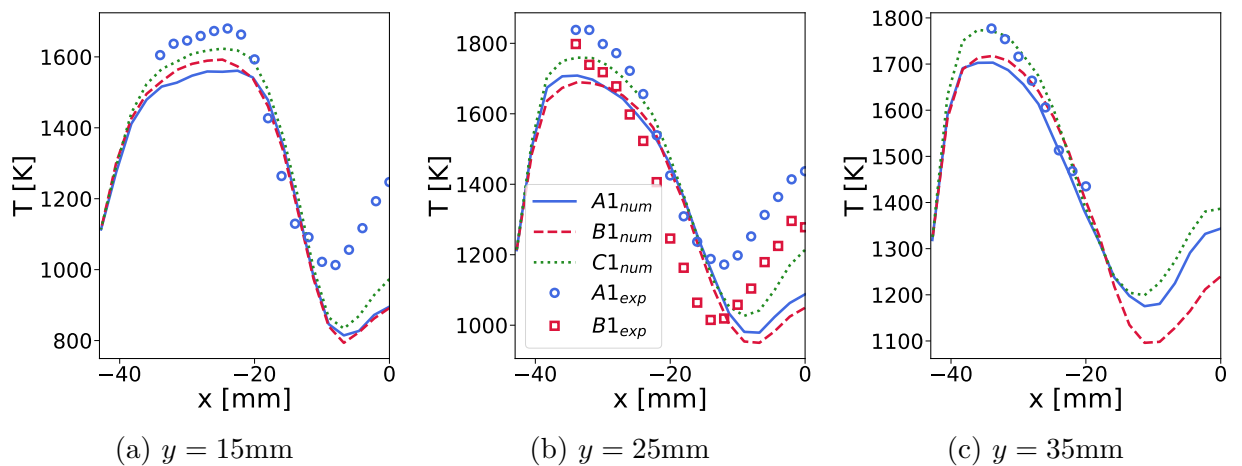


Figure 10.8: Radial temperature profiles at $y = 15$ mm, $y = 25$ mm and $y = 35$ mm for A1, B1 and C1. Experimental results are added for A1 and B1.

Concerning the radial profiles (Fig. 10.8), A1 shows a slightly higher temperature than B1. As for the axial profile, the experimental trend is reproduced, but the differences are smaller for the LES than for the experiments. C1 (and A1 and $y > 35$ mm) shows a higher temperature in the central region and C1 also exhibits a higher temperature in the ORZ.

As a conclusion, AVBP is able to show an impact of fuel on flame position and shape, and for A1 and B1, the experimental trend is responded, although the differences are smaller numerically. These differences are due to physical reasons, since the setup used in the three cases and the averaging time has not changed between the different fuels. The

aim of next sections is to analyse the complex effects of multi-component fuel on flame structure.

10.2 Spray flame structures

The goal of this section is to analyse the differences between the fuels, from evaporation to combustion. Section 10.2.1 analyse the fuel evaporation. Section 10.2.2 explains how the evaporation field impacts the temperature field. Finally, Section 10.2.3 analyses the pollutant emissions fields and proposes first conclusions on the "best" alternative fuel in the SSB configuration.

10.2.1 Fuel evaporation

As explained in Chapter 7, the flame foot is the key region to study the stabilisation mechanism in the combustion chamber. Therefore, evaporation characteristics are investigated for the three fuels to explain how pre-evaporation happens and affects the flame. To start with, the time-averaged mass fraction fields of each component for the three surrogates are displayed in Fig. 10.9. Note that the mass fractions are also tangentially-averaged. Solid black lines representing 10 and 50 percent of the maximum are displayed as well.

Looking at the maximum values, B1 is much more evaporated than A1 and C1, which is consistent with the faster evaporation of B1 compared to the two other fuels. Second, when looking at the different components fields for each fuel, it appears that:

- for A1, methyl-cyclohexane evaporates very fast downstream the injection system and shows a much lower concentration further downstream. Xylene slightly evaporates close to the injection system as well, but as it is not a very reactive species, it evaporates on the sides of the flame. Finally, n-dodecane slightly evaporates close to the injection system, but releases a larger amount of vapour much downstream.
- for B1, iso-octane evaporates directly after the injection system, and the field looks like the cyclohexane one for A1. Iso-dodecane also evaporates near the injection system, but also shows a high mass fraction for higher y values ($y = 20$ mm). Finally, iso-cetane exhibits a very low mass fraction maximum and is located on the side of the flame.
- for C1, iso-dodecane evaporates downstream the injection system, but also depicts high values for higher y values ($y = 20$ mm). Decalin and methyl-naphthalene evaporate roughly at the same location.

These vapour distributions are coherent with the 0D analyses in Section 8.1.2. The use of a multi-component surrogate model coupled to a multi-component evaporation model shows different component distributions according to the fuel tested. The next point is to analyse how these fields affect the flame and the burning modes.

To start with, the instantaneous fuel mass fraction is defined:

$$Y_F^{inst} = Y_F + \sum_{c=cells} \frac{\dot{e}_{F,c} \Delta t}{m_c^g} \quad (10.1)$$

with $\dot{e}_{F,c}$ the evaporation rate evaluated at the cell centre in a given iteration, Δt the time-step and m_c^g the gaseous mass of the cell. This definition enables to consider the total

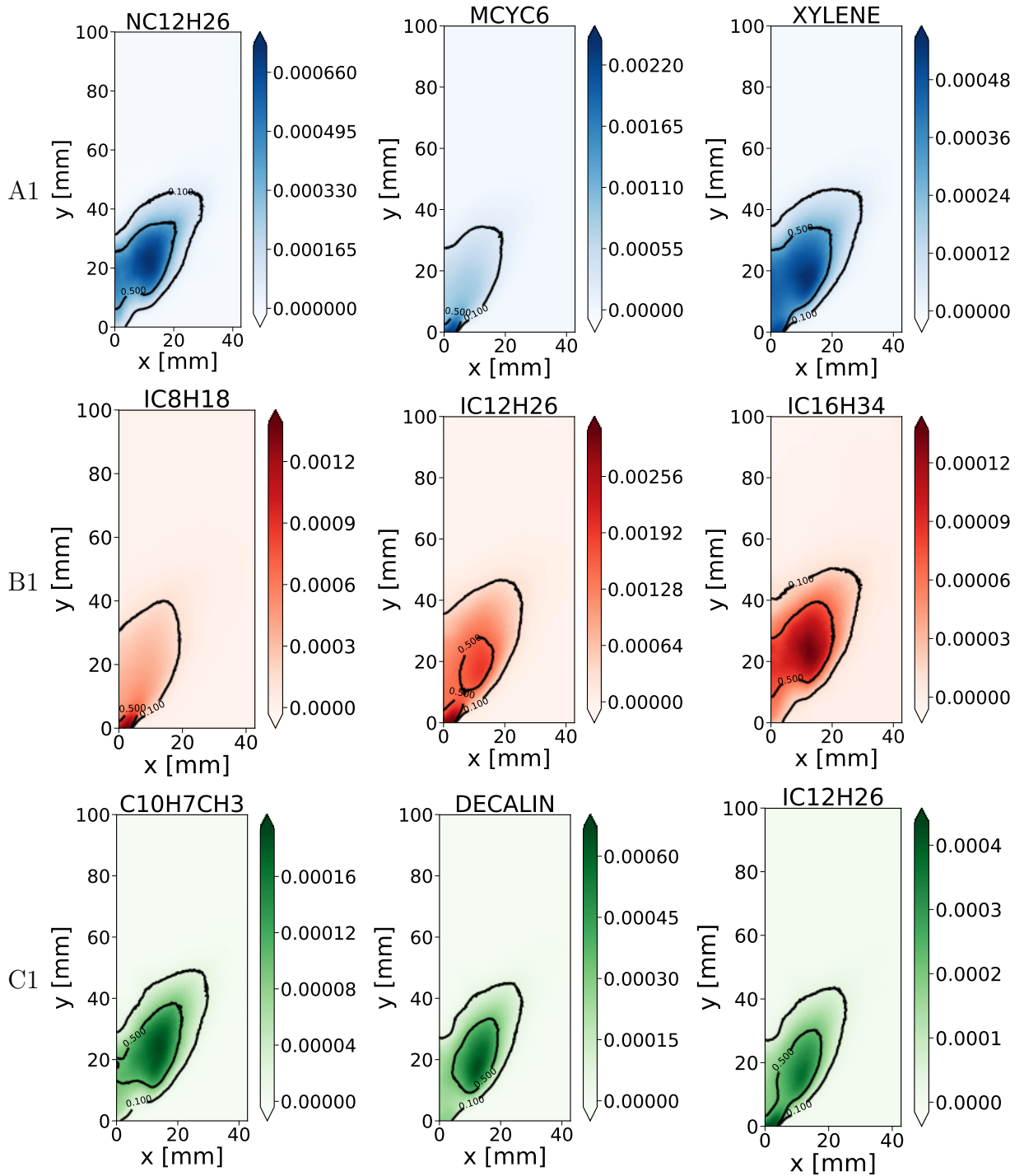


Figure 10.9: Time-averaged mass fraction fields for each component of A1 (top), B1 (middle) and C1 (bottom) fuel species. Isolines at 10 and 50 percent of the maximum value are added (solid black lines).

mass of fuel (both gaseous and liquid) available to burn. Such definition enables to build a contour plot representing the fuel efficiency defined in Section 7.2.2 for A1, B1 and C1 in Fig. 10.10. A threshold has been set $Y_F^{inst} > 10^{-6}$ to avoid zones where there would not be any fuel. The colorbar, represented by a Maxwell triangle is in three directions, and each direction represents a dominant component in the local blend.

The simpler plot to analyse is B1 as the most important component is $IC_{12}H_{26}$ by far,

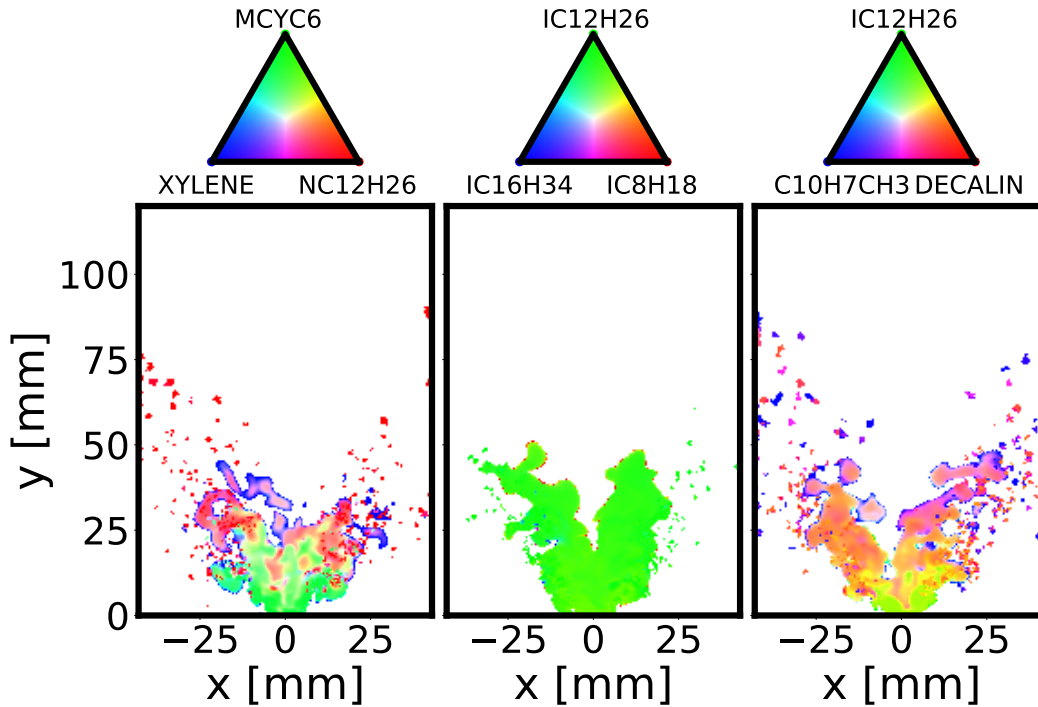


Figure 10.10: Instantaneous fields of $Y_F^{eff,inst}$ for $Y_F^{inst} > 10^{-6}$ for A1, B1 and C1 fuel.

which is dominant everywhere in the flame. On the edges of the flame shape, tiny red zones can be seen, which is explained by $IC_{12}H_{26}$ reacting faster than IC_8H_{18} . Droplet combustion is visible, but here again testifies the presence of iso-dodecane in the droplets. No clear region of iso-cetane is visible in the graph. The fuel seems to react mostly near the flame front, even if some droplets are burning in the ORZ.

For A1 fuel, on the contrary, the flame looks interestingly very much stratified in terms of components. Indeed, at the flame foot, methyl-cyclohexane in green is the dominant species as it has already evaporated in the injection system. Approaching the ORZ, n-dodecane, the major fuel species in the droplet, slightly becomes the most dominant species. It is interesting to see that xylene only dominates at the edge of the flame, even if it evaporates slightly after methyl-cyclohexane. At the central line, on the top of the flame, methyl-cyclohexane and xylene remain together without any n-dodecane. Indeed, n-dodecane is the latest to evaporate and is thus mostly present in the form of droplets, which will continue to release fuel directly in the ORZ and in the far field.

For C1, iso-dodecane is the first species to evaporate and dominates the flame root. However, it is quickly replaced by the major species, decalin, with a zone where both components co-exist. Finally, in the upper branches of the flame, a mix of decalin and methyl-naphthalene is predominant. Contrary to A1, and because there is no strong variation between evaporation and chemistry of the species, the fuel area does not extend towards the ORZ.

To quantify the observed effects of differential evaporation, local gaseous equivalence ratios and the absolute difference between the blend effective composition and the local composition for the cold flow ($T < 1000K$) is shown in Fig. 10.11 for A1, B1 and C1. This definition is useful when looking at the dominant mass fraction at a given location.

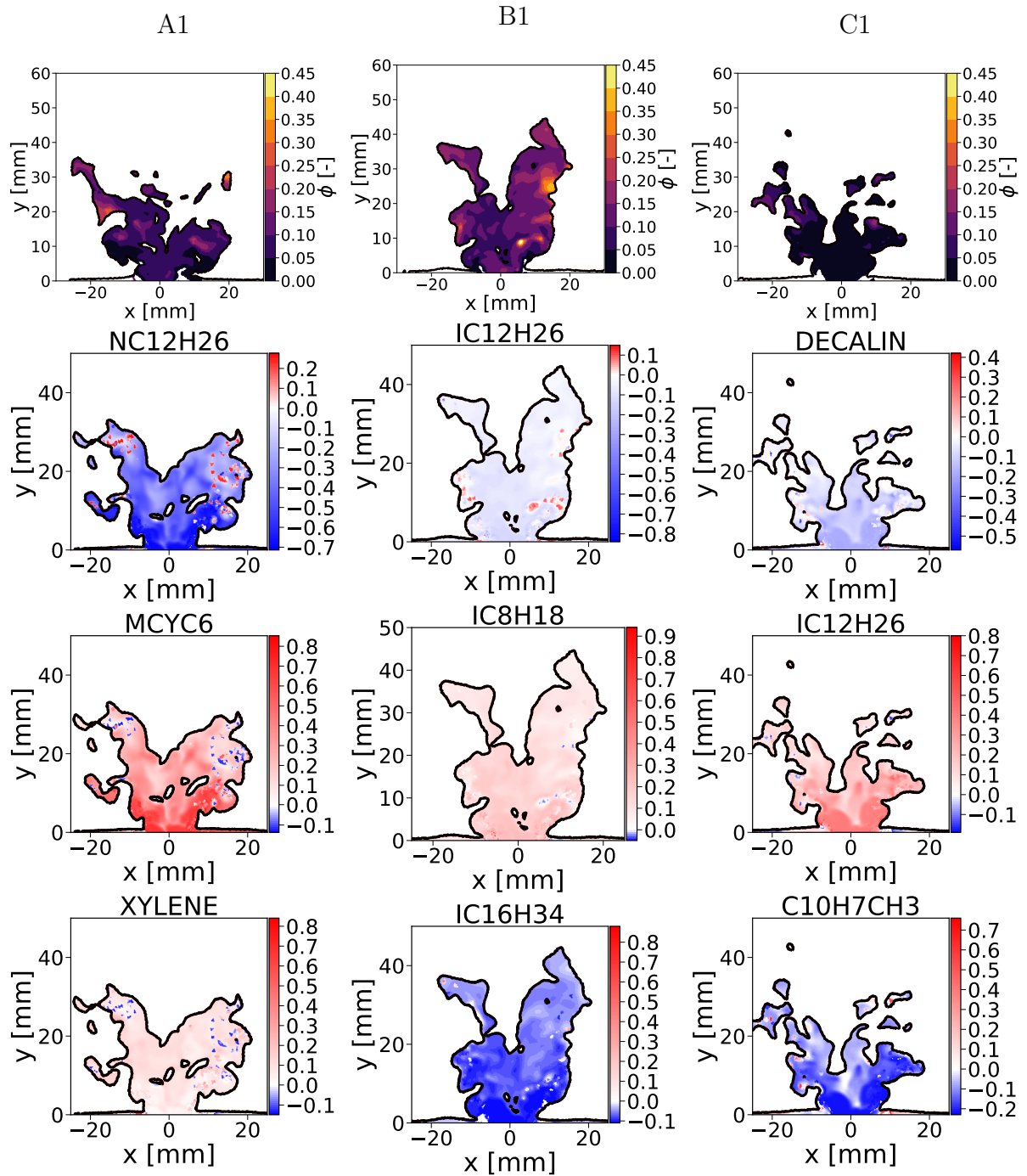


Figure 10.11: Gaseous local equivalence ratio (first row) and absolute difference between blend and local composition: $Y^{eff} - Y_{liq}^{ref}$ (last three rows) for A1 (first column), B1 (second column) and C1 (last column) for $T < 1000$ K.

First, the gaseous local equivalence ratio is lower than the global equivalence ratio ($\phi_g = 0.8$). B1 shows a higher local equivalence ratio, due to a higher level of pre-evaporation, which leads to a greater laminar flame speed and a lower CO mass fraction.

Second, the absolute difference $Y^{eff} - Y_{liq}^{ref}$ with the reference composition is bounded between $-Y_{liq}^{ref}$ and $1 - Y_{liq}^{ref}$ which shows the difference between the expected composition if no preferential evaporation occurred and the real case. A strong blue colour means that

the species is largely below the initial value and a strong red colour that it is largely above, before combustion. Results mainly confirm what the semi-liquid 1D spray premixed flame shows (see Section 8.2.2):

- for A1 (left column), methyl-cyclohexane MCYC6 takes a much larger part in the pre-evaporated fresh gases than it has in the initial blend. As a contrary, n-dodecane NC12H26 burns the latest and out of the pre-evaporated zones, except for several droplets that have already been consumed because of their small sizes, visible through the small points on the graphs. Xylene evaporates slightly more than the reference value. Therefore, because of the pre-evaporation and the lower efficiency of xylene compared to n-dodecane in terms of burning, the flame is slower with a lower temperature than the corresponding spray flame with the initial blend composition everywhere in the domain.
- for B1, iso-octane evaporates faster than the two other components and is therefore slightly higher than what is expected. Iso-dodecane is slightly below the reference values and iso-cetane has not started evaporation or very little, as it is the last one to evaporate. Pre-evaporation here has a relatively small influence on the flame dynamics because the three components exhibit roughly the same characteristics.
- for C1, iso-dodecane evaporates more than the initial composition, and decalin, the main species in the fuel, slightly less. Methyl-naphthalene has not evaporated except at the centre of the flame. Contrary to A1, the higher contribution of iso-dodecane in the pre-evaporated part leads to a higher flame velocity and temperature than the corresponding flame with the initial blend composition everywhere.

As a conclusion, starting from the inherent chemistry of the surrogates, 1D calculations made in previous section help to identify two important aspects influencing the flame. First, the droplet size influences the spray penetration in the ORZ, i.e a larger diameter leads to a less pre-evaporated flame, meaning that the final temperature and the laminar flame speed are lower. Second, the pre-evaporated composition may modulate the influence of the two-phase flow. According to this analysis, A1, even though having the largest of the flame speed, shows a higher diameter spray (see Section 10.1.1) with a downgraded pre-evaporation because of xylene, which would normally lead to lower laminar flame speeds and lower temperature. On the contrary, B1, with a slightly lower flame speed and lower final temperature, shows neutral pre-evaporation effects and lower two-phase characteristics. C1, with a lower laminar flame speed and a higher temperature, finally shows a higher diameter effect but an efficient pre-evaporation. With this in mind, the next section investigates the impact of the fuel evaporation on the thermal field.

10.2.2 Combustion regime

Knowing that the pre-evaporated area is weak in terms of fuel released and that quantities are pre-evaporated following the preferential evaporation analysed in Section 8.1, the influence of the fuel burning in the ORZ and the impact on the related field can be described. With the previous analysis in mind, the hexbin and temperature scatter plots of the different fuel compositions can be drawn on the whole domain (Fig. 10.12) to highlight the link between evaporation and combustion. Purple boxes represent the initial blend compositions. Here again, a threshold has been set for $Y_F^{inst} > 10^{-6}$.

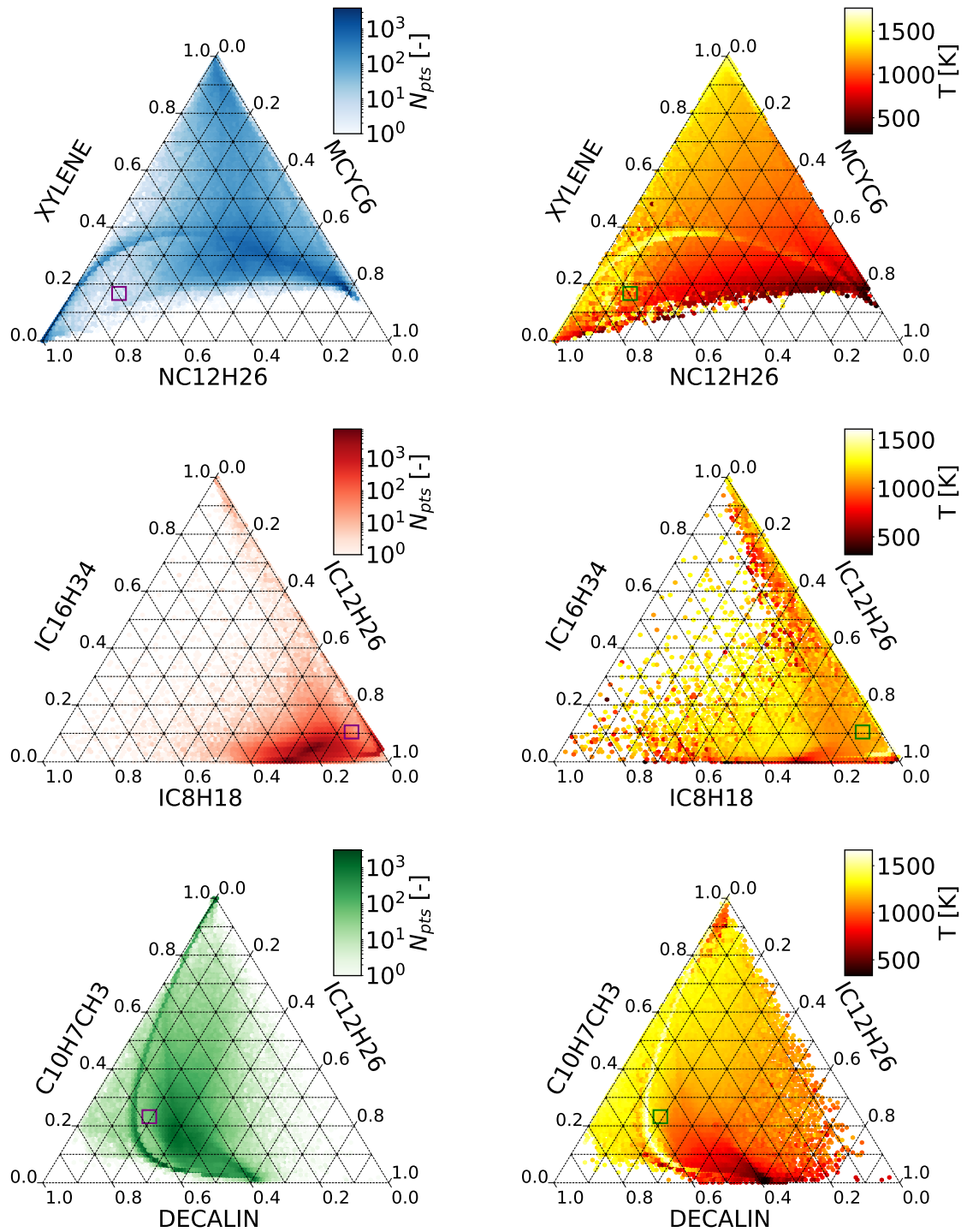


Figure 10.12: Hexbin (left) and temperature scatter (right) plots vs $Y_F^{inst,eff}$ at $0 < y < 10$ mm for A1, B1 and C1 components.

For A1, points are spread all around the graph, except for pure methyl-cyclohexane. Indeed, and even at the flame foot (represented by low temperature on the temperature scatter plot), methyl-cyclohexane and xylene have already slightly evaporated. Only a few points burn at the blend composition, testifying that the evaporation is very different for the fuel species. Yellow areas in the temperature scatter plot represent, for the top of the

triangle, pure gaseous xylene burning and droplet evaporation for the yellow line going from methyl-cyclohexane burning to pure n-dodecane burning. The hexbin plot suggests that a majority of points are located at $Y_{NC12H26}^{eff} = 0.2$, $Y_{MCYC6}^{eff} = 0.5$ and $Y_{XYLENE}^{eff} = 0.3$, which shows the fast evaporating behaviour of methyl-cyclohexane and xylene, even if they are theoretically not the predominant species in the blend.

For B1, most points are very close to the initial composition, slightly shifted towards a greater value of iso-octane, and smaller values of iso-cetane and iso-dodecane. The spread is not important, some values may reach the extrema of pure iso-dodecane and pure iso-cetane. The droplet burning, in yellow on the temperature scatter plot, lays very close to the pure iso-dodecane region. The cold zone is not visible here, because too many points are located in the same area, justifying that the points are not moving in the flame.

For C1, points are also spread all around the graph. Pure iso-dodecane and pure decalin are however fairly hardly reached. The fuel starts burning with a mix of decalin and iso-dodecane (black points). When reaching a higher temperature, the part of methyl-naphthalene becomes more important. Points displayed with the highest temperature also corresponds to droplets burning fast in the ORZ, which can contain a mix of the three components, depending on the size of the droplets. Most points are located nearby the expected composition, with $Y_{DECALIN}^{eff} = 0.5$, $Y_{IC12H26}^{eff} = 0.3$ and $Y_{C10H7CH3}^{eff} = 0.2$.

For the three surrogates, points with a higher temperature correspond to the points burning as two-phase flow. This is a big difference compared to the 1D two-phase premixed flame. Indeed, droplets burning in the ORZ can induce additional energy and heat to the flame, which is not the case in the 1D flame because the flame temperature is already the adiabatic temperature. As a consequence, larger mean diameter size, leading to a longer spray, influences the flame deeper and could explain why A1 and C1 stabilises at higher temperature than B1. This can be illustrated with scatter plots of temperature versus local gaseous equivalence ratio for the three surrogates, displayed in Fig. 10.13.

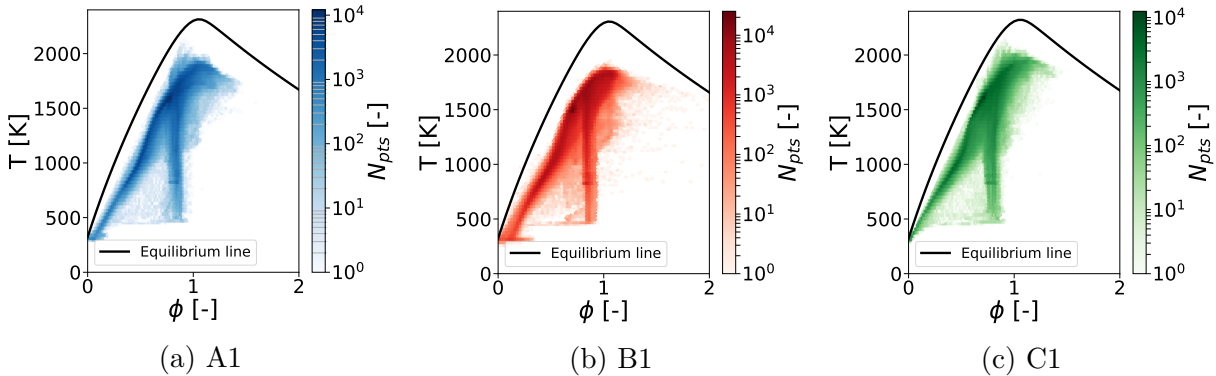


Figure 10.13: Scatter plot of temperature versus the local equivalence ratio ϕ for A1 (left), B1 (middle) and C1 (right). The equilibrium line is drawn in black.

The three plots look very similar at first glance. When comparing A1 and B1 plots, the highest temperature reached seems lower for B1 than for A1. These statements seem to assess that higher diameters seem to add another dynamics for the flame, explaining the thermal behaviour for the fuels. C1 surrogate keeps closer to the equilibrium line with a higher temperature than the two other fuels, featuring fewer rich regions.

To investigate why some fuels show more rich points than others, Takeno fields with pyrolysis products contoured by $HRR > 10 \text{ MW/m}^3$ and for $\nabla Y_F > 10^{-6}$ and $\nabla Y_{O_2} >$

10^{-6} are displayed Fig. 10.14 for A1, B1 and C1.

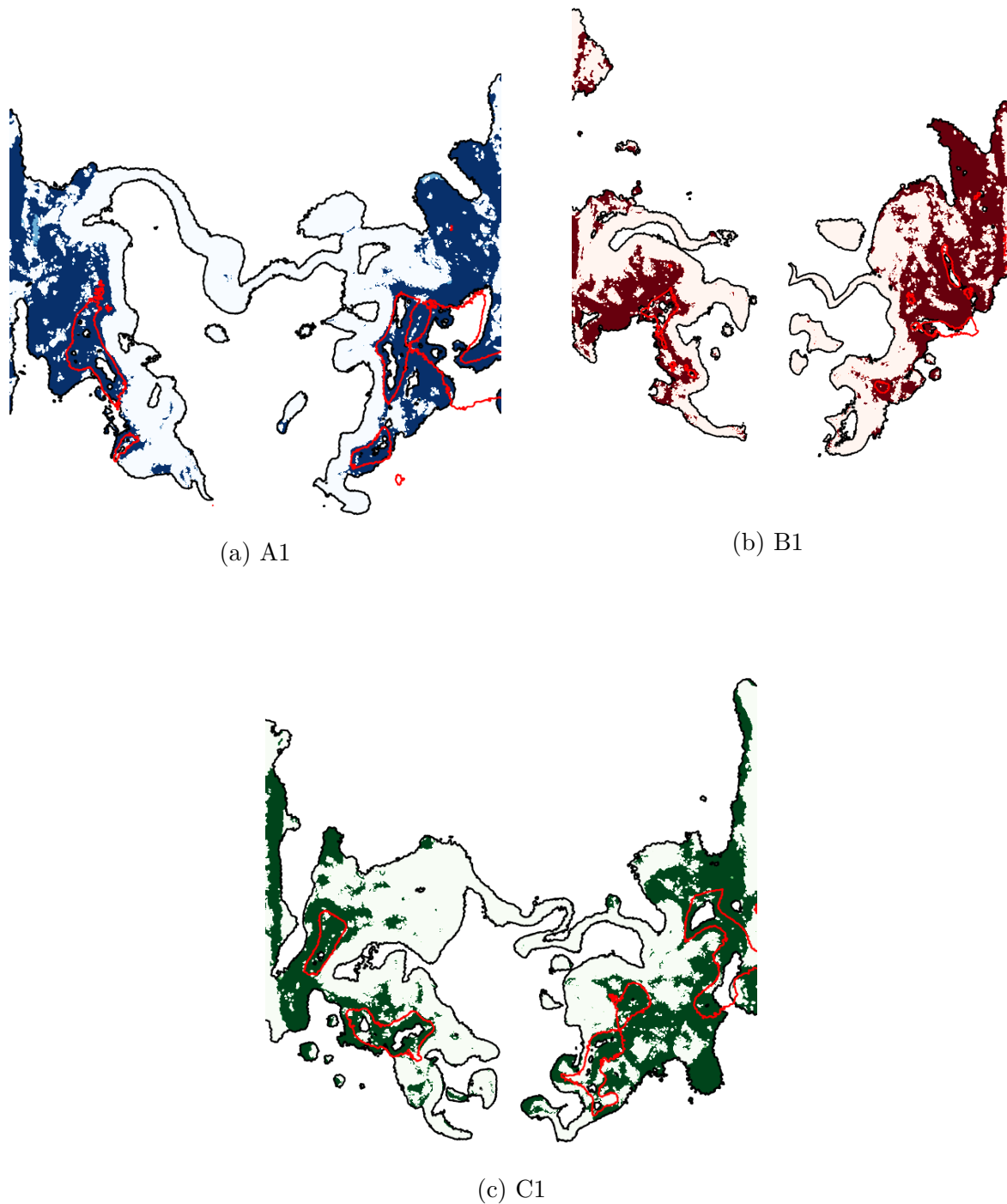


Figure 10.14: Vertical and horizontal cuts of instantaneous Takeno field for $HRR > 10 \text{ MW/m}^3$ for A1, B1 and C1. Premixed zones in white, diffusion zones in dark and stoichiometric isocontour in red. The dotted lines represent the location of the cuts.

Regimes do not change completely between the fuels: every surrogate exhibits a fully premixed flame, due to the pre-evaporation, followed by a stratified field due to the two-phase flow. The stratified area seems to be more extended for A1 and C1 than for B1,

depicting their higher initial diameter. A small difference in the flame topology is that B1 show fewer diffusion gaseous zone in the burnt gases, contrary to A1 and C1, which is due to their bigger droplet diameter.

The mean proportion of a given flame regime multiplied by the heat release rate Ta^{HRR} , defined Section 3.3.3.3, is displayed in Fig. 10.15 as well as $Ta^{\dot{\omega}}$ the flame regime multiplied by the component source terms with error bars representing the variance of the results.

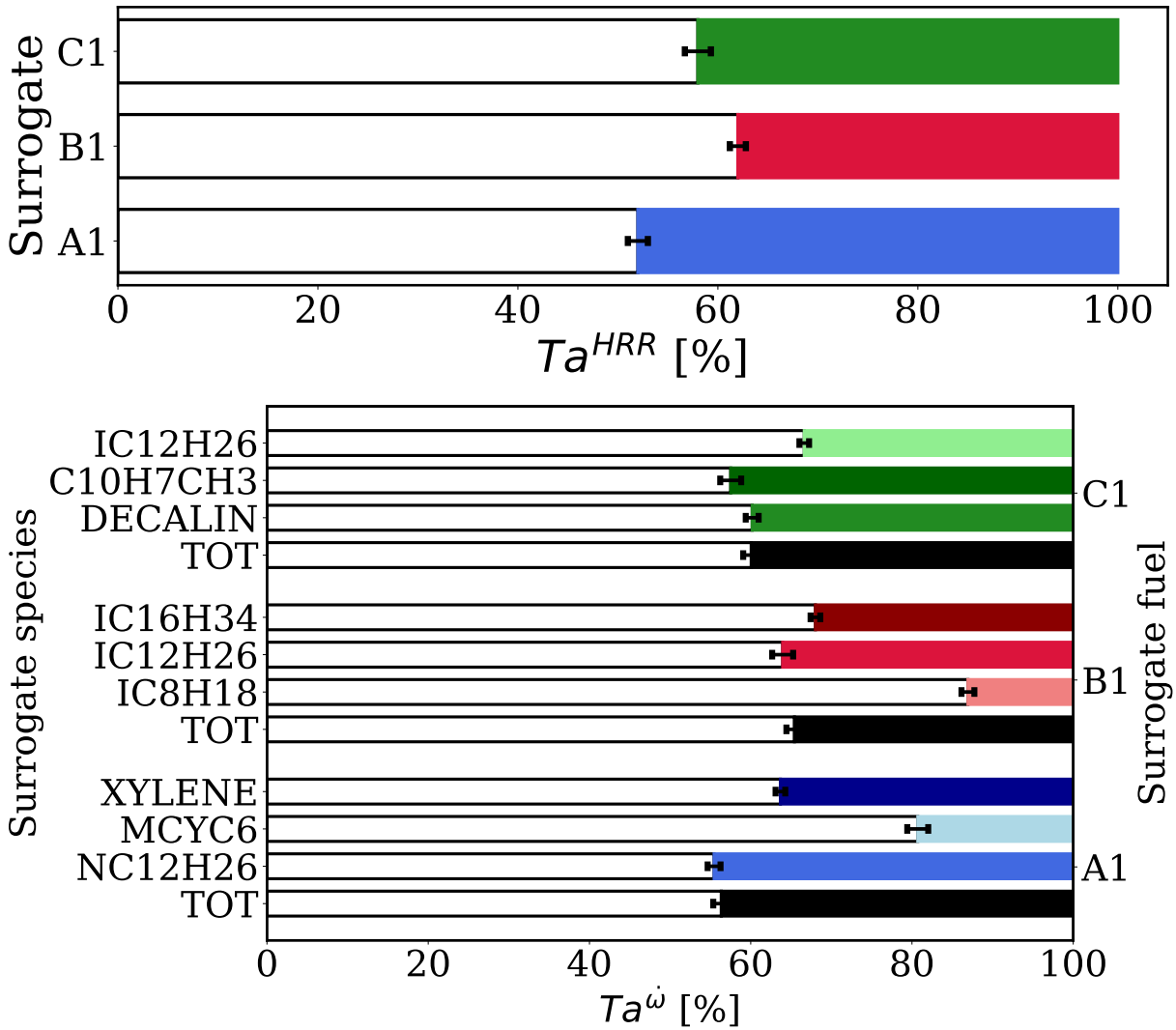


Figure 10.15: Flame regime proportion for A1, B1 and C1 and for the individual fuel components. Premixed in white and diffusion in colour.

Looking at the heat release rate Takeno, B1 seems to be the one burning the most in premixed mode, followed by C1 and then A1. The three flames exhibit a higher proportion of premixed mode than diffusion mode.

Looking at the fuel source term Takeno, the total contribution is first looked at, and results show the same tendency as for the heat release rate field. When analysing which species produces more premixed or diffusion flame regions, the main fuels (NC12H26 for A1, IC12H26 for B1 and DECALIN for C1) are found to produce a premixed quantity which get close to the one accounting for the three fuels. Both IC8H18 for B1 and MCYC6 for A1, as expected since they are the most volatile species, give a more premixed contribution

to the flame than the total fuel contribution. In the middle, XYLENE for A1, IC16H34 for B1 and XYLENE for C1 are lying in between those volatile fuels and the main fuel. Finally, C10H7CH3 leads to higher diffusion area because it mainly burns in the burnt gases area.

Consequences are the following. A1 shows many gaseous diffusion flame regions that account for a high power of the flame. B1 also shows diffusion areas, but they account for less flame power. C1 shows fewer diffusion areas than B1, but it seems to account for more of the power than B1. The reason for this is the pre-evaporation: for B1, droplets are massively consumed near the flame front generating real diffusion flames, whereas for C1, droplets are massively consumed in the far field. Looking at A1 and C1 fields, one may wonder why diffusion flames areas are promoted for A1 compared to C1. Since xylene and n-dodecane show a reverse order for the evaporation and the chemical phenomena, xylene is present in the ORZ but not consumed directly which creates areas with higher fuel loading that is consumed at the moment with n-dodecane, leading to higher local equivalence ratio.

As a conclusion, the flame structures depicted in Section 10.1 are a direct consequence of the two-phase flow dynamics and the fuel pre-evaporation impacting the thermal field. First, the total amount of fuel still to be burnt in the hot gases environment brought by the droplets modifies the flame structure. Second, the order of release between the fuel components influence the combustion efficiency. Both parameters induce stratified premixed flame, with a flame regime that is a result of these two previous parameters, defined in the SAF.

Of course, real fuels are made up of several different carbon molecules for the different species classes, as shown in Section 7.1.1. Therefore, results shown here represent extreme cases where one class is reduced to one carbon molecule. Discretising the different species as done here has the advantage of highlighting the major class behaviour and was able to explain the differences shown in the experiments.

10.2.3 Towards optimised SAF

The temperature fields induce several pollutant predictions that can as well be compared with the 1D flame computations. First Section 10.2.3.1 presents the consequences of the flame shapes on CO , CO_2 with an extension towards NO_x . Second, a discussion is made on the best candidate as SAF in terms of flame stabilisation (Section 10.2.3.2) and LBO (Section 10.2.3.3).

10.2.3.1 Pollutants

The first consequence of using different fuels is the impact on the overall CO_2 production, shown in Table 10.3 for A1, and extended here for B1 and C1. Theoretical values result from a Cantera equilibrium calculation, and the numerical values are the time-averaged values measured on a plane in the exit duct.

	A1	B1	C1
Theoretical value	0.162	0.1578	0.1705
Numerical value	0.1588	0.156480	0.165216

Table 10.3: Comparison of theoretical and numerical final fuel mass fractions for A1, B1 and C1.

Numerical values are very close to the experimental ones, with a relative error less than 2%. Comparing values between the three fuels shows that more carbon dioxide is released when burning C1 fuel as B1 and A1. This is a direct consequence of the H/C ratio, as highlighted in Equation 7.10. As shown in Table 7.2, since A1 has a higher H/C ratio ($H/C = 2$) compared to C1 ($H/C = 1.7$), less CO_2 is produced. Conversely, A1 has a lower H/C ratio than B1 ($H/C = 2.17$) and therefore produces more CO_2 .

CO mass fraction was measured above the exit duct experimentally. This probe being placed in the free atmosphere, it prevented us from comparing the measurements to the computations. Eventually, only CO and NO concentrations for A1 have been provided. Therefore, to have an idea on the fuel sensitivity to CO production, fields of time-averaged CO mass fractions are displayed in Fig. 10.16 for the three fuels.

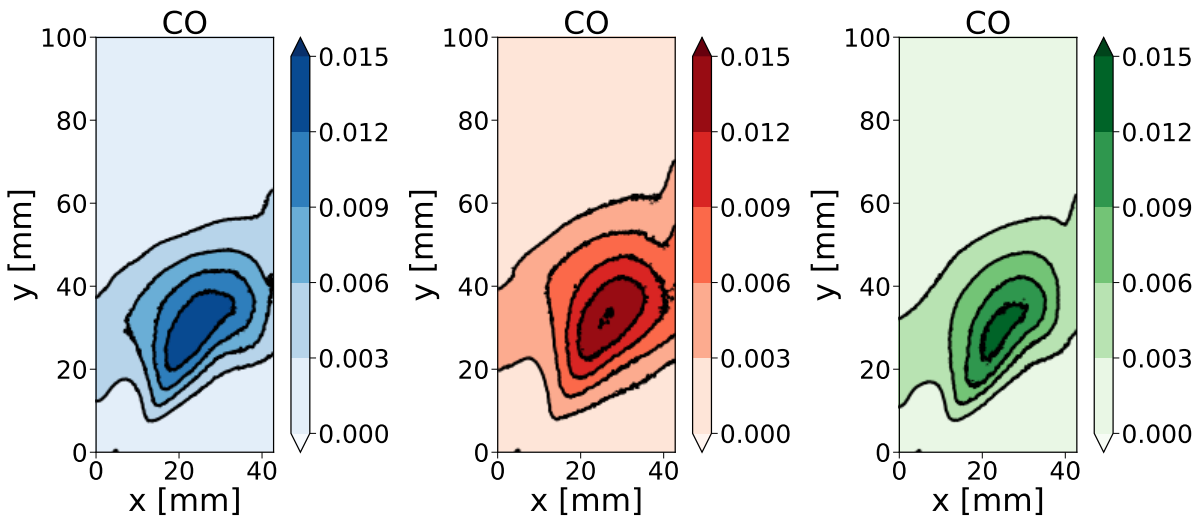


Figure 10.16: Time-averaged CO mass fraction field for A1 (left), B1 (middle) and C1 (right).

CO production for C1 is slightly lower than for A1 and B1, which themselves show very similar levels. The two-phase 1D premixed flame gave a higher concentration for A1 and nearly the same for B1 and C1. The local equivalence ratio in the ORZ must then have an impact on the CO produced. Indeed, the diffusion regions that may be found for A1 increases the amount of CO compared to C1. B1 was expected to be lower than A1, because the pre-evaporation is higher and the preferential evaporation is in favour of less CO, as shown in Section 8.2.3. However, the flame structure leading to numerous diffusion flame regions leads to a higher CO mass fraction.

As the temperature is higher for those fuels and that the thermal NO_x pathway is dominant, NO_x emissions are expected to be higher for A1 and especially in the C1 and B1 cases. This first guess should be confirmed by rederiving reduced chemistries including the NO_x pathways and re-performing LES for the 3 fuels.

10.2.3.2 Best SAF candidate in terms of flame stabilisation

The flame stabilisation and the amount of pollutant produced, for a given power level delivered, naturally depends on:

- the fuel **liquid distribution**, that impacts the evaporation timescale τ_{ev} .

- the **chemistry** of the fuel components that impact the capability of the mixture to ignite fast (auto-ignition time τ_{ig}) and to react fast (chemical time τ_c).

These timescales are valid for any turbulent spray flame with complex kinetics. When including complex surrogate models, an additional phenomenon appears: the **preferential evaporation** of the surrogate components also has to be considered as it redistributes the local mass fractions temporally, and thus spatially. As a consequence, the local combustion is modified, leading to different H/C ratios and different combustion regimes.

Rich mixture fraction and high temperature areas should be avoided in the flame, because they respectively promote CO and NO_x production. Those regions are created because of the late evaporation of some components of the surrogates and are a direct consequence of the two-phase flow modulated with the pre-evaporation behaviour. The high temperatures observed in the ORZ are then a coupling between the chemistry, the flame regime created and the heat losses to be accounted for. As a consequence, and as the objective is to reduce the creation of emissions, the H/C ratio should be the highest so that the species would react fast and burn efficiently at low temperature. The spray should not evaporate too quick to avoid strong diffusion areas. Conversely, if the spray evaporation is too long, higher temperatures may be reached locally. Therefore, one may build an optimal blend to limit the pollutant emissions. Finally, preferential evaporation should not lead to the creation of diffusion areas by inverting the order between the evaporation and the chemical reaction, as for the A1 flame with XYLENE and NC12H26.

However, other requirements should be fulfilled when employing SAF, namely ignition and extinction. Therefore, LBO resistance is investigated in the next paragraph.

10.2.3.3 Towards LBO resistance

As far as LBO is concerned, the analysis of [107] on the fuel properties can be carried out here. Indeed, the parameters that may differ when considering different fuels are the following:

- Atomisation properties, which were not considered in this study as mentioned in Section 8.1. B1 is supposed to give finer droplets than A1 and C1.
- Evaporation properties differ for A1 and C1 compared to B1.
- Chemical properties, which are almost the same for the three fuels tested here.

Evaporation properties are supposed to be the most influencing parameter for the extinction phenomenon, especially with the analyses made in Section 9.3.2, stating that the flame stabilisation depends mainly on the capability of the droplets to burn in the ORZ. As a consequence, B1 is expected to resist less to lean blow-out than A1 and C1 because of its lower characteristic diameter.

For pure chemistry, LBO limit is not dependent on the H/C ratio [295] because, even if it is strongly correlated to the Derived Cetane Number (DCN), the DCN is difficult to correlate to the H/C ratio [316]. Therefore, LBO limit could be different for the fuels studied when considering the pure chemistry, even if their combustion dynamics are not very different.

As a consequence, results are completely reversed for the LBO limit: B1, that was a good candidate in terms of flame stabilisation as it should produce fewer pollutants, is found to be the less resisting to the LBO because of its efficient combustion.

10.3 Conclusion

The SSB using the three multi-component surrogates with complex kinetics (A1, B1 and C1) were computed. LES was able to capture the differences between A1 and B1 fuels for which measurements were provided. The differences in terms of temperature profiles could be explained by the two-phase flow dynamics and the preferential evaporation phenomenon, inducing different stratification fields for the fuels. The resulting pollutants were estimated, with a CO_2 level depending greatly on the equilibrium state. CO emissions were surprisingly very much the same between A1 and B1 and lower for C1. NO emissions are expected to be larger for A1 and C1 due to the higher temperatures.

Conclusions on the fuel have been drawn for the stabilised flame and the extinction:

- The H/C ratio must be kept high to maximise the combustion and minimise the final CO_2 , then avoiding aromatic species and promoting linear, branched and, to a certain extent, cyclic alkanes. A trade-off may be found to maximise the H/C and the DCN for a better flame resistance.
- Diameter should be kept optimum, i.e. low enough to avoid rich diffusion flame zones and high temperatures that are prone to create CO and NO_x , but high enough to be resistant to the LBO phenomenon.
- Preferential evaporation should conserve the same order between evaporation and chemical consumption to avoid late release of the fuel in burnt gases area, promoting diffusion areas.

Therefore, replacing some of the branched alkane with linear alkane species to enable a slightly bigger diameter while conserving the combustion efficiency of linear and branched species can be thought of, and is what is done for HEFA alternative fuel, which is one of the best candidate for SAF at the moment in the industry and already tested in aeroplanes within VOLCAN project. VOLCAN (VOL avec Carburants Alternatifs Nouveaux) is a French project in which Airbus, SAFRAN, Dassault Aviation, ONERA, DGAC, France Relance and the French Ministry of Transport are involved. The objective is to prove the operability of the current aircraft architecture to fly with 100% of alternative fuels, whereas the current legislation limits their use to a 50% blend with kerosene. CERFACS develops the fuel model and the simulation tools for SAFRAN in the project¹.

¹<https://www.safran-group.com/fr/espace-presse/principaux-acteurs-aeronautiques-francais-feront-voler-monocouloir-100-carburant-alternatif-fin-2021-2021-06-10>

Chapter 11

Conclusion and perspectives

11.1 Conclusion

The aim of this PhD was to study the impact of the fuel modelling in aeronautical burner and to evaluate numerically the LBO phenomenon. For this purpose, in the context of JETSCREEN project, the Spray-Stabilised Burner (SSB) from DLR was computed. Before simulating and analysing the complex 3D chamber, several chemical and spray processes needed to be analysed.

Firstly, the surrogates were analysed through the chemical spectrum. Three Analytically Reduced Chemistries (ARCs) were developed and tested, showing a good accuracy compared to the detailed mechanism. Several canonical cases (0D equilibrium, 0D time evolving reactor, 1D premixed flame) were computed to validate this mechanism and have been further analysed in order to investigate the different reactivities of the surrogates. Especially, the poorer reactivity of the aromatic compared to the other species was recovered. Pollutant productions were estimated, showing no real difference in terms of CO and CO_2 mass fractions unlike NO_x which seemed to be higher for C1 than the two other fuels. Soot could not be evaluated, but a methodology has been proposed. Aside from this validation, Zeldovich assumption, stating that 5 to 10 points are sufficient to discretise correctly the flame front of a 1D premixed flame, has been extended to ARC mechanisms. A further analysis of the reaction rates showed that the flame actually stabilises through a reaction-diffusion mechanism, where the discretisation of the fuel source term has a leading role in the flame spatial accuracy.

Second, two-phase flow modelling and properties were compared to the DLR experimental work and showed good accuracy. 1D spray flames were computed with pre-evaporation to see the difference with the gaseous flame in terms of overall properties and pollutants. The pre-evaporation in the gaseous phase has a slight impact on the laminar flame speed and heat release rate for a given fuel, since it redistributes the power given per species. Pollutants do not to change much with the liquid phase, but NO_x and soot emissions could not directly be estimated. Besides, a planar spray counterflow diffusion flame with a poly-disperse distribution was computed and analysed. The flame structure displayed a heat release rate field with two peaks showing the same intensity. With the help of monodisperse case, the second peak could be attributed to three major combustion behaviours: the gaseous diffusion flame contribution, the droplets vaporising in it and the premixed contribution of the droplets resisting the temperature field and evaporating after the flame front in the oxidiser side. A single droplet combustion algorithm was tested and compared with the previous calculation, showing the same overall flame structure but a different

behaviour on the oxidiser side as the droplets would evaporate more rapidly. Finally, the overall flame power led to the conclusion that the combustion regime is changing with the droplet size and include more premixed contribution with bigger diameters, which is well captured by the heptane/O₂ ARC chemistry that was developed for the study.

The swirl-stabilised spray flame was finally computed. The non-reacting flow showed a very good agreement with the experimental PIV. Prior to the reacting case, the input Rosin-Rammler distribution, measured experimentally in hot conditions, was fitted to the experimental data thanks to an uncertainty analysis. The simple BFER and the complex Jet-A1 surrogates were compared and showed differences in terms of flame reactivity and stabilisation. However, the three-component surrogate showed a much more complex field in the stratified area.

Then, LBO was experimentally tested by the DLR on the three fuels. Before simulating LBO, the flame was converged towards a lower operating point to evaluate the characteristic timescales and the important quantities near LBO. The ORZ was found to control the flame stabilisation and took too long to apply a step-like approach correctly. Near LBO, useful markers to detect the LBO event were identified. To get rid of the long computation time of adaptation, extinction was tested by igniting the combustion chamber at different fixed equivalence ratios and see if the flame may stabilise or not. After the characteristic convergence time-step, the flame seemed to stabilise at $\phi = 0.45$ and is extinct at $\phi = 0.40$, showing that LBO is occurring in-between those equivalence ratios. However, those results may be compromised by a non-adapted atomisation and wrong wall temperatures.

Finally, the SSB flame with multi-component fuel modelling and complex chemistry was stabilised and converged for three fuels. Spray differences were well captured, and the flame stabilisation was in accordance with the experimental data for A1 and B1 fuels. Preferential evaporation is still visible in the flame and gives a stratification of the fuel species released. The flame shows some stratified areas, because of the multi-component behaviour and the two-phase flow dynamics. The preferential evaporation, the heat losses and the flame structures induced by it are the key parameters that concluded on the flame shapes which were not featuring in the simple 1D two-phase premixed flames. Analysis on pollutants depicted a higher *CO* production for A1 and B1 due to the richer combustion generated in the ORZ. The “best” fuel suggested is then a trade-off for the flame stability and the LBO, with a high H/C ratio, an optimal diameter and a preferential evaporation that does not mix evaporation timescales and chemical timescales.

11.2 Perspectives

New questions arise from the work summarised in the previous paragraph, either to improve it or to clarify some ideas that were tackled but not investigated.

The study on the flame discretisation may lead to two perspectives:

- a flame refinement methodology can be deduced from the findings made previously. For a light fuel, such as methane, the fuel source term is covering the same area as the heat release rate, therefore refining the fuel source term means refining the heat release rate and the flame is well-discretised. For heavier fuels, however, the pyrolysis area is located much more ahead from the biggest heat release rate zone. A conclusion of this study would be that refining the source term and slightly less the rest of the flame front (that is to say, just enough for the intermediate species to be well discretised) could be a smart manner of refining a flame.

- as well as refining a canonical flame, choosing the right area where to thicken a flame front is also a topic of interest, and this study suggests that the right location to thicken a flame would be the species source term and not the heat release rate.

For evaporation concerns, as depicted in chapter 8, soot and NO_x pollutants should be estimated and especially the link between two-phase flow properties and their production. Eventually, the surrogate influence should be tested, namely the number of species used on the accuracy of the results found.

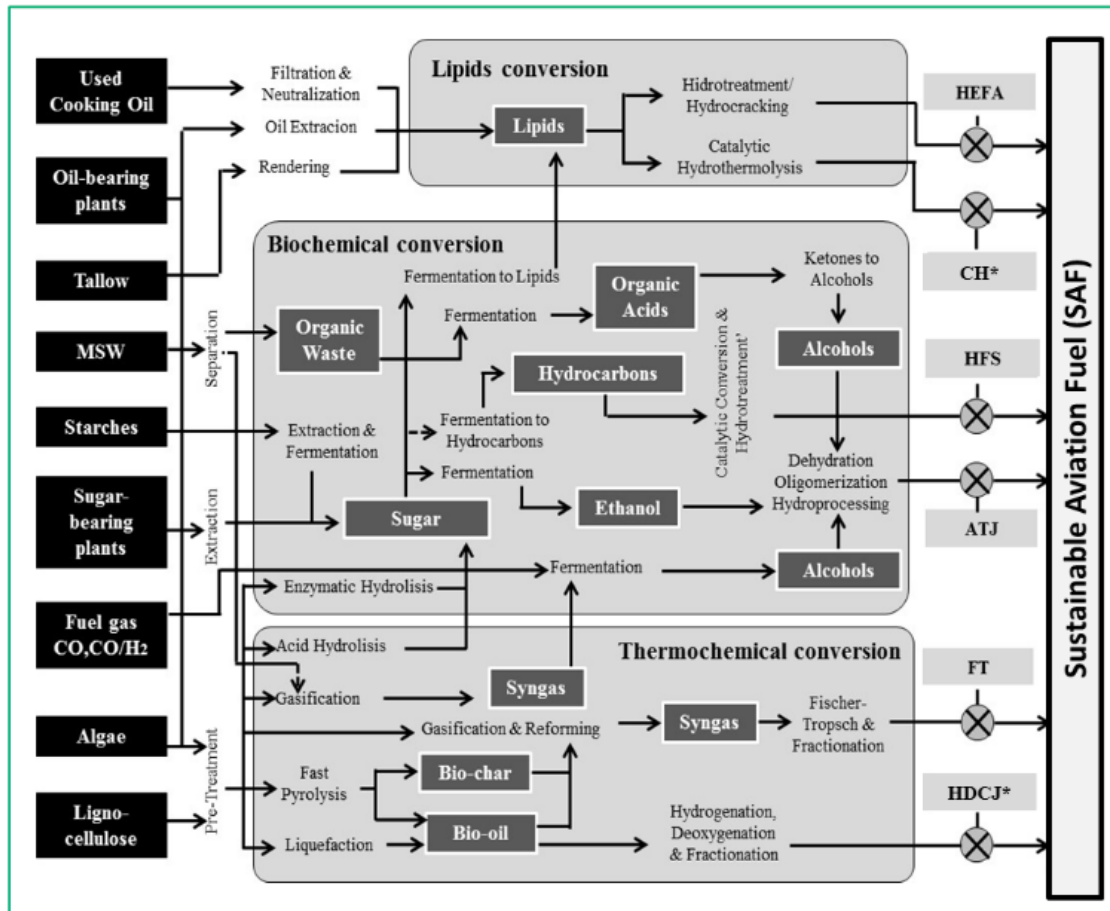
The counterflow diffusion flame configuration is a great start for several developments. Indeed, parameters playing on the thickness evolution of a two-phase flow diffusion flame compared to the purely gaseous equivalent were never investigated as done for the premixed flame in [266] where a correlation was found for the flame thickness and other flow parameters. Furthermore, this two-phase flame was computed with n-heptane and oxygen, which are showing a different behaviour from multi-component fuels. The exercise could then be repeated with complex surrogates to evaluate the impact of the modelling on the canonical structure.

For the SSB, several perspectives may be highlighted. To start with, data are available for Readijet and HEFA fuels, but the mechanism was not derived, and they were not tested in the SSB even if experimental works from the DLR exist. This could provide new lights on different fuel behaviours and precise the methodologies that this PhD has started to tackle. Other surrogate models could be applied on other schemes to see the difference in terms of flame structure. Single fuel data are as well available in Grohmann's paper [110] and could be simulated. More precisely, an ARC emulating kerosene could be tested to separate more accurately the complex kinetics effects from the surrogates one. High pressure cases should be investigate, especially as far as the evaporation is concerned and the role it has on the flame shape. For pollutants, NO_x and CO were measured by the DLR, but not taken into account in this work. Setting up a scheme that takes into account the pollutant predictions accurately would enable the comparison with the experiment and assess for the good reproduction of the experimental work. Furthermore, even though the thickening value was not high in the fields presented in chapter 9, the major part of uncertainty in the simulation must come from the combustion/turbulence modelling, as the thickening methodology is often not derived for two-phase flow multi-component complex chemistry. Emphasis should be made on the future on checking if the combustion/turbulence interactions are correctly modelled by the thickened flame modelling. Atomisation at the end of the swirler lips as well as a secondary atomisation model were not applied and should be taken into account. As the flame regimes are concerned, Takeno Index with pyrolysis products has shown good results in the SSB burner. However, when considering flames that are not only monitored by a premixed stratified flame but also real diffusion flames, their combustion regime may not be adequately identified. Therefore, the flame structure must be analysed in more simple cases.

For LBO, when changing the operating point, fixing the temperature is a very big assumption and may lead to some errors because the walls influence the thermal quantities. Second, atomisation properties need to be determined near extinction. Eventually, LBO limit was found with extinction from scratch but was not compared to a ramp extinction due to the long characteristic timescales. A work then needs to be done on the mesh to reduce the number of points. Multi-component LBO calculations could be tested and compared to the BFER calculation, with the methodology derived here. Indeed, for such complex surrogates, the converging quickness might not be the same as for simple surrogates. Besides, the chemistry, such as the importance of formaldehyde or of low tem-

perature paths for instance, could be investigated. LBO dependency to evaporation and/or chemistry then could be investigated.

Appendix Intro : SAF



*CH: Catalytic hydrothermolysis – not yet approved

HDCJ: Hydrotreated depolymerized cellulosic to jet – not yet approved

Figure 1: Detailed SAF pathways from [132].

Appendix A : Flame spatial discretisation

Species sensibility analysis

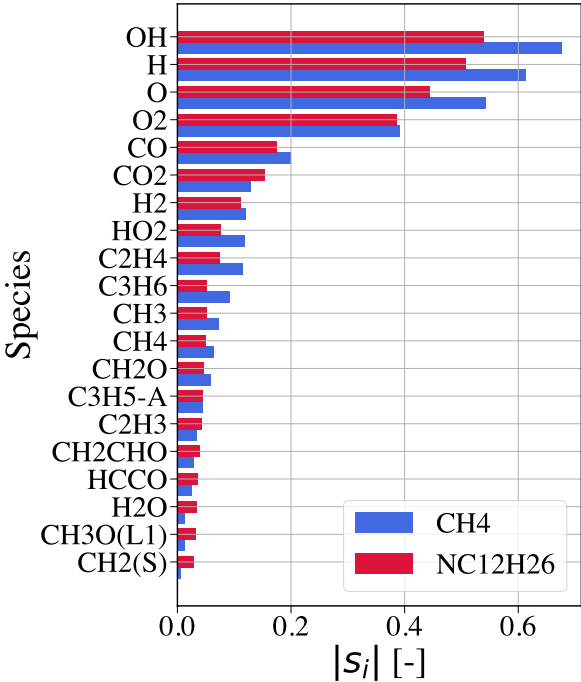


Figure 2: Sensibility analysis for CH₄/air and NC₁₂H₂₆/air flame at $T = 400$ K, $P = 1$ bar and $\phi = 1.0$.

Reaction rate proportion

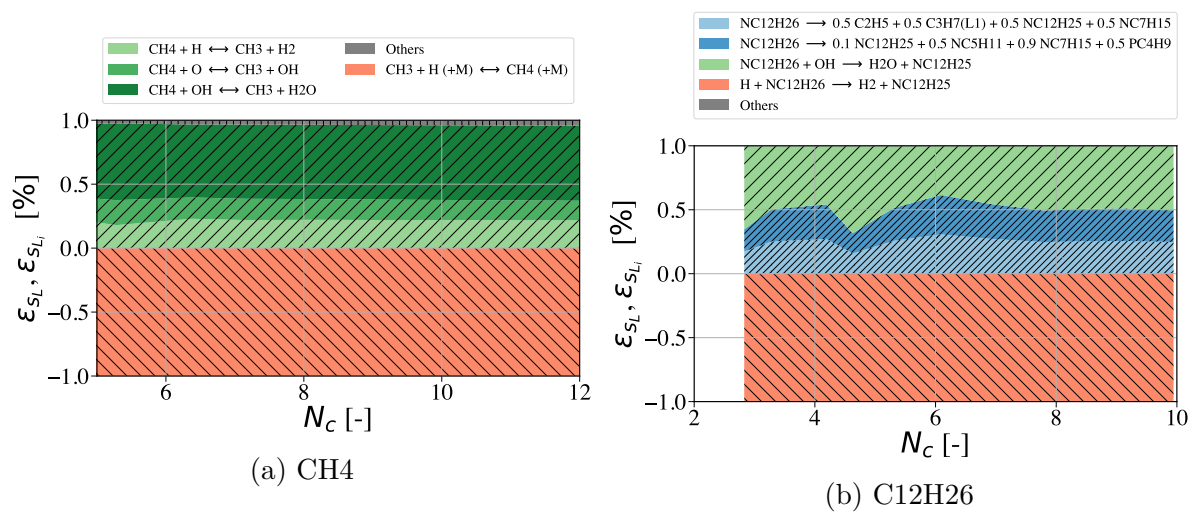
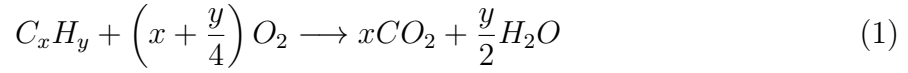


Figure 3: Proportion of the positive (resp. negative) reaction rate compared to the sum of positive (resp. negative) reaction rate.

Appendix B : Analysis of gaseous chemical processes

Final products mass fraction

Let's consider the following combustion equation:



Lean case The following advancement table is derived Table 1 for the lean case.

$C_xH_y + (x + \frac{y}{4})O_2 \longrightarrow xCO_2 + \frac{y}{2}H_2O$			
n_{Fuel}^{init}	$n_{O_2}^{init}$	0	0
$n_{Fuel}^{init} - \xi = 0$	$n_{O_2}^{init} - (x + \frac{y}{4})\xi$	$x\xi$	$\frac{y}{2}\xi$

Table 1: Advancement table for any hydrocarbon in the lean side.

Therefore:

$$X_{H_2O} = \frac{n_{H_2O}}{n_{H_2O} + n_{CO_2} + n_{O_2} + n_{N_2}} \quad (2)$$

By considering that $n_{N_2} = 3.76n_{O_2}$ and as $\xi = n_{Fuel}^{init}$:

$$X_{H_2O} = \frac{y/2n_{Fuel}^{init}}{y/2n_{Fuel}^{init} + xn_{Fuel}^{init} + 4.76n_{O_2}^{init} - (x + \frac{y}{4})n_{Fuel}^{init}} \quad (3)$$

By dividing the numerator and the denominator by x and n_{Fuel}^{init} :

$$X_{H_2O} = \frac{\frac{y/x}{2}}{\frac{y/x}{4} + 4.76\frac{n_{O_2}^{init}}{xn_{Fuel}^{init}}} \quad (4)$$

As $H/C = y/x$ and $\phi_g = (x + y/4)n_{Fuel}^{init}/n_{O_2}^{init}$:

$$X_{H_2O} = \frac{\frac{H/C}{2}}{\frac{H/C}{4} + 4.76\frac{1 + \frac{H/C}{4}}{\phi_g}} \quad (5)$$

And as $n_{CO_2} = x\xi = \frac{2}{H/C}n_{H_2O}$:

$$X_{CO_2} = \frac{1}{\frac{H/C}{4} + 4.76\frac{1 + \frac{H/C}{4}}{\phi_g}} \quad (6)$$

$C_xH_y + (x + \frac{y}{4})O_2 \longrightarrow xCO_2 + \frac{y}{2}H_2O$			
n_{Fuel}^{init}	$n_{O_2}^{init}$	0	0
$n_{Fuel}^{init} - \xi$	$n_{O_2}^{init} - (x + \frac{y}{4})\xi = 0$	$x\xi$	$\frac{y}{2}\xi$

Table 2: Advancement table for any hydrocarbon in the rich side.

Rich case The following advancement table is derived Table 2 for the lean case.

Therefore:

$$X_{H_2O} = \frac{n_{H_2O}}{n_{H_2O} + n_{CO_2} + n_F + n_{N_2}} \quad (7)$$

By considering that $n_{N_2} = 3.76n_{O_2}$:

$$X_{H_2O} = \frac{y/2\xi}{y/2\xi + x\xi + 3.76n_{O_2}^{init} + n_F^{init} - \xi} \quad (8)$$

By dividing the numerator and the denominator by ξ and replacing ξ by its value:

$$X_{H_2O} = \frac{\frac{y}{2}}{\frac{y}{2} + x + 3.76(x + y/4) + \phi_g - 1} \quad (9)$$

As $H/C = y/x$:

$$X_{H_2O} = \frac{\frac{H/C}{2}}{\frac{H/C}{2} + 1 + 3.76(1 + H/C/4) - 1/x} \quad (10)$$

Leading a dependency on the number of carbon atoms for the water mass fraction.

LHV calculation

At $T_0 = 298.15$ K, it is known that:

$$h_{C-H} = 413 \text{ kJ/mol} \quad (11)$$

$$h_{C-C} = 348 \text{ kJ/mol} \quad (12)$$

$$h_{C=C} = 614 \text{ kJ/mol} \quad (13)$$

$$h_{C\equiv C} = 839 \text{ kJ/mol} \quad (14)$$

$$h_{O_2} = h_{O=O} = 495 \text{ kJ/mol} \quad (15)$$

$$h_{CO_2} = 2h_{C=O} = 1598 \text{ kJ/mol} \quad (16)$$

$$h_{H_2O} = 2h_{O-H} = 926 \text{ kJ/mol} \quad (17)$$

The molar LHV LHV_{mol} can therefore be calculated through the following formula:

$$LHV_{mol} = xh_{CO_2} + \frac{y}{2}h_{H_2O} - \left(x + \frac{y}{4}\right)h_{O_2} - h_F \quad (18)$$

As for $x = 1$ atom of carbon in a hydrocarbon molecule, the number of hydrogen can be calculated:

$$y = 2(x - d + 1 - r - 2t) \quad (19)$$

with x the number of carbons, d the number of double bond (replacing 2 atoms of hydrogen), r the number of cycles (replacing 2 atoms of hydrogen as well) and t the number of triple bonds (replacing 4 atoms of hydrogen). The impact on the fuel enthalpy is the following:

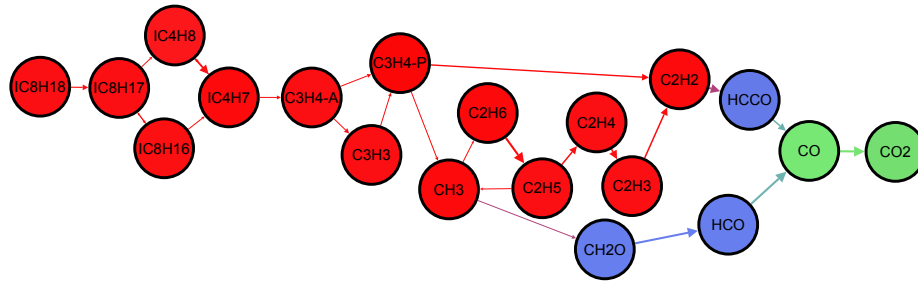
$$h_F = dh_{C=C} + th_{C\equiv C} + yh_{C-H} + (x - 1 + r - d - t)h_{C-C} \quad (20)$$

Indeed, if the number of carbon is fixed, for a linear molecule, the fuel enthalpy should be equal to the C-H bond enthalpy times the number of C-H bonds (the same as the number of hydrogen) and the C-C bond enthalpy times the number of carbon minus one as there is one less link than the total number of carbons. To that, the double and triple links must be replaced by their equivalent energy $h_{C=C}$ and $h_{C\equiv C}$. Finally, a cycle adds a $C - C$ bond to the molecule.

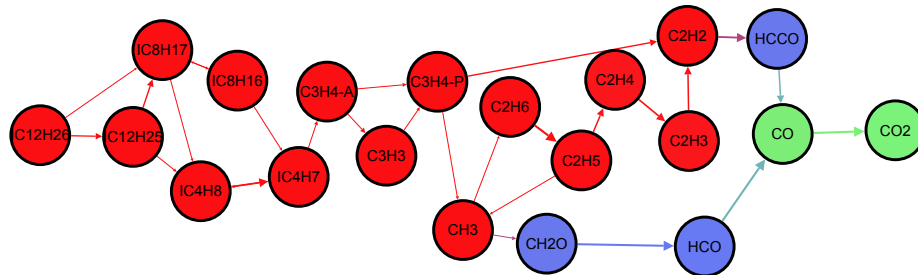
Eventually, when all the calculations are performed, the following formula is derived :

$$LHV_{mol} = 407x + 100y + 82d + 205t = 607x + 200 - 118d - 200r - 195t \quad (21)$$

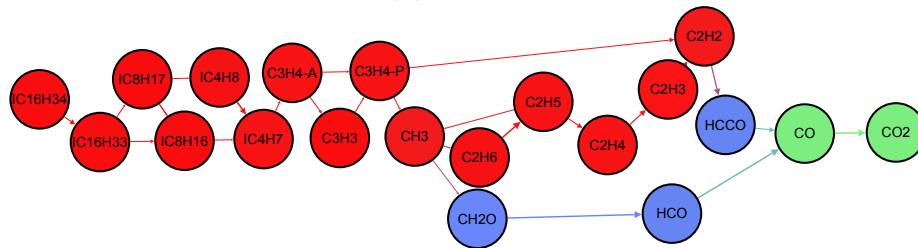
Chemical pathways for B1 and C1



(a) IC8H18



(b) IC12H26



(c) IC16H34

Figure 4: Chemical pathways for B1 fuel species at $T = 400K$, $P = 1$ bar and $\phi = 1.0$.

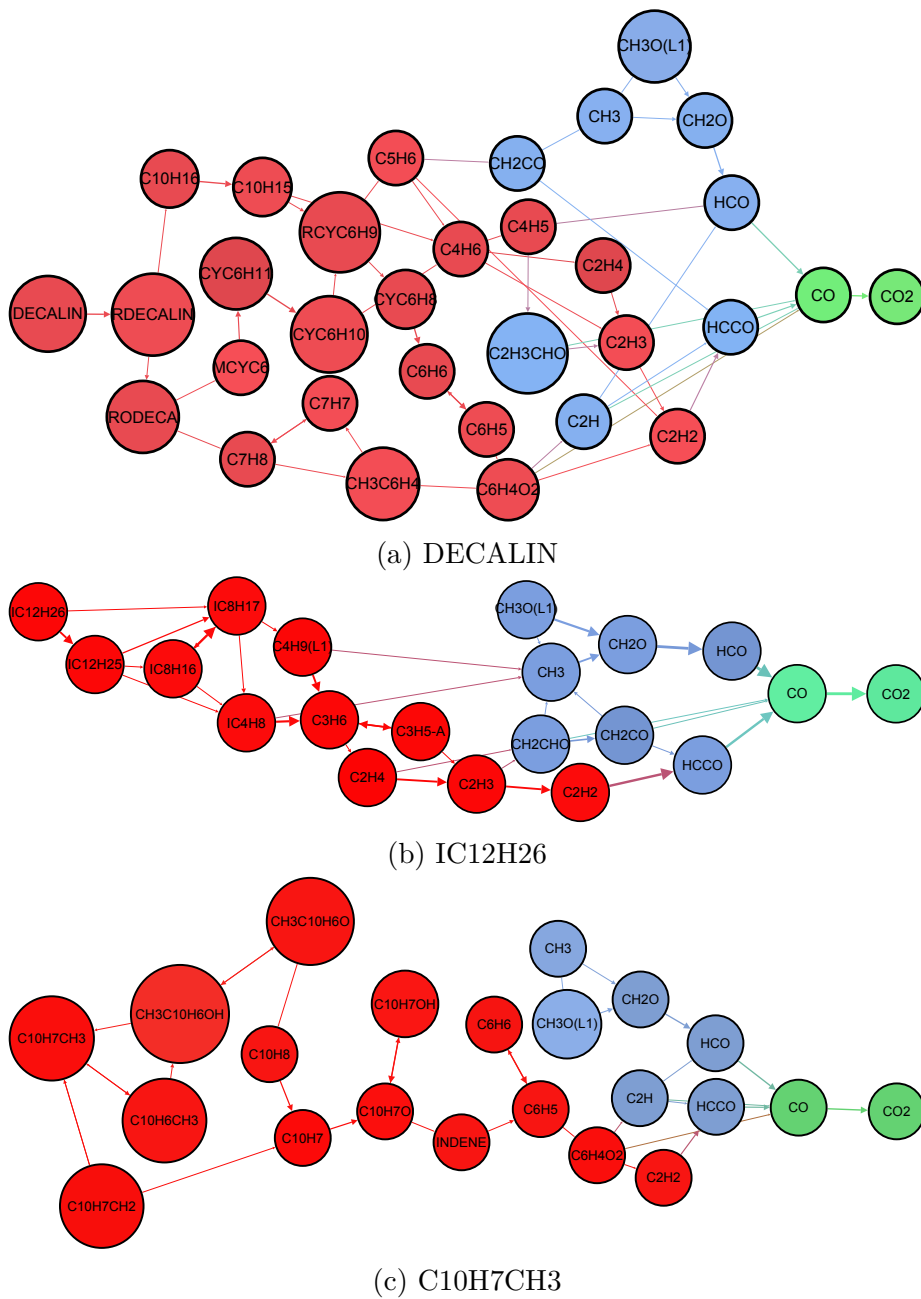


Figure 5: Chemical pathways for C1 fuel species at $T = 400K$, $P = 1$ bar and $\phi = 1.0$.

Premixed flame reaction rates for B1 and C1

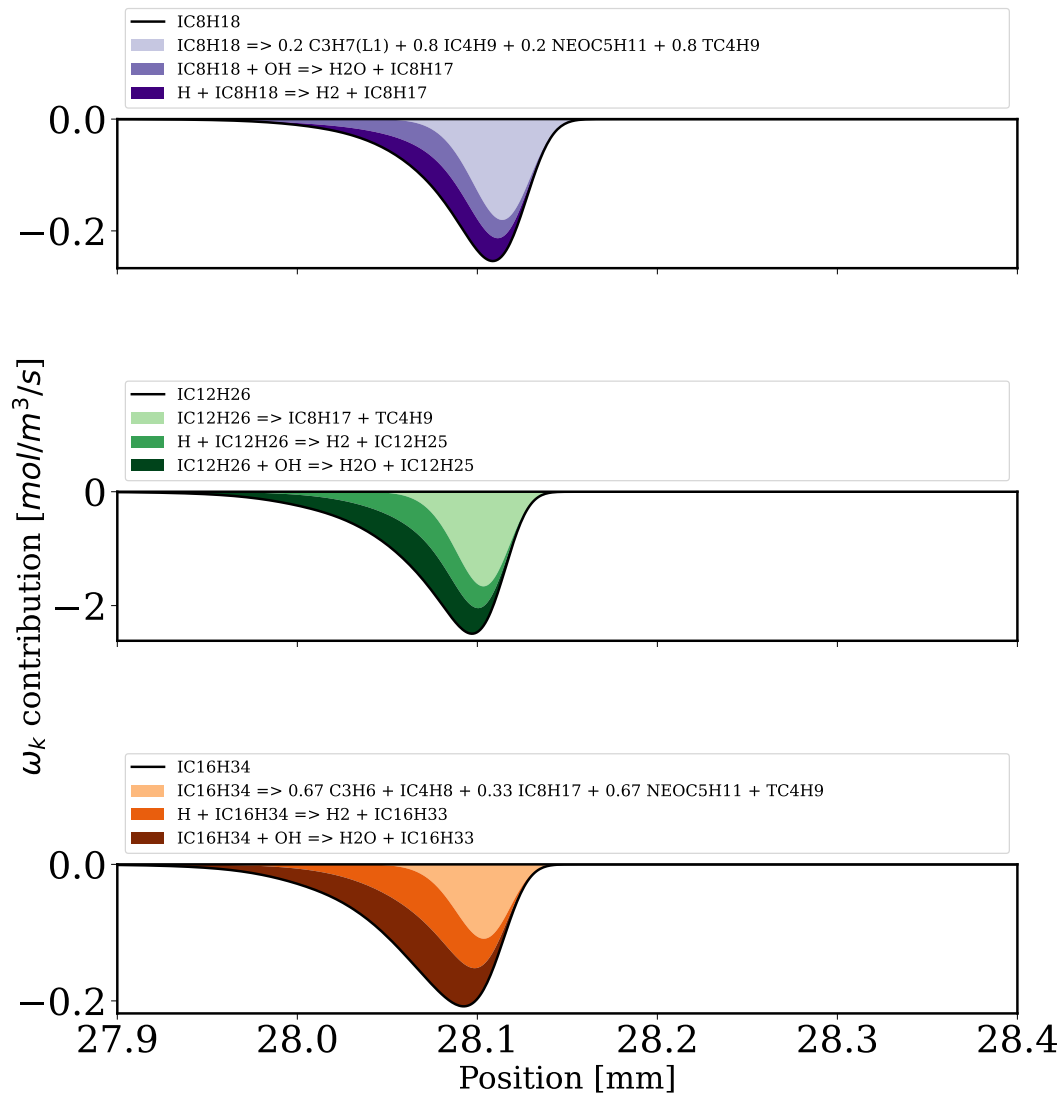


Figure 6: Source term for the B1 components and their reaction contributions at $T = 400$ K, $P = 1$ bar and $\phi = 1$.

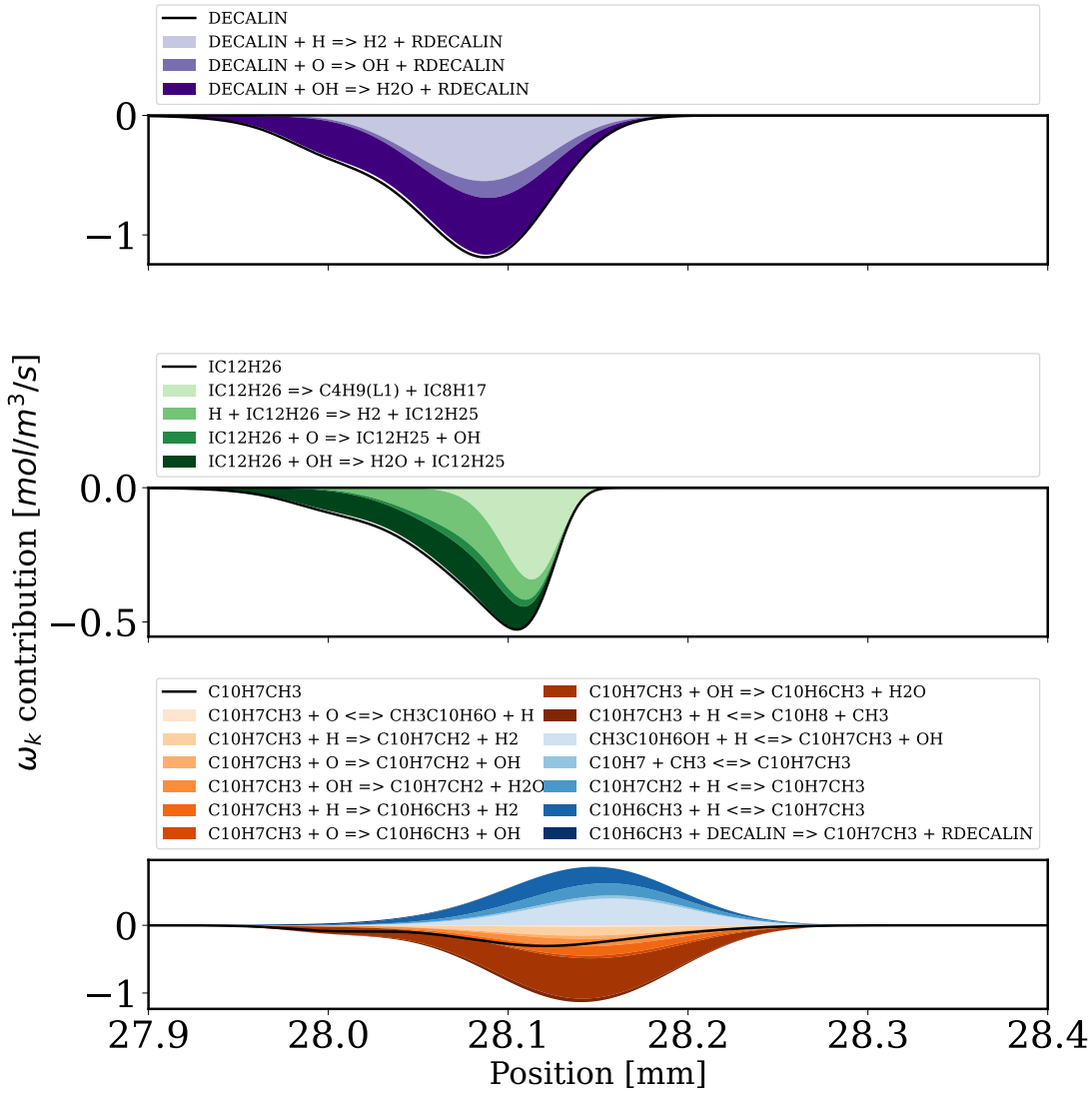


Figure 7: Source term for the C1 components and their reaction contributions at $T = 400$ K, $P = 1$ bar and $\phi = 1$.

List of Schmidt and Prandtl numbers for the mechanisms

BFER scheme

The Schmidt number for BFER are displayed Table 3. The Prandtl number Pr for BFER is $Pr = 0.7$.

Species	$C_{10}H_{20}$	O_2	CO	CO_2	H_2O	N_2
Sc	0.7	0.7	0.7	0.7	0.7	0.7

Table 3: Schmidt numbers Sc for the BFER scheme.

A1 scheme

The Schmidt number for ARC A1 are displayed Table 4. The Prandtl number Pr for ARC A1 is $Pr = 0.67$.

Species	N_2	H_2	H	O_2	O	H_2O
Sc	0.741	0.206	0.125	0.743	0.485	0.555
Species	OH	H_2O_2	HO_2	CO	CO_2	CH_4
Sc	0.494	0.753	0.748	0.753	0.949	0.682
Species	CH_3	CH_2O	C_2H_6	C_2H_5	C_2H_4	C_2H_2
Sc	0.679	0.862	0.996	0.988	0.776	0.818
Species	C_3H_6	$C_3H_5 - A$	C_3H_3	C_4H_6	C_6H_6	NC_5H_{10}
Sc	1.034	1.053	1.064	1.27	1.549	1.497
Species	CYC_6H_{10}	<i>XYLENE</i>	$MCYC_6$	$NC_{10}H_{21}$	$NC_{12}H_{25}$	$NC_{12}H_{26}$
Sc	1.559	1.903	1.769	2.484	2.753	2.754
Species	$NC_{10}H_{20}$	$C_4H_7(L_1)$	$C_3H_7(L_1)$	$CH_3O(L_1)$	$C_7H_7(L_1)$	$C_4H_8(L_1)$
Sc	2.482	1.25	1.227	0.882	1.753	1.39

Table 4: Schmidt numbers Sc for the ARC A1 scheme.

B1 scheme

The Schmidt number for ARC B1 are displayed Table 4. The Prandtl number Pr for ARC B1 is $Pr = 0.714$.

Species	N_2	H_2	H	O_2	O	H_2O
Sc	0.679	0.204	0.122	0.7408	0.477	0.551
Species	OH	H_2O_2	HO_2	CO	CO_2	CH_4
Sc	0.486	0.744	0.739	0.744	0.936	0.670
Species	CH_3	CH_2O	C_2H_6	C_2H_5	C_2H_4	C_2H_3
Sc	0.667	0.853	0.983	0.975	0.766	0.815
Species	C_2H_2	C_2H	C_3H_6	$C_3H_5 - T$	$C_3H_4 - P$	$C_3H_4 - A$
Sc	0.807	0.799	1.023	1.041	1.057	1.057
Species	C_2H_3CHO	IC_4H_8	IC_4H_7	IC_8H_{18}	IC_8H_{16}	$IC_{16}H_{34}$
Sc	1.363	1.376	1.239	1.978	1.974	3.208
Species	$IC_{12}H_{26}$					
Sc	2.735					

Table 5: Schmidt numbers Sc for the ARC B1 scheme.

C1 scheme

The Schmidt number for ARC C1 are displayed Table 4. The Prandtl number Pr for ARC C1 is $Pr = 0.708$.

Species	N_2	H_2	H	O_2	O	H_2O
Sc	0.677	0.202	0.121	0.731	0.474	0.545
Species	OH	CO	CO_2	CH_4	CH_3	CH_2O
Sc	0.483	0.739	0.942	0.666	0.663	0.845
Species	C_2H_5	C_2H_4	C_2H_2	CH_2CO	C_4H_6	C_4H_2
Sc	0.968	0.761	0.802	1.0	1.247	1.23
Species	CYC_6H_{10}	IC_8H_{16}	C_7H_8	C_6H_5O	$C_6H_5C_2H$	$INDENYL$
Sc	1.534	1.959	1.728	1.650	1.772	1.909
Species	$C_{10}H_7CH_3$	$CH_3C_{10}H_6O$	$DECALIN$	$RDECALIN$	$NC_{12}H_{26}$	$IC_{12}H_{25}$
Sc	2.13	2.156	2.047	2.046	2.712	2.711
Species	$C_{10}H_{15}$	$C_6H_9(L_1)$	$C_4H_8O(L_1)$	$C_4H_8(L_1)$	$CH_3O(L_1)$	
Sc	2.043	1.617	1.555	1.366	0.864	

Table 6: Schmidt numbers Sc for the ARC C1 scheme.

Appendix C : Spray counterflow diffusion flame

Additional fields of interest

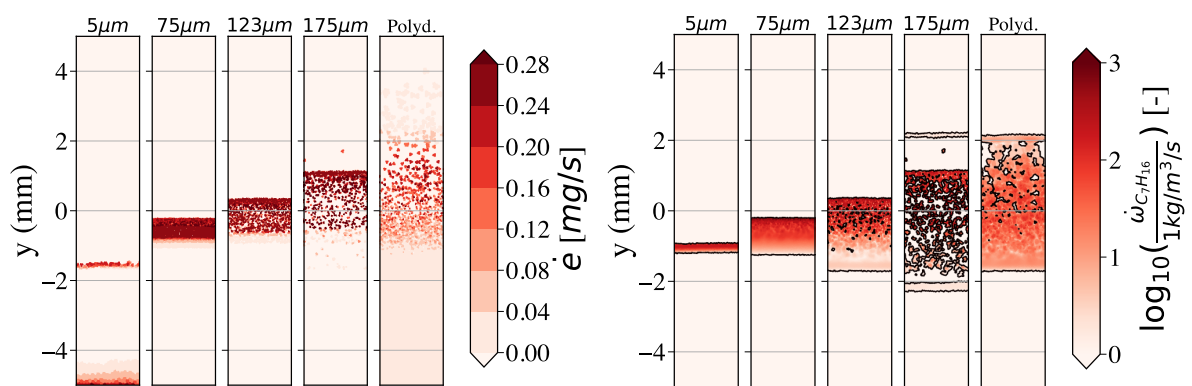


Figure 8: Evaporation rate (left) and source term (right) fields for $d_p = 5\mu\text{m}$, $d_p = 75\mu\text{m}$, $d_p = 123\mu\text{m}$, $d_p = 175\mu\text{m}$ and the polydisperse configuration.

Appendix D : 3D computation

Calculation timescales for the different fuels

To determine the resources demanded to run the computations, the required number cpu time is calculated with :

$$n_{ch} = n_{proc}n_{nodes}t_{simu} \quad (22)$$

with n_{ch} the number of core per hour of calculation used, n_{proc} the number of processors, n_{nodes} the number of nodes per processors and t_{simu} the real time of a simulation, calculated by:

$$t_{simu} = \frac{t_{run}}{(n_{ite/sec} * \Delta t)} \quad (23)$$

with t_{run} the physical time measured, $n_{ite/sec}$ the number of iteration by second and Δt an approximation of the timestep of the simulation. The following table compares the results for BFER, A1, B1 and C1 for $\Delta t = 10^{-8}$ s, $t_{run} = 5$ ms, $n_{proc} = 15$ and $n_{nodes} = 36$:

Fuel	$n_{ite/sec}$ [s^{-1}]	t_{simu} [h]	n_{ch} [CPUh]
2S	2.68	51.82	27985
A1	1.42	97.81	52817
B1	1.63	85.21	46013
C1	1.45	95.78	51721

Table 7: Required computational resources for 2S, A1, B1 and C1 to simulate 5 ms of physical time.

Averaged fields of some mass fractions

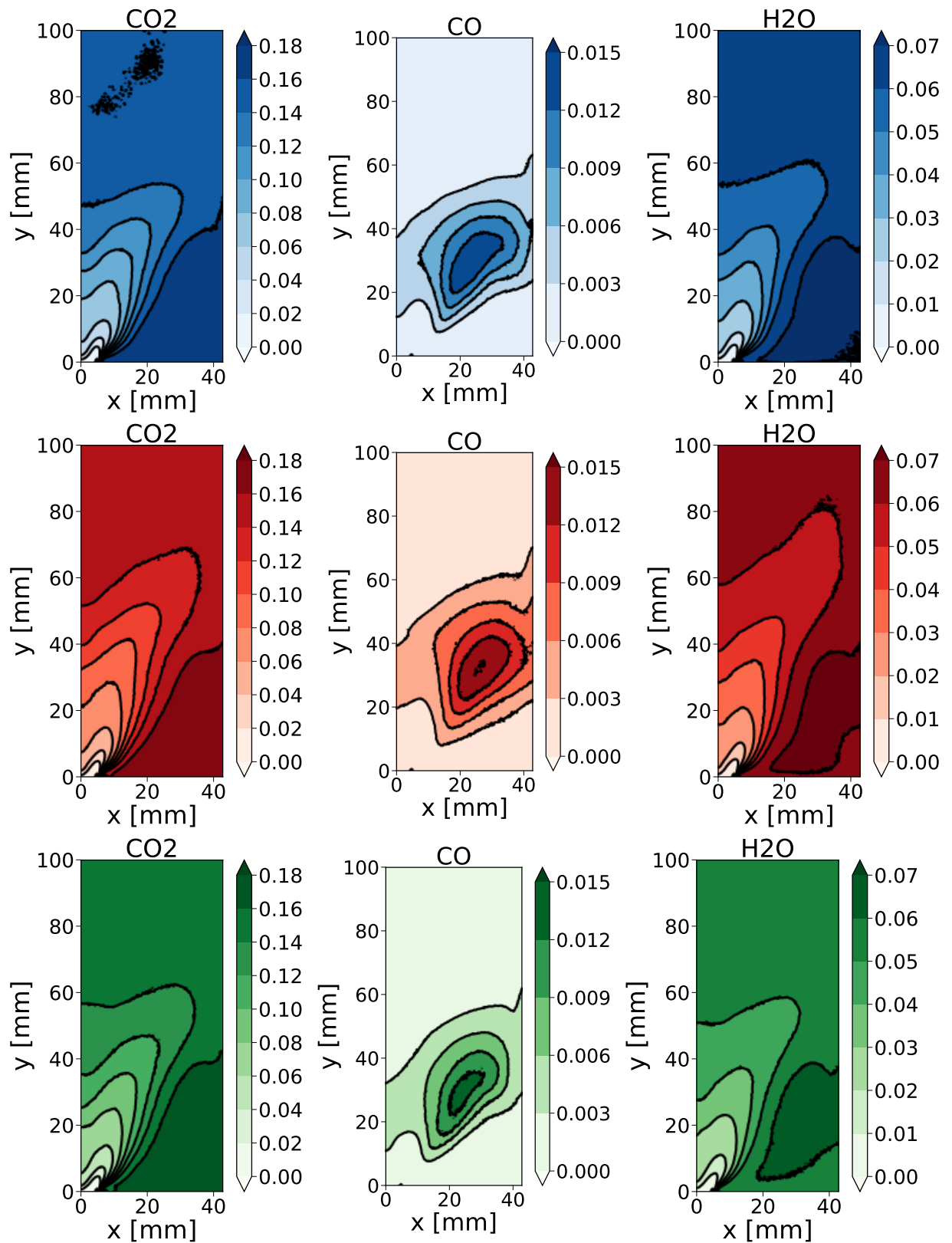


Figure 9: Average mass fraction fields of A1, B1 and C1 CO , CO_2 and H_2O species coloured by iso-lines at 10 and 50 percent of the maximum value.

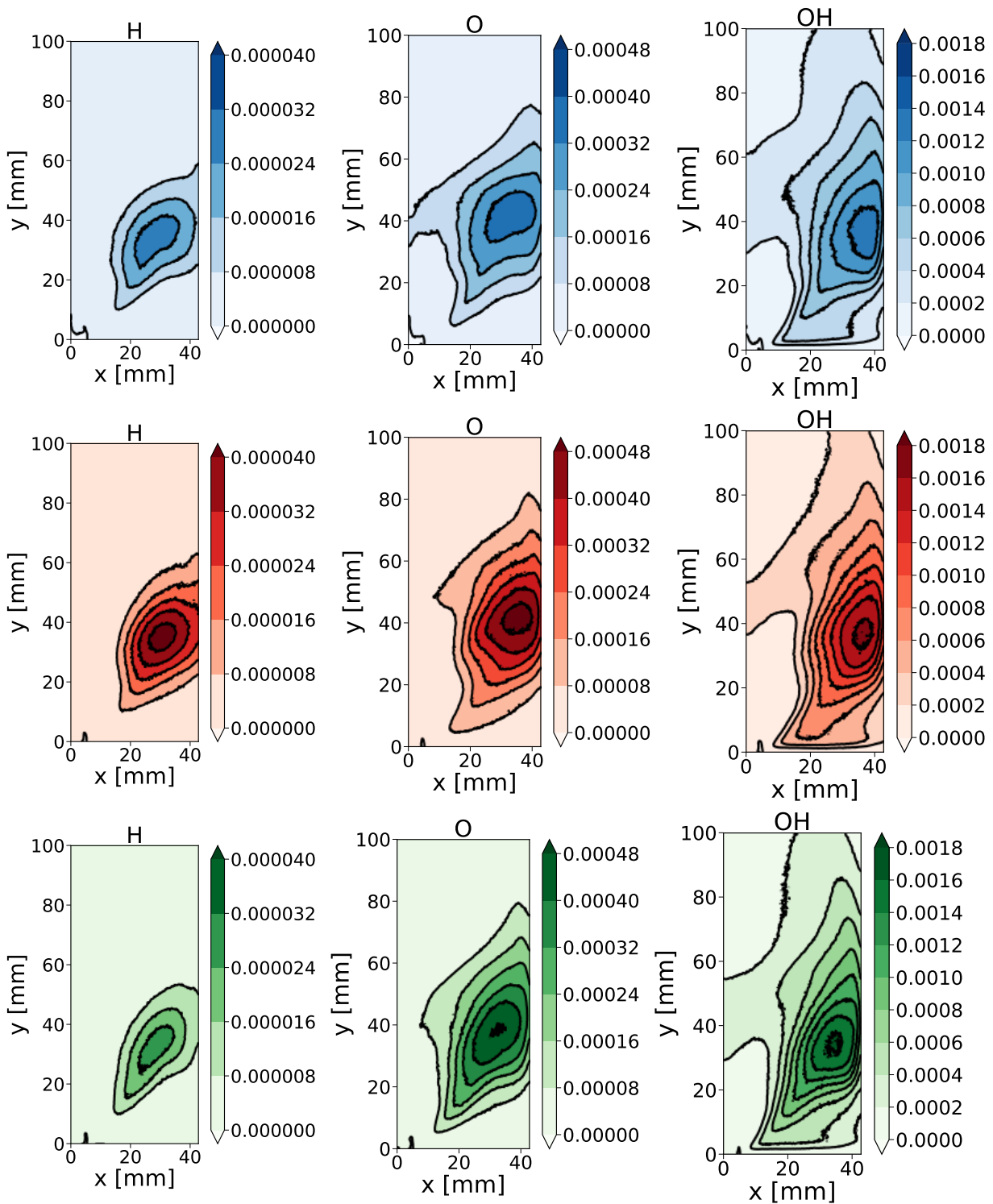
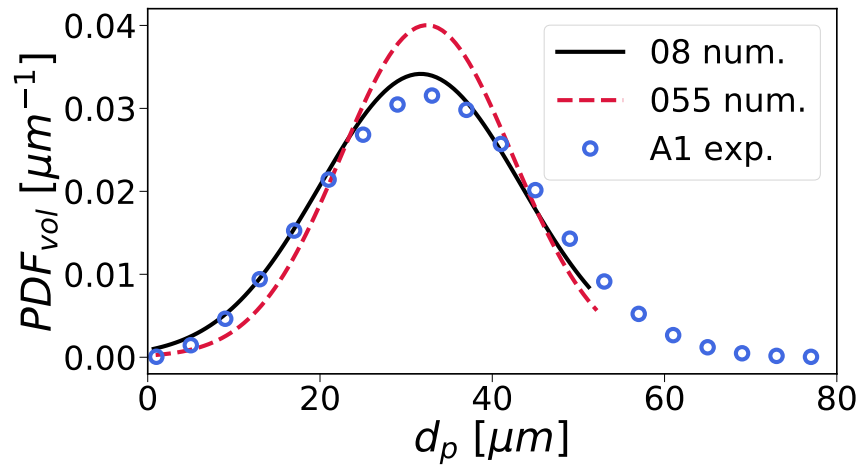


Figure 10: Average mass fraction fields of A1, B1 and C1 O , H and OH species coloured by iso-lines at 10 and 50 percent of the maximum value.

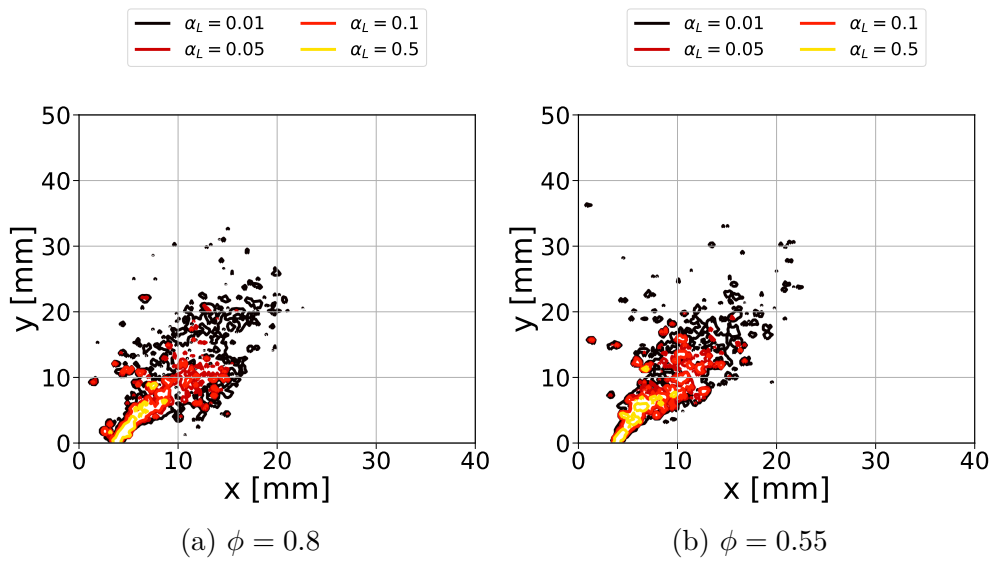
Appendix E : LBO computation

Others fields of stabilized and NBO flames



(a) $\phi = 0.55$

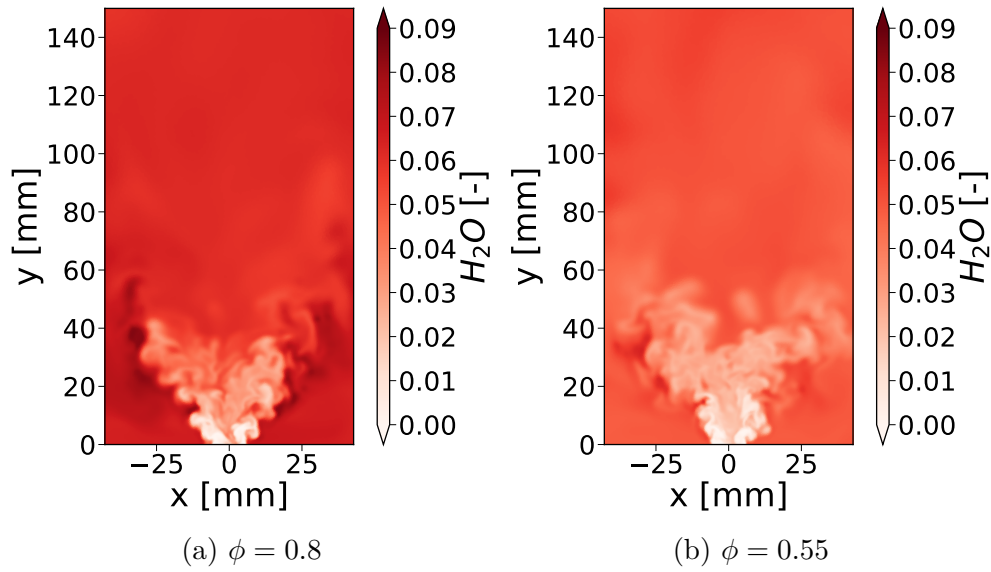
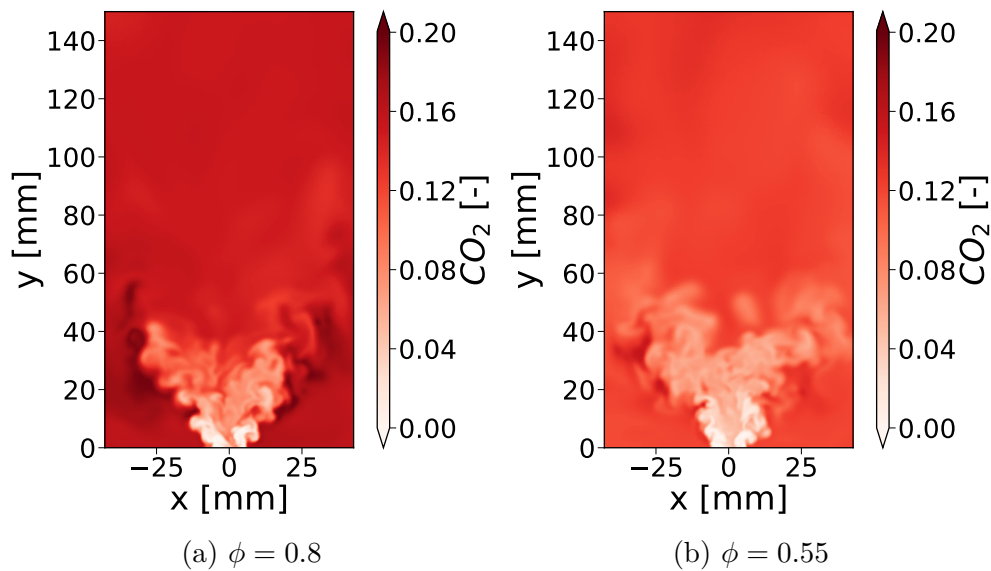
Figure 11: Time-averaged diameter PDF for $y = 25$ mm on 10 ms.



(a) $\phi = 0.8$

(b) $\phi = 0.55$

Figure 12: Instantaneous cuts of conditional liquid loading fields.

Figure 13: Instantaneous cuts of H_2O mass fraction fieldsFigure 14: Instantaneous cuts of CO_2 mass fraction fields

Variable evolution

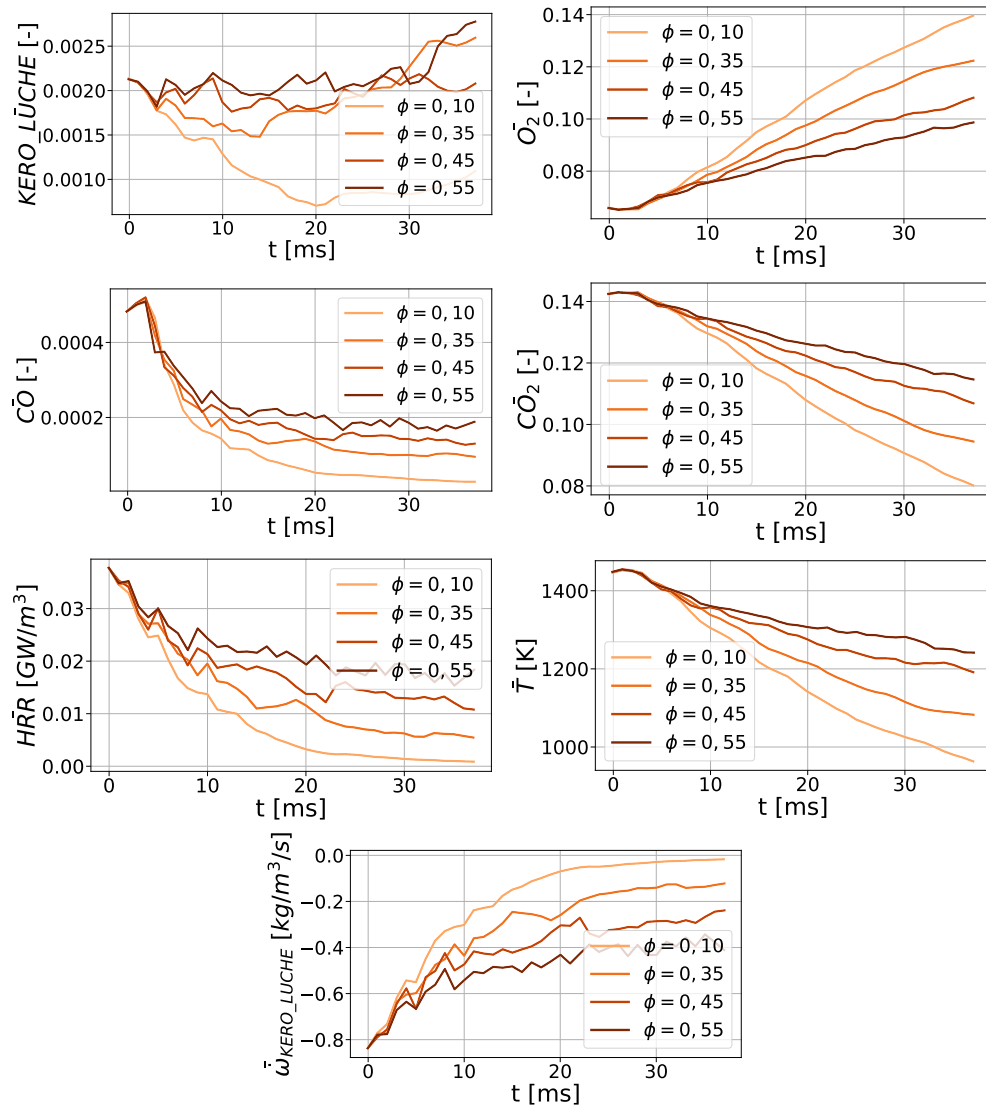


Figure 15: 2S mean species and thermochemical variables below $y = 60$ mm as a function of the time for the different steps.

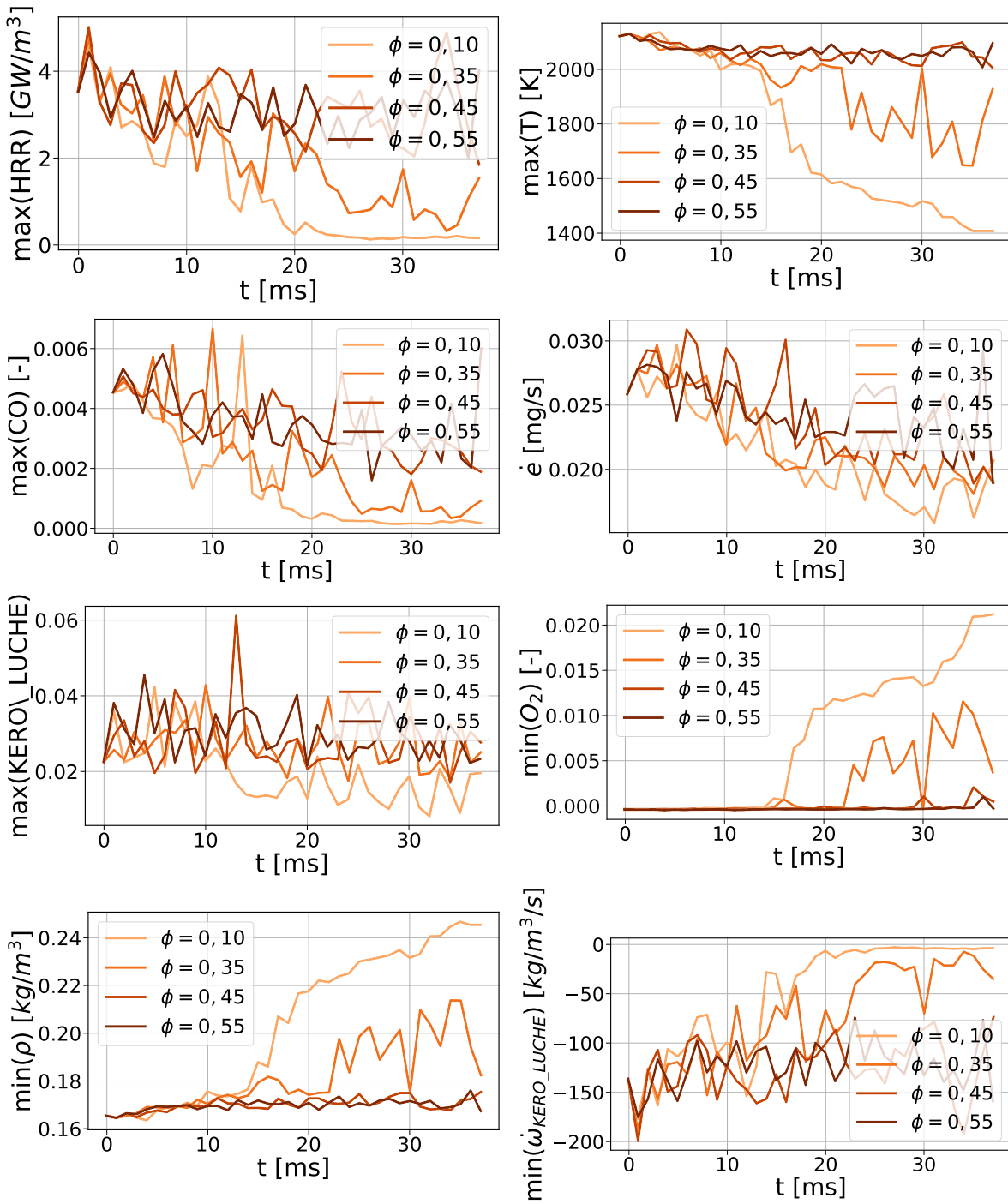


Figure 16: 2S minimum and maximum variables below $y = 60$ mm as a function of the time for the different steps.

Wall temperature demonstration

Let's imagine a cube completely filled with burnt gases. The following system of equation is then written:

$$\begin{aligned} C_{P,final}^{0.8} T_{final}^{0.8} &= C_{P,ad}^{0.8} T_{ad}^{0.8} - Q_{wall}^{0.8} \\ C_{P,final}^{0.45} T_{final}^{0.45} &= C_{P,ad}^{0.45} T_{ad}^{0.45} - Q_{wall}^{0.45} \end{aligned} \quad (24)$$

with Q_{wall} the wall heat losses, T_{final} the final temperature obtained in the burner and T_{ad} the adiabatic temperature of the operating point. The superscript 0.8 represents variables associated to the wall temperatures adapted for the stabilised case and 0.45 for the adapted wall values, that is wanted. The goal of this demonstration is to know $Q_{wall}^{0.45}$ by the knowledge of every variable associated to 0.8 superscript and $T_{ad}^{0.45}$ from simple equilibrium calculations.

The expression of Q_{wall} is :

$$Q_{wall} = kS \frac{T_{ext} - T_{in}}{e} \quad (25)$$

with $T_{ext} = T_{wall}$ the external temperature, $T_{in} = T_{final}$ the internal temperature, e the wall thickness, S the wall surface and k the wall heat conductivity. As e , S and k are supposed not to change between the different cases, the preceding equations can be reformulated:

$$\frac{Q_{wall}^{0.45}}{Q_{wall}^{0.8}} = \frac{C_{P,final}^{0.45} T_{final}^{0.45} - C_{P,ad}^{0.45} T_{ad}^{0.45}}{C_{P,final}^{0.8} T_{final}^{0.8} - C_{P,ad}^{0.8} T_{ad}^{0.8}} = \frac{T_{final}^{0.45} - T_{wall}^{0.45}}{T_{final}^{0.8} - T_{wall}^{0.8}} \quad (26)$$

By supposing that:

$$r = \frac{C_{P,final}^{0.45} T_{final}^{0.45}}{C_{P,ad}^{0.45} T_{ad}^{0.45}} = \frac{C_{P,final}^{0.8} T_{final}^{0.8}}{C_{P,ad}^{0.8} T_{ad}^{0.8}} \quad (27)$$

The relation can be rewritten:

$$\frac{Q_{wall}^{0.45}}{Q_{wall}^{0.8}} = r \quad (28)$$

and therefore:

$$T_{final}^{0.45} = r T_{final}^{0.8} \frac{C_{P,final}^{0.8}}{C_{P,final}^{0.45}} \quad (29)$$

Finally, if $C_{P,final}^{0.45} = C_{P,final}^{0.8}$, then:

$$T_{wall}^{0.45} = r T_{wall}^{0.8} \quad (30)$$

Bibliography

- [1] B. Abramzon and W. Sirignano, “Droplet vaporization model for spray combustion calculations,” *International Journal of Heat and Mass Transfer*, vol. 32, no. 9, pp. 1605–1618, 1989.
- [2] U. F. A. Administration, “Airplane flying handbook,” in 2004.
- [3] M. Alves Fortunato, *Jetscreen - d1.1 - report about the fuel strategy*, 2017.
- [4] K. Annamalai and W. Ryan, “Interactive processes in gasification and combustion. part i: Liquid drop arrays and clouds,” *Progress in Energy and Combustion Science*, vol. 18, no. 3, pp. 221–295, Jan. 1, 1992.
- [5] “Are aviation biofuels ready for take off?” <https://www.iea.org/commentaries/are-aviation-biofuels-ready-for-take-off>. (Mar. 18, 2019).
- [6] R. Aris, G. R. Gavalas, and K. G. Denbigh, “On the theory of reactions in continuous mixtures,” *Philosophical Transactions of the Royal Society of London. Series A, Mathematical and Physical Sciences*, vol. 260, no. 1112, pp. 351–393, Sep. 1, 1966, Publisher: Royal Society.
- [7] A. Ateshkadi, V. Mcdonell, and G. Samuelsen, “Lean blowout model for a spray-fired swirl-stabilized combustor,” *Proceedings of the Combustion Institute*, vol. 28, pp. 1281–1288, Dec. 31, 2000.
- [8] AVBP Development Team, *AVBP Documentation Release 7.8*, 2021.
- [9] L. Backer, “Generating reduced mechanisms for realistic multi-component fuel combustion,” Accepted: 2019-10-15T16:51:20Z, Ph.D. dissertation, Aug. 30, 2019.
- [10] S. Balachandar and J. K. Eaton, “Turbulent dispersed multiphase flow,” *Annual Review of Fluid Mechanics*, vol. 42, no. 1, pp. 111–133, 2010.
- [11] D. R. Ballal and A. H. Lefebvre, “Weak extinction limits of turbulent heterogeneous fuel/air mixtures,” *Journal of Engineering for Power*, vol. 102, no. 2, pp. 416–421, 1980.
- [12] —, “Weak extinction limits of turbulent flowing mixtures,” *Journal of Engineering for Power*, vol. 101, no. 3, pp. 343–348, Jul. 1, 1979.
- [13] —, “Flame propagation in heterogeneous mixtures of fuel droplets, fuel vapor and air,” *Symposium (International) on Combustion*, vol. 18, no. 1, pp. 321–328, 1981, Eighteenth Symposium (International) on Combustion.
- [14] A. Barke, C. Thies, J.-L. Popien, *et al.*, “Life cycle sustainability assessment of potential battery systems for electric aircraft,” *Procedia CIRP*, The 28th CIRP Conference on Life Cycle Engineering, March 10 - 12, 2021, Jaipur, India, vol. 98, pp. 660–665, Jan. 1, 2021.

- [15] M. Barrère and F. A. Williams, “Comparison of combustion instabilities found in various types of combustion chambers,” *Symposium (International) on Combustion*, vol. 12, no. 1, pp. 169–181, Jan. 1, 1969.
- [16] M. Bastian, S. Heymann, and M. Jacomy, “Gephi: An open source software for exploring and manipulating networks,” 2009.
- [17] L. P. Bayvel and Z. Orzechowski, *Liquid atomization*. Taylor & Francis, 1993.
- [18] R. W. Bilger, “Conditional moment closure for turbulent reacting flow,” *Physics of Fluids A: Fluid Dynamics*, vol. 5, no. 2, pp. 436–444, Feb. 1993, Publisher: American Institute of Physics.
- [19] —, “Turbulent jet diffusion flames,” *Progress in Energy and Combustion Science*, vol. 1, no. 2, pp. 87–109, Jan. 1, 1976.
- [20] R. Bilger, “A mixture fraction framework for the theory and modeling of droplets and sprays,” *Combustion and Flame*, vol. 158, pp. 191–202, Feb. 15, 2011.
- [21] C. Bischof, A. Carle, P. Khademi, and A. Mauer, “The ADIFOR 2.0 system for the automatic differentiation of fortran 77 programs,” Jul. 26, 1995.
- [22] D. Black, D. S. Crocker, and C. Smith, “Transient lean blowout modeling of an aero low emission fuel injector,” in *39th AIAA/ASME/SAE/ASEE Joint Propulsion Conference and Exhibit*, ser. Joint Propulsion Conferences, American Institute of Aeronautics and Astronautics, Jul. 20, 2003.
- [23] S. Blakey, L. Rye, and C. W. Wilson, “Aviation gas turbine alternative fuels: A review,” 2011.
- [24] S. Blanchard, Q. Cazères, and B. Cuenot, “Chemical modeling for methane oxy-combustion in liquid rocket engines,” *Acta Astronautica*, vol. 190, pp. 98–111, Jan. 1, 2022.
- [25] J. Blazek, “Chapter 1 - introduction,” in *Computational Fluid Dynamics: Principles and Applications (Third Edition)*, J. Blazek, Ed., Oxford: Butterworth-Heinemann, Jan. 1, 2015, pp. 1–5.
- [26] R. J. Blint, “The relationship of the laminar flame width to flame speed,” *Combustion Science and Technology*, vol. 49, no. 1, pp. 79–92, Sep. 1, 1986, Publisher: Taylor & Francis _eprint: <https://doi.org/10.1080/00102208608923903>.
- [27] P. Bogaeviski, *Algebraic Methods In Nonlinear Perturbation Theory - Applied Mathematical Sciences*. New York, Ny, U.s.a.: Springer, May 1991.
- [28] M. Boileau, G. Staffelbach, C. Benedicte, T. Poinso, and C. Bérat, “LES of an ignition sequence in a gas turbine engine,” *Combustion and Flame*, vol. 154, pp. 2–22, Jul. 15, 2008.
- [29] P. Boivin, “Reduced-kinetic mechanisms for hydrogen and syngas combustion including autoignition,” Ph.D. dissertation, 2012.
- [30] R. Borghi, “Turbulent combustion modelling,” *Progress in Energy and Combustion Science*, vol. 14, no. 4, pp. 245–292, Jan. 1, 1988.
- [31] R. Borghi, “Background on droplets and sprays,” 1996.
- [32] C. T. Bowman, “A shock-tube investigation of the high-temperature oxidation of methanol,” *Combustion and Flame*, vol. 25, pp. 343–354, Aug. 1, 1975.

- [33] M. Braun-Unkhoff and U. Riedel, “Alternative fuels in aviation,” en, *CEAS Aeronautical Journal*, vol. 6, no. 1, pp. 83–93, Mar. 2015.
- [34] M. Braun-Unkhoff, U. Riedel, and C. Wahl, “About the emissions of alternative jet fuels,” *CEAS Aeronautical Journal*, vol. 8, no. 1, pp. 167–180, Mar. 1, 2017.
- [35] J. D. Buckmaster, Ed., *The Mathematics of Combustion*, Frontiers in Applied Mathematics, University of Illinois: Society for Industrial and Applied Mathematics, Jan. 1, 1985, 260 pp.
- [36] T. D. Butler and P. J. O’Rourke, “A numerical method for two dimensional unsteady reacting flows,” *Symposium (International) on Combustion*, vol. 16, no. 1, pp. 1503–1515, Jan. 1, 1977.
- [37] S. Candel, F. Lacas, N. Darabiha, and J.-C. Rolon, “Group combustion in spray flames,” *Multiphase Science and Technology*, vol. 11, no. 1, 1999, Publisher: Begel House Inc.
- [38] L. M. Cantu, J. Grohmann, W. Meier, and M. Aigner, “Temperature measurements in confined swirling spray flames by vibrational coherent anti-stokes Raman spectroscopy,” en, *Experimental Thermal and Fluid Science*, vol. 95, pp. 52–59, Jul. 2018.
- [39] Q. Cazeres, “Analysis and reduction of chemical kinetics for combustion applications,” Ph.D. dissertation, Jul. 13, 2021.
- [40] Q. Cazères, P. Pepiot, E. Riber, and B. Cuenot, “A fully automatic procedure for the analytical reduction of chemical kinetics mechanisms for computational fluid dynamics applications,” *Fuel*, vol. 303, p. 121 247, 2021.
- [41] F. Charlette, C. Meneveau, and D. Veynante, “A power-law flame wrinkling model for LES of premixed turbulent combustion part i: Non-dynamic formulation and initial tests,” *Combustion and Flame*, vol. 131, no. 1, pp. 159–180, Oct. 1, 2002.
- [42] G. Chaussonet, “Modeling of liquid film and breakup phenomena in large-eddy simulations of aeroengines fueled by airblast atomizers,” Ph.D. dissertation, May 13, 2014.
- [43] G. Chen and A. Gomez, “Counterflow diffusion flames of quasi-monodisperse electrostatic sprays,” *Symposium (International) on Combustion*, vol. 24, no. 1, pp. 1531–1539, Jan. 1992.
- [44] J. -. Chen, J. A. Blasco, N. Fueyo, and C. Dopazo, “An economical strategy for storage of chemical kinetics: Fitting in situ adaptive tabulation with artificial neural networks,” *Proceedings of the Combustion Institute*, vol. 28, no. 1, pp. 115–121, Jan. 1, 2000.
- [45] H. H. Chiu, H. Y. Kim, and E. J. Croke, “Internal group combustion of liquid droplets,” *Symposium (International) on Combustion*, Nineteenth Symposium (International) on Combustion, vol. 19, no. 1, pp. 971–980, Jan. 1, 1982.
- [46] H. H. Chiu and T. M. Liu, “Group combustion of liquid droplets,” *Combustion Science and Technology*, vol. 17, no. 3, pp. 127–142, Dec. 1, 1977, Publisher: Taylor & Francis _eprint: <https://doi.org/10.1080/00102207708946823>.
- [47] C. H. Cho, H. S. Han, C. H. Sohn, and J. S. Han, “Ignition delay time and oxidation of a kerosene aviation fuel and a blended jet50-bio50 fuel,” *ACS Omega*, vol. 6, no. 40, pp. 26 646–26 658, Oct. 12, 2021, Publisher: American Chemical Society.

- [48] C. T. Chong and S. Hochgreb, "Spray flame structure of rapeseed biodiesel and jet-a1 fuel," *Fuel*, vol. 115, pp. 551–558, Jan. 2014.
- [49] F. Christo, A. Masri, E. Nebot, and T. Turanyi, "Utilising artificial neural network and repro-modelling in turbulent combustion," in *Proceedings of ICNN'95 - International Conference on Neural Networks*, vol. 2, Nov. 1995, 911–916 vol.2.
- [50] O. Colin, F. Ducros, D. Veynante, and T. Poinsot, "A thickened flame model for large eddy simulations of turbulent premixed combustion," *Physics of Fluids*, vol. 12, pp. 1843–1863, Jul. 1, 2000, ADS Bibcode: 2000PhFl...12.1843C.
- [51] O. Colin and M. Rudgyard, "Development of high-order taylor-galerkin schemes for LES," *Journal of Computational Physics*, vol. 162, pp. 338–371, 2000.
- [52] O. Colin, "Simulations aux grandes échelles de la combustion turbulente prémélangée dans les statoréacteurs," These de doctorat, Toulouse, INPT, Jan. 1, 2000.
- [53] A. Cook and J. Riley, "Subgrid-scale modeling for turbulent reacting flows," *Combustion and Flame*, vol. 112, pp. 593–606, Mar. 1, 1998.
- [54] A. W. Cook and J. J. Riley, "A subgrid model for equilibrium chemistry in turbulent flows," *Physics of Fluids*, vol. 6, no. 8, pp. 2868–2870, Aug. 1994, Publisher: American Institute of Physics.
- [55] B. Cuenot, F. Shum-Kivan, and S. Blanchard, "The thickened flame approach for non-premixed combustion: Principles and implications for turbulent combustion modeling," *Combustion and Flame*, p. 111702, Sep. 4, 2021.
- [56] A. Cuoci, A. Frassoldati, T. Faravelli, and E. Ranzi, "A computational tool for the detailed kinetic modeling of laminar flames: Application to c2h4/CH4 coflow flames," *Combustion and Flame*, vol. 160, no. 5, pp. 870–886, May 1, 2013.
- [57] H. J. Curran, "Developing detailed chemical kinetic mechanisms for fuel combustion," *Proceedings of the Combustion Institute*, vol. 37, no. 1, pp. 57–81, Jan. 1, 2019.
- [58] P. Dagaut, A. El Bakali, and A. Ristori, "The combustion of kerosene: Experimental results and kinetic modelling using 1- to 3-component surrogate model fuels," *Fuel*, vol. 85, pp. 944–956, May 1, 2006.
- [59] P. Dagaut and S. Gai"l, "Kinetics of gas turbine liquid fuels combustion: Jet-a1 and bio-kerosene," in *Volume 2: Turbo Expo 2007*, Montreal, Canada: ASMEDC, Jan. 1, 2007, pp. 93–101.
- [60] M. J. Davis and R. T. Skodje, "Geometric investigation of low-dimensional manifolds in systems approaching equilibrium," *The Journal of Chemical Physics*, vol. 111, no. 3, pp. 859–874, Jul. 15, 1999, Publisher: American Institute of Physics.
- [61] S. Davis, A. B. Mhadeshwar, D. Vlachos, and H. Wang, "A new approach to response surface development for detailed gas-phase and surface reaction kinetic model optimization," *International Journal of Chemical Kinetics*, 2003.
- [62] R. M. DeConto and D. Pollard, "Contribution of antarctica to past and future sea-level rise," *Nature*, vol. 531, no. 7596, pp. 591–597, Mar. 2016.
- [63] O. Delabroy, F. Lacas, B. Labegorre, and J.-M. Samaniego, "Paramètres de similitude pour la combustion diphasique," *Revue Générale de Thermique*, vol. 37, no. 11, pp. 934–953, Dec. 1, 1998.

- [64] W. S. Derr and A. M. Mellor, “Characteristic times for lean blowoff in turbine combustors,” *Journal of Propulsion and Power*, vol. 3, no. 4, pp. 377–380, Jul. 1, 1987, Publisher: American Institute of Aeronautics and Astronautics.
- [65] R. Djouad and B. Sportisse, “Some reduction techniques for simplifying atmospheric chemical kinetics,” *Air pollution modelling and simulation*, p. 235, 2002.
- [66] S. Dooley, S. H. Won, F. M. Haas, *et al.*, “Development of reduced kinetic models for petroleum-derived and alternative jet fuels,” *50th AIAA/ASME/SAE/ASEE Joint Propulsion Conference*, AIAA Propulsion and Energy Forum, Jul. 25, 2014.
- [67] J. Driscoll and C. Rasmussen, “Correlation and analysis of blowout limits of flames in high-speed airflows,” *Journal of Propulsion and Power*, vol. 21, no. 6, pp. 1035–1044, 2005.
- [68] F. L. Dryer, “Chemical kinetic and combustion characteristics of transportation fuels,” *Proceedings of the Combustion Institute*, vol. 35, no. 1, pp. 117–144, Jan. 1, 2015.
- [69] A. M. Dunker, “The decoupled direct method for calculating sensitivity coefficients in chemical kinetics,” *The Journal of Chemical Physics*, vol. 81, no. 5, pp. 2385–2393, Sep. 1, 1984, Publisher: American Institute of Physics.
- [70] —, “The reduction and parameterization of chemical mechanisms for inclusion in atmospheric reaction-transport models,” *Atmospheric Environment (1967)*, vol. 20, no. 3, pp. 479–486, Jan. 1, 1986.
- [71] A. Dvorjetski and B. Greenberg, “Steady-state and extinction analyses of counterflow spray diffusion flames with arbitrary finite evaporation rate,” *Combustion Science and Technology*, vol. 174, pp. 187–208, Jul. 2002.
- [72] A. Dvorjetski and B. Greenberg, “Small stokes number analysis of counterflow spray diffusion flames,” Jan. 2005.
- [73] J. K. Eaton and J. R. Fessler, “Preferential concentration of particles by turbulence,” *International Journal of Multiphase Flow*, vol. 20, pp. 169–209, Aug. 1, 1994.
- [74] G. Eckel, J. Grohmann, L. Cantu, *et al.*, “LES of a swirl-stabilized kerosene spray flame with a multi-component vaporization model and detailed chemistry,” en, *Combustion and Flame*, vol. 207, pp. 134–152, Sep. 2019.
- [75] T. Edwards and L. Maurice, “Surrogate mixtures to represent complex aviation and rocket fuels,” *Journal of Propulsion and Power*, vol. 17, pp. 461–466, Mar. 1, 2001.
- [76] EEA. “TERM 2017: Mixed progress for europe’s transport sector in meeting environment, climate goals.” (2017), [Online]. Available: <https://www.eea.europa.eu/highlights/term-2017-mixed-progress-for> (visited on 11/15/2021).
- [77] —, “Trends and projections in europe 2017.” (2017), [Online]. Available: <https://www.eea.europa.eu/publications/trends-and-projections-in-europe-2017> (visited on 11/15/2021).
- [78] M. Efthymiou, “The fundamentals of environmental regulation of aviation: A focus on EU emissions trading scheme,” *Aeronautics and Aerospace Open Access Journal*, vol. Volume 5, Issue 1 Feb. 10, 2021, Publisher: MedCrave Publishing.

- [79] G. Eggenpieler and S. Menon, "Combustion and emission modelling near lean blow-out in a gas turbine engine," *Progress in Computational Fluid Dynamics*, vol. 5, Jan. 1, 2005.
- [80] G. Eggenpieler and S. Menon, "Structure of locally quenched swirl stabilized turbulent premixed flames," *42nd AIAA Aerospace Sciences Meeting and Exhibit*, Aerospace Sciences Meetings, Jan. 5, 2004.
- [81] M. E. of Energy. "Alternative fuels and vehicle," Encyclopedia.com. (Jan. 24, 2022).
- [82] —, "Fluid mechanics," Encyclopedia.com. (Jan. 24, 2022).
- [83] L. Esclapez, P. Ma, and M. Ihme, "Large-eddy simulation of fuel effect on lean blow-out in gas turbines," Dec. 1, 2015.
- [84] L. Esclapez, P. C. Ma, E. Mayhew, *et al.*, "Fuel effects on lean blow-out in a realistic gas turbine combustor," *Combustion and Flame*, vol. 181, pp. 82–99, Jul. 1, 2017.
- [85] G. Faeth, "Spray atomization and combustion," in *24th Aerospace Sciences Meeting*. 1986.
- [86] A. Favre, "Statistical equations of turbulent gases," *Problems of hydrodynamics and continuum mechanics*, pp. 231–266, 1969.
- [87] A. Felden, "Development of analytically reduced chemistries (arc) and applications in large eddy simulations (les) of turbulent combustion," Ph.D. dissertation, Jun. 2017.
- [88] E. Fermi, P. Pasta, S. Ulam, and M. Tsingou, "Studies of the nonlinear problems," May 1955.
- [89] H. S. Findlay and C. Turley, "Chapter 13 - ocean acidification and climate change," in *Climate Change (Third Edition)*, T. M. Letcher, Ed., Elsevier, Jan. 1, 2021, pp. 251–279.
- [90] B. Fiorina, O. Gicquel, L. Vervisch, S. Carpentier, and N. Darabiha, "Approximating the chemical structure of partially premixed and diffusion counterflow flames using FPI flamelet tabulation," *Combustion and Flame*, vol. 140, pp. 147–160, Feb. 1, 2005.
- [91] M. Fortunato, "Fuel composition - GCxGC," 2019.
- [92] R. Fox, "Quadrature-based moment methods for polydisperse multiphase flows," *CISM International Centre for Mechanical Sciences, Courses and Lectures*, Jan. 1, 2014.
- [93] N. Franck and F. Ducros, "Subgrid-scale stress modelling based on the square of the velocity gradient tensor," vol. 62, pp. 183–200, Sep. 1999.
- [94] B. Franzelli, E. Riber, M. Sanjosé, and T. Poinso, "A two-step chemical scheme for kerosene-air premixed flames," *Combustion and Flame*, vol. 157, no. 7, pp. 1364–1373, Jul. 2010.
- [95] B. Franzelli, A. Vié, and M. Ihme, "Characterizing spray flame-vortex interaction: A spray spectral diagram for extinction," *Combustion and Flame*, vol. 163, pp. 100–114, 2016.
- [96] A. Frassoldati, A. Cuoci, T. Faravelli, E. Ranzi, C. Candusso, and D. Tolazzi, "Simplified kinetic schemes for oxy-fuel combustion," Jan. 1, 2009.

- [97] M. Frenklach, K. Kailasanath, and E. S. Oran, “Systematic development of reduced reaction mechanisms for dynamic modeling,” NTRS Author Affiliations: Pennsylvania State University, Pennsylvania State Univ., U.S. Navy, Naval Research Laboratory, Washington NTRS Document ID: 19870046713 NTRS Research Center: Legacy CDMS (CDMS), Jan. 1, 1986.
- [98] M. Frenklach, “Monte carlo simulation of hydrogen reactions with the diamond surface,” *Physical Review B*, vol. 45, no. 16, pp. 9455–9458, Apr. 15, 1992, Publisher: American Physical Society.
- [99] N. Garcia Rosa, P. Villedieu, J. Dewitte, and G. Lavergne, “A new droplet-wall interaction model,” presented at the 10th International Conference on Liquid Atomization and Spray Systems, ICLASS 2006, Oct. 24, 2008.
- [100] M. Germano, U. Piomelli, P. Moin, and W. H. Cabot, “A dynamic subgrid-scale eddy viscosity model,” *Physics of Fluids A: Fluid Dynamics*, vol. 3, no. 7, pp. 1760–1765, Jul. 1, 1991, Publisher: American Institute of Physics.
- [101] A. F. Ghoniem, “Needs, resources and climate change: Clean and efficient conversion technologies,” *Progress in Energy and Combustion Science*, vol. 37, no. 1, pp. 15–51, Feb. 2011.
- [102] R. G. Gilbert, K. Luther, and J. Troe, “Theory of thermal unimolecular reactions in the fall-off range. II. weak collision rate constants,” *Berichte der Bunsengesellschaft für physikalische Chemie*, vol. 87, no. 2, pp. 169–177, 1983.
- [103] D. G. Goodwin, H. K. Moffat, and R. L. Speth, *Cantera: An object-oriented software toolkit for chemical kinetics, thermodynamics, and transport processes*, <http://www.cantera.org>, Version 2.1.2, 2014.
- [104] M. Gorokhovski, “The stochastic lagrangian model of drop breakup in the computation of liquid sprays,” *Atomization and Sprays*, vol. 11, pp. 505–519, Sep. 1, 2001.
- [105] J. B. Greenberg, “An analysis of multiple flames in counterflow spray combustion,” 1996.
- [106] “Gri 30 mechanism.” (), [Online]. Available: http://www.me.berkeley.edu/gri_mech/.
- [107] J. Grohmann, B. Rauch, T. Kathrotia, W. Meier, and M. Aigner, “Influence of Single-Component Fuels on Gas-Turbine Model Combustor Lean Blowout,” en, *Journal of Propulsion and Power*, vol. 34, no. 1, pp. 97–107, Jan. 2018.
- [108] J. Grohmann, “Experimentelle Untersuchungen zum Einfluss von Kohlenwasserstoffen auf das Verbrennungsverhalten drallstabilisierter Sprayflammen,” Ph.D. dissertation, Jan. 2019.
- [109] J. Grohmann, W. Meier, and M. Aigner, “Gas Turbine Model Combustor Emissions of Liquid Single-Component Fuels,” en, in *Volume 4A: Combustion, Fuels and Emissions*, Charlotte, North Carolina, USA: American Society of Mechanical Engineers, Jun. 2017, V04AT04A011.
- [110] J. Grohmann, W. O’Loughlin, W. Meier, and M. Aigner, “Comparison of the Combustion Characteristics of Liquid Single-Component Fuels in a Gas Turbine Model Combustor,” en, in *Volume 4A: Combustion, Fuels and Emissions*, Seoul, South Korea: American Society of Mechanical Engineers, Jun. 2016, V04AT04A010.

- [111] J. Grohmann, B. Rauch, T. Kathrotia, W. Meier, and M. Aigner, "Investigation of differences in lean blowout of liquid single-component fuels in a gas turbine model combustor," en, in *52nd AIAA/SAE/ASEE Joint Propulsion Conference*, Salt Lake City, UT: American Institute of Aeronautics and Astronautics, Jul. 2016.
- [112] E. Gutheil, "Structure and extinction of laminar ethanol-air spray flames," *Combustion Theory and Modelling*, vol. 5, no. 2, pp. 131–145, 2001.
- [113] C. Habchi, "Développement de modèles d'atomisation secondaire et d'interactions spray-paroi en les décrits par une approche lagrangienne dans avbp," IFPEN, Technical report, 2005.
- [114] —, "Modélisation de l'interaction spray-film liquide par une approche lagrangienne incluant splashing et évaporation.," IFPEN, 2005.
- [115] C. Habchi, "New correlations for leidenfrost and nukiyama temperatures with gas pressure application to liquid film boiling simulation," Jan. 1, 2010.
- [116] G. Hannebique, "Study of the two-phase flow flame structure in aeronautical burners," Ph.D. dissertation, Apr. 9, 2013.
- [117] F. H. Harlow, "Fluid dynamics in group t-3 los alamos national laboratory: (LA-UR-03-3852)," *Journal of Computational Physics*, vol. 195, no. 2, pp. 414–433, Apr. 10, 2004.
- [118] K. Harstad and J. Bellan, "A model of reduced kinetics for alkane oxidation using constituents and species: Proof of concept for n-heptane," *Combustion and Flame*, vol. 157, no. 8, pp. 1594–1609, Aug. 2010, Number: 8 Publisher: Elsevier.
- [119] D. Harvey, "A guide to global warming potentials (GWPs)," *Energy Policy*, vol. 21, pp. 24–34, Feb. 1, 1993.
- [120] V. R. Hasti, P. Kundu, G. Kumar, S. A. Drennan, S. Som, and J. P. Gore, "A numerical study of flame characteristics during lean blow-out in a gas turbine combustor," in *2018 Joint Propulsion Conference*, Cincinnati, Ohio: American Institute of Aeronautics and Astronautics, Jul. 9, 2018.
- [121] G. C. Hegerl, H. v. Storch, K. Hasselmann, B. D. Santer, U. Cubasch, and P. D. Jones, "Detecting greenhouse-gas-induced climate change with an optimal fingerprint method," *Journal of Climate*, vol. 9, no. 10, pp. 2281–2306, Oct. 1, 1996, Publisher: American Meteorological Society Section: Journal of Climate.
- [122] J. L. Hess and A. M. O. Smith, "Calculation of potential flow about arbitrary bodies," *Progress in Aerospace Sciences*, vol. 8, pp. 1–138, Jan. 1, 1967.
- [123] J. Hirschfelder, C. Curtiss, and R. Bird, *Molecular Theory Of Gases And Liquids*. 1954.
- [124] J. O. Hirschfelder, C. F. Curtiss, and D. E. Campbell, "The theory of flame propagation. IV," *The Journal of Physical Chemistry*, vol. 57, no. 4, pp. 403–414, Apr. 1, 1953, Publisher: American Chemical Society.
- [125] C. W. Hirt and B. D. Nichols, "Volume of fluid (VOF) method for the dynamics of free boundaries," *Journal of Computational Physics*, vol. 39, no. 1, pp. 201–225, Jan. 1, 1981.
- [126] "Http://creckmodeling.chem.polimi.it." ()
- [127] "Https://www.ansys.com/products/fluids/ansys-chemkin-pro." ()

- [128] B. Hu, Y. Huang, F. Wang, and F. Xie, "CFD predictions of LBO limits for aero-engine combustors using fuel iterative approximation," *Chinese Journal of Aeronautics*, vol. 26, no. 1, pp. 74–84, Feb. 2013.
- [129] B. Hu, Q. Zhao, and J. Xu, "Predicting lean blowout limit of combustors based on semi-empirical correlation and simulation," *Journal of Propulsion and Power*, vol. 32, no. 1, pp. 108–120, Jan. 1, 2016, Publisher: American Institute of Aeronautics and Astronautics.
- [130] S. Humer, A. Frassoldati, S. Granata, *et al.*, "Experimental and kinetic modeling study of combustion of JP-8, its surrogates and reference components in laminar nonpremixed flows," *Proceedings of the Combustion Institute*, vol. 1, no. 31, pp. 393–400, 2007.
- [131] N. Iafrate, "Simulation aux grandes échelles diphasique dans les moteurs downsizes à allumage commande," Ph.D. dissertation, 2016.
- [132] ICAO, *Sustainable aviation fuels guide*, 2018.
- [133] J. J. D. Anderson, "Some reflections on the history of fluid dynamics," in *The Handbook of Fluid Dynamics*. R.W Johnson, CRC Press, vol. 469, Oct. 25, 2002.
- [134] T. Jaravel, "Prediction of pollutants in gas turbines using large eddy simulation," Ph.D. dissertation, Apr. 2016.
- [135] S. Jerzembeck, N. Peters, P. Pepiot-Desjardins, and H. Pitsch, "Laminar burning velocities at high pressure for primary reference fuels and gasoline: Experimental and numerical investigation," *Combustion and Flame*, vol. 156, no. 2, pp. 292–301, 2009.
- [136] C. Ji, Y. L. Wang, and F. N. Egolfopoulos, "Flame studies of conventional and alternative jet fuels," *Journal of Propulsion and Power*, vol. 27, no. 4, pp. 856–863, Jul. 2011.
- [137] W. P. Jones and R. P. Lindstedt, "Global reaction schemes for hydrocarbon combustion," *Combustion and Flame*, vol. 73, no. 3, pp. 233–249, Sep. 1, 1988.
- [138] S. de Jong, K. Antonissen, R. Hoefnagels, L. Lonza, M. Wang, and M. Junginger, "Life-cycle analysis of greenhouse gas emissions from renewable jet fuel production," *Biotechnology for Biofuels*, vol. 10, Mar. 14, 2017.
- [139] S. de Jong, R. Hoefnagels, J. Stralen, *et al.*, "Renewable jet fuel in the european union - scenarios and preconditions for renewable jet fuel deployment towards 2030," Feb. 2017.
- [140] M. Kaltschmitt and U. Neuling, Eds., *Biokerosene: Status and Prospects*, Berlin, Heidelberg: Springer Berlin Heidelberg, 2018.
- [141] D. Kang, D. Kim, V. Kalaskar, A. Violi, and A. L. Boehman, "Experimental characterization of jet fuels under engine relevant conditions - part 1: Effect of chemical composition on autoignition of conventional and alternative jet fuels," *Fuel*, vol. 239, pp. 1388–1404, Mar. 2019.
- [142] F. Karsenty, "Etude expérimentale et modélisation de la cinétique de combustion de carburants aéronautiques alternatifs synthétiques et de mélanges-modèles," Ph.D. dissertation, 2014.

- [143] G. B. Kauffman, "Lavoisier and the chemistry of life: An exploration of scientific creativity (holmes, frederic lawrence)," *Journal of Chemical Education*, vol. 62, no. 12, A327, Dec. 1, 1985, Publisher: American Chemical Society.
- [144] J. Keck and D. Gillespie, "Rate-controlled partial-equilibrium method for treating reacting gas mixtures," *Combustion and Flame*, pp. 237–241, 1971.
- [145] R. J. Kee, M. E. Coltrin, and P. Glarborg, *Chemically Reacting Flow: Theory and Practice*. Wiley, Mar. 4, 2005, 884 pp., Google-Books-ID: Vm2XHwyNK7EC.
- [146] A. R. Kerstein, W. T. Ashurst, and F. A. Williams, "Field equation for interface propagation in an unsteady homogeneous flow field," *Physical Review A*, vol. 37, no. 7, pp. 2728–2731, Apr. 1, 1988, Publisher: American Physical Society.
- [147] A. Al-Khateeb, J. Powers, and S. Paolucci, "On the necessary grid resolution for verified calculation of premixed laminar flames," *Communications in Computational Physics*, vol. 8, no. 2, pp. 304–326, 2010.
- [148] W.-W. Kim, J. J. Lienau, P. R. Van Slooten, M. B. Colket III, R. E. Malecki, and S. Syed, "Towards modeling lean blow out in gas turbine flameholder applications," *Journal of Engineering for Gas Turbines and Power*, vol. 128, no. 1, pp. 40–48, Mar. 1, 2004.
- [149] A. de Klerk, "Fischer-tropsch process," in *Kirk-Othmer Encyclopedia of Chemical Technology*, John Wiley & Sons, Ltd, 2013, pp. 1–20.
- [150] A. Y. Klimenko, "Multicomponent diffusion of various admixtures in turbulent flow," *Fluid Dynamics*, vol. 25, no. 3, pp. 327–334, May 1, 1990.
- [151] W. Klöpffer and B. Grahl, "Life cycle assessment (LCA): A guide to best practice," *Life Cycle Assessment (LCA): A Guide to Best Practice*, pp. 1–396, Apr. 14, 2014.
- [152] E. Knudsen and H. Pitsch, "A general flamelet transformation useful for distinguishing between premixed and non-premixed modes of combustion," *Combustion and Flame*, vol. 156, no. 3, pp. 678–696, Mar. 1, 2009.
- [153] A. Kolmogorov, "The local structure of turbulence in incompressible viscous fluid for very large reynolds' numbers," *Akademiia Nauk SSSR Doklady*, vol. 30, pp. 301–305, Jan. 1, 1941, ADS Bibcode: 1941DoSSR..30..301K.
- [154] P. D. Kourdis and D. A. Goussis, "Glycolysis in *saccharomyces cerevisiae*: Algorithmic exploration of robustness and origin of oscillations," *Mathematical Biosciences*, vol. 243, no. 2, pp. 190–214, Jun. 2013.
- [155] D. Kretschmer and J. Odgers, "Modeling of gas turbine combustors—a convenient reaction rate equation," *Journal of Engineering for Power*, vol. 94, no. 3, pp. 173–180, Jul. 1, 1972.
- [156] K. K.-y. Kuo, *Principles of Combustion*, John Wiley & Sons. New Jersey, 2005.
- [157] P. Kurzawska and R. Jasiński, "Overview of sustainable aviation fuels with emission characteristic and particles emission of the turbine engine fueled ATJ blends with different percentages of ATJ fuel," *Energies*, vol. 14, p. 1858, Mar. 26, 2021.
- [158] D. Laera, P. W. Agostinelli, L. Selle, *et al.*, "Stabilization mechanisms of CH₄ premixed swirled flame enriched with a non-premixed hydrogen injection," *Proceedings of the Combustion Institute*, vol. 38, no. 4, pp. 6355–6363, Jan. 1, 2021.

- [159] K. J. Laidler, “The development of the arrhenius equation,” *Journal of Chemical Education*, vol. 61, no. 6, p. 494, Jun. 1, 1984, Publisher: American Chemical Society.
- [160] N. Lamarque, “Schémas numériques et conditions limites pour la simulation aux grandes échelles de la combustion diphasique dans les foyers d’hélicoptère.,” Ph.D. dissertation, Dec. 6, 2007.
- [161] F. Laurent, “Numerical analysis of eulerian multi-fluid models in the context of kinetic formulations for dilute evaporating sprays,” *ESAIM: Mathematical Modelling and Numerical Analysis*, vol. 40, pp. 431–468, 2006.
- [162] C. K. Law, “Asymptotic theory for ignition and extinction in droplet burning,” *Combustion and Flame*, vol. 24, pp. 89–98, Feb. 1, 1975.
- [163] P. Lax and B. Wendroff, *Systems of conservation laws*. 1960.
- [164] P. Le Clercq, N. Doué, M. Rachner, and M. Aigner, “Validation of a multicomponent-fuel model for spray computations,” in *47th AIAA Aerospace Sciences Meeting including The New Horizons Forum and Aerospace Exposition*, American Institute of Aeronautics and Astronautics, 2009.
- [165] R. Le Dortz, “Détermination des caractéristiques fondamentales de combustion de pré-mélange air-kérosène, de l’allumage à la vitesse de flamme : Représentativité de surrogates mono et multi-composants,” Ph.D. dissertation, Jun. 19, 2018.
- [166] R. Lebas, T. Menard, P. A. Beau, A. Berlemont, and F. X. Demoulin, “Numerical simulation of primary break-up and atomization: DNS and modelling study,” *International Journal of Multiphase Flow*, vol. 35, no. 3, pp. 247–260, Mar. 1, 2009.
- [167] D. Lebiez, “Computing minimal entropy production trajectories: An approach to model reduction in chemical kinetics,” *The Journal of chemical physics*, vol. 120, pp. 6890–7, May 1, 2004.
- [168] D. S. Lee, D. W. Fahey, A. Skowron, *et al.*, “The contribution of global aviation to anthropogenic climate forcing for 2000 to 2018,” *Atmospheric Environment*, vol. 244, p. 117834, Jan. 1, 2021.
- [169] A. H. Lefebvre and R. Ballal Dilip, *Gas turbine combustion: alternative fuels and emissions Lefebvre Arthur H., Ballal Dilip R.* Librairie Lavoisier, 2010.
- [170] A. H. Lefebvre, “Fuel effects on gas turbine combustion—ignition, stability, and combustion efficiency,” *Journal of Engineering for Gas Turbines and Power*, vol. 107, no. 1, pp. 24–37, Jan. 1, 1985.
- [171] A. H. Lefebvre and V. G. McDonell, *Atomization and sprays*, Second edition. Boca Raton London New York: CRC Press, Taylor & Francis Group, 2017, 284 pp., OCLC: 1012431126.
- [172] S. Lei and H. Yong, “An overview of methodologies to predict lean blowout limits for gas turbine combustors,” in *2019 16th International Bhurban Conference on Applied Sciences and Technology (IBCAST)*, ISSN: 2151-1411, Jan. 2019, pp. 709–718.
- [173] P. A. Leonard and A. M. Mellor, “Correlation of lean blowoff of gas turbine combustors using alternative fuels,” *Journal of Energy*, vol. 7, no. 6, pp. 729–732, Nov. 1, 1983, Publisher: American Institute of Aeronautics and Astronautics.

- [174] S. Li and F. Williams, "Counterflow heptane flame structure," *Proceedings of the Combustion Institute*, vol. 28, no. 1, pp. 1031–1038, 2000.
- [175] T. H. Lin, C. K. Law, and S. H. Chung, "Theory of laminar flame propagation in off-stoichiometric dilute sprays," *International Journal of Heat and Mass Transfer*, vol. 31, no. 5, pp. 1023–1034, May 1, 1988.
- [176] A. Liñán, "The asymptotic structure of counterflow diffusion flames for large activation energies," *Acta Astronautica*, vol. 1, no. 7, pp. 1007–1039, Jul. 1, 1974.
- [177] F. A. Lindemann, S. Arrhenius, I. Langmuir, N. R. Dhar, J. Perrin, and W. C. M. Lewis, "Discussion on "the radiation theory of chemical action"," *Transactions of the Faraday Society*, vol. 17, no. 0, pp. 598–606, Jan. 1, 1922, Publisher: The Royal Society of Chemistry.
- [178] J. C. Livengood and P. C. Wu, "Correlation of autoignition phenomena in internal combustion engines and rapid compression machines," *Symposium (International) on Combustion*, vol. 5, no. 1, pp. 347–356, Jan. 1, 1955.
- [179] J. P. Longwell, E. E. Frost, and M. A. Weiss, "Flame stability in bluff body recirculation zones," *Industrial & Engineering Chemistry*, vol. 45, no. 8, pp. 1629–1633, Aug. 1, 1953, Publisher: American Chemical Society.
- [180] T. Løvs, D. Nilsson, and F. Mauss, "Automatic reduction procedure for chemical mechanisms applied to premixed methane/air flames," *Proceedings of the Combustion Institute*, vol. 28, no. 2, pp. 1809–1815, 2000.
- [181] Lu and C. K. Law, "Systematic approach to obtain analytic solutions of quasi steady state species in reduced mechanisms," *The Journal of Physical Chemistry A*, vol. 110, no. 49, pp. 13 202–13 208, Dec. 1, 2006, Publisher: American Chemical Society.
- [182] L. Lu, S. R. Lantz, Z. Ren, and S. B. Pope, "Computationally efficient implementation of combustion chemistry in parallel PDF calculations," *Journal of Computational Physics*, vol. 228, no. 15, pp. 5490–5525, Aug. 20, 2009.
- [183] T. Lu and C. K. Law, "A criterion based on computational singular perturbation for the identification of quasi steady state species: A reduced mechanism for methane oxidation with NO chemistry," *Combustion and Flame*, vol. 154, no. 4, pp. 761–774, Sep. 1, 2008.
- [184] —, "A directed relation graph method for mechanism reduction," *Proceedings of the Combustion Institute*, vol. 30, no. 1, pp. 1333–1341, 2005.
- [185] —, "A directed relation graph method for mechanism reduction," *Proceedings of the Combustion Institute*, vol. 30, no. 1, pp. 1333–1341, Jan. 2005.
- [186] J. Luche, "Obtention de modèles cinétiques réduits de combustion - Application à un mécanisme du kérosène," Ph.D. dissertation, 2003, p. 329.
- [187] T. S. Lundgren, "Distribution functions in the statistical theory of turbulence," *The Physics of Fluids*, vol. 10, no. 5, pp. 969–975, May 1967, Publisher: American Institute of Physics.
- [188] K. Luo, H. Pitsch, M. G. Pai, and O. Desjardins, "Direct numerical simulations and analysis of three-dimensional n-heptane spray flames in a model swirl combustor," *Proceedings of the Combustion Institute*, vol. 33, no. 2, pp. 2143–2152, Jan. 1, 2011.

- [189] Z. Luo, T. Lu, M. J. Maciaszek, S. Som, and D. E. Longman, "A reduced mechanism for high-temperature oxidation of biodiesel surrogates," *Energy & Fuels*, vol. 24, no. 12, pp. 6283–6293, Dec. 16, 2010, Publisher: American Chemical Society.
- [190] U. Maas and S. B. Pope, *Simplifying chemical kinetics: Intrinsic low-dimensional manifolds in composition space. combustion and flame*, 1992.
- [191] J. Malcolm W. Chase, *NIST-JANAF thermochemical tables*. 1998.
- [192] F. E. Marble and J. Broadwell, "The coherent flame model for turbulent chemical reactions. final report 1 mar 75–31 jan 77," 1977.
- [193] P. Marmottant and E. Villermaux, "On spray formation," *Journal of Fluid Mechanics*, vol. 498, pp. 73–111, Jan. 10, 2004.
- [194] J. C. Massey, Z. X. Chen, M. Stöhr, W. Meier, and N. Swaminathan, "On the blow-off correlation for swirl-stabilised flames with a precessing vortex core," en, *Combustion and Flame*, A dedication to Professor Kenneth Noel Corbett Bray, vol. 239, p. 111 741, May 2022.
- [195] F. Mauß, D. Keller, and N. Peters, "A lagrangian simulation of flamelet extinction and re-ignition in turbulent jet diffusion flames," *Symposium (International) on Combustion*, vol. 23, no. 1, pp. 693–698, Jan. 1991.
- [196] E. Mayhew, C. M. Mitsingas, B. McGann, *et al.*, "Spray characteristics and flame structure of jet a and alternative jet fuels," in *55th AIAA Aerospace Sciences Meeting*, Grapevine, Texas: American Institute of Aeronautics and Astronautics, Jan. 9, 2017.
- [197] M. Mehl, M. Pelucchi, and P. Osswald, "Understanding the compositional effects of SAFs on combustion intermediates," *Frontiers in Energy Research*, vol. 10, 2022.
- [198] M. Mehl and M. Pelucchi, "JETSCREEN - d2.5 - report about the high temperature regime regarding auto-ignition, combustion and soot.," 2020.
- [199] P. Mehta, "Aviation waste management: An insight," vol. 5, pp. 179–186, Jan. 1, 2015.
- [200] S. Menon, "Multi-scale modeling for LES of engineering designs of large-scale combustors," in *42nd AIAA Aerospace Sciences Meeting and Exhibit*, ser. Aerospace Sciences Meetings, American Institute of Aeronautics and Astronautics, Jan. 5, 2004.
- [201] M. Mikami, S. Miyamoto, and N. Kojima, "Counterflow diffusion flame with poly-disperse sprays," *Proceedings of the Combustion Institute*, vol. 29, pp. 593–599, Dec. 2002.
- [202] H. Mongia, M. Vermeersch, and T. Held, "A simple reactor-based approach for correlating lean blowout of turbopropulsion engine combustors," 37th Joint Propulsion Conference and Exhibit, Jul. 8, 2001.
- [203] H. Mongia, M. Vermeersch, and T. Held, "Data reduction and analysis (DRA) for emissions and lean blowout," Jan. 6, 2003.
- [204] V. Moureau, P. Domingo, and L. Vervisch, "From large-eddy simulation to direct numerical simulation of a lean premixed swirl flame: Filtered laminar flame-pdf modeling," *Combustion and Flame*, vol. 158, no. 7, pp. 1340–1357, 2011, Publisher: Elsevier.

- [205] C. J. Mueller, J. F. Driscoll, D. L. Reuss, M. C. Drake, and M. E. Rosalik, "Vorticity generation and attenuation as vortices convect through a premixed flame," *Combustion and Flame*, vol. 112, no. 3, pp. 342–358, Feb. 1, 1998.
- [206] C. Mundo, M. Sommerfeld, and C. Tropea, "Droplet-wall collisions: Experimental studies of the deformation and breakup process," *International Journal of Multiphase Flow*, vol. 21, no. 2, pp. 151–173, Apr. 1, 1995.
- [207] T. Nagy and T. Turányi, "Relaxation of concentration perturbation in chemical kinetic systems," *Reaction Kinetics and Catalysis Letters*, vol. 96, pp. 269–278, Apr. 1, 2009.
- [208] M. Nakamura, F. Akamatsu, R. Kurose, and M. Katsuki, "Combustion mechanism of liquid fuel spray in a gaseous flame," *Physics of Fluids*, vol. 17, no. 12, p. 123301, Dec. 1, 2005, Publisher: American Institute of Physics.
- [209] K. Narayanaswamy and P. Pepiot, "Simulation-driven formulation of transportation fuel surrogates," *Combustion Theory and Modelling*, vol. 22, no. 5, pp. 883–897, Sep. 3, 2018.
- [210] K. Narayanaswamy, H. Pitsch, and P. Pepiot, "A component library framework for deriving kinetic mechanisms for multi-component fuel surrogates: Application for jet fuel surrogates," *Combustion and Flame*, vol. 165, pp. 288–309, Mar. 2016.
- [211] P. C. Nassini, D. Pampaloni, R. Meloni, and A. Andreini, "Lean blow-out prediction in an industrial gas turbine combustor through a LES-based CFD analysis," *Combustion and Flame*, vol. 229, p. 111391, Jul. 1, 2021.
- [212] A.-M. Nassur, D. Léger, M. Lefèvre, *et al.*, "Effects of aircraft noise exposure on heart rate during sleep in the population living near airports," *International Journal of Environmental Research and Public Health*, vol. 16, no. 2, p. 269, Jan. 2019.
- [213] A. Neophytou and E. Mastorakos, "Simulations of laminar flame propagation in droplet mists," *Combustion and Flame*, vol. 156, no. 8, pp. 1627–1640, Aug. 1, 2009.
- [214] U. Niemann, K. Seshadri, and F. A. Williams, "Accuracies of laminar counterflow flame experiments," *Combustion and Flame*, vol. 162, no. 4, pp. 1540–1549, Apr. 1, 2015.
- [215] M. S. Okino and M. L. Mavrouniotis, "Simplification of mathematical models of chemical reaction systems," *Chemical Reviews*, vol. 98, no. 2, pp. 391–408, Apr. 2, 1998.
- [216] H. Olguin and E. Gutheil, "Influence of evaporation on spray flamelet structures," *Combustion and Flame*, vol. 161, no. 4, pp. 987–996, 2014.
- [217] S. Osher and R. Fedkiw, "Level set methods and dynamic implicit surfaces," *Applied Mechanics Reviews*, vol. 57, no. 3, B15, Jun. 10, 2004.
- [218] P. Oßwald, J. Zinsmeister, T. Kathrotia, *et al.*, "Combustion kinetics of alternative jet fuels, part-i: Experimental flow reactor study," *Fuel*, vol. 302, p. 120735, Oct. 2021.
- [219] N. Ouarti, "Modélisation de l'allumage d'un brouillard de carburant dans un foyer de turbomachine," Ph.D. dissertation, 2004.

- [220] J. P. Legier, T. Poinso, and D. D. Veynante, “Dynamically thickened flame model for premixed and non-premixed turbulent combustion,” *Proceedings of the Summer Program*, Jan. 2000.
- [221] A. Panchal, R. Ranjan, and S. Menon, “Effect of chemistry modeling on flame stabilization of a swirl spray combustor,” *Conference: 2018 Joint Propulsion Conference*, Jul. 9, 2018.
- [222] D. Paulhiac, “Modélisation de la combustion d’un spray dans un brûleur aéronautique,” Ph.D. dissertation, Apr. 2015.
- [223] F. Pecquery, V. Moureau, G. Lartigue, L. Vervisch, and A. Roux, “Modelling nitrogen oxide emissions in turbulent flames with air dilution: Application to LES of a non-premixed jet-flame,” *Combustion and Flame*, vol. 161, no. 2, pp. 496–509, Feb. 2014, Publisher: Elsevier.
- [224] J. H. A. M. Peeters, “Aviation and air pollution,” in *Studies in Environmental Science*, ser. Air pollution in the 21st century, T. Schneider, Ed., vol. 72, Elsevier, Jan. 1, 1998, pp. 601–613.
- [225] P. Pepiot and J. M. Tishkoff, “Automatic strategies to model transportation fuel surrogates a dissertation submitted to the department of mechanical engineering and the committee on graduate studies of stanford university in partial fulfillment of the requirements for the degree of doctor of philosophy,” Ph.D. dissertation, 2008.
- [226] P. Pepiot-Desjardins and H. Pitsch, “An efficient error-propagation-based reduction method for large chemical kinetic mechanisms,” *Combustion and Flame*, vol. 154, no. 1, pp. 67–81, 2008.
- [227] A. Pestre, “Phd of pestre, in progress,” Ph.D. dissertation, INP Toulouse, Toulouse, 2022.
- [228] N. Peters and J. Warnatz, *Numerical Methods in Laminar Flame Propagation*. 1982.
- [229] J. Piehl, L. Bravo, W. Acosta, G. Kumar, S. Drennan, and O. Samimi-Abianeh, “On predictions of fuel effects on lean blow off limits in a realistic gas turbine combustor using finite rate chemistry,” presented at the ASME Turbo Expo 2018: Turbo-machinery Technical Conference and Exposition, American Society of Mechanical Engineers Digital Collection, Aug. 30, 2018.
- [230] H. Pitsch. “<https://www.itv.rwth-aachen.de/downloads/flamemaster/>.” (1990).
- [231] H. Pitsch and N. Peters, “A consistent flamelet formulation for non-premixed combustion considering differential diffusion effects,” *Combustion and Flame*, vol. 114, no. 1, pp. 26–40, Jul. 1998.
- [232] S. L. Plee and A. M. Mellor, “Flame stabilization in simplified prevaporizing, partially vaporizing, and conventional gas turbine combustors,” *Journal of Energy*, vol. 2, no. 6, pp. 346–353, Nov. 1, 1978, Publisher: American Institute of Aeronautics and Astronautics.
- [233] T. Poinso, “Prediction and control of combustion instabilities in real engines,” *Proceedings of the Combustion Institute*, vol. 36, no. 1, pp. 1–28, Jan. 1, 2017.
- [234] T. J. Poinso and S. K. Lelef, “Boundary conditions for direct simulations of compressible viscous flows,” *Journal of Computational Physics*, vol. 101, no. 1, pp. 104–129, Jul. 1, 1992.

- [235] T. Poinsot and D. Veynante, *Theoretical and Numerical Combustion*. Jan. 1, 2005, vol. 28.
- [236] S. B. Pope, “Computations of turbulent combustion: Progress and challenges,” *Symposium (International) on Combustion*, Twenty-Third Symposium (International) on Combustion, vol. 23, no. 1, pp. 591–612, Jan. 1, 1991.
- [237] —, “The evolution of surfaces in turbulence,” *International Journal of Engineering Science*, vol. 26, no. 5, pp. 445–469, Jan. 1, 1988.
- [238] —, “Computationally efficient implementation of combustion chemistry using in situ adaptive tabulation,” *Combustion Theory and Modelling*, vol. 1, no. 1, pp. 41–63, Jan. 1, 1997.
- [239] J. Powers and S. Paolucci, “Accurate spatial resolution estimates for reactive supersonic flow with detailed chemistry,” *AIAA JOURNAL*, vol. 43, Apr. 1, 2005.
- [240] A. Prasad, “Prasad, a.k.: Stereoscopic particle image velocimetry. exp. fluids 29(2), 103-116,” *Experiments in Fluids*, vol. 29, Aug. 7, 2000.
- [241] G. Pretzier, “A new method for numerical Abel-inversion,” *Zeitschrift für Naturforschung A*, vol. 46, no. 7, pp. 639–641, Jul. 1, 1991, Publisher: De Gruyter.
- [242] T. S. Project, “Pouvoir voler en 2050 : Quelle aviation dans un monde contraint ?” Mar. 2021.
- [243] K. Prommersberger, G. Maier, and S. Wittig, “Validation and application of a droplet evaporation model for real aviation fuel,” in *In: RTO AVTSymposium on Gas Turbine Engine Combustion Emissions and Alternative Fuels, Lisbon, Portugal 1998. 1999. S. 16.1-16.13. (RTO MP-14.)* 1999.
- [244] R. Przysowa, B. Gawron, T. Białocki, A. Łęgowik, J. Merkisz, and R. Jasiński, “Performance and emissions of a microturbine and turbofan powered by alternative fuels,” *Aerospace*, vol. 8, p. 25, Jan. 21, 2021.
- [245] I. Puri and P. Libby, “Droplet behavior in counterflowing streams,” *Combustion Science and Technology*, vol. 66, pp. 267–292, Aug. 1989.
- [246] Y. Ra and R. D. Reitz, “A vaporization model for discrete multi-component fuel sprays,” *International Journal of Multiphase Flow*, vol. 35, no. 2, pp. 101–117, Feb. 1, 2009.
- [247] H. Rabitz, M. Kramer, and D. K. Dacol, “Sensitivity analysis in chemical kinetics,” *Annual Review of Physical Chemistry*, 1983.
- [248] R. Rajasegar, C. Mitsingas, E. Mayhew, Q. Liu, T. Lee, and J. Yoo, “Development and characterization of additive-manufactured mesoscale combustor array,” *Journal of Energy Engineering*, vol. 144, Feb. 26, 2018.
- [249] R. Ranjan, A. Panchal, G. Hannebique, and S. Menon, “Towards numerical prediction of jet fuels sensitivity of flame dynamics in a swirl spray combustion system,” Jul. 25, 2016.
- [250] W. E. Ranz and W. R. J. Marshall, “Evaporation from drops. parts i & II,” *Chemical Engineering Progress*, no. 48, pp. 141–146, 1952.
- [251] E. Ranzi, A. Frassoldati, R. Grana, *et al.*, “Hierarchical and comparative kinetic modeling of laminar flame speeds of hydrocarbon and oxygenated fuels,” en, *Progress in Energy and Combustion Science*, vol. 38, no. 4, pp. 468–501, Aug. 2012.

- [252] E. Ranzi, A. Frassoldati, A. Stagni, M. Pelucchi, A. Cuoci, and T. Faravelli, “Reduced Kinetic Schemes of Complex Reaction Systems: Fossil and Biomass-Derived Transportation Fuels: REDUCED KINETIC SCHEMES OF COMPLEX REACTION SYSTEMS,” en, *International Journal of Chemical Kinetics*, vol. 46, no. 9, pp. 512–542, Sep. 2014.
- [253] F.-M. Raoult, “Loi générale des tensions de vapeur des dissolvants,” pp. 1430–1433, 1882.
- [254] M. Rein, “Interactions between drops and hot surfaces,” in *Drop-Surface Interactions*, M. Rein, Ed., ser. CISM International Centre for Mechanical Sciences, Vienna: Springer, 2002, pp. 185–217.
- [255] “Renewables 2020 data explorer,” www.iea.org. (Nov. 10, 2020).
- [256] J. Reveillon and L. Vervisch, “Analysis of weakly turbulent dilute-spray flames and spray combustion regimes,” *Journal of Fluid Mechanics*, vol. 537, pp. 317–347, 2005.
- [257] R. Rezende, J. Barros, and V. Perez, “General aviation 2025 - a study for electric propulsion,” in *2018 Joint Propulsion Conference*. Jul. 9, 2018.
- [258] E. Riber, M. Moreau, O. Simonin, and B. Cuenot, “Development of euler-euler LES approach for gas-particle turbulent jet flow,” presented at the ASME 2006 2nd Joint U.S.-European Fluids Engineering Summer Meeting Collocated With the 14th International Conference on Nuclear Engineering, American Society of Mechanical Engineers Digital Collection, Sep. 5, 2008, pp. 1663–1672.
- [259] N. Rimbart and G. Castanet, “Crossover between rayleigh-taylor instability and turbulent cascading atomization mechanism in the bag-breakup regime,” *Physical Review E*, vol. 84, no. 1, p. 016318, Jul. 29, 2011.
- [260] N. Rizk and H. Mongia, “Gas turbine combustor design methodology,” in *22nd Joint Propulsion Conference*, eprint: <https://arc.aiaa.org/doi/pdf/10.2514/6.1986-1531>, American Institute of Aeronautics and Astronautics, 1986.
- [261] N. K. Rizk and H. C. Mongia, “Three-dimensional combustor performance validation with high-density fuels,” *Journal of Propulsion and Power*, vol. 6, no. 5, pp. 660–667, 1990, Publisher: American Institute of Aeronautics and Astronautics.
- [262] N. Rizk and A. Lefebvre, “Internal flow characteristics of simplex swirl atomizers,” *Journal of Propulsion and Power*, vol. 1, no. 3, pp. 193–199, May 1, 1985, Publisher: American Institute of Aeronautics and Astronautics.
- [263] P. J. Roache, “Quantification of uncertainty in computational fluid dynamics,” *Annual Review of Fluid Mechanics*, vol. 29, no. 1, pp. 123–160, 1997.
- [264] A. Robinson, R. Calov, and A. Ganopolski, “Multistability and critical thresholds of the greenland ice sheet,” *Nature Climate Change*, vol. 2, no. 6, pp. 429–432, Jun. 2012.
- [265] B. Rochette, E. Riber, and B. Cuenot, “Effect of non-zero relative velocity on the flame speed of two-phase laminar flames,” *Proceedings of the Combustion Institute*, vol. 37, no. 3, pp. 3393–3400, 2019.
- [266] B. Rochette, “Modeling and simulation of two-phase flow turbulent combustion in aeronautical engines,” These de doctorat, Toulouse, INPT, Jun. 25, 2019.
- [267] D. Rosenberg, “A method to measure flame index in turbulent partially-premixed flames,” Ph.D. dissertation, May 1, 2014.

- [268] M. R. Roussel and S. J. Fraser, “Accurate steady-state approximations: Implications for kinetics experiments and mechanism,” *The Journal of Physical Chemistry*, vol. 95, no. 22, pp. 8762–8770, Oct. 1, 1991, Publisher: American Chemical Society.
- [269] P. Roy, N. El Moçaid, S. Ricci, *et al.*, “Comparison of polynomial chaos and gaussian process surrogates for uncertainty quantification and correlation estimation of spatially distributed open-channel steady flows,” *Stochastic Environmental Research and Risk Assessment*, 2017.
- [270] P. Roy, S. Ricci, R. Dupuis, R. Campet, J.-C. Jouhaud, and C. Fournier, “Batman: Statistical analysis for expensive computer codes made easy,” *The Journal of Open Source Software*, 2018.
- [271] S. Ruoff, *Jetscreen - d6.2 - impact of fuel on LBO (experimental and numerical work)*, 2017.
- [272] A. Saber, T. Lundström, and J. G. Hellström, “Turbulent modulation in particulate flow: A review of critical variables,” *Engineering*, vol. 07, pp. 597–609, Jan. 1, 2015.
- [273] O. Samimi Abianeh and C. P. Chen, “A discrete multicomponent fuel evaporation model with liquid turbulence effects,” *International Journal of Heat and Mass Transfer*, vol. 55, no. 23, pp. 6897–6907, Nov. 1, 2012.
- [274] M. Sanjose, “Evaluation de la méthode Euler-Euler pour la simulation aux grandes échelles des chambres à carburant liquide,” Ph.D. dissertation, p. 109.
- [275] M. Sanjosé, J. M. Senoner, F. Jaegle, B. Cuenot, S. Moreau, and T. Poinso, “Fuel injection model for euler-euler and euler-lagrange large-eddy simulations of an evaporating spray inside an aeronautical combustor,” *International Journal of Multiphase Flow*, vol. 37, no. 5, pp. 514–529, Jun. 1, 2011.
- [276] M. Sanjosé, T. Lederlin, G. L.Y.M., *et al.*, “LES of two-phase reacting flows,” *Studying Turbulence Using Numerical Simulation Databases - XII : Proceedings of the 2008 Summer Program*, pp. 251–263. Aug. 26, 2010.
- [277] B. D. Santer, K. E. Taylor, T. M. L. Wigley, *et al.*, “A search for human influences on the thermal structure of the atmosphere,” *Nature*, vol. 382, no. 6586, pp. 39–46, Jul. 1996, Bandiera_abtest: a Cg_type: Nature Research Journals Number: 6586 Primary_atype: Research Publisher: Nature Publishing Group.
- [278] J. Sauter, *Die Grössenbestimmung der im Gemischnebel von Verbrennungskraftmaschinen vorhandenen Brennstoffteilchen (Mitteilung aus dem Laboratorium für technische Physik der Technischen Hochschule München)*. VDI, 1926.
- [279] L. Schiller and A. Naumann, “A drag coefficient correlation,” *Zeitschrift des Vereins Deutscher Ingenieure*, vol. 77, pp. 318–320, 1935.
- [280] D. J. Seery and C. T. Bowman, “An experimental and analytical study of methane oxidation behind shock waves,” *Combustion and Flame*, vol. 14, no. 1, pp. 37–47, Feb. 1, 1970.
- [281] J.-M. Senoner, “Simulations aux grandes échelles de l’écoulement diphasique dans un brûleur aéronautique par une approche euler-lagrange,” Jun. 9, 2010.
- [282] V. Shastry, “Simulation of multicomponent spray combustion in gas turbine engines,” These en préparation, Toulouse, INPT, 2022.

- [283] V. Shastry, Q. Cazerres, B. Rochette, E. Riber, and B. Cuenot, “Numerical study of multicomponent spray flame propagation,” *Proceedings of the Combustion Institute*, Oct. 7, 2020.
- [284] F. Shum-Kivan, J. Santiago, A. Verdier, *et al.*, “Experimental and numerical analysis of a turbulent spray flame structure,” Ph.D. dissertation, 2017.
- [285] J. A. Sidey, P. M. Allison, and E. Mastorakos, “The effect of fuel composition on swirling kerosene flames,” *55th AIAA Aerospace Sciences Meeting*, 2017, `_eprint: https://arc.aiaa.org/doi/pdf/10.2514/6.2017-0383`.
- [286] W. Sirignano and C. F. Edwards, “Fluid dynamics and transport of droplets and sprays,” 2010.
- [287] J. Smagorinsky, “General circulation experiments with the primitive equations,” *Monthly Weather Review*, vol. 91, no. 3, pp. 99–164, 1963.
- [288] A. Smallbone, A. Bhave, A. Coble, S. Mosbach, M. Kraft, and R. McDavid, “Identifying optimal operating points in terms of engineering constraints and regulated emissions in modern diesel engines,” *SAE 2011 World Congress and Exhibition*, Apr. 12, 2011.
- [289] C. Smith, D. Nickolaus, T. Leach, B. Kiel, and K. Garwick, “LES blowout analysis of premixed flow past v-gutter flameholder,” in *45th AIAA Aerospace Sciences Meeting and Exhibit*, ser. Aerospace Sciences Meetings, American Institute of Aeronautics and Astronautics, Jan. 8, 2007.
- [290] L. D. Smoot, W. C. Hecker, and G. A. Williams, “Prediction of propagating methane-air flames,” *Combustion and Flame*, vol. 26, pp. 323–342, Feb. 1, 1976.
- [291] S. Solomon, D. Qin, M. Manning, *et al.*, “Chapter 2: Changes in atmospheric constituents and radiative Forcing,” Solomon, s., d. qin, m. manning, z. chen, m. marquis, k.b. averyt, m. tignor and h.l. miller,” in *Contribution of Working Group I to the Fourth Assessment Report of the Intergovernmental Panel on Climate Change, 2007*, Cambridge University Press, Cambridge, United Kingdom and New York, NY, USA, 2007.
- [292] D. B. Spalding, “The combustion of liquid fuels,” in *4th Symposium on Combustion*, Pittsburgh, 1953, pp. 847–864.
- [293] D. B. Spalding, “Development of the eddy-break-up model of turbulent combustion,” *Symposium (International) on Combustion*, vol. 16, no. 1, pp. 1657–1663, Jan. 1, 1977.
- [294] D. B. Spalding and W. R. Hawthorne, “The theory of flame phenomena with a chain reaction,” *Philosophical Transactions of the Royal Society of London. Series A, Mathematical and Physical Sciences*, vol. 249, no. 957, pp. 1–25, Mar. 22, 1956, Publisher: Royal Society.
- [295] R. Stachler, J. Heyne, S. Stouffer, J. Miller, and M. Roquemore, “Investigation of combustion emissions from conventional and alternative aviation fuels in a well-stirred reactor,” Jan. 9, 2017.
- [296] B. E. Stapper, W. A. Sowa, and G. S. Samuelson, “An experimental study of the effects of liquid properties on the breakup of a two-dimensional liquid sheet,” *Journal of Engineering for Gas Turbines and Power*, vol. 114, no. 1, pp. 39–45, Jan. 1, 1992.

- [297] M. Stöhr, S. Ruoff, B. Rauch, W. Meier, and P. Le Clercq, “Droplet vaporization for conventional and alternative jet fuels at realistic temperature conditions: Systematic measurements and numerical modeling,” *Proceedings of the Combustion Institute*, vol. 38, no. 2, pp. 3269–3276, Jan. 1, 2021.
- [298] G. G. Stokes, “On the effect of the internal friction of fluids on the motion of pendulums,” *Transactions of the Cambridge Philosophical Society*, 1850.
- [299] G. Sturgess and D. Shouse, “A hybrid model for calculating lean blowouts in practical combustors,” in *32nd Joint Propulsion Conference and Exhibit*, eprint: <https://arc.aiaa.org/doi/pdf/10.2514/6.1996-3125>, American Institute of Aeronautics and Astronautics, 1996.
- [300] G. J. Sturgess, D. G. Sloan, A. L. Lesmerises, S. P. Heneghan, and D. R. Ballal, “Design and development of a research combustor for lean blowout studies,” presented at the ASME 1990 International Gas Turbine and Aeroengine Congress and Exposition, American Society of Mechanical Engineers Digital Collection, 1990.
- [301] W. Sun, Z. Chen, X. Gou, and Y. Ju, “A path flux analysis method for the reduction of detailed chemical kinetic mechanisms,” *Combustion and Flame*, vol. 157, no. 7, pp. 1298–1307, Jul. 1, 2010.
- [302] S. Taing, A. R. Masri, and S. B. Pope, “PDF calculations of turbulent nonpremixed flames of h₂co₂ using reduced chemical mechanisms,” *Combustion and Flame*, vol. 95, no. 1, pp. 133–150, Oct. 1, 1993.
- [303] J. Tamim and W. Hallett, “A continuous thermodynamics model for multicomponent droplet vaporization,” *Chemical Engineering Science*, vol. 50, no. 18, pp. 2933–2942, Sep. 1995.
- [304] A. S. Tomlin, T. Turányi, and M. J. Pilling, “Chapter 4 mathematical tools for the construction, investigation and reduction of combustion mechanisms,” in *Comprehensive Chemical Kinetics*, ser. Low-Temperature Combustion and Autoignition, M. J. Pilling, Ed., vol. 35, Elsevier, Jan. 1, 1997, pp. 293–437.
- [305] T. Turányi, “Reduction of large reaction mechanisms,” *undefined*, 1990.
- [306] T. Turányi, “Parameterization of reaction mechanisms using orthonormal polynomials,” *Computers & Chemistry*, vol. 18, no. 1, pp. 45–54, Mar. 1, 1994.
- [307] ———, “Sensitivity analysis of complex kinetic systems. tools and applications,” *Journal of Mathematical Chemistry*, vol. 5, no. 3, pp. 203–248, Sep. 1, 1990.
- [308] T. Turányi and A. S. Tomlin, *Analysis of Kinetic Reaction Mechanisms*. Berlin, Heidelberg: Springer Berlin Heidelberg, 2014.
- [309] A. Umemura and S. Takamori, “Percolation theory for flame propagation in non- or less-volatile fuel spray: A conceptual analysis to group combustion excitation mechanism,” *Combustion and Flame*, vol. 141, no. 4, pp. 336–349, Jun. 1, 2005.
- [310] S. Vajda, P. Valko, and T. Turányi, “Principal component analysis of kinetic models,” *International Journal of Chemical Kinetics*, vol. 17, no. 1, pp. 55–81, 1985.
- [311] A. Violi, S. Yan, E. G. Eddings, *et al.*, “Experimental formulation and kinetic model for JP-8 surrogate mixtures,” *Combustion Science and Technology*, vol. 174, no. 11, pp. 399–417, Nov. 1, 2002.

- [312] P. Vozka, D. Vrtiška, P. Šimáček, and G. Kilaz, “Impact of alternative fuel blending components on fuel composition and properties in blends with jet a,” *Energy & Fuels*, vol. 33, no. 4, pp. 3275–3289, Apr. 18, 2019, Publisher: American Chemical Society.
- [313] L. H. J. Wachters and N. A. J. Westerling, “The heat transfer from a hot wall to impinging water drops in the spheroidal state,” *Chemical Engineering Science*, vol. 21, no. 11, pp. 1047–1056, Nov. 1, 1966.
- [314] K. J. E. Walsh, S. J. Camargo, T. R. Knutson, *et al.*, “Tropical cyclones and climate change,” *Tropical Cyclone Research and Review*, vol. 8, no. 4, pp. 240–250, Dec. 1, 2019.
- [315] H. Wang, X. You, A. V. Joshi, *et al.* “[Http://ignis.usc.edu/USC_mech_ii.htm](http://ignis.usc.edu/USC_mech_ii.htm),” ().
- [316] Y. Wang, Y. Cao, W. Wei, D. F. Davidson, and R. K. Hanson, “A new method of estimating derived cetane number for hydrocarbon fuels,” *Fuel*, vol. 241, pp. 319–326, Apr. 1, 2019.
- [317] J. Wei and J. C. W. Kuo, “Lumping analysis in monomolecular reaction systems. analysis of the exactly lumpable system,” *Industrial & Engineering Chemistry Fundamentals*, vol. 8, no. 1, pp. 114–123, Feb. 1, 1969, Publisher: American Chemical Society.
- [318] C. R. Wilke, “A viscosity equation for gas mixtures,” *The Journal of Chemical Physics*, vol. 18, no. 4, pp. 517–519, Apr. 1, 1950, Publisher: American Institute of Physics.
- [319] J. Wirtz, B. Cuenot, and E. Riber, “Numerical study of a polydisperse spray counterflow diffusion flame,” *Proceedings of the Combustion Institute*, vol. 38, no. 2, pp. 3175–3182, Jan. 1, 2021.
- [320] A. Wood, W. Hwang, and J. Eaton, “Preferential concentration of particles in homogeneous and isotropic turbulence,” *International Journal of Multiphase Flow*, vol. 31, pp. 1220–1230, Oct. 1, 2005.
- [321] Y. Wu, “Experimental investigation of laminar flame speeds of kerosene fuel and second generation biofuels in elevated conditions of pressure and preheat temperature,” Ph.D. dissertation, INSA de Rouen, 2016.
- [322] N. Wunderling, M. Willeit, J. F. Donges, and R. Winkelmann, “Global warming due to loss of large ice masses and arctic summer sea ice,” *Nature Communications*, vol. 11, no. 1, p. 5177, Oct. 27, 2020.
- [323] H. Yamashita, M. Shimada, and T. Takeno, “A numerical study on flame stability at the transition point of jet diffusion flames,” *Symposium (International) on Combustion*, vol. 26, no. 1, pp. 27–34, Jan. 1, 1996.
- [324] S. Yang, Y. Ra, R. D. Reitz, B. VanDerWege, and J. Yi, “Development of a realistic multicomponent fuel evaporation model,” *Atomization and Sprays*, vol. 20, no. 11, 2010, Publisher: Begel House Inc.
- [325] C. L. Yaws, *Transport Properties of Chemicals and Hydrocarbons*, ser. Knovel. 2009.
- [326] J. B. Zeldowitsch and D. A. Frank-Kamenetzki, “A theory of thermal propagation of flame,” in *Dynamics of Curved Fronts*, P. Pelcé, Ed., San Diego: Academic Press, Jan. 1, 1988, pp. 131–140.

- [327] C. Zhang, X. Hui, Y. Lin, and C.-J. Sung, “Recent development in studies of alternative jet fuel combustion: Progress, challenges, and opportunities,” *Renewable and Sustainable Energy Reviews*, vol. 54, pp. 120–138, Feb. 1, 2016.
- [328] H. Zhang and S. Yang, “Multicomponent transcritical flow simulation based on in situ adaptive tabulation of vapor-liquid equilibrium solutions,” Jan. 4, 2021.
- [329] X. Zheng, T. Lu, and C. Law, “Experimental counterflow ignition temperatures and reaction mechanisms of 1,3-butadiene,” *Proceedings of The Combustion Institute*, vol. 31, pp. 367–375, Jan. 31, 2007.
- [330] X. Zhu, A. A. Khateeb, T. F. Guiberti, and W. L. Roberts, “NO and OH* emission characteristics of very-lean to stoichiometric ammonia-hydrogen-air swirl flames,” *Proceedings of the Combustion Institute*, vol. 38, no. 4, pp. 5155–5162, Jan. 1, 2021.
- [331] T. Zirwes, F. Zhang, P. Habisreuther, *et al.*, “Identification of flame regimes in partially premixed combustion from a quasi-DNS dataset,” *Flow, Turbulence and Combustion*, vol. 106, no. 2, pp. 373–404, Feb. 1, 2021.
- [332] E. Zukoski and F. Marble, “The role of wake transition in the process of flame stabilization on bluff bodies,” Ph.D. dissertation, Jan. 1, 1955, pp. 167–180.

